HIGH ENERGY PULSED LIQUID LASER

GTE LABORATORIES, INCORPORATED

PREPARED FOR
OFFICE OF NAVAL RESEARCH
ADVANCED RESEARCH PROJECTS AGENCY

30 AUGUST 1974

UNCLASSIFIED

SECURITY CLASSIFICATION OF THIS PAGE (When Data Entered)

REPORT DOCUMENTATION PAGE		READ INSTRUCTIONS BEFORE COMPLETING FORM
1. REPORT NUMBER	2. GOVT ACCESSION NO.	3. RECIPIENT'S CATALOG NUMBER AD-787 895
4. TITLE (and Subtitle) HIGH ENERGY PULSED LIQUID LASER		5. TYPE OF REPORT & PERIOD COVERED Final Technical Report 1 July 1967 - 31 March 1974
		6. PERFORMING ORG. REPORT NUMBER TR 74-826.1
7. AUTHOR(s) H. Samelson, R. Kocher		8. CONTRACT OR GRANT NUMBER(s) N00014-68-C-0110
9. PERFORMING ORGANIZATION NAME AND ADDRESS GTE Laboratories Incorporated 40 Sylvan Road Waltham, Mass. 02154		10. PROGRAM ELEMENT, PROJECT, TASK AREA & WORK UNIT NUMBERS ARPA No. 1806 Amendment No. 9
11. CONTROLLING OFFICE NAME AND ADDRESS U. S. Navy Office of Naval Research Washington, D. C.		12. REPORT DATE 30 August 1974 13. NUMBER OF PAGES 430
14. MONITORING AGENCY NAME & ADDRESS(if different from Controlling Office) Same as block 11.		15. SECURITY CLASS. (of this report) Unclassified 15a. DECLASSIFICATION/DOWNGRADING SCHEDULE

16. DISTRIBUTION STATEMENT (of this Report)

Qualified requestors may obtain copies of this report from DDC.

17. DISTRIBUTION STATEMENT (of the abstract entered in Block 20, if different from Report)

18. SUPPLEMENTARY NOTES

19. KEY WORDS (Continue on reverse side if necessary and identify by block number)

Neodymium liquid laser; high average power laser; hydrodynamic model

20. ABSTRACT (Continue on reverse side if necessary and identify by block number)

This report covers the research on inorganic liquid lasers which commenced on July 1, 1967 and came to a conclusion on March 26, 1974. The objectives of the project were to evaluate inorganic liquid laser materials in high average power and high brightness applications. The first part of this was achieved by the construction of a repetitively pulsed system and operating it at average power levels in excess of 400 watts, with an overall efficiency of more than 2%. It is estimated that, with relatively straightforward modification, average power levels of 1 kW could be

DD FORM 1 JAN 73 1473 EDITION OF 1 NOV 65 IS OBSOLETE

UNCLASSIFIED

SECURITY CLASSIFICATION OF THIS PAGE (When Data Entered)

attained. The high brightness goal was not achieved. There is some doubt that sufficiently good beam quality could be maintained through the amplifier for high brightness applications. It is clear that further research effort is necessary to complete this part of the evaluation.

The reported work is comprehensive in that it extends from research on the laser materials to system design and construction. In the course of this project, not only have the laser properties been investigated in great detail but considerable light has also been shed on the hydrodynamics and optical properties of laser liquids in turbulent flow. The nature of the radial thermal gradient in the flowing liquid, and its optical consequences, have been investigated theoretically and a degree of experimental verification of the model was achieved.

This report is divided into the following technical sections:

The chemistry and properties of liquid laser materials - this includes a detailed discussion of the preparation of the solutions as well as a comprehensive discussion of the chemistry. Also included are the scattering and stimulated scattering properties and a compilation of the known and estimated physical constants of the laser solutions.

Liquid laser systems - this includes both static and circulatory systems and the details of system, sub-system and component design.

The hydrodynamic and thermo-optical properties of liquid lasers - this is a theoretical analysis of the very complex processes involved in turbulent flow and the degree of experimental verification we have been able to achieve is also presented.

Laser and amplifier behavior (static and circulatory) - here the high average power performance is described and evaluated. In addition, a variety of interesting and potentially useful properties, such as self Q-switching and mode locking are described. The limitations of inorganic liquid systems in terms of nonlinearities and optical quality is discussed.

HIGH-ENERGY PULSED LIQUID LASER

Contract No. N00014-68-C-0110

ARPA Order Number:	1806, Amendment No. 9	Date of Report:	30 August 1974
Project Code Number:	421	Contract Expiration Date:	31 March 1974
Date of Contract:	1 July 1967	Project Scientist:	H. Samelson
Amount of Contract:	$654,603.00	Telephone:	617-890-8460

ACKNOWLEDGMENT

This research was supported by the Advanced Research Projects Agency of the Department of Defense and was monitored by the Office of Naval Research under Contract No. N00014-68-C-0110.

DISCLAIMER

The views and conclusions contained in this document are those of the authors and should not be interpreted as necessarily representing the official policies, either expressed or implied, of the Advanced Research Projects Agency or the U. S. Government.

GTE LABORATORIES INCORPORATED
Waltham, Massachusetts 02154

ABSTRACT

This report covers the research on inorganic liquid lasers which commenced on July 1, 1967 and came to a conclusion on March 26, 1974. The objectives of the project were to evaluate inorganic liquid laser materials in high average power and high brightness applications. The first part of this was achieved by the construction of a repetitively pulsed system and operating it at average power levels in excess of 400 watts, with an overall efficiency of more than 2%. It is estimated that, with relatively straightforward modification, average power levels of 1 kW could be attained. The high brightness goal was not achieved. There is some doubt that sufficiently good beam quality could be maintained through the amplifier for high brightness applications. It is clear that further research effort is necessary to complete this part of the evaluation.

The reported work is comprehensive in that it extends from research on the laser materials to system design and construction. In the course of this project not only have the laser properties been investigated in great detail but considerable light has also been shed on the hydrodynamics and optical properties of laser liquids in turbulent flow. The nature of the radial thermal gradient in the flowing liquid, and its optical consequences, have been investigated theoretically and a degree of experimental verification of the model was achieved.

This report is divided into the following technical sections:

- The chemistry and properties of liquid laser materials — this includes a detailed discussion of the preparation of the solutions as well as a comprehensive discussion of the chemistry. Also included are the scattering and stimulated scattering properties and a compilation of the known and estimated physical constants of the laser solutions.
- Liquid laser systems — this includes both static and circulatory systems and the details of system, sub-system and component design.

- The hydrodynamic and thermo-optical properties of liquid lasers — this is a theoretical analysis of the very complex processes involved in turbulent flow and the degree of experimental verification we have been able to achieve is also presented.
- Laser and amplifier behavior (static and circulatory) — here the high average power performance is described and evaluated. In addition, a variety of interesting and potentially useful properties, such as self Q-switching and mode locking are described. The limitations of inorganic liquid systems in terms of nonlinearities and optical quality are discussed.

ACKNOWLEDGMENTS

A project as extensive as this one must have had contributions from a large number of people. Only two authors' names appear on this report (H. Samelson and R. Kocher), but they feel it is only appropriate to acknowledge other people who have made substantial contributions. Moreover, three people (A. Lempicki, C. Brecher and K. French) have made comments and criticism on various parts of this report, and in so doing, have improved it.

At the contributor level, the work of A. Lempicki, C. Brecher, V. A. Brophy, S. Reich, W. Watson, K. French, S. L. Shapiro, R. R. Alfano, R. Pappalardo, D. Miller and A. Heller has been of great significance. In particular, it should be noted that A. Lempicki had the major part of the supervisory responsibility. It is also appropriate to acknowledge the invaluable technical assistance of S. Kellner, J. Lech, and C. N. Fallier for their dedication to the daily details of the experimental work. The assistance of G. Sears, T. J. Illing, G. Alexander, W. Kohler, T. Waszak, W. Pollack, R. Bache and T. Califano in various phases of the work deserve recognition.

The Design Shop under K. Weise, the Glass Shop under K. Early, the Machine Shop under P. Riggio and the Optical Shop under J. Steiner have been a bulwark of support throughout the effort.

It is a pleasure to acknowledge the support of L. R. Bloom as well as W. F. Nelson and F. J. Reid in their administrative capacity.

Finally, all of the above contributors are grateful to the Office of Naval Research and to A. R. P. A. for their encouragement and financial assistance.

CONTENTS

CONTENTS (Continued)

CONTENTS (Continued)

CONTENTS (Continued)

ILLUSTRATIONS

ILLUSTRATIONS (Continued)

ILLUSTRATIONS (Continued)

ILLUSTRATIONS (Continued)

ILLUSTRATIONS (Continued)

ILLUSTRATIONS (Continued)

ILLUSTRATIONS (Continued)

ILLUSTRATIONS (Continued)

ILLUSTRATIONS (Continued)

TABLES

TABLES (Continued)

TABLES (Continued)

1. INTRODUCTION

The use of the liquid phase as the host for laser active species has expanded at an extraordinarily rapid rate in recent years. This aspect of laser work began some twelve years ago with the europium chelate laser and received a great impetus four years later with the extension of that work to neodymium based solutions and organic luminophors. The inorganic and organic branches of liquid laser work differ markedly in techniques and applications, but they both have in common those aspects that are concerned with the liquid nature of the medium. It is the circulability of this phase that has made possible the interesting and useful, or potentially useful, developments that have emerged from the research effort. Associated with the movement of the liquid, there arise a variety of hydrodynamic and thermo-optical problems that add another dimension to laser research.

This report is devoted to the inorganic branch of liquid laser research. All but a small part of this has appeared in scattered and incomplete form in the Semi-Annual Technical Summary Reports associated with the contract. The Final Report has been used as a vehicle to gather these fragments into a unified and coherent form. In this way, we can see better what the accomplishments were and what the possible directions are.

The body of the subsequent report consists of six sections of technical substance and two of related interest. These are as follows:

The subject matter of these technical sections deals in detail only with the work performed at the GTE Laboratories but, for completeness, other related work is mentioned and discussed.

2. THE CHEMISTRY AND PROPERTIES OF LIQUID LASER MATERIALS

The materials part of inorganic liquid lasers represents one of the more interesting and, at the same time, one of the more frustrating aspects of this field of research. The liquid phase was the last in which laser action was observed, and held the promise for solving many problems relating to high average power, damage and cost. In many ways this promise has been fulfilled but the chemistry and physics of the materials, inorganic (Nd^{+3}) or organic (dye), have always presented a serious obstacle to the full realization of the potentials.

In this section the chemistry and the properties of inorganic liquid laser materials is presented. We start with a brief discussion of the fluorescence behavior of rare earth ions in solution since the understanding of this problem forms the basis for the concept of aprotic solvent systems. This is followed by the chemistry of the principal aprotic solvent systems — $SeOCl_2$ and $POCl_3$. The differences between these are pointed out and some of the still obscure points are indicated. Then, following the presentation of the spectroscopic properties of the laser solutions, the problems connected with scattering and stimulated scattering processes are discussed. Finally, the physical properties of those materials are listed and the gaps in the available data pointed out.

2.1 THE CHEMISTRY OF LIQUID LASER SYSTEMS

2.1.1 Fluorescence of Rare Earth Ions in Solution

For the most part, the inorganic rare earth ions exhibit very little fluorescence in liquid systems. The basic reason for this is the low mass of the hydrogen atom and correspondingly high vibrational energy of the OH group; the most common component of the customary solvents of inorganic chemistry. In the normal process of the dissolution of ionic salts in solvents, a considerable amount of work must be expended in separating the charged components of the solute. In fact, simply considering the magnitude of the electric field surrounding small positive ions and the mobility of the dipoles in high dielectric solvents, it is obvious that a much lower system energy can be achieved by having the dipoles surround the ion. In this way the net charge is distributed over a much larger surface area and the system rendered more stable. This phenomenon is known as solvation and, in general, the nearest neighbor solvation shell has a symmetry

closely related to the symmetry of the orbital hybridization of the bonding electronic states of the cation. The interaction between the solvent and the cation is strong and, in solution, the species to consider is a cationic complex with a fairly tightly-bound inner dipolar solvation shell embedded in successively larger, more mobile solvation shells.

The excitation of the cationic rare earth complex is identical to that of rare earth ions in any host, and the excitation energy is degraded until the system finds itself in the conventional emitting states. These states are usually the lowest ones of the excited manifold and are separated by a gap in energy from the highest states of the ground manifold. Some typical examples are given in Table 2-1. This relatively small amount of energy can be taken up by a relatively few O-H phonons (see Table 2-1), and

the rare earth ion is then in the ground manifold and decays nonradiatively to the ground state. The substitution of heavy water for ordinary water increases the number of phonons required, as shown in Table 2-1, and decreases the probability of the nonradiative process; the fluorescence yield increases. This quenching behavior of water relative to heavy water is illustrated graphically in the Stern-Volmer type plot of Figure 2-1.[1]

TABLE 2-1

FACTORS ENTERING INTO THE FLUORESCENCE QUENCHING OF RARE EARTH IONS IN SOLUTION

Ion (+3)	Emitting State Energy (cm^{-1})	Highest Ground Manifold Energy (cm^{-1})	Δ cm^{-1}	Number of Phonons	
				OH	OD
Sm	17800	10500	7300	≥ 2	~ 3
Eu	17000	5000	12000	≥ 3	~ 5
Tb	20500	6000	14500	≥ 4	~ 6
Dy	21000	13000	8000	≥ 2	≥ 3

In these terms it is qualitatively easy to understand the behavior of rare earth chelates whose fluorescence yield, even in solution, is very high.[2-4] The most common chelating agents, β-diketones, occupy the nearest neighbor (bonding) sites on the rare-earth ion. The light hydrogen containing bonds are removed some distance from the point of excitation and are less effective in the quenching process. A variety of these systems have functioned as lasers[5,6] but they are subject to chemical effects[7] and are plagued by an extremely intense pump band absorption rendering them rather inefficient. Neodymium, in this kind of system, does not fluoresce; but if the second nearest hydrogens are replaced by fluorine,[8] a neodymium-chelate system will fluoresce and does lase.

These studies made it abundantly clear that the solvent played a key role in the fluorescence quenching of rare earth ions in solution, and that the way around the difficulty was to employ heavy atom solvents. Then the solvation shell would consist of molecules or dipoles having only low energy vibrations, and the radiative relaxation process would compete successfully with the nonradiative ones. The basic solvent must then have no protons and this leads quite naturally into the field of aprotic chemistry. When one, in addition, considers the requirements on dielectric constant for solubility

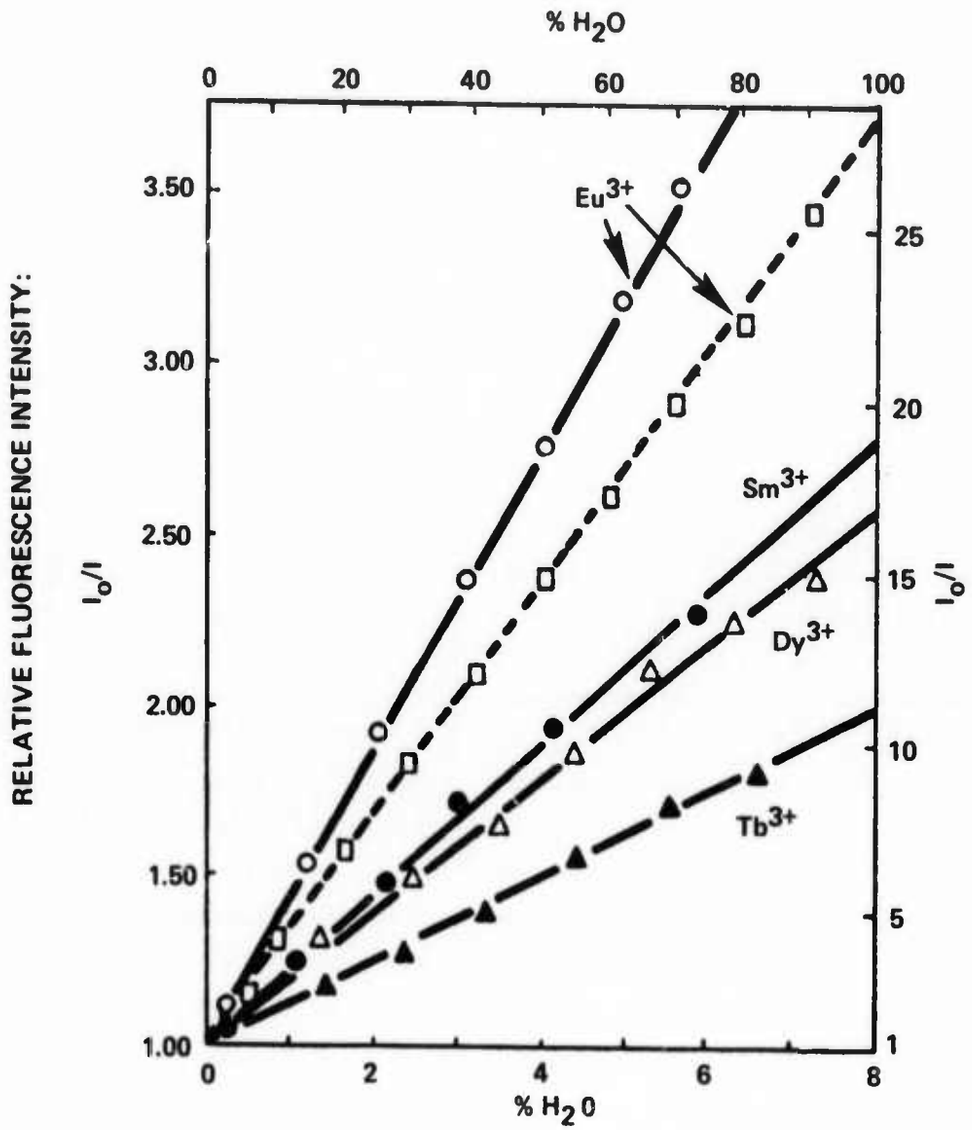

Figure 2-1. Quenching of the Luminescence of Rare Earth Ions in D_2O. Top and right hand scales are for the dashed line.

and optical transpareney to make laser proeesses feasible, two solvents, $SeOCl_2$ and $POCl_3$, stand out.[9] Both of these solvents have been used and in the following seetions we will eonsider their chemistry in some detail. In addition, we will deseribe the speetroseopy of Nd^{+3} in these solvents, the physieal properties of the solutions and their nonlinear optieal behavior.

2.1.2 Aprotie Solvents

Both $SeOCl_2$ and $POCl_3$ are aprotie solvents witn dieleetrie constants of 46 and 14 respeetively. Indeed, their use in this applieation is based on the absence of hydrogen. One can even write parallel equations for the solution of Nd_2O_3 in these solvents as follows:

$$Nd_2O_3 + 3\ SnCl_4 + 3\ SeOCl_2 \rightarrow 2\ Nd^{+3} + 3\ SnCl_6^{-2} + 3\ SeO_2 \qquad (2\text{-}1)$$

$$Nd_2O_3 + 3\ SnCl_4 + 6\ POCl_3 \rightarrow 2\ Nd^{+3} + 3\ SnCl_6^{-2} + 3\ P_2O_3Cl_4 \qquad (2\text{-}2)$$

The similarity is, however, deceptive because while reaction (Eq. 2-2) does proceed, the solubility of Nd_2O_3 in $POCl_3$:$SnCl_4$ is so small as to render it useless as a laser solution. The ehemistry of the two types of laser solutions is different; the one for $SeOCl_2$ being like an aprotie acid-base system while that for $POCl_3$ is, as will be seen later, like a ehelate system in an aprotie solvent. For this reason, we will eonsider the ehemistries separately and begin with that of the $SeOCl_2$ solutions.

2.1.2.1 Preparation of $SeOCl_2$ Laser Solutions

The eomponents for these solutions are $SeOCl_2$, Nd_2O_3 and a Lewis aeid such as $SnCl_4$ or $SbCl_5$. In general, all these materials with the exeeption of $SbCl_5$ (reagent grade available from J. T. Baker is aeeeptable) have to be purified. The neodymium oxide, even the purest grade, has usually absorbed some earbon dioxide and water from the atmosphere. This is purified by roasting in air to a eonstant weight at 950°C.

The purification of $SeOCl_2$ is aeeomplished by distillation. Sinee at higher temperatures it deeomposes into Cl_2, SeO_2 and Se_2Cl_2, the distillations (two are required) are earried out under reduced pressure. In the first, the boiling point is kept down to 90°C. In the seeond distillation, it is earried out at 40°C to remove selenium monoehloride and the distilled selenium oxychloride is obtained as a light straw-colored

liquid. The degree to which the proton contamination has been reduced is shown in Figure 2-2; the bands in the 3000 - 3500 cm^{-1} region are indicative of the hydrogen contamination.

The purification of the $SnCl_4$ is somewhat more difficult. Simple distillation alone is not effective, since separation is achieved during the distillation, but the hydrogen containing compounds recombine with the $SnCl_4$ in the distillate. The most effective means found for purification is by distillation under a constant flow of dry nitrogen through a Vigreux column packed with alumina. The degree of success is, again, shown by the infrared spectra in Figure 2-3, in which the double peak at 3600 cm^{-1} is due to hydrogenic containing components. An alternative technique, passing the $SnCl_4$ through a column of basic alumina, has been used by Heller,[10] Shepherd,[11] and Hunt and Shepherd,[12] but the one outlined here is most effective.

To prepare the laser solution, Nd_2O_3 is dissolved in $SeOCl_2$ acidified with $SnCl_4$ (in a volume ratio of 5:1). Now, once again, a step is taken to remove any hydrogen contamination. The resulting mixture is distilled at a pressure of 40 mm Hg until a constant boiling point of 90°C is reached. The solution is then reconstituted by adding $SnCl_4$ and $SeOCl_2$ until the final solution has the desired composition: 0.3M in Nd^{+3} and 1M in Sn. With this procedure, the bleaching step (addition of $KClO_3$) previously used by Heller,[8] is not necessary. Solutions prepared in this manner have a fluorescence lifetime of about 260 μs and an infrared spectrum as illustrated in Figure 2-4 for the dry solution.

The preparative details have been described for those solutions using $SnCl_4$ as the Lewis acid and for an "acid" solution, that is, an excess of $SnCl_4$. The composition of the solutions can be varied in terms of the particular Lewis acid used, whether it is in excess or stoichiometric (acid or neutral solutions) or whether there is an excess of chloride ion present (a basic solution). The two acids studied in some detail by Heller,[8] $SnCl_4$ and $SbCl_5$, do not lead to marked differences in the properties of the solutions. More significant differences occur on going from acid-to-neutral-to-basic solutions. In this order, the fluorescence lifetime decreases and some solubility problems appear. For the laser work, acid $SnCl_4$ solutions were most convenient and effective. In view of the negligible quantity of work done with other types of solutions, further discussion is limited to the acid $SnCl_4$ type and reference is made to Heller's[13] work for a discussion of the others.

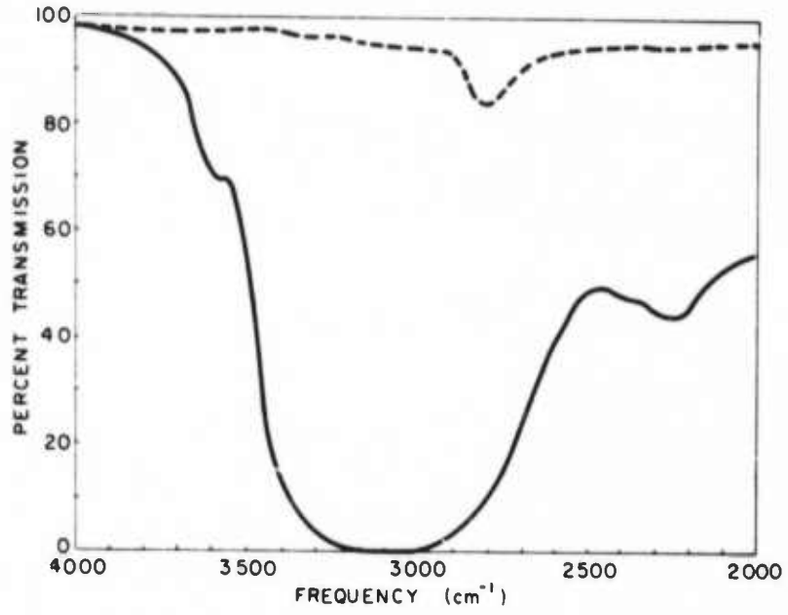

Figure 2-2. Absorption Spectrum of $SeOCl_2$

— Water Contaminated Material
--- Carefully Purified Material

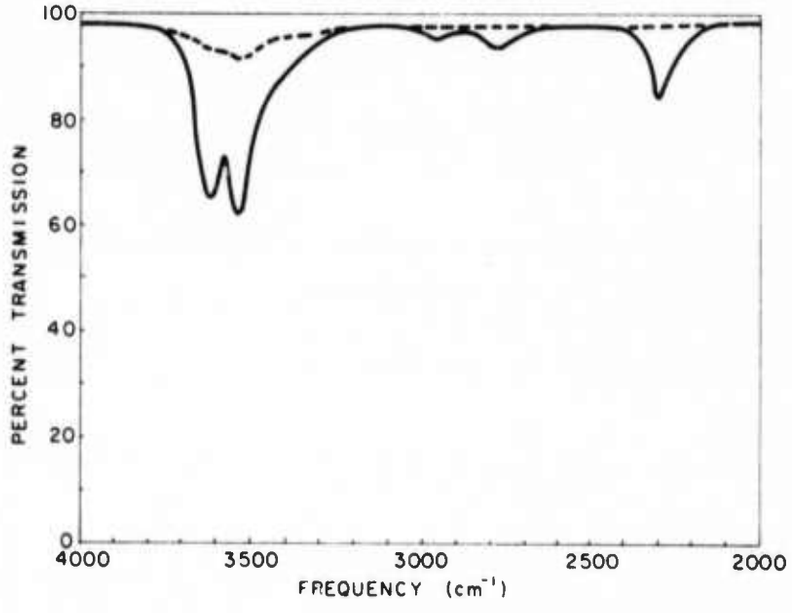

Figure 2-3. Absorption Spectrum of $SnCl_4$

— Water Contaminated Material
--- Carefully Purified Material

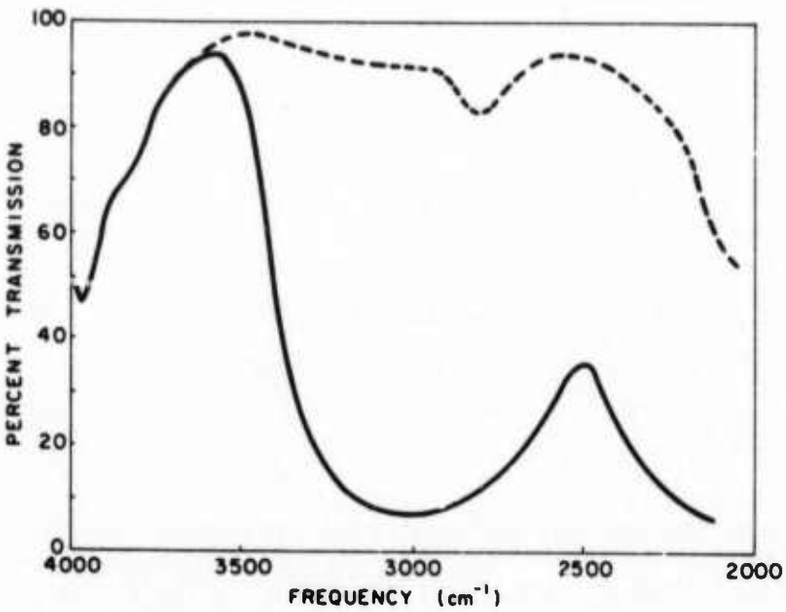

Figure 2-4. Absorption Spectrum of Laser Solutions

— Water Contaminated

--- Dry

2.2.2.2 Preparation of $POCl_3$ Liquid Laser Solutions

There are two different types of solutions based on the $POCl_3$ solvent. In the first of these, $SnCl_4$ is the additive and in the second, $ZrCl_4$ is used. While ostensibly these compounds play the role of a Lewis acid the chemistry is, in fact, very different. There is indeed considerable doubt expressed by Van Wazer[14] that there is an acid-base chemistry in $POCl_3$ similar to that in $SeOCl_2$. The preparative techniques reflect the different chemistry.

The materials required for these solutions are: $POCl_3$, $SnCl_4$, $ZrCl_4$, $Nd(CF_3COO)_3$ and Nd_2O_3. The purification of $SnCl_4$ and Nd_2O_3 were described earlier and $ZrCl_4$ is used as received in the anhydrous state. $Nd(CF_3COO)_3$ is prepared by dissolving Nd_2O_3 in trifluoroacetic acid, evaporating the resulting solution and drying in a vacuum oven at 60°C for several days. $POCl_3$, as received, is wet (see spectrum b in Figure 2-5) and is made anhydrous by distillation from lithium. The $POCl_3$ is first refluxed with lithium for several hours and then distilled. About 10% of the volume is taken as a first fraction and then the distillate collected (B. P. 105-106°C). The following precautions are always taken. First, the receiver is always dried in an oven at 110°C for at least one hour before being put on the system. Second, the receiver is taken from the oven and put on the system as quickly as possible so that it is still hot when put in place. Third, those points at which the distillation apparatus (see Figure 2-5) are connected to the atmosphere are protected by drying tubes filled with drierite. Fourth, as with the distillation of $SeOCl_2$, all ground glass joints are connected by using Teflon sleeves. The spectrum of dry $POCl_3$ is shown in Figure 2-5(a). The degree of water contamination can be estimated by using the calibration curve shown in Figure 2-7. In general, if the collected $POCl_3$ has a water contamination in excess of 10 ppm it is redistilled.

Ionic salts are only slightly soluble in $POCl_3$ and this is true of most Nd salts. In anhydrous $POCl_3$, there is doubt that $NdCl_3$ is at all soluble. The first such solutions reported by Blumenthal, Ellis and Grafstein[15] were relatively dilute and the solubility, as will be seen next, was probably the result of water contamination. Other work in the $POCl_3$:$SnCl_4$ solvent has been reported by Collier et al.,[16] Kato and Shimoda,[17,18] P. M. Buzhinskii et al.,[19] A. V. Aristov et al.,[20] M. E. Zhabotinsky et al.,[21] H. Sergent et al.[22] and Brun and Caro.[23] In many cases, preparative procedures are not described and it is, therefore, difficult to evaluate the results. We shall describe a procedure, developed in this work, which provides excellent laser solutions.

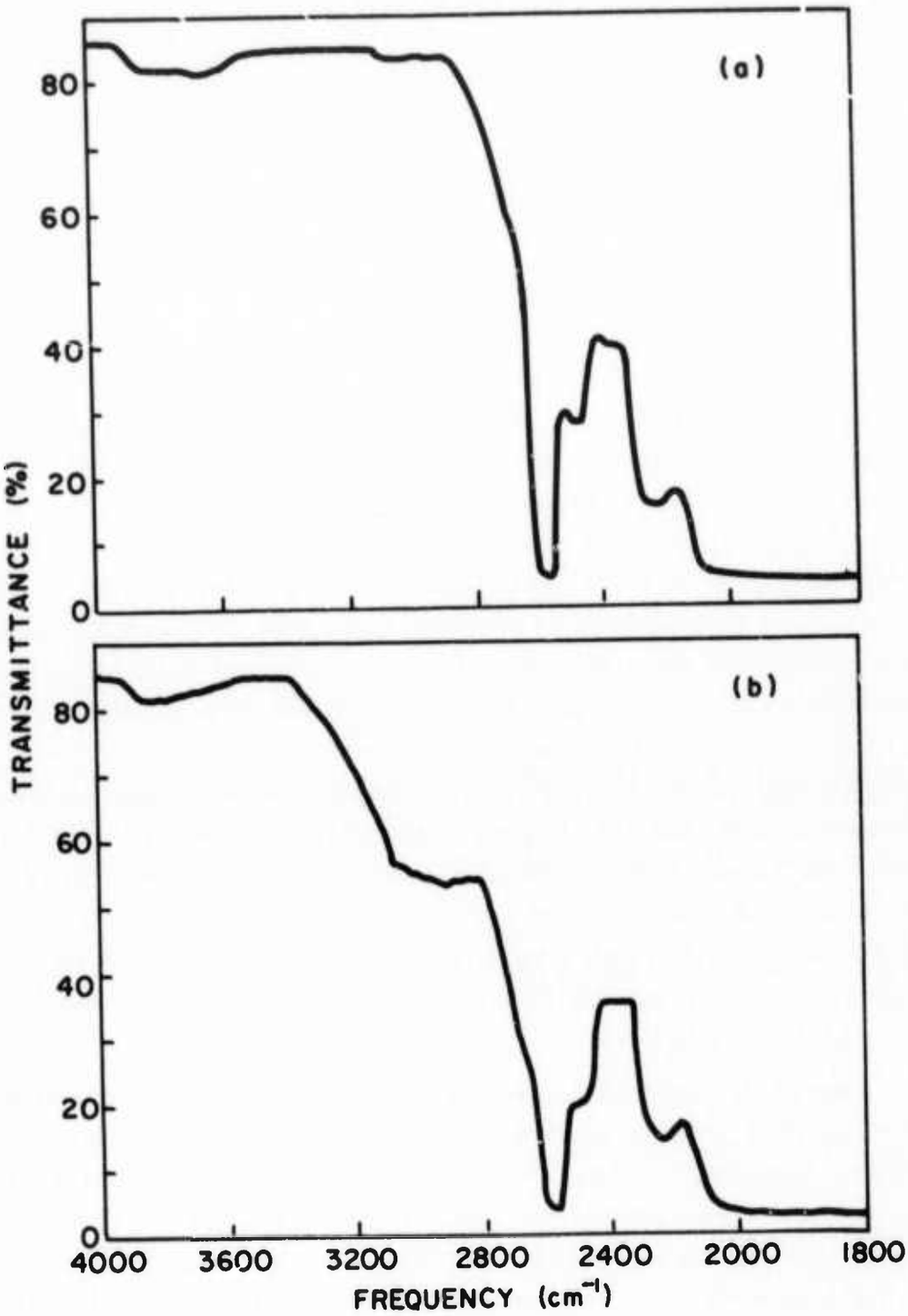

Figure 2-5. Infrared Spectra of $POCl_3$
a) Dry
b) Contaminated with Water

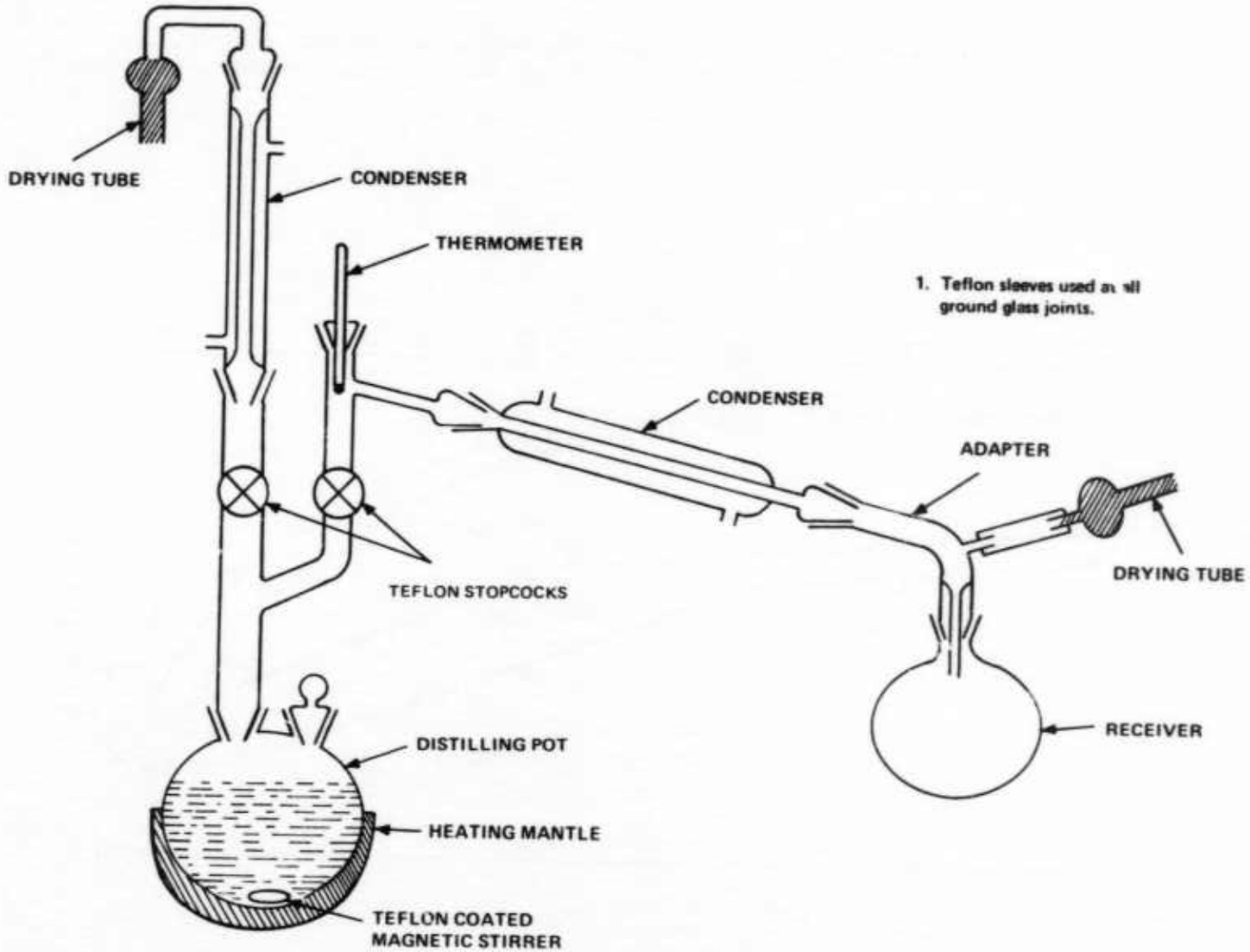

Figure 2-6. Distillation Apparatus

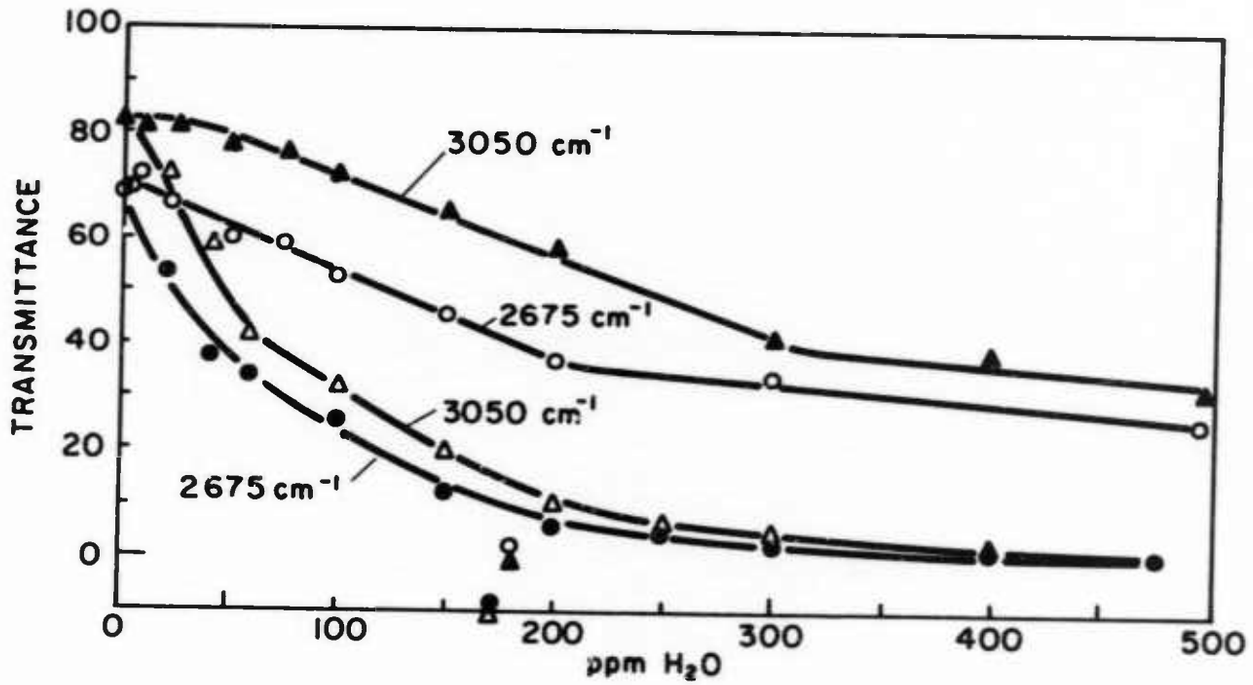

Figure 2-7. Transmission at 3050 cm^{-1} and 2675 cm^{-1} of $POCl_3$ with Various Amounts of Water Added. For the upper two curves the ppm H_2O scale is 10% of the one indicated.

Starting with anhydrous Nd_2O_3 and an anhydrous 5:1 volume mixture of $POCl_3$ and $SnCl_4$, there is virtually no dissolution even on boiling. If, however, water in the molar ratio of 1:10 is added to the $POCl_3$:$SnCl_4$ solution, the Nd_2O_3 dissolves. The resulting solution is rendered anhydrous by distilling off half the solvent and then reconstituting the solution by the addition of an appropriate amount of the anhydrous solvent mixture. In all the work we have done with such solutions, they have been found to be stable except under two conditions. The solutions are sensitive to water content in that the fluorescence is quenched (fluorescence lifetime shortened) by water contamination. Secondly, the solubility of $SnCl_4$ is limited and, at the concentration required, the solution is nearly saturated. Therefore, decreases in temperature (below about 20°C) lead to a precipitate of, presumably, the adduct $SnCl_4 \cdot 2\ POCl_3$. This is more an inconvenience, however, since it can be redissolved simply by raising the temperature.

In the course of research on Lewis acids and $POCl_3$ systems, several new systems were developed. The first indication was the use by Schimitschek[24] of $ZrCl_4$, $TiCl_4$ and BBr_3 to enhance the fluorescence yield of $Nd(ClO_4)_3$ dissolved in $POCl_3$. The perchlorate is the only Nd^{+3} salt, which seems to dissolve readily in $POCl_3$. Shortly after this, Brecher and French, and Schimitschek went over to the use of $Nd(CF_3COO)_3$ as the source of Nd^{+3} in these solutions. A preparative procedure, developed in this work, is now described.

A solution of $POCl_3$ and $ZrCl_4$ is made so that the concentration of $ZrCl_4$ is 1.5 times the desired Nd^{+3} concentration. The appropriate amount of $Nd(CF_3COO)_3$ is then added and the solution warmed until the evolution of gaseous CF_3COCl ceases. The solution is then filtered by being forced through a fine fritted disc funnel and then distilled to about one half its volume. The final step is to dilute the solution to its original concentration by the addition of anhydrous $POCl_3$.

These solutions have been used extensively in the bulk of the recent inorganic liquid laser work. They have some advantages and some disadvantages. These solutions are rather insensitive to water contamination, however, excessive contamination leads to a precipitate of, presumably, $ZrOCl_2$ resulting in instant termination of laser activity. Considerable laser and chemical work on these solutions has been reported by Schimitschek,[25,26] Weichselgartner and Perchermeier,[27] Fill,[28] Andreou,[29,30] Selden,[31,32] and Brecher and French.[33]

2.1.3 Discussion

The comparative chemistries of the $SeOCl_2$ and $POCl_3$ as solvents for Nd^{+3} depend on the relative acidities of these compounds. $SeOCl_2$ has a well known and well documented aprotic acid-base chemistry, in which $SeOCl^+$ and Cl^- are the acid and base corresponding to H^+ and OH^- in the water system. In addition, the high dielectric constant indicates that the $SeOCl_2$ molecule can readily function as a dipolar solvation entity just as H_2O does in the common water system. Thus, the partial equations leading to the overall Eq. (2-1) are:

$$SnCl_4 + 2\ SeOCl_2 \rightleftarrows SnCl_6^{2-} + 2\ SeOCl^+$$

and

$$6\ SeOCl^+ + Nd_2O_3 \rightarrow 2\ Nd^{+3} + 3\ SeOCl_2 + 3\ SeO_2 \qquad (2\text{-}3)$$

and the Nd^{+3} is solvated by $SeOCl_2$.

In the case of $POCl_3$, however, it has been pointed out that water is essential in preparing the solutions. Water is known to react with $POCl_3$ to form, among other products, dichlorophosphoric acid:

$$H_2O + POCl_3 \rightarrow HPO_2Cl_2 + HCl \qquad (2\text{-}4)$$

This acid in turn reacts with Nd_2O_3 as follows:

$$6\ HPO_2Cl_2 + Nd_2O_3 \rightarrow 2\ Nd(PO_2Cl_2)_3 + 3\ H_2O \qquad (2\text{-}5)$$

The overall reaction being:

$$3\ H_2O + 6\ POCl_3 + Nd_2O_3 \rightarrow 2\ Nd(PO_2Cl_2)_3 + 6\ HCl \qquad (2\text{-}6a)$$

With $NdCl_3$ or $Nd(CF_3COO)_3$ the equations are as follows:

$$3\ H_2O + 3\ POCl_3 + NdCl_3 \rightarrow Nd(PO_2Cl_2)_3 + 6\ HCl \qquad (2\text{-}6b)$$

$$Nd(CF_3COO)_3 + 3\ POCl_3 \rightarrow Nd(PO_2Cl_2)_3 + 3\ CF_3COCl \qquad (2\text{-}6c)$$

In the absence of a Lewis acid, the dichlorophosphate is unstable in $POCl_3$ and the reaction proceeds:

$$Nd(PO_2Cl_2)_3 + 3\ POCl_3 \rightarrow NdCl_3 + 3\ P_2O_3Cl_4 \qquad (2\text{-}7)$$

and the $NdCl_3$ precipitates from solution solvated by 5 molecules of $POCl_3$. The key question is the role of the Lewis acid.

This role is the stabilization of the $PO_2Cl_2^-$ anion so that the equilibrium of Eq. (2-7) is shifted to the left and the Nd^{+3} species is soluble. It is the Lewis acid character of $SnCl_4$, its ability to combine and hold $PO_2Cl_2^-$, that stabilizes this species and leads to compounds of the type:

$$Nd(PO_2Cl_2SnCl_4)_{3-n}\ (SnCl_5\ POCl_3)_n\ (n = 0, 1, 2) \qquad (2\text{-}8)$$

thus, rendering the solution stable. The particular compounds described by Eq. (8) have no net charge in keeping with the low dielectric constant of $POCl_3$. The primary coordination sphere of the Nd^{+3} would contain -O-P only. The introduction of water would lead to the introduction of the stronger OH bond in the solvation sphere and subsequent fluorescence quenching.

A different picture emerges when $ZrCl_4$ is used as the Lewis acid, because of the greater strength of the Zr-O bond. This results in a reaction to form the neutral $Zr(PO_2Cl_2)$ species and would lead to coordination species of the type:

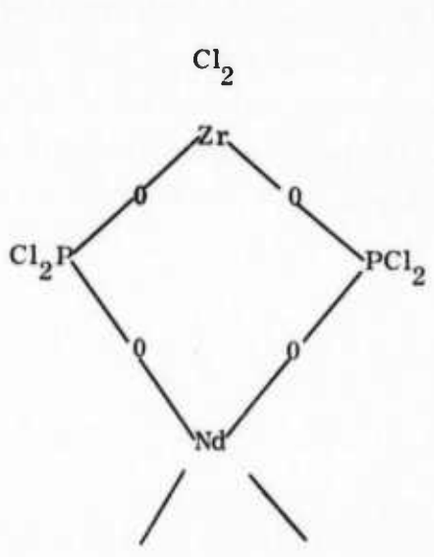

When water is added to this solution one observes an immediate drop in the fluorescence lifetime as expected. However, in time this lifetime returns to its original value. The reaction can be viewed in the following manner.

$$H_2O + POCl_3 \rightarrow HPO_2Cl_2 + HCl$$

$$2\ HPO_2Cl_2 + ZrCl_4 \rightarrow Zr(OH)_2Cl_2 + 2\ POCl_3$$

$$Zr(OH)_2Cl_2 \rightarrow ZrOCl_2 + H_2O \qquad (2\text{-}9)$$

or the overall reaction:

$$H_2O + ZrCl_4 \rightarrow ZrOCl_2 + 2\ HCl$$

the second or third of the above reactions presumably being slow, but finally resulting in $ZrOCl_2$, which is insoluble in $POCl_3$.

The basic chemistry and the identification of many of the intermediate compounds in the complex- and still-imperfectly understood chemistry of $POCl_3$ solutions has been worked out by Schimitscheck[35-37] and by Brecher and French[34] during the course of this research. The latter work is included as Appendix B and C and provides a more detailed description and discussion of the chemistry.

Many other Lewis acids have been used in the $POCl_3$ solvent. A brief list taken from Weichselgartner and Pechermeier[27] is given in Table 2-2. It is difficult to evaluate this work to a greater extent than is given in the table, since each system requires its own development and this obviously has not been done. Even this list is rather incomplete since such obvious candidates as Hf, Ti, B and perhaps Ga have not been tried. Since the chemistry in $POCl_3$ is so varied, there may yet be interesting results to be obtained.

TABLE 2-2

Nd^{+3} APROTIC SOLVENT SYSTEMS

Solvent	Lewis Acid	Fluorescence Lifetime μs	Laser
$POCl_3$	$AlCl_3$	330	Yes
$VOCl_3$	$SnCl_4$	70	----
$PSCl_3$	$AlCl_3$	100	Not Tried
$SOCl_2$	$AlCl_3$	---	----

2.2 SPECTROSCOPIC PROPERTIES

The spectroscopic properties and the physical properties bear on two different aspects of the laser application. The former are concerned primarily with the way in which the laser medium absorbs radiation and converts it into fluorescence. This provides information on the efficiency of the processes as well as on the cross-section of the laser transition, a particularly important parameter. In addition, it bears on the chemistry of the materials used and to some extent on the nature of the fluorescence line broadening. In this area we have a reasonably complete picture. From a laser point of view such physical properties as; the index of refraction and its temperature dependence, the viscosity, and the thermal conductivity are significant factors in the flow characteristics and the thermo-optical performance of the laser liquid. In this area the information is rather sparse. Here we shall indicate what is known and later, during considerations of flow and thermal effects we will have to estimate or guess at some of the quantities.

2.2.1 Spectroscopic Properties of the Laser Solutions

2.2.1.1 The Absorption Spectra

Over most of the visible and near infrared regions of the spectrum, illustrated in Figure 2-8, the characteristic spectrum of Nd^{+3} is observed. The $SeOCl_2$-based solutions exhibit a sharp absorption edge just above 4000 Å and a similar one is observed just above 3000 Å for $POCl_3$ solutions. These steeply rising absorption edges are due to the solvent and probably play only a minor role in laser behavior. The longer wavelength

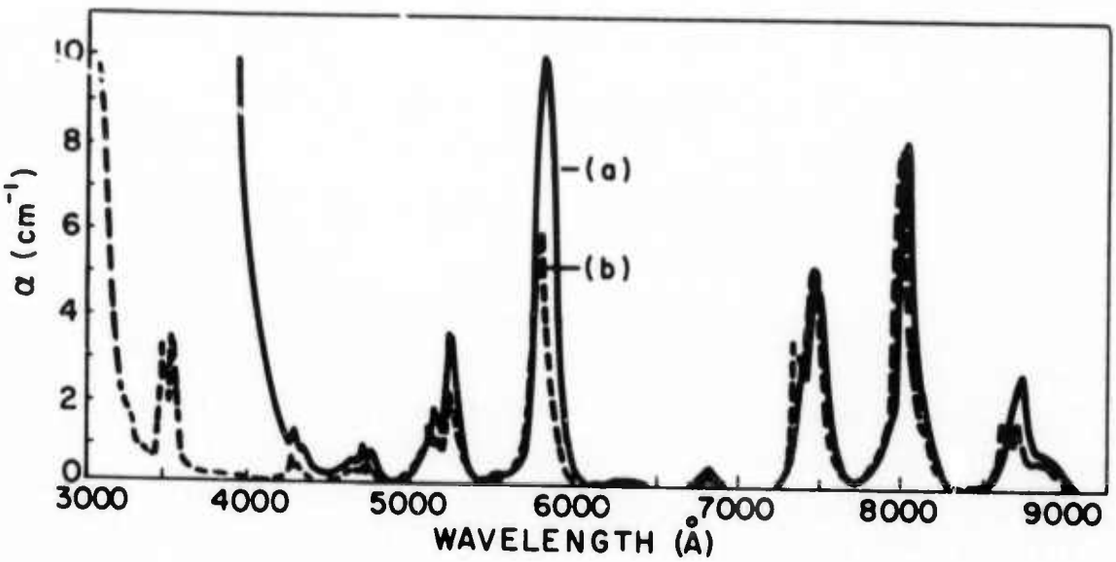

Figure 2-8. Absorption Spectrum of 0.3M Nd^{+3} Laser Solutions

a) $SeOCl_2$:$SnCl_4$

b) $POCl_3$:$SnCl_4$

absorption of $SeOCl_2$ will result in more heat absorption from the flash lamps while the 3500 Å absorption band of Nd^{+3} available in $POCl_3$ solutions, will contribute very little to the pumping efficiency.

The spectrum of Nd^{+3} in $POCl_3$ is shifted slightly to the blue with respect to that in $SeOCl_2$. The $POCl_3$ spectrum in Figure 2-8 is for a solution having $SnCl_4$ as the acid, but there is virtually no change when $ZrCl_4$ is used. Figure 2-9 compares the absorption spectra of Nd^{+3} in $POCl_3$:$ZrCl_4$, $SeOCl_2$:$SnCl_4$ and in Schott laser glass LG55. The gross characteristics of the spectra are similar, but there is somewhat more structure evident in the glass spectrum. The absorption bands in all three cases are broad, so we would expect pumping efficiency in the liquid to be as good as in glass. There is evidence that the broadening in the liquid is homogeneous which, in general, is not the case in glass.

2.2.1.2 The Emission Spectrum

The emission spectrum of Nd^{+3} shows the characteristic emission from the $^4F_{3/2}$ to the $^4I_{9/2,11/2}$, and $_{13/2}$ at 0.88, 1.05 and 1.3μ, respectively. The first of these is, of course, the resonance transition. The 1.3μ transition is weak and contains a relatively small fraction of the total energy emitted. Therefore, we shall confine our discussions to the 0.88 and 1.05μ regions.

The emission spectrum of Nd^{+3} in $SeOCl_2$:$SnCl_4$ is illustrated in Figure 2-10 over a range of concentration of Nd^{+3} differing by a factor of 100. It is clearly seen that there are no changes in the spectral shape other than those expected at the short wavelength end of the resonance transition. We thus conclude that the emission is probably from a single species or that different species have insignificant variations in optically thin spectra. Were there significantly different species, say in degree or type coordination (solvation), the shapes of the spectra over this concentration range would change reflecting the shift in equilibrium between the species.

The spectra for $SeOCl_2$:$SnCl_4$ and $POCl_3$:$SnCl_4$ are compared in Figure 2-11. The major effects to be noted here are: first, the blue shift corresponding to the one in absorption; a change in the relative distribution between the transitions to the $^4I_{9/2}$ and $^4I_{11/2}$, reflecting an increased probability to the $^4I_{11/2}$ in $POCl_3$; and relatively insignificant changes in the shapes. The comparison between the liquid systems and LG55 glass is shown in Figure 2-12, again showing the marked similarity of the different systems. In a later section concerning the absorption cross-section,

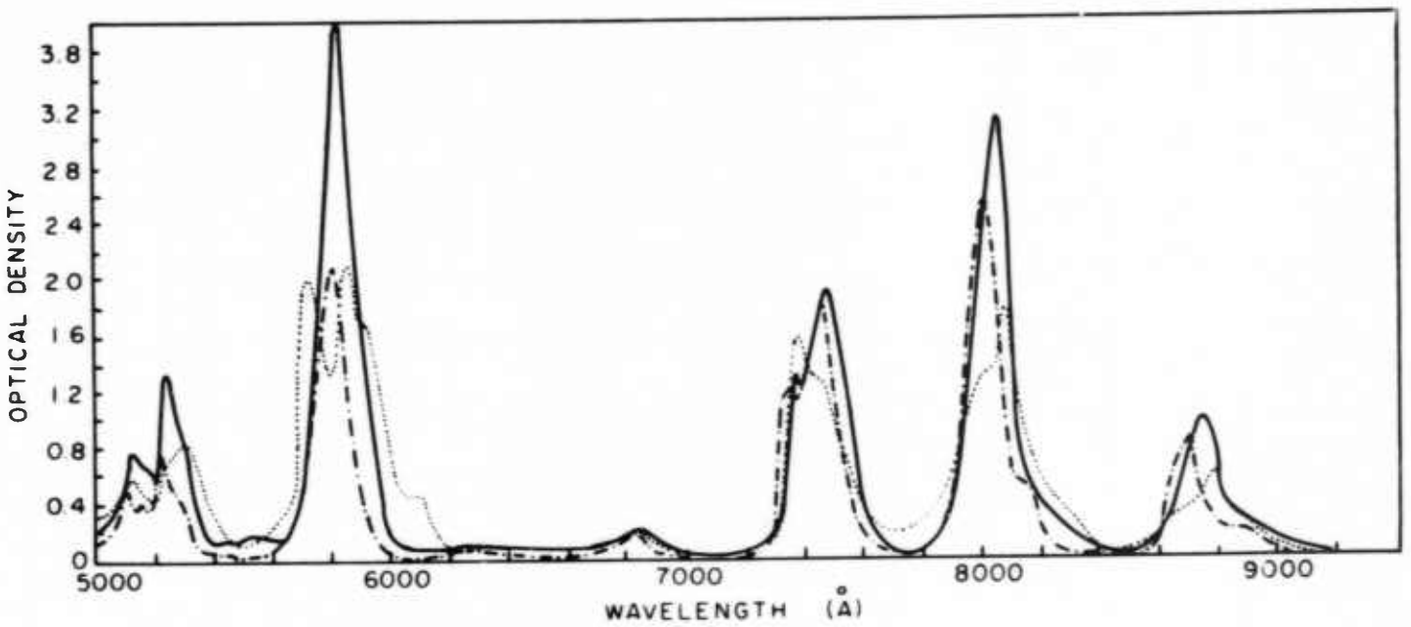

Figure 2-9. Absorption Spectra of Nd^{+3} in $SeOCl_2$, $POCl_3$ and Glass

— $SeOCl_2$

—·—· $POCl_3$

..... Glass

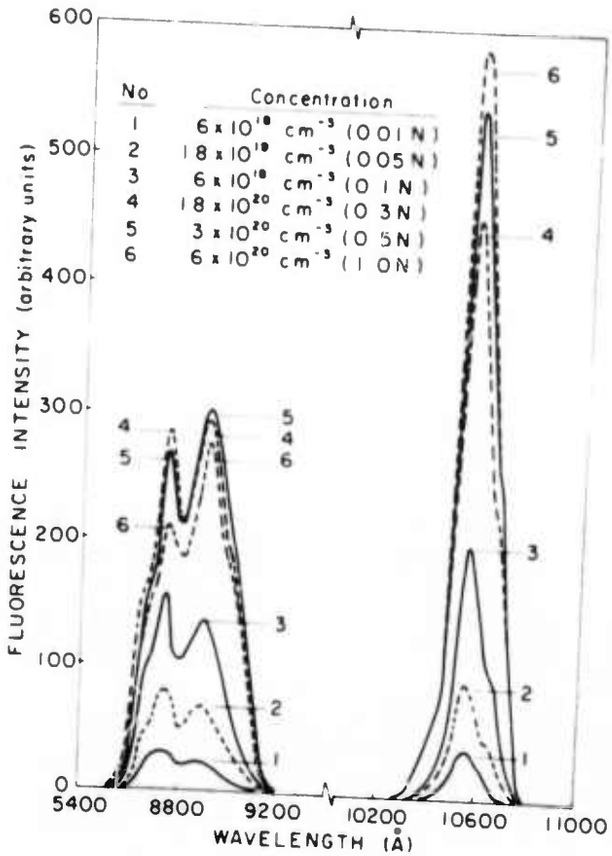

Figure 2-10. Fluorescence Spectra of Nd^{+3}:$SeOCl_2$ Laser Solutions at Various Concentrations

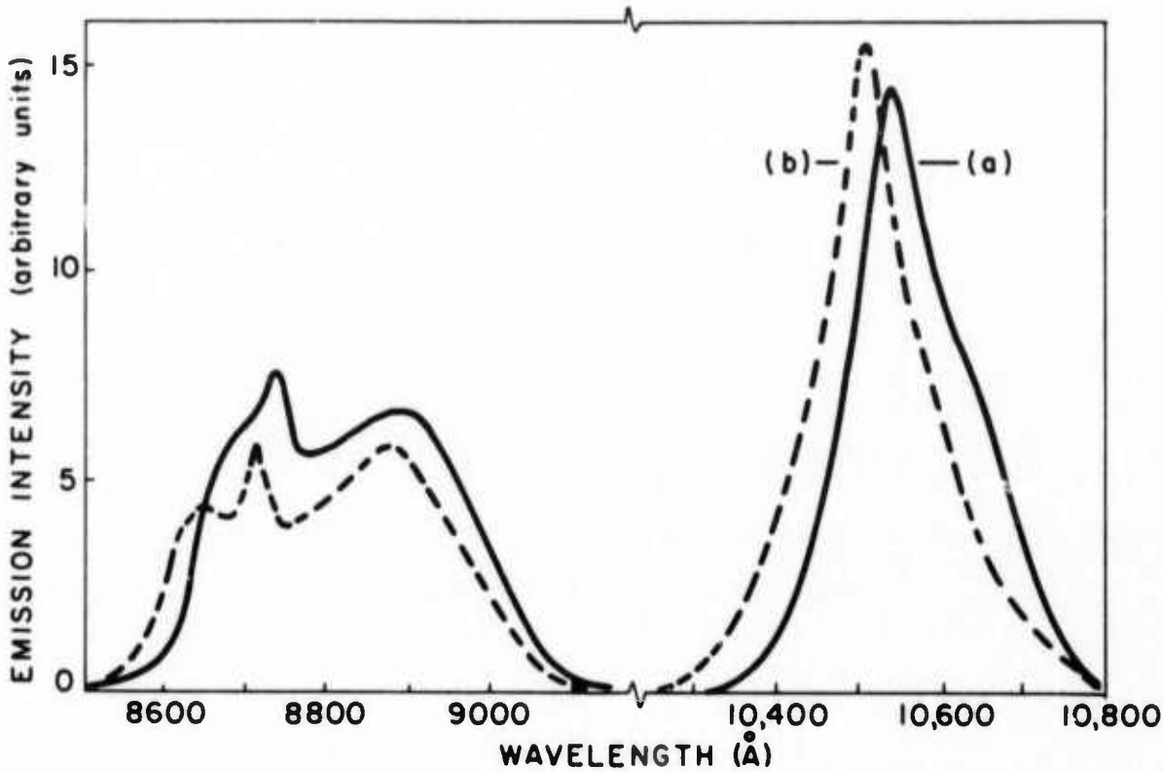

Figure 2-11. Emission Spectra of 0.3M Nd^{+3} Laser Solutions

a) $SeOCl_2$:$SnCl_4$

b) $POCl_3$:$SnCl_4$

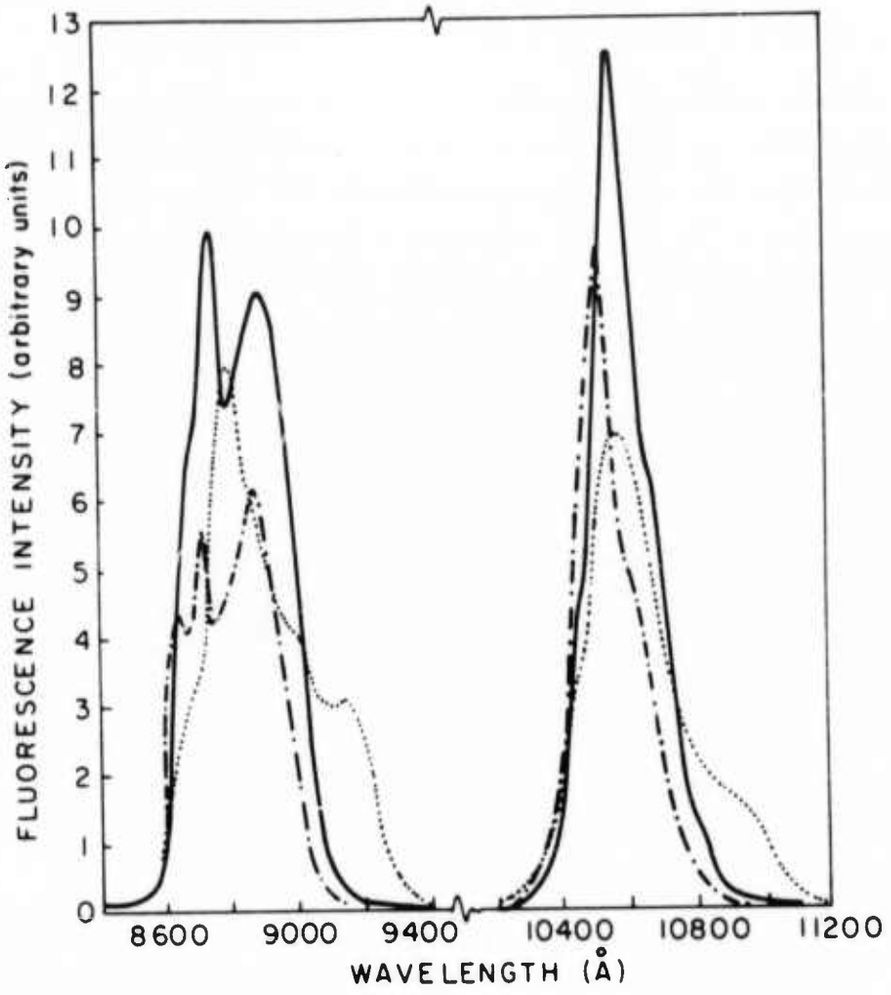

Figure 2-12. Emission Spectra of Nd^{+3} in $SeOCl_2$, $POCl_3$ and LG55

— $SeOCl_2$

—·—· $POCl_3$

..... Glass

we shall provide a more detailed discussion of some spectroscopic features required for the calculation of the cross-section.

2.2.2 The Fluorescence Decay Time

The fluorescence decay time is a sensitive indicator of the environment of Nd^{+3} ion. This measures the competition between the radiative and nonradiative processes in the relaxation of the Nd^{+3} ion from the emitting state.

In general, the fluorescence lifetime increases with increasing concentration of Lewis acid up to the stoichiometrically required amount, as illustrated in Figure 2-13. Stoichiometry is based on the quantities as defined by Eqs. (2-1) and (2-2). When $SnCl_4$ is used as the Lewis acid, the lifetime reaches a maximum at stoichiometry and then remains constant. This is taken to mean that the environment surrounding the Nd^{+3} reaches its stable configuration at this point and is unchanged thereafter. Below stoichiometry, the coordination is more open and allows for interactions that result in nonradiative quenching. Chemically, this is accompanied by a marked instability and a tendency for precipitation to occur in such solutions. When $ZrCl_4$ is used as the Lewis acid, the behavior above stoichiometry is different, as shown in Figure 2-14. As a function of Lewis acid concentration, the fluorescence lifetime has a rather well defined peak at stoichiometry, falling off above it as well as below. Indeed, the rate at which it falls off depends not on the ratio of $ZrCl_4$ and Nd^{+3}, but on the concentration of $ZrCl_4$, as would be expected in the event that a new species were being formed. That this is probably the case is indicated by the new emission lines that appear as the $ZrCl_4$ concentration is increased, as shown in Figure 2-15. The $ZrCl_4$ is interacting with the coordination sphere, probably opening up the structure and allowing nonradiative interactions to occur.

The difference in behavior observed with $ZrCl_4$, as opposed to $SnCl_4$ as the Lewis acid, is also found in the behavior of lifetime as a function of Nd^{+3} concentration. This is illustrated in Figure 2-16. The increasing lifetime with increasing Nd^{+3} concentration seen in solutions with $SnCl_4$ as the Lewis acid are expected as a result of the trapping of resonance radiation. With $ZrCl_4$, however, just the reverse is observed. The difference is attributed to the bidentate nature of the coordination resulting with $ZrCl_4$. The coordinating groups form rings and these coordinating species can just as well "bridge" or connect two Nd^{+3} ions. In so doing, the Nd^{+3} ions can interact and the result is quenching. The mechanism is that an excited Nd^{+3} ion and one in the

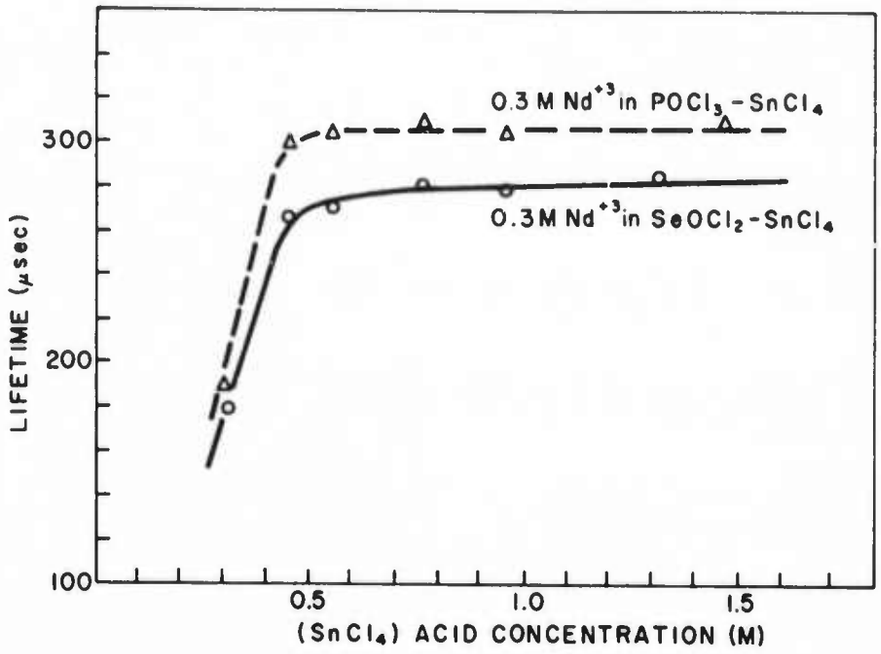

Figure 2-13. Fluorescence Decay Time of 0.3M Nd^{+3} in $SeOCl_2$:$SnCl_4$ and $POCl_3$:$SnCl_4$ as Function of Lewis Acid Concentration (at 300°K)

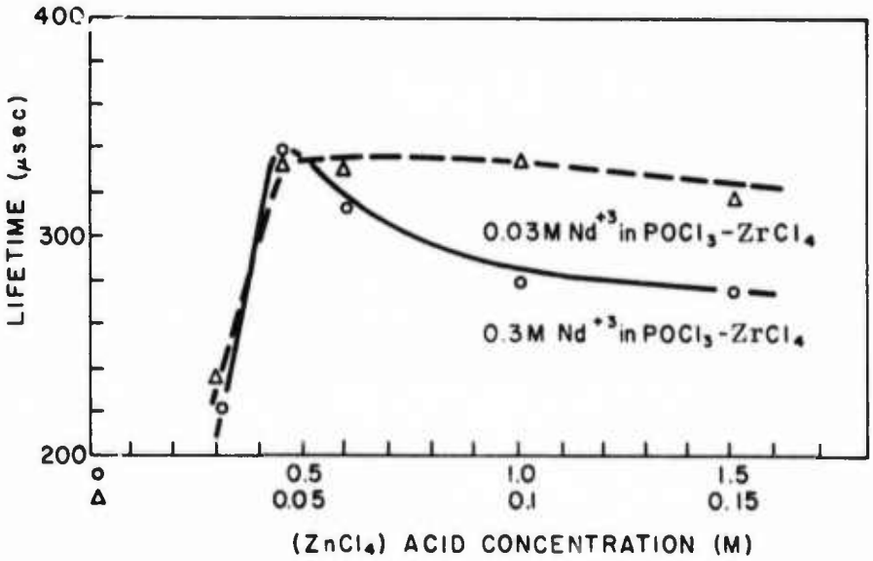

Figure 2-14. Fluorescence Decay Time of Nd^{+3} in $POCl_3$:$ZrCl_4$ as Function of Lewis Acid Concentration (at 300°K)

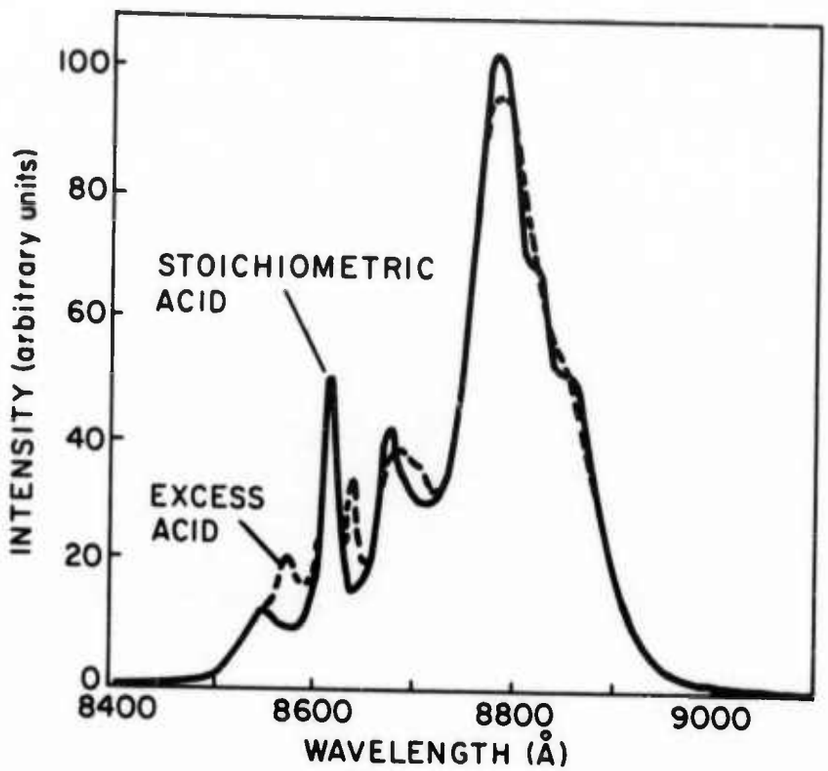

Figure 2-15. Emission Spectrum of 0.3M Nd^{+3} Solutions in $POCl_3$:$ZrCl_4$ Solutions as a Function of Lewis Acid Concentration (at 100°K)

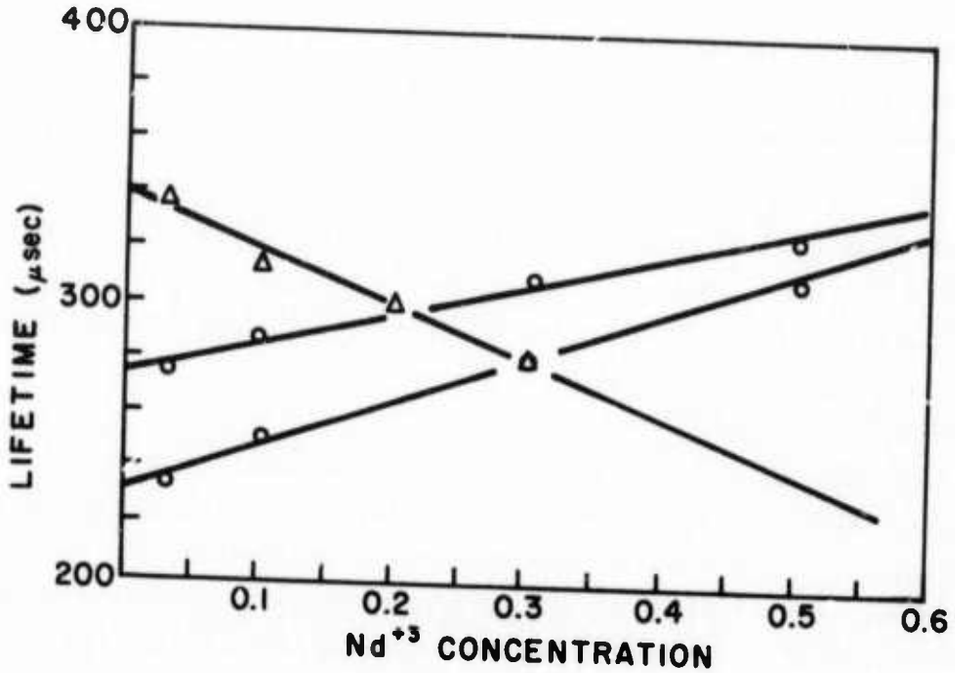

Figure 2-16. Fluorescence Decay Time of Nd^{+3} Aprotic Solutions at Stoichiometric Acidity as Function of Nd^{+3} Concentration (at 300°K)

ground state interact to leave both in the $^4I_{15/2}$ from which both relax nonradiatively. This behavior is observed in many hosts.[38, 39] Such a mechanism is, of course, enhanced by a high Nd^{+3} concentration.

The final factor entering into the fluorescence lifetime is the protic contamination. We shall consider specifically water. In both $POCl_3$, using $SnCl_4$ and $SeOCl_2$ solutions, an increase in such contamination results in a marked decrease in the fluorescence lifetime. In the case of $ZrCl_4$, however, the fluorescence lifetime will ultimately recover. As noted before, this is attributed to the reaction of H_2O and $ZrCl_4$ which removes the protons from solution but results in the precipitation of $ZrOCl_2$.

The behavior of the fluorescence lifetime is consistent with the chemical model developed earlier. In the case of solutions using $ZrCl_4$ as Lewis acid, it adds further confirmation to the structure already presented for the Nd^{+3} complex in the solution.

2.2.3 The Absorption Cross-Section

With the possible exception of fluorescence efficiency, the absorption cross-section is probably the most important spectroscopic parameter for estimating laser performance. This is the factor entering all gain considerations whether in the oscillator or amplifier mode. In determining the absorption cross-section, one also determines the stimulated emission coefficient since, as shown by Einstein,[40] the two are equal. In the case of Nd^{+3}, where the terminal level of the laser transition lies about 2000 cm^{-1} above the ground state, it is experimentally difficult to obtain a sufficient population in this state to get a measurable absorption. In practice then, one obtains this information by indirect methods. In the case of Nd^{+3}, we take advantage of the fact that the resonance transition and the laser transition arise from the same excited states. In the subsequent discussions we shall outline the procedure,[41] also used by others,[42, 43] and present the results on Nd^{+3} solutions.

The basic equations for the derivation are given by Mitchell and Zemansky:[44]

$$\int k(\nu)\,d\nu = \frac{\lambda_0^2}{8\pi n^2}\frac{g_2}{g_1}\frac{N_1}{t_{21}}\left(1 - \frac{g_1}{g_2}\frac{N_2}{N_1}\right) \simeq \frac{\lambda_0^2}{8\pi n^2}\frac{g_2}{g_1}\frac{N_1}{t_{21}} \qquad (2\text{-}10)$$

$$f_{12} = \frac{mcn}{N_1\pi e^2}\int k(\nu)\,d\nu = 37.680\,\frac{n}{N_1}\int k(\nu)\,d\nu \qquad (2\text{-}11)$$

and the combined equations:

$$f_{12}t_{21} = \frac{mc}{8\pi^2 e^2 n}\frac{g_2}{g_1}\lambda_0^2 = \frac{1.499}{n}\frac{g_2}{g_1}\lambda_0^2 \qquad (2\text{-}12)$$

where

$k(\nu)$ = the absorption constant (cm^{-1}) at frequency ν

N_i = the population of state i

λ_0 = the peak wavelength of the transition

n = the index of refraction

g_i = the degeneracy of state i

f_{12} = the oscillator strength of transition 1, 2

m, e = the electronic mass charge

c = the velocity of light

t_{21} = the radiative lifetime of the transition

In this case, we determine the oscillator strength of the resonance transition which has an easily measured absorption. Then, using Eq. (2-12), t_{21} is readily determined. Now, since the laser and resonance fluorescence arise from the same excited state, the ratio of the radiative lifetimes is the ratio of fluorescence intensities. This determines t_{laser} and then the cross-section, σ, is obtained from:

$$\sigma = \frac{\lambda_0^2}{8\pi n^2 \Delta\nu}\frac{1}{t_{laser}} \qquad (2\text{-}13)$$

where $\Delta\nu$ is the half width of the fluorescence line.

To carry out this calculation, a more detailed knowledge of the emission and absorption spectra are required than has thus far been presented. In Figure 2-17 we show the emission spectra of Nd^{+3} in $SeOCl_2$ and $POCl_3$ at liquid nitrogen temperature, while Figure 2-11 presents the same information at room temperature. The absorption spectra at liquid nitrogen temperature are shown in Figure 2-18, and in Figure 2-19 there is the absorption spectrum of Nd^{+3} in $SeOCl_2$ at room temperature.

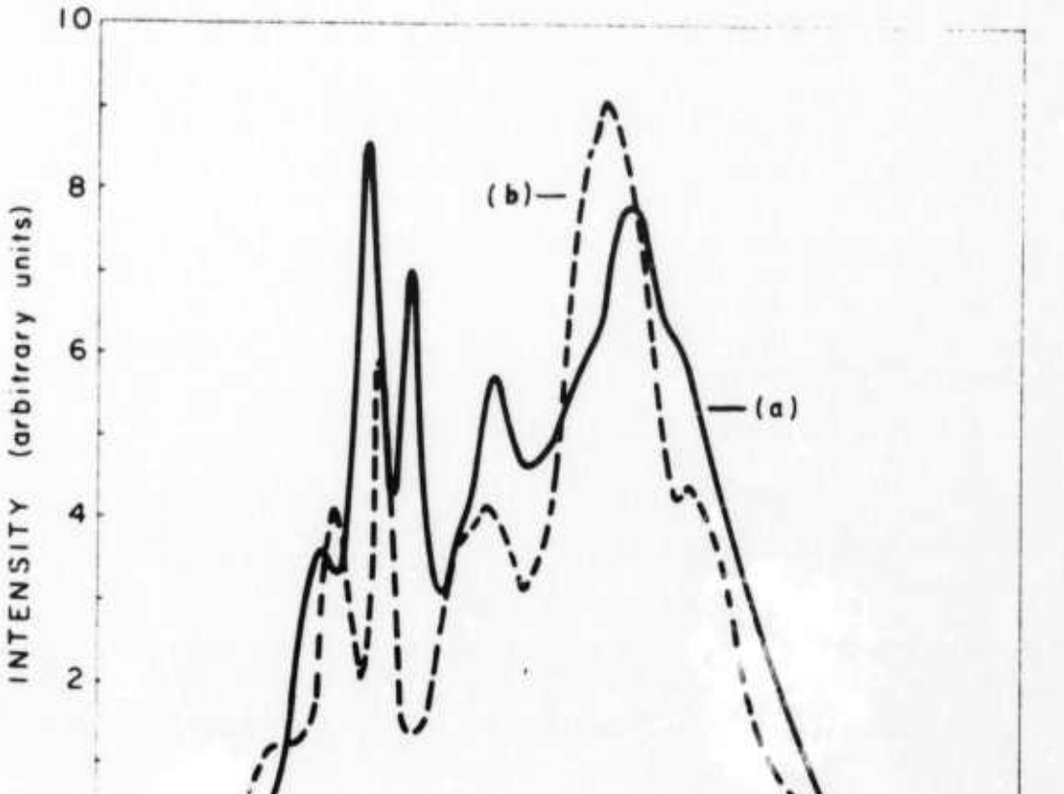

Figure 2-17. Emission Spectrum of 0.3M Nd^{+3} Solutions at 100°K

— $SeOCl_2$

--- $POCl_3$

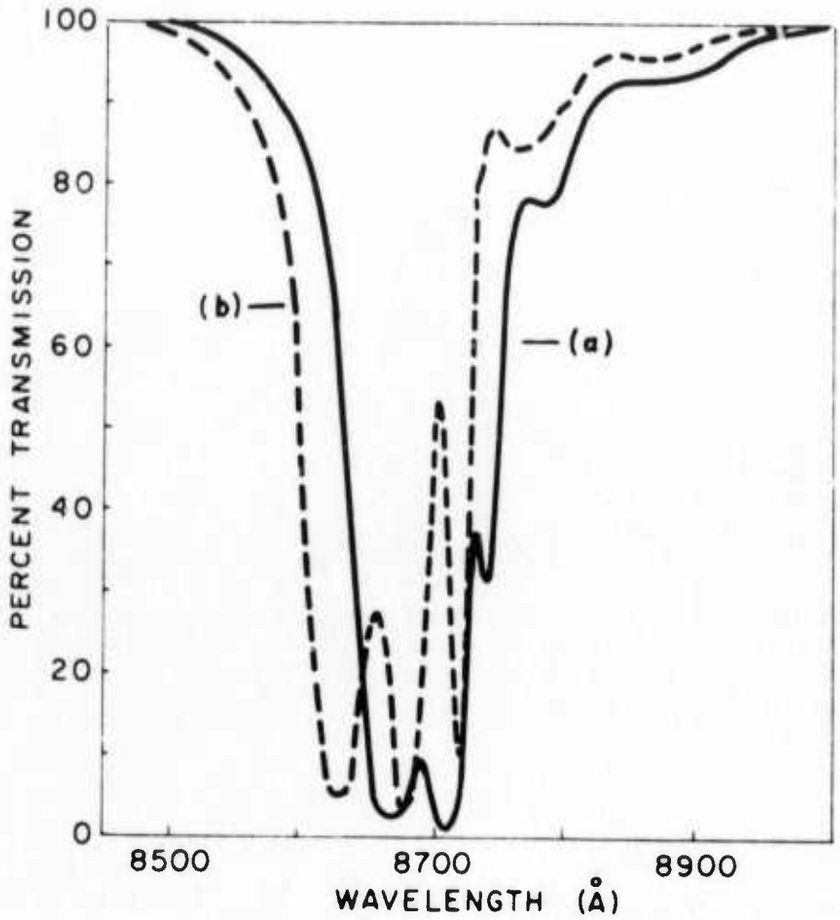

Figure 2-18. Absorption Spectrum of 0.3M Nd^{+3} Solutions at 100°K

a) $SeOCl_2$

b) $POCl_3$

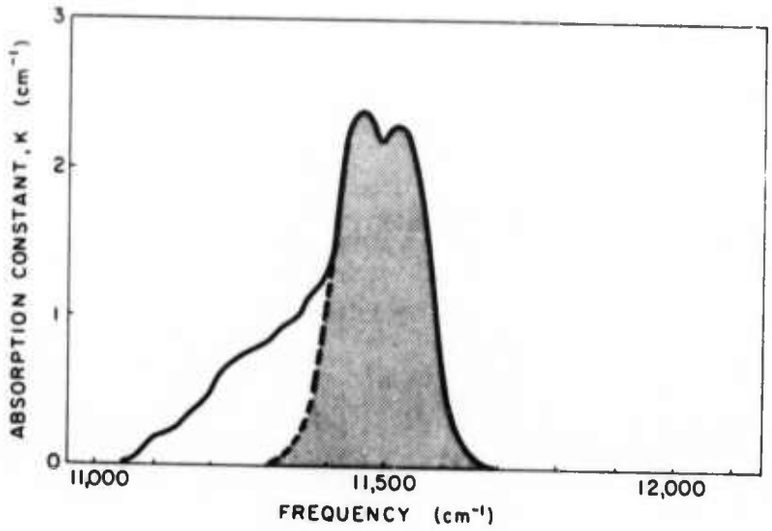

Figure 2-19. Absorption Spectrum of $^4I_{9/2} - {}^4F_{3/2}$ Transition of Nd^{+3}

Comparison of the emission and absorption speetra at room and liquid nitrogen temperatures reveal that the prineipal peak frequencies are the same, but the narrower lines at the lower temperature provide more resolution and an easier identifieation of the transition frequeneies. An analysis of the speetra leads to the results given in Table 2-3 and the energy level strueture in Figure 2-20. These results are characteristie for the stoiehiometrie solutions and indieate a low symmetry as would be expeeted. Tolstoi[45] presents a somewhat eonflicting set of results (Table 2-3) for the $POCl_3$:$SnCl_4$ solvent at liquid He temperatures. In their report, the method of solution preparation is not clearly stated. In addition, they find varying speetroseopic results depending on the rate of cooling, and they provide no information on intermediate temperatures whieh might help resolve the differenees. Furthermore, Tolstoi finds evidence for three different emitting speeies in Nd^{+3}:$POCl_3$:$SnCl_4$ solutions at liquid helium temperatures. Breeher and French,[34] investigating Eu^{+3} in this solvent, also found evidenee for multiple speeies, but this was usually under strongly acid eonditions. Clearly defined single speeies were found generally under stoichiometrie eonditions. Considering these factors, it is probably most appropriate to use the values for the energy levels found in our work and shown in Figure 2-20.

TABLE 2-3

COMPONENTS OF THE $^4F_{2/2}$–$^4I_{9/2}$ TRANSITION OF Nd^{3+} (0.3M) IN $SeOCl_2$ AND $POCl_3$

$SeOCl_2$			$POCl_3$	
Wavelength, Å	Energy, cm^{-1}	Assignment*	Wavelength, Å	Energy, cm^{-1}
8668	11,537	b-1	8628	11,590
8705	11,488	a-1	8679	11,522
8738	11,444	b-2	8718	11,471
8778	11,393	a-2	8768	11,405
		b-3		
8801	11,362	a-3	8805	11,357
8865	11,280	b-4		
8905	11,230	a-4	8889	11,250
8950	11,173	b-5	8960	11,162
~8990	11,123	a-5		

*Components of the $^4I_{9/2}$ level are numbered eonsecutively from the ground state (1); for the $^4F_{3/2}$ level, a denotes the lower component and b the higher.

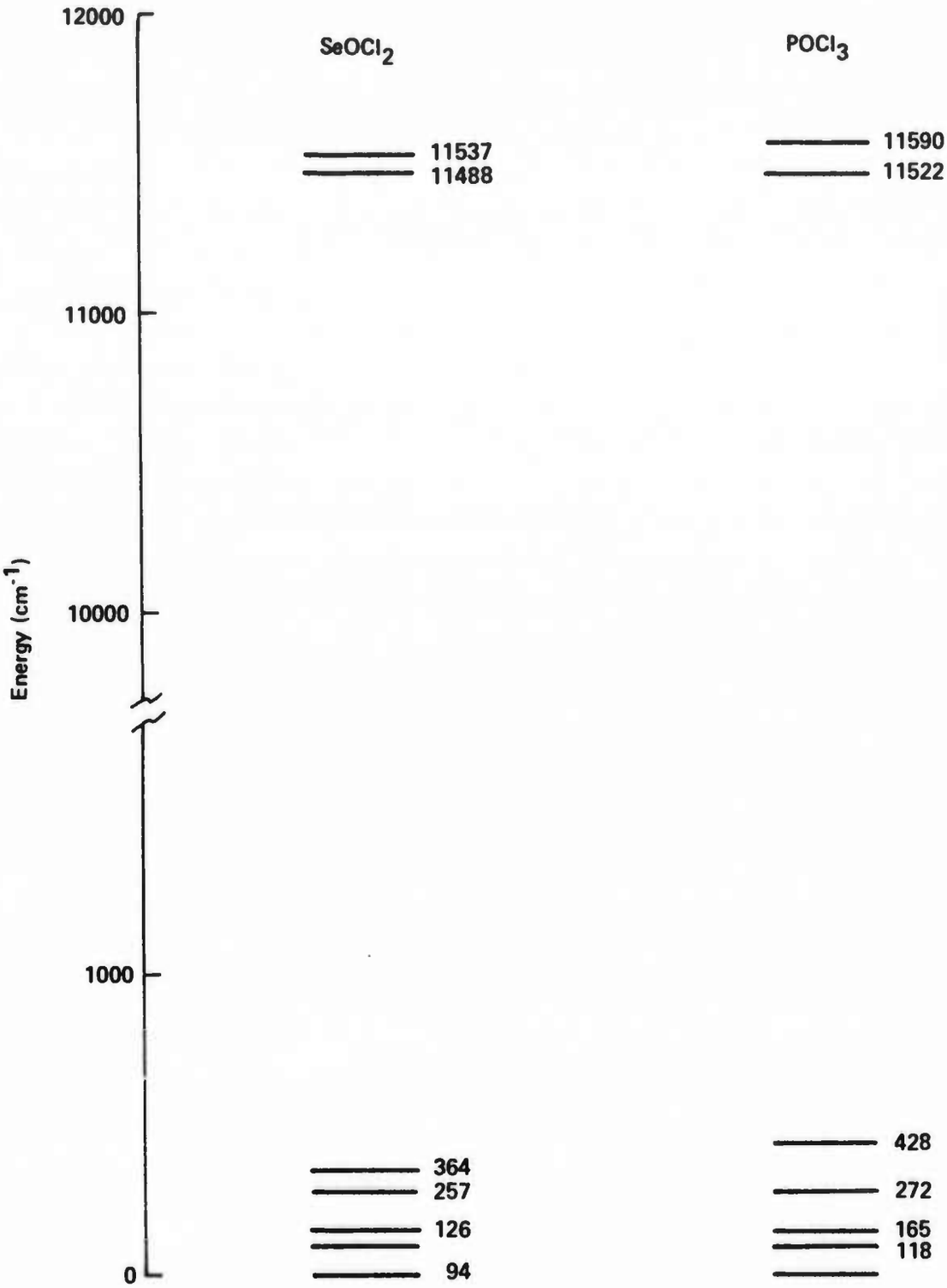

Figure 2-20. Energy Level Structure of Nd in $SeOCl_2$ and $POCl_3$

The establishment of the energy levels enables us to evaluate the partition function (using only the $^4I_{9/2}$ levels) and thus, to determine the population of the ground state. Separating out the spectroscopic contribution of the 8705 Å ($SeOCl_2$) or 8679 Å ($POCl_3$) transition enables us to calculate $\int k(\nu)d\nu$. Application of Eq. (11) then leads to a value for f_{12} and the use of Eq. (2-12) provides t_{21}. Partitioning the fluorescence emission in the laser transition and the resonance transition, in terms of the number of photons, leads to the radiative lifetime in the laser transition. Here, care must be taken to work with more and more dilute solutions until a constant ratio is found, and the effect of the self-absorption in the resonance transition eliminated. Finally, the application of Eq. (2-12) gives the desired cross-section. Table 2-4 lists the results of these measurements and compares them with the results of others.

TABLE 2-4

ABSORPTION CROSS-SECTION AND FLUORESCENCE LIFETIME FOR LIQUID LASER SOLUTIONS

	Absorption Cross-Section σ (cm^2) $\times 10^{20}$	Fluorescence Lifetime (μs) (Calculated)	Decay Time (μs) (Observed)
$SeOCl_2$:$SnCl_4$	7.66[a]	290	280
	7.8[b]	280	280
$POCl_3$:$SnCl_4$	9.6[b, c]	310	290
	5.6[d] (Method 1)		
	8.3[d] (Method 2)	350	350
	8.5[d] (Method 3)		
	8.1[e]		
	10.0[f]		
	7.8[g]		
	20.0[h]		
$POCl_3$:$ZrCl_4$	9.6	350[i]	340

(a) Ref. 41
(b) Ref. 23
(c) Ref. 24
(d) Ref. 47
(e) Ref. 49
(f) Ref. 48
(g) Ref. 46
(h) Ref. 21
(i) Estimate based on similarity between spectra of $POCl_3$:$ZrCl_4$ and $POCl_3$:$SnCl_4$.

The value obtained by Birnbaum and Gelbwachs[46] (g) assumes a knowledge of the quantum efficiency that is a difficult quantity to obtain. Collier et al.[47] (d) evaluate the absorption cross-section by three different methods: the first is based on the spontaneous fluorescence drop occurring when a Q-switched probe pulse is amplified through the pumped liquid medium; the second is similar to the technique of Samelson, Heller and Brecher;[41] and the third is based on direct absorption. Their results are in general agreement with the other workers. In fact, Boling and Dube'[48] (f) indicate a valid correction to the calculation of Collier et al., in their application of Method 2, which changes their value to one in better agreement with Brecher and French (b, c). Belan et al.[49] (e), using Method 1 of Collier et al., obtain a value on the low side but higher than Collier.

The over-all conclusion is that the cross-section for Nd^{+3} in these solutions lies between 8 and 10×10^{-20} cm^2. This is compared with values for other typical Nd^{+3} systems in Table 2-5. The cross-sections of the liquids are about a factor of 2 or 3 higher than glass, and nearly an order of magnitude smaller than for crystals, indicating that liquids will have lower thresholds than glasses and greater energy storage than crystals.

TABLE 2-5

ABSORPTION CROSS SECTION FLUORESCENCE LIFETIME AND LASER WAVELENGTH OF Nd^{+3} IN VARIOUS HOSTS

Nd^{+3} Host	Fluorescence Lifetime (μs)	Cross-Section $cm^2 \times 10^{20}$	Laser Wavelength (μm)
YAG	240	88.0	1.064
$CaWO_4$	165	41.0	
$POCl_3$:$SnCl_4$	290	9.6	1.051
$POCl_3$:$ZrCl_4$	350	9.6	1.051
$SeOCl_2$:$SnCl_4$	280	7.8	1.055
ED-2 Glass	310	4.5	1.061
LG55 Glass	560	2.1	1.058

It is also interesting to observe that the ratio of observed-to-calculated fluorescence lifetime is close to unity for liquids (values greater than unity suggest a calculational error), which indicates a quantum efficiency also close to unity. This is in conflict with a value of 0.49 determined experimentally by Schimitschek[50] for a $POCl_3$:$ZrCl_4$ solution. It should be pointed out, however, that the solution used by Schimitschek did not correspond to the stoichiometric composition used in laser work but, in fact, had an excess of Lewis acid. This excess would lead to nearly a 20% reduction in fluorescence lifetime (characteristic of quenching) and multiple Nd^{+3} species in solution. It is then doubtful that the value of 0.49 for the quantum efficiency is characteristic of "laser" solutions.

Substantial contributions to Nd^{+3} laser solutions in aprotic solvents were made in the open literature during the course of the work performed under this contract. In these papers there are more detailed discussions and descriptions of the experimental work, and the publications relating to the solution preparation and the spectroscopy are included as Appendix A, B, and C.

2.3 BRILLOUIN, RAYLEIGH AND STIMULATED-BRILLOUIN AND-RAMAN SCATTERING

In liquid laser solutions of the type involving Nd^{+3} in aprotic solvents, the Nd^{+3} containing molecule or ion is a large, polarizable species. As such, these can constitute effective scattering centers and contribute to transmission losses. In addition, some laser properties as self Q-switching and spectral broadening, to be discussed later, raised the possibility that stimulated scattering processes, either Brillouin or Rayleigh wing, could be playing a role. Stimulated Raman scattering represents a laser loss, in that laser energy appears at another frequency. Consequently, the work described in this section was undertaken. The description given in this section is a brief condensation of the published work contained in Appendix D and E. These should be consulted if more detail is desired.

2.3.1 Brillouin and Rayleigh Scattering

One important respect in which Brillouin and Rayleigh scattering differs from Raman scattering is that the frequencies to which they give rise are well within the fluorescence line width of the laser transition and, in fact, within 1 cm^{-1} of the peak fluorescence. Raman scattering on the other hand lies well outside the fluorescence band. Here we will only consider the results interpreted in terms of a thermodynamic model.

The simplest theoretical treatment is based on the thermodynamic consideration of a structureless continuum. This is in essence the original approach used by Einstein.[51] The dependence of the variation of dielectric constant $\Delta\epsilon$ on temperature fluctuations is neglected in comparison with its dependence on the density fluctuations. Assuming a single-phase system, the following expression is derived for the intensity of the scattered light:[52, 53]

$$I = I_0 \frac{\pi^2 V}{2\lambda^4 L^2} \left(\rho \frac{\partial \epsilon}{\partial p}\right)_T^2 \beta_T kT \, (1 + \cos^2\theta) \tag{2-14}$$

where

ϵ = dielectric constant

I_0 is the intensity of the incident unpolarized light

V is the scattering volume

λ is the wavelength of the incident light

L is the distance from the scattering volume to the point where I is measured

ρ is the density

β_T is the isothermal compressibility

θ is the angle between the k vectors of the incident and scattered light

Most of the quantities in Eq. (2-14) are external parameters, since they depend on the experimental geometry and the excitation conditions. The only internal parameters characterizing the scatterer are ρ, $(\partial\epsilon/\partial\rho)_T$, and β_T. The experimental data on scattering intensity and the theory are conveniently connected via the scattering coefficient R_θ:

$$R_\theta = \frac{I}{I_0} \frac{L^2}{V} \, (\text{cm}^{-1}) \tag{2-15}$$

By comparison with Eq. (2-14), it is easy to express the theoretical value of R_θ as a function of the excitation wavelength, the scattering angle, and the physical properties of the scatterer as follows:

$$R_\theta = \frac{\pi^2}{2\lambda^4} \left(\rho \frac{\partial \epsilon}{\partial \rho}\right) \beta_T \, kT \, (1 + \cos^2\theta) \tag{2-15'}$$

The following simple relation connects the scattering coefficient for $\theta = 90°$ with the corresponding extinction coefficient, h, of a nonabsorbing medium:[52]

$$h = \frac{16}{3}\pi R_{90} \tag{2-16}$$

The extinction coefficient is defined from the expression connecting the initial and final intensities of a light beam after it has traversed a homogeneous medium of length x (cm):

$$I = I_0 e^{-hx} \tag{2-17}$$

The measured scattering coefficient for a laser solution can then be converted into an extinction coefficient and, as such, inserted into the expression for the gain characteristic of a laser medium, nonabsorbing at the frequency under consideration. A slight modification of Eq. (2-16) leads to a connection between the scattering coefficient per unit volume R'_{90} and the cross-section for scattering:

$$h' = \frac{16}{3}\pi R'_{90} \tag{2-16'}$$

and

$$h' = N\sigma_{sc} \tag{2-16''}$$

N being the number density of scattering centers and σ_{sc} the scattering cross-section per particle.

So far, no spectral distribution of the scattered light has been considered. A preliminary discussion of the spectral characteristics of the scattered light can be derived from the following considerations: In Eq. (2-14) the fluctuations of the density $\overline{\Delta\rho^2}$ have been expressed as a function of the coefficient of isothermal compressibility β_T. Alternatively, $\overline{\Delta\rho^2}$ can be expressed in terms of pressure and entropy fluctuations, $\overline{\Delta p^2}$ and $\overline{\Delta S^2}$:

$$I = I_{adiabatic} + I_{isobaric} = VG\left[\left(\frac{\partial\epsilon}{\partial\rho}\right)_T^2\left(\frac{\partial\rho}{\partial p}\right)_S^2\overline{\Delta p^2} + \left(\frac{\partial\epsilon}{\partial\rho}\right)_T^2\left(\frac{\partial\rho}{\partial S}\right)_p^2\overline{\Delta S^2}\right] \tag{2-18}$$

with G an "external" parameter, not containing quantities characterizing the scatterer. The pressure fluctuations obey a wave equation and will propagate, while the entropy fluctuations obey a flow equation and will not propagate. Pressure fluctuations cause Doppler-type scattering with change in frequency, while entropy fluctuations will cause no change in frequency. The first term in Eq. (2-18) gives rise to Brillouin scattering, the other to Rayleigh scattering. Brillouin scattering in a given direction will be maximized when Bragg's relation is satisfied and

$$2n\Lambda.sn\left(\frac{1}{2}\theta\right)=\lambda \tag{2-19}$$

where n is the index of refraction of the medium for the wavelength λ of the incident light and Λ is the wavelength of density waves involved in the scattering event. From Eq. (2-13), the following relation (Landau-Placzek formula) is obtained for the ratio of the intensity of the Rayleigh and Brillouin components of the scattered light:

$$I_{\text{isobaric}}/I_{\text{adiabatic}} = \frac{\beta_T - \beta_S}{\beta_S} = \gamma - 1 \tag{2-20}$$

where γ is the ratio of the specific heats c_p/c_v. The relative frequency shift in the scattered radiation due to pressure fluctuations can be derived from Eq. (2-21):

$$\Delta\omega/\omega_0 = 2n\ (v/c)\ \sin\frac{1}{2}\theta \tag{2-21}$$

From the measurement of $\Delta\omega$, ω_0, θ, and n, the value of the hypersound velocity v can be deduced.

Depolarization Effects

Both Rayleigh and the Brillouin scattering are completely polarized because only isotropic fluctuations of the refractive index have been considered so far. Depolarization effects on the expression of the scattered intensity can be formally introduced by the use of the empirical parameter Δ_u as follows:[52, 53]

$$I\left(1+\frac{\Delta_u(1+\rho_u)}{\rho_u-\Delta_u}\right) \tag{2-22}$$

$$\rho_u = i_x/i_z \tag{2-23}$$

$$\Delta_u = i_x/(I_z + i_x) \qquad (2\text{-}24)$$

where

I is the scattered intensity inclusive of scattering due to orientation fluctuations

i_x and i_z are the intensity components of the depolarized scattered light in the scattering plane and normal to it, respectively

u stands for unpolarized incident light.

The expression for the scattering coefficient then becomes:

$$R_{90} = \frac{\pi^2}{2\lambda^4} \rho \left(\frac{\partial \epsilon}{\partial \rho}\right)^2_T \beta_T kT \frac{6+6\Delta_u}{6-7\Delta_u} \qquad (2\text{-}25)$$

The term $(6+6\Delta_u)/(6-7\Delta_u)$ is known as the Cabannes correction factor.

The solutions used in the experimental work are described in Table 2-6.

TABLE 2-6

COMPOSITION AND PREPARATION OF LASER SOLUTION SAMPLES

Sample	Components (25:1)	Nd Content (Mole/Liter)	Filtered	Filter Porosity
A	$POCl_3$:$SnCl_4$	0.3	Yes	Fine
B	$POCl_3$:$SnCl_4$	0.3	Yes	Fine
C	$POCl_3$:$SnCl_4$	0.3	Yes	Medium
D	$POCl_3$:$SnCl_4$	0.3 [$Nd(TFA)_3$]	Yes	Ultrafine
E	$POCl_3$:$SnCl_4$	0.3		
F	$POCl_3$:$SnCl_4$	0.3	Yes	Ultrafine
G	$POCl_3$:$ZrCl_4$	0.3 [$Nd(TFA)_3$]	Yes	Fine
H	$SeOCl_2$:$SnCl_4$	0.3	No	
I	$SeOCl_2$:$SnCl_4$	0.5	No	
J	$SeOCl_2$:$SnCl_4$	0.3	No	
K	$SeOCl_2$:$SnCl_4$	0.1	No	

Unless otherwise specified, Nd_2O_3 was used to provide the Nd^{+3} ion. In the other cases the trifluoroacetate (TFA) was used. The less corrosive $POCl_3$ based solutions were filtered prior to use as stated in Table 2-6.

A typical experimental result is illustrated in Figure 2-21 and the measured values of the Brillouin triplet spacing and values of the hypersound velocities obtained from Eq. (2-21) are listed in Table 2-7.

The FWHM for the depolarized Rayleigh-wing scattering in some of the systems investigated are listed in Table 2-8. Only solutions based on $SeOCl_2$ gave any appreciable Rayleigh-wing scattering. The FWHM was largest for $SeOCl_2$ (i.e., 0.204 cm^{-1}), and tended to decrease with increasing Nd concentration. The Brillouin scattering from the laser solutions does not show unusual features, either with respect to the intensity of the two Brillouin components or with respect to the over-all triplet spacing. The derived values of the hypersound velocity are within the range of the values obtained for simple liquids. Table 2-9 lists the value of the scattering coefficients of the solutions investigated. These were obtained by using values reported in the literature for the scattering coefficient of benzene: 15×10^{-6} cm^{-1} for R_{90} from benzene under 5461-Å excitation.[52] The corresponding scattering coefficients at 6328 and 10600 Å were derived from the inverse fourth-power relation [Eq. 2-14)] involving λ and are listed in Table 2-9, columns 3 and 4. Finally the scattering coefficients were changed into the corresponding extinction coefficients which are listed in the last two columns of Table 2-9.

It would appear that at 1.06μ, the scattering losses, even for the solutions based on $POCl_3$, would be of the order of 0.02% cm^{-1}. These are less than 10% of the lowest observed values found for dynamic loss in laser liquids and may be considered negligible.

2.3.2 Stimulated Raman and Brillouin Scattering

The large and polarizable Nd^{+3} containing molecules in inorganic liquid laser solutions could readily result in nonlinear processes arising from the interaction of the medium with the pulse undergoing amplification. It is possible that such processes would limit the power capabilities of an oscillator or amplifier based on the liquid media or limit their mode of operation. The principal nonlinear processes of concern are stimulated Raman scattering (SRS), stimulated Brillouin scattering (SBS) and self-focusing.

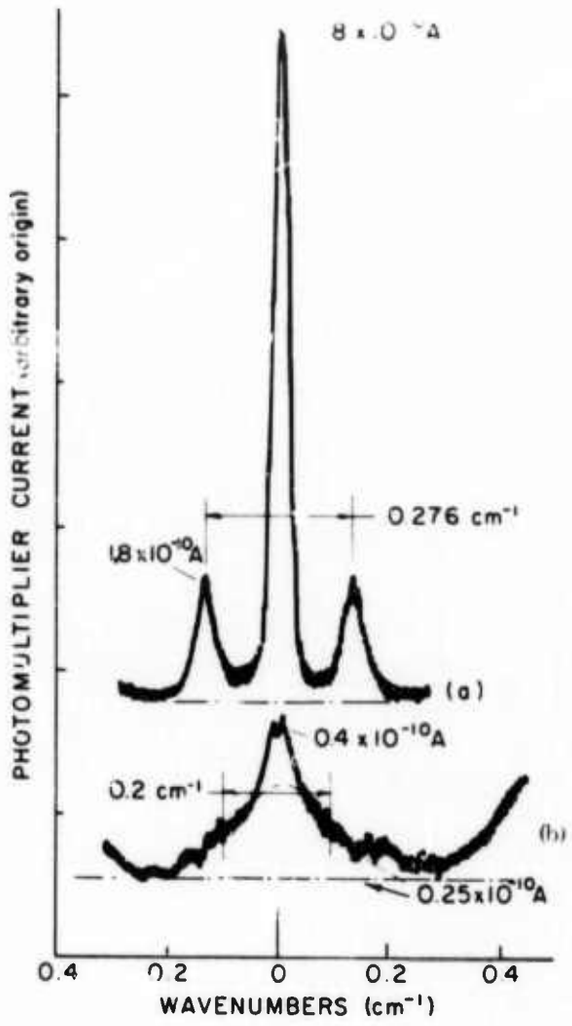

Figure 2-21. Detail of the Spectral Distribution of Scattered Light at 90° from $SeOCl_2$

TABLE 2-7

BRILLOUIN-TRIPLET SPACINGS; REFRACTIVE INDEX OF SOLUTIONS AND DERIVED VALUES OF HYPERSOUND VELOCITY

Solution	Brillouin-Triplet Spacing[a] (cm^{-1})	Other Measurements (cm^{-1})	Spacing in SBS (cm^{-1})[b]		Refractive Index	Hypersound Velocity (m/sec)	
			Predicted[c]	Observed[d]		This Work[e]	Other Measurements
$SnCl_4$	0.180		0.272	0.232	1.508[l]	800	803[d,g]
$POCl_3$	0.215 ± 0.005		0.277	0.234	1.457[f]	990	837[c,g]
$POCl_3$:$SnCl_4$ (25:1)	0.215 ± 0.005		0.277	0.294			
A	No Splitting Observed[h]						
B	0.235 ± 0.010		0.302	0.36	1.4879[i]	1060	1266[d,g]
G	0.220 ± 0.010		0.283		1.4873		
C	No Splitting Observed[h]						
F	0.225 ± 0.005		0.290				
D	0.225 ± 0.005		0.302				
E	0.230 ± 0.005						
$SeOCl_2$	0.275 ± 0.005		0.354	0.356[d]	1.648[f]	1120	1130
$SeOCl_2$:$SnCl_4$				0.356[d]			1129
H	0.290 ± 0.005		0.373	j			
I	0.315 ± 0.010		0.405				
J	0.295 ± 0.005		0.380		1.671[f]	1180	
K	0.285 ± 0.005		0.367	0.380[d]		1188	
Benzene	0.325 ± 0.005	0.330[k]			1.5011[l]	1450	1500

[a] Under 6328 — Å excitation; 90° scattering.

[b] Under 6943 — Å excitation; backward scattering.

[c] Assuming no variation in the product nv from 6328 to 6943 Å.

[d] Reference 54; Eq. (2-21).

[e] Values derived using Eq. (2-21) and observed Brillouin-triplet spacing at 6328 Å.

[f] Interpolated value at 6328 Å.

[g] Same as footnote (e), for backward scattering at 6943 Å.

[h] Because of intense Rayleigh scattering.

[i] R. Kocher (private communication).

[j] No Brillouin components observed in stimulated backward scattering measurements.

[k] Reference 55.

[l] Index of refraction at 5893 Å (sodium lines).

TABLE 2-8

OBSERVED RAYLEIGH-WING SCATTERING

Solution	Observed FWHM (cm^{-1})	Relaxation Time (10^{-11} s)
$SeOCl_2$	0.204	5.2
H	0.128	8.3
J	0.112	9.5
K	0.180	5.9

TABLE 2-9

DERIVED VALUES OF SCATTERING COEFFICIENTS R_{90} (cm^{-1}) AND EXTINCTION COEFFICIENT h (FROM $I = I_{0e}^{-hx}$) FOR LASER SOLUTIONS

The Value of $R_{90} = 15 \times 10^{-6}$ cm^{-1} for Benzene at 5461 Å was Used in Conjunction with Formula (2-16).

Solution	R_{90} (6328 Å) ($\times 10^6$ cm^{-1})	R_{90} (1.06μ) ($\times 10^6$ cm^{-1})	h (at 6328 Å) ($\times 10^4$ cm^{-1})	h (at 1.06μ) ($\times 10^4$ cm^{-1})
$SeOCl_2$	16.8	2.13	2.82	0.356
H	37.8	4.8	6.32	0.805
I	30.2	3.84	5.02	0.645
J	39.5	5.0	6.6	0.838
K	19.3	2.45	3.26	0.41
$POCl_3$	5.55	0.70	0.93	0.117
B	60.0	7.6	10.0	1.27
C	470.0	59.5	79.0	9.95
D	47.0	5.95	7.9	0.99
E	73.0	9.25	12.2	1.55
F	59.0	7.5	9.9	1.25
G	84.0	10.65	14.1	1.785
Benzene	8.4	1.07	1.41	0.18

From the intensities of the spontaneous Raman spectra, estimates of the SRS gain can be made. The spontaneous linewidth and intensities of the vibrational Raman lines of $POCl_3$ and $SeOCl_2$ were measured in the pure liquids and in laser solutions. Raman linewidths and integrated intensities were then compared with CS_2, for which the SRS gain per unit length[56] should be 60×10^{-3} I_0 if the CS_2 linewidth is taken as 0.5 cm^{-1} (57) and where I_0 is in MW/cm^2. The gain value for $POCl_3$ was found by measuring its integrated intensity relative to that of CS_2 and correcting for the linewidth, since the intensity per unit frequency width at the peak is the relevant parameter in SRS.[58]

Spontaneous Raman spectra of pure $POCl_3$ and pure $SeOCl_2$ are shown in Figure 2-22. The most intense line in the $POCl_3$ Raman active vibrational spectrum is the P-Cl vibration at 488 cm^{-1}. The line is strong and comparable in total integrated Raman intensity to the 656 cm^{-1} line of CS_2. In a Nd^{+3}:$POCl_3$ laser solution a weak new Raman line appears shifted ~5 cm^{-1} to the red of the 488 cm^{-1} $POCl_3$ line. Its intensity is enhanced relative to the main line at higher molar concentrations of Nd^{+3}. The presence of the new line depends upon the presence of the components (other than Nd^{+3} or $POCl_3$) in the laser solution. When Nd^{+3} was removed from the solution, the line was still present. The intensity of the line is proportional to the amount of acid in the solution, i.e., the more acid, the stronger the line. The main effect of the extra components of the laser solution that are not present in pure $POCl_3$ is to reduce the intensity of the 488 cm^{-1} line proportionate to the amount of added components.

The 386 cm^{-1} Se-Cl vibration is the most intense feature of the $SeOCl_2$ Raman spectra. In a pure $SeOCl_2$ solution, the 386 cm^{-1} line has a complex structure ~18 cm^{-1} wide. In the laser solution of Nd^{+3} $SeOCl_2$, as in $POCl_3$, a new line appears shifted to the red of the 386 cm^{-1} line by ~5 cm^{-1}. When Nd^{+3} is removed from the laser solution, the extra line is still present, indicating that the other components of the laser solution are responsible for this new line. At the highest molar concentrations studied (10^{-2} molar), the red-shifted line is nearly as intense as the main Raman line.

Theory[58] states that the most intense spontaneous Raman lines will appear in SRS. The gain[59] per unit length for SRS is given by:

$$g = \frac{8\pi c N}{h \omega_s^2 n^2} \frac{d\sigma}{d\Omega} \frac{1}{\Delta\nu_L \otimes \Delta\nu} \qquad (2\text{-}26)$$

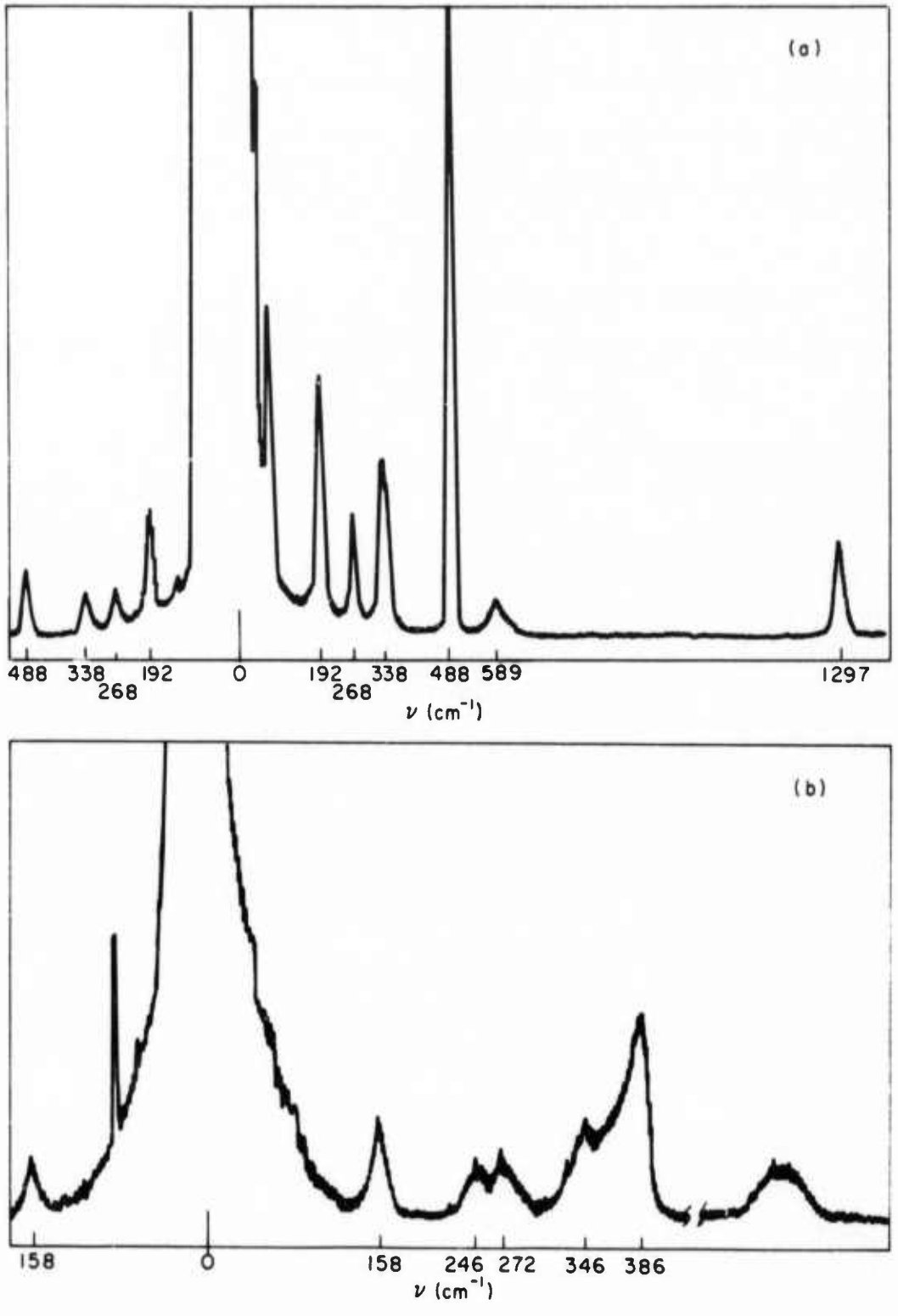

Figure 2-22. Raman Spectrum of Pure PCl_3 (a) and $SeOCl_2$ (b)

where

$d\sigma/d\Omega$ is the differential scattering cross-section

$\Delta\nu$ the Raman linewidth in cm^{-1}

$\Delta\nu_L$ the laser linewidth in cm^{-1}

ω_s the angular frequency of Stokes radiation

N is the number of molecules per cm^3

$\Delta\nu_L \otimes \Delta\nu$ is the convolution of the linewidths of the pump and Raman radiation, respectively, (e.g., for Lorentzian line shapes $\Delta\nu_L \otimes \Delta\nu = \Delta\nu_L + \Delta\nu$). Under single-mode excitation, $\Delta\nu_L \otimes \Delta\nu = \Delta\nu$.

The integrated Raman intensities of the 488 cm^{-1} $POCl_3$ and 386 cm^{-1} $SeOCl_2$ lines relative to CS_2 were measured, and with a knowledge of the Raman linewidths, the gain was computed. The peak intensity of the Raman line in $POCl_3$, relative to the peak intensity of the 656 cm^{-1} CS_2 line, was measured as 0.05 ± 0.01; and the peak intensity of the $SeOCl_2$ line, relative to the CS_2 line, was measured as 0.06 ± 0.01. Spontaneous data predicts a Raman gain per unit length of $\sim 2.7 \times 10^{-3}$ I_0 in $POCl_3$ and 3.2×10^{-3} I_0 in $SeOCl_2$ where I_0 is in MW/cm^2. The gains in $SeOCl_2$ and $POCl_3$ are about the same, because the peak intensity per unit bandwidth is approximately the same.

A single-longitudinal and single-transverse mode Korad ruby laser was used to measure Raman gains in the inorganic liquids. This laser consists of a sapphire etalon output reflector, a 1-mm aperture, a four-inch ruby rod, a Kodak Q-switch dye cell antireflection coated at the ruby wavelength, and a 100% reflectivity rear output reflector. SRS and SBS gains were measured in pure $POCl_3$, $POCl_3$ doped with dimer ($P_2O_3Cl_4$), and $E_u(TFA)_3$:$POCl_3$:$ZrCl_4$. The objective was to isolate nonlinear effects produced by the other components of the laser solution — dimers such as $P_2O_3Cl_4$ or complexes such as $POCl_3$:$ZrCl_4$ and those effects produced by the rare earth ions — Nd^{+3} itself. The solution doped with europium ions was used to simulate a neodymium-doped solution, because a neodymium solution absorbs the 6943 Å ruby wavelength.

The curve of SRS intensity vs. laser intensity for pure $POCl_3$ is plotted in Figure 2-23. Only forward Raman scattering was observed from $POCl_3$. Backward SRS from $POCl_3$ was measured to be ≤ 0.01 of the forward scattering at the power levels of the experiment. Theoretically, the forward-to-backward ratio is unity under steady-state conditions, but its theoretical value is computed in the absence of backward SBS which experimentally is present and competing against the back SRS light.

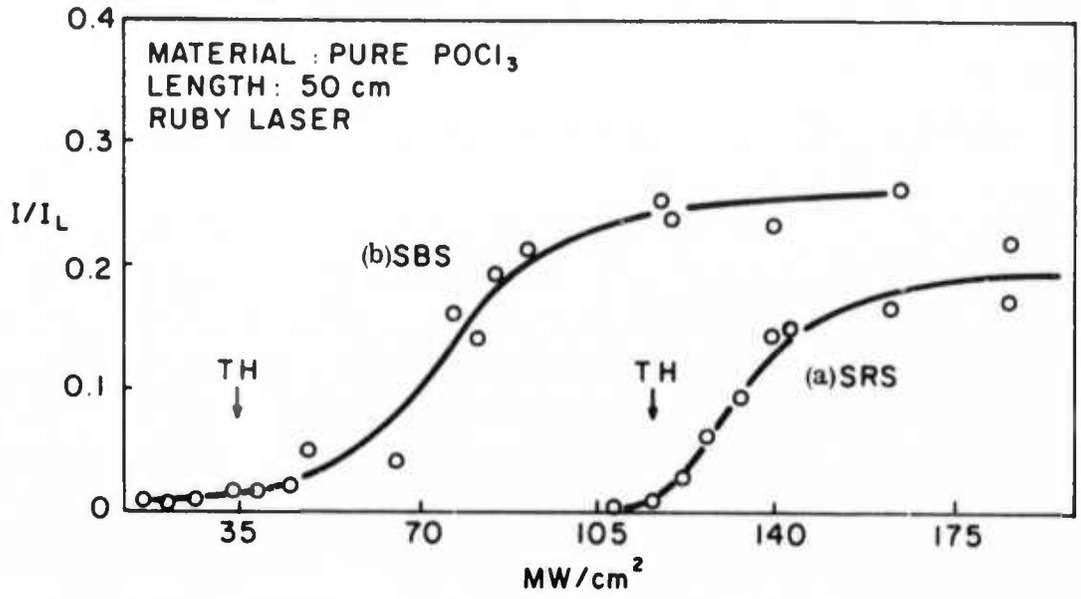

Figure 2-23. SRS and SBS Curves in $POCl_3$ Versus Ruby Single-Mode Laser Intensity

As seen from Figure 2-23, substantial Raman conversion occurs over a length of 50 cm at powers of ~100 MW/cm^2. The Brillouin scattering curve is also shown in Figure 2-23. A large amount of laser conversion to SBS takes place at ≃20 MW/cm^2. At the powers where substantial Raman conversion begins, ~20 percent of the laser has been depleted into backward Brillouin scattering. At the highest laser powers in this experiment, as much as 40% of the laser beam is converted to SBS and 30% to SRS light.

The curves of Raman and Brillouin intensities vs. laser power reach saturation regions at high powers, because of laser depletion into SRS and SBS. The laser depletion was further verified by observing that the laser beam intensity, transmitted through the cell, decreased as the SBS and SRS built up. The Raman gain was measured from the beginning portion of the Raman curve to be ~0.33 cm^{-1} at 128 MW/cm^2.

When $POCl_3$ was doped with dimer ($P_2O_3Cl_4$), the only apparent difference in the Raman curve was a slight increase in the Raman threshold by approximately 20%, corresponding apparently to the approximate percentage of the volume taken up by the dimer. When $POCl_3$ was doped with its dimer plus a rare earth (europium), the threshold for Raman scattering increased still further. These results show that at these laser powers only pure $POCl_3$ is responsible for SRS, and the rare earth ions and the additional liquid components act like inactive participants in SRS.

At the powers used in this experiment (128 MW/cm^2), the SRS gain calculated from the spontaneous Raman emission is 0.3 cm^{-1} while the actual measured SRS gain is ~0.33 cm^{-1}. The rough agreements of the calculated and measured values indicate that self-focusing is not playing a dominant role. Since the gain figures are close, we can get a reasonable picture of the role of Raman scattering inside a laser cavity by using the experimental SRS gain value. Electronic self-focusing due to the rare earth ions in the $POCl_3$ solution is not present, since the laser solution has a higher threshold and a similar gain as the pure $POCl_3$ solution. Self-focusing, due to the orientational Kerr effect, might be expected since the reorientation time of a $POCl_3$ molecule is ~10^{-11}s. However, we were unable to photograph self-focusing.

To summarize the experimental results, (1) large amounts of Raman conversion occur only at high power and long cell lengths, typically 100 MW/cm^2 and ℓ = 50 cm; (2) the threshold and conversion efficiency for SRS in laser solutions are comparable to many non-self-focusing liquids. In long-pulse operation, no limitations on laser performance is to be expected from nonlinear effects.

A more complete description of the stimulated scattering effects is provided in Appendix E, and Appendix F describes the measurement of the Kerr constant in $SeOCl_2$.

2.4 PHYSICAL PROPERTIES OF APROTIC SOLVENT SOLUTIONS

The physical properties of these laser solutions are important quantities in the design of laser systems. The index of refraction and its temperature dependence play a significant role in system design and in understanding the thermo-optical behavior of the laser. Other constants, such as viscosity, thermal conductivity, density and heat capacity are basic in the design of circulatory systems and in controlling the thermal gradients. Some of these have been measured but, for the most part, there are gaps in our knowledge. In this section we will present the available information and indicate the deficiencies.

2.4.1 The Index of Refraction

The index of refraction of selenium oxychloride and selenium oxychloride based solutions was determined by a team from the National Bureau of Standards. For this work they used a hollow glass prism constructed from carefully fabricated plane parallel slabs, and they measured the deflection of a collimated beam at different frequencies. The results are presented in the first six entries in Table 2-10. The measurements on $POCl_3$:$SnCl_4$ and $POCl_3$:$ZrCl_4$ were made at a later time using a minor variation of the same technique.

2.4.2 Viscosity and Density

The viscosity measurements were made with an Ostwald viscosimeter using an 80% glycerine-water solution η(viscosity) = 45.86 cp (centipoise) as a calibrating fluid. A negative pressure of 150 Hg was maintained at the efflux end of the viscosimeter to keep the measurement times at a reasonable level. The results of these measurements are listed in Table 2-11.

For solutions containing $SnCl_4$, both in $SeOCl_2$ and $POCl_3$, the viscosity increases markedly with increasing concentration of the Lewis acid. The lowest viscosity (for a stable solution) attainable with $SeOCl_2$ is 9 cp while with $POCl_3$ it is 6.3 cp. The laser solution, using $ZrCl_4$, has a viscosity of about 5 cp which is the lowest.

TABLE 2-10

REFRACTIVE INDEX OF LASER SOLUTIONS

Material	Refractive Index at				Accuracy	Temperature (°C)
	0.5086μm	0.6678μm	0.7947μm	1.083μm		
$SeOCl_2$	1.66500	1.64188	1.63333	1.62437	$\pm 3 \times 10^{-5}$	22.9
$SeOCl_2$:$SnCl_4$ (25:5)	1.67875	1.65579	1.64717	1.63826	$\pm 4 \times 10^{-5}$	22.9
$SeOCl_2$:$SnCl_4$ (29.5:0.5)	1.66689	1.64379	1.63522	1.62625	$\pm 2 \times 10^{-5}$	22.5
0.3M Nd^{+3} Laser Solution $SeOCl_2$:$SnCl_4$	1.69079	1.66733	1.65852	1.64929	$\pm 3 \times 10^{-5}$	22.8
0.03M Nd^{+3} Laser Solution $SeOCl_2$:$SnCl_4$	1.67701	1.65394	1.64541	1.63640	$\pm 1 \times 10^{-5}$	22.7
$SnCl_4$	1.51847	1.50536	1.50027	1.49491	$\pm 2 \times 10^{-5}$	22.3
		0.6328μm		1.06μm		
0.3M Nd^{+3} Laser Solution $POCl_3$:$SnCl_4$		1.4879		1.4789	$\pm 5 \times 10^{-4}$	
0.3M Nd^{+3} Laser Solution $POCl_3$:$ZrCl_4$		1.4873		1.4783	$\pm 5 \times 10^{-4}$	

TABLE 2-11[a]

VISCOSITY AND DENSITY OF LASER SOLUTIONS

Solution	Viscosity (cp)	Density (gcm^{-3})
$SeOCl_2$	3.0	
$SeOCl_2$:0.3M Nd^{+3}:2.45M $SnCl_4$	190.0	
$SeOCl_2$:0.3M Nd^{+3}:1.45M $SnCl_4$	27.0	
$SeOCl_2$:0.3M Nd^{+3}:0.45M $SnCl_4$	9.0	
$POCl_3$	1.01	1.645
$POCl_3$ with 1% H_2O	1.09	
$POCl_3$:0.3M Nd^{+3}:1.33M $SnCl_4$	10.42	1.91
$POCl_3$:0.3M Nd^{+3}:1M $SnCl_4$ (Comm[b])	6.32	1.86
$POCl_3$:0.3M Nd^{+3}:0.45M $ZrCl_4$ (Comm[b])	5.40	1.79
$POCl_3$:0.3M Nd^{+3}:0.45M $ZrCl_4$	3.95	1.78

[a]All measurements made at 25°C.

[b]Commercial material supplied by Sylvania Chemical and Metallurgical Division, Towanda, Pennsylvania.

2.4.3 Passive Scattering Losses

The molecular entities in the inorganic liquid laser solutions are large and may even be small chain polymers. As such, these may give rise to yet another kind of scattering, that could function as a loss mechanism. The possibility of such a loss, which we designate as a passive loss, was investigated.

These investigations were carried out by three different methods; a transmission measurement, a right angle scattering measurement, and by determining how the insertion of such a solution in the cavity affected the threshold of a cw Nd^{+3} YAG laser and comparing this with a known loss. This is called the static loss. The transmission measurement is difficult to carry out precisely at the levels of loss involved. The scattering measurement is performed by passing a He-Ne laser beam through the solution, and measuring the radiation scattered at a right angle to the beam. This has to be calibrated by reference to one of the other two methods. The details of the experimental methods are discussed in detail in Appendix G. The results of these measurements are given in Table 2-12.

TABLE 2-12

LIGHT SCATTERING AND TRANSMISSION LOSS IN VARIOUS LIQUIDS

Material	Light Scatter (Arbitrary Units)	Transmission Loss at 1.06μ (% per cm)	Method
Water	0.15	>1.0	Transmission[a]
Ethanol	0.25	>1.0	Transmission[a]
Benzene	1.0	>1.0	Transmission[a]
CCl_4	0.4	0.10	Static Loss
$POCl_3$	0.4	0.10	Static Loss
$POCl_3 + ZrCl_4$	0.6		
$H_2O + ZrCl_4$	0.5	>1.0	Transmission[a]
H_2O + Nd (TFA)$_3$	0.4	>1.0	Transmission[a]
0.3M Nd^{+3} in $POCl_3$-$ZrCl_4$	2.5	0.16	Static Loss
		0.2-0.3	Transmission
(Contaminated with H_2O)	4.5	0.26	Static Loss
(Contaminated with H_2O)	15.0	0.60	Static Loss
0.9M $P_2O_3Cl_4$ in $POCl_3$	0.8		Static Loss

[a] Loss values greater than 1% per cm by direct transmission measurement indicate that absorption band in the medium, rather than scattering is a major loss.

A number of significant points were revealed by the measurements. The laser solutions must be filtered to prevent a high scattering loss. Hence, all solutions studied in detail were filtered through an ultrafine sintered glass frit having a nominal pore size of 1μ. Measurements were made on many different solutions, although not all methods were used on all samples. The solutions studied include:

1) Pure liquids: water, alcohol, benzene, CCl_4, $SeOCl_2$, $POCl_3$.

2) Mixtures of various components: $SeOCl_2 + SnCl_4$, $POCl_3 + SnCl_4$, $POCl_3 + ZrCl_4$, $Nd(CH_3COO)_3 + H_2O$.

3) Various standard laser solutions: 0.3M Nd^{+3} in $SeOCl_3 + SnCl_4$, in $POCl_3 + SnCl_4$, in $POCl_3 + ZrCl_4$, with and without H_2O contamination.

4) Dilutions of standard laser solutions with pure solvent: 0.1M and 0.03M Nd^{+3}; solutions prepared by reaction of sodium trifluoroacetate with $POCl_3$ to produce various concentrations of $P_2O_3Cl_4$.

The results of the measurements are listed in Table 2-12. To summarize the more important points: all the pure components of the laser solutions ($POCl_3$, $POCl_3 + ZrCl_4$, $SeOCl_2$, Nd^{+3} in H_2O), as well as some other pure liquids (alcohol, water) give scattering measures of 0.1-0.5; however, when Nd^{+3} is present in the $POCl_3$ or $SeOCl_2$ mixture, the scattering measure is 2.5-3.0, a factor of 6-8 higher. It is also noteworthy that the ratio of the scattering values for the two pure solvents CCl_4 and benzene (0.4) is in good agreement with that found by others (0.37).[60]

A linear correlation was found between the scattering values and the transmission losses, which ranged between 0.1% and 0.3% per cm. The scattering loss for the pure $POCl_3$ liquid comes out as about 0.015% per cm at 1.06μ and the absorption loss as about 0.06% per cm. The latter value is higher than expected, probably due to trace amounts of contamination by H_2O which has a significantly intense absorption of 1.06μ. The scattering loss for the complex itself is 0.1% per cm at 0.3M concentration.

$POCl_3$ solutions that have been contaminated with H_2O, even if subsequently dehydrated by distillation, invariably have high scattering (of the order of 10 or higher), high loss (greater than 0.5% per cm) and are also quite viscous. This is attributed to an excessively high concentration of polyphosphoryl chloride polymer. Reduction of the viscosity can be accomplished by addition of PCl_5 (which selectively degrades this polymer), but the scattering does not go below the "base level" of 2.5, and further addition of PCl_5 causes the Nd^{+3} to precipitate. Since solutions containing only the

polyphosphoryl chloride polymer gave scattering values considerably less than laser solutions of equal polymer concentration, it would appear that the scattering entity is a complex containing both Nd^{+3} and the polymer.

From this work we conclude that:

1) A distinct scattering loss is characteristic of those aprotic liquid laser solutions, even after all particulate matter is removed.

2) This scattering loss can be reduced to a minimum value intrinsic to the medium, below which we cannot go without deleterious chemical effect.

3) The scattering appears to be caused by a highly polarizable complex of Nd^{+3} and $P_2O_3Cl_4$ (and also longer polymeric phosphoryl chlorides). The latter compounds are components of the $POCl_3$-based laser solution and are essential to the solubility of the active ion.

4) A laser solution (0.3M Nd^{+3} in $POCl_3$-$ZrCl_4$) has a loss corresponding closely to the absorption loss at 1.06μ and is a good laser medium.

2.4.4 Other Physical Properties

The other physical properties that are of interest are the thermal conductivity and the specific heat. For these there is little or no information, and we have not made any such measurements.

Birnbaum and Gelbwachs[46] report a heat capacity of 0.22 cal/g°C for Nd:$POCl_3$:$ZrCl_4$ solutions, but give no reference, nor do they indicate making the measurement themselves. The most extensive report of physical properties is made by Zhabotinsky et al.[21] who give the following: heat capacity: 0.32 cal/g°C; coefficient of volume expansion: 10^{-3}/°C; density: 1.88 gcm^{-3}; viscosity: 4.23 cp at 20°C; refractive index: 1.525 at 20°C; and a temperature dependence of refractive index: $(-5 \pm 2) \times 10^{-4}$/°C at 20°C. The authors do not specify the Lewis acid used with $POCl_3$ and state that they used a number of systems. From the information given, particularly with respect to refractive index and density, it appears that the Lewis acid is $SnCl_4$. We have assumed that they are correct in stating that these values are typical for such systems. This is probably so since the majority component, by far, is $POCl_3$.

2.5 DISCUSSION AND SUMMARY

From the work presented in this section, the general conclusion is that substantial progress has been made in our understanding of how to make these solutions and how they work. The preparative procedures require a meticulous attention to detail and extreme care and quality control is essential if a good, long-lasting laser solution is to be made. Many of the details of the chemistry and structure of the molecules are still unclear; what is also unclear is how important these details are to the laser performance itself. However, it is possible that such knowledge could be helpful in terms of understanding solution stability. Finally, on a purely chemical basis, it would be of great interest to study the behavior of other Lewis acids in $POCl_3$; it is already clear that they all do not behave similarly. In terms of physical properties, it would be extremely useful to have more and better information on the thermal and mechanical properties of the solutions, particularly on how they depend on the chemical composition.

3. LIQUID LASER SYSTEMS — STATIC AND CIRCULATORY

Since we are concerned with a liquid active laser medium, we can expect to find some unique features. Even though this is a condensed phase, it is obvious that some form of container or cell is required and for static and circulatory liquid lasers, this feature requires some explanation. The system design considerations center around the chemical properties of this particular set of liquids, but by and large, the laser system physically resembles other solid state lasers. In the case of a circulatory liquid laser, flow characteristics must be taken into account.

The first section is concerned with static systems. This is relatively brief and, for the most part, traces out the development of laser cells. The bulk of the material relates to circulatory systems. The details of the design considerations involved in such systems represents a major contribution and must form the basis for any continuation of this work. The presentation centers principally around the last system we built but the evolution of the various components such as pumps, cells, etc., is also given so that future investigators can avoid some of the pitfalls and traps into which we stumbled.

3.1 STATIC LIQUID LASERS

3.1.1 Cells

To achieve laser oscillation the liquid can actually be contained in any kind of transparent enclosure. The extreme example of this is a simple one-cm diameter sphere. Such an enclosure was designed to study certain fluorescence properties but the experiment was defeated because the fluorescence exhibited nonlinear or supralinear behavior when excited by a flash lamp. While actual oscillation was not observed in this case (probably the input energy to the flash lamp was not high enough), the next simplest case did produce a laser. This cell was, in effect, nothing more than a piece of quartz sealed off rather arbitrarily at each end. The laser solution was admitted through a side arm which was then sealed. When the solution was excited, laser oscillations were observed; this is illustrated in Figure 3-1. Such an arrangement is indicative only of the high gain of the material and would be of no value for the acquisition of quantitative information.

The first cells used are illustrated in Figure 3-2. The tube ends and windows were finished as parallel and as optically flat as possible. The windows were optically contacted to the tube and these quartz components diffusion bonded to make a permanent

seal. The liquid was admitted through the side arm which was closed by the tapered stopper. Such cells had many drawbacks. First, during the heat treatment involved in the diffusion bonding, the parallelism of the end windows was degraded; often by as much as 15 minutes/arc. Second, the single entry port was an insufficient shock absorber and the cells, when subjected to high input energy flashes, frequently ruptured at the opposite end. The rupture did not occur at the diffusion bond but at some point up to about 2 mm into the cell. Thirdly, the cells were difficult to clean and, finally, were consistent only with a plane parallel geometry.

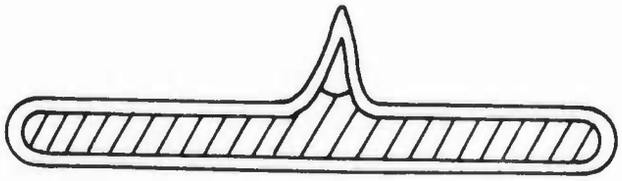

Figure 3-1. Primitive Flame-Sealed Laser Cell

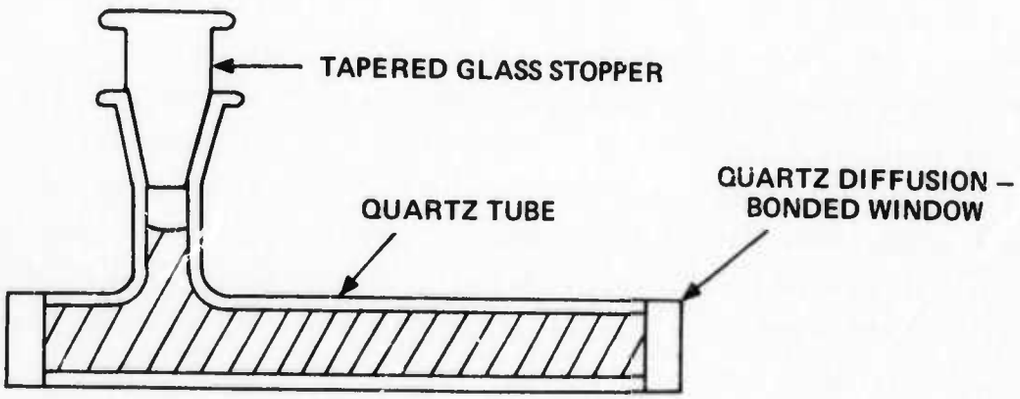

Figure 3-2. Quartz Diffusion-Bonded Laser Cell

A major advance was achieved when the windows were made demountable. Such cells were in every way similar to the diffusion bonded cells except that an O-ring groove was cut into the end of the cell body. The windows were compressed onto the cell and held in place by two stainless steel washers connected by three tie rods; this is illustrated in Figure 3-3. The tension in the tie rods was adjusted by tightening the nuts on the tie rods. Since these were independently adjustable, there was a certain amount of play even after interference rings became visible between the cell window and body and parallelism could usually be achieved. The entire structure was made possible by a Teflon covered O-ring seal. These consist of a silicone O-ring encased in a Teflon tube sealed on itself so that no liquid permeated the Teflon to attack the silicone rubber. These cells had the advantages of being easy to clean and dry, involved no costly diffusion bonding step and offered great flexibility. The latter aspect is best illustrated by the ease with which such parameters as bore diameter and window thickness and configuration could be altered. The windows could be fabricated with Brewster angle terminations on one side and a flat on the other. They were even made with two different Brewster angles, one appropriate for the air-quartz interface and the other for the liquid-quartz interface. Finally, the cell body could be made of Pyrex instead of quartz. The use of two expansion volumes eliminated the rupture problem; the use of tie rods probably also helped. The major disadvantage of this structure was that the rods obscured some flash lamp radiation.

The final modification is illustrated in Figure 3-4. This type of cell is basically identical to the simple demountable cell except that the cell body ends are thickened and machined into a conical shape. The windows are now held on by two stainless steel washers. The one outside the cell window is the same as in the earlier demountable cell. The second ring has a large enough opening so that it fits over the thickened cell body end and the washer opening is tapered at the same angle as the cell body. A split nylon sleeve sits between the cell body and stainless steel washer. The two washers are drawn together by three screws until the cell window is contacted to the cell body. This design eliminates the tie rods but introduces an umpumped liquid volume. This is removed by counter boring thickened ends and extending the window by a "nosepiece" arrangement so that the liquid-quartz interface occurs where the laser liquid is being pumped.

The results reported in this section were obtained with one or another of the types of cells described; the bulk of it with the demountable cell shown in Figure 3-3 and, unless otherwise specified, it can be assumed that such a cell was used.

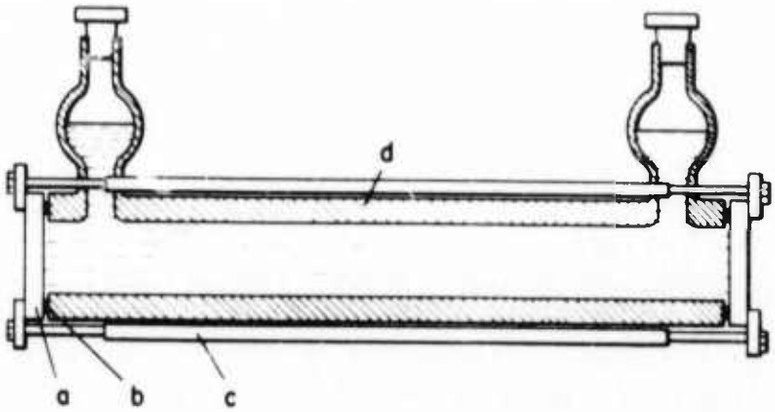

Figure 3-3. Laser Cell: (a) cell windows, (b) Teflon-coated silicone O-ring, (c) Invar tie rods, (d) cell body.

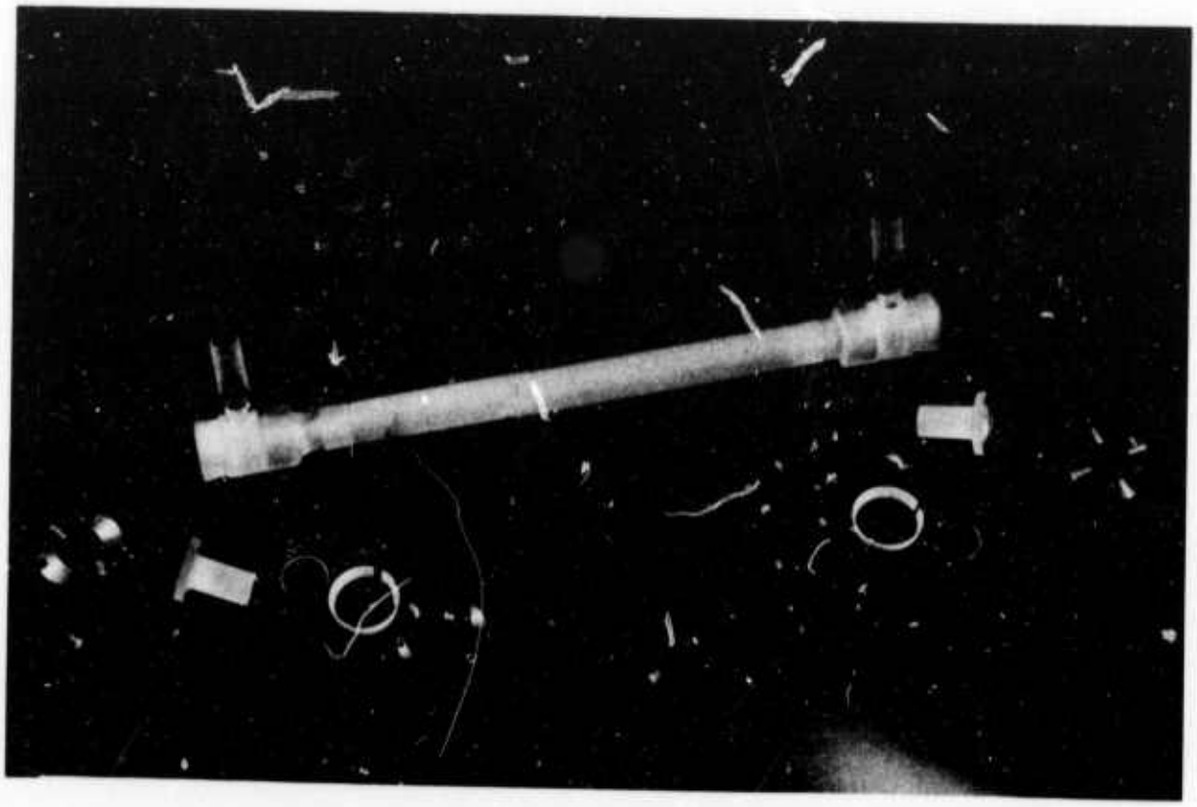

Figure 3-4. Laser Cell, Disassembled. Shown in photograph are the cylindrical cell, the plug windows and the components required to assemble the cell.

3.1.2 Flash Heads

All flash heads used two lamps located as close as possible to the cell. The lamp-cell configuration was tightly enclosed in a wrapping of 5-mil aluminum which also served as the means for introducing the external trigger pulse. The cell and lamps protruded through two mica-lex end plates which served as a support. The box-like flash enclosure was completed by metal sides and base and a demountable metal top. The optical resonator consisted of two external mirrors aligned by an autocollimator so that the cell faces and the mirrors were parallel. Most of the experimantal work on static lasers was done with a plane parallel resonator.

3.2 CIRCULATORY SYSTEMS

It became apparent very early in this work that, because of the spectroscopic and physical characteristics of the liquid medium, the most natural application of the liquid laser medium was in the generation of high average output powers in a repetitively flash-pumped mode of operation. The liquid laser medium has unique advantages in the high average power mode of operation. Since all flash-lamp pumped lasers are relatively inefficient, a large fraction of the input power to the device will appear as heat to be removed. At a minimum, the amount of heat that must be dissipated in Nd^{+3} lasers under flash excitation must equal the amount of laser output power. A more realistic estimate might be twice the maximum expected output power. Thus, we see that if we desire to construct a long-pulse oscillator with an average power output of 500 watts, we must reckon on dissipating about one kilowatt of heat in the laser medium. This is a serious problem in solid-state Nd^{+3} lasers where the only means of removing this heat is by thermal conduction. As an example, consider a 1/2-inch diameter by 6-inch long YAG rod whose thermal conductivity, K, is 0.07 watts cm^{-1} $°C^{-1}$.[61] Let us assume we wish to generate an average output power of 500 watts from this rod and therefore must dissipate about one kilowatt of heat in the rod. The average heat generated per unit volume is, therefore,

$$W_i = \frac{10^3 \text{ watts}}{\pi r_o^2 L} \simeq 50 \text{ watts cm}^{-3}$$

The temperature difference between the center of the rod and the rod outside surface will be given by:[62]

$$T_{CL} - T_o = W_i^2 \frac{r_o^2}{4K} \simeq 70°C$$

if we assume that the heat generation, W_l, is uniform across the rod diameter. Such a large temperature differential must lead to a large refractive index change across the rod, assuming that the rod will withstand the radial stress imposed by such a large thermal gradient.

In liquid laser media the situation is quite different. First of all, if we circulate the liquid through the laser cell, a large portion of this heat can be removed from the active region by the mass transport of the liquid, which is then cooled in an external heat exchanger. If we consider a repetitively flash-pumped laser in which several cell volumes of laser liquid are exchanged between each succeeding shot, this process can dissipate more than 80% of the heat generated during the pulse. The rest of the heat load is dissipated by forced convection in the radial direction. It is important to note that even though the thermal conductivity of the laser liquid is about a factor of 10 smaller than that of YAG, the radial transport of heat in the liquid is greatly aided by the flow of the liquid so that the heat transport rate in the liquid laser is, in general, much larger than that in the crystalline YAG.

The design and construction of the circulatory system for the Nd^{+3} laser liquid presents a set of unique problems for the laser designer. These arise partly from the chemical properties of the inorganic liquid laser medium and partly from the use of a liquid as the active laser medium. Some of the problems are then unique to this laser and others to the general class of liquid lasers. These unique problems, forming a set of design constraints for the construction of the system, are detailed below.

a) The laser liquid $POCl_3$:$ZrCl_4$:Nd^{+3} is an acid which will attack most materials. For example, most rubbers (natural and synthetic) are hardened to the point of brittleness because the liquid leaches out the plasticizers. The problem of gasket seals for the laser circulatory system is, therefore, made more difficult.

b) The laser liquid is a powerful dessicant, absorbing water any possible way. Above a certain level, water absorbed in the solution causes a precipitate, $ZrOCl_2$, resulting in a large and rapid increase in optical scattering which destroys laser action in the liquid. In general, a water contamination level of 100 ppm in a freshly-made sample of laser liquid is the upper limit tolerable, although several batches of liquid have precipitated at water levels in a factor of five lower than this. As a result, water contamination must be reduced and maintained at 20 ppm in the circulatory system liquid to be assured of stable operation.

c) The circulatory system must be carefully designed to avoid hydrodynamic instabilities (cavitation) while maintaining a large volume flow rate through the laser cell(s). Typical values for Reynold's Numbers in the system are on the

order of 10,000 (turbulent flow regime). Because of this, pipe bends, unions and couplings must be designed to avoid flow separations and sharp pressure drops.

d) A high optical quality must be maintained in the laser cells. This means that scattering from abraded particles in the laser solution must be kept to an absolute minimum. The laser cells themselves must be designed for a well-mixed, stable fluid flow pattern for best optical performance. In addition, good optical coupling must be provided between the laser cells and flashlamps.

e) Because of the corrosive nature and moderate health hazard of the solvents used in the laser liquid, adequate safety margins must be built into the circulatory system to protect against breakage or catastrophic seal failures. It should be noted that, although we have experienced many problems working with these laser solutions over the years, we have never had a catastrophic system failure that might have endangered the health and safety of any project personnel.

The above considerations eventually lead to the construction of a hermetically-sealed circulatory system with multiple laser cells arranged in a series flow combination. The ability to have more than one laser cell in the circulatory system points out an important economy factor for the Nd^{+3} liquid laser, in that a single pump and heat exchanger are capable of operating several liquid laser cells. A schematic drawing of the most recent system constructed is shown by Figure 3-5, demonstrating just this point.

In this diagram, Head 1 is a 4-lamp, quad-ellipse flash enclosure pumping a 7/8-inch I. D. by 10 inches long laser cell; Head 2 is a two-lamp, dual-ellipse flash enclosure around a 5/8-inch I. D. by 10 inches long laser cell; and Head 3 is another two-lamp, dual-ellipse enclosure surrounding a 1/2-inch I. D. by 6-1/2 inches long cell. With the proper power supplies and flashlamp driving circuits, the system is also capable of operation in an oscillator-amplifier mode.

The only item in the circulatory system which is not self-explanatory is the "free surface" shown between Heads 1 and 2. This consists of a vertical standpipe topped by a half-filled spherical chamber of about 0.5 liters capacity located midway on the connecting pipe between the two laser heads. This arrangement has two functions; the first is to act as a sort of shock absorber for the pressure wave generated in the liquid by the rapid thermal expansion of the fluid in the laser cells under flash excitation.

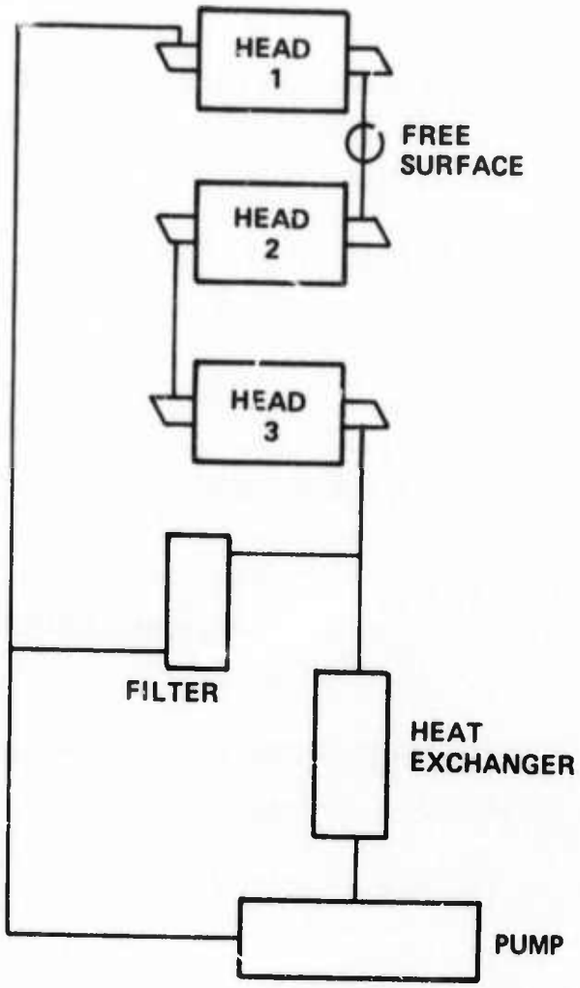

Figure 3-5. Liquid Laser Circulatory Schematic Diagram

The second function of the arrangement is provided by connecting the top of the spherical chamber to a large (5 liters) gas ballast. By means of an external source of dry nitrogen, the static pressure of the entire system can be regulated above or below ambient. As the surface of the liquid in the standpipe is also the highest point in the circulatory system: this also provides a convenient means of collecting and releasing bubbles from the system when filling.

In this section we will describe in detail the design and the factors affecting the design of the circulatory system, and the cells. We will also describe the flash enclosures, the cooling system and the power supply.

3.2.1 Circulatory System Design and Calculations

One of the most important factors in the design of the circulatory system is the system pressure vs. volume flow rate characteristic. This curve along with the pump pressure head vs. volume flow rate information enables us to determine the system flow as a function of either pumpshaft rpm or power supply setting. The pump data is usually supplied by the manufacturer but the system data must be calculated from the geometry of each of the components and the physical constants of the laser liquid. Because of the importance of establishing the operating characteristics of the system, these calculations will be presented for the latest liquid laser system shown schematically in Figure 3-5.

3.2.1.1 System Pressure Head Calculations

In general, the pressure drop across an element ma be written in the form:

$$\Delta p = p_1 - p_2 = \rho g(y_2 - y_1) + (\rho/2)(v_1^2 - v_2^2) \qquad (3\text{-}1)$$

Where:

p_1, p_2 = pressure at points 1, 2

v_1, v_2 = mean stream velocities at 1, 2

y_1, y_2 = mean channel height at 1, 2

ρ = fluid density

g = acceleration due to gravity

Dividing each side of the equation by ρg, we arrive at Bernoulli's equation:

$$\frac{p_1 - p_2}{\rho g} = (y_2 - y_1) + \frac{1}{2g}(v_1^2 - v_2^2) \qquad (3\text{-}2)$$

where each term in this equation has the dimension of length. The reduced pressure terms in this form are called heads and in English units are measured in feet. Descriptively, Eq. (3-2) states that the total head across an element is equal to the static head drop plus the dynamic head loss and is strictly applicable only to an inviscid, incompressible fluid under irrotational flow. If we consider only liquids which can be assumed to be incompressible, the liquid viscosity and flow separation in a confining channel leading to rotational flow patterns must modify this equation. The general engineering approach to this problem divides the dynamic head loss term into two parts:

$$\text{dynamic head loss} = \text{expansion or compression head} + \text{friction head loss} \qquad (3\text{-}3)$$

and proceeds through theory and experiment to express these in terms of factors involving the physical properties of the liquid. A complete exposition of this development is beyond the scope and needs of this report, so we shall simply present the commonly-used results pertinent to our calculations.

One of the most important of the dimensionless quantities used in fluid mechanics is the Reynolds Number, R_e, for an average-fluid flow velocity, V, in a channel of hydraulic radius, r_h, given by:

$$R_e = 4 V r_h (\rho/\mu) \qquad (3\text{-}4)$$

Where:

ρ = fluid density (gm cm^{-3})

μ = dynamic viscosity (poise = gm cm^{-1} sec^{-1})

r_h = hydraulic radius = $\dfrac{\text{channel cross-sectional area}}{\text{wetted perimeter}}$ (cm)

$= \dfrac{\pi r^2}{2\pi r} = \dfrac{r}{2}$ for a cylindrical pipe of radius r.

The volume rate of flow Q in the channel of cross-sectional area A is given by:

$$Q = AV (cm^3\ sec^{-1}) \qquad (3\text{-}5)$$

Eq. (3.4), therefore, becomes in a cylindrical pipe of diameter D = 2r,

$$R_e = \frac{4Q\rho}{\pi D \mu} \qquad (3\text{-}6)$$

Three distinct conditions of fluid flow are identified by ranges of the Reynold's Number, as follows:

$$\begin{aligned} R_e &< 2000 \quad : \text{ laminar flow} \\ 2000 < R_e &< 3000 \quad : \text{ transition flow} \\ R_e &> 3000 \quad : \text{ turbulent flow} \end{aligned} \tag{3-7}$$

Under laminar flow conditions, the velocity profile of the fluid flow across the pipe diameter is parabolic. Under extreme turbulence, this profile flattens out over the central region of the pipe and becomes more steep near the pipe wall. A further discussion of the properties of turbulent vs. laminar flows will be presented later.

In general, the friction head loss, H_f, for incompressible fluid flow in smooth bore circular pipes may be written as:

$$H_f = f\left(\frac{L}{D}\right)\frac{V^2}{2g} \tag{3-8}$$

Where:

L, D = pipe length, diameter
V = average flow velocity [from Eq. (3-5)]
g = acceleration due to gravity (32.2 ft sec^{-2} or 981 cm sec^{-2})
f = dimensionless friction factor.

The value of this friction factor can be well approximated in the laminar and turbulent flow regions as:[63]

$$\begin{aligned} f &= \frac{64}{R_e} \quad \text{(laminar flow)} \\ &= \frac{0.316}{R_e^{1/4}} \quad \text{(turbulent flow)} \end{aligned} \tag{3-9}$$

The second dynamic head loss term in Eq. (3-3), the expansion or compression head loss, H_e or H_c, may be defined similarly to Eq. (3-8) as:

$$H_e, H_c = \left(K_e, K_c\right)\frac{V^2}{2g} \tag{3-10}$$

In this case, the average fluid velocity, V, is defined as that in the <u>smaller</u> of the joining pipe cross-sections. The constants, K_e, K_c, have been measured and are most conveniently presented in graphical form as functions of the cylindrical pipe diameter ratio (diameter smaller pipe/diameter larger pipe). Such a graph is shown as Figure 3-6.[64] A third

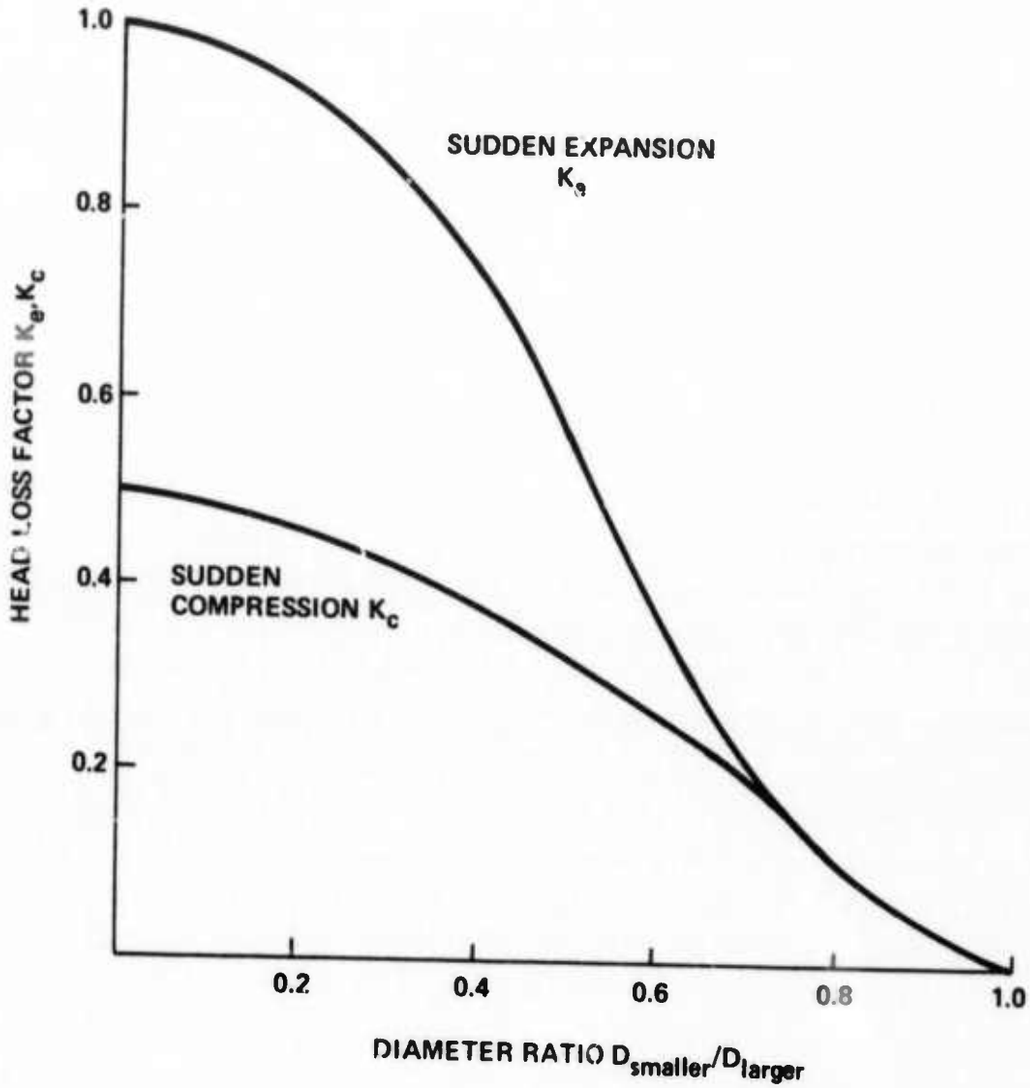

Figure 3-6. Expansion and Contraction Head Loss Factors as a Function of Pipe Diameter Ratio

dynamic head loss term arises in bent tubes or tubing elbow couplings. If the flow in the pipe is turbulent (as it is in almost all of the calculations we will encounter), this loss can be expressed formally by an equation like Eq. (3-10) with a head loss factor, K_b, which is a rather complicated function of the radius of the bend relative to the pipe diameter, the angular degree of the bend and the Reynold's Number of the flow. Such factors as used in the calculations are taken from the design charts and graphs of reference 64.

As an actual example of these calculations as applied to the design of the latest Nd^{+3} liquid laser system, these formulae will be applied to each of the elements in turn of the system as shown in Figure 3-5. A brief description of the component precedes each calculation (presented in tabular form). The head losses of the components in series in the circulation loop are then summed to yield the system pressure head loss. A particle filter in a bypass loop with volume flow rate less than 10% of the main loop is then assumed so that the bypass flow may be neglected with respect to the main loop flow. Flow through the bypass is reduced by the addition of a constriction in the loop to achieve this. Finally, the pump head characteristics are introduced to determine the system operating characteristics. Final estimates of system head losses are considered accurate to only about ±20% but, because of the largely quadratic dependence of H on Q, the final estimates of system volume flow-rates and Reynold's Numbers should be accurate to ±10%. In this calculation, the circulating fluid is assumed to be the Nd^{+3} liquid laser solution with a density $\rho = 1.8$ gm cm^{-3}, and a dynamic viscosity of $\mu = 5$ centipoise $= 5 \times 10^{-2}$ gm cm^{-1} sec^{-1}.

3.2.1.2 Liquid Laser Cells

Three laser cells of different active lengths and internal diameters are used in this system. These cells can be visualized as consisting of identical entrance and exit chambers connected by a cylindrical flow tube. In all three cells, the entrance and exit chambers are identical; only the flow tube joining them is changed in length and internal diameter to meet the individual laser requirements. The individual cell dimensions and design parameters are show by Table 3-1.

The type of cell used is illustrated in Figure 3-7. The body of the cell is Pyrex tubing of the appropriate bore diameter and wall thickness. Sealed to each end of the tube is a truncated conical Pyrex end piece having a centrally located hole the same size as the bore diameter of the tube. In actual fabrication, one conical piece is first attached and a water jacket of appropriate dimensions slipped over the unfinished

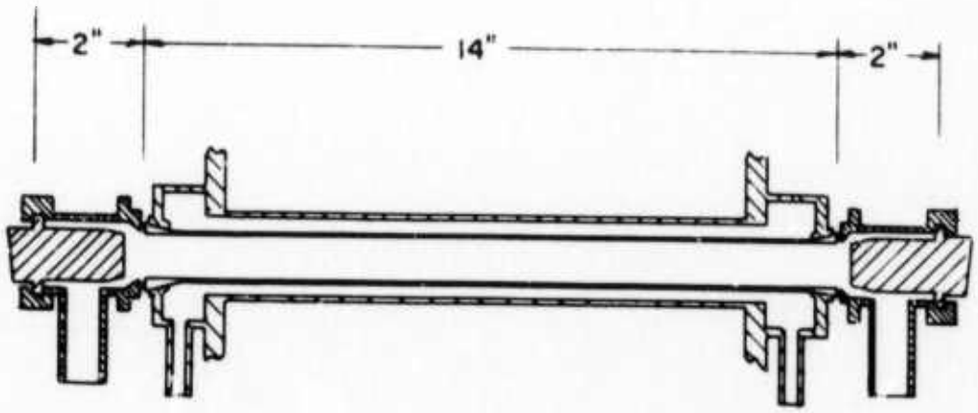

Figure 3-7. Cutaway View of Actual Water-Jacketed Laser Cell Demonstrating Cell Assembly

TABLE 3-1

CELL DIMENSIONS AND FLASH HEADS FOR LIQUID LASER SYSTEM

Item	Head 1	Head 2	Head 3
Flash Enclosure	Quad Ellipse	Dual Ellipse	Dual Ellipse
Number of Lamps	4	2	2
Pumped Cell Length	10 inches	10 inches	6-1/2 inches
Cell Bore Diameter	7/8-inch (2.2 cm)	5/8-inch (1.6 cm)	1/2-inch (1.3 cm)
Cell Active Volume	100 cm^3	50 cm^3	20 cm^3
E_{input}/pulse (maximum)	4000 joules	2000 joules	750 joules
Maximum Rep. Rate	5 pps	10 pps	20 pps
Laser Cell Wall Thickness	0.14 cm	0.10 cm	0.08 cm
Thickness of Water Coolant Layer	0.31 cm	0.20 cm	0.14 cm
Glass Water Jacket Thickness	0.10 cm	0.10 cm	0.10 cm
O. D. of Glass Water Jacket	3.32 cm	2.40 cm	1.90 cm

end and then the second conical piece is added. The thick ends of the cell are ground and polished to be flat and parallel. Teflon-covered O-rings are used to seal the finished cell body to nickel plenum chambers consisting of a nickel tube with an inlet pipe at right angles which is terminated with a bead to mate to a Corning glass pipe used for connecting the circulatory system. The assembled cell is then completed at each end by a two-inch thick homosil quartz window. The end of the window facing the liquid and the nickel transition piece are both tapered as they approach the cell entrance so that the window diameter matches the cell diameter. The annular space between the window and the nickel transition piece is made to have an area as close as possible equal to the cell cross-section. In this way the velocity of the liquid, on entering the cell, changes in direction only but not in speed.

The volume enelosed by the niekel transition pieee acts as a plenum chamber. There is vigorous mixing as the liquid flow enters and is diverted by the nosepiece of the cell window. The flow then assumes a new direetion and the liquid enters onto its journey down the cell (pipe). Figure 3-8 is a full-scale drawing showing the detailed eonstruetion of the nickel plenum chambers at either end of the laser eell.

Dynamie head losses for the laser eells are ealeulated by modeling the eell as a series of pipe expansions, eompressions and right angle bends in the niekel plenum chambers plus a pipe frietion head due to flow through the aetive region of the eell. Sinee a flow expansion at one region of the entranee plenum chamber is a flow eompression at the exhaust plenum, the niekel ehambers may be treated simultaneously. With refer-enee to the eell schematie of Figure 3-9, the entire eell model can be visualized as the following:

a) an expansion (contraction) from A_o to A_1
b) right angle bend (2) at effeetive area A_1
e) expansion (eompression) from area A_1 to A_2
d) right angle bend (2) at area A_2
e) expansion (eompression) from area A_2 to A_3
f) right angle bend (2) at area A_3
g) compression (expansion) from area A_3 to A_4
h) friction loss through pipe.

As a numerical example, we will ealeulate the head losses for the cell with a bore diameter of 7/8 inches (22.2 mm) and a pipe length of 14 ineh̃es (35.5 cm). From the dimensions of Figure 3-9, the respeetive eross-seetional areas for the eell are:

$$A_0 = \pi (0.500 \text{ in})^2 = 0.485 \text{ in}^2$$

$$A_1 = \pi (0.437 \text{ in})^2 = 0.601 \text{ in}^2$$

$$A_2 = \pi [(0.665 \text{ in})^2 - (0.500 \text{ in})^2] = 0.604 \text{ in}^2$$

$$A_3 = \pi (0.875 \text{ in})(0.281 \text{ in}) = 0.772 \text{ in}^2$$

$$A_4 = \pi (0.437 \text{ in})^2 = 0.601 \text{ in}^2$$

a) $\sqrt{A_1/A_0} = 0.875$

From the graph of Figure 3-6,

$$K_e, K_e = 0.04$$

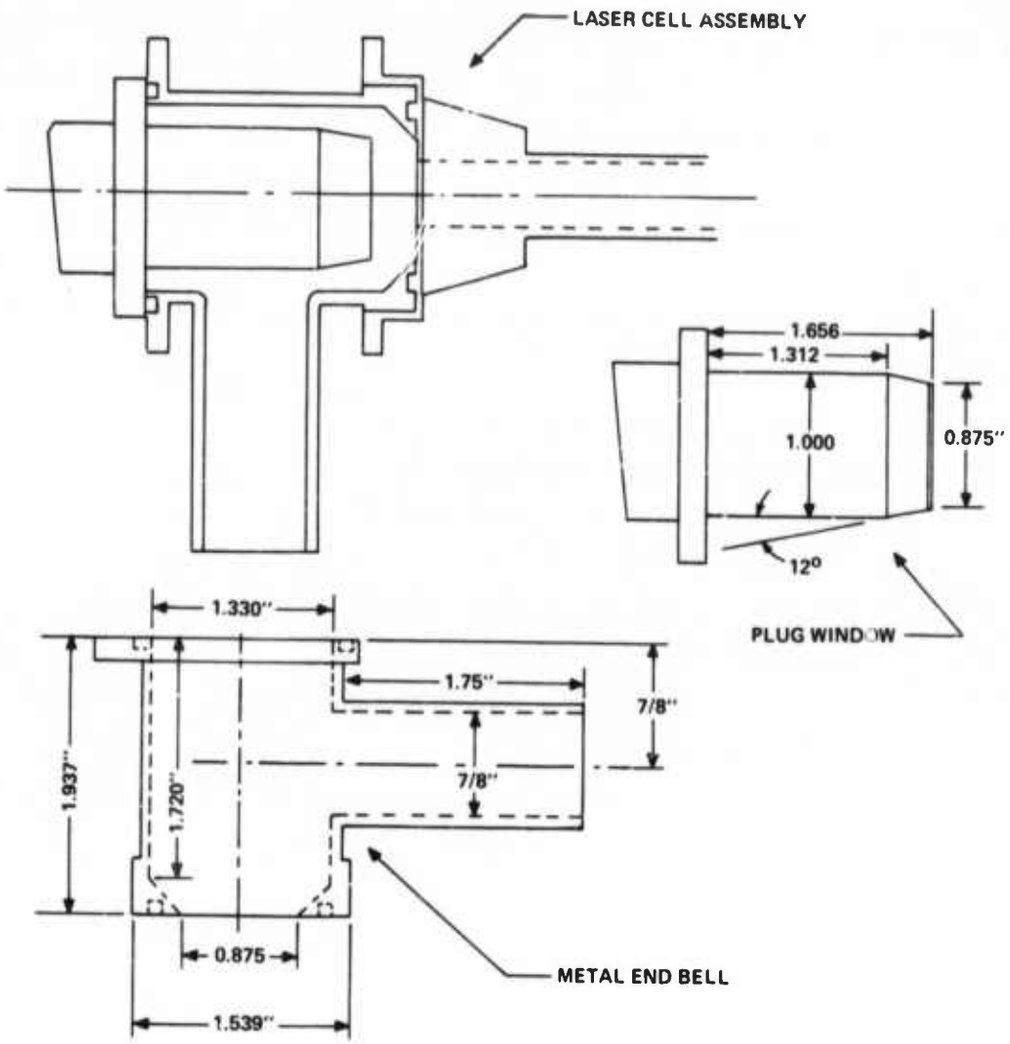

Figure 3-8. Detail Showing Nickel Plenum Chamber at End of Laser Cell.

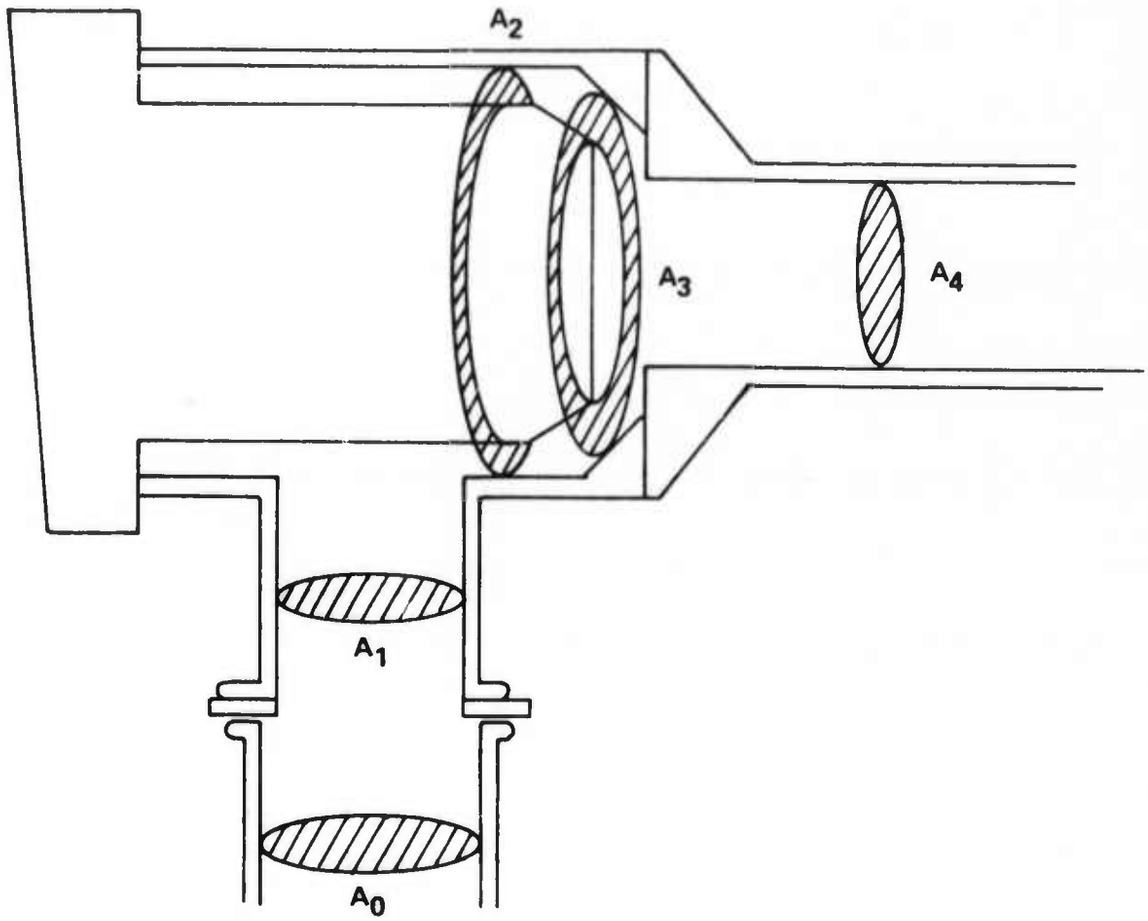

Figure 3-9. Schematic of Laser Cell End Showing Cross-Sectional Areas used for Head Loss Calculations

and,

$$H_a = \left(K_e + K_c\right) \frac{V^2}{2g} = 0.08\left(\frac{V_1^2}{64.4}\right)$$

where:

V_1 = average flow velocity in the 7/8-inch pipe section (ft sec^{-1})

$$V_1 = \frac{2.22\times10^{-3}Q}{\pi r^2} = 0.533\,Q$$

where:

Q = volume flow rate (gallons min^{-1})

Therefore,

$$H_a(ft) = 3.51\times10^{-4}Q^2$$

b) Assume that the Reynold's Number of the flow is on the order of 10,000 so that

$$K_b = 0.27.$$

Therefore:

$$H_b(ft) = (0.27+0.27)\frac{V^2}{2g} = \frac{0.54}{64.4}V^2 = 2.38\times20^{-3}Q^2$$

c) $\sqrt{A_1/A_2} = 0.996$ and $K_e, K_c = 0.001$

$$V_2^2 = \frac{1}{0.996}V_1^2 = 1.005\,V_1^2$$

$$H_c(ft) = \frac{0.002}{64.4}(1.005)(0.533\,Q)^2 = 0.89\times10^{-4}Q^2$$

d) $K_b = 0.27$

$$H_d(ft) = (0.54)\frac{V_2^2}{2g} = \frac{0.54}{64.4}(1.005)(0.533\,Q)^2 = 2.39\times10^{-3}Q^2$$

e) $\sqrt{A_2/A_3} = \sqrt{\frac{0.604}{0.772}} = 0.884$; $K_e, K_c = 0.05$

$$H_e(ft) = (0.1)\frac{V_2^2}{2g} = \frac{0.1}{64.4}(1.005)(0.533\,Q)^2 = 4.41\times10^{-4}Q^2$$

f) $K_b = 0.27$ $\quad V_3 = \left(\frac{A_2}{A_3}\right)V_2 = (0.783)(1.005)\,V_1 = 0.786\,V_1$

$$H_f(\text{ft}) = (0.54)\,\frac{V_3^2}{2g} = \frac{0.54}{64.4}\,(0.619)\,(0.533\,Q)^2 = 1.47 \times 10^{-3}\,Q^2$$

g) $\sqrt{A_4/A_3} = \sqrt{0.601/0.772} = \sqrt{0.779} = 0.881; \quad K_e, K_c = 0.05$

$$H_g(\text{ft}) = (0.1)\,\frac{V_4^2}{2g} = \frac{0.1}{64.4}\,(1.008)\,(0.533\,Q)^2 = 4.43 \times 10^{-4}\,Q^2$$

Summing a) through g):

$$H'(\text{ft}) = H_a + \ldots + H_g = 7.57 \times 10^{-3}\,Q^2$$

h) The friction loss through the cell pipe is calculated using the friction factor from Eqs. (3-9) and (3-8) in the form:

$$H_h(\text{ft}) = f\left(\frac{14\text{ in}}{7/8\text{ in}}\right)\frac{V_4^2}{2g} = f\,\frac{16}{64.4}\,V_4^2$$

The total head losses for this cell and the two other cells used in the laser system are compiled by Table 3-2. The Reynold's Number, R_e, of the flow through the pipe section of the laser cell is also included for later use.

3.2.1.3 Heat Exchanger

A schematic cross-section of the laser liquid heat exchanger is shown as Figure 3-10. The device is of the shell and tube type with city water as the cooling medium surrounding 24 nickel tubes through which the laser liquid flows. The cooling tubes terminate at the entrance and exit at the plenum chambers in the shape of hemispheric cavities. The entering laser liquid stream strikes a conical flow diverter in the entrance chamber to help redirect the stream to the cooling tubes. The entire unit is mounted vertically on the output flange of the pump so that any bubbles contained in the fluid are naturally exhausted from the device.

From a fluid mechanical viewpoint, the device can be analyzed for pressure heads as follows:

a) A free expansion (compression) loss from the connecting tubing to the plenum chambers.

b) A free compression (expansion) loss of the equally-divided flow from the plenum chambers to the cooling tubes.

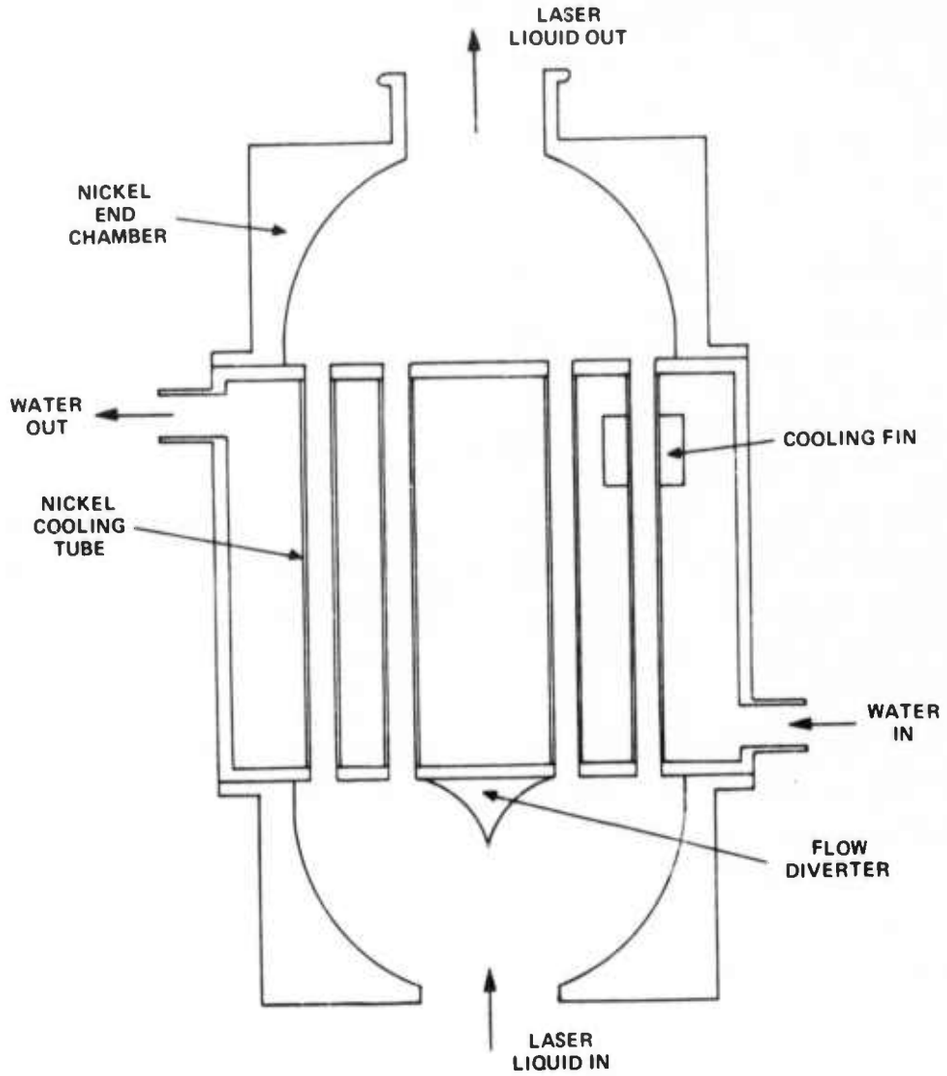

Figure 3-10. Schematic Diagram of Heat Exchanger

TABLE 3-2

DYNAMIC HEAD LOSSES (FEET) AND REYNOLD'S NUMBERS FOR THREE LASER CELLS USED IN THE LIQUID LASER SYSTEM

	7/8 in bore × 10 in long				5/8 in bore × 10 in long				1/2 in bore × 6-1/2 in long				
Q (GPM)	R_e	H′	H_h	H_{cell}	R_e	H′	H_h	H_{cell}	R_e	H′	H_h	H_{cell}	H_{total}
1	1300	0.076	0.010	0.02	1820	0.020	0.034	0.05	2280	0.052	0.075	0.13	0.20
2	2600	0.030	0.028	0.06	3640	0.081	0.116	0.20	4550	0.206	0.253	0.46	0.72
3	3910	0.068	0.069	0.14	5450	0.183	0.235	0.42	6830	0.464	0.514	0.98	1.54
4	5210	0.121	0.122	0.24	7270	0.325	0.389	0.71	9110	0.826	0.851	1.68	2.63
5	6510	0.189	0.178	0.37	9090	0.508	0.575	1.08	11380	1.290	1.257	2.55	4.00
6	7810	0.272	0.251	0.52	10910	0.731	0.791	1.52	13660	1.858	1.730	3.59	5.63
7	9120	0.371	0.332	0.70	12730	0.995	1.036	2.03	15930	2.528	2.266	4.79	7.52
8	10420	0.485	0.417	0.91	14550	1.299	1.309	2.61	18210	3.302	2.862	6.16	9.68
9	11720	0.613	0.531	1.14	16360	1.644	1.608	3.25	20490	4.180	3.517	7.70	12.09
10	13020	0.757	0.639	1.40	18180	2.030	1.934	3.96	22760	5.160	4.229	9.39	14.75
11	14320	0.915	0.763	1.68	20000	2.456	2.285	4.75	25040	6.244	4.997	11.24	17.67
12	15630	1.090	1.004	1.99	21820	2.923	2.661	5.58	27320	7.430	5.819	13.25	20.82

c) Fluid friction head loss for the flow through the cooling tubes.

The calculation of each contribution is again shown below:

a) We shall assume the hemispheric entrance and exit chambers act as true plenums in that the flow transitions from the connecting tubing to the chamber volumes can be idealized as a free expansion and compression at the respective ends of the device ($K_e = 1.0$, $K_c = 0.5$). Letting the mean flow velocity in the 1-inch diameter connecting tubing to designated by V_1 (ft/sec), we therefore have:

$$H_a(\text{ft}) = \left(K_e + K_c\right)\frac{V_1^2}{2g} = \frac{1.0 + 0.5}{2(32.2)}\,V_1^2 = 2.33 \times 10^{-2}\,V_1^2$$

If the volume flow rate of liquid is Q gallons min^{-1}, we can convert this to cubic feet per second as:

$$Q'(\text{ft}^3\text{sec}^{-1}) = 2.22 \times 10^{-3}\,Q\,(\text{GPM})$$

The mean flow velocity, V_1, in the connecting tubing can therefore be calculated by dividing Q' by the cross-sectional area (ft^2) of the tubing. We therefore have:

$$V_1(\text{ft sec}^{-1}) = \frac{Q'(\text{ft}^3\,\text{sec}^{-1})}{5.45\times10^{-3}\,\text{ft}^2} = 0.407\,Q$$

The head loss, H_a, is therefore:

$$H_a(\text{ft}) = (2.33\times10^{-2})\times(0.407\,Q)^2 = 3.86 \times 10^{-3}\,Q^2$$

b) Assuming the flow is equally divided among the 24 cooling tubes, the volume flow rate $Q_t = Q/24$. The internal diameter of the nickel cooling tubes is 3/16-inch and the mean flow velocity through each of the tubes is therefore:

$$V_{3/16}(\text{ft sec}^{-1}) = \left(\frac{Q'}{24}\right)\times\frac{1}{\pi\,r_0^2} = \frac{2.22\times10^{-3}\,Q}{24\times\pi\times(1/128)^2} = 0.483\,Q$$

The expansion and compression head losses at either end of the entrance to the tubes is therefore:

$$H_b(\text{ft}) = \left(K_e + K_c\right)\frac{V_{3/16}^2}{2g} = \left(\frac{1.5}{64.4}\right)\times(0.483\,Q)^2 = 5.44 \times 10^{-3}\,Q^2$$

c) The friction loss for the flow through the cooling tubes may be calculated by using Eq. (3-8) where the ratio of length (6 inches) to tubing I. D. (3/16 inches) is L/D = 32.

Therefore:

$$H_c(\text{ft}) = f\left(\frac{L}{D}\right)\frac{V^2_{3/16}}{2g} = f\left(\frac{32}{64.4}\right) \times (0.483\,Q)^2 = (0.116) \times f \times Q^2$$

The "friction factor" f may be calculated from Eq. (3-9) and the Reynold's Number of the flow through the cooling tubes as defined by Eq. (3-6).

The calculated partial head losses H_a, H_b and H_c are shown as a function of system volume flow rate, Q, on Table 3-3 for the heat exchanger along with the sum of the partial head losses and the Reynold's Number, R_e, for the flow through the exchanger cooling tubes.

TABLE 3-3

HEAD LOSSES AND REYNOLD'S NUMBERS FOR HEAT EXCHANGER USED IN THE LIQUID LASER SYSTEM

Q (GPM)	R_e	H_c (feet)	$H_a + H_b$ (feet)	$H_a + H_b + H_c$ (feet)
1	253	0.028	0.009	0.04
2	506	0.112	0.037	0.15
3	759	0.167	0.083	0.25
4	1012	0.221	0.148	0.37
5	1265	0.311	0.231	0.54
6	1518	0.401	0.333	0.73
7	1771	0.532	0.453	0.99
8	2024	0.662	0.593	1.26
9	2277	0.820	0.750	1.57
10	2530	0.979	0.926	1.90
11	2783	1.163	1.059	2.22
12	3037	1.347	1.333	2.68

3.2.1.4 Connecting Tubing

The three laser cells, pump and heat exchanger are all connected together using Corning Beaded Pipe and couplers (1-inch I. D.). The entire system is laid out with gentle slopes to the piping so that there is one unique high point to the circulation loop (the "free surface" previously described) where bubbles trapped in the laser liquid can eventually collect outside of the main fluid stream. In this particular system, the pump, heat exchanger and bypass filter (to be described) are located beneath an aluminum table top which forms a convenient reference surface for mounting the three laser heads described earlier. The total length of pipe required for connecting the components described amounted to 63 inches.

In addition to the friction loss through the connecting pipe, head losses also arise at the three right angle sweep bends in the tubing, the six pipe couplings used for joining sections of the beaded pipe sections and the 1-inch I. D. to 1-1/2-inch I. D. nickel transition coupler necessary at the pump input port. The individual contributions to the head loss are calculated below:

a) Head loss at 1-inch to 1-1/2-inch transition.

This is an expansion loss with diameter ratio (0. 67). From the head loss factor graph of Figure 3-6 we find:

$$K_e = 0.26$$

so that:

$$H_a(\text{ft}) = \frac{K_e}{2g}\left(V_1\right)^2 = \frac{0.26}{64.4}(0.407\,Q)^2 = 6.70 \times 10^{-4}\,Q^2$$

b) Head loss at beaded pipe couplers.

The internal diameter of the Corning beaded pipe couplers is roughly 95% of that of the pipe. Fluid flowing through the coupling, therefore, undergoes a rapid compression and expansion. Consulting Figure 3-6 once again we find:

$$K_e, K_c \simeq 0.015$$

so that for the six couplers used:

$$H_b(\text{ft}) = 6 \times \frac{\left(K_e + K_c\right)}{2g}\left(V_1\right)^2 = \frac{0.18}{64.4}(0.407\,Q)^2 = 4.6 \times 10^{-4}\,Q^2$$

c) Head loss at sweep bends.

As mentioned earlier, flow separation occurring at bends in the pipe leads to a head loss across the element. This effect can usually be expressed as a head loss factor, K_b, similarly to the K_e, K_c we have used above. The magnitude of K_b depends on the ratio of pipe diameter to radius of the bend, the angular sweep of the bend and the Reynold's Number of the flow through the pipe. As mentioned previously, Reference 64 contains graphs and charts which may be used to estimate K_b. In our case, we estimate from this data that:

$$K_b \simeq 0.40$$

and

$$H_c(\text{ft}) = 3 \times \frac{K_b}{2g} \left(V_1\right)^2 = \frac{1.20}{64.4} (0.407\,Q)^2 = 3.09 \times 10^{-3}\, Q^2$$

since there are three bends.

d) Head losses at miscellaneous points in the circulation loop.

Not mentioned previously are four tee joints let into the circulation loop. Two of these are for conducting roughly 10% of the main flow through the filter bypass loop. Another tee occurs at the standpipe leading to the free surface and a fourth tee is let into the side of the pipe to mount a thermocouple finger for monitoring liquid temperature out of the flow-stream. As a good approximation, we can assume that the liquid in the side-arm of these tees is stagnant except for the inevitable eddy motion that occurs at the juncture of the side-arm to the pipe. This slight flow distortion across the location of the side-arm leads to a separation of the flow-stream lines and a pressure drop across the tee. A conservative estimate of this effect might be to model this stagnant side-arm tee to the case of an expansion followed by a compression from the effective radius, r, of the pipe to the radius r + d/8 where d is the internal diameter of the side-arm of the tee. In the case where the side-arm and pipe are the same diameter, d = 2r and the effective diameter ratio of the transition would be 1/1.25 = 0.8. In this case:

$$K_e, K_c = 0.105$$

and, for the four tees we have in this system:

$$H_d = 4 \times \frac{(0.10510 \cdot 105)}{2g} \left(V_1\right)^2 = \frac{0.84}{64.4} (0.407 Q)^2 = 2.15 \times 10^{-3} Q^2$$

e) Friction head loss through 63 inches of 1-inch I. D. pipe.

This calculation is similar to that of c) in the heat exchanger. Again, the Reynold's Number, R_e, is calculated for the flow through the pipe, the friction factor, f, is estimated from Eq. (3-10) and the head loss determined.

Table 3-4 shows the Reynold's Number of the flow in the connecting pipe, the friction head, H_e, generated thereby and the sum of $H_a + H_b + H_c + H_d$ as:

$$H_a + H_b + H_c + H_d = (0.67 + 0.46 + 3.09 + 2.15) \times 10^{-3} Q^2 \text{ (feet)}$$

$$= 6.37 \times 10^{-3} Q^2.$$

TABLE 3-4

HEAD LOSSES AND REYNOLD'S NUMBERS FOR PIPING SYSTEM USED IN THE LIQUID LASER SYSTEM

(GPM)	R_e	H_e (feet)	$H_a + H_b + H_c + H_d$ (feet)	H_{total} (feet)
1	816	0.006	0.006	0.01
2	1633	0.012	0.026	0.04
3	2449	0.025	0.057	0.08
4	3266	0.039	0.102	0.14
5	4082	0.060	0.160	0.22
6	4900	0.080	0.230	0.31
7	5716	0.106	0.313	0.42
8	6533	0.132	0.408	0.54
9	7349	0.163	0.516	0.68
10	8166	0.195	0.637	0.83
11	8982	0.231	0.770	1.00
12	9800	0.268	0.918	1.19

3.2.1.5 Total System Head Losses and Filter Bypass Loop

The totals from Table 3-2, 3-3 and 3-4 must be summed to give the system head losses as a function of flow rate Q through the main circulation loop. This summation is displayed by Table 3-5.

TABLE 3-5

SYSTEM HEAD LOSS VS. VOLUME FLOW RATE Q
THROUGH MAIN CIRCULATION LOOP

(GPM)	H_{cells} (feet)	$H_{heat\ exchanger}$ (feet)	H_{loop} (feet)	H_{system} (feet)	$H_{filter\ loop}$ (feet)
1	0.20	0.04	0.01	0.3	0.2
2	0.72	0.15	0.04	0.9	0.8
3	1.54	0.25	0.08	1.9	1.6
4	2.63	0.37	0.14	3.1	2.8
5	4.00	0.54	0.22	4.8	4.2
6	5.63	0.73	0.31	6.7	5.9
7	7.52	0.99	0.42	8.9	7.9
8	9.68	1.26	0.54	11.5	10.2
9	12.09	1.57	0.68	14.3	12.8
10	14.75	1.90	0.83	17.5	15.6
11	17.67	2.22	1.00	20.9	18.7
12	20.82	2.68	1.19	24.7	22.0

The construction of the bypass filter loop must now be considered. As can be seen in Figure 3-6, a liquid filter is connected between the output of the heat exchanger and the input of the pump. The pressure appearing across the filter circuit as a function of main loop volume flow rate, Q, appears in the last column of Table 3-5. We must, therefore, design the bypass filter loop to have this dynamic head loss at a corresponding volume flow rate of 0.1Q. This is most simply accomplished by adding a flow-constricting element in series with the filter in the bypass loop. The element is

chosen so that the sum of the dynamic head loss of the element plus that of the filter just equals the drop across the filter circuit from Table 3-5.

The filter selected for use in the laser system is a fritted quartz cylinder of 0.5 ft^2 surface area and 2-micron porosity manufactured by Chem-Flow, Inc. Head loss as a function of flow rate through the filter as estimated from the manufacturer's data for this unit is shown as the second column on Table 3-6. The first column of this Table lists the desired loop characteristic from Table 3-5 data. The third column is the difference of column one values and column two and is thus the head loss characteristic of the desired flow control element.

TABLE 3-6

BYPASS LOOP HEAD LOSSES VS. BYPASS LOOP VOLUME FLOW RATE Q_B

Q_B (GPM)	H_{loop} (feet)	H_{filter} (feet)	$H_{loop} - H_{filter}$ (feet)	$H_{constriction}$ (feet)
0.1	0.2	0.01	0.2	0.3
0.2	0.8	0.05	0.7	0.8
0.3	1.6	0.10	1.5	1.7
0.4	2.8	0.17	2.6	2.8
0.5	4.2	0.25	3.9	4.2
0.6	5.9	0.34	5.6	5.8
0.7	7.9	0.45	7.4	7.6
0.8	10.2	0.57	9.6	9.6
0.9	12.8	0.70	12.1	11.7
1.0	15.6	0.84	14.8	14.1
1.1	18.7	0.99	17.7	16.7
1.2	22.0	1.16	20.8	19.4

This element used as the flow control can, in principle, be any device which would constrict the bypass loop fluid flow rate. In our case, because we desired to avoid flow separation problems and possible cavitation, we selected a long, narrow pipe ($L/D > 10$) with a gradual taper at either end. The friction head loss of this pipe

therefore serves to limit the flow through the bypass loop. The final column of Table 3-6 shows the calculated friction head loss for a 3.5-mm I. D. pipe of length 11 cm (L/D ~ 30). A piece of glass pipe of these dimensions was selected from stock, the ends of the pipe were flared to mate with the Corning beaded pipe couplers and a glass reinforcing cylinder was bonded outside of this thin tube to make the unit mechanically more rugged.

3.2.1.6 Pump Characteristics and System Operating Conditions

The pump is one of the most critical elements in the circulatory loop in that the ultimate in purity and stability of the laser liquid is necessary for best laser results and this is only possible if contamination of the liquid by water vapor from leaks to the atmosphere or abraded or dissolved materials from the pump are kept to a minimum. In terms of pump requirements, it therefore is clear that almost any direct means for transmitting the driving power to the pump impeller creates a shaft-seal problem both in terms of packing material and atmospheric leakage. The best and thus far only long-lived solution to this problem has been found in a hermetically sealed, magnetically-coupled pump manufactured by the Liquid Dynamics Corporation as schematically illustrated in Figure 3-11. The driving power is electromagnetically transmitted from a rotating field to a soft iron core encapsulated in a nickel case. The impeller, pump casing and rotor housing are all fabricated from Carpenter 20 stainless steel, and the bushings, journals and associated locating hardware in contact with the liquid are either alumina or stainless steel. In the pump, as well as in the rest of the system, the liquid comes into contact only with the materials toward which it is nonreactive or with which it reacts exceedingly slowly as determined by corrosion tests.[65] The pump has been operated above and below atmospheric pressure and has proven to be reliable and tight with respect to leaks.

The pump output characteristics (pressure head developed vs. volume flow rate) with motor control setting (proportional to shaft rpm) as a parameter are shown on Figure 3-12. Note that while the manufacturer's data gives the total head developed by the pump, H_p, as a function of pump flow rate, ($Q_p = Q + Q' = 1.1Q$), the curve for the total system head, H_s, from Table 3-5 was calculated only for the main loop flow rate, Q. To plot both curves on the same graph, we must add the bypass loop volume flow rate, $Q' = 0.1Q$, to the data on Table 3-5.

The intersection of the system head loss curve and the pump output curves give the pressure head and total system flow rate at any given motor control setting. This data is replotted as Figure 3-13 where we have now plotted the main loop volume

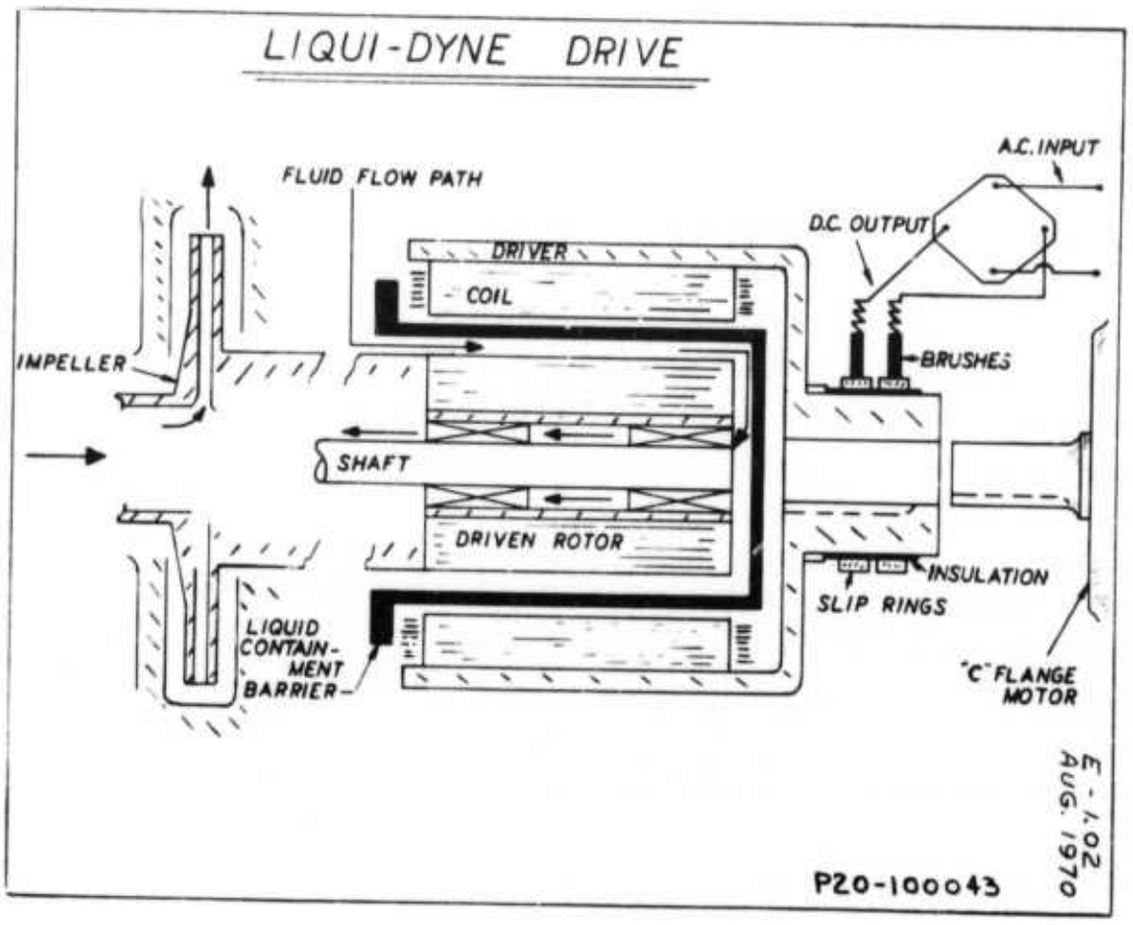

Figure 3-11. Cross-Section of Circulating Pump Manufactured by Liquid Dynamics, Inc.

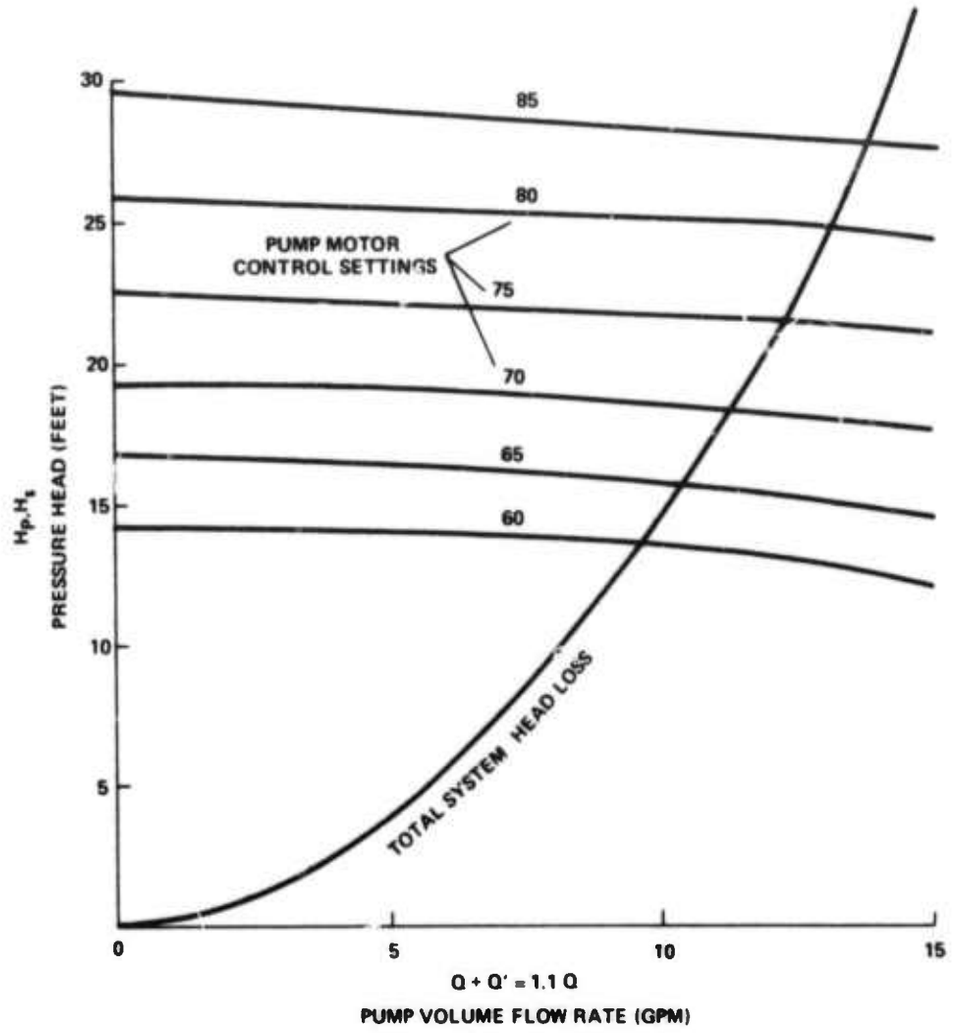

Figure 3-12. Pump Output Characteristics and System Head Loss

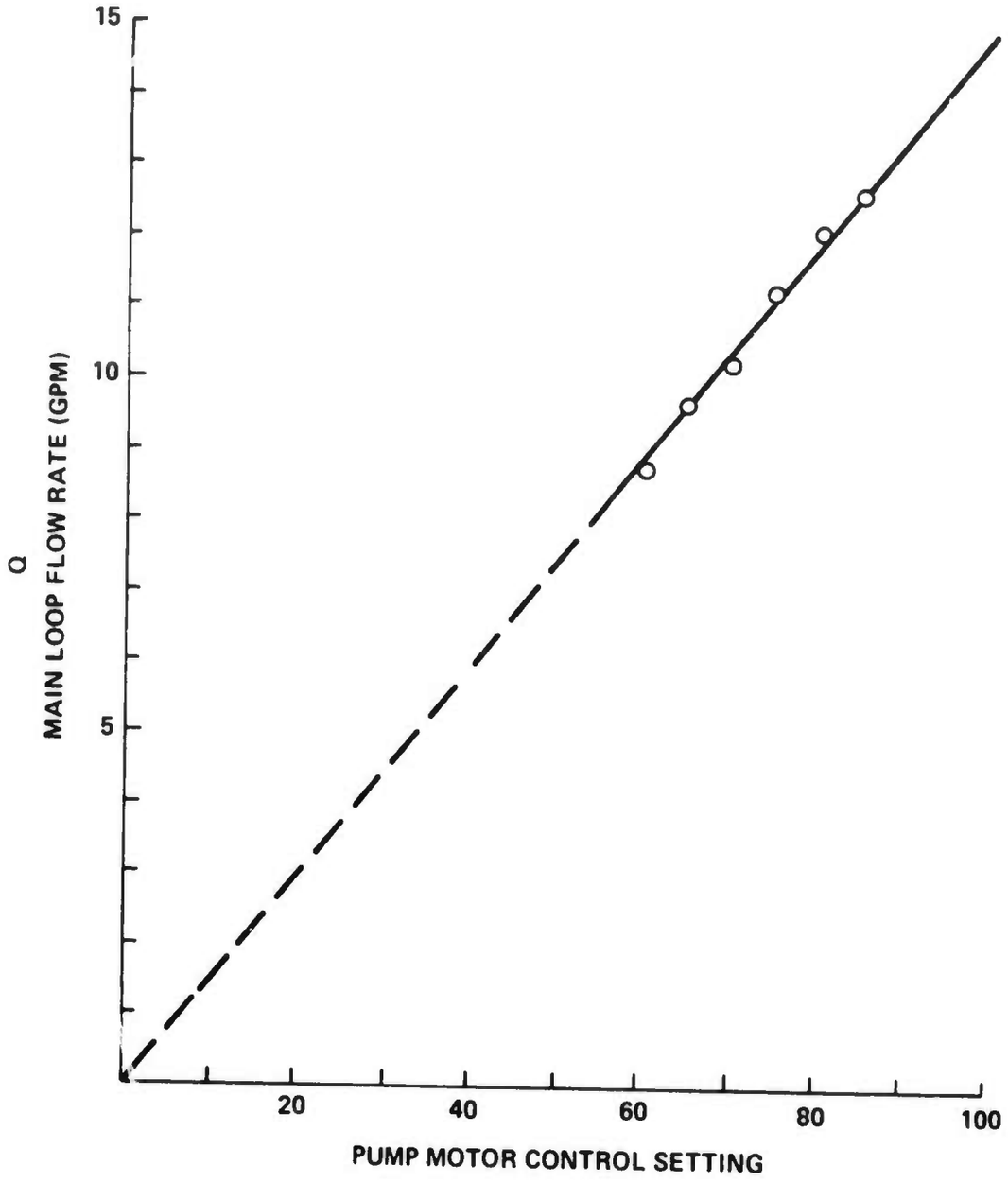

Figure 3-13. Main Loop Volume Flow Rate Q Vs. Pump Motor Control Setting.

flow rate, Q, against the pump motor control setting. As may be seen, the experimental points may be extrapolated by a straight line to the origin. This linear relationship between the volume flow rate, Q, and motor control setting is fortuitous. Since the Reynold's Number for the flow through each of the laser cells is directly proportional to Q and inversely proportional to the I. D. of the cell [from the definition of Eq. (3-6)], Figure 3-14 is a direct result of Figure 3-13 and again shows a linear relationship. It will be noted that on Figure 3-14, the pump motor control setting has an indicated upper limit of 50 due to cavitation in the system. This cavitation occurs in the smallest laser cell at a Reynold's Number of about 17,000. At this Reynold's Number, flow separation seems to occur in the output plenum chamber of the laser cell where the rapidly moving liquid encounters the cell end window and makes a simultaneous right angle bend and expansion. The phenomena of cavitation exhibits itself in an abrupt generation of bubbles from the dissolved gas in the laser liquid. These bubbles are carried along in the fluid stream and lead to a great increase in laser losses. As long as operation of the system is restricted to pump speeds below this critical point, optical quality of the liquid is excellent and no problems arise.

3.2.2 Water Contamination Control of the Laser Liquid and Circulatory System Materials

This part of the report is divided into two parts; the first is concerned with the measurement of the level of water contamination of the circulatory system and a test of its tightness. In addition, the question of tolerable levels of water contamination is considered. The second part evaluates the potential construction materials for those parts of the pump that come into contact with the laser solution. This essentially determines the chemical compatibility of satisfactory materials with the laser solutions.

3.2.2.1 Measurement of the Water Contamination in the Circulatory System of the $POCl_3$ Based inorganic Liquid Laser

The development of technically significant liquid lasers depends critically on the understanding and control of the competitive radiative and nonradiative decay processes from the excited state. In the particular case of inorganic liquid lasers this is complicated by the fact that most solvents contain protons which are extremely efficient in enhancing the nonradiative decay processes and thus severely inhibiting efficient laser capability.

One approach to overcome the problem is the use of aprotic solvent systems. A number of such systems are available and the two that showed the greatest promise

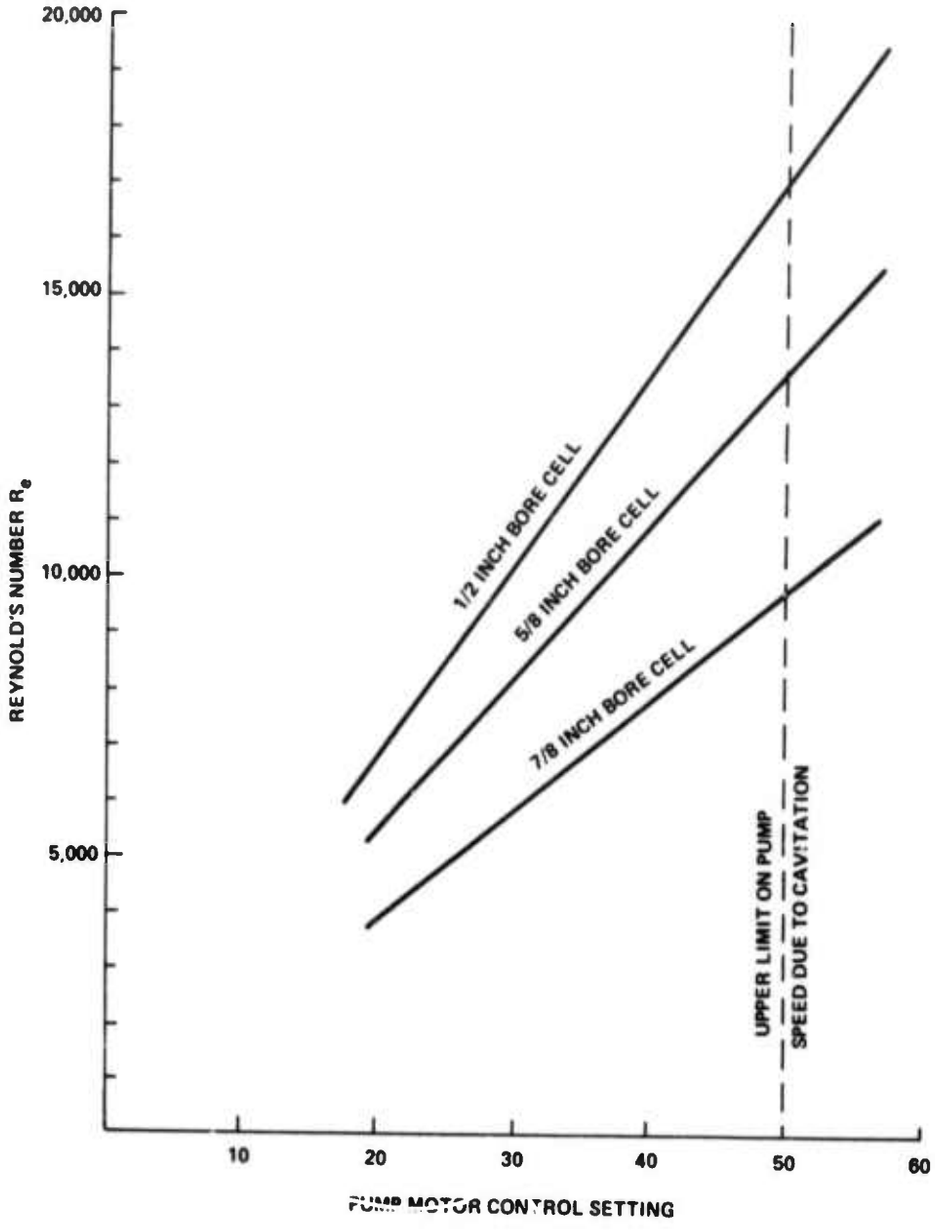

Figure 3-14. Reynold's Number for Flow Through All Laser Cells Vs. Pump Motor Control Setting

were based on $SeOCl_2$ and $POCl_3$.[66, 67] In these systems, in addition to the aprotic solvent and active ion, a Lewis acid is required to enhance the solubility of the laser active component to practical levels. Research effort ultimately resulted in two efficient laser solutions: $SeOCl_2$:$SnCl_4$: Nd^{+3}.[68, 69] The chemistry of these solutions is different but both are exceedingly sensitive to water contamination in, however, different ways. In the $SeOCl_2$ system, water contamination immediately results in significant nonradiative deactivation as evidence by a decrease in both fluorescence intensity and excited state lifetime. The $POCl_3$-based system is much less sensitive to protic contamination but continued exposure to water results in the precipitation of $ZrOCl_2$ and ultimately a decrease in fluorescence lifetime. In this case the usefulness of the laser materials is completely vitiated by the appearance of even the slightest precipitate which occurs well before any degradation in the lifetime becomes evident.

There is no major problem in preparing either of these laser materials in large quantities almost completely free of any protic contamination. Nor is there any problem in storing them for, apparently, indefinite periods of time if reasonable precautions are taken. However, their final use in a real, practical laser requires extensive manipulation and circulation of the solution. This use involves the risk of protic contamination and raises the question of the techniques required for successful manipulation of the solution.

In the simplest terms the problem is to transfer dry laser solution to a dry laser circulatory system and maintain an acceptable level of dryness. The actual transfer operation has been achieved many times and poses no problem more difficult than the techniques for handling up to six liters of solution at one time. More difficult are the following tasks:

1) To dry out the circulatory system.

2) To ascertain when the circulatory system has reached a satisfactory level of dryness and is sufficiently leak-tight so that water contamination does not accumulate.

3) To determine an upper limit to the tolerable level of water contamination.

Actually the first task is reasonably straightforward. The pure solvent itself, $POCl_3$, is an extremely efficient dessicant since it reacts with water irreversibly. The basic difficulty is to measure quantitatively the water content of $POCl_3$. This then is the first problem.

The absorption spectrum of $POCl_3$ as obtained from a Perkin-Elmer Model 700 Spectrophotometer is shown in Figure 3-15. The key regions of interest are the flat part from 3200 to 3400 cm^{-1}, the weak band at 3050 cm^{-1}, the shoulder at 2675 cm^{-1} and broadband at 2500 to 2600 cm^{-1}. These spectral characteristics are associated with an O-H or P-O-H vibration.[70] This is the species that must be examined since the water contaminant reacts rather rapidly with $POCl_3$ resulting in $HOPOCl_2$ and HCl. As the water contamination becomes more extensive, the transmission at these frequencies decreases and the band between 2500 and 2600 cm^{-1} becomes broader. The spectrum of "wet" $POCl_3$ is shown in Figure 3-16.

A quantitative measure of the water contamination is complicated by the difficulty of obtaining and keeping dry $POCl_3$. Lanning and Cukor, using 10-cm cells and $POCl_3$ freshly distilled from lithium were able to establish a calibration curve as shown in Figure 3-17. The ppm H_2O represent the actual amounts added to the $POCl_3$ by means of a Hamilton microliter syringe. These results were extended to higher levels of water contamination as shown in Figure 3-18 by measuring the spectra in 1-cm cells. All these results were obtained on a Model 621 Perkin-Elmer spectrometer. The nonlinearity of the calibration curve close to the orign is presumably due to a small but unknown quantity of water present in the freshly distilled $POCl_3$.

Figure 3-19 shows the results for the same solutions when run on the Perkin-Elmer Model 700 in a cell length of 0.9 cm. The line designated 2675 cm^{-1} is derived from an original $POCl_3$ sample that was significantly drier to begin with, and to which water was added, using the same microliter syringe. Figure 3-20 illustrates the results when plotted as a function of ℓnT. The curves of Figures 3-19 and 3-20 serve to calibrate the water contamination.

Figures 3-21(a) and 3-21(b) present spectra of the actual laser solution, dry and wet, respectively. In this case the main sensitivity resides in the 2675 cm^{-1} shoulder and this is used to measure the degree of wetness. This is estimated by using the calibration curve for this frequency in $POCl_3$.

The laser circulatory system was shown in Figure 3-5. The liquid used to fill the system is transferred to the system by pressure through a valve near the pump. When the system is filled this valve is shut off, the free surface is pressurized and the liquid is ready for circulation.

In practice, the system is first filled with dry $POCl_3$ to dry out the interior of the circulatory system. The dryness of the system is determined by noting the wetness

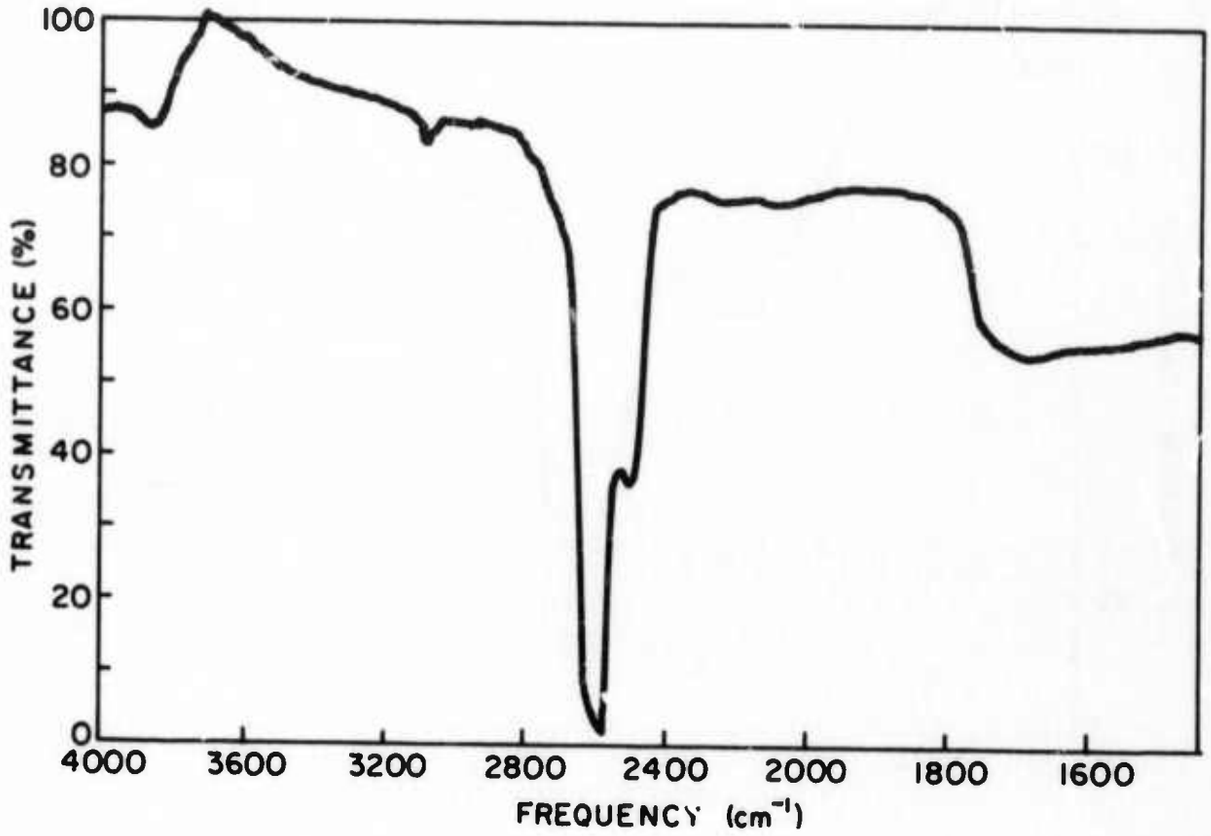

Figure 3-15. Infrared Spectrum of Dry $POCl_3$

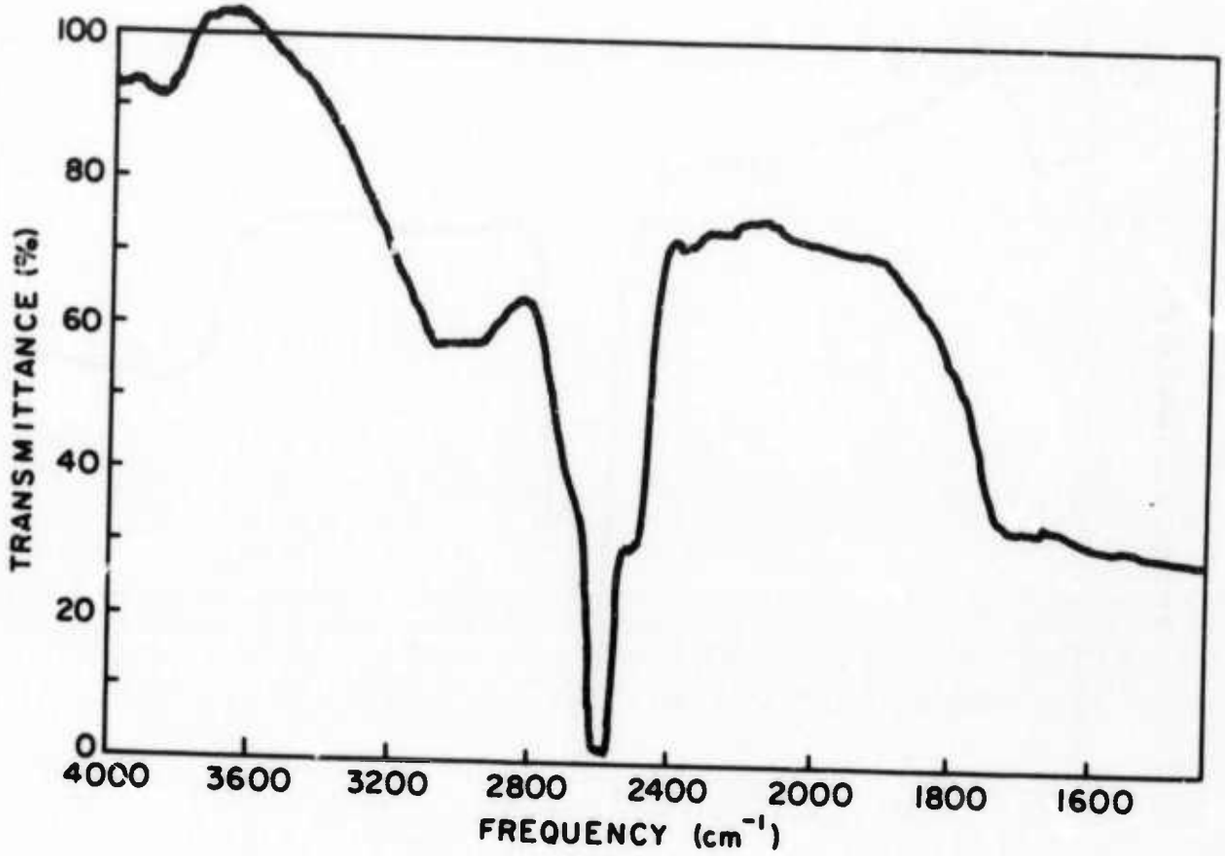

Figure 3-16. Infrared Spectrum of $POCl_3$ Containing 40 ppm Added Water

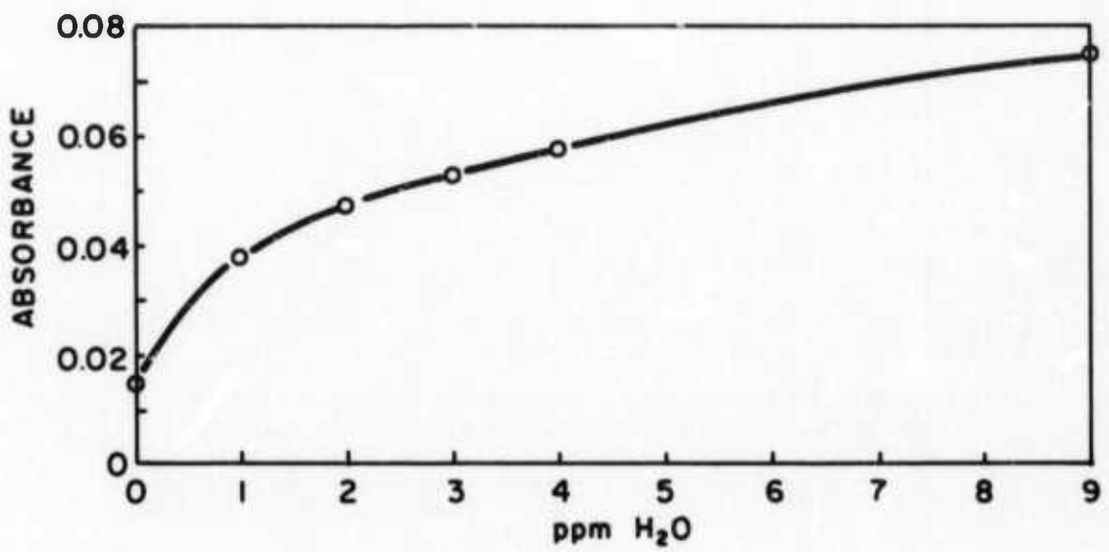

Figure 3-17. Calibration Curve of Water Contamination from 0 to 10 ppm in $POCl_3$. From work of Lanning and Cukor.

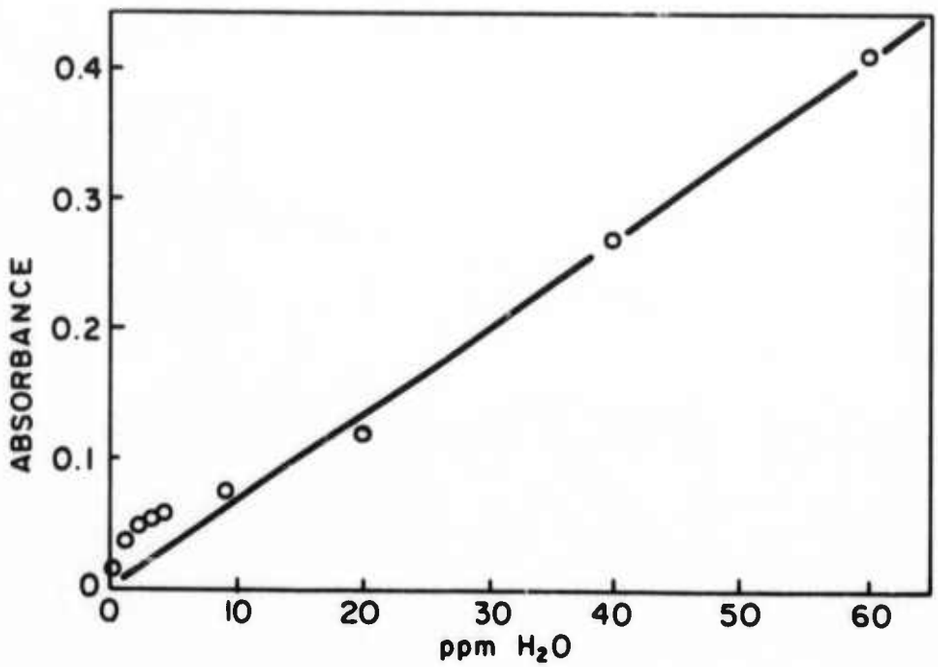

Figure 3-18. Calibration Curve of Water Contamination from 0 to 60 ppm in $POCl_3$. From work of Lanning and Cukor.

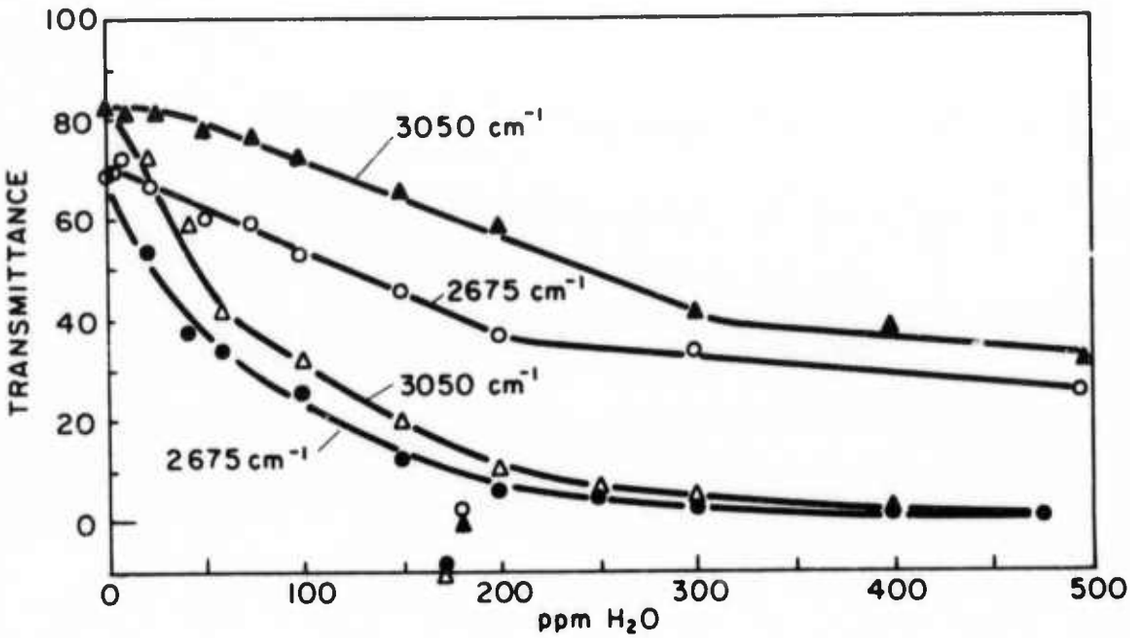

Figure 3-19. Transmission at 3050 cm^{-1} and 2675 cm^{-1} of $POCl_3$ with Various Amounts of Water Added. For the upper two curves the ppm H_2O scale is 10 percent of the one indicated.

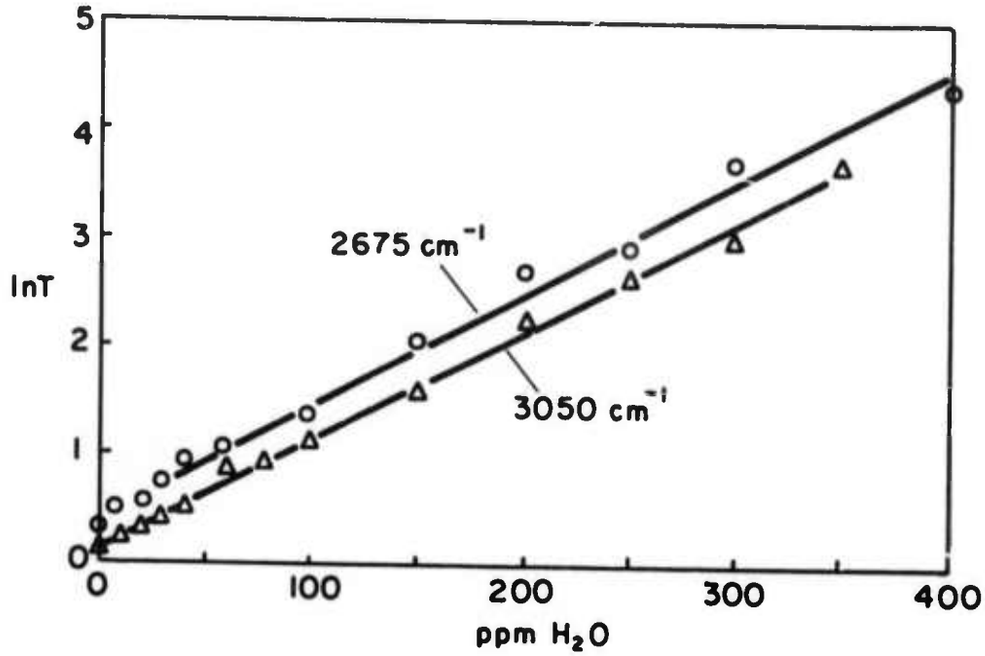

Figure 3-20. Absorption Constant of $POCl_3$ at 2675 and 3050 cm^{-1} with Different Amounts of Added Water

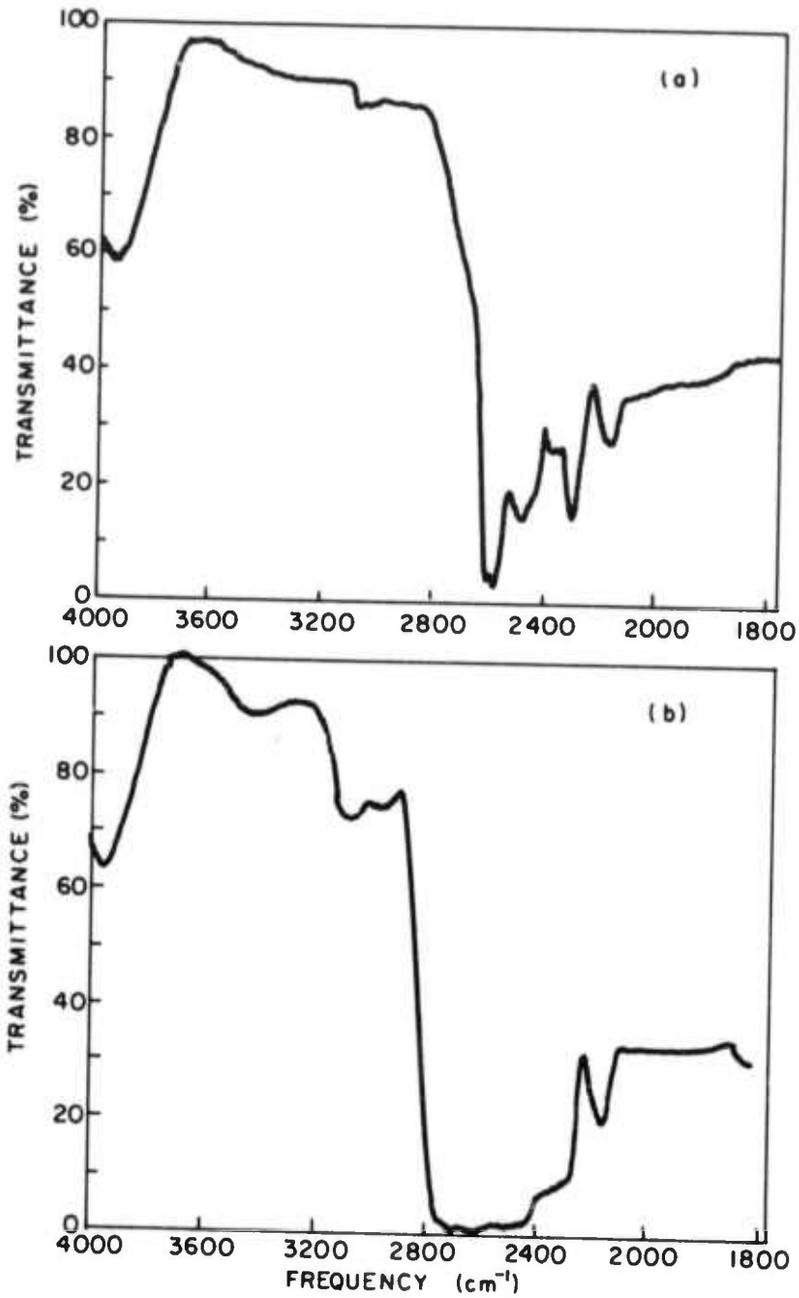

Figure 3-21. (a) Infrared Spectrum of Dry Laser Solution;
(b) Infrared Spectrum of Wet Laser Solution.

level of the $POCl_3$ being circulated after the water content has reached a steady level. If the water content continues to increase with time, this is taken as an indication that there is a leak in the system. To be sure that the sample withdrawn from the circulating system represents accurately the material in the system, a special apparatus illustrated in Figure 3-22 is used. The basic idea is that the entire receiving system is flushed with dry nitrogen before and after the sample is withdrawn so that no residual $POCl_3$ remains in the receiving system after the sample is withdrawn. If this is not done, the trapped $POCl_3$ comes into contact with the atmosphere, becomes wet, and contaminates the next sample.

The results of the application of the drying technique and the measurement to an actual circulatory system are illustrated in Figure 3-23. As is seen, most of the water in the circulatory system was extracted with the first $POCl_3$ fill. Even on the first filling there is a strong tendency of the water contamination level to saturate with time, indicating that there are no, or at the worst only very small leaks. The second and third fillings show a stronger tendency to saturate and a much lower absolute level of water contamination. After the third $POCl_3$ filling was drained, the system was filled with laser solution.

Figure 3-24 shows the spectrum of the laser solution after use in the laser system for 69 days. From a comparison with the spectra in Figure 3-21, it is evident that there is no significant water contamination. The extent of contamination of the laser solution over a period of six weeks is shown in Figure 3-25. Over this period of time there appears to be a very slight tendency for the water contamination level to increase, but the scatter in the points is too great for this to be a firm conclusion. After 100 days, the laser solution is as efficient as at the start of the experiment.

It is clear that there is a problem associated with the preparation of absolutely anhydrous $POCl_3$ and that its reactivity with water involves a serious risk of contamination on handling or in use. The problem with the laser solution is that at some level of water contamination, $ZrOCl_2$ begins to precipitate thus terminating the effectiveness of the laser.

As has been seen, even with the uncertainties in the precise level of water contamination a level of less than 50 ppm can be maintained in the laser circulating system for long periods of time. To determine the deleterious effects of contamination at this level, an experiment was set up in which laser solution deliberately contaminated at a level of 100 ppm was put in sealed containers. Over a period of three months, none of these showed any sign of precipitation. Furthermore, at this level the fluorescence

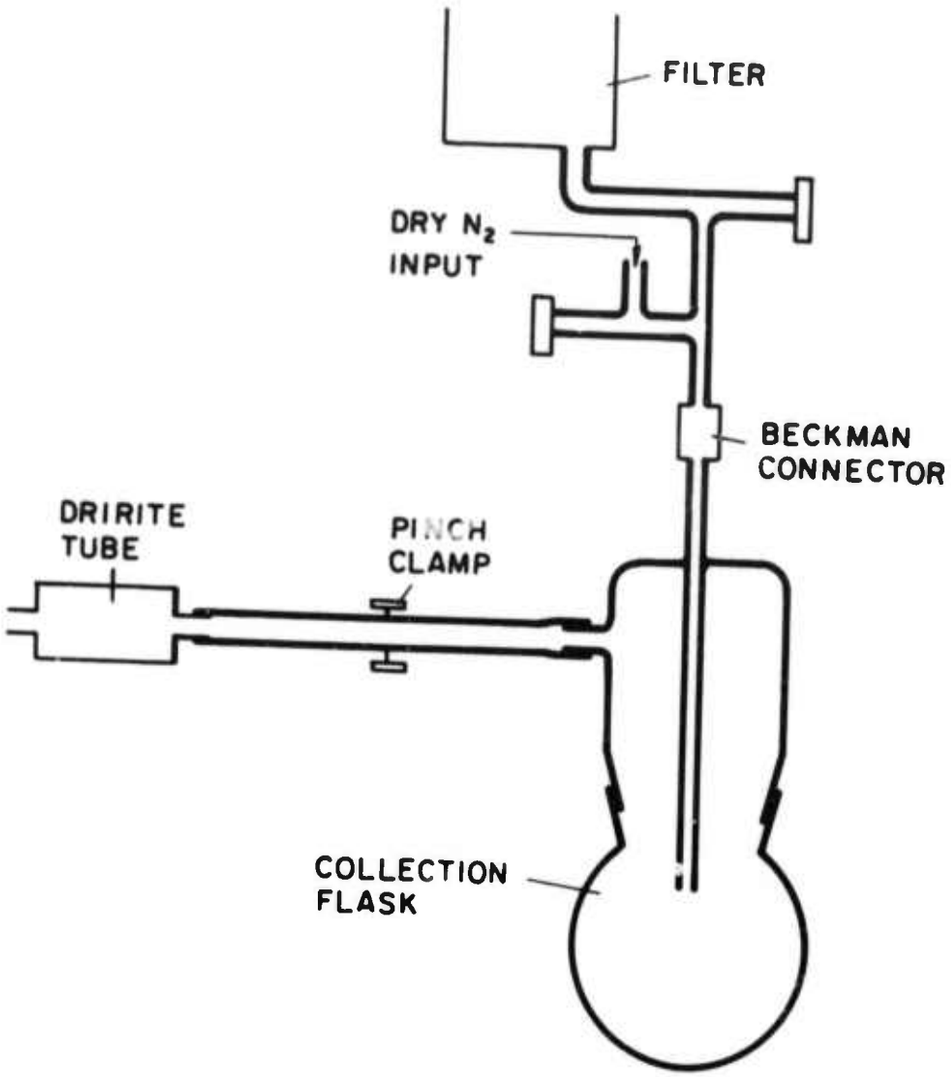

Figure 3-22. Collection System for Obtaining Samples of Liquid In Circulatory System

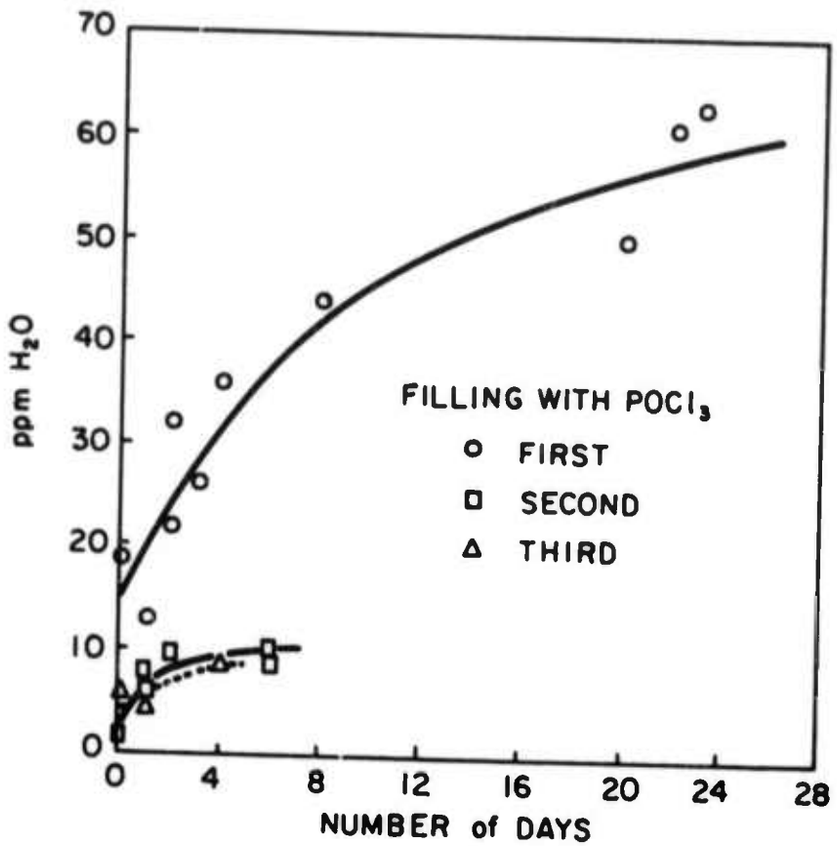

Figure 3-23. Water Level Contamination of Successive Fills of Circulatory System with Dry $POCl_3$

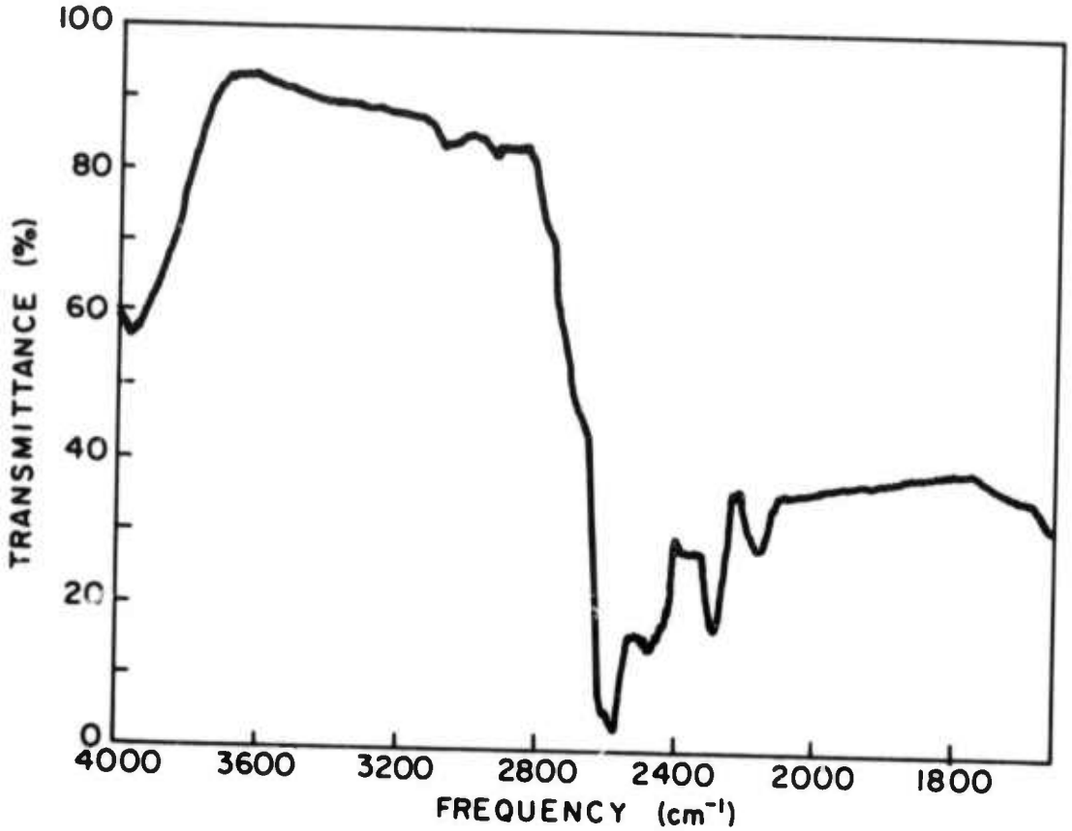

Figure 3-24. Spectrum of Laser Solution after Use in Laser System for 69 Days

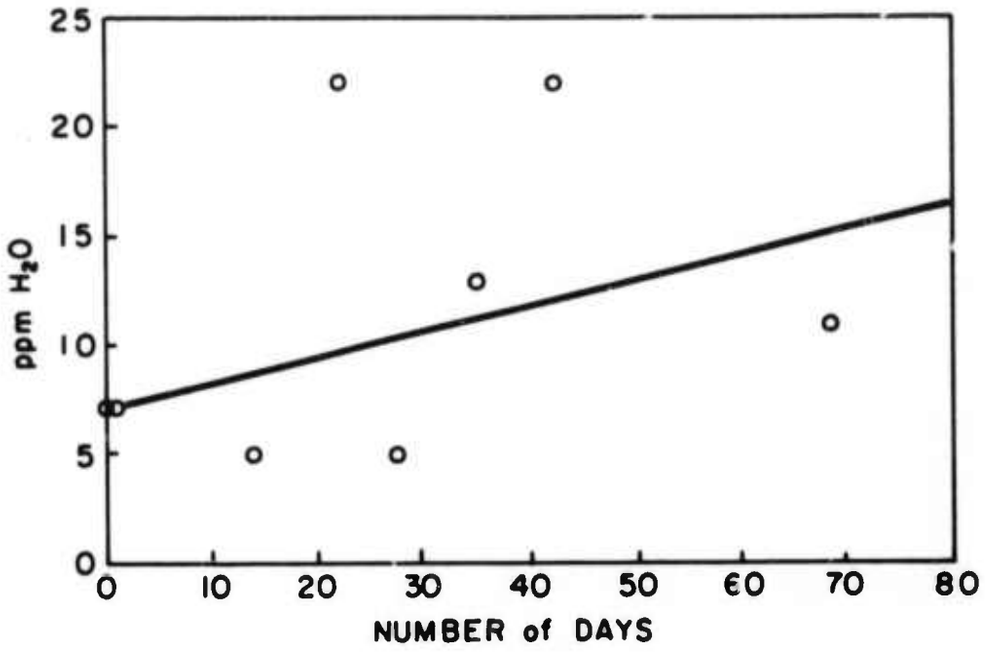

Figure 3-25. Water Contamination Level of Laser Solution as a Function of Time of Use

lifetime of the laser solution is not at all affected. The 100 ppm then appears to be a realistic safe level of contamination.

3.2.2.2 Investigation of Materials for Circulatory System

In the design of an inorganic liquid laser system one of the most important factors is the selection of materials for the circulatory system. It is vital that these materials be stable to the laser liquid and lead to no deterioration of these properties of the laser liquid essential to the laser process. In early systems only Pyrex glass, Teflon (virgin), nickel 200, 316 stainless steel, and mercury were used. Even though the last two were known to dissolve at a slow rate, they did not affect the fluorescence lifetime of Nd^{+3} and were at least acceptable.

The first circulatory systems, however, were inadequate and the central difficulty was the circulatory pump. In general, pumps deriving their motive power by means of a shaft coupled to an external driving motor were considered unsuitable. All such schemes involve a shaft seal to limit communication between the pumped liquid and the external environment. In the present application, unless the liquid isolation is complete and achieved by a totally inert seal material, the circulatory system, and the laser, will, as experience has shown, have a very short life indeed.

The conceptual problem of the pump was solved when the idea of a "canned" pump was reopened. A version of such a pump was used in the earlier liquid laser work based on the selenium oxychloride solvent system. This solvent system so limited the choice of materials for constructing the pump that to seek the assistance of commercial pump manufacturers was totally impractical. Our own pump designs were limited in torque transmission so that the pressure head required to achieve adequate flow for a high-average-power, high-repetition-rate laser system were not available.

The advent of $POCl_3$-based systems relieved some of the material compatibility problems and stimulated the search for a commercial pump source. This was not a trivial problem. Most such pumps are based on electromagnetic coupling to provide the driving power. Consequently, large amounts of heat are dissipated in the circulated fluid. In our application this is not acceptable since it puts an excessive burden on the cooling system. However, a pump manufacturer, Liquid Dynamics Inc., has recently marketed such a pump for the chemical and drug industry and has a minimum heat dissipation in the driving circuit.

The basic design of the pump is illustrated in Figure 3-26. The key components with regard to materials compatibility are the impeller, pump casing, liquid containment barrier, and the can encapsulating the ferromagnetic material essential for torque transmission. The work to be detailed describes the requirements for material selection and the tests performed on them. Aside from compatibility with the laser solution, it is essential that the pump material be non- or weakly magnetic, have a high electrical resistance, and be readily castable or machinable. Within these restrictions the materials tested are listed in Table 3-7 along with their composition. The pump manufacturer suggested the use of Carpenter 20 steel because this is the material customarily used in the construction of the pump.

TABLE 3-7

COMPOSITION OF MATERIALS TESTED

	Fe	Cr	Ni	Residual
316 Stainless Steel	0.65	0.17	0.14	0.04 (Mn, Si, Cu)
Carpenter 20 Steel	0.30	0.30	0.34	0.06 (Mo, Cu)
Hastelloy B	0.05	0.01	0.635	(Mo, 28; Cu, V)
*Tophet 30	0.015	0.30	0.68	0.01 (Al)
*Tophet A	-	0.30	0.70	--
Inconel X	0.07	0.15	0.73	0.05 (Al, Si, Mn, Cu)
Ni 200	0.004	-	0.99	0.066 (Mn, Si, Cu)
**Brass	-	-	-	~0.6 Cu, 0.4 Zn

*High resistance alloy suggested by R. Steinitz of Wilbur Driver Company.

**This was not tested as a pump material. It was thought that nickel-plated brass might be used as piping in the circulatory system.

The tests were carried out in the following manner. Samples of the material to be tested were put into one-half inch diameter Pyrex test tubes and a constriction put near the top of the tube. The tube and sample were dried in a vacuum oven, and when dry, were quickly transferred to a dry box where they were filled with laser solutions to between one-half and two-thirds the tube volume. The tubes were then tipped off quickly

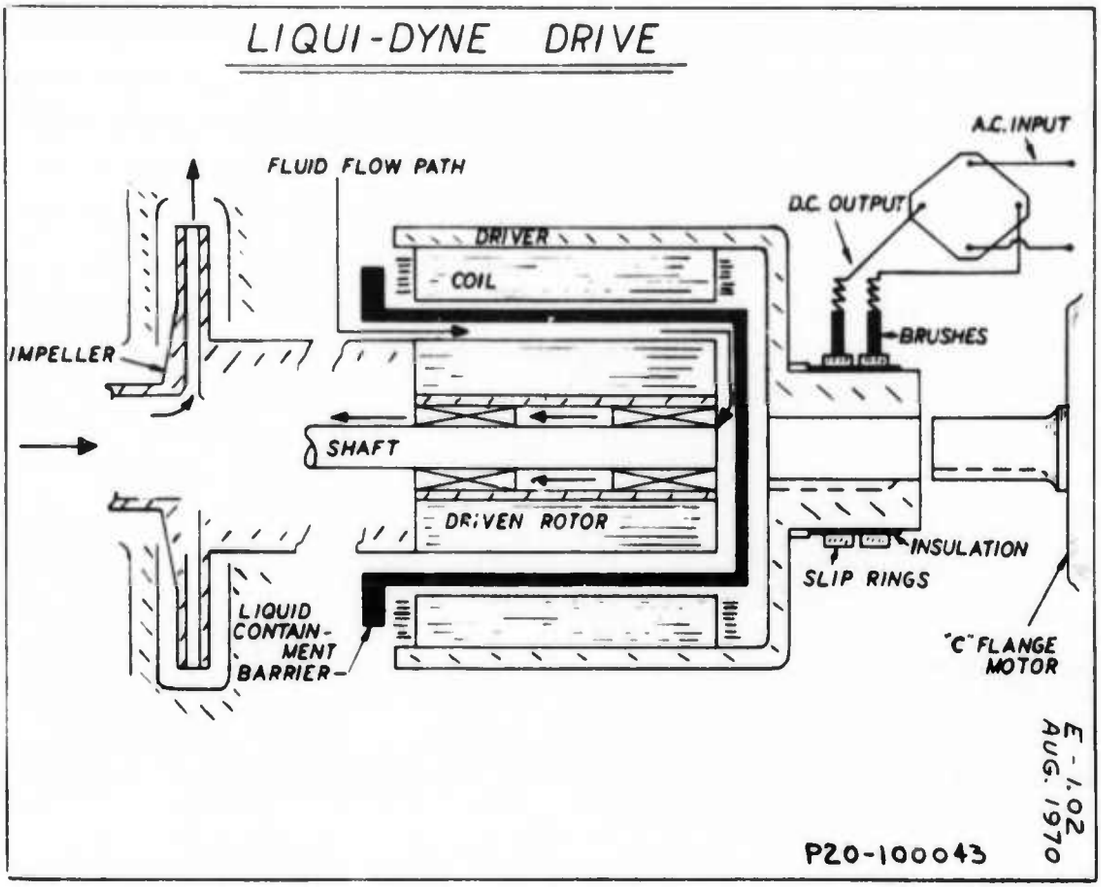

Figure 3-26. Liquid Dynamics, Inc. Pump Design

with precaution taken to ensure as little water contamination as possible. The tubes were then put into cans and held in place by crushed paper and batting, and, to stimulate the effect of a moving, circulating liquid, the cans were rolled on a rolling mill. In addition to a number of tubes for each material, a set of "control" tubes containing only the laser liquid alone were set up. Sample tubes were opened at periodic intervals and analyses for the various elemental components were carried out using the techniques of atomic absorption. Before the tubes were opened for analysis, a visual inspection of the solution was made and the fluorescence lifetime determined. The results of the analyses at times of 10, 48 and 55 days are given in Tables 3-8 and 3-9. In each table, the contamination from the control samples (Pyrex tube and laser solution alone) is subtracted from the total contamination in the tubes with the various materials to provide a measure of the corrosion rate of the material itself. From these data, the corrosion rates given in Table 3-10 were calculated.

TABLE 3-8

SAMPLE ANALYSES AFTER TEN DAYS

Sample Description	Ni (ppm)	Fe (ppm)	Cr (ppm)	Cu (ppm)	Zn (ppm)	Raw Total (ppm)	ppm Above Control Sample
Inconel X	2.2	4.5	1.2	1.2	-	9.1	2.3
Ni-plated on Brass	2.0	3.3	-	1.2	1.9	8.4	1.6
Ni 200	2.6	4.4	1.4	0.9	-	9.3	2.5
Tophet A	1.4	3.6	1.2	1.3	-	7.5	0.7
316 Stainless Steel	1.6	6.0	1.5	-	-	8.9	2.1
Tophet 30	1.2	3.6	1.2	1.2	-	7.2	0.4
Control Sample	1.5 (22%)	2.8 (41%)	1.1 (16%)	1.4 (21%)	-	6.8	-

TABLE 3-9

SAMPLE ANALYSES AFTER 48 AND 55 DAYS

	ppm Above Control Samples					Total (ppm)
	Ni	Fe	Cr	Cu	Zn	
Inconel X (55 days)	3.8 (22%)	11.3 (65%)	1.0 (6%)	0.2 (1%)	1.1 (6%)	17.4
Ni-plated Brass (55 days)	14.0 (36%)	11.3 (29%)	-	6.2 (16%)	6.9 (18%)	38.4
Ni 200 (55 days)	21.7 (93%)	1.4 (6%)	-	0.2 (1%)	-	23.3
Tophet A (55 days)	0.4 (27%)	1.4 (23%)	-	-	-	1.8
316 SS (55 days)	3.2 (16%)	12.5 (64%)	3.2 (20%)	-	-	19.4
Control (55 days)	4.1 (31%)	4.6 (35%)	-	1.6 (12%)	2.8 (21%)	13.1
Tophet 30 (48 days)	0.2 (6%)	-	-	-	3.3 (94%)	3.5
Carpenter 20 (48 days)	5.2 (45%)	3.7 (31%)	2.7 (23%)	0.2 (1%)	-	11.9
Carpenter 20 (48 days)	2.3 (46%)	1.5 (30%)	1.0 (20%)	0.2 (4%)	-	5.0
Carpenter 20 (48 days)	3.1 (44%)	2.1 (30%)	1.6 (23%)	0.2 (3%)	-	2.0
Controls (3) (48 days)	4.8 (42%)	3.3 (29%)	0.3 (3%)	1.5 (13%)	1.4 (12%)	11.3

TABLE 3-10

CORROSION RATES OF VARIOUS MATERIALS IN Nd^{+3} LASER SOLUTION

Material	Corrosion Rate ($ppm \cdot in^{-2} \cdot day^{-1}$)
Pyrex (4 control samples)	0.020
Tophet A	0.070
Tophet 30	0.155
Carpenter 20 (3 samples)	0.22
Inconel X	0.41
316 Stainless Steel	0.45
Nickel 200	0.53
Ni-plated Brass	0.93

Of the possible materials that might be used for pump construction, Tophet A had by far the lowest corrosion rate. However, both Tophet materials are difficult to machine or work and their application would have been pursued only in the event that other materials were at a very serious disadvantage. A very interesting result is that Carpenter 20 steel, the one normally used in pump construction, has a very low corrosion rate. This rate is in fact less than half that of nickel 200, which had previously been successfully used in our own pumps.

Visual inspection of the tubes during the corrosion tests showed two main characteristics. First, after a period of time, a white precipitate formed. Attempts to obtain analyses of the precipitates were not very successful but tended to indicate that the precipitate was $ZrOCl_2$. This usually precipitates when the laser solution becomes wet. The plated samples often produced a flaky black deposit. This seemed to be the plating itself, and this development obviated the testing of plated material. It is suspected that the flaking occurred because insufficient care was taken in preparing the metal or alloy surface for plating. The plated brass did not show such a precipitate but did show a significant corrosion rate, part of which was undoubtedly brass.

The lifetime tests showed that, within experimental error, there was no change in the fluorescence decay time. This indicated that the dissolved material themselves would present no difficulties.

The results of this materials study are twofold. First, the customarily used material, Carpenter 20 steel, was found to be slightly better than nickel 200. The latter material had been used as prior basic pump material with considerable success, so the same success can be expected from Carpenter 20 steel. In addition, it was also shown that Pyrex glass piping is superior to nickel-plated brass since it has a lower corrosion rate.

3.2.3 Pumps for the Nd^{+3} Liquid Laser

In this section, the general problem of pumps for the liquid laser system will be discussed and a review of the several types of pumps constructed for this application will be presented leading up to the development of the final design used in the present system. The experience gained in trying to develop a suitable means for circulating this admittedly difficult-to-handle laser liquid in small-volume systems can be useful in many applications where conditions may not be so severe but in which the circulated fluid must be maintained in as leak-free a system as possible. This section will review past methods and pumps used for circulating the laser liquid and describe the advantages and shortcomings of each.

3.2.3.1 Pressure-Vacuum Reciprocating Flow System

The initial attempt to flow the laser liquid through a flash-excited cell or cuvette was not by means of a liquid pump. The laser liquid used in this system was based on $SeOCl_2$ and, because of the limited list of materials compatible with this liquid, the arrangement shown by Figure 3-27 was used. The laser liquid as contained in two identical reservoirs and the laser cell beneath them. The laser cell used in this system was a primitive version of the final design but without the plug window-nozzle arrangements at either end. The liquid was simply let into the cell through sidearms at either end of the cell which were connected to the bottoms of the respective reservoirs. The operation of this system was such that the liquid was made to flow first in one direction and then in the other through the laser cell. This was accomplished by alternatively connecting the top of the reservoir flasks to vacuum and dry pressurized nitrogen gas by means of a glass four-way valve which was turned by a low-speed electric motor. The arrangement thus provides two complete flow cycles, back and forth, for each complete revolution of the valve. One complete velocity cycle of the liquid through the cell measured by means of stroboscopic observation of the liquid height in one of the reservoirs is shown by Figure 3-28. In the arrangement used for the data of Figure 3-28, the valve

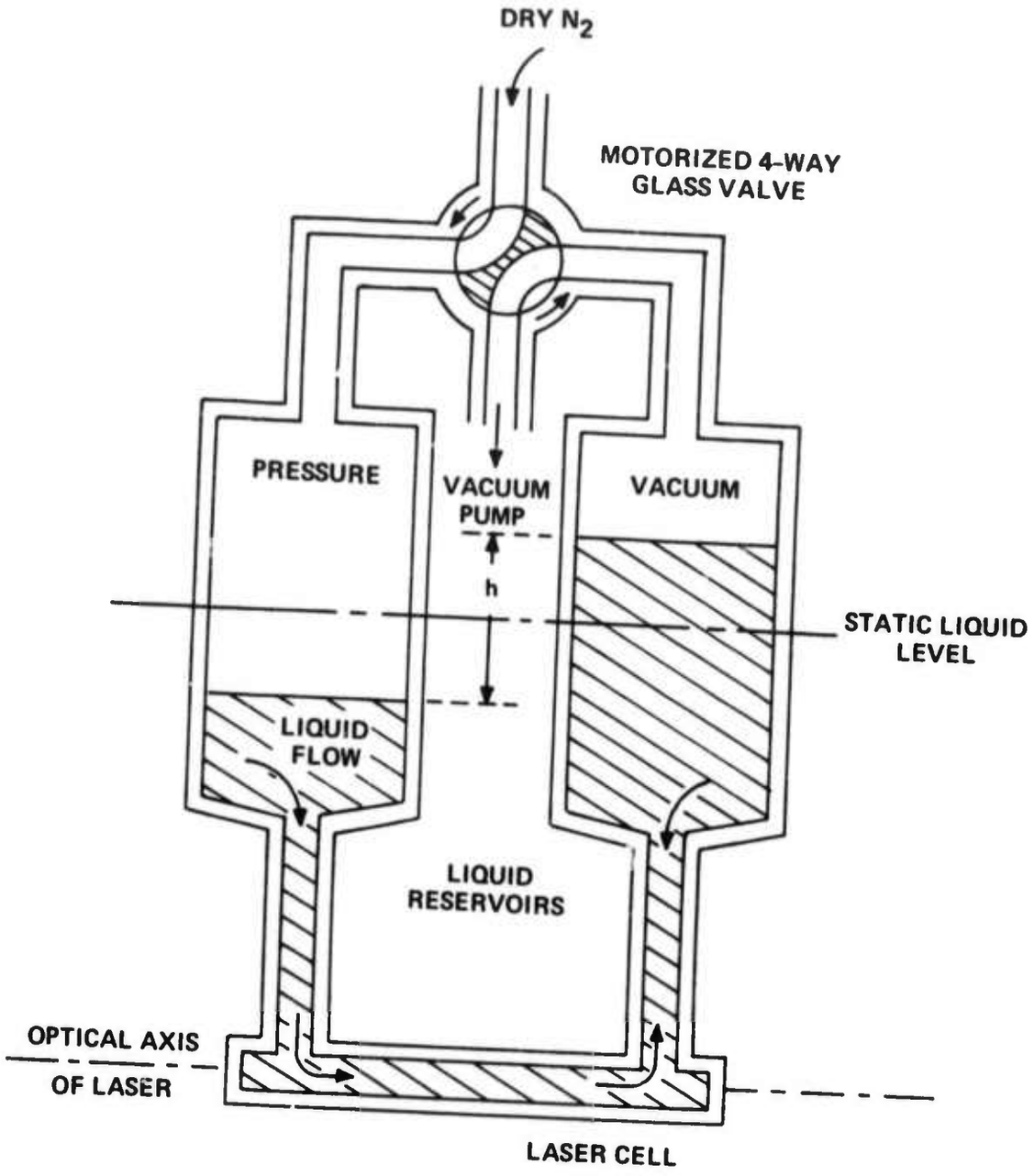

Figure 3-27. Push-Pull Reciprocating Flow System

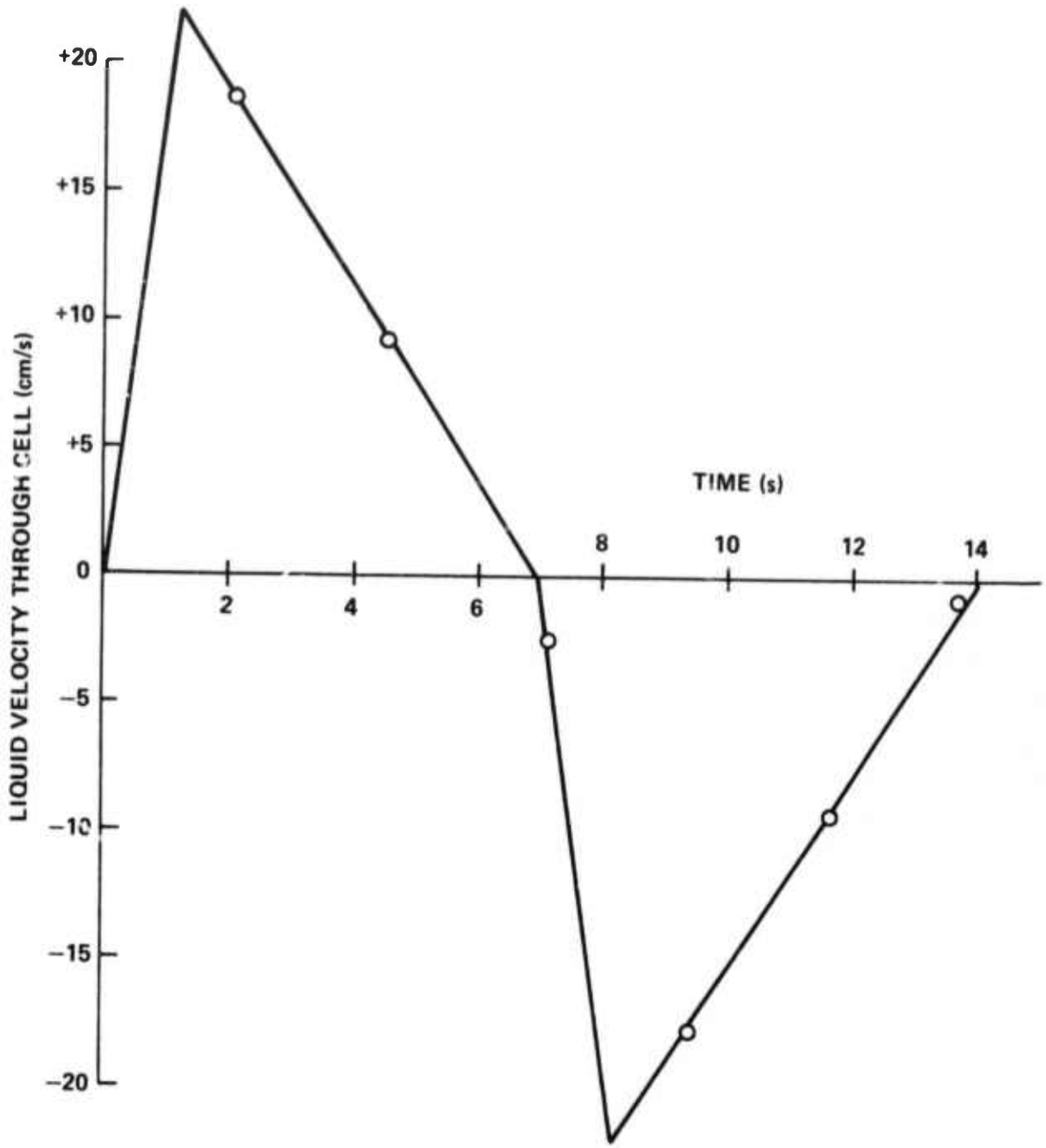

Figure 3-28. Laser Liquid Velocity Through Cell for Push-Pull Pumping System

motor speed was set so the valve made one complete turn every 28 seconds. The velocity waveform (extrapolated by straight lines in the Figure) therefore has a period of 14 seconds.

Peak liquid flow velocity in this arrangement could be varied by changing the nitrogen gas pressure and vacuum pumping rate simultaneously. Peak fluid velocity was proportional to the maximum liquid level difference in the reservoirs (shown as h on Figure 3-28). Firing of the flashlamps was synchronized to the liquid flow cycle by means of a microswitch and cam fastened to the valve drive motor so that the lamps could be flashed at any time during the flow cycle.

The prime advantage of this sytem is that contamination of the liquid could only be by means of water vapor since there are no moving parts in direct contact with liquid to generate abraided particles. The entire wetted portion of the system was constructed of either glass or Teflon, which were the most inert construction materials known at the time. If proper care was taken to make sure that the nitrogen feed gas was well-dried, the system would, in principle, be contamination-free. There were several disadvantages, the main one being that the nitrogen pressure and vacuum pumping rate had to be carefully adjusted to prevent: (a) pulling the liquid entirely over into one reservoir or the other by using too large a difference between nitorgen feed and vacuum pumping rate, (b) having the magnitude of the nitrogen pressure so great as to risk blowing the system apart at the tubing couplings, or (c) making the pumping rate so high as to gradually decrease the average pressures at the top of the reservoirs to the point where the high vapor pressure of the laser liquid caused the fluid to boil. Another disadvantage was that a steady-state flow was never developed through the laser cell since the liquid velocity was continually changing. It, therefore, was clear that reproducible results under repetitive pulsing could only be obtained by firing the lamps every half-cycle (at best) of the fluid flow. Practical considerations of liquid density and viscosity along with required nitrogen pressures and pumping rates would, therefore, limit the repetition rate to about one shot every two seconds.

3.2.3.2 Magnetically-Coupled All-Teflon Pump

To overcome the disadvantages of the reciprocating-flow system, a series of pumps were constructed. At the outset, it was clear that we desired a centrifugal pump design as opposed to a positive displacement pump (although one of the several pumps constructed or purchased was of the latter type). This choice was based on the fact that positive displacement pumps are more prone to cavitation of the liquid than

centrifugal due to the more abrupt acceleration of the fluid in the pump. It is also easier to regulate flow with a centrifugally-pumped system by means of a valve in series with the pump.

The first pump designed and constructed was a magnetically-coupled centrifugal pump[71, 72] shown by Figure 3-29. The casing, impeller and cover plate were machined out of a Teflon block. To the back of the impeller was attached a cylindrical Teflon capsule containing a stack of magnets. The casing had a thin-walled extension into which the magnet capsule could be inserted and about which a hollow stack of magnets could be rotated to cause the impeller to spin. The external magnets were driven at 1140 rpm by an electric motor.

The diameter of the impeller was 4 inches and the vanes were 3/8-inch high; the magnet capsule was 1.5 inches in diameter and 4 inches deep. With this pump, which was driven by a variable-speed motor, a laser liquid of 12-centipoise viscosity was pumped through a 6-inch cell of 10-mm bore diameter. Figure 3-30 is a plot of the flow rate versus motor speed.

This pump suffered from a lack of torque transmission due to the relatively weak permanent magnets used as impeller and drive units. Even after design and construction changes, the magnetic coupling could not be made strong enough to transmit enough power to the circulating fluid without slippage. Another problem developed due to the fact that the laser liquid (using the $ScOCl_2$-based liquid in this case) would harden the virgin Teflon surfaces of the pump. For the thin-walled casing of the impeller magnets, this meant that abrasion of the chemically-hardened surface occurred when the casing rubbed against the surrounding pump parts and eventually leakage was observed. This pump showed, however, that the principle of a magnetically-coupled pump would work. The main problem remained of devising a strong enough coupling between motor drive and impeller. With the extremely limited choice of materials compatible with the $SeOCl_2$ laser liquid, the problem was insurmountable. As eventual developments showed, with a bit more leeway of available materials (using the $POCl_3$ liquid), these problems were capable of resolution and this type of design was ultimately the one adapted for the liquid laser system.

3.2.3.3 Positive-Displacement Diaphragm Pump

The next pump used to circulate the laser liquid was a commercial, positive displacement pump rated at 5 liters per minute with a maximum outlet pressure of 20 psig.[72] A system was designed for circulating the liquid through a 6-inch cell of

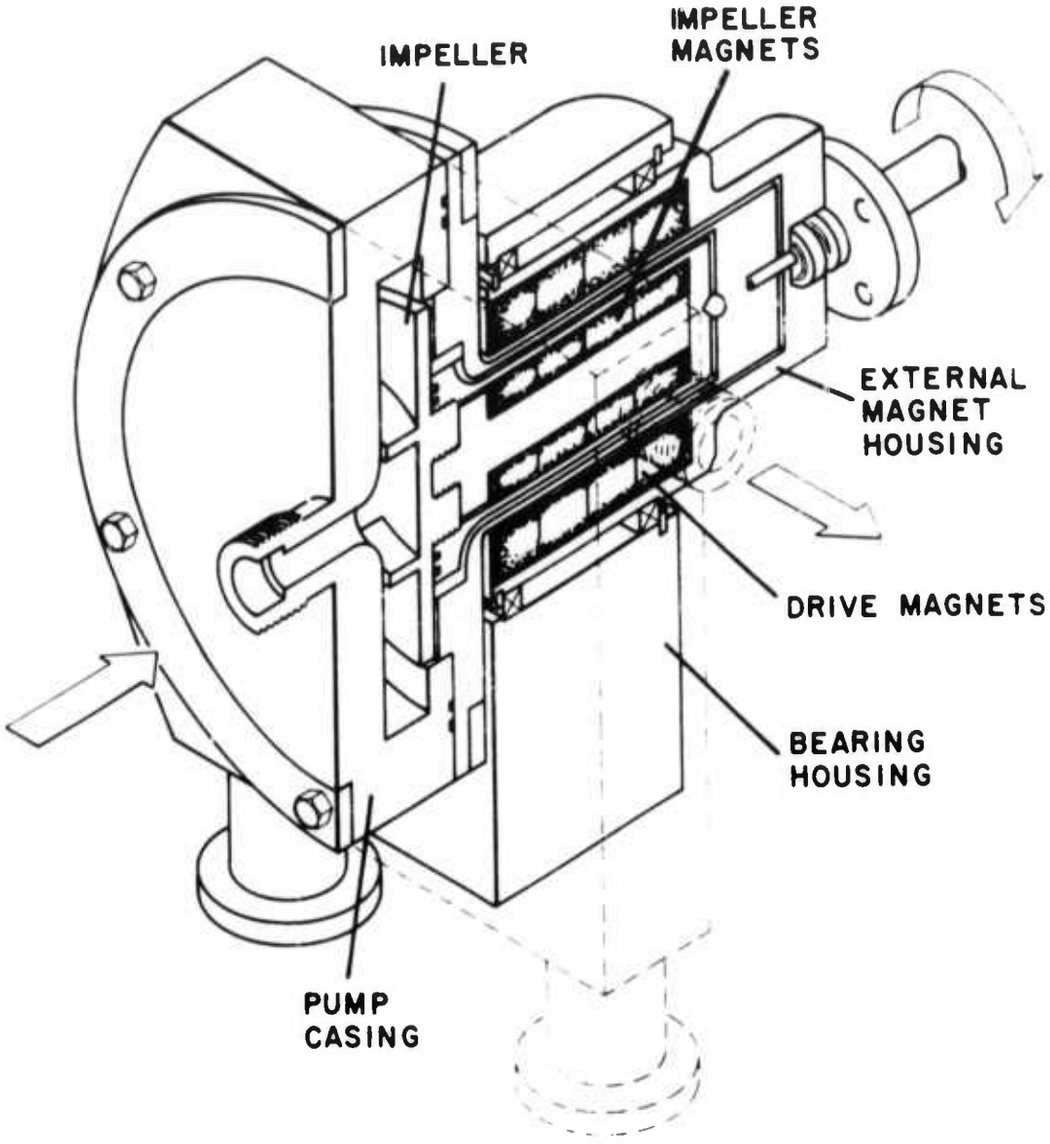

Figure 3-29. Teflon Pump Assembly

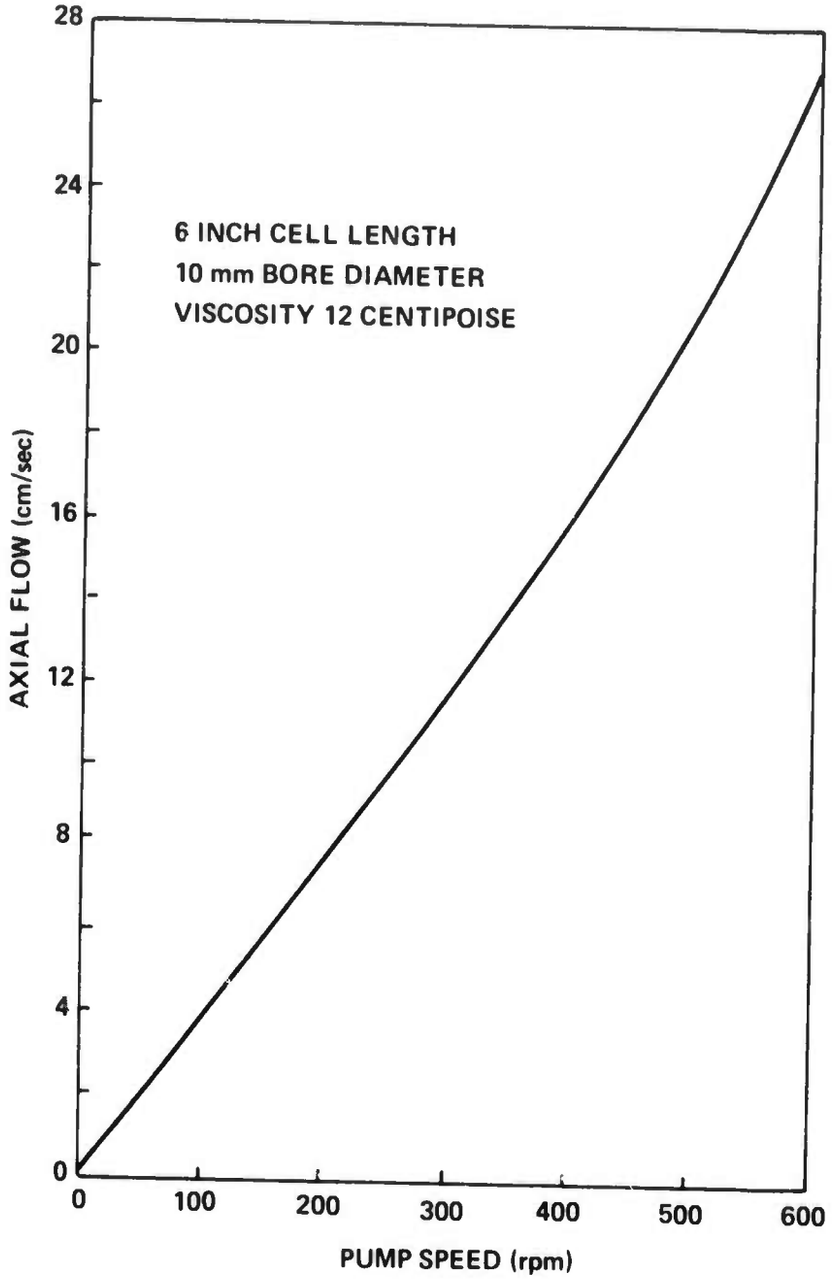

Figure 3-30. Plot of Axial Flow Velocity in the Cell as a Function of Pump rpm

5-mm bore. It was calculated that the maximum allowable pressure would not be exceeded if a 6-centipoise liquid was used, provided the system had an air chamber or some other device to take up the shock of the delivery stroke. Trials were made with acetone, water and finally the laser liquid. This pump made it possible to test lasing on a rapidly flowing liquid. The splashing of the liquid in the air chamber, however, created bubbles so that the pump could be operated for only a few minutes at a time. The bubbles escaped from the liquid on stopping the pump. When the system was taken apart if was found that the Teflon diaphragms had lost much of their pliability and that there was considerable corrosion of the metal parts. No holes or ruptures were found; some permeation appeared to have occurred.

Another pump was then developed which was also a positive displacement type, but which had diaphragms having greater resistance to the permeation of solvents. This pump was rated at 5200 cm^3 per minute and had a dial that set the flow to an indicated percentage of the maximum by altering the length of stroke. An expansion chamber that had a spring loaded diaphragm was used instead of the air chamber to smooth the flow from this pump. There was no difficulty with bubbles in this sytem, and the pump could be left running for hours at a time. There is some question, however, whether the pump continued to deliver the indicated rate of flow after a relatively short period of operation. Upon disassembly, the diaphragms again appeared to have failed through chemical hardening. Further development of this pump was abandoned due to the diaphragm problem.

3.2.3.4 Ceramic and Quartz Pumps with Labyrinth Shaft Seals

After the failure of the diaphragm positive displacement pumps, a series of centrifugal pumps were constructed. By this time, it had become clear that what was desired was a pump that would have volume flow rates in excess of several gallons per minute at moderate heads. This requirement was to be met using a laser liquid ($SeOCl_2$) of density 2.4 gm cm^{-3} and viscosity 12 cp. These design constraints implied that up to 1/2 hp electric motors were necessary to drive the pump at the requisite flow and head values. It was, therefore, felt that only a direct shaft coupling between the impeller and drive motor was capable of transmitting the torque and the problem of making a leak-proof rotating shaft seal was thus directly addressed.

The initial attempt in this direction was to make the length of the shaft seal as long as possible (labyrinth shaft seal). Two such pumps, one of ceramic and the other of synthetic quartz, were eventually constructed[73] and these are shown as Figures 3-31, 3-32 and 3-33. The shaft seal in these pumps consisted of a close-fitting impeller shaft

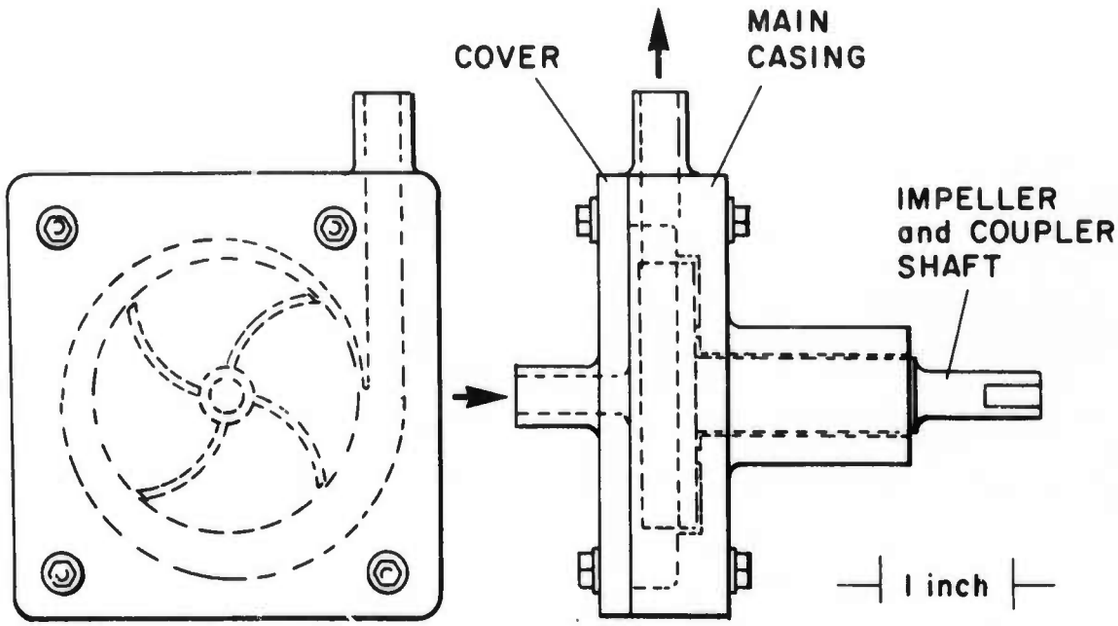

Figure 3-31. Diagram of Ceramic Pump

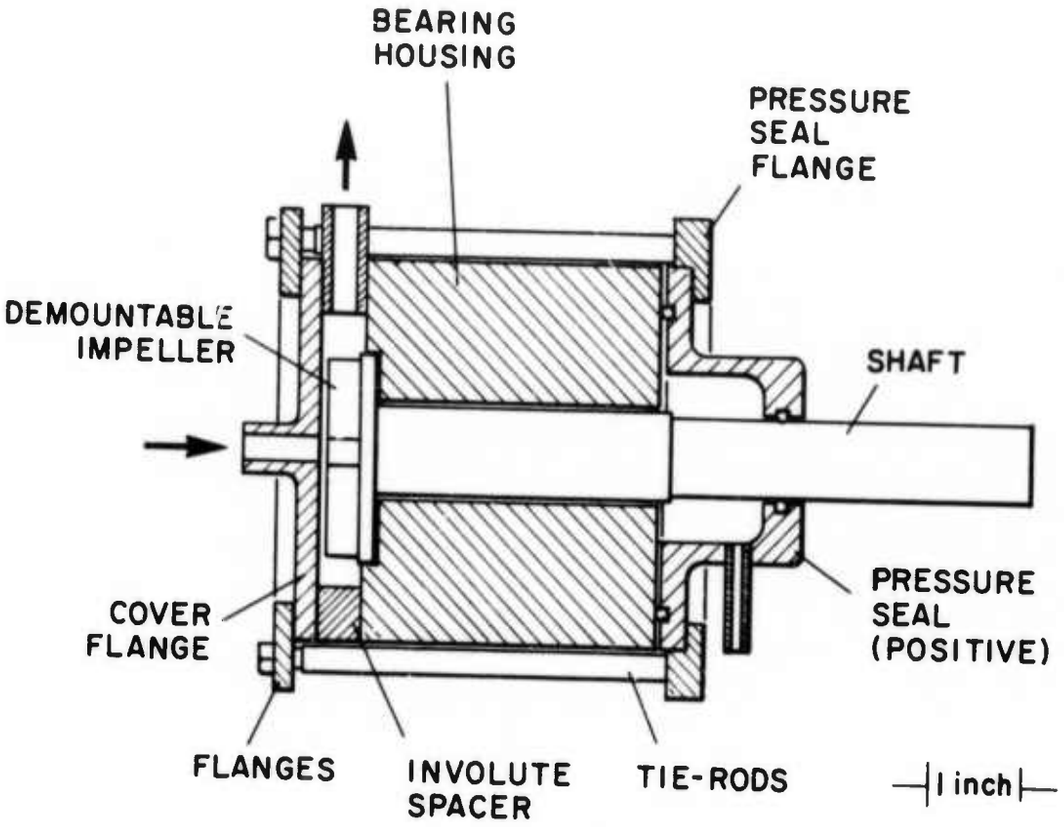

Figure 3-32. Diagram of Quartz Pump

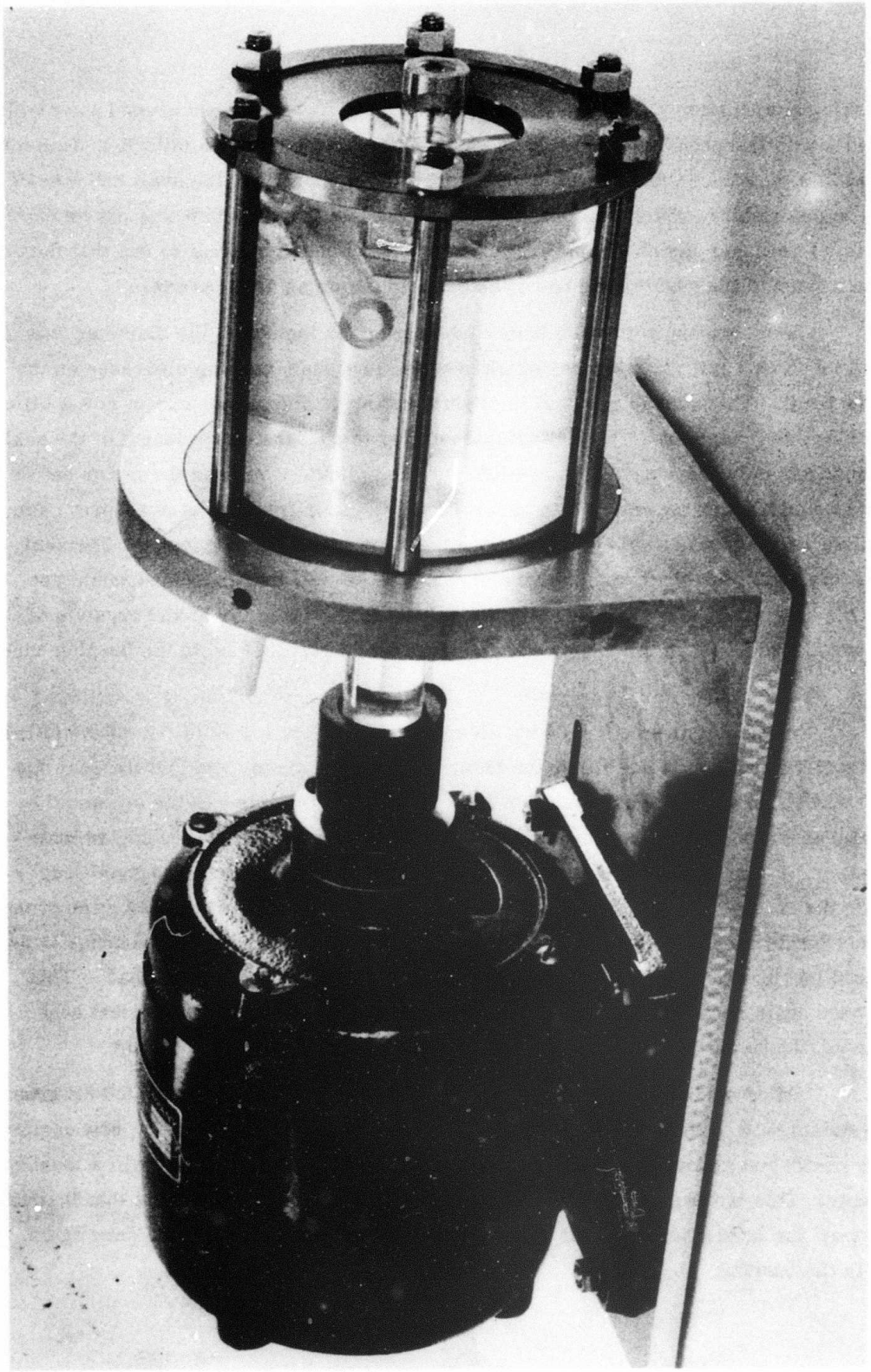

Figure 3-33. Photograph of Quartz Pump

and bushing combination. Both the shaft and bushings were centerless ground and highly polished for a clearance between shaft and bushing of from 0.2 to 0.5 mils (5 to 12 microns). This small a clearance did not lead to good results. In operation, the shaft had a tendency to bind in the bushing, which was probably due to the fact that the shaft was not lubricated by a film of the laser liquid. In several attempts, the binding became so bad that the shaft became welded to the bushing and had to be pressed out on an arbor press.

In an attempt to provide better lubrication for the shaft, the diameter was increased by about 1 mil (25 microns) which resulted in a shaft-bushing clearance on the order of 1 mil. This change resulted in slightly better performance, except now a different problem was manifest. The laser liquid seemed to coat the entire length of the shaft seal, but after only a few days of operation, the laser liquid film near the motor end of the seal would become saturated with absorbed water vapor from the atmosphere. The immediate result of this would be a dramatic increase in the film viscosity. The seal area at this end of the shaft would, therefore, not be so well lubricated and would get hot. This heat would evaporate some of the solvent in the laser liquid and crystals of $SnCl_4$ would form. When this happened, the shaft would rapidly bind in the bushing once again.

Increasing the shaft-bushing clearance by another 0.5 mils (12 microns) led to still a third problem; now, either the laser liquid would simply leak out the seal due to the hydrostatic head of the circulation system or the water vapor in the air would be gradually absorbed and diffuse through the laser liquid film in the seal to contaminate the system. Figure 3-32 shows a modification to the seal in the form of a small cup added to the rear of the seal to try to prevent this latter failure mode. This attempt met with only limited success in that when the pump was running, the natural tendency is for the liquid lubricating the shaft to be drawn toward the impeller end of the shaft. This would once again lead to an under lubrication of the motor end of the seal, local heat generation, lubricant evaporation, more heat and eventual binding of the shaft.

Other modifications tried included prelubricating the shaft with a TFE grease (which was dissolved by the laser liquid and led to eventual failure in the by-now common binding mode) and grooving the shaft in the bearing area in an attempt to form a local reservoir. This latter change decreased the bearing area to such an extent that it could not support the lateral torque loads of the pump in operation and the shaft, once again, bound in the bushing.

3.2.3.5 Mercury Shaft Seals and Nickel Pumps

With the advent of the $POCl_3$-based laser solutions, more materials were found compatible with the liquid. In particular, mercury and the purest grade of commercially available nickel (Nickel 200) were found satisfactory for pump applications. The latter material in the form of either formed sheet stock or large bulk pieces and was used to fashion pump involutes, impellers, cover plates and tubing. Another major advantage was Nickel 200, the first metal found compatible with an aprotic laser liquid, had a decidedly better thermal conductivity than any previous materials and could, therefore, be used in an effective heat exchanger for the laser liquid.

To make optimum use of this breakthrough, new and larger laser systems were designed to operate at average output powers of up to 500 watts repetitively-pulsed at rates up to 5 pps. These design goals represented almost an order-of-magnitude increase over previous operational limits. Along with the goal of higher outputs and repetition rates came the requirement for larger and more reliable pumps. Since pump heads and flow rate requirements were increased, drive motor power also had to increase to one horsepower and more. The assembled pump-drive motor unit became a prodigious piece of mechanical engineering and construction which exceeded 100 pounds in weight. A comparison of the size of the involute and impeller of one of the two such pumps constructed entirely in our laboratories and shown as Figure 3-34 with the previous generation of pumps as exemplified by Figure 3-33, demonstrates this dramatic increase.

The discovery that mercury was nonreactive with the new $POCl_3$-based laser solutions cast new light on the prevalent shaft seal problems. As was clear during the previous work on the labyrinth shaft seals, the concept would work in principle if the problem of lubricant evaporation or contamination by absorbed water vapor at the shaft seal end could be solved. Mercury, in the form of a liquid dam seal, seemed to be the answer to this problem. Figures 3-35(a) and 3-35(b) show two moderately successful attempts in this direction. The first figure, 3-35(a), shows a pump with a nickel involute and impeller with a ceramic shaft and bushing combination which functions as a labyrinth seal as described in the previous section. A modest groove was ground into the inside of the bushing near the drive motor end to act as a well for mercury which was introduced into the well by means of a nipple through the bushing. The mercury, therefore, acts as a dam and prevents the laser solution in the pump and seal area from coming in contact with the atmosphere. Evaporation or contamination of the liquid

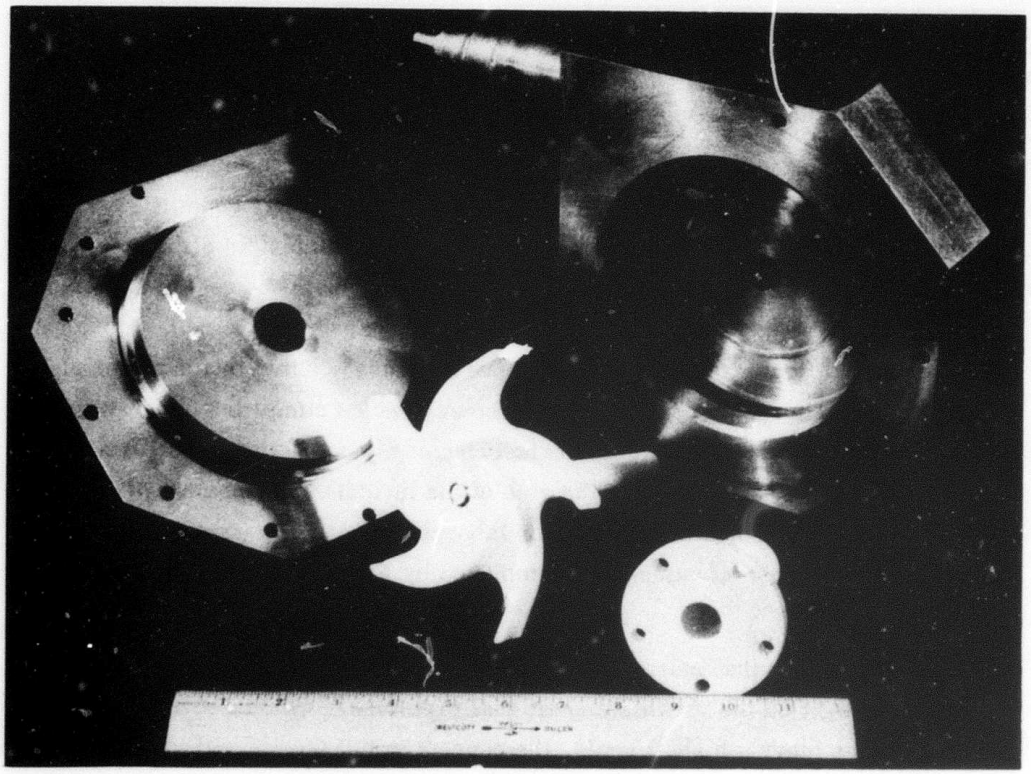

Figure 3-34. Circulatory Pump, Disassembled, Showing the Impeller, Housing, Involute, Shaft and Bushing

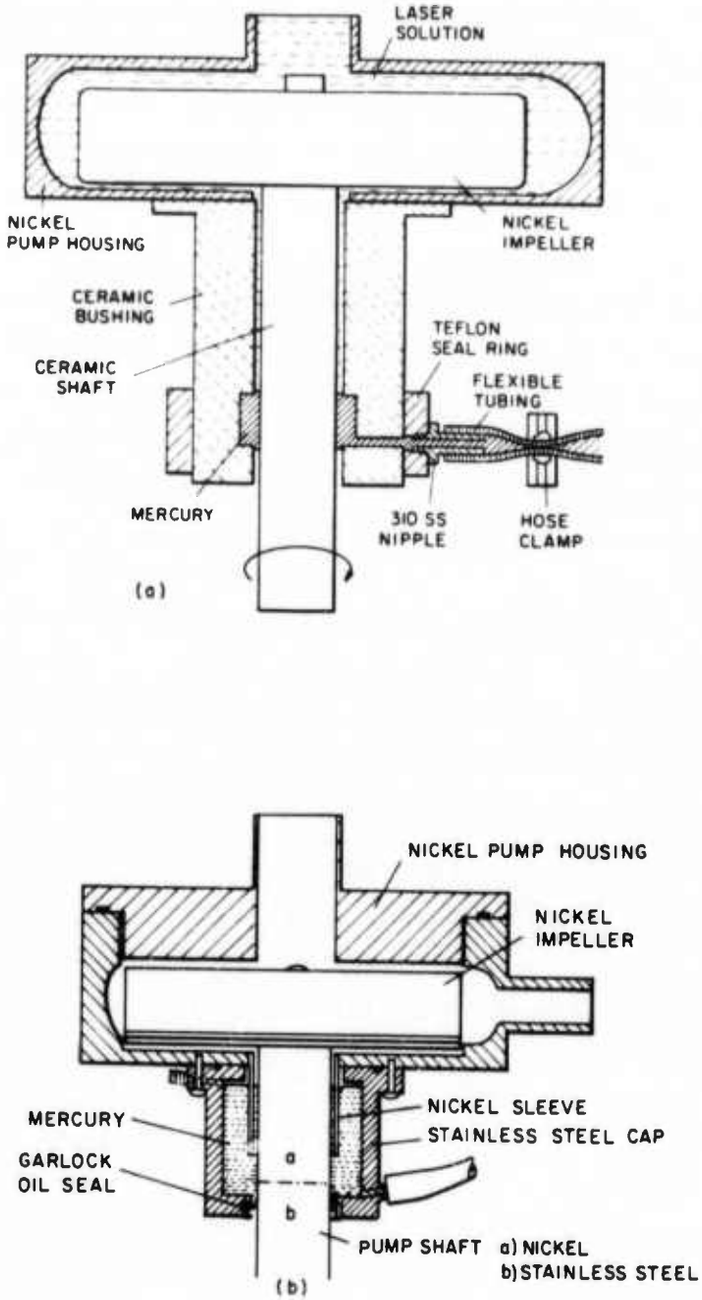

Figure 3-35. (a) Schematic drawing of circulatory pump used in Q-switched oscillator; shows first working model of mercury dam seal. (b) Schematic drawing of laser circulatory pump used in oscillator/amplifier; shows a second design of mercury dam seal.

lubricating the labyrinth seal is thereby avoided. This concept was proven by eventual operation of this pump for several months without any contamination of the laser liquid. Operating characteristics of these pumps in actual laser systems are shown by Figure 3-36. In these two figures, the points accompanied by numbers indicate the number of laser cell volumes exchanged per second at a given pump shaft, rpm. In both these systems, volume flow rates through the laser cells were large enough to give turbulent flow (Reynold's Number greater than 3000).

The two pumps, shown by Figure 3-35, represent our final attempts at developing a rotating shaft seal for the aprotic liquid laser. As such, the effort was deemed a qualified success, judging from how long the pumps would operate before failure. In these final seals, we separated the function of alignment of the shaft-bushing combination by using an external set of bearnings for locating the pump shaft in the labyrinth (bushing). The external bearings, therefore, took up the shaft side thrust under running conditions and especially during start-up and slow-down. The ultimate embodiment of the labyrinth concept was thus the design shown in Figure 3-35(b) where the ceramic bushing was replaced with a nickel sleeve sitting inside a stainless steel cup which was partially filled with mercury. This final design allowed us to construct the pump with parts wetted by the laser liquid made exclusively of nickel. The Garlock oil seal shown at the bottom of the stainless cup was a simple rubber lip seal whose only purpose was to contain the mercury in the cup.

The design functioned extremely well in principle but did have a few minor flaws in practice. One flaw was that the length of the nickel sleeve and the volume of mercury in the cup had to be carefully chosen. The problem here was that under operation the pump develops a reduced pressure at the rear of the impeller where it joins the shaft. The natural result is that the mercury in the stainless steel cup behaves as a manometer; if the pressure of the air above the mercury surface in the cup becomes larger than that above the mercury between the shaft and sleeve, the latter level will rise. At a sufficiently large dynamic pump head, the mercury will rise so far as to spill out into the pump itself and get into the circulated laser liquid. In contradistinction to this behavior, if the static liquid head above the mercury between the shaft and sleeve was larger than that above the mercury in the cup, mercury would be forced out of the shaft-sleeve area and laser liquid would enter the cup. The most common failure mode for the entire seal arrangement was the destruction of the secondary Garlock oil seal through poor lubrication and overheating. It was found that this seal had to be regularly lubricated with a good grease to maintain the elasticity of the rubber lip element. When this was done, relatively long periods of operation (up to several months) were possible.

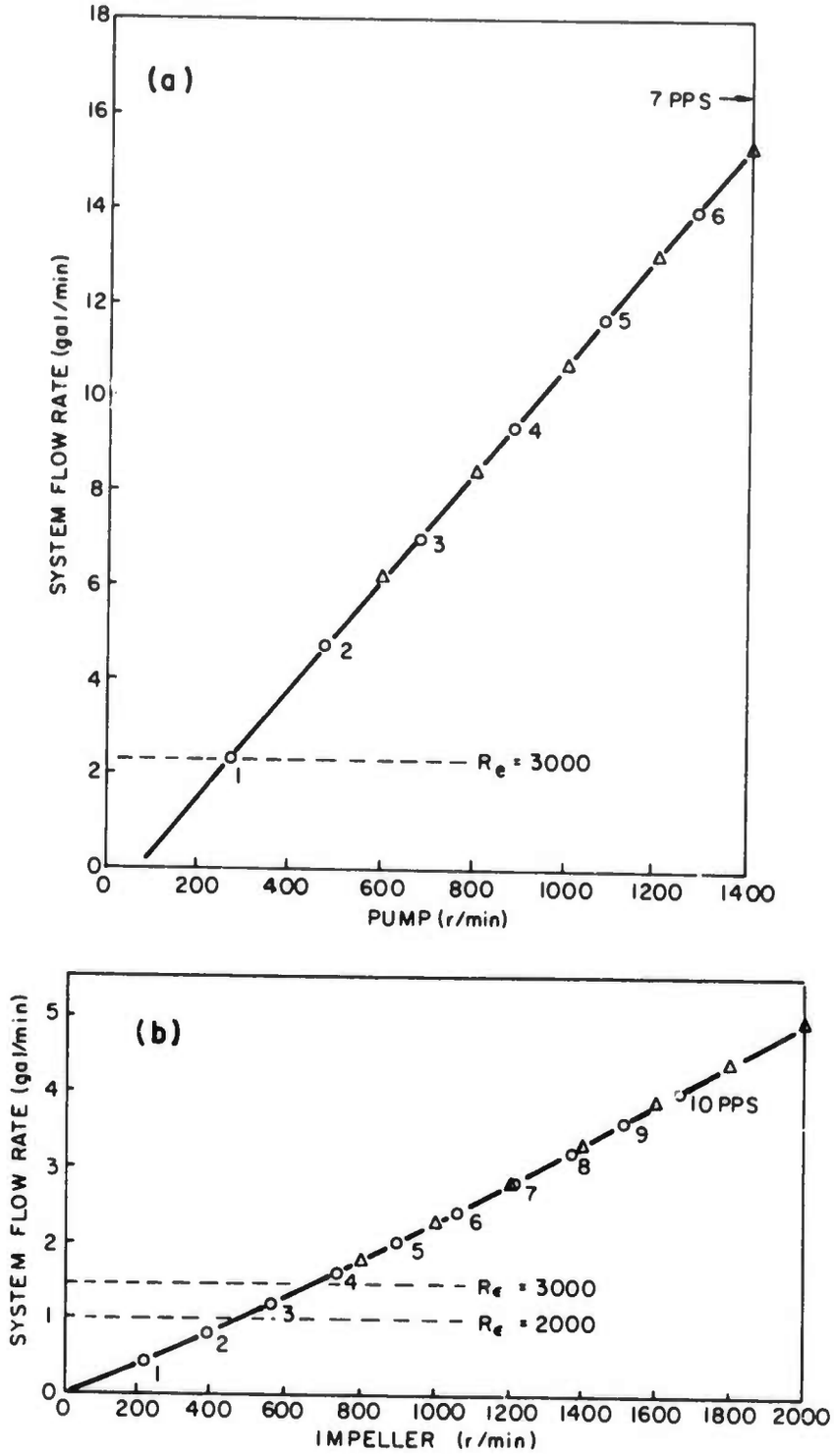

Figure 3-36. (a) Flow operating conditions of the liquid laser oscillator/amplifier system; (b) Flow operating conditions; Q-switched oscillator laser system

3.2.3.6 Liquidyne Pump

Toward the middle of 1970, we first became aware of a manufacturer of a "canned" or magnetically-coupled pump through contact with Mr. A. P. Frass of the Nuclear Reactor Division at the Oak Ridge National Laboratory. The application at Oak Ridge for this pump was the circulation of radioactive molten salts where obviously zero leakage was a must. Our subsequent visit to the manufacturer, Liquid Dynamics Corporation of Southampton, PA, revealed to us that the components of this pump were cast, forged or welded from a high-nickel stainless steel (Carpenter 20). The success and availability of this pump thus stimulated a materials testing program (the results of which were presented in Section 3.2.2.2) with a component redesign and modifications as necessary to adapt this pump to our use. A schematic diagram of this pump has already been presented as Figure 3-26.

Two identical pumps were eventually constructed and delivered in mid-1971. These pumps have served without a single case of failure in our liquid laser systems since then, a tribute to the conservative engineering and material qualification efforts expended over the lifetime of this project on this thorny problem.

3.2.4 Laser Cells for the Circulatory Liquid Laser

Materials used as the active media for condensed-phase lasers must have exceptionally good optical properties. For low-threshold and high-efficiency laser operation, the scattering of the light within the laser material by tiny inclusions or bubbles must be kept extremely low. Similarly, lens aberrations of the laser material can degrade the output and raise the oscillation threshold by destroying the ideal resonator cavity mode spectrum. When a liquid is used as the active laser medium, small temperature differences can produce index of refraction gradients large enough to seriously degrade the laser performance. By circulating the laser liquid, one can hope to realize the dual advantages of homogenizing small thermally induced refractive index gradients and dissipating flash lamp-produced heat in a simple external heat exchanger. These potential advantages make the circulating liquid laser an obvious candidate for a reliable high-average-output laser. From a device viewpoint, it therefore becomes imperative to establish for liquid laser cells design criteria based on sound hydrodynamic principles in order to maintain the inherently good optical properties of isothermal liquids.

Optical properties of a flowing liquid are primarily related to the nature of the liquid itself. The perfect optical liquid would be composed of small, rigid and preferably spherical molecules. Such a liquid would exhibit small scattering losses and have a low viscosity. At the present stage of material development, the aprotic liquid laser materials in use in Nd^{+3} liquid lasers do not possess all of these ideal properties. This does not necessarily imply that these liquids will not perform satisfactorily as a laser medium.

With these points in mind, we set up a program to test a variety of prototype designs for circulating laser cells using a standarized apparatus to evaluate overall optical performance of the cell. Most of these prototype cells were made of plastic (to simulate glass in the actual cell) and instead of the corrosive laser liquid, a glycerin-water solution of roughly the same viscosity (10 centipoise) as the laser liquid was used. This arrangement allowed inexpensive rapid experiments on many types of cells, resulting in the establishment of consistent and practical design guidelines for the liquid laser cell.

3.2.4.1 Test Procedure

A schematic drawing of the test setup is shown by Figure 3-37. The fluid flow system consists of a small positive-displacement pump, a large beaker filled with the glycerin-water mixture and a "mixing bottle" along with connecting tubing. The "mixing bottle" is a 5-inch long by 1-3/4-inch OD glass cylinder filled with 3/8-inch long by 3/8-inch OD glass cylinders rather loosely packed. As the figure shows, it is placed just before the input port of the laser cell and serves to smooth out any local temperature inhomogeneities in the entering fluid stream. Because of the design of the pump used in this particular system, it was impossible to keep the fluid flow rate constant for all the different cells investigated; however, this limitation was not found to be significant for the purpose of these experiments.

The optical arrangement works as follows.[74] The helium-neon gas laser generates a collimated red (6328 Å) beam of small diameter which is expanded by a small Newtonian telescope to overfill the aperture of the cell under test. A variable stop is then adjusted to the aperture of the cell and a 100-lines/inch Ronchi grating is placed behind the stop. Lenses L_1 and L_2 constitute another telescope which focuses the image of the Ronchi grating on the screen to be photographed by the camera. In practice, L_1 is fixed and L_2 is adjusted to focus, in turn, the near-field and far-field images of the grating on the screen. For convenience, let us call the combination of the laser cell and the lens L_1 and new lens L'.

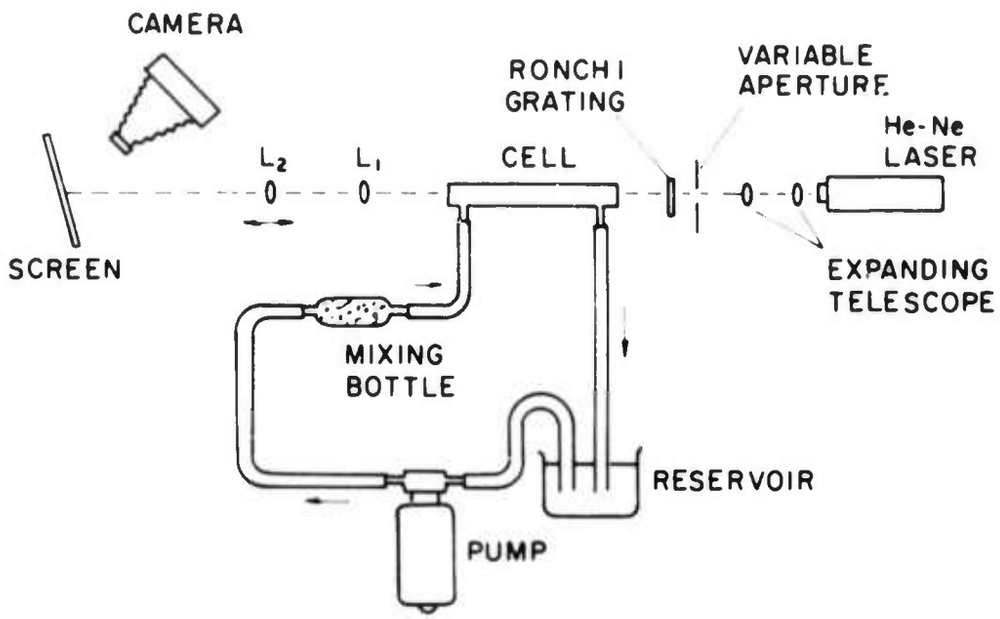

Figure 3-37. Optical Test Setup

In the near field, lens L′ will form a real image of the grating, R, at the point, P, as shown in Figure 3-38(a). Lens L_2 projects this image onto the screen, S, as a real noninverted image composed of a set of parallel lines. The parallelism of the image lines on the screen is a measure of distortion (variation of magnification of lens L′ away from the axis of the system), while the distortion of focus of the lines is a measure of the monochromatic aberrations (spherical aberration, coma and astigmatism) of the compound lens L′.

The far-field image of the grating is the image of the diffraction pattern of the grating, R, formed by the compound lens, L′, at its principal focal plane, S′, as shown by Figure 3-38(b). As is well known, the diffraction pattern of the Ronchi grating is a series of individual parallel-line images spaced according to the formula:

$$\sin\theta = \eta\left(\frac{\lambda}{d}\right) \qquad \eta = 0, 1, 2 \ldots$$

$\lambda = 6328\,\text{Å}$

d = grating spacing = 10^{-2} inches.

Since $\lambda/d = 2.5 \times 10^{-3}$, the line pattern will be equally-spaced for $\eta \leq 6$. Because the diffraction pattern is at infinity, the compound lens, L′, will form an image of a regular series of small dots at its principal focal plane, S′, which is only terminated because of the aperture of L′. The lens, L_2, is then adjusted to focus this image on the screen, S. The far-field pattern may also be described as the result of the transfer function of the lens, L′, acting on the spatial Fourier transform of the Ronchi grating (i.e., the decomposition of the light wave transmitted by the grating into a series of plane waves with wave vectors $\underline{k}_n$ where $|\underline{k}_n|$ = constant). It then becomes obvious that both the far-field and near-field images contain exactly the same information about the transfer function of the lens L′; however, in a different form in each case. Figure 3-39 shows typical far-field patterns expected for various distortions and aberrations in the optical performance of the cell along with the ideal pattern.

Aside from these regular and constant lens deformations due to the flowing liquid, there may also be present transient optical degradations due to bubbles, fluctuating thermal gradients, etc., in the moving liquid. These phenomena will also show characteristic figures in both the near and far-field patterns. Both the transient and steady imperfections in the optical quality of the flowing fluid are related to fluid stream behavior observed by eye under white light illumination of the cell perpendicular to the optic axis. The glycerin-water solution can be made to entrain small air bubbles as tracers of the flow through the cell for this purpose.

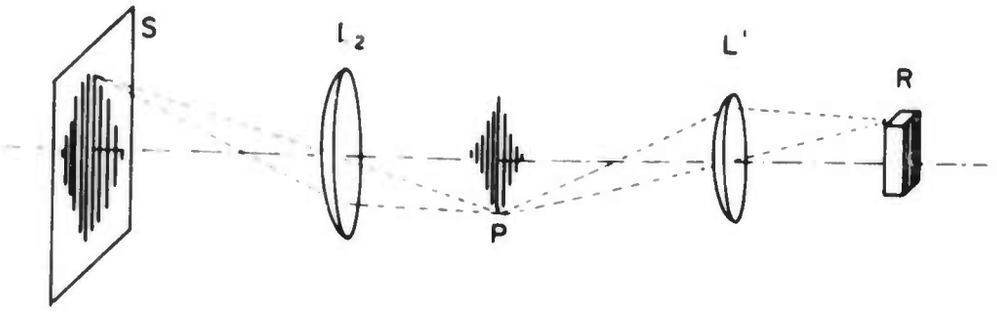

(a) NEAR FIELD OF RONCHI GRATING R

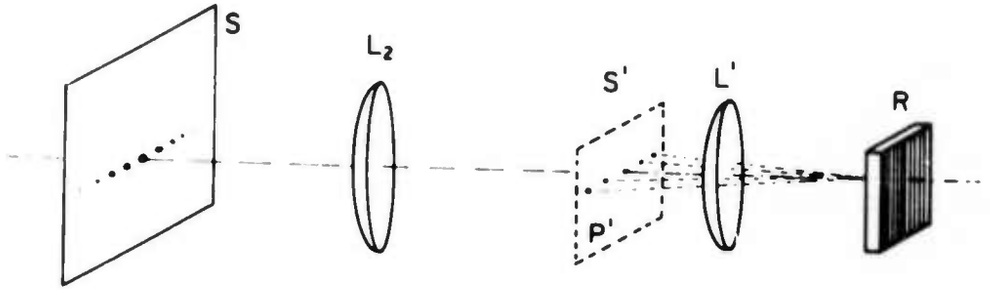

(b) FAR FIELD OF RONCHI GRATING R

Figure 3-38. Near- and Far-Field Images of a Ronchi Grating under Monochromatic Illumination

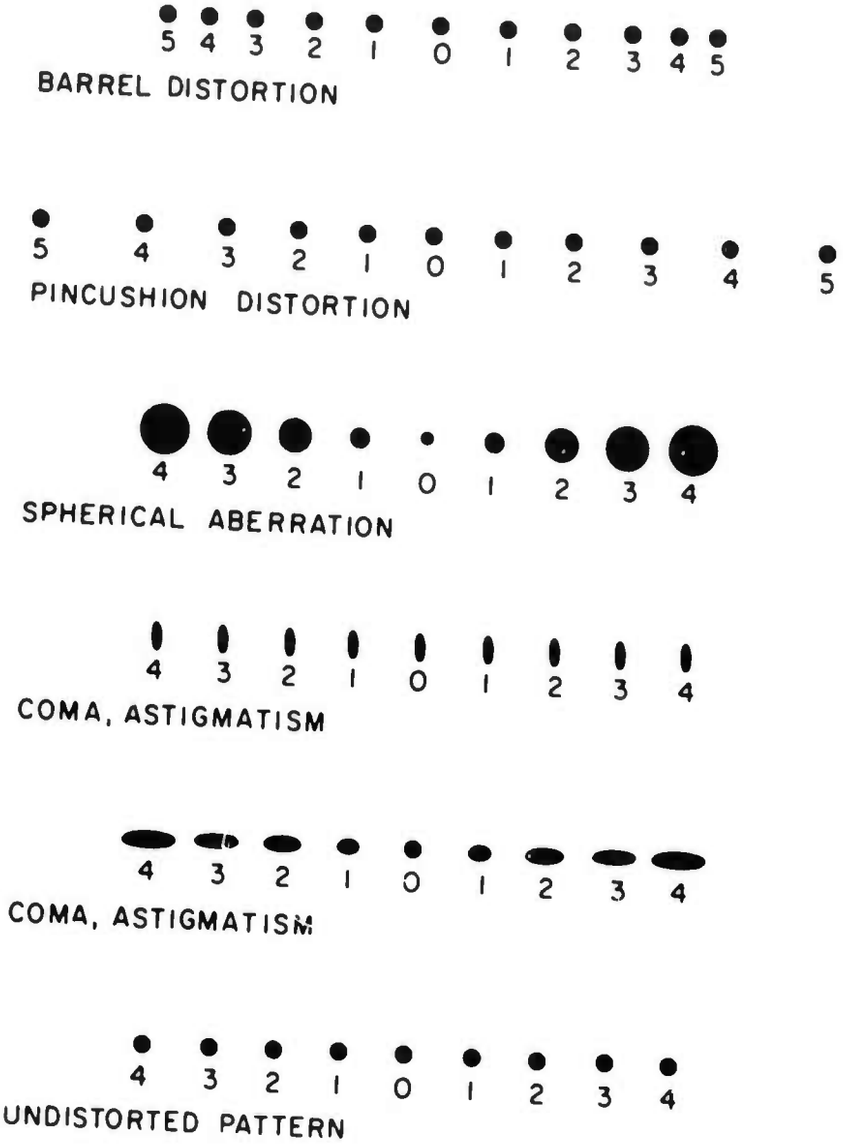

Figure 3-39. Far-Field Patterns for Various Forms of Lens Distortion and Aberrations

3.2.4.2 Results

This section presents the observations for four basic types of cells for the liquid laser: one small, longitudinal-flow cell designed to be used in a cw laser; two designs for a larger, longitudinal-flow cell to be used in a high-average-power pulsed-laser system; and a small, transverse-flow cell again designed for a cw application. Photographs of the near- and far-field patterns will be presented, and observed fluid-flow characteristics of the cell will be discussed with reference to the observed optical properties of the cell.

3.2.4.2.1 Small, Longitudinal-Flow Cell

This cell is a "barbell" type as shown in Figure 3-40. The respective dimensions of the cell are:

A = 3 inches
B = 5-1/4 inches
C = 6 inches
D = 3-1/4 inches
Cell bore = 3/16 inch.

To have a flow with a Reynold's Number greater than 3000 (turbulent flow), such a cell requires a flow volume of better than 1.5 gal/min.

Two series of photographs were taken with this cell in the system. The first series was with a small ceramic pump (centrifugal type) which was designed to be used with the aprotic laser solutions. With the cell, this pump gave a system flow volume of about 0.5 gal/min for a Reynold's Number of about 1000 (laminar flow). The pictures of the near and far fields for this situation are shown in Figure 3-41. The small positive displacement pump was then used in place of the ceramic pump and gave a flow volume of about 1.5 gal/min (turbulent flow). Figure 3-42 shows the results.

Figure 3-41(c) shows a distortion of the near-field close to the axis of the cell and Figure 3-41(d) shows a blurring of the first two orders of the far-field pattern. The two photos indicate a barrel distortion near the optical axis with rather strong blurring due to small scale variations of the index of refraction. All these effects are due to temperature inhomogeneities in the liquid. As Figure 3-40 shows, the fluid stream is purposely given a rotary motion at the entrance bells to the cell. The purpose of this is to mix any large-scale temperature variations before the liquid enters the

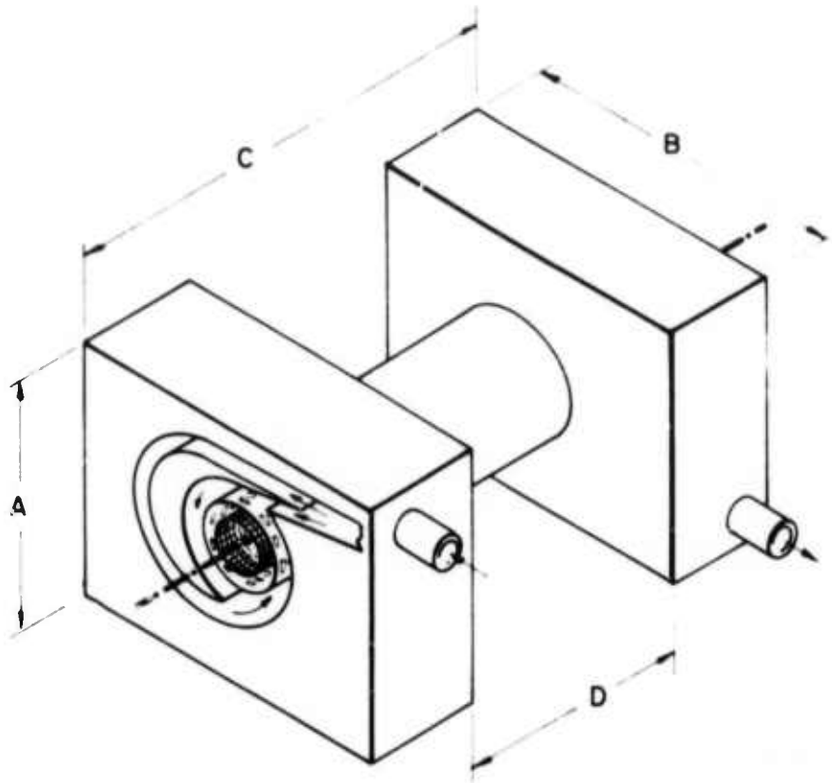

Figure 3-40. "Barbell" Cell

(a) Near field; flow-static

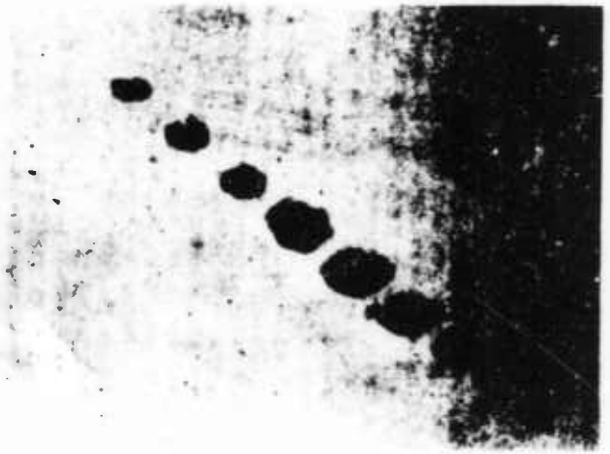

(b) Far field; flow-static

(c) Near field; flow ~ 0.5 gal/min.

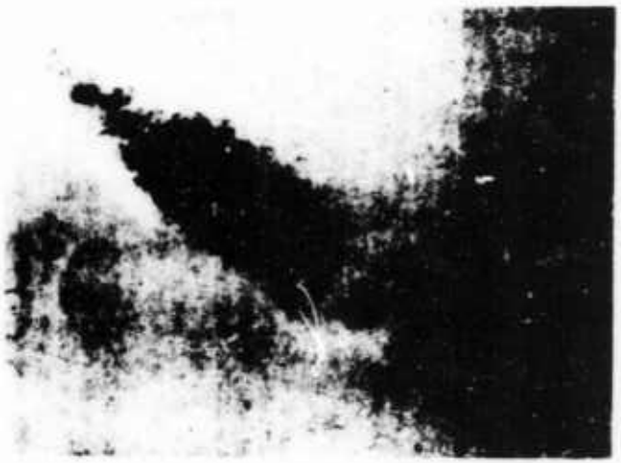

(d) Far field; flow ~ 0.5 gal/min.

Figure 3-41. Near- and Far-Field Flow Patterns for the "Barbell" Cell. Laminar flow (~ 0.5 gal/min)

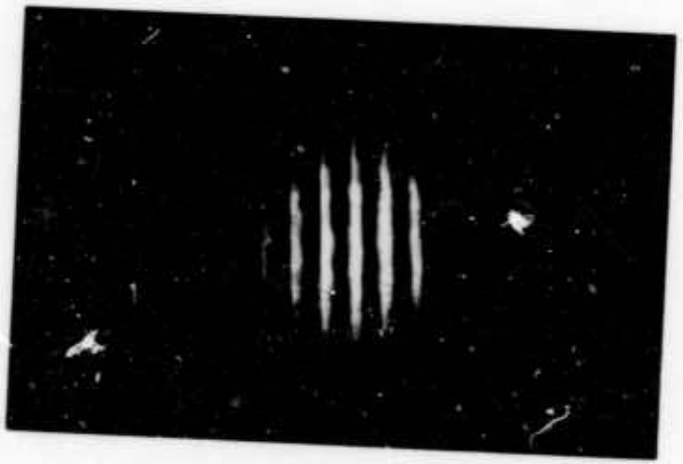

(a) Near Field; Flow - Static

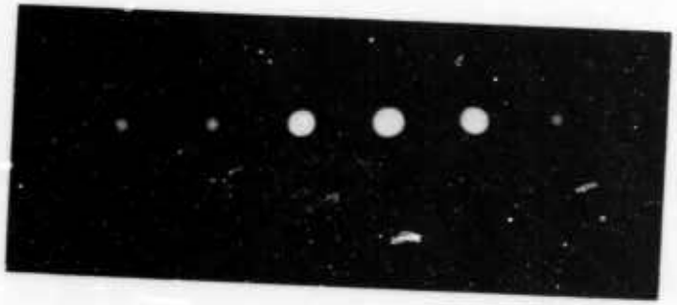

(b) Far Field; Flow - Static

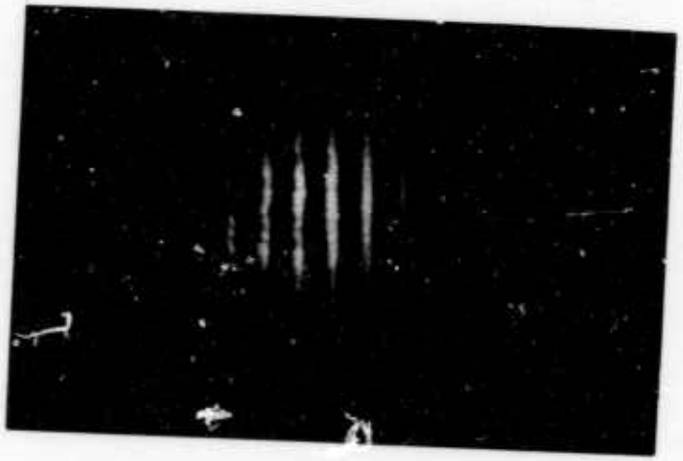

(c) Near Field; Flow ~ 1.5 gal/min.

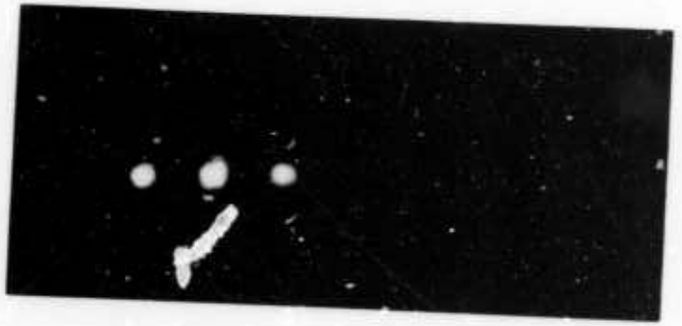

(d) Far Field; Flow ~ 1.5 gal/min.

Figure 3-42. Near- and Far-Field Flow Patterns for the "Barbell" Cell. Turbulent flow.

optical path. The two sets of screens shown in the figure are designed to produce a pressure drop from the outside chamber of the end bell to the optic axis of the cell so that the rotary motion will be broken up and damped out before the liquid reaches the optic path inside the cell. Apparently, this does not happen, and because the flow through the cell is laminar, this rotary motion persists throughout the cell length. A stable radial temperature gradient may therefore be established and produce the distortion observed in Figure 3-41(c). Similarly, because of the rotation of the flow through the cell, small-scale temperature fluctuations may be "trapped" near the optic axis and produce the scattering of the light beam which results in the blurring shown in Figure 3-41(d).

Figures 3-42(c) and 3-42(d) show the great improvement in optical quality obtained in this cell by increasing the flow rate so that the flow throughout the cell length is turbulent. In this case, the rotation of the fluid stream is damped as it goes through the cell and the improved mixing of small thermal fluctuations reduces the blurring of the far field. The barrel distortion seen in Figure 3-41(c) also disappears in Figure 3-42(c) for the same reason. The implication of these results is that if a particular cell has gross optical distortion due to the liquid flow patterns under a laminar flow situation, these distortions may be considerably lessened by increasing the flow volume so that a turbulent flow develops along the optical path.

3.2.4.2.2 Large "Nautilus" Cell

This cell, which is made of glass, is shown in Figure 3-43. The cell was designed, making use of the above observations, for a high-average-power liquid laser system. A 5-gal/min flow rate is necessary to establish a turbulent flow through the central 11-inch region. As may be seen from Figure 3-43, the incoming fluid is given a swirling motion in the entrance bell by placing the feed tube off to one side. This establishes a rotary flow down through the cell to the exit bell which acts as a small plenum chamber. The optical ends of the cell are cut at the Brewster angle.

The positive displacement pump delivered about 5.5 gal/min through this cell, and a good turbulent flow was assured. At this flow rate, a vortex was formed in the entrance bell on the window surface. It was fairly stable in location, but was outside the optical path of the beam through the cell and did not interfere with the optical quality of the images photographed. The photographs of both near and far fields for this cell are shown in Figure 3-44. As can be seen, no recognizable distortion in either the far- or near-field patterns can be discerned when the liquid is flowing. Futhermore,

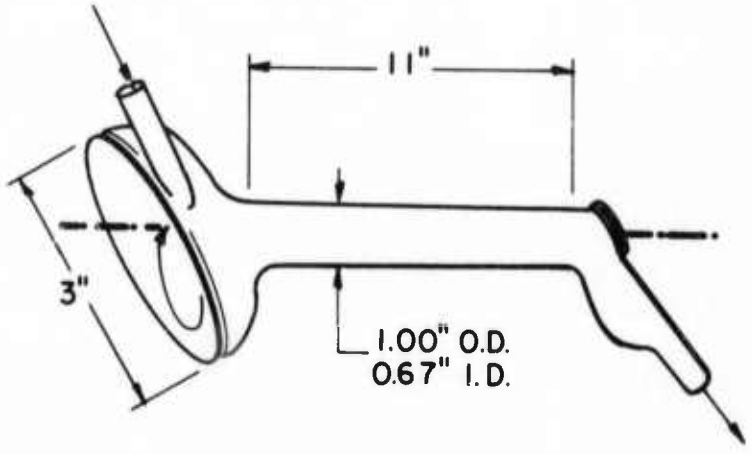

Figure 3-43. "Nautilus" Cell

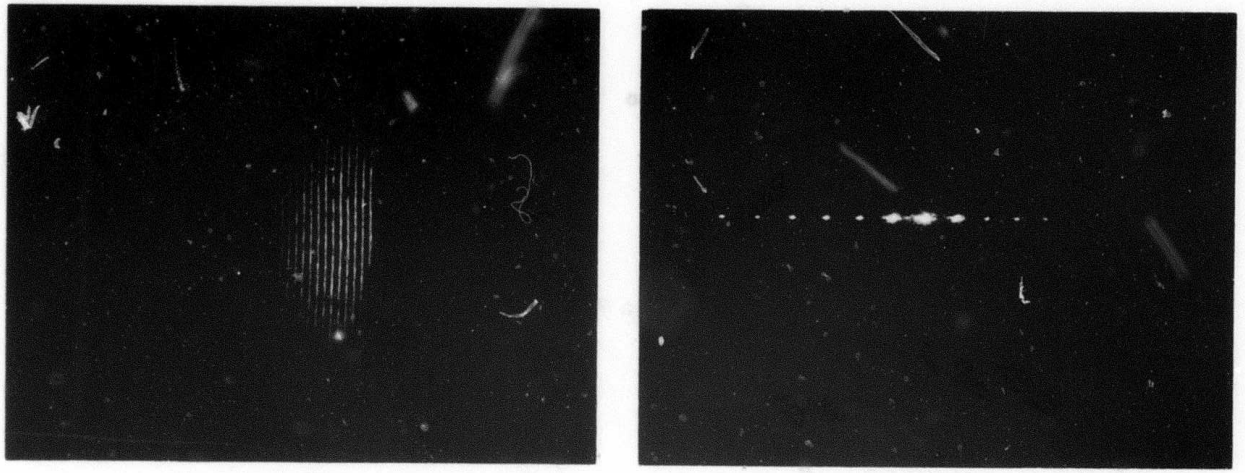

(a) Near field; flow - static.

(b) Far field; flow - static.

(c) Near field; flow ~ 5.5 gal/min.

(d) Far field; flow ~5.5 gal/min.

Figure 3-44. Near- and Far-Field Flow Patterns for the "Nautilus" Cell

the patterns remained undistorted even when the central tube section was heated by the flame of a match. This demonstrated in a very concrete manner that a good fully developed turbulent flow was obtained through the cell and that the optical quality of the cell as a whole was completely unaffected by the thermal condition of the cell wall.

3.2.4.2.3 Large "Nozzle" Cell

A section drawing of this type of cell is shown as in Figure 3-45. The bore of this cell is the same as that of the previous cell (0.67-inch) and the tube length is also the same (11 inches). The hydrodynamic design, however, is quite different. Fluid flow is not stablized by a rotary motion through the cell. The entering (and exiting) fluid is forced under pressure from a small annular chamber through a nozzle formed by a tapered plug laser window and the cell body. The flow through this nozzle should have a high Reynold's Number and flow separation should occur over the length of the cell noted as the transition region of Figure 3-45. There will thus be a pressure drop across the region which will establish the flow pattern for the rest of the length of the cell. If the nozzle is properly designed in such a cell, the large-scale turbulence induced in this transition region should be rapidly damped out. Of course, the question of flow stability arises in this design and is not easily answered by simple analysis for all nozzle geometries and fluid flow rates. For this reason, we constructed the whole cell assembly of plastic and designed the cell so that various plastic nozzle chambers could be attached to the main cell body and modified until a good flow pattern and optical performance was obtained.

Several observations of the flow patterns in the cell should be mentioned. In all the nozzle configurations tested (i.e., varying the depth of penetration of the tapered plug window into the nozzle throat and the size of annular entrance chamber), a stable flow pattern was observed in the "transition region." This pattern is formed because of an unequal pressure distribution across the throat area of the nozzle due to the asymmetric fluid flow into the entrance chamber. One nozzle variation was tried with slots cut into the cell throat area parallel to the axis of the cell to try to relieve the pressure difference as well as to damp out the rotation of the fluid, but this attempt failed and the pattern was even worse than before.

It is significant, however, that the observed optical patterns of the far- and near-fields were both free of distortion and sensibly identical for all variations of nozzle geometry used. This is a result of the fact that, even with a stable flow pattern present

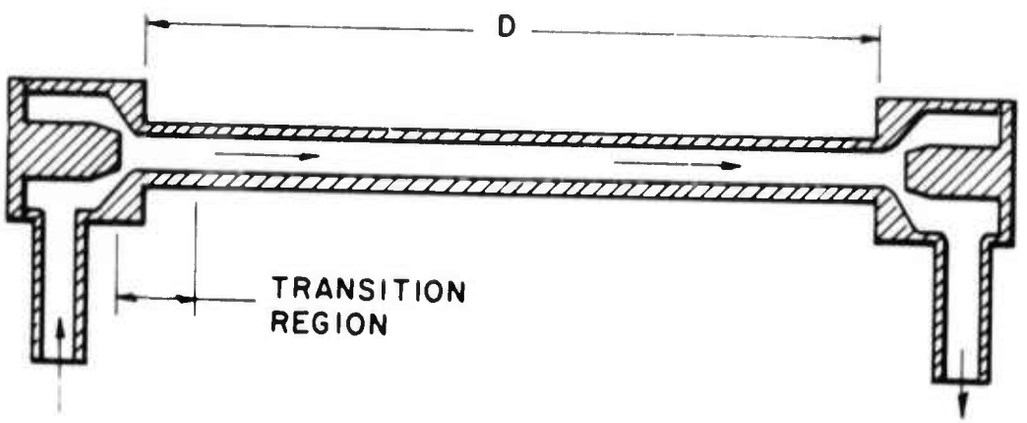

Figure 3-45. "Nozzle" Cell and Transition Region Flow Pattern

in the transition region, rapid and thorough mixing of the flowing liquid obtained throughout the optical path of the cell. The optical patterns through the cell were, as in the "Nautilus" cell, completely unaffected by heating the cell wall. A good indication of the fine optical performance of this design is indicated by Figure 3-46. Because of the inherently larger dynamic impedance of this cell design, the measured flow rate through this cell was 2.8 gal/min which gives a Reynold's Number of about 2000 through the cell length. Thus, even though the flow through this cell is probably closer to a laminar flow than a turbulent flow, no small or large scale distortions are apparent on the photographs. Because of the compactness and simplicity of construction of this design, this type of cell was used in all subsequent laser systems.

3.2.4.2.4 Small "Torah" Cell

This final cell design is different from the preceding ones in that the fluid flow is perpendicular to the optic axis of the laser as shown in Figure 3-47. This design allows for a faster laser pulse repetition rate, and, in fact, this cell is a plastic prototype of a glass cw liquid laser cell. The dimensions of the device are:

Cell length (D)	= 3 inches
Channel length (l)	= 3-1/2 inches
Channel width (w)	= 1/8 inch
End bell ID	= 2 inches.

The purpose of the screens shown in the entrance and exit bells is to establish a uniform pressure drop along the channel length and an even flow pattern through the central channel.

It is difficult to establish theoretically a unique flow rate required for a turbulent flow through the central channel section. The best estimate is that the flow rate should be 2 gal/min or better for the onset of a turbulent flow. The flow rate actually observed with this sytem was indeed 2 gal/min. The liquid flow pattern observed through the channel was stable and uniform at this flow rate.

The photographs in Figure 3-48 show an interesting phenomena. For this setup, the grating lines were lined up parallel to the flow and the input beam size was adjusted to overfill the rectangular cell aperture. In this case, the narrow channel of the cell (1/8 inch) acted as a diffraction object itself, and Figures 3-48(b) and 3-48(d) clearly show secondary maxima inside the normal grating diffraction patterns. A fine

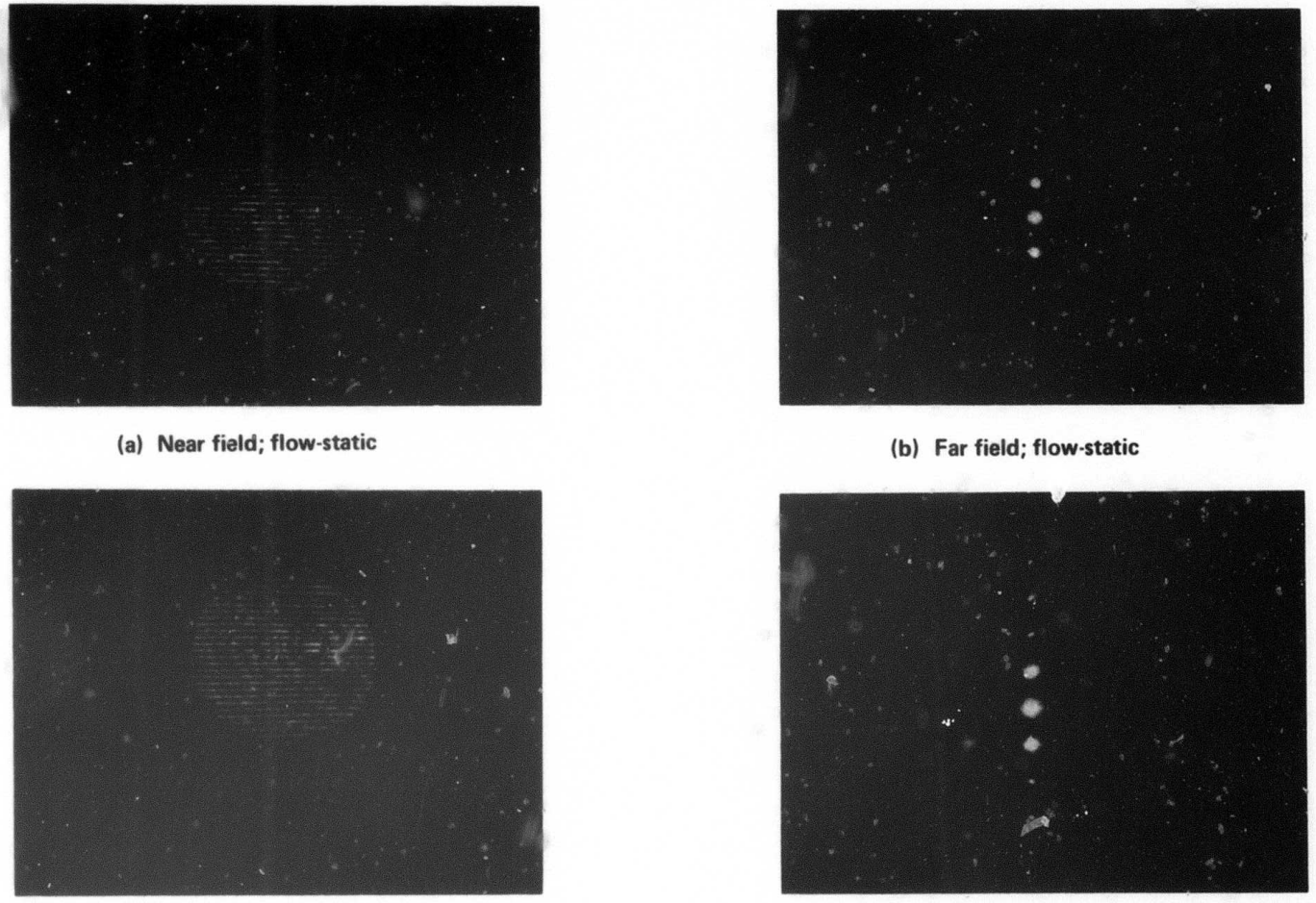

(a) Near field; flow-static

(b) Far field; flow-static

(c) Near field; flow ~ 2.8 gal/min.

(d) Far field; flow ~ 2.8 gal/min.

Figure 3-46. Near- and Far-Field Flow Patterns for the "Nozzle" Cell

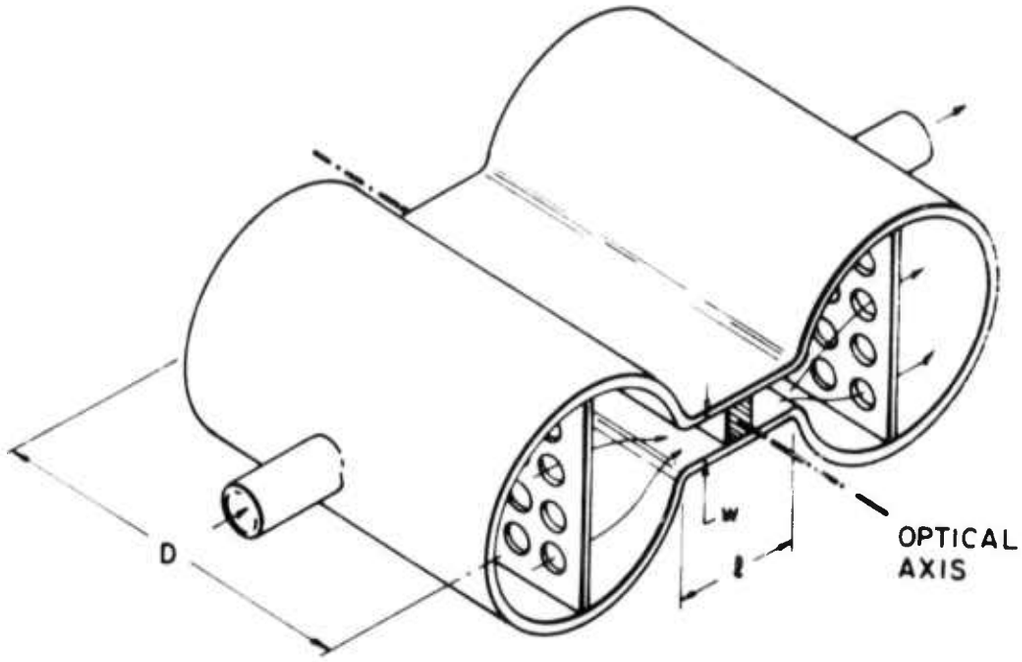

Figure 3-47. "Torah" Cell

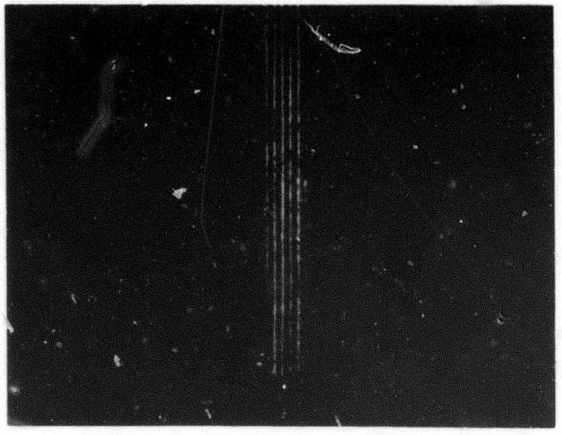

(a) Near field (magnified); flow-static

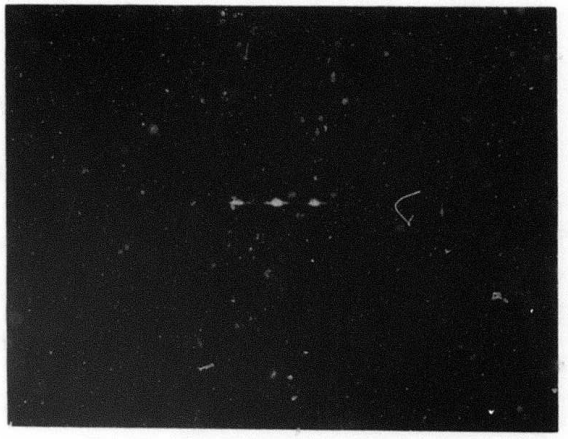

(b) Far field; flow-static

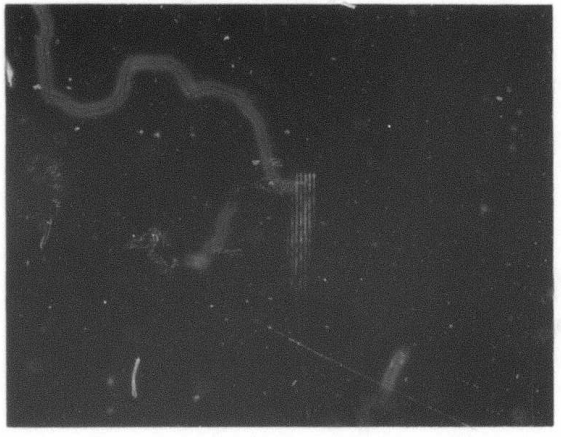

(c) Near field; flow ~ 2 gal/min.

(d) Far field; flow ~ 2 gal/min.

Figure 3-48. Near- and Far-Field Flow Patterns for the "Torah" Cell

structure can also be seen in the magnified photograph of the near-field with the liquid static [Figure 3-48(a)]. Although the near-field photographs show sharp and clear lines, the far-field photographs indicate an astigmatic aberration in this cell. Figure 3-48(b) shows this most clearly for the static case. This occurs because of the asymmetry of the rectangular channel. The difference in temperature between the cell wall and the liquid causes a thermal distortion of the index of refraction in the liquid across the small channel. This effect is reduced somewhat when the fluid is moving as Figure 3-48(d) shows; however, the flow appears to be inadequate to eliminate it entirely.

The cell showed a good even flow through the active cell channel. The flow appeared stable and smooth although, as the photographs indicate, because of the channel asymmetry, astigmatism may present a problem unless the flow rate is increased beyond the 2 gal/min rate used here. The results shown by this cell were considered encouraging enough so that an all-glass design of this type was considered for a small cw liquid laser cell.

3.2.4.2.5 Tests of Small "Nozzle" Cell Under CW Arc Lamp Excitation

The results above receive considerable support from our Air Force-sponsored research[75] into the feasibility of a cw aprotic liquid laser. In this work it was found that as the arc lamp power loading on the cell increased, the undistorted cross-section of the liquid in the cell decreased due to a radial temperature gradient. This is illustrated in Figure 3-49 which shows a near-field pattern of a 100-line-per-inch Ronchi grating photographed through the liquid laser cell. In Figure 3-49(a) the power loading was 0 watts; in Figure 3-49(b) it was 34 watts and the lamps had been on for two minutes. After a longer time the pattern degenerated to that shown in Figure 3-49(c). As the flow speed and Reynold's Number increased, the undistorted volume at a given power loading also increased, as shown in Figure 3-50. It was, however, found that this corrective measure alone was not adequate since the ultimate flow speed was limited by the pump. Further experiments showed that a water jacket was extremely beneficial in controlling this problem. With this addition, the temperature of the liquid and of the cell wall was independently adjustable, the direction of heat flow controlled and the magnitude of the heat flow significantly reduced. The results of measurements with a water-jacketed cell indicated that the decrease in undistorted laser volume was significantly reduced.

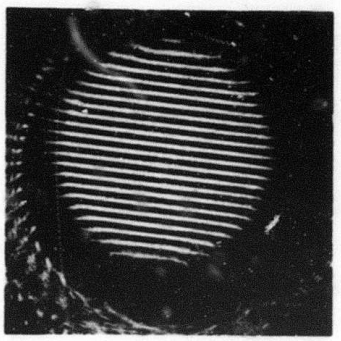

(a)

0
4200

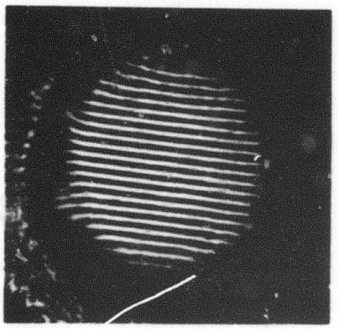

(b)

34
4200

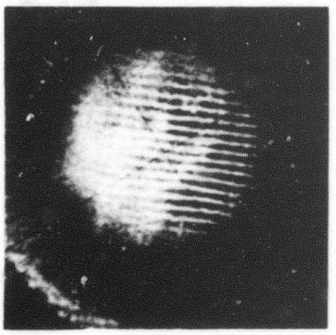

(c)

34
4200

Figure 3-49. Near-Field Patterns of 100-Line-Per-Inch Ronchi Grating. Grating Photographed Through Liquid Laser Cell. Reynold's Number = 4200. (a) power loading = 0 watts; (b) power loading = 34 watts, photograph taken after lamps turned on; (c) same power loading as (b) but after several minutes.

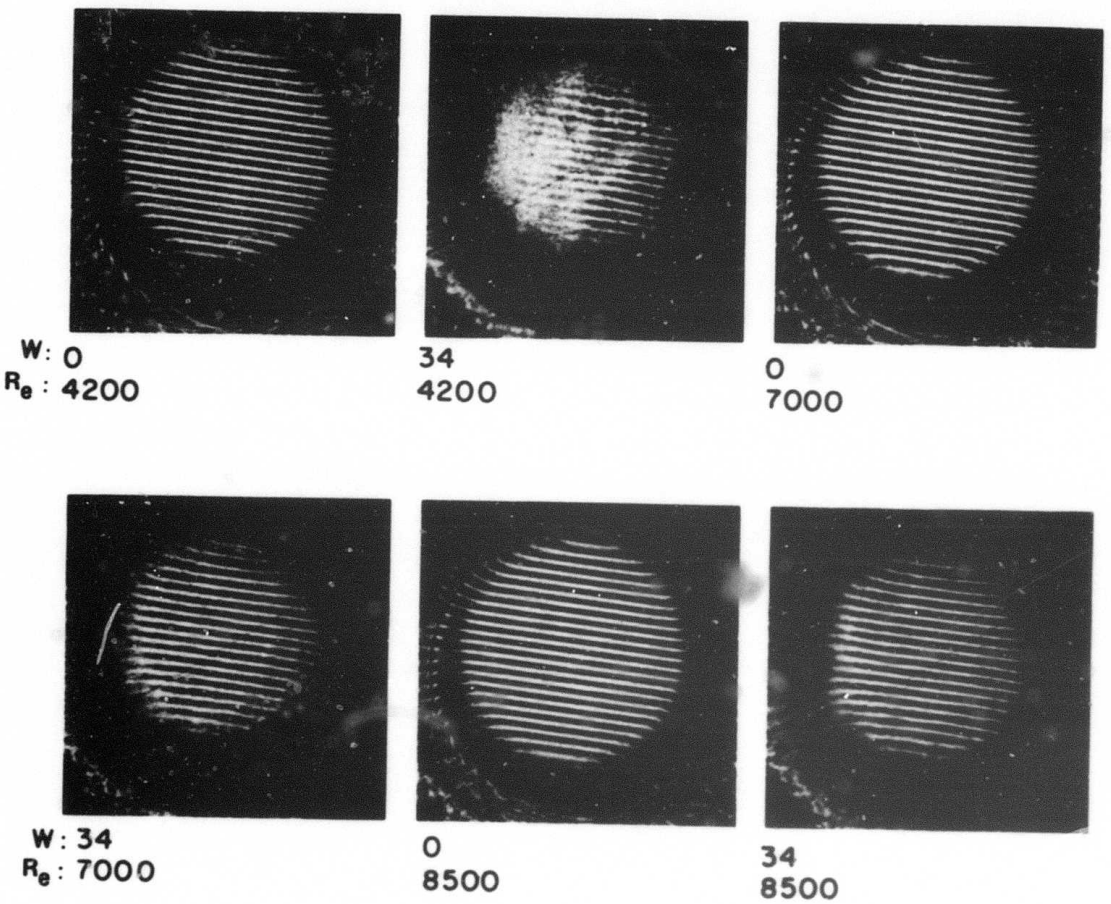

Figure 3-50. Near-Field Patterns of 100-Line-Per-Inch Ronchi Grating. Photographed Through Liquid Laser Cell. Flow speed (R_e Reynold's Number) and power loading (W) are variable.

3.2.4.3 Laser Cells and Water Jackets

As has been shown in Section 3.2.4.2, the addition of a water jacket helps to improve the cell optical performance. One important factor in this is to design the laser cell, water-jacket geometry for optimum optical coupling of the flash lamp radiation while at the same time decreasing the radial thickness of the water layer used for cooling the cell wall. By shrinking this water layer and maintaining a high volume flow rate and Reynold's Number, the heat transfer efficiency from the laser cell wall to the water coolant is increased.

As an aid in discussing the optimization of the design, Figure 3-51 shows a schematic cross-section of the laser cell-water jacket assembly. The center of the cell assembly is located at point C, the outer radius of the glass water jacket is R, and the thickness of the water jacket is denoted by t. The outer radius of the laser cell is r and the inner radius is ρ. The figure shows a tangential light ray entering the assembly at point M. This ray is refracted by the water-jacket assembly to strike the laser cell tangentially at point 0. The laser cell wall thickness, $r - \rho$ is chosen such that the ray then strikes the laser liquid tangentially at point P. The latter condition is assured by the relation:

$$n_2 r = n_1 \rho ; \; r = \left(\frac{n_1}{n_2} \right) \rho \tag{3-11}$$

Referring to the figure, we have for the incident ray at point M,

$$\begin{aligned} n_1 \sin \theta_1 &= \sin (\pi/2) \\ \sin \theta_1 &= 1/n_1 \end{aligned} \tag{3-12}$$

and at point N,

$$\sin \theta_2 = \frac{R \sin \theta_1}{R-t} = (1/n_1) \; \frac{R}{R-t} \tag{3-13}$$

Then, from Snell's Law:

$$\sin \theta_3 = (1/n_2) \; \frac{R}{R-t} \tag{3-14}$$

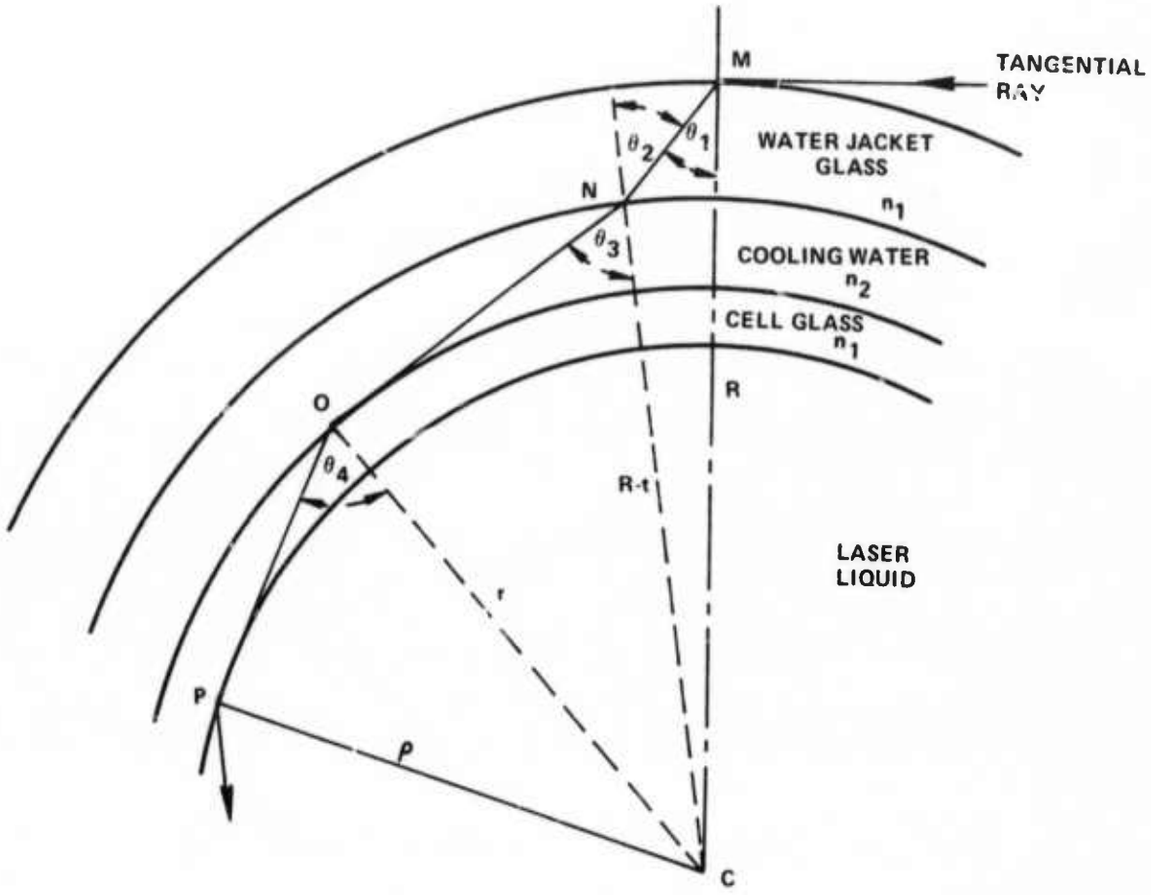

Figure 3-51. Optical Situation on Focusing the Pump Radiation into the Laser Cell

In addition:

$$\frac{r}{\sin\theta_3} = \frac{R-t}{\sin(\pi/2)} = R-t$$

Thus,

$$\sin\theta_3 = \frac{r}{R-t} = \frac{R}{n_2}\ \frac{1}{R-t} \tag{3-15}$$

$$r = R/n_2$$

We must impose the constraint at the point N that the angle of incidence, θ_2, does not lead to total reflection, i.e.,

$$\sin\theta_3 \leq 1 \tag{3-16}$$

Using Eq. (3-14), we have:

$$\frac{R}{n_2}\left(\frac{1}{R-t}\right) \leq 1$$

$$R \leq n_2(R-t) \tag{3-17}$$

$$t \leq R\left(1 - \frac{1}{n_2}\right)$$

Eqs. (3-11), (3-15) and (3-17) serve to define the design constraints given a desired cell bore radius, ρ, and cell and water-jacket material (Pyrex, $n_1 = 1.45$) with water ($n_2 = 1.33$) as the cell coolant.

3.2.5 Flash Excitation Equipment

3.2.5.1 Flash Enclosures

The flash enclosures (reflectors) used for focusing pumping radiation from the flashlamps into the laser liquid were quite similar to those used in Nd^{+3} glass or YAG systems. They were basically of two types over the course of this work: close-coupled enclosures and imaging enclosures. The former type usually consisted of simply wrapping a polished metal (typically silver) sheet around the flashlamps and the laser cell. The sheet thus served to confine the flashlamp radiation so that it would be predominantly absorbed in the laser liquid. One such enclosure is shown as Figure 3-52.

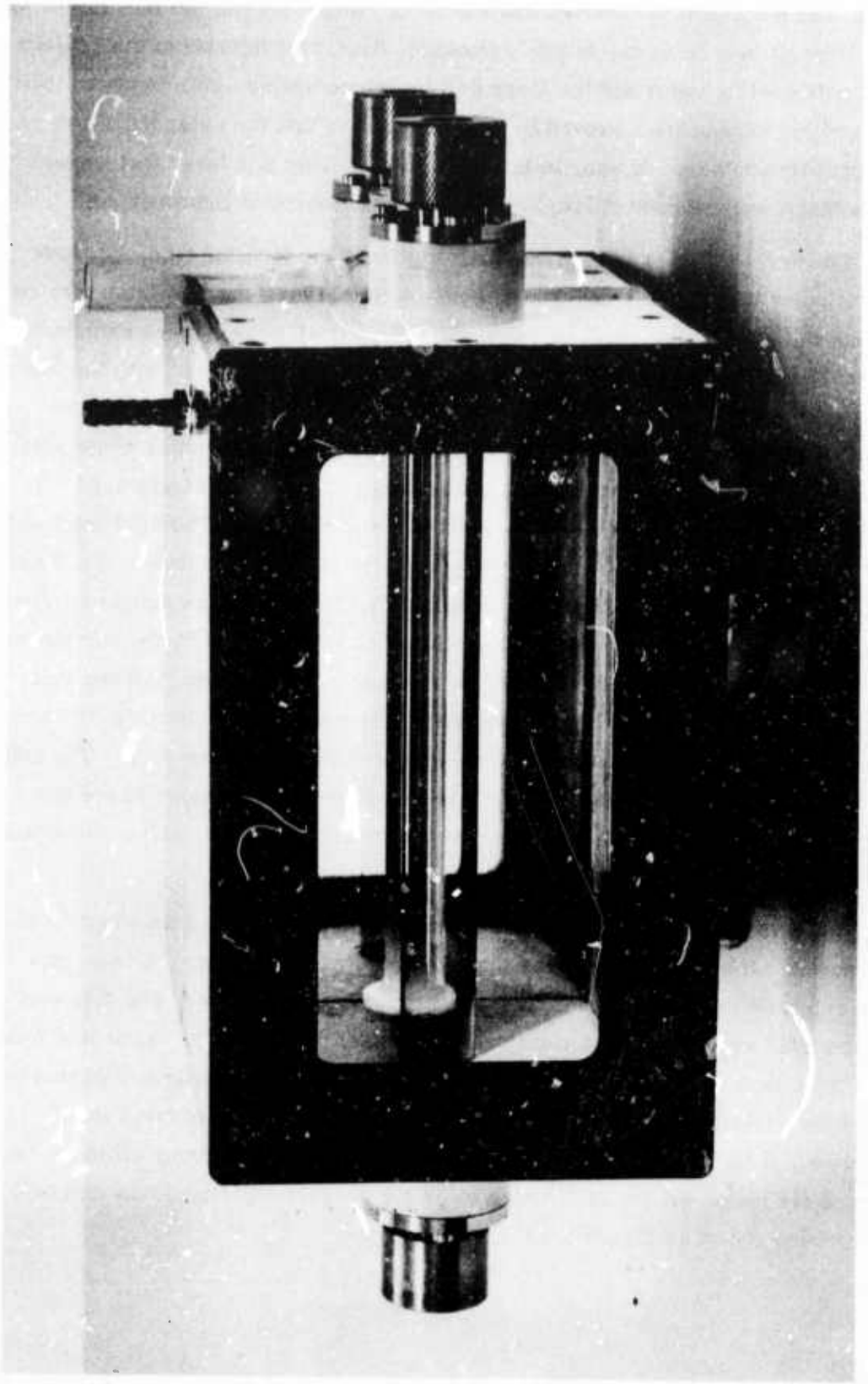

Figure 3-52. The Two-Lamp Close-Coupled Flash Head Used in the Q-Switched Oscillator Unit

In this photo, the metal foil is removed and the water jackets for the two flashlamps and the laser cell itself may be seen. In this enclosure, the entire interior of the enclosure was flooded with cooling water and the laser cell therefore has no water jacket of its own. This cooling arrangement proved to be inadequate in that the water therefore became hot under repetitive pulsing. It was, in fact, the results from this laser that showed conclusively that a water-jacketed laser cell was a most desirable improvement.

The second type of flash enclosures used was the focusing type. In these units, the reflector had an elliptical cross-section which imaged the flashlamp located at one focus onto the laser cell located at the other focus. In all cases, these enclosures used multiple flashlamps and the enclosure cross-section was multi-elliptical with the laser cell situated at a focus common to all the ellipses. One such enclosure utilizing two flashlamps is shown by Figure 3-53. The laser cell shown in place on this photo also lacks a water jacket. An enclosure utilizing four lamps is shown as Figure 3-54. In this last enclosure, the laser cell is surrounded by a water jacket. The flash enclosures shown by Figures 3-53 and 3-54 are basically commercially available units. They are manufactured by Research Incorporated of Minneapolis, Minn., and marketed as infrared radiant heating chambers. In this use, the laser cell is replaced by the sample rod to be heated and the flashlamps are replaced by resistance rod heaters. All the units are cast of aluminum with internal labyrinths for water-cooling the enclosure. The reflecting surface is polished aluminum which we use as-is for our laser work. The only modifications we make to the commercial unit is to replace the end plates of the enclosure with ones we manufacture in our shop to mount the flashtubes, cell cooling jacket hardware, etc., required for our application.

We have not paid much attention to the optical perfection of the imaging in these enclosures. The reason for this is that the effective cell diameter (taking into account the refraction in the cell water jacket as mentioned in Section 3.2.4.3 is comparable to the latus rectum (the chord through either foci perpendicular to the line joining the foci). Under such circumstances, the imaging of the flashtube at the cell cannot be too good and the enclosure must function as a cross between a close-coupled and a focusing device. It is, however, a fact that the best long-pulse oscillator efficiency we have observed (44 joules out for 1650 joules in or 3.8 percent efficiency) was obtained with the enclosure shown as Figure 3-53.

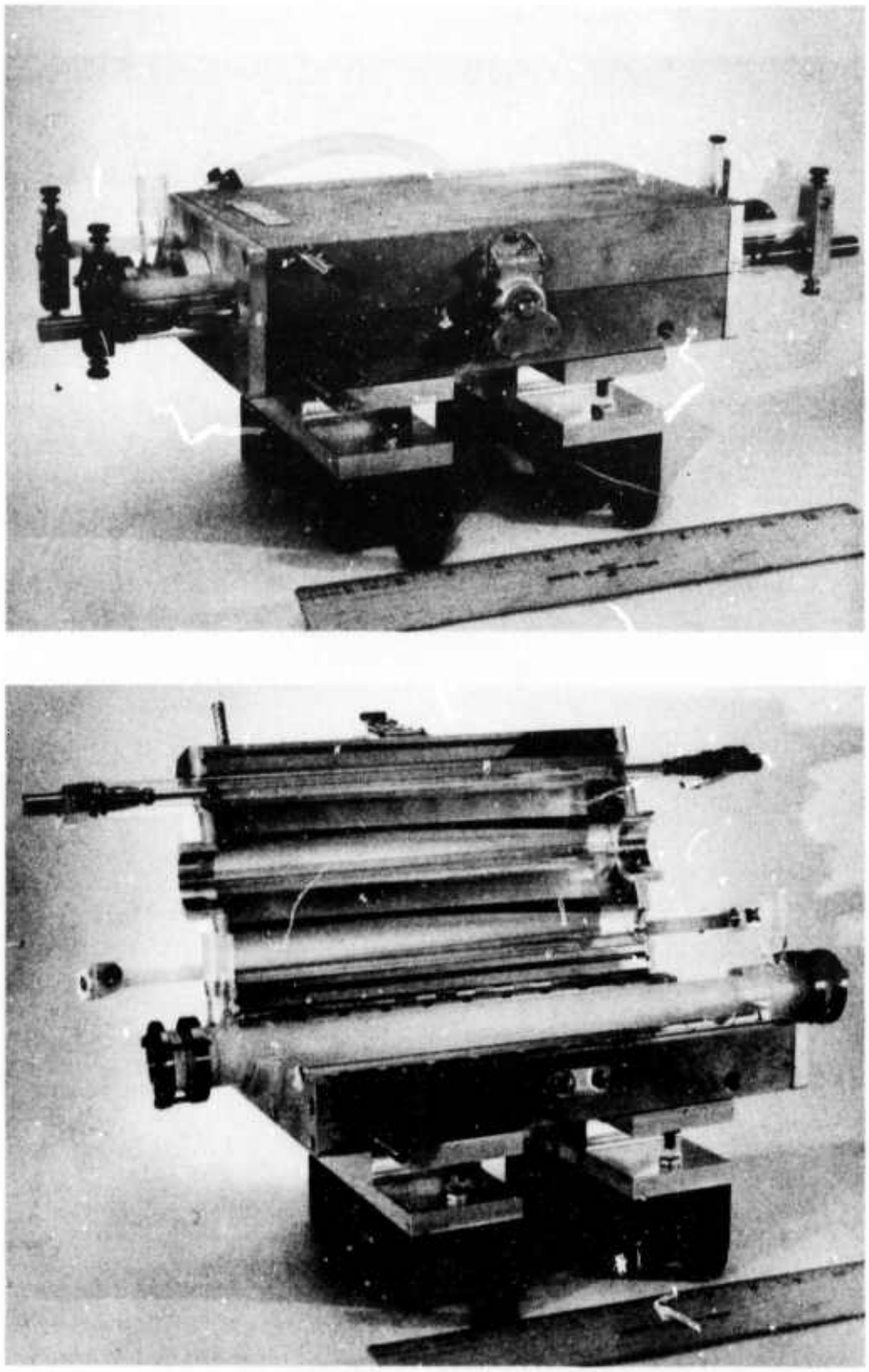

Figure 3-53. Assembled Flash Head, Laser Cell and Flash Lamps

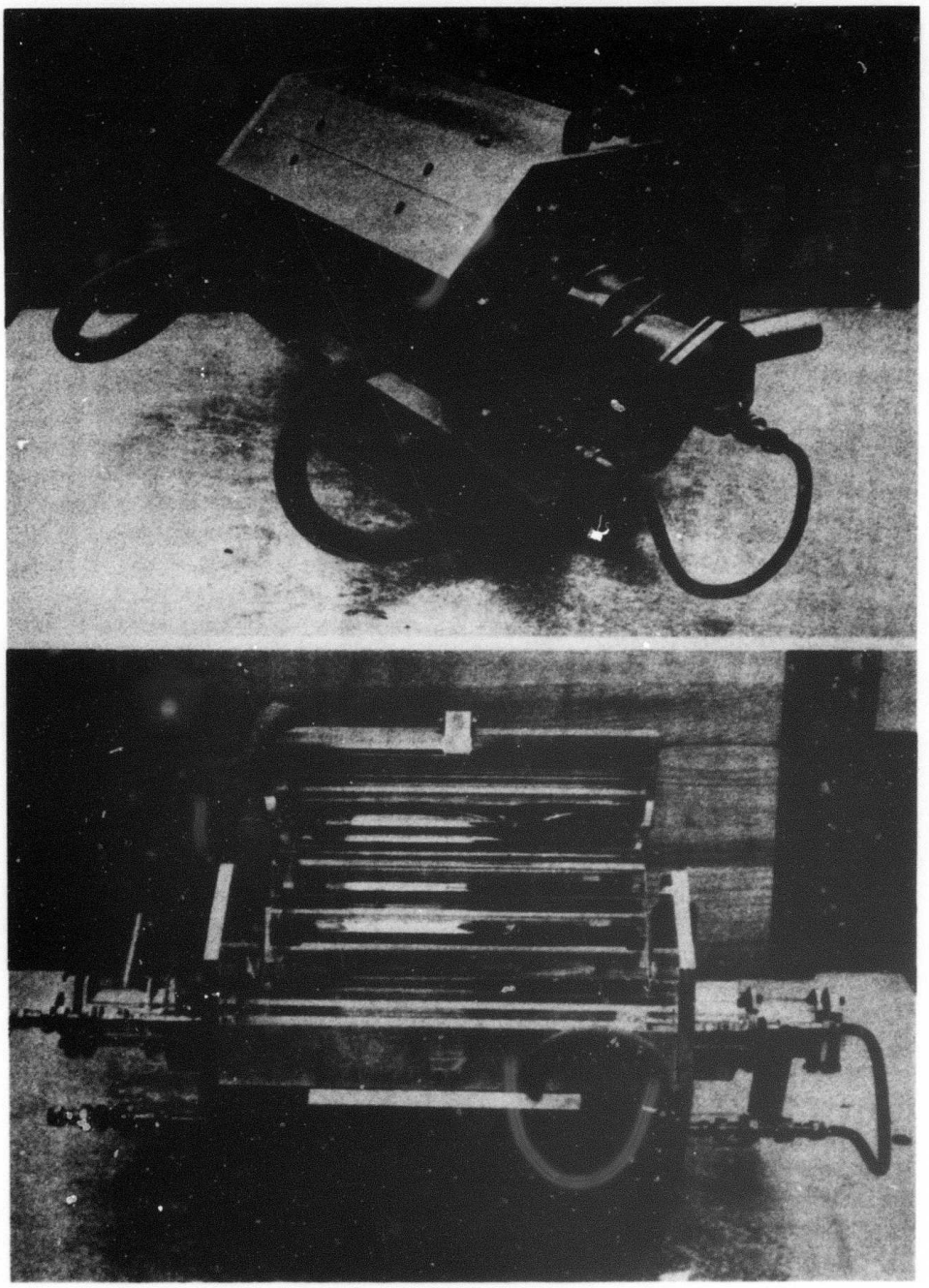

Figure 3-54. Assembled Four-Lamp Focused Flash Enclosure with Cell in Place

3.2.5.2 Flashlamp PFN's and Trigger Circuits

The selection of the flashlamps to be used and the design of the pulse-forming network (PFN) used to drive them is based on the popular method of Markiewicz and Emmett.[76] In our cases, we specify the total electrical input energy (joules) to the flashlamps necessary to obtain a desired amount of long-pulse oscillator output assuming an overall conversion efficiency on the order of 2 percent (which gives a conservative estimate of input energy requirements in general). Thus, if we desire a long-pulse output of 50 joules, we must assume that we will want to put up to 2500 joules of electrical energy into the flashlamps. The next most important specification is the flashlamp pulse duration. Since all our liquid lasers have been designed to function primarily as long-pulse oscillators and amplifiers, a roughly square-topped lamp current was assumed with pulse duration on the order of 600 μs. The final specification necessary is the maximum capacitor bank (PFN) voltage to be used. This is in general set by the power supply available. In most of the repetitively-pulsed work we have done, this voltage was 5000 volts. These three specifications, along with the design limitation that the flashlamps be run at no more than 10 percent of their explosion energy per pulse, are enough to completely specify the lamps to be used and the PFN configuration in the following manner:

The energy (joules) stored in the PFN is given by,

$$E = 1/2\ CV^2 \tag{3-18}$$

where C is the total bank capacitance (in farads) and V is the maximum bank voltage (volts). From the given specifications (V = 5 kV, E = 2500 J), we calculate that the desired PFN capacitance is C = 200 μF. Requiring that the lamp current pulse be square-topped means that the PFN used must be a delay-line type as shown by Figure 3-55(a). As is well-known from circuit analysis, such a combination of L's and C's must have a characteristic impedance:

$$Z = \sqrt{\frac{L_1}{C_1}} = \sqrt{\frac{L_2}{C_2}} = \ldots = \sqrt{\frac{L_n}{C_n}} \tag{3-19}$$

to be balanced. Furthermore, to avoid current reversal in the circuit, the characteristic impedance of the line must be matched to the load; i.e.,

$$R = Z = \sqrt{\frac{L_i}{C_i}} \tag{3-20}$$

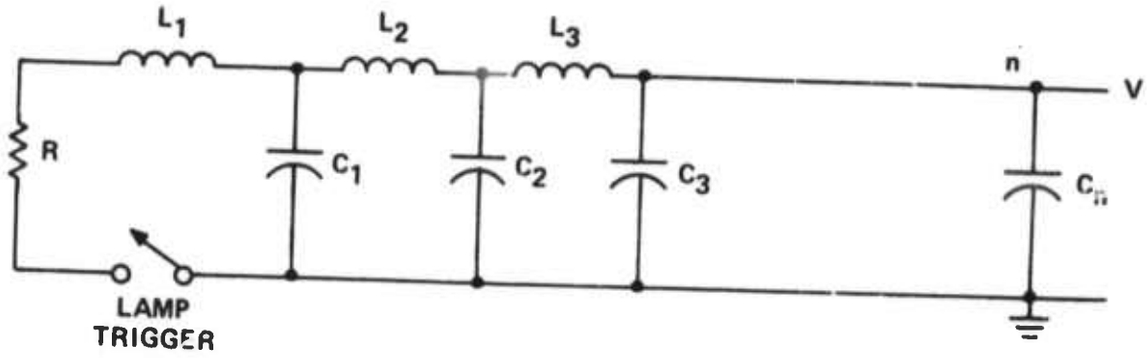

(a) Delay Line PFN (n-Sectioned)

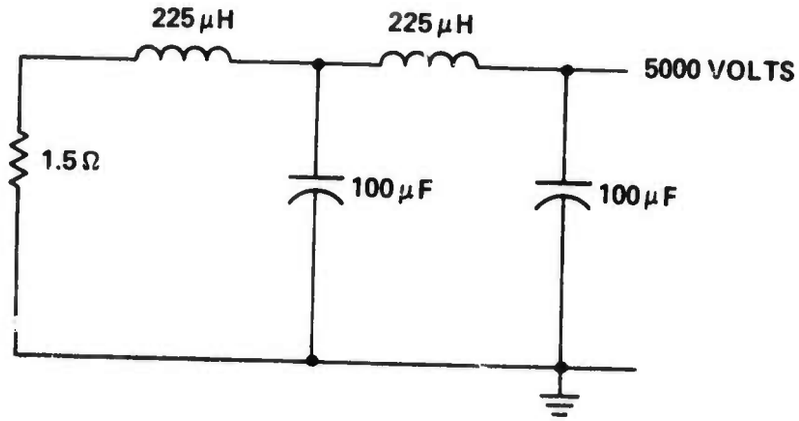

(b) Two-Section PFN as Calculated from Text

Figure 3-55. Delay Line PFN's for Flashlamp Driving Circuit

In the matched line case, the duration of the lamp current pulse will be:

$$\tau = 2Z\sum_i C_i = 2Z\,C_{total} = 2R\,C_{total} \qquad (3\text{-}21)$$

In our example, if $\tau = 600\ \mu s$, $C_{total} = 200\ \mu F$, we find that the flashlamp load and the PFN characteristic impedance must be $R = Z = 1.5$ ohms. In the case of a two-section PFN, as shown by Figure 3-55(b), the value of the section inductance will be:

$$L = Z^2 C = (1.5\ \Omega^2)\ (100\ \mu F) = 225\ \mu H$$

The high-pressure xenon flashlamps act as nonlinear circuit elements whose resistance may be phenomenologically expressed as:

$$R(ohms) = \frac{1.27\,\ell}{\sqrt{I\,D}} \qquad (3\text{-}22)$$

where:

ℓ = electrode spacing (cm)
D = lamp internal diameter (cm)
I = current through lamp (amperes)

The instantaneous power dissipated in the lamp load is:

$$P = I^2 R = \left(\frac{1.27\,\ell}{D}\right) I^{3/2} \qquad (3\text{-}23)$$

Expressing the lamp resistance in terms of the power dissipation:

$$R = \left(\frac{1.27\,\ell}{D}\right)^{4/3} \left(\frac{1}{P}\right)^{1/3} \qquad (3\text{-}24)$$

Now, the maximum power dissipation in the lamp load in the hypothetical case we have been considering is:

$$P = \frac{E}{\tau} = \frac{2500\ J}{0.6 \times 10^{-3}\ sec} \approx 4.1 \times 10^6\ watts$$

We can, therefore, solve for the length to diameter ratio for the flashlamp load as:

$$\left(\frac{1.27\,\ell}{D}\right)^{4/3} = R(P)^{1/3} = (1.5)(4.1\times10^{6})^{1/3} = (1.5)(1.6\times10^{2}) = 240$$

$$\frac{\ell}{D} = (240)^{3/4} \times \left(\frac{1}{1.27}\right) = \frac{61}{1.27} = 48$$

Thus, if the required flashlamp arc length is 10 inches (25.4 cm) and we wish to use two flashlamps connected in series, the total lamp arc length is 50.8 cm. The calculation shows that the required lamp I. D. is:

$$D = \frac{\ell}{48} = \frac{50.8\,\text{cm}}{48} \approx 11\ \text{mm}$$

Such calculations give a flashlamp specification for a particular PFN (or vice-versa) for a load matching only at one particular PFN voltage because of the non-linear impedance characteristics of the flashlamp. Because the worst case in terms of lamp and capacitor life occurs under the condition of current reversal (lamp impedance smaller than PFN characteristic impedance), the design point for the lamp-PFN circuit is taken as the maximum bank voltage (energy input). At lower bank voltages, the lamp impedance is larger than the PFN characteristic impedance and the pulse has a tendency to lengthen.

Current risetime in the pulse is largely controlled by the number of sections in the PFN delay line. It can be show that, if the PFN is made up of n identical sections, the current risetime, τ_r, will be given by:

$$\tau_r = Z\,C_n = \frac{Z\,C_{total}}{n} = \frac{\tau}{2\,n} \qquad (3\text{-}25)$$

Therefore, if we make the PFN out of too many sections (in order to get a "clean" square-topped current pulse), the risetime of the pulse must get very short. In most PFN's we have constructed, we used a two-section PFN. The resulting current waveform has a total rise and fall time amounting to about 1/2 the total pulse duration. This selection allows the lamps to be safely limited in peak current without the possibility of current reversal while at the same time having a flash pulse which is consistent with good long-pulse oscillator performance as well as acceptable amplifier gain.

A separate problem in the PFN design is the provision for triggering the flashlamps. On the order of 10 milliseconds after the current pulse through the lamps has extinguished, ambipolar diffusion of the ions in the lamp gas to the walls of the flashlamp returns the flashlamp to a nonconducting state. The PFN may then be charged to voltage without the lamps "breaking down" and prematurely dumping the PFN energy; however, once the bank is brought to the desired voltage, a means must be provided for injecting mobile charge carriers into the lamp gas so that it becomes a conductor again. Two different means are traditionally used for this flashlamp "triggering." The first is called "external" or "parallel" triggering and involves capacitively-coupling a high voltage and frequency pulse signal to the lamp gas by means of a small wire wrapped around the outside of the flashlamp. The signal ionizes enough of the gas to form mobile charges which, because of the high voltage across the lamp electrodes, can be be accelerated and in an avalanching process form an arc channel in the gas. The second method (series injection triggering) involves rapidly raising the potential of one of the lamp electrodes above the breakdown potential of the gas in the lamp. The triggering signal must have enough current capability to form an arc streamer through the gas which can act as a conducting path for the main bank discharge current. The method most commonly used for this is to use a saturable core transformer for generating the high voltage pulse at the lamp electrode above ground. The secondary of this transformer is therefore part of the PFN. By using a saturable core transformer, the secondary can thus present a relatively low inductance under core saturation from the bank discharge current while being capable of high voltage generation in the unsaturated condition from a large winding ratio between secondary and primary.

In most of the liquid laser systems constructed, we have used the series injection triggering method because it is just as effective at low PFN voltages as at high voltages. The potential disadvantage of the trigger transformer being part of the PFN was overcome by constructing a special transformer with a relatively low saturated inductance (125 microhenries) and high secondary rms current capability (150 amps). The transformers were manufactured by Saratoga Industries to our specifications. The completed PFN's used in the most recent three-head liquid laser system are shown as Figures 3-56(a) and 3-56(b).

3.2.5.3 High Average Power Supplies

The power supplies used to charge the capacitors in the PFN must be capable of a high average power. The maximum capability of the unit was set by requiring that

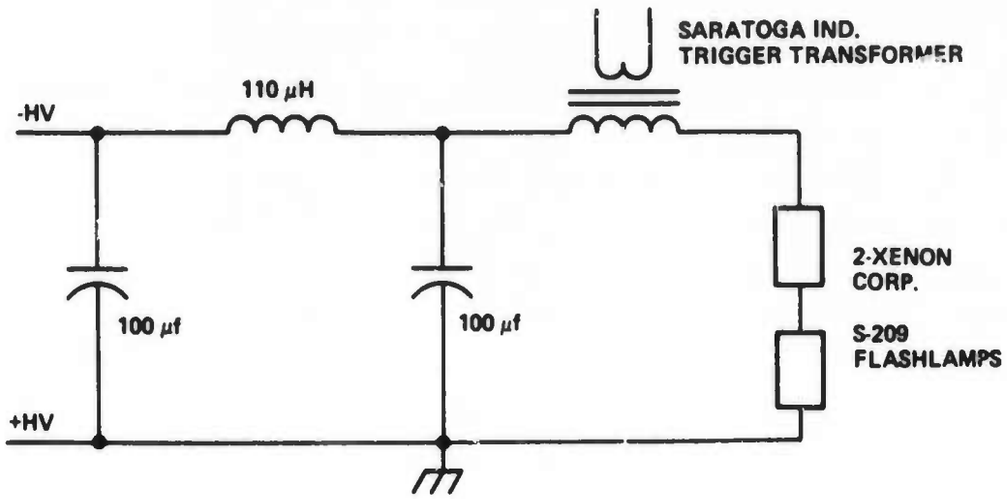

(a) Pulse Forming Network for Two Largest Laser Heads

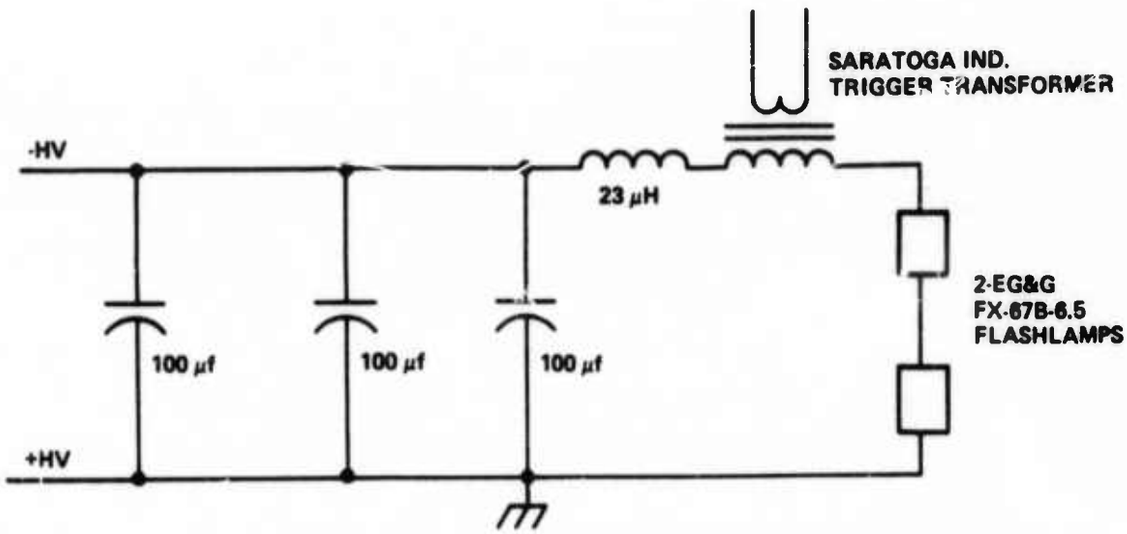

(b) Pulse Forming Network for Smallest Laser Head

Figure 3-56

the maximum input to the PFN be 4000 joules per pulse at a repetition frequency of 5 pps (20 kilowatts average power). The power supply for this laser is manufactured by Systomation, Inc. The key element in this supply is a monocyclic circuit designed by Steinmetz and adapted for SCR switching. Power from a three-phase line is fed into an LC network arranged to operate as a resonant circulator at the line frequency. Power is extracted from this network through another network tuned to the three-phase high-voltage transformer. Three pairs of SCR's are used as shunts on the primary side of the transformer; when the desired voltage is reached on the capacitor bank the SCR's close and stop the charging current. The resonant nature of the circulator limits the current through the SCR's for protection against damaging surges. The entire circuit acts as a constant-current supply with primary over-voltage and over-current protection. In addition, the design of the SCR controlling circuit allows for a charging accuracy of approximately 0.1 percent of the desired capacitor bank voltage at the maximum charge rate. The supply is rated for an output of 30 kW to the capacitor bank. At a pulse repetition rate of six pps, 5000 joules per pulse can be delivered to the flashlamps. The pulse repetition rate and the energy delivered to the lamps can, of course, be varied provided the total power is 30 kW or less. In actual use, no more than 20 kilowatts is normally allowed because of flashlamp cooling limitations.

3.2.6 Cooling System and Heat Exchangers

Two separate cooling systems are used in the liquid laser system. One system uses temperature-regulated deionized water for cooling the laser cell via the cell water jacket and is also used for cooling the flashlamps. This system is a closed-loop system with the deionized water being circulated through the cell water jacket, flashlamps and a stainless steel heat exchanger by means of a plastic centrifugal pump. The deionized water temperature is sensed at the output of the heat exchanger. A time-proportional controller activates a solenoid valve on the domestic water line to regulate the output temperature to ± 0.1°C. The deionized water is also bypassed to an internal loop which includes a particle filter, deionizer cartridges and a resistivity monitor to maintain the quality of the coolant. The heat exchanger, pump, cartridges, controller, etc., comprise a commercial cooling system manufactured by Systomation, Inc., the builders of our power supply described earlier. This cooling system derives its electrical power from, and interfaces with, the logic systems inside of the M-60 power supply. The system is therefore so arranged that, in the event of loss of cooling, the power supply shuts down automatically to prevent damage to the laser system.

A second independent cooling system uses ordinary tap water with a time-proportional temperature controller identical to that in the previous system to regulate the temperature of the laser liquid by means of a specially-constructed all-nickel heat exchanger. A schematic of the laser cooling and control circuits are shown as Figure 3-57. The figure shows both the laser liquid temperature control system and the deionized water system previously described.

Of the two cooling systems, the deionized water system dissipates the most heat because it cools the flashlamps. We estimate that about 80% of the electrical power dissipated in the flashlamps must be handled by this system. The remaining 20% goes largely into heat dissipated by the second cooling system. A breakdown of the power dissipated by the two cooling systems assuming a 10 kW input to the flashlamps, is shown below:

	Deionized Water System	Laser Liquid Cooling System
Flashlamp Heat	7500 W	-
Cell Water Jacket	500 W	-
Laser Output Power	-	500 W
Laser Liquid Heat	-	1500 W
Liquid Pump Friction	-	500 W
Totals	8000 W	2500 W

The extra 500 watts dissipated in the laser liquid arises from the friction of the circulated laser liquid as well as heat caused by the electromagnetic drive of the "canned" pump previously described.

In operation, the cooling systems used in the liquid laser system seemed quite adequate, at least for the relatively short periods of operation used in the experiments to be described. Certainly, the deionized water system was more than adequate because it was designed by the manufacturer to dissipate the entire 30 kW capability of the power supply while we only used it to occasionally dissipate about half this amount (16 kW). The deionized water temperature was monitored near the input to the laser cell water jacket and this temperature rarely varied more than 0.1°C during the course of an experiment. This excellent control is a testament to the sensitive proportional controller and well-designed heat exchanger used in this sytem. The system used for maintaining the temperature of the laser liquid was not as accurate even though the

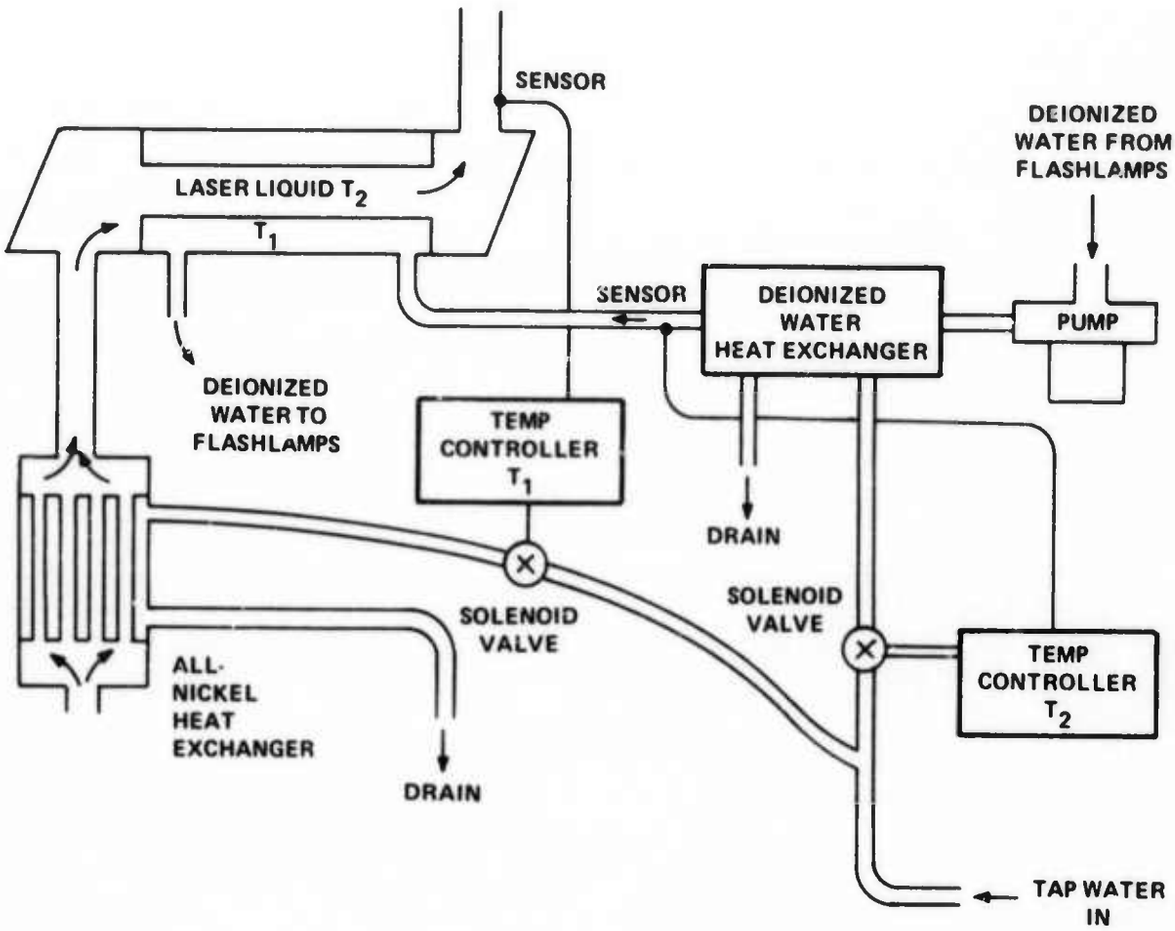

Figure 3-57. Liquid Laser Cooling and Control Circuit

same time-proportional controller was used here. Under operation, the liquid temperature showed tendency to rise about 0.3°C near the end of a run. The system would then start "hunting" about the set temperature. We suspect that the heat transfer efficiency of the all-nickel heat exchanger (designed and manufactured in our own shop) was not as high as it could have been had we been able to purchase nickel tubing in the proper gauge. Also, the heat exchanger had to be made as small as possible to minimize the quantity of laser liquid used in the system, as well as to fit the physical layout of the laser system. Photos of the heat exchanger disassembled and in place on top of the pump in the laser system are shown by Figures 3-58 and 3-59, respectively.

The completely assembled laser system is shown in Figure 3-60 showing the circulatory system (below table top level) and Figure 3-61 showing the three laser heads on the table top. In Figure 3-60, the circulatory pump and heat exchanger are clearly evident in the right-hand portion, the gas ballast system and nanometer in the left, and the trigger transformers in the lower left. The three laser heads in Figure 3-61 are 6.5 inch dual ellipse in the extreme left, a ten inch dual ellipse in the center, and a ten inch quadruple ellipse in the right.

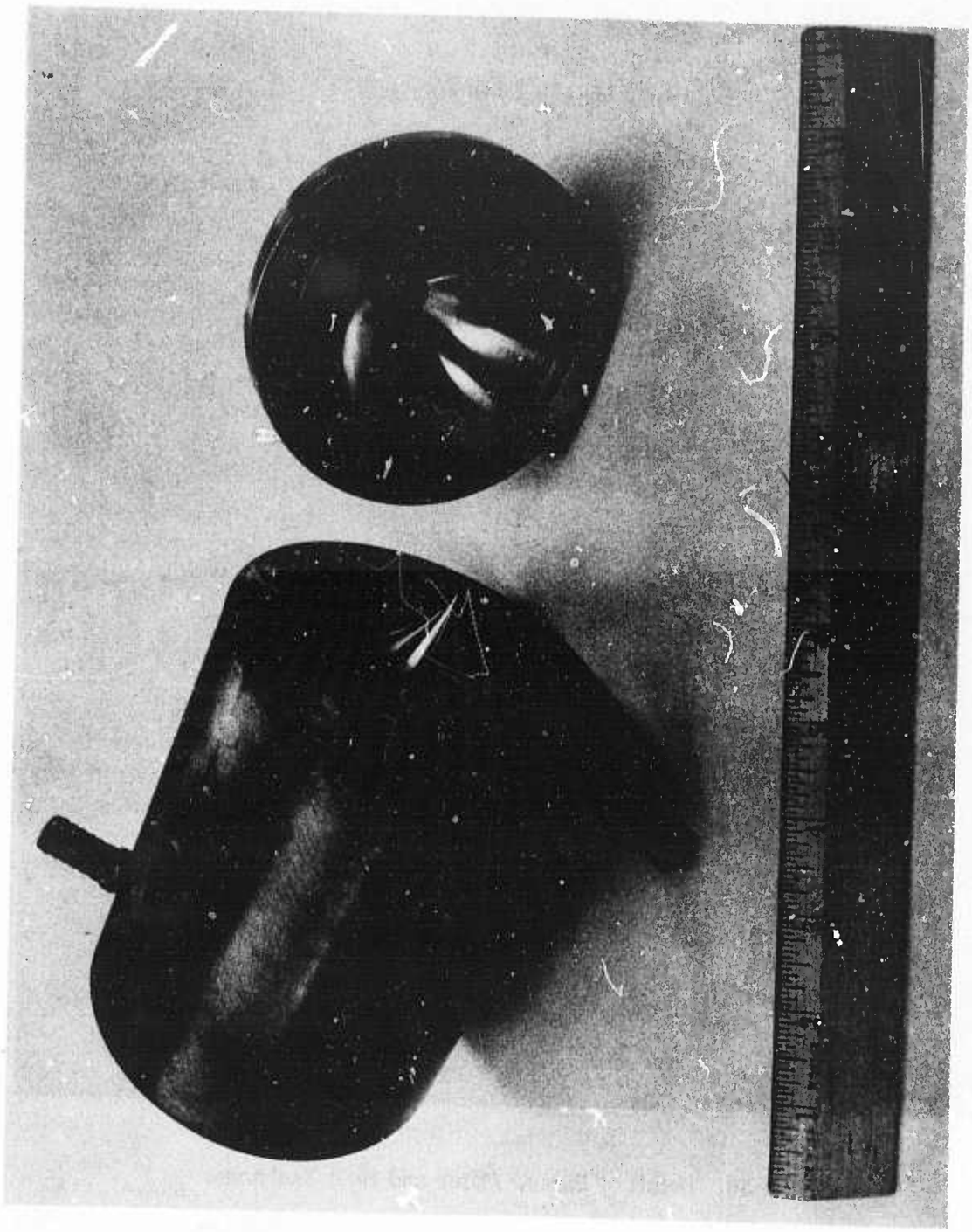

Figure 3-58. Heat Exchanger

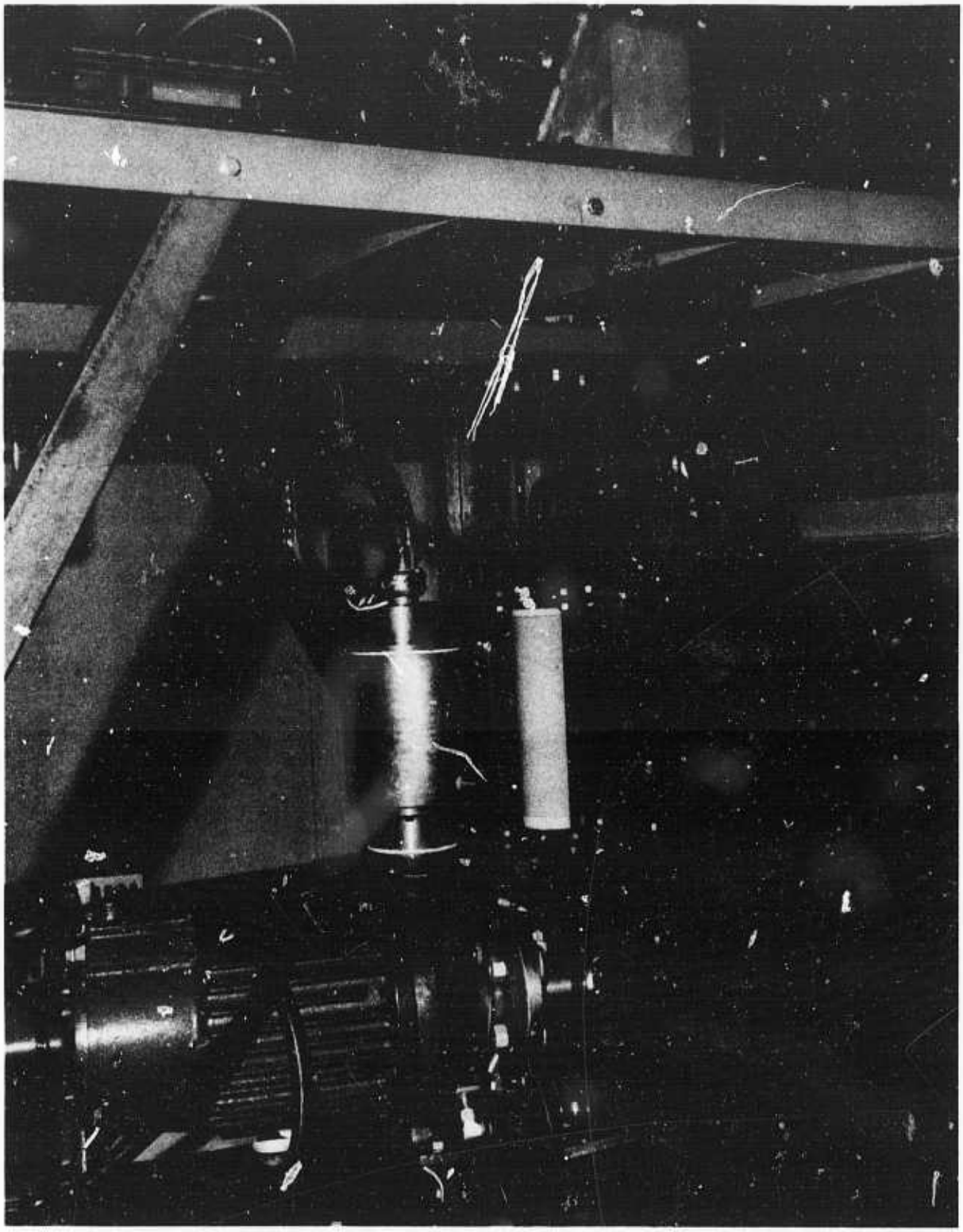

Figure 3-59. Detail of Pump, Filter and Heat Exchanger

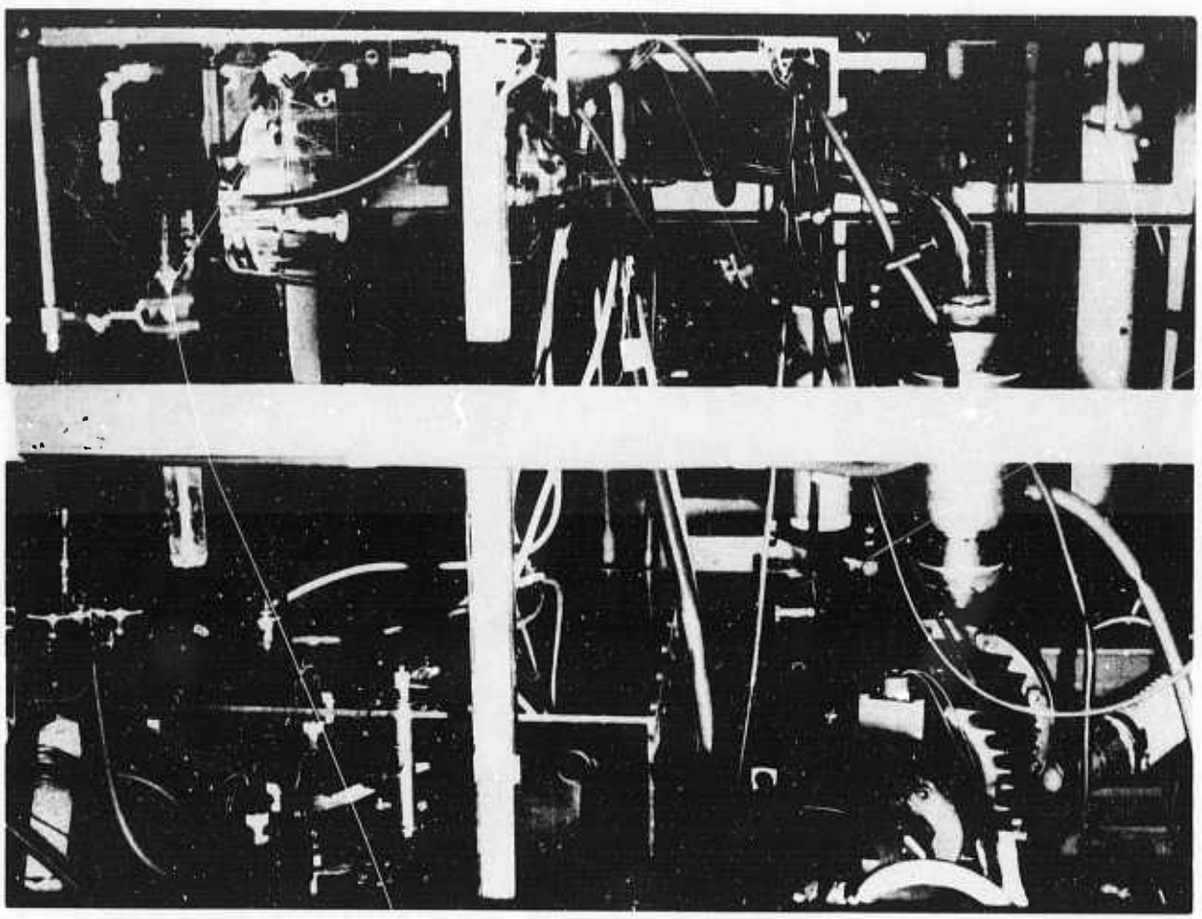

Figure 3-60. Photograph of the Plumbing and Drive Parts of the Liquid Laser System. The vertical meter stick is attached to the manometer used to measure the pressure above the free surface. In the lower left is the triggering circuit and in the upper left the gas ballast. In the center right the filter and heat exchanger can be readily identified along with the piping used in the circulatory system. The circulatory pump is in the lower right.

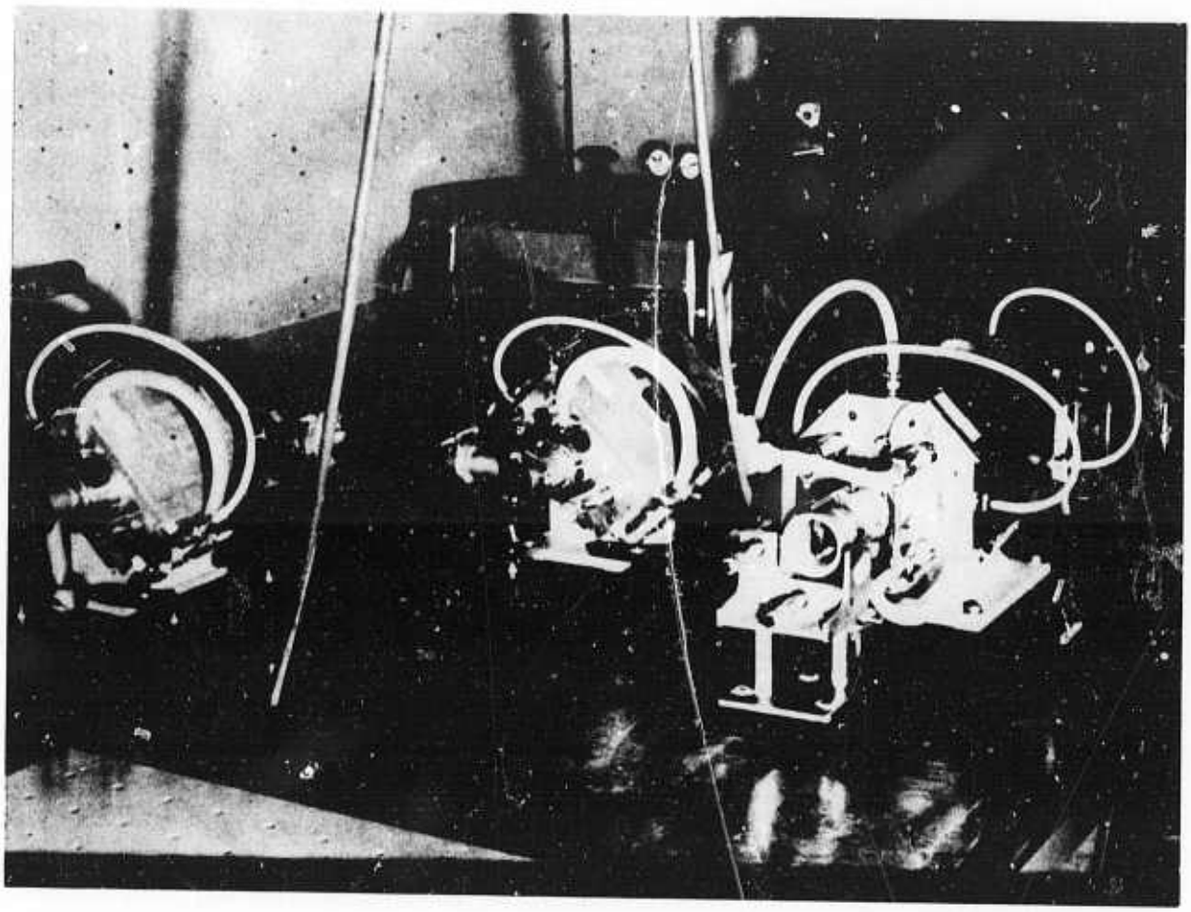

Figure 3-61. Photograph of the Liquid Laser System Showing the Three Laser Heads. In the extreme left is the 6.5 inch dual elliptical laser head; in the center the 10 inch dual elliptical laser head and on the right the 10 inch quadruple elliptical laser head. The standpipe and free surface arrangement can be seen at the rear of the table between the two 10 inch heads.

4. THE HYDRODYNAMIC AND THERMO-OPTICAL PROPERTIES OF LIQUID LASERS

In all condensed phase optically-pumped lasers, conversion efficiency and beam quality are affected by the temperature distribution induced by the optical pumping process. These thermal effects are virtually unavoidable, because only part of the absorbed pump energy appears as laser emission; the remainder appears as heat. Because of the spatial nonuniformity of the energy absorbed in the laser medium and its virtually instantaneous degradation into heat, thermal gradients are induced in the active medium during the pumping pulse, as has been observed by many workers.[76-85] The actual temperature rise in a laser rod has been estimated to range from 3 to 8°C[78, 80, 81, 83, 86] depending on the material, rod cooling and flashlamp input energy. For practical laser rods, flashlamp absorption nonuniformity is such that the outer circumference of the rod reaches a higher temperature than the central core. Thermo-optical distortions, therefore, arise from both the change in index of refraction with temperature, dn/dT, and the material linear expansion coefficient, dL/dT. In addition, solid state materials possess nonzero, stress-optic coefficients which contribute optical birefringent effects.

In addition to the pump induced distortion occurring during the laser pulse, repetitive pulsing introduces a cumulative heat transport problem. From this point of view, the thermal recovery or relaxation time of the system is important, since it limits the repetition rate. This has been variously estimated to range from a minimum of perhaps 2s to much higher values[83, 85, 86] depending on material thermal conductivity and heat capacity, cooling conditions and pumping energy.

The use of a liquid laser medium provides another approach to the latter problem. In such devices, the active medium can be exchanged for each flashlamp pulse, thus, providing a new isothermal sample for each shot. There is still, however, the flash induced distortion to contend with. Since dn/dT for the laser liquid, Nd^3:$POCl_3$:$ZrCl_4$ is negative, the liquid under flash excitation behaves like a converging lens as Malyshev et al.[87, 88] have shown. Quelle,[79] in his theoretical analysis of the thermal problem, has shown that the large dn/dT characteristic of liquids (between 10 and 100 times greater than for solids) tends to magnify the effects of a temperature differential in a liquid or limit the acceptable input pump energy. Furthermore, in tubular flow, the liquid adjacent to the tube wall is not exchanged at nearly the same

average rate as the core liquid. Thus, the tube wall and the contiguous liquid boundary layer constitute a region in which the principal means of heat dissipation is thermal conduction. A laser cell configuration, such as described in the previous section, provides for an outer coolant jacket for heat removal from the cell wall.

In this section, we address ourselves primarily to the calculation of the temperature gradient that exists in a liquid under turbulent flow contained by a glass tube where the liquid centerline temperature is maintained at a value T_{CL}, and the external cell wall coolant is set at a temperature T_0. We shall then analyze the optical properties of the liquid medium using Fermat's principal and ray optics. The calculation will involve only the nonoptically pumped medium under steady-state conditions. The calculation will, however, establish a starting point for a discussion of the laser properties of a liquid medium.

4.1 THE HYDRODYNAMIC MODEL

The analysis of the thermal characteristics of a liquid laser is based on the hydrodynamics of the circulating liquid. In detail, we are interested in temperature distribution of a fluid under turbulent flow through a pipe. The experimental laser cell, to which the analysis is to be applied, is illustrated in Figure 4-1(a). The region to be considered is the active length L (of inside diameter D) between the interior faces of the cell windows. A section of the cell is shown in Figure 4-1(b). The bulk circulating laser liquid is maintained at a centerline temperature T_{CL} and the external cooling water is maintained at a temperature T_0.

The hydrodynamic analysis of turbulent flow in a pipe is very complicated and incomplete at best. Most descriptions are semiempirical in nature. The more tractable results are obtained for the case of fully developed flow that is established some distance after the liquid has entered the pipe. A value of 10D (where D is the pipe internal diameter) is a rough measure of this distance[62] and $L > 10D$ is not satisfied in some of the experimental cases to be discussed later. However, the plenum chamber of the laser cell has a tapered entry into the cell pipe, and this assists the rapid establishment of a fully developed flow throughout the active region of the laser cell.

Under fully developed flow, the average velocity in the axial (z) direction at any radius r is independent of time, distance down the tube (z) and angular position in the tube. In addition, the mean radial velocity, $\bar{v}_r$, is zero but there are nonzero fluctuations of velocity, v'_r, in the radial and axial directions. Hence, the mean flow

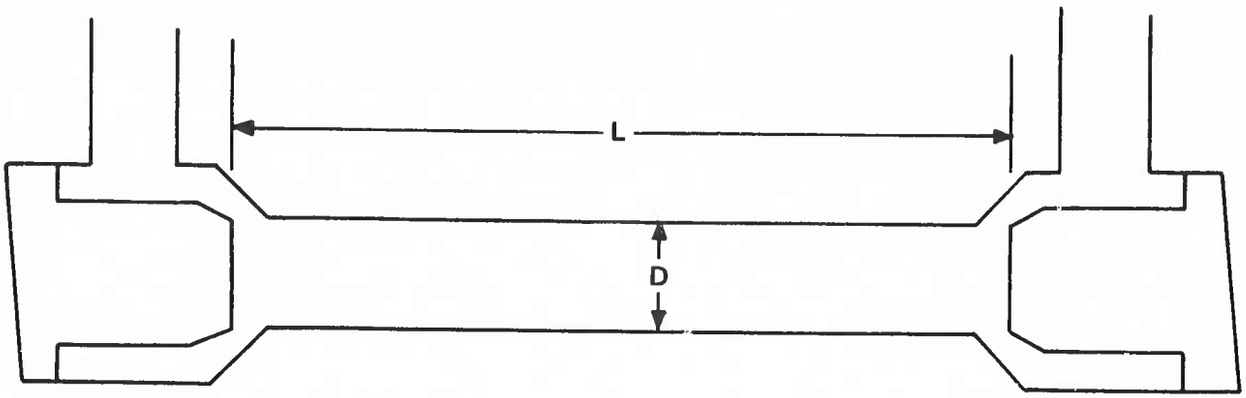

(a) Side View (Without Water Jacket).

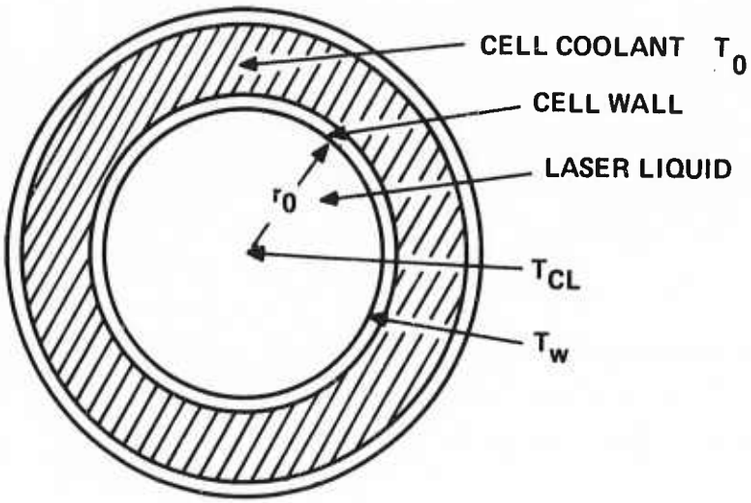

(b) Cross Section Showing Water Jacket.

Figure 4-1. Schematic Drawings of a Water-Jacketed Laser Cell.

in the axial direction, $\bar{v}_z$, is one dimensional but the turbulent fluctuations at any point are two dimensional.

For such a system, since the liquid is incompressible, the pertinent equations are the Navier-Stokes equation (with no body forces);

$$\mu \nabla^2 \vec{v} = \nabla p + \rho \vec{v} \cdot \nabla \vec{v} + \frac{\partial \vec{v}}{\partial t} \tag{4-1}$$

and the equation of continuity:

$$\rho \nabla \cdot \vec{v} = 0 \tag{4-2}$$

where

μ is the dynamic viscosity

p is the pressure

ρ is the density

In addition, there is the energy balance equation:

$$k \nabla^2 T = \rho C_p (\vec{v} \cdot \nabla T) + \frac{\partial T}{\partial t} \tag{4-3}$$

where

T is the temperature

C_p is the heat capacity

k is the thermal conductivity.

The conditions of turbulent flow are introduced into the problem by Eq. (4-4) which states that the instantaneous value available in a turbulent flow field is given by the mean value (the barred quantity) and a fluctuating part (the primed quantity):

$$\begin{aligned} v &= \bar{v} + v' \\ T &= \bar{T} + T' \\ p &= \bar{p} + p' \end{aligned} \tag{4-4}$$

Eqs. (4-1) and (4-3) undergo considerable simplification when the conditions of steady state and fully developed flow are imposed. For flow in a pipe, we have $\vec{v}$ and T as functions of r only, and the time derivatives are zero. Then, putting Eq. (4-4) into Eqs. (4-1) and (4-3) and using the continuity equation, [Eq. (4-2)], and the fact that the time averages of the primed quantities are zero, we obtain the time averaged equations:

$$\frac{1}{\rho}\frac{\partial p}{\partial z} + \frac{1}{r}\frac{\partial}{\partial r}\left[r\left(v_r' v_z' - \nu\frac{\partial v}{\partial r}\right)\right] = 0 \qquad (4\text{-}5)$$

and

$$\frac{\partial T}{\partial z} + \frac{1}{r}\frac{\partial}{\partial r}\left[r\left(v_r' T' - \alpha\frac{\partial T}{\partial r}\right)\right] = 0 \qquad (4\text{-}6)$$

where the unprimed quantities are the mean values [the barred quantities in Eq. (4-1)] and $\nu = \frac{\mu}{\rho}$ and $\alpha = \frac{k}{\rho C_p}$. In Eq. (4-5), the first term represents the pressure forces, the second represents the forces arising from turbulent fluctuations, and the last represents viscous shear forces. In Eq. (4-6), the first term represents heat transport by convection; the second, heat transfer due to turbulent fluctuations; and the last represents heat transfer by molecular conduction.

The quantities involved in the radial derivatives of Eqs. (4-5) and (4-6) are apparent fluxes of momentum and heat. The first component in each case is a quantity arising from the turbulent nature of the flow, while the second component is identical to that found in laminar flow alone. Using Prandtl's concept of eddy diffusivity, we can define:

$$-\left(\overline{v_r' T'}\right) = \epsilon_h \frac{\partial T}{\partial r} \qquad (4\text{-}7)$$

and

$$-\left(v_r' v_z'\right) = \epsilon_m \frac{\partial v}{\partial r}$$

so that Eqs. (4-5) and (4-6) become:

$$\frac{1}{\rho}\frac{\partial p}{\partial z} = \frac{1}{r}\frac{\partial}{\partial r}\left[r\left(\epsilon_m + \nu\right)\frac{\partial v}{\partial r}\right] \qquad (4\text{-}8)$$

and

$$v \frac{\partial T}{\partial z} = \frac{1}{r} \frac{\partial}{\partial r} \left[r \left(\epsilon_h + \alpha \right) \frac{\partial T}{\partial r} \right] \tag{4-9}$$

The simultaneous solution of Eqs. (4-8) and (4-9) will provide the temperature distribution in the flowing liquid. First, we consider the integration of Eq. (4-8). At the wall, since the flow there is laminar,

$$\epsilon_m = 0, \frac{\tau}{\rho} = -\nu \frac{dv}{dr} \text{ and } \frac{\tau_0}{\rho} = -\nu \frac{dv}{dr}\Big|_{r_0}$$

where τ is the shear stress in the fluid and τ_0 is the shear stress of the fluid acting on the tube wall. Then,

$$+ \frac{d}{dr} r \left[\frac{\tau}{\rho} \right] = - \frac{r}{\rho} \frac{dp}{dz} = \frac{\tau}{\rho} + \frac{r}{\rho} \frac{d\tau}{dr}$$

Integrating over the limits 0 and r_0:

$$r_0 \frac{\tau_0}{\rho} = - \frac{r_0^2}{2\rho} \frac{dp}{dz}$$

or

$$- \frac{1}{\rho} \frac{dp}{dz} = \frac{2\tau_0}{\rho r_0}$$

The general integral is:

$$r \left(\epsilon_m + \nu \right) \frac{dv}{dr} = \int \frac{r}{\rho} \frac{dp}{dz} dr = - \frac{2\tau_0}{\rho r_0} \int r dr = - \frac{\tau_0}{\rho} \left(\frac{r^2}{r_0} \right)$$

or

$$\left(\epsilon_m + \nu \right) \frac{dv}{dy} = \frac{\tau_0}{\rho} \left(1 - \frac{y}{r_0} \right) \tag{4-10}$$

where $y = r_0 - r$.

Similarly, a consideration of the heat flow, Eq. (4-9) leads to the equation:

$$\frac{q/A_0}{\rho c_p}\left(1 - \frac{y}{r_0}\right) = -(\alpha + \epsilon_h)\frac{dT}{dy} \tag{4-11}$$

where q/A_0 is the heat flux from the wall into the fluid.

Eqs. (4-10) and (4-11) are formally similar in the variables v and T. Dividing Eq. (4-11) by Eq. (4-10) leads to a differential equation for $\frac{dT}{dy}$ in terms of $\frac{dv}{dy}$, other material and system constants, and the ratio

$$\frac{\alpha + \epsilon_h}{\nu + \epsilon_m}.$$

These equations may be integrated by assuming an explicit form for the flow velocity field v(y). For this purpose, a modified form of the "universal velocity distribution" due to Von Karman[89] is used as defined below:

$$v^+ = y^+ \qquad 0 \le y^+ \le 5$$

$$v^+ = 5.0 \ell n y^+ - 3.05 \qquad 5 \le y^+ \le 30$$

$$v^+ = 5.5 + 2.5 \ell n y^+ \qquad 30 \le y^+ \le \frac{y_0^+}{2}$$

$$v^+ = 6.75 + 2.5 \ell n \frac{y_0^+}{2} - 5\left(1 - \frac{y^+}{y_0^+}\right)^2 \qquad \frac{y_0^+}{2} \le y^+ \le y_0^+$$

where

$$v^+ + \frac{v}{\sqrt{\tau_0/\rho}}$$

$$y^+ = \frac{1}{\nu}(r_0 - r)\sqrt{\frac{\tau_0}{\rho}}$$

$$y_0^+ = \frac{1}{\nu}\sqrt{\frac{\tau_0}{\rho}}\, r_0$$

The four regions of application of this function have historically been defined as, respectively, the laminar sublayer (near the wall), the buffer or transition sublayer, the turbulent sublayer and the core. In the latter two regions, $\epsilon_h \gg \alpha$ and $\epsilon_m \gg \nu$, and the ratio ϵ_h/ϵ_m is designated as E. Experimental values of E range from 0.9 to 1.7, and in the absence of detailed information, a value of E = 1 is generally assumed. In the laminar sublayer, flow is governed by viscous forces and α and ν dominate to the degree where we can neglect ϵ_h and ϵ_m. In the buffer layer, all four quantities e_h, α, e_m and ν must be retained.

The actual integration of first Eq. (4-10) and then Eq. (4-11) for each of the four regions will not be shown here for brevity. The interested reader is referred to the original paper by R. Martinelli[90] for the details in the first three regions. By extension of these calculations, the calculation of the core distribution is straightforward. The result of these calculations is, therefore, an explicit expression for the radial temperature distribution for a liquid flowing through a pipe with centerline temperature T_{CL} and wall temperature T_w. The following equations display this distribution:

$$\frac{T_{CL} - T(r)}{T_{CL} - T_w} = 1 - \frac{Pr\ (y/y_1)}{D} \tag{4-12}$$

$$0 \le y = r_0 - r \le y_1$$

$$= 1 - \frac{Pr + \ell n\left[1 + Pr\left(\frac{y}{y_1} - 1\right)\right]}{D} \tag{4-13}$$

$$y_1 \le y \le y_2$$

$$= 1 - \frac{Pr + \ell n\ (1+5\ Pr) + 0.5\ \ell n\left[\frac{Re}{30}\sqrt{\frac{f}{8}}\left(\frac{y}{r_0}\right)\right]}{D} \tag{4-14}$$

$$y_2 \le y \le \frac{r_0}{2}$$

$$= 1 - \frac{Pr + \ell n\ (1+5\ Pr) + 0.5\ \ell n\left[\frac{Re}{60}\sqrt{\frac{f}{8}}\right] + \left[0.25 - \left(1 - \frac{y}{r_0}\right)^2\right]}{D} \tag{4-15}$$

$$\frac{r_0}{2} \le y \le r_0$$

where

$$\text{Pr} = \text{Prandtl number} = \frac{\nu}{\alpha} \text{ (a value of 10 appears to be appropriate for the laser liquid)}$$

$$y_1 = \frac{10 r_0}{(0.198)\text{Re}^{7/8}}$$

$$y_2 = 6y_1$$

$$\text{Re} = \text{Reynolds number of flow} = \frac{v_{max}\,(2r_0)}{\nu}$$

$$f = \text{pipe "friction factor"} = \frac{0.0791}{\text{Re}^{1/4}}$$

$$D = \text{Pr} + \ell n\,(1 + 5\,\text{Pr}) + 0.5\,\ell n\left(\frac{\text{Re}}{60}\sqrt{\frac{f}{8}}\right) + 0.25$$

Eqs. (4-12) to (4-15) and the subsequent definitions, obtained from the Martinelli analysis, allow the calculation of the temperature distribution of the flowing laser liquid in the cell as a function of the radius. These results apply to the case where there is a constant temperature difference between the centerline (T_{CL}) and inner wall (T_w) temperature. The results are not applicable to the case where the centerline temperature is varying due to the addition of heat from an external source (flashlamps).

4.2 APPLICATION OF THE HYDRODYNAMIC SOLUTION TO THE LIQUID LASER

The solution to the hydrodynamic problem for the temperature distribution of a liquid flowing in a pipe is given by Eqs. (4-12) to (4-15), in which the solution is expressed in terms of the centerline temperature and the inner wall temperature. A typical example of what such a distribution might look like is shown in Figure 4-2. The centerline temperature is reasonably well-approximated by the bulk temperature of the flowing liquid; the inner wall temperature is more difficult to determine. Referring to Figure 4-1(b), it is seen that in addition to the bulk laser liquid temperature, the only other temperature that is readily measured and known is that of the external cell coolant, T_0. The first problem, then, is to estimate T_w in terms of T_{CL}, T_0 and the flow characteristics. The knowledge of T_w enables us to apply Eqs. (4-12) to (4-15) and obtain the temperature distribution.

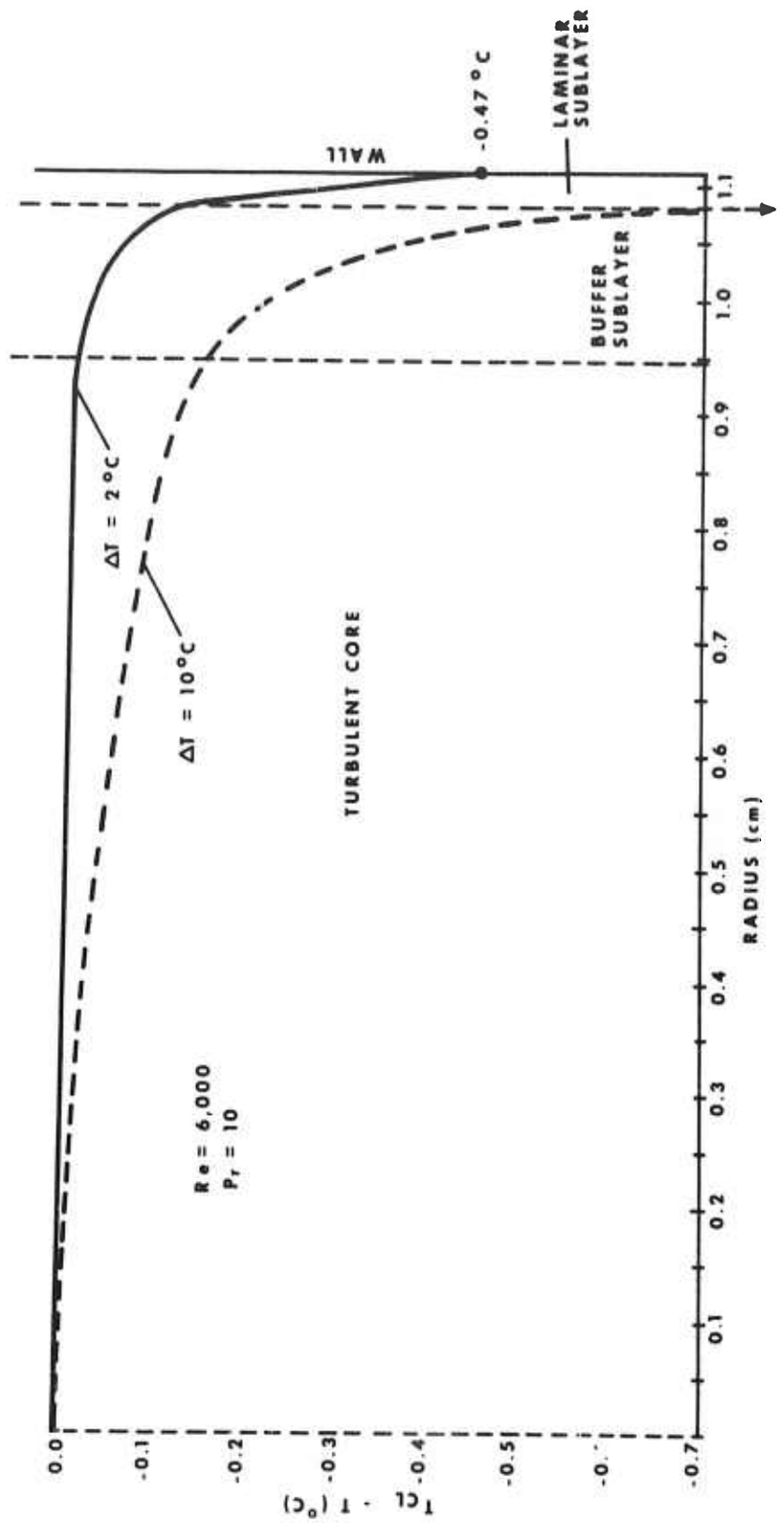

Figure 4-2. Typical Radial Temperature Profiles in the Liquid Laser Cell. Two values of $\Delta T = T_{CL} - T_0$ are shown. In this case, Re = 6,000, r_0 = 1.11 cm, Pr = 10.

If there is no external heat source, the radial flow of heat is determined by the temperature difference $T_{CL} - T_0$ and the volume flow rate through the cell. At the boundary between the liquid and the cell (inner cell wall) there will exist a temperature which, in the steady state, is determined by the heat arriving at the cell wall by forced convection from the liquid and the conductive heat flow through the cell wall.

For the latter we can write:

$$\frac{dQ}{dt} = - K_w A \frac{dT}{dx} \tag{4-16}$$

where

$\frac{dQ}{dt}$ = the heat flow per unit time

K_w = the thermal conductivity of the Pyrex cell wall

A = the surface area

$\frac{dT}{dx}$ = the temperature gradient in the wall at the interface

Assuming a uniform thermal conductivity for the cell wall, and also assuming that the cell coolant represents an infinite heat sink in intimate contact with the outside of the cell, the temperature gradient across the cell wall will be constant and of magnitude $(T_w - T_0)/t$. The flat plate approximation used here is valid since

$\frac{r_0 + t}{r_0} < 1.4$,[91] where t is the cell wall thickness. Eq. (4-16), therefore, becomes

$$\frac{dQ}{Adt} = - K_w \left(\frac{T_w - T_0}{t} \right) \tag{4-17}$$

The heat transfer under forced convection from the laser liquid to the cell wall can be approximated by the calculation[92] of the Nusseult number, Nu:

$$Nu = \frac{2hr_0}{K_L} \approx 0.27 \, (Re)^{0.8} \, (Pr)^{1/3} \tag{4-18}$$

where the surface heat transfer coefficient, h, is defined as:

$$h = \frac{dQ/dt}{A\left(T_{CL} - T_w\right)} = \frac{dQ/dt}{2\pi r_0 L\left(T_{CL} - T_w\right)} \tag{4-19}$$

and K_L is the thermal conductivity of the laser liquid. Combining Eqs. (4-18) and (4-19) and using Pr = 10 for the laser liquid, we obtain:

$$\frac{dQ}{Adt} = K_L \beta \left(\frac{T_{CL} - T_w}{r_0}\right) \tag{4-20}$$

where $\beta = 2.91 \times 10^{-2} \times Re^{0.8}$. In the steady state, the rate at which heat arrives at the wall [Eq. (4-20)] equals the rate at which it is transmitted through the wall [Eq. (4-17)]. Hence, equating (4-17) and (4-20), T_w is found to be:

$$T_w - T_0 = \left(T_{CL} - T_0\right) \frac{\beta K_L / r_0}{\beta K_L / r_0 + K_w / t} = \left(T_{CL} - T_0\right) \frac{1}{1 + \frac{K_w}{\beta K_L} \frac{r_0}{t}} \tag{4-21}$$

As an example, consider a set of experimental conditions described by Re = 9900 and Pr = 10 in a cell of r_0 = 1.1 cm and t = 0.14 cm. The physical constants for a Pyrex glass wall and the laser liquid Nd^{+3}:$ZrCl_4$:$POCl_3$ are given in Table 4-1. For the case $T_{CL} - T_0 = 10°C$, we find $T_w - T_0 = 7.7°C$; the bulk of the temperature drop occurs across the cell wall. With this value of T_w, one can obtain the solutions for $(T_{CL} - T)/(T_{CL} - T_w)$ as given by Eqs. (4-12) to (4-15). For the conditions specified in the above example, this function:

$$\left(\frac{T_{CL} - T}{T_{CL} - T_w}\right) = 1 - \left(\frac{T_w - T}{T_w - T_{CL}}\right)$$

is plotted against the radius r in Figure 4-3. The radii r_2 and r_1 shown on the graphs are the respective boundaries of the buffer sublayer and laminar sublayers. Also drawn to scale on this figure is the actual laser cell wall thickness t. It is important to note that of the total 2.3°C temperature drop between the centerline and the wall less than 7% (0.16°C) occurs up to r = 1.0 cm (the onset of the buffer layer). Most of the temperature drop occurs in the buffer and laminar layers.

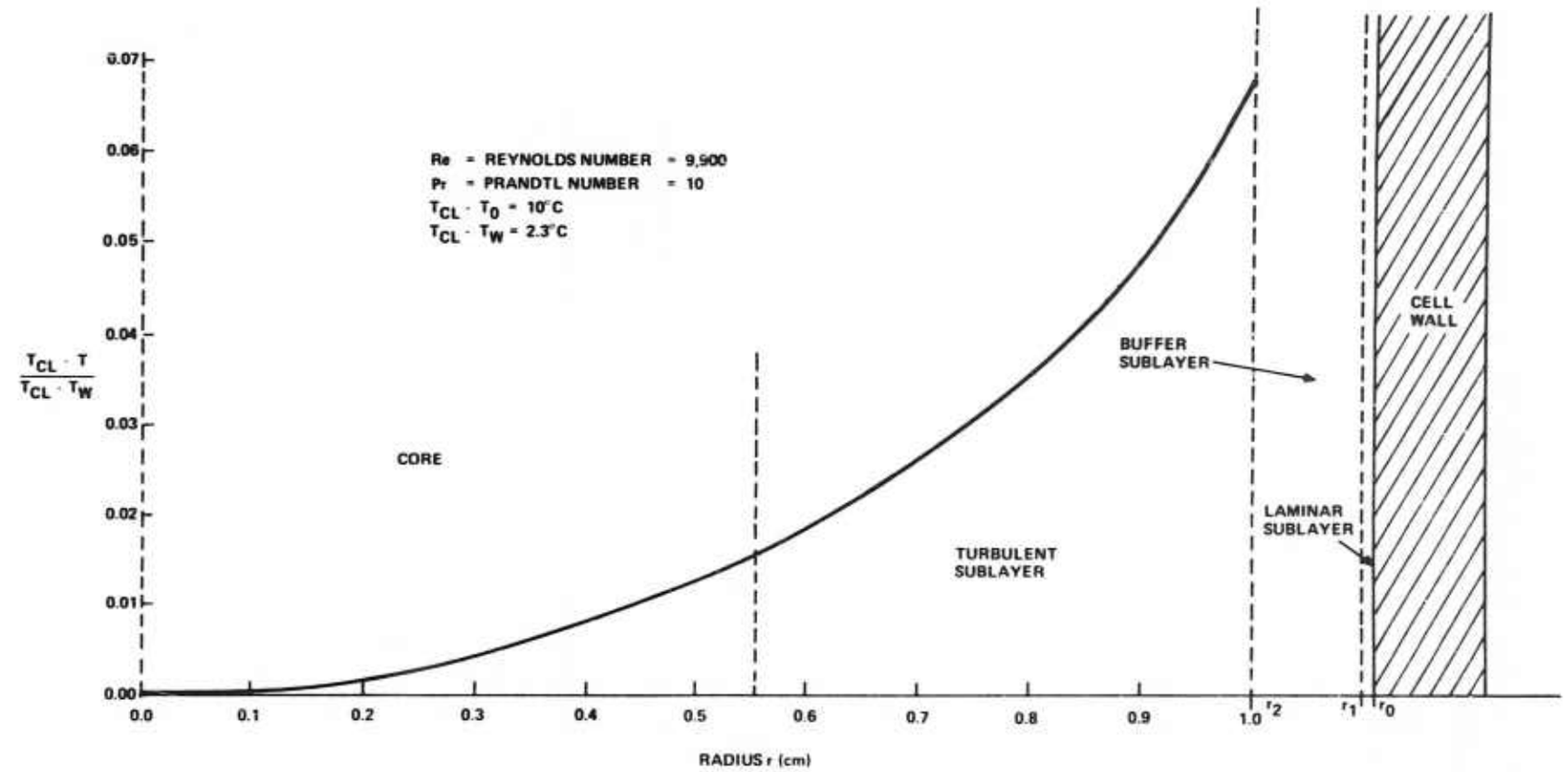

Figure 4-3. Computer Calculation of Temperature Profile Across the Laser Cell. Parameters are Re = 9900, Pr = 10. $T_{CL} - T_0 = 10°C$, cell wall thickness = 0.14 cm. The cell wall thickness as well as the four liquid sublayer thicknesses are drawn to scale.

TABLE 4-1

PHYSICAL CONSTANTS OF LASER LIQUID AND LASER CELL

Thermal conductivity of Pyrex (K_{Pyrex}):	2.7×10^{-3} cal • cm^{-1} • s^{-1} • $°C^{-1}$
Density of laser liquid (ρ_L):	1.8 g • cm^{-3}
Index of refraction of liquid ($\lambda = 1.06\mu$, T = 20°C) N_o:	1.4783
Change of index with temperature $\frac{dn}{dT}$:	-4.5×10^{-4} $°C^{-1}$
Specific heat of liquid (C_p):	0.320 cal • gm^{-1} • $°C^{-1}$
Prandtl number of laser liquid (Pr):	10
Dynamic viscosity (μ):	5 centipoise = 5×10^{-2} gm • s^{-1} • cm^{-1}
Thermal conductivity of liquid $K_{liquid} = \frac{C_p \mu}{Pr}$:	1.6×10^{-3} cal • cm^{-1} • s^{-1} • $°C^{-1}$
$T_{CL} - T_0$:	10°C
$T_{CL} - T_w$:	2.3°C

Let us now consider the index of refraction gradient $n'(r)$, Eq. (4-22):

$$\frac{dn}{dr} = \frac{dn}{dT}\frac{dT}{dr} \tag{4-22}$$

is readily integrated to give:

$$n(r) - n(0) = \frac{dn}{dT}\int_0^r \frac{dT}{dr}dr = \frac{dn}{dt}\left(T_r - T_{CL}\right) \tag{4-23}$$

if we assume $\frac{dn}{dT}$ is constant. Limiting ourselves to the turbulent layer and core and using Eqs. (4-14) and (4-15), it is then readily shown that:

$$n(0) - n(r) = \frac{dn}{dT}\left(T_{CL} - T_{w}\right)\left\{1 - \frac{Pr + \ell n\,[1+5\,Pr] + 0.5\,\ell n\left(\frac{Re}{30}\sqrt{\frac{f}{8}}\right)\left[1 - \frac{r}{r_0}\right]}{D}\right\} \qquad (4\text{-}24)$$

for

$$\frac{r_0}{2} \le r \le r_2$$

$$n(0) - n(r) = \frac{dn}{dT}\left(T_{CL} - T_{w}\right)\left\{1 - \frac{Pr + \ell n\,[1+5\,Pr] + 0.5\,\ell n\left(\frac{Re}{60}\sqrt{\frac{f}{8}}\right) + \left[0.25 - \left(\frac{r}{r_0}\right)\right]^2}{D}\right\} \qquad (4\text{-}25)$$

for

$$0 \le r \le \frac{r_0}{2}$$

where D is the same quantity defined in Eqs. (4-12) to (4-15). By straightforward differentiation:

$$n'(r) = \frac{dn}{dr} = \left(\frac{-dn}{dT}\right)\left(T_{CL} - T_{w}\right)\frac{1}{r_0 \times D}\left(\frac{0.5}{1 - r/r_0}\right) \qquad (4\text{-}26)$$

for

$$\frac{r_0}{2} \le r \le r_2$$

and

$$n'(r) = \left(\frac{-dn}{dT}\right)\left(T_{CL} - T_{w}\right)\left(\frac{2}{r_0 \times D}\right)\frac{r}{r_0} \qquad (4\text{-}27)$$

for

$$0 \le r \le \frac{r_0}{2}$$

Eqs. (4-24) and (4-25) describe the radial variation of the refractive index as a function of the material and flow characteristics, and the imposed temperature differential, $T_{CL} - T_0$, since $T_w - T_0$ can be calculated according to Eq. (4-21). Further, Eqs. (4-26) and (4-27) express directly the radial refractive index gradient. Eqs. (4-26) and (4-27) will be applied in the next section to obtain the optical properties of the laser medium.

4.3 OPTICAL CHARACTERISTICS OF THE LASER MEDIUM UNDER STEADY-STATE CONDITIONS

For condensed phase lasers, thermo-optical effects arise from the optical excitation energy degraded as heat. In an Nd^{+3} based laser, whose principal absorption bands are at 5800 Å, 7400 Å, 8000 Å and 8800 Å, with a laser emission at 1.06μ, about 50% of the absorbed pump energy is dissipated as heat. For solid state devices there are, in addition, stress-optic effects which complicate the problem. These do not exist in a fluid medium that is subject only to thermo-optical effects.

Thermo-optical effects are of two sorts. The first occurs during the excitation pulse and arises from nonuniform absorption of pump power. This occurs very rapidly and the distortion introduced by this process is present for each pulse in a train. The bulk of the excited liquid and the associated heat are swept away after the pulse. However, there is a residue in the laminar and buffer layers that is not exchanged as rapidly as the turbulent core; this gives rise to the second effect which occurs on the repetitive application of pulsed energy and is more or less a function of average power. The thermal residues of successive pulses accumulate until the temperature gradient and resulting heat conduction are large enough to balance the increment from each pulse. The radial temperature gradient gives rise to a radial refractive index gradient that distorts the beam in the amplifying medium and results in a marked reduction of output.

In this section we shall, for simplicity, discuss the optical consequences in terms of the second effect. We will set up a radial thermal gradient through control of T_0 and T_{CL} $(T_{CL} > T_0)$ the external cell coolant and the bulk temperature of the liquid laser material. As has been shown in the previous section, under these conditions the radial thermal gradient can be calculated and, given this thermal gradient, the refractive index gradient and its effect on the propagated wave will be evaluated. Optical measurements on the pure $POCl_3$ solvent and the actual laser solution under flow conditions will be correlated with these theoretical results in Section 4.6. The actual application of these results to laser experiments will be considered later.

A light ray, entering normally at the centerline of the laser cell, will propagate undeviated. Rays entering normally at values of $r \neq 0$ will deviate from the normal. In fact, since dn/dT and dT/dr have the same sign, the liquid medium will behave as a diverging lens. This is schematically illustrated in Figure 4-4. The analysis we will give, based on this figure, is taken from Riedel and Baldwin;[82, 83] other approaches have been given by Quelle[79] and Winston and Gudmundson.[93]

The optical path length, S, of a ray entering at $z = 0$, $r = r_1$, and leaving at $z = L$, $r = r_2$, is given by:

$$S = \int_0^L n(r) \sqrt{1 + r'^2}\, dz = \int_0^L G(r, r', z)\, dz \tag{4-28}$$

where $r' = \frac{dr}{dz}$. Applying Fermat's principle, $\delta S = 0$, leads to the differential equation:

$$\frac{\partial G}{\partial r} - \frac{d}{dz}\frac{\partial G}{\partial r'} = 0$$

$$\frac{dn(r)}{dr}\left(1 + r'^2\right) - nr'' = 0 \tag{4-29}$$

If we let $q = r'$ and integrate the resulting equation, we find:

$$\frac{1}{2\left(1+q^2\right)} = \ell n\, C_1 n(r) \tag{4-30}$$

where C_1 is a constant of integration. This is evaluated by the boundary condition $q\left(r_1\right) = r_1' = 0$. Then:

$$C_1 = \frac{1}{n(r_1)\, e^{1/2}}$$

and

$$-\frac{1}{2\left(1+q^2\right)} = \ell n \left[\frac{n(r)}{n(r_1)\, e^{1/2}}\right] \tag{4-31}$$

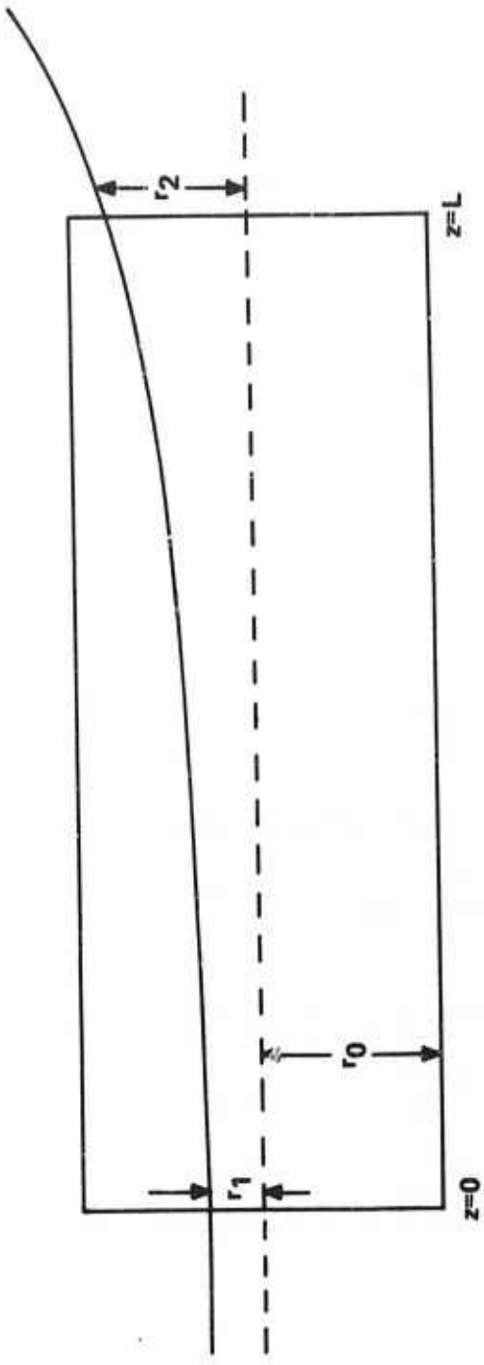

Figure 4-4. Simplified Ray Diagram of the Laser Cell.

Eq. (4-31) can now be brought into the form:

$$\pm \int \left[\frac{1}{2 \ell n \frac{n(r)}{n\, r_1}} - 1 \right]^{1/2} dr = \int dz = z + C_2 \qquad (4\text{-}32)$$

In the turbulent core, where dT/dr is slowly varying, we express n(r) as follows:

$$n(r) = n_0 + \frac{dn}{dt} \left[T(r) - T_{CL} \right] \qquad (4\text{-}33)$$

and using Eqs. (4-24) and (4-25),

$$n(r) = n(r_1) + \left(\frac{dn}{dT}\right) \left[\frac{0.5 \left(T_{CL} - T_w\right)}{D} \right] \ell n \left[\frac{R_e}{30} \sqrt{\frac{f}{8}} \left(\frac{r_0 - r}{r_0 - r_1} \right) \right] \qquad (4\text{-}34)$$

$$r_2 \leq r,\ r_1 \leq \frac{r_0}{2}$$

and

$$n(r) = n(r_1) + \left(\frac{dn}{dT}\right) \left(\frac{T_{CL} - T_w}{D} \right) \left[\left(\frac{r_1}{r_0} \right)^2 - \left(\frac{r}{r_0} \right)^2 \right] \qquad (4\text{-}35)$$

$$\frac{r_0}{2} \leq r,\ r_1 \leq r_0$$

Both expressions may be written in the form:

$$\frac{n(r)}{n(r_1)} = 1 + \frac{C_0}{n(r_1)} F(r, r_1)$$

where

$$|C_0| = \left(\frac{dn}{dT}\right) \left(\frac{T_{CL} - T_w}{D} \right) \simeq 10^{-5}$$

$$|F(r, r_1)| \simeq \left(\frac{r_0}{r} \right)^2$$

The insertion of either Eqs. (4-34) or (4-35) into Eq. (4-32) leads to an equation that is not readily integrable.

Over the turbulent layer and core, $n(r)/n(r_1)$ is a slowly varying function, and can be expanded in a Taylor series:

$$\frac{n(r)}{n(r_1)} = 1 + \frac{n'(r_1)}{n(r_1)}(r - r_1) + \frac{n''(r_1)}{2n(r_1)}(r - r_1)^2 + \cdots\cdots \tag{4-36}$$

If we limit ourselves to only the first terms, the expansion of $e^{-a(r-r_1)}$ with

$$a = \frac{n'(r_1)}{n(r_1)}$$

has the same form as Eq. (4-36). The justification for using this approximation lies in the value of $n'(r_1)$. In general, over the turbulent layer and core, as we have seen, the radial change in temperature is small (0.16°C for $T_{CL} - T_0 = 10°C$). Furthermore, dn/dT is very small, hence

$$\frac{n'(r_1)}{n(r_1)}$$

is very small. Again, over the turbulent layer and core the curvature of T as a function of r is small and $n''(r_1)$ is also small.

From Eqs. (4-26) and (4-27) we find, using the first order approximation $n(r_1) \simeq n_0$:

$$a = \frac{n'(r_1)}{n(r_1)} \simeq \left(\frac{-dn}{dT}\right)\left(\frac{T_{CL} - T_w}{n_0 \times r_0}\right)\left(\frac{1}{D}\right)\left(\frac{0.5}{1 - r_1/r_0}\right) \tag{4-37}$$

in the turbulent layer and

$$a = \frac{n'(r_1)}{n(r_1)} = \left(\frac{-dn}{dT}\right)\left(\frac{T_{CL} - T_w}{n_0 \times r_0}\right)\left(\frac{1}{D}\right)\left(\frac{2r}{r_0}\right) \tag{4-38}$$

in the core.

Substituting $\frac{n(r)}{n(r_1)} \simeq e^{-a(r-r_1)}$ into Eq. (4-32) and integrating, we find:

$$z + C_2 = \pm \frac{1}{2a} \left\{ \sqrt{2a\ (r-r_1)} \left[1 - 2a\ (r - r_1)\right]^{1/2} + \sin^{-1} \left[2a\ (r - r_1)\right] \right\}^{1/2} \quad (4\text{-}39)$$

C_2 is determined from the boundary condition that at $z = 0$, $r = r_1$; this leads to $C_2 = 0$. Then, using the fact that $a \ll 1$, neglecting $2a\ (r - r_1)$ with respect to 1 and expanding the arcsine function, we obtain

$$a^2 z^2 = 2a\ (r - r_1)$$

or

$$r - r_1 = \frac{a}{2} z^2 = 1/2 \frac{n'(r_1)}{n(r_1)} z^2 \quad (4\text{-}40)$$

This says that a ray entering the laser cell normally, but off the cylinder axis, follows a parabolic path and, since $n'(r)$ changes faster than $n(r)$, the curvature of the ray is greater the further it is removed from the centerline.

4.4 BEAM PROPAGATION THROUGH THE TURBULENT LASER MEDIUM

The parabolic relationship derived in the previous section for the ray path has two important consequences. First, a ray entering the medium at ($z = 0$, $r \neq 0$) leaves the medium ($z = L$) at some angle (>0) with respect to the z axis. Secondly, due to the curvature of the ray path, there is a phase variation across the beam in a plane normal to the propagation direction after a traversal of the medium. In this section, we consider these two factors in more detail.

From the laser cell schematic of Figure 4-5, the definitions of the quantities shown therein and Snell's law, we can write for the emerging ray:

$$n(r_2) \sin \gamma(r_2) = \sin \varphi(r_2) \quad (4\text{-}41)$$

At r_2,

$$\frac{dr}{dz} = \tan \gamma(r_2).$$

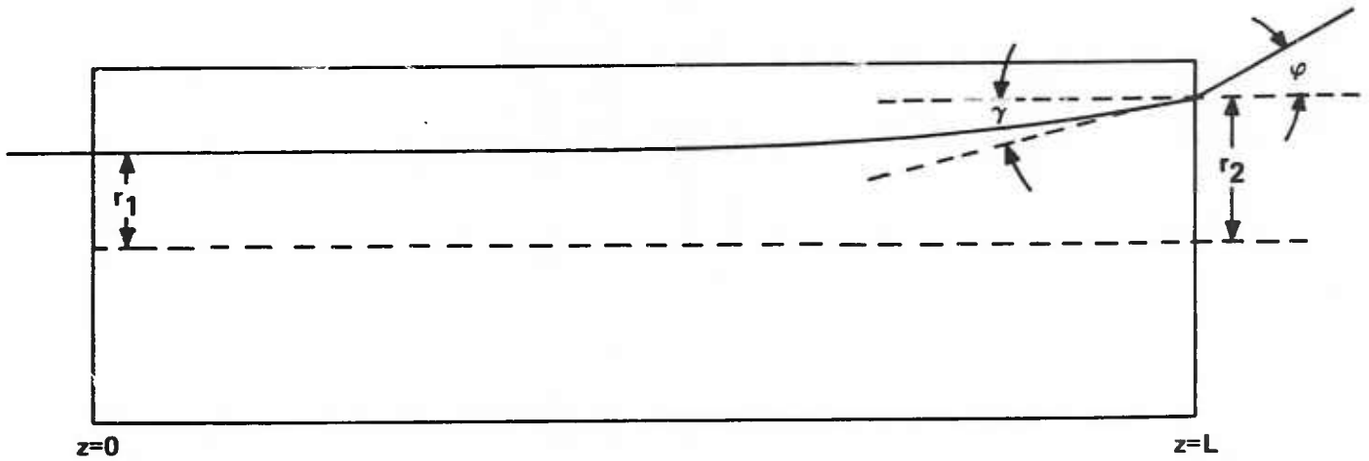

Figure 4-5. Laser Cell Ray Diagram Showing Ray Exit Angles γ and φ.

From Eq. (4-40), we find:

$$\frac{dr}{dz}\Big|_{r_2} = \frac{n'(r_1)}{n(r_1)} L = \tan \gamma(r_2)$$

and then:

$$\sin \varphi(r_2) = n(r_2) \sin \left[\tan^{-1} \frac{n'(r_1)}{n(r_1)} L \right]$$

For the system involved $n'(r_1) \ll L$ and $n(r_1)$, so:

$$\tan \gamma(r_2) = \sin \gamma(r_2) = \gamma(r_2)$$

then:

$$\sin \varphi(r_2) = n(r_2) \frac{n'(r_1)}{n(r_1)} L$$

However, since $n(r_2) \cong n(r_1)$ and $n'(r_1)L \ll 1$, then $\varphi(r_2) = n'(r_1)L$. The refractive index gradient $n'(r)$ increases with r so that $\varphi(r_2)$ increases with increasing r_1. At some value of $r_1 = r_a$, the emergence angle $\varphi(r_2)$ will be large enough so that in a plane parallel resonator, or one with large radius of curvature mirrors, the emerging ray will "walk off" or have a very high loss. From this picture, the laser is then self-apertured at this value of r_a, in general smaller than the turbulent core. The extent of the self-aperturing will depend on the index of refraction gradient and hence, on flow conditions and $\Delta T = T_{CL} - T_0$.

With the development of the ray path in the medium, the change in phase for a ray propagating through the laser cell off-axis, measured relative to the on-axis ray, can be calculated. Consider the case of a plane wave entering the cell as shown in Figure 4-6.

The optical path length of the ray propagating along the axis of the cell and striking the observation plane OP placed a distance d_0 from the output end of the cell is:

$$P(0) = n_0 L + d_0 \qquad (4\text{-}42)$$

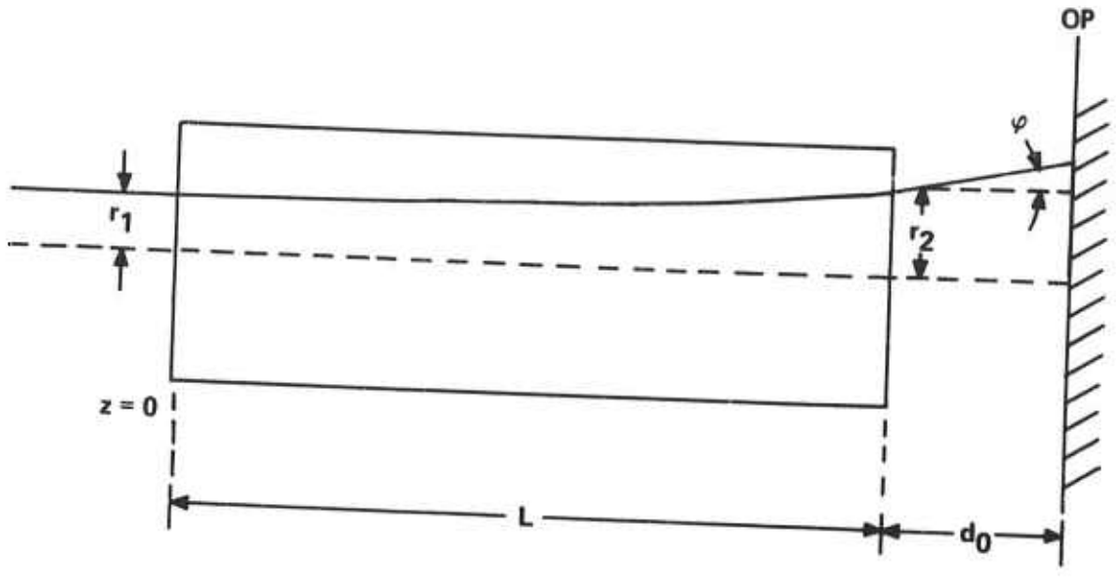

Figure 4-6. Ray Diagram of the Laser Cell for a Plane Wave Input.

The optical path length of a ray entering the cell at radius r_1 and striking the OP plane will be:

$$P(r_1) = S(r_1) + \frac{d_0}{\cos \varphi(r_2)} \tag{4-43}$$

Now:

$$S(r_1) = \int_0^L n(r) \sqrt{1 + r'^2}\, dz \tag{4-44}$$

and, using Eq. (4-31), we find:

$$S(r_1) = \int_{r_1}^{r_2} = \frac{n(r)\, dr}{\sqrt{2 \ell n \left[n(r)/n(r_1)\right]}} \tag{4-45}$$

Using Eqs. (4-36), (4-40), and the exponential approximation for $\frac{n(r)}{n(r_1)}$, we obtain:

$$S(r_1) = \frac{n(r_1)\sqrt{2}}{a} \int_0^{\frac{aL}{\sqrt{2}}} e^{y^2}\, dy \tag{4-46}$$

where $y^2 = a(r - r_1)$. Since $y^2 \ll 1$, we expand the exponential in Eq. (4-46), retain only the first two terms and integrate to get:

$$S(r_1) = n(r_1)\, L \left(1 + \frac{a^2 L^2}{6}\right) \tag{4-47}$$

Since $\varphi(r_2)$ is small, we can expand the second term in Eq. (4-43) as:

$$\frac{d_0}{\cos \varphi(r_2)} \simeq d_0 \left[1 + \frac{\varphi^2(r_2)}{2}\right]$$

As we have seen before, we may approximate to the same order:

$$\varphi(r_2) \simeq n'(r_1) L$$

Substituting into Eq. (4-43), we have

$$P(r_1) = n(r_1) \left\{ L + \frac{L^3}{6} \left[\frac{n'(r_1)}{n(r_1)}\right]^2 \right\} + d_0 \left\{1 + \frac{L^2}{2} \left[n'(r_1)\right]^2 \right\} \tag{4-48}$$

Subtracting Eq. (4-42) from Eq. (4-48), we find the optical path length difference at the observation plane for the two beams

$$P(r_1) - P(0) \equiv \Delta P(r_1) = \left[n(r_1) - n_0\right] L + L^2 \left[\frac{L}{6n(r_1)} + \frac{d_0}{2}\right] \left[n'(r_1)\right]^2 \tag{4-49}$$

Again, we may approximate to the same order of accuracy as previously used $n(r_1) \simeq n_0$, so that the first term in Eq. (4-49) vanishes compared to the last two. We, therefore, are left the final result:

$$\Delta P(r_1) = L^2 \left(\frac{L}{6n_0} + \frac{d_0}{2}\right) \left[n'(r_1)\right]^2 \tag{4-50}$$

4.5 OPTICAL MEASUREMENTS OF A LIQUID WITH AN IMPOSED RADIAL TEMPERATURE GRADIENT UNDER TURBULENT FLOW CONDITIONS

In this section, two independent optical methods are used to measure the radial index gradient in a liquid laser cell. The cell used for these measurements was the largest one on the recent three-head laser system described in Section 3.2. A sketch of the cell actually used has been previously shown as Figure 3-7. In the experiments to be described, two different liquids were circulated through the laser cell — the pure $POCl_3$ solvent and the actual Nd^{+3}:$POCl_3$:$ZrCl_4$ laser liquid. These liquids have different physical properties that are compared in the following table.

TABLE 4-2

PHYSICAL CONSTANTS OF LASER LIQUID AND $POCl_3$

Constant	Units	$POCl_3$	Laser Liquid
Density (ρ)	$gm \cdot cm^{-3}$	1.645	1.8
Dynamic Viscosity	$gm \cdot cm^{-1} \cdot sec^{-1}$ (poise)	0.010645	0.005
dn/dT	$^{\circ}C^{-1}$	-6×10^{-4}*	-6×10^{-4}
Specific Heat (cp)	$cal \cdot gm^{-1} \cdot {}^{\circ}C^{-1}$	0.38*	0.32
Thermal Conductivity (k)	$cal \cdot cm^{-1} \cdot {}^{\circ}C^{-1} \cdot sec^{-1}$	1.6×10^{-3}*	1.6×10^{-3}
Prandtl Number $\left(P_r = \frac{c_p \mu}{K}\right)$	---	2.5*	10.0

*Estimated values

Of the two liquids, the pure $POCl_3$ solvent has the larger uncertainty of the actual value of the indicated physical constants. The values listed in Table 4-2 are the best approximations we could make in lieu of actual reported data. Since these factors enter into the estimate of the Prandtl Number of the liquid, we estimate that any one of the three quantities indicated may be off from the actual value by as much as a factor of two.

These two liquids were circulated in the laser system at a set pump speed, but, because of their different physical properties, a different Reynold's Number for the flow resulted (R_e = 25,600 for the $POCl_3$ and 5980 for the laser solution). For each liquid, the temperature of the cell water jacket coolant (T_0) was varied while keeping the flowing liquid temperature (T_{CL}) constant. In this way, a variable, steady-state

thermal (and index of refraction) gradient could be established across the radius of the flowing liquid. The results of the previous section were used to calculate this gradient for the two liquids used. The experimental results to be described are, therefore, a direct check of the validity of the preceding theory.

4.5.1 Calculation of the Induced Radial Temperature Gradients

We first calculate the refractive index gradient dn(r)/dr from Eq. (4-27) of Section 4.2. Since the data to be compared to theory was taken on a cell whose aperture was restricted by an external iris with diameter $d < r_0$ = internal radius of laser cell, only those equations in Section 4.2 will apply where $0 \leq r \leq r_0/2$. The index gradient is therefore given by:

$$n'(r) = \left(\frac{-dn}{dT}\right)\left(T_{CL} - T_w\right)\frac{2r}{r_0^2 \times D}$$

where

$$D = P_r + \ell n\,(1 + 5\,P_r) + 0.5\,\ell n\left[\frac{R_e}{60}\sqrt{\frac{f}{8}}\right] + 0.25$$

In the cases we will be considering, the following parameters apply:

Quantity	With $POCl_3$	With Laser Solution
r_0	1.1 cm	1.1 cm
P_r	2.5	10
R_e	25600	5980
f	6.25×10^{-3}	9.0×10^{-3}
dn/dT	$-6 \times 10^{-4}\ °C^{-1}$	$-6 \times 10^{-4}\ °C^{-1}$
D	8.86	14.785

The centerline, cell-wall temperature difference $T_{CL} - T_w$ must be calculated from the applied temperature difference $T_{CL} - T_0$ and the estimated cell wall thermal conductivity, etc., as was done in Section 4.2, Eq. (4-21).

$$T_{CL} - T_w = T_{CL} - T_0 - (T_w - T_0) = \left[T_{CL} - T_0\right]\left[1 - \frac{1}{1 + \left(\frac{K_w}{K_L}\right)\left(\frac{r_0}{\beta t}\right)}\right]$$

$$= \left[T_{CL} - T_0\right]\left[\frac{r_0 \times K_w}{\beta t K_L + r_0 K_w}\right] = A\left[T_{CL} - T_0\right]$$

Again, using the data from Table 4-1 in Section 4.2 and the relevant physical parameters for this laser cell:

Quantity	With $POCl_3$	With Laser Solution
r_0	1.1 cm	1.1 cm
t	0.14 cm	0.14 cm
K_w (Pyrex)	0.0027 cal $\cdot$ cm^{-1} $\cdot$ sec^{-1} $\cdot$ °C^{-1}	0.0027 cal $\cdot$ cm^{-1} $\cdot$ sec^{-1} $\cdot$ °C^{-1}
K_L	0.0016 cal $\cdot$ cm^{-1} $\cdot$ sec^{-1} $\cdot$ °C^{-1}	0.0016 cal $\cdot$ cm^{-1} $\cdot$ sec^{-1} $\cdot$ °C^{-1}
$\beta = 0.0135\ P_r^{1/3}\ R_e^{0.8}$	61.6	30.54
A	0.177	0.303

Combining the results from these two tables, we find that:

$$\frac{dn}{dr} = 2\left(T_{CL} - T_0\right)\left(\frac{-dn}{dT}\right)\left(\frac{A}{r_0^2\ D}\right)r \equiv 2\left(T_{CL} - T_0\right)\alpha r \qquad (4\text{-}51)$$

$$\alpha = 0.984 \times 10^{-5}\ °C^{-1} \cdot cm^{-2} \text{ for } POCl_3$$

$$= 1.017 \times 10^{-5}\ °C^{-1} \cdot cm^{-2} \text{ for laser solution}$$

Integrating Eq. (4-51) directly, we find

$$n(r_a) - n(0) = \int_0^{r_a} \frac{dn}{dr}\, dr = \alpha \left(T_{CL} - T_0\right) r_a^2 \qquad (4\text{-}52)$$

We again must note that the quadratic form of Eq. (4-52) applies only over the range of the experiments to be presented next; i.e., when $r_a < r_{0/2}$.

4.5.2 Effective Focal Length of Laser Cell — Telescopic Measurement

In this series of experiments, the "effective focal length" f_c of the laser cell is measured using a Davidson autocollimator-telescope to project an illuminated reticle pattern at a known distance from the principle plane of the telescope. The experimental arrangement is shown in Figure 4-7(a). An aperture, set to a diameter of one centimeter (r_0 for this cell), was placed between the telescope and the laser cell and an aluminized flat reflector was placed on the other side of the laser cell. The experiment consisted of decreasing the temperature of the coolant in the laser cell water jacket (T_0) while keeping the bulk temperature of the circulating $POCl_3$ or laser liquid (T_{CL}) constant. Since for both liquids dn/dT is negative and $T_{CL} > T_0$, the liquid in the laser cell will behave as a diverging lens. The effective optical setup of this experiment is shown in Figure 4-7(b). We note that the laser cell must be considered as a thick lens, and that d_1 and d_3 represent the respective distances from the principal planes of the laser cell to the telescope and the flat reflector. In the experiments, the focal length of the telescope f_T was varied until the projected reticle pattern through the telescope was brought into focus. We furthermore adjusted the spacing of the reflector from the laser cell so that $d_3 = d_1 = d$. Under these conditions, the focal length of the laser cell f_c may be calculated as follows:

The first lens L_1 (the telescope) forms a virtual image of the reticle pattern at an image distance i_1 from L_1 given by the focal length of the telescope

$$i_1 = f_T \qquad (4\text{-}53)$$

The second lens L_2 (the laser cell) will form a virtual image of the reticle pattern to the right of L_2, a distance i_2 given by the lens formula

$$\frac{1}{i_2} = \frac{-1}{f_c} - \frac{1}{0_2} = \frac{-1}{f_c} - \frac{1}{i_1 - d} = \frac{-1}{f_c} - \frac{1}{f_T - d}$$

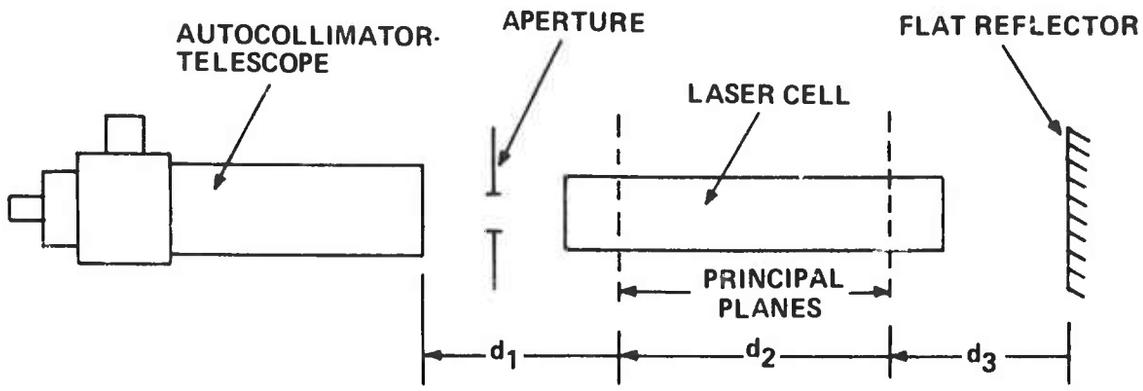

(a) OPTICAL SETUP

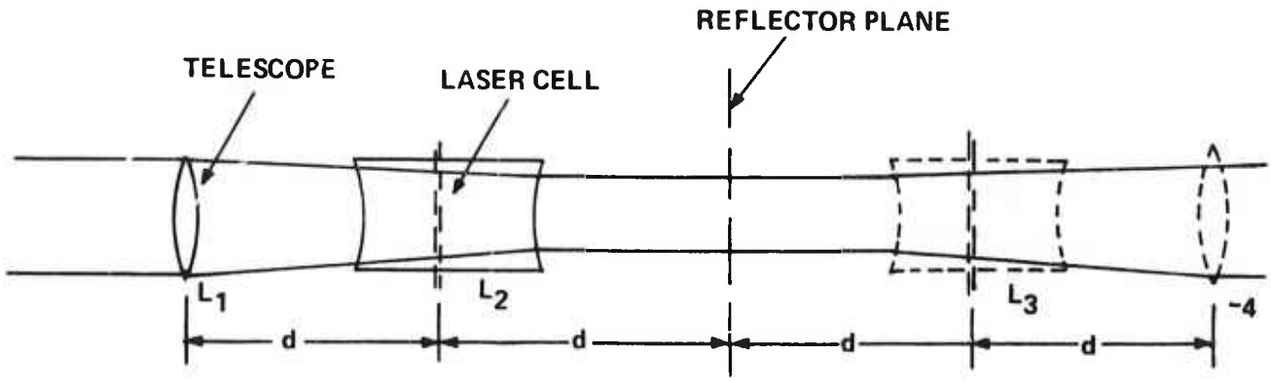

(b) EFFECTIVE OPTICAL SYSTEM

Figure 4-7. Autocollimator-Telescope Setup for Measuring Effective Focal Length of Laser Cell

Thus:

$$i_2 = \frac{f_c\,(f_T - d)}{d - f_c - f_T} \tag{4-54}$$

The third lens L_3 (the virtual lens of the cell caused by the reflecting mirror) will form a real image of the reticle, a distance i_3 to the left given by

$$\frac{1}{i_3} = \frac{-1}{f_c} - \frac{1}{i_2 - 2d} = \frac{-1}{f_c} - \frac{1}{\frac{f_c(f_r - d)}{d - f_c - f_T} - 2d}$$

After a bit of algebra, we arrive at

$$i_3 = \frac{f_c^2 f_T + d f_c^2 + 2d f_c f_T - 2d^2 f_c}{2d^2 - 2d f_c - 2d f_T + f_c^2} \tag{4-55}$$

The image of the telescope in the mirror L_4 will form a virtual image of the reticle pattern at infinity. Therefore,

$$\frac{1}{i_4} = \frac{1}{f_T} - \frac{1}{d + i_3} = \frac{1}{\infty} = 0$$

and

$$f_T - d = i_3 \tag{4-56}$$

By substituting from Eq. (4-55) into Eq. (4-56), we may solve for f_c in terms of f_T and d. When this is done, a simple result obtains

$$f_c = d - f_T \tag{4-57}$$

Substituting Eq. (4-57) into Eq. (4-54), we find that the image distance of L_2 is at infinity, and therefore, the lens combination L_1, L_2 acts as a Galilean telescope. At any rate, Eq. (4-57) is the important result we need relating the "effective cell focal length" f_c to the measured telescope focal length f_T. In the setup, d was estimated to be about 15 cm and was, in general, negligible as regards the actual recorded

values of f_T. To an excellent approximation, then, we can say $f_c = f_T$ and the measured cell focal lengths are reported as this below.

Let us now return to the results of Section 4.5.1. There it was shown that, over the cell radius $0 < r < r_{0/2}$, the index of refraction of the cell can be well-approximated as a quadratic [see Eq. (4-52)].

$$n(r) - n(0) = \alpha \left(T_{CL} - T_0\right) r^2$$

or

$$n(r) = n(0)\left[1 + 2\left(\frac{r^2}{b^2}\right)\right] \tag{4-58}$$

where

$$b^2 = \frac{2n(0)}{\alpha \left(T_{CL} - T_0\right)}$$

and

$$b^2 > 1 \tag{4-59}$$

For such a lens-like medium, Kogelnik[94] has shown that the medium behaves as a diverging lens of focal length

$$f = \frac{-|b|}{2n(0)\sinh\frac{2L}{|b|}} \tag{4-60}$$

and the principal planes are located a distance δ from the ends of the cell given by

$$\delta = \frac{|b|}{2n(0)}\tanh\frac{L}{|b|} \tag{4-61}$$

where L is the length of the cell = 25.4 cm.

We note that we will have $T_{CL} - T_0 \geq 1°C$ and that, for both $POCl_3$ and the laser solution, $\alpha \sim 10^{-5}$. Therefore, using the definition Eq. (4-59),

$$b^2 = \frac{2n(0)}{\alpha\left(T_C - T_0\right)} \sim \frac{3}{10^{-5}} = 3 \times 10^5 \text{ cm}^2$$

$$|b| \sim 5 \times 10^2 \text{ cm and } \frac{2L}{|b|} \sim 0.2$$

In this order, we can approximate $\sinh \frac{2L}{|b|} \simeq \frac{2L}{|b|}$ and rewrite Eq. (4-60) as

$$f = \frac{b^2}{4n(0)L} = \frac{2n(0)}{4\alpha\left(T_{CL} - T_0\right)n(0)\,L} = \frac{1}{2\alpha L\left(T_{CL} - T_0\right)} \tag{4-62}$$

Table 4-3 presents a comparison between the effective focal length f, calculated by Eq. (4-62) for the laser cell and that actually measured (f_c) using the telescope arrangement.

TABLE 4-3

COMPARISON OF CALCULATED AND EXPERIMENTAL FOCAL LENGTHS FOR LASER CELL (FOR $POCl_3$ AND LASER SOLUTION)

	Temperature Difference $T_{CL} - T_0$(°C)	Calculated f_c (Meters)	Observed f_c (Meters)
Using $POCl_3$	1.1	-18.1	-100.0
	2.3	-10.9	- 45.0
	2.8	- 7.25	- 29.0
	3.1	- 6.60	- 23.0
Using Laser Solution	1.0	-27.5	- 42.0
	1.5	-18.6	- 21.5
	2.0	-13.8	- 18.5
	2.35	-11.8	- 16.0
	2.95	- 9.75	- 12.0

The observed focal lengths are, in both cases, larger than those predicted by the calculation. The observed index of refraction gradient dn/dr is, therefore, smaller than the calculated value. The ratio of observed focal length to calculated focal length is:

$$\frac{f_c \text{ (calculated)}}{f_c \text{ (observed)}} = 4.33 \text{ for } POCl_3$$

$$= 1.32 \text{ for laser solution.}$$

Combining Eq. (4-62), (4-59) and (4-51), we see that

$$f_c \text{ (calc.)} \sim \frac{b^2}{4n_0 L} = \frac{2n_0/\alpha \left(T_{CL} - T_0\right)}{4n_0 L} = \frac{4n_0\, r/n'(r)}{4n_0 L} = \frac{r}{Ln'(r)} \qquad (4\text{-}63)$$

The calculation of the index gradient at radius r $[n'(r)]$ is shown best by Eq. (4-51). Note that the index gradient is proportional to dn/dT and depends critically on the estimation of the liquid Nusseult number as was shown in Section 4.2. The point here is that the physical constants for $POCl_3$ as shown in Table 4-2 are not as well known as for the laser liquid. As was mentioned, we estimate an uncertainty of a factor of two for the $POCl_3$ quantities. The cumulative effect of these uncertainties can well explain the factor of four discrepancy between measured and calculated values of the cell focal length. On the other hand, the better known values for the laser liquid result in good agreement between calculated and experimental focal lengths.

4.5.3 Index Gradient of Laser Cell — Interferometer Measurement

The radial index of refractive gradient $n'(r)$ existing in the laser cell may be observed directly using an interferometer. This has been done by several investigators[95-97] to measure flash-induced optical path length changes inside a laser rod. We used a method similar to that used by Sims, Stein and Roth[98] to observe the steady-state radial index gradient induced by the temperature difference $T_{CL} - T_0$ in the liquid flowing through the laser cell. A sketch of the experimental setup is shown as Figure 4-8. A diffraction-limited, pulsed YAG laser was used as a source of collimated 1.064μ wavelength light. The laser was a Sylvania Model 610 YAG laser, modified for flash pumping and Q-switching. The laser output consisted of a single pulse of energy 1.5 mJ of duration 20 ns FWHM. The laser beam was almost a pure TEM_{00} mode (with just a bit of the

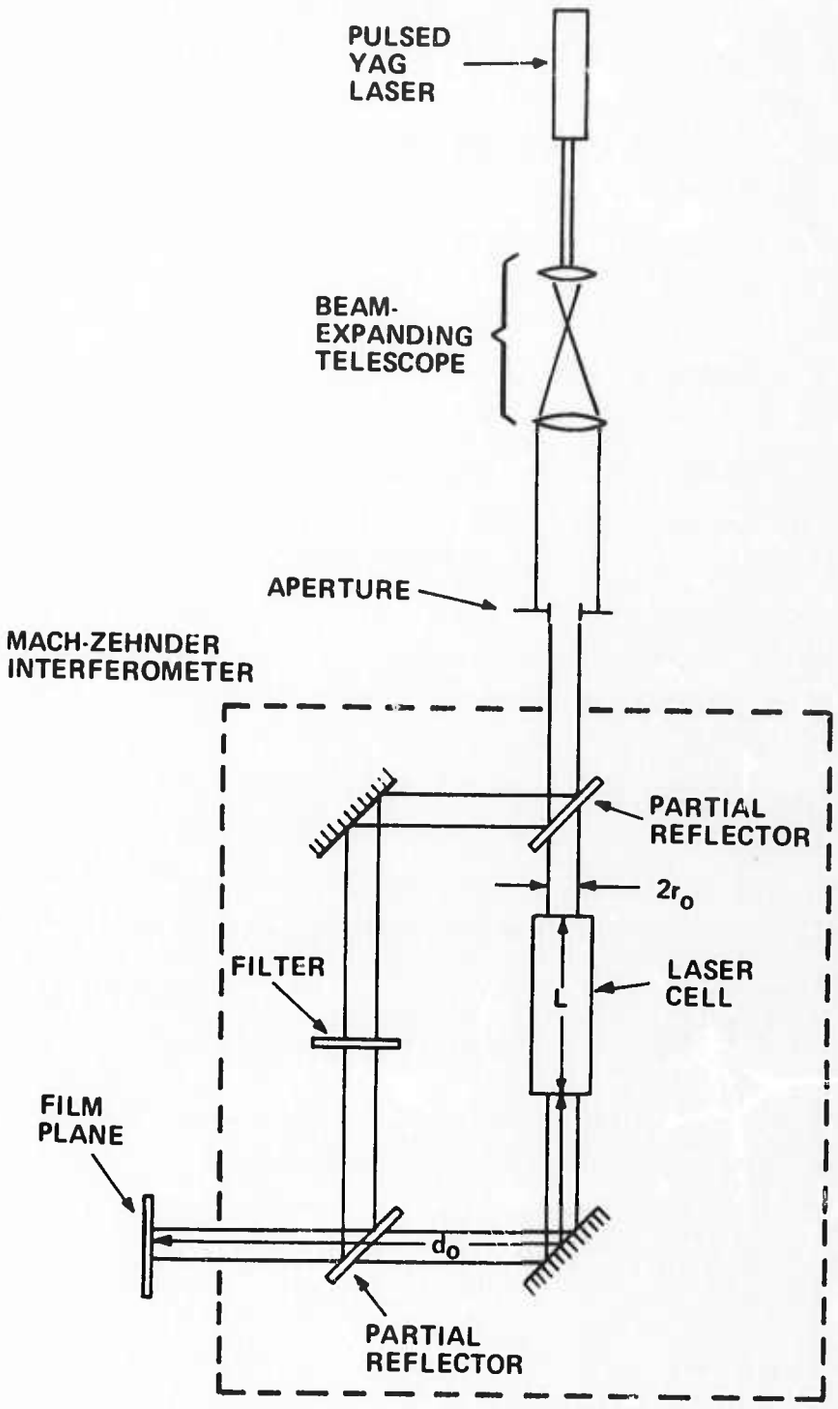

Figure 4-8. Laser-Interferometer Experiment for Observing Index of Refraction Gradients in the Liquid Laser Cell.

next TEM_{01}* mode present) with a far-field half beam divergence angle of 0.34 mrad. This raw laser beam was expanded by the 5X telescope and passed through an aperture of one cm diameter. A Mach-Zehnder interferometer was constructed with the laser cell in one side. A neutral density filter could be inserted in the other side of the interferometer to improve the fringe visibility. The interferometer was aligned using a He-Ne laser to produce fringes of constant inclination at the film plane located a distance d_0 from the exit end of the laser cell, as shown in Figure 4-8. The aperture placed in the YAG beam also produced a weak "bullseye" diffraction pattern on the film plane which aided in establishing the optical center of the laser cell. Interference patterns were recorded on Polaroid IR film. A representative selection of the interferograms produced are shown in Figure 4-9.

To measure the phase changes recorded on these interferograms, a straight line was drawn through the center of the photo, running roughly through the centers of curvature of the fringes. Distances on the film were measured between neighboring dark and light fringes (path differences of $\lambda/2$). When this data is plotted as cumulative optical path length difference from one side of the photo against radius from the centerline of the cell, the results shown in Figure 4-10 are produced. The points forming the straight line on this figure were measured on the cell when $\Delta T = T_{CL} - T_0 = 0$. The curved line shown was generated from data points for $\Delta T = 5°C$. If we subtract the ordinate (path length) differences of the first, linear curve from the second data set, the "reduced" data set forms a parabola. A proper representation of the data set is thus given by:

$$\Delta P = \text{optical path length difference} = Ar^2 + Br \qquad (4\text{-}64)$$

The raw data from the interferograms was fit using a least-squares to the form shown by Eq. (4-64). In the data thus reduced, the linear term is generated by the alignment of the interferometer and is, within experimental error, constant for all the photos measured. The quadratic coefficient A, on the other hand, is a function of the temperature differential $T_{CL} - T_0$.

Referring back to Section 4.4, we had calculated the optical path length difference for a ray entering the cell at radius r, P(r), and a ray propagating along the centerline of the cell, P(c). In the absence of any temperature differential ($\Delta T = 0$), these optical paths are equal. The expression given by Eq. (4-50), therefore, gives the optical path difference as measured on the interferograms as

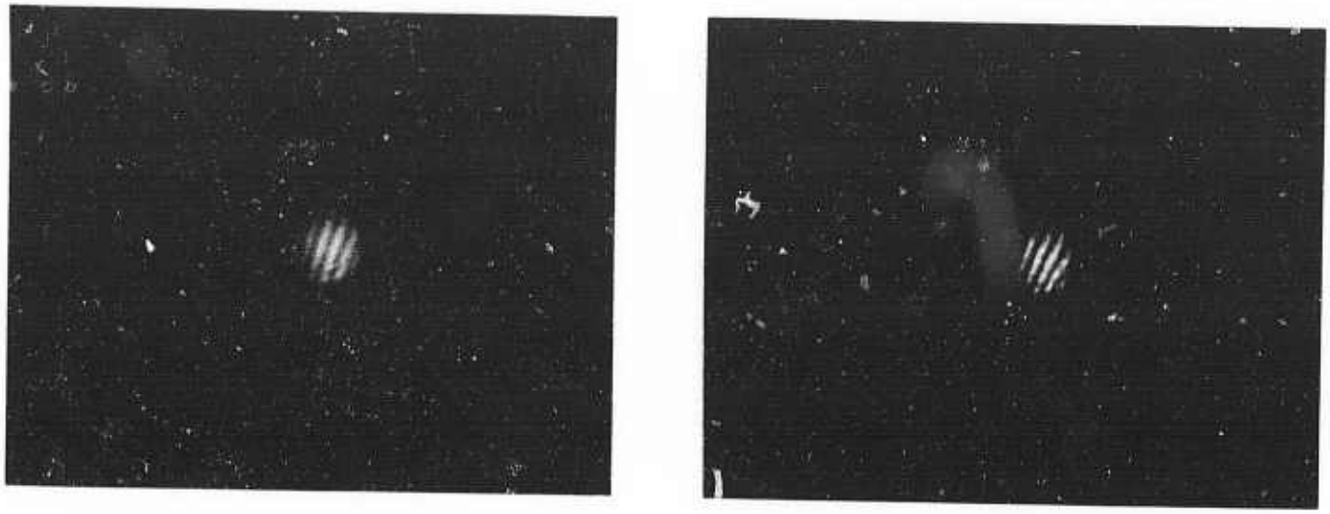

(a) $\Delta T = 0$

(b) $\Delta T = 2.5°C$

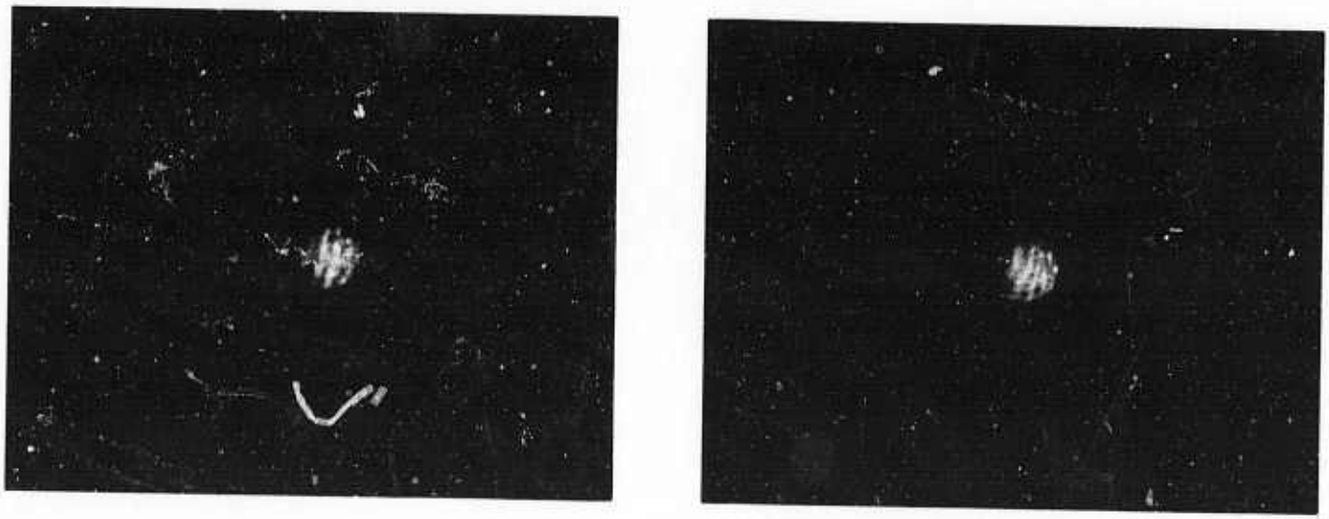

(c) $\Delta T = 4°C$

(d) $\Delta T = 5°C$

Figure 4-9. Mach-Zehnder Interferograms of Laser Cell Using $POCl_3$ with Different Values of $\Delta T = T_{CL} - T_0$.

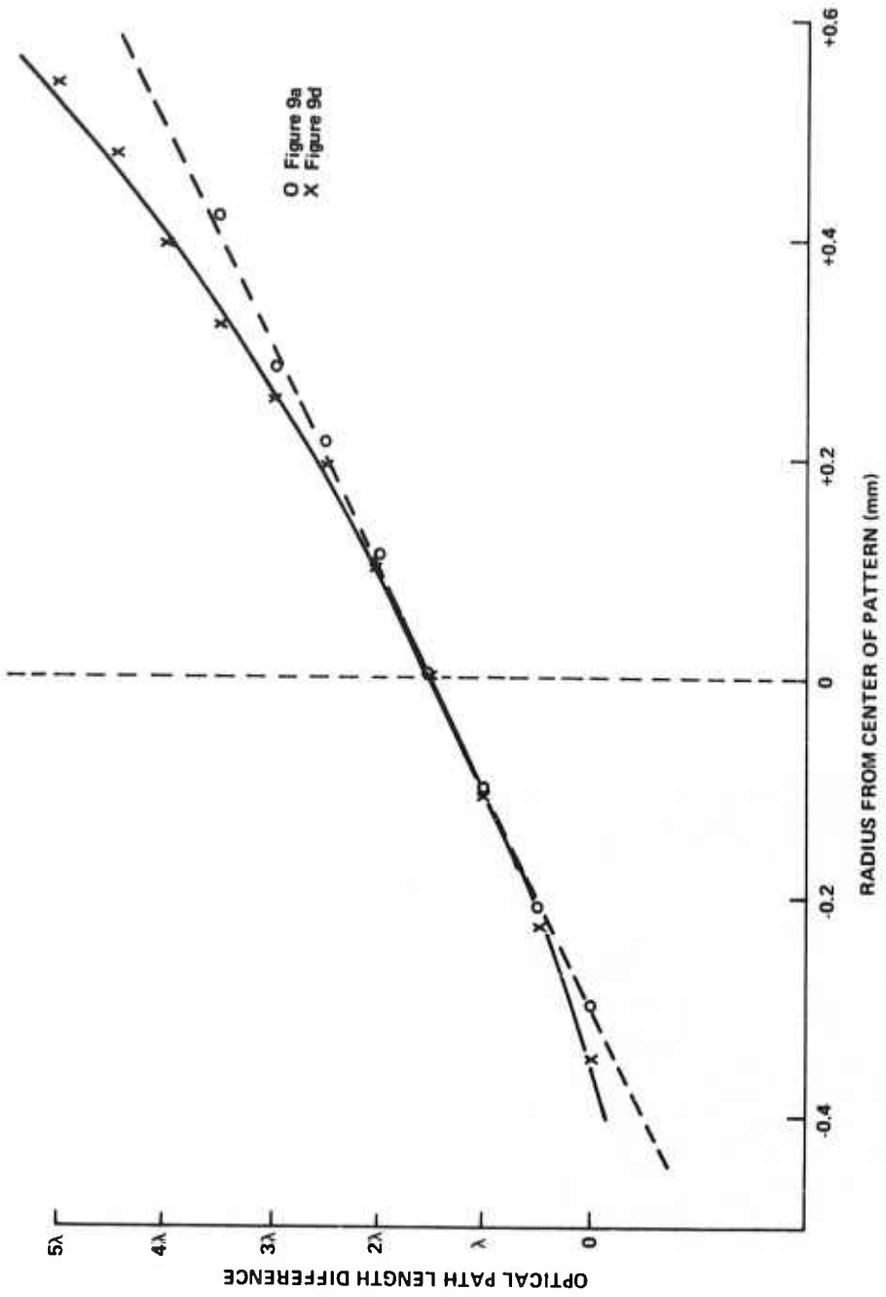

Figure 4-10. Data From Interferogram Shown as Figures 4-9(a) and 4-9(d) $\Delta T = 0$, 5°C; Using $POCl_3$

$$\Delta P(r) = L^2 \left(\frac{L}{6n_0} + \frac{d_0}{2} \right) [n'(r)]^2 \tag{4-65}$$

Using the results of Eq. (4-51), this becomes

$$\Delta P(r) = 4\,\alpha^2\, L^2 \left(\frac{L}{6n_0} + \frac{d_0}{2} \right) (T_{CL} - T_0)^2\, r^2 \tag{4-66}$$

The factors to the left of r^2 are identical to the measured values of A from the experiment. Table 4-4 gives a comparison between the experimental and calculated values for this quantity.

TABLE 4-4

COMPARISON OF CALCULATED AND EXPERIMENTALLY DETERMINED PATH LENGTH QUADRATIC COEFFICIENT $\Delta P(r) = Ar^2 + Br$

	Temperature Difference $T_{CL} - T_0$ (°C)	A Calculated (cm^{-1})	A Measured (cm^{-1})
Using $POCl_3$	1.0	2.06×10^{-5}	1.32×10^{-5}
	2.5	1.29×10^{-4}	3.93×10^{-5}
	4.0	3.30×10^{-4}	3.49×10^{-5}
	5.0	5.15×10^{-4}	2.71×10^{-4}
Using Laser Solution	2.0	8.77×10^{-5}	3.10×10^{-5}
	4.0	3.55×10^{-4}	1.63×10^{-4}

Although the agreement is only fair, it must be emphasized that the calculated values are based on a model (Martinelli calculation) for the turbulent flow properties that have never been applied before to a calculation of the optical properties of flowing liquids. In view of the necessary approximations made in the calculation, along with the uncertainty in physical properties of the liquids, the agreement represented above (within an order of magnitude in all cases) is reasonable for validating the original model and the preceding calculations.

4.5.4 Radial Index Gradients Under Flash-Pumping in the Laser Cell

This section presents the results of extending the work reported in the preceding section to the case of flash excitation of the liquid flowing through the laser cell. The radial index gradients induced by the combination of the imposed temperature differential, and that resulting from absorption of the pump radiation in the flowing liquid were measured using the Mach-Zehnder interferometer shown on Figure 4-8. A delayed trigger circuit was added to fire the liquid laser flashlamps and synchronize them to the Q-switched YAG pulse. The arrangement was such that the liquid laser lamps would fire a predetermined time, ranging from 250 to 600 microseconds, before the YAG laser pulse would probe the medium. In general, varying this time delay showed that the flash-induced, thermal gradient became stronger as the delay time was increased for both the laser liquid and the pure $POCl_3$ solvent. This observation is in complete agreement with results reported for laser rods by several authors.[95-98] We, therefore chose a time delay (400 μs) corresponding to the peak of fluorescence emission of the laser solution under these pumping conditions, and studied the radial gradients induced as a function of input energy to the flashlamps. This was done for both the laser liquid and the $POCl_3$ solvent. The following set of Mach-Zehnder interferograms, Figure 4-11, are representative of the data set for this experiment.

The data were reduced from photos similar to those shown on Figure 4-11 by the same method described in Section 4.5.3. The quadratic coefficient A(cm^{-1}) of the optical path length difference was calculated by a least-squares analysis of the raw data to the form shown by Eq. (4-64). The coefficients thus calculated are shown in Table 4-5.

As may be seen from Table 4-5, the flash-induced gradients are larger in the laser solution than in the $POCl_3$, because of the greater absorption by the laser solution of the pump radiation. Also, the table shows that the gradient induced by the flash pumping is larger than that resulting from the imposed temperature differential. If we assume that the induced index of refraction in the liquids has the quadratic form

$$n(r) = n_0 \left(1 + \frac{p}{2} r^2\right) \tag{4-67}$$

Then:

$$n'(r) = n_0 pr \tag{4-68}$$

(a) $\Delta T = 0°C$
$E_{in} = 0$

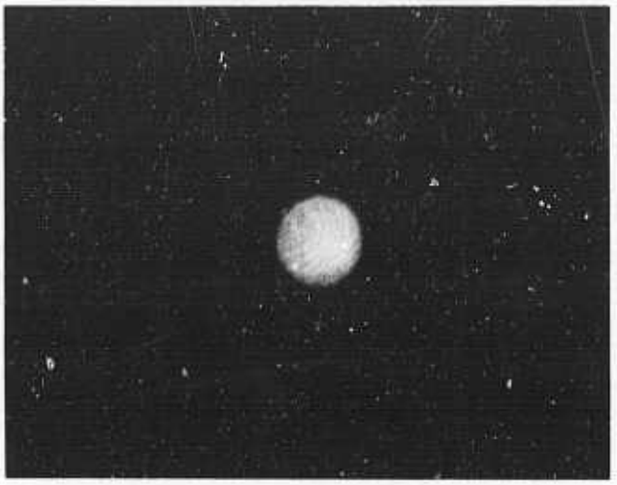

(b) $\Delta T = 0°C$
$E_{in} = 1000J$

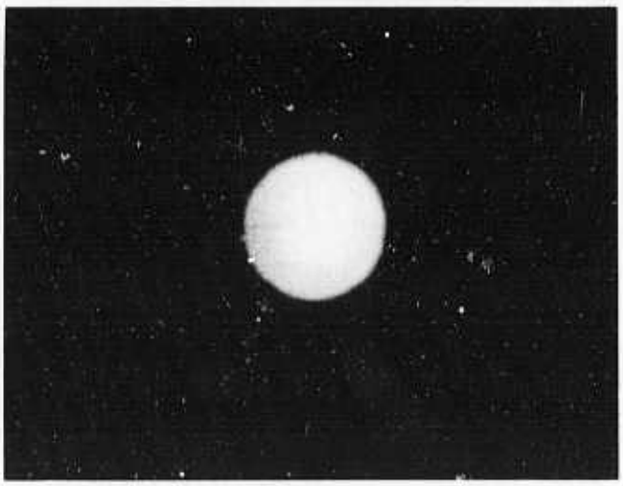

(c) $\Delta T = 0°C$
$E_{in} = 1500J$

(d) $\Delta T = 0°C$
$E_{in} = 2000J$

Figure 4-11. Mach-Zehnder Interferograms of Laser Cell Using Laser Solution with $\Delta T = T_{CL} - T_0 = 0$ and Different Values of Flashlamp Input Energy

TABLE 4-5

PATH LENGTH QUADRATIC COEFFICIENTS A(cm^{-1}) MEASURED FOR LASER SOLUTION AND $POCl_3$ $\Delta P(r) = Ar^2 + Br$

Temperature Difference $T_{CL} - T_0$ (°C)	Using $POCl_3$			
	Flashlamp Input Energies			
	0	1000 J	2000 J	3000 J
0	0	1.8×10^{-4}	2.79×10^{-4}	4.07×10^{-4}
1.0	0.13×10^{-4}	---	3.00×10^{-4}	---
2.5	0.39×10^{-4}	---	4.01×10^{-4}	---
4.0	0.35×10^{-4}	---	---	---
5.0	2.71×10^{-4}	---	4.21×10^{-4}	---
	Using Laser Solution			
$T_{CL} - T_0$ (°C)	0	1000 J	1500 J	2000 J
0	0	2.54×10^{-4}	5.92×10^{-4}	10.48×10^{-4}
2.0	0.31×10^{-4}	5.05×10^{-4}	---	---
4.0	1.63×10^{-4}	5.84×10^{-4}	---	12.48×10^{-4}

Substituting this into Eq. (4-65) and equating the resulting factor of r^2 to the measured coefficient A, we can solve for the factor p (cm^{-2}) as

$$p(cm^{-2}) = \left[\frac{A}{n_0^2 L^2 \left(\frac{L}{6n_0} + \frac{d_0}{2} \right)} \right]^{1/2} \tag{4-69}$$

The values of the coefficient p, thus determined, are shown on Table 4-6.

TABLE 4-6

VALUES OF COEFFICIENT p CALCULATED FROM DATA OF TABLE 5*

Temperature Difference $T_{CL}-T_0$ (°C)	Using $POCl_3$			
	Flashlamp Input Energies			
	0	1000 J	2000 J	3000 J
0	0	-3.97×10^{-5}	-4.89×10^{-5}	-5.90×10^{-5}
1.0	1.06×10^{-5}	----	-5.07×10^{-5}	----
2.5	1.84×10^{-5}	----	-5.86×10^{-5}	----
4.0	1.72×10^{-5}	----	----	----
5.0	4.82×10^{-5}	----	-6.01×10^{-5}	----
	Using Laser Solution			
$T_{CL}-T_0$ (°C)	0	1000 J	1500 J	2000 J
0	0	-4.67×10^{-5}	-7.14×10^{-5}	-11.88×10^{-5}
2.0	1.63×10^{-5}	-6.58×10^{-5}	----	----
4.0	3.64×10^{-5}	-7.06×10^{-5}	----	-10.32×10^{-5}

*Note: The values of p for $E_{in} \neq 0$ are negative because the flash-induced distortion causes the liquid to behave as a converging lens.[87,88]

Substituting from Eqs. (4-51) and (4-68), we find

$$n'(r) = n_0\, pr = 2\left(T_{CL}-T_0\right)\alpha r$$

$$p = \frac{2\alpha}{n_0}\left(T_{CL}-T_0\right) = q\left(T_{CL}-T_0\right) \qquad (4\text{-}70)$$

where

$q = 1.331\times10^{-5}\ °C^{-1}\ cm^{-2}$ for $POCl_3$

$= 1.378\times10^{-5}\ °C^{-1}\ cm^{-2}$ for laser solution.

Eq. (4-70) shows that the measured value for p should be directly proportional to $\Delta T = T_{CL} - T_0$, with a coefficient calculable from the physical properties of the liquid. Using the data from the first columns of Table 4-6, we can calculate an average measured value for this quantity as:

$$q_{meas.} = 0.71 \times 10^{-5}\ ^\circ C^{-1}\ cm^{-2} \text{ for } POCl_3$$

$$= 0.86 \times 10^{-5}\ ^\circ C^{-1}\ cm^{-2} \text{ for laser solution.}$$

The measured quantities are again within a factor of two of the calculated quantities showing good agreement with theory. If we now assume that this measured quantity p varies linearly with the amount of flashlamp energy absorbed in the liquid and is, therefore, linear in flashlamp input energy, i.e.,

$$p(\Delta T, E_{in}) = (q \times \Delta T) - (m \times E_{in}) \tag{4-71}$$

The first row of data in Table 4-6 allows us to calculate an average value of m as

$$m = 2.80 \times 10^{-5}\ kJ^{-1}\ cm^{-2} \text{ for } POCl_3$$

$$= 5.12 \times 10^{-5}\ kJ^{-1}\ cm^{-2} \text{ for laser solution.}$$

The data thus show that due to the larger amount of energy absorbed from the flashlamp radiation, the flash induced distortions in the laser liquid are larger than in the pure $POCl_3$ solvent. We can calculate the effective focal length induced in the laser cell by equating the form Eq. (4-67) to Eq. (4-58), whence we have:

$$b = \sqrt{\frac{4}{p}} \tag{4-72}$$

and the focal length (negative) of the laser cell is given by Eq. (4-60) as

$$f = \frac{-1}{\sqrt{p} n_0 \sinh \sqrt{p}\, L} \tag{4-73}$$

We now can recalculate the effective focal lengths observed by this method, and compare these to the ones observed directly using the autocollimating telescope listed in Table 4-3. The results are shown in Table 4-7.

TABLE 4-7

EFFECTIVE FOCAL LENGTHS OF LASER CELL CALCULATED FROM THEORY AND OBSERVED USING TWO INDEPENDENT METHODS (FOR $POCl_3$ AND LASER SOLUTION)

	Temperature Difference $T_{CL} - T_0$ (°C)	Calculated f (m)	Observed f	
			Telescope (m)	Interferometer (m)
Using $POCl_3$	1.1	-18.1	-100.0	-33.8
	2.3	-10.9	- 45.0	-16.2
	2.8	- 7.25	- 29.0	-13.8
	3.1	- 6.60	- 23.0	-12.0
Using Laser Solution	1.0	-27.5	- 42.0	-30.6
	1.5	-18.6	- 21.5	-20.5
	2.0	-13.6	- 18.5	-15.4
	2.35	-11.8	- 16.0	-13.1
	2.85	- 9.75	- 12.0	-10.8

As is apparent from Table 4-7, the observed results from the interferometer experiments fall between the observed focal lengths using the autocollimating telescope and the calculated focal lengths from the theory. The agreement between all these sets of numbers is very good but is, once again, better for the laser solution measurements than for the $POCl_3$, due to the uncertainties in the physical constants of the $POCl_3$, which probably contribute an error of a factor of two or more to the calculated effective focal lengths for the first four rows in Table 4-7. The fact that better estimates are available for the laser solution result in better agreement between theory and observations.

A final observation on these data is that the interferometer results allow one to estimate the flash-induced lens produced in the liquid in the absence of an initial temperature gradient across the laser cell $\left(T_{CL} - T_0 = 0\right)$. We can apply the averaged results from Table 4-6 to Eq. (4-73) to obtain this. Figure 4-12 shows the estimated focal length of the laser cell in diopters (diopters = 1/focal length in meters) plotted against flashlamp input energy for the large 4-lamp laser cell. As may be seen from the graph, this relation is linear. It should be recalled that the induced focal length of the laser cell is positive[87, 88] and, therefore, the laser acts as a converging lens. Figure 4-12 shows that, with the system filled with the laser liquid, focal lengths as short as one meter may be generated by energy inputs of 5000 J to the flashlamps.

4.6 DISCUSSION

The actual temperature and index of refraction profile across the liquid in the laser cell is a composite of that imposed by the temperature differential $T_{CL} - T_0$, and that caused by absorption of the pump radiation. In the most common case, we usually set $T_{CL} - T_0 > 0$. Since dn/dT for the laser liquid is negative, this results in the liquid acting as a diverging lens. The absorption of pump radiation, on the other hand, results in the liquid near the cell wall becoming warmer than that near the centerline of the cell with the result that the liquid acts as a converging lens. Under a single-shot condition, if the situation is such that $T_{CL} - T_0 > 0$, at some time during the flashlamp pump pulse or at some particular energy input at a given time during the laser flashlamp pulse, the laser liquid will appear to act neither as a converging nor a diverging lens. This condition (at a time delay of 400 μs from the start of the laser flashlamp pulse) may be derived by setting Eq. (4-71) equal to zero.

$$\frac{\Delta T}{E_{in}} = \frac{m}{q} = \frac{2.8}{0.71}\ ^\circ C\ kJ^{-1}\ 4.0^\circ C\ kJ^{-1} \text{ for } POCl_3$$

$$= \frac{5.12}{0.86} = 6.0\ ^\circ C\ kJ^{-1} \text{ for laser solution}$$

In the experiments described, a 400 μs delay was selected because this time corresponded to the peak of the 1.052μ fluorescence emission of the laser liquid in this laser cell. For this time delay and the input energies used shown on Table 4-6, it is clear that none of the temperature differentials used would satisfy the above requirements. This requirement also indicates that for flashlamp inputs above 3000 J, a temperature differential of about 20°C would be required. Meeting this requirement would hardly seem practical under normal circumstances.

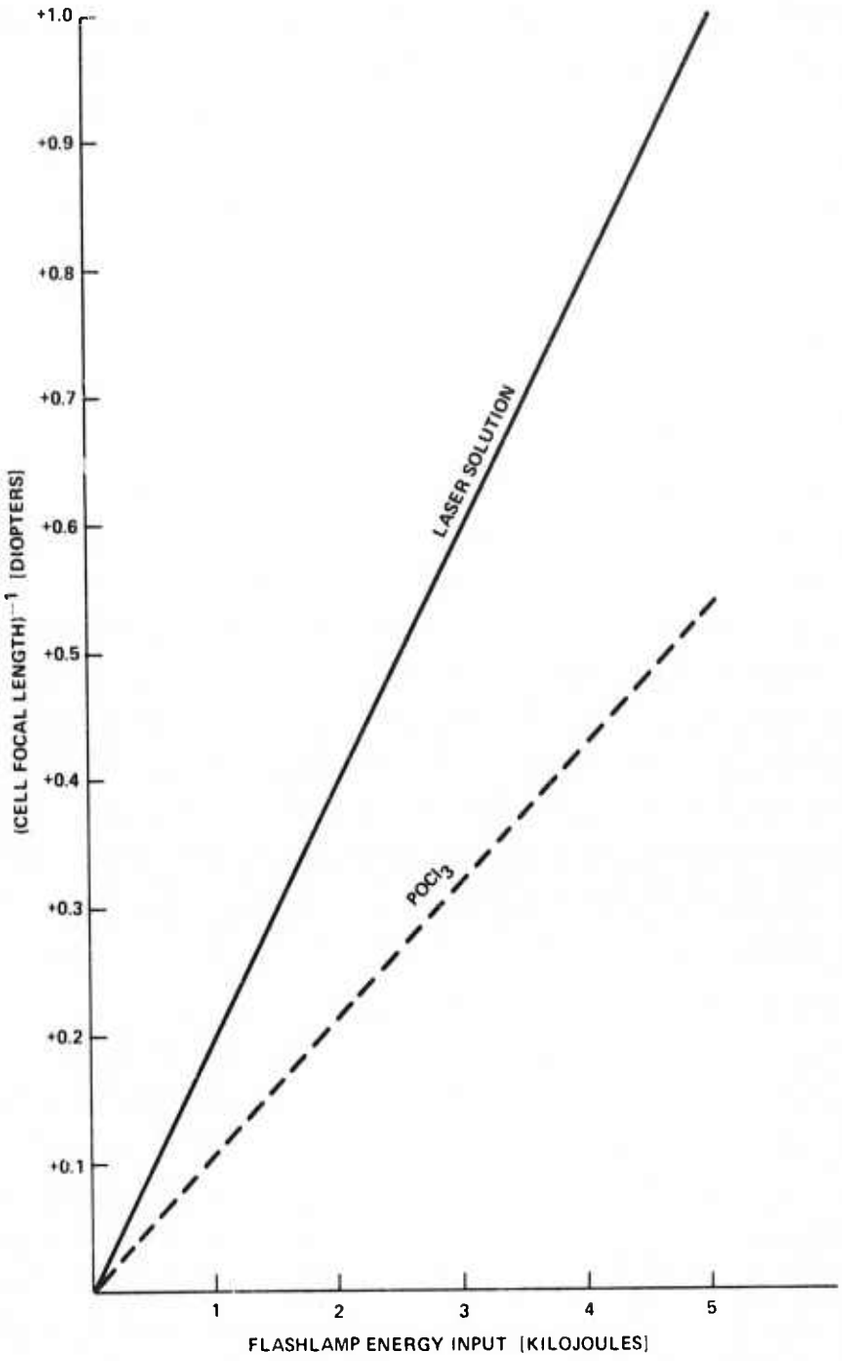

Figure 4-12. Estimated Focal Length of the Laser Cell in Diopters

In any event, the flash-induced gradients in the laser liquid are not really radially-symmetrical as a glance at the photo of Figure 4-11(c) will prove. Since the cell is being pumped by four flashlamps in a quadruple elliptical flash enclosure, the lamp radiation is not completely uniform over the cross-section of the laser cell, and the photo rather clearly shows the lamp positions at about 1, 4, 7 and 10 o'clock. This distortion was even worse on the other two-lamp dual elliptical heads used on the laser system. In principle, this distortion could be removed by using either a helical flashlamp or many linear flashlamps with a diffusing glass cylinder around the outside of the laser cell. Both alternatives were not practical on the present liquid laser system for reasons of time availability.

Although the externally-applied temperature differential $T_{CL}-T_0$ could not be made large enough to be helpful in reducing beam divergence of the liquid in the amplifier mode, it could be adjusted to optimize the laser output in a long-pulse, repetitively-pulsed oscillator mode as will be shown in the next section. In these experiments, the externally-impressed initial temperature differential, $T_{CL}-T_0$, was used to offset the temperature rise (under repetitive pulsing) of the relatively stagnant laminar and buffer sublayers in the liquid. In this case, the flash-induced distortions were still present for each lamp pulse, but the cumulative effect of repeated lamp pulses could be compensated. The net result was that the laser could be operated at average input powers in the kilowatt range while maintaining the same pulse output energies as measured under single-shot conditions.

One final word should be mentioned here concerning the optical properties of the flowing liquid. The actual microscopic velocity field in the liquid under steady-state turbulent conditions is a very complex affair. At the very beginning of the Martinelli calculation [Eq. (4-4)], we divided the temperature, pressure and velocity variables into mean values plus time and space dependent fluctuations. We then stated that the time average of the fluctuating part of these variables vanished to reduce the Navier-Stokes, energy-balance and continuity equations to soluble forms. In point of fact, these fluctuations are non-zero over the time scale of most laser phenomena. A good example of the importance of these fluctuations may be seen in the photos of Figure 4-9. In these pictures, it is apparent that the interference fringes do not only bend more as the temperature differential is increased, but they also become less distinct due to the larger fluctuations caused by the increasing differential. The fluctuations in the turbulent liquid are revealed in these photographs because the source of illumination here was

Q-switched laser with a 20 ns pulse duration. On this time scale, the time average of these fluctuations is nonzero. On the other hand, the photos of Figure 4-11 do not show the same degree of fluctuations. This is because the flash-induced temperature gradient across the laser cell has not yet (400 μs) had enough time to be mixed by the turbulent flow of the laser liquid and establish fluctuations due to shear forces at the liquid boundary layer near the cell wall.

5. STATIC MODE LASER CHARACTERISTICS

Long pulse oscillator experiments were carried out in both static and circulatory modes. The initial laser work on aprotic solvent systems was, of course, carried out on static systems. The requirement that the solutions be made and maintained anhydrous presented a new set of conditions on the construction of laser cells. These, in turn, led to interesting and novel solutions especially in terms of the materials used because of the corrosiveness or sensitivity of the solutions. The actual laser work itself resulted in the discovery of several new laser effects, some of which have become understood and, at least one, which is still a bit of a mystery. Because of the fluidity of the medium, the pulse repetition rate in the static mode was restricted to very low values and average power was, of necessity, limited. In the circulatory mode the main objective of the work was the achievement of high average output powers; values in excess of 400 watts were achieved. The first part of this section presents the physical model for the laser. The analysis leads to equations which are of considerable value in the understanding of the laser behavior. Following this, the laser properties of the static systems are described. We also describe such properties as dynamic loss, efficiency, the effects of material parameters, a self Q-switching, Q-switching,mode locking, and spectral broadening. The next section is concerned with circulatory systems and high average output power. The output properties of the laser are related, as far as possible, to the hydrodynamic and thermo-optical model developed in Section 4.

5.1 PHYSICAL MODEL FOR DESCRIBING THE LASER OUTPUT PROPERTIES

To describe the behavior of a laser, we require the solution to two equations; one involves the population of the excited state based on the pumping rate and the relaxation kinetics of the system, and the other describes the photon flux. In the strictest sense, these are two coupled, non-linear, differential equations and there are no simple solutions in a closed form. There are, however, a number of simplifying assumptions and approximations which do allow the basic features to become clear, since they result in solutions to the equations that lend themselves readily to comparison with experimental results.

The use of these assumptions and approximations actually serves to separate these two equations by taking advantage of two properties: first, below oscillation threshold or in the absence of a resonator the stimulated emission term is so small that it is negligible with respect to other relaxation processes; and second, above threshold, the population of the upper laser level is fixed and all the pump energy is

converted to laser radiation. Even so, the solutions are not so readily obtained. The kinetic equation cannot be easily solved for an arbitrarily shaped excitation pulse. Solutions in closed form can be obtained for two extreme cases; a delta function excitation (i.e., very short compared to the fluorescence lifetime), or an infinitely long excitation pulse. In practice, for the Nd^{+3} system, neither of these obtains in the usual type of pulsed laser systems. However, the latter is a more appropriate assumption and leads to what is generally called the steady-state approximation.

The energy level system of Nd^{+3}, for laser purposes, is readily idealized to a 4-level system as illustrated in Figure 5-1.

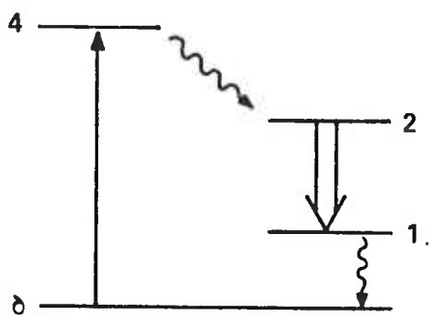

Figure 5-1. Four-Level System

Level 1 is the lower laser level, Level 2 is the upper laser level, Level 0 is the ground state and Level 4 is the states that ultimately result in the population of Level 2. The kinetic equations appropriate to such a system are[99,100]

$$\frac{dN_2}{dt} = R_2 - \frac{N_2}{\tau} - (N_2 - N_1)\,W$$

$$\frac{dN_1}{dt} = R_1 - \frac{N_1}{t_1} + \frac{N_2}{\tau_{sp}} + (N_2 - N_1)\,W \qquad (5\ )$$

where:

N_i = the population density of Nd^{+3} in state i

R_i = the pumping rate/cm^3 to state i

t_1 = the decay rate of state 1

τ_{sp} = the spontaneous transition probability between states 2 and 1

τ = the decay time of level 2

W = the induced transition rate between levels 1 and 2

Assuming a steady state ($\frac{d}{dt} = 0$) or the long pump pulse approximation, the solution for $N_2 - N_1$ is:

$$(N_2 - N_1) = \frac{R_2\tau - (R_1 + \delta R_2)\, t_1}{1 + \left[\tau + (1-\delta)t_1\right]W} \tag{5-2a}$$

where δ is τ/τ_{sp}. In all cases of practical interest $t_1 \ll \tau$ and

$$\Delta N = N_2 - N_1 = \frac{R_2\tau}{1 + W\tau} \tag{5-2b}$$

Furthermore, below threshold $W\tau \ll 1$, hence:

$$\Delta N = R_2\tau \tag{5-2c}$$

The quantity $R_2\tau$ is designated as ΔN^0, that is the population that would result if there were no stimulated emission.

Above threshold, the inversion is fixed at a value ΔN_T by the gain saturation and Eq. (5-2b) yields:

$$W\Delta N = \frac{\Delta N^0 - \Delta N_T}{\tau} \tag{5-3}$$

This is the rate of stimulated emission per unit volume into the cavity.

In terms of cavity power it is:

$$P_c = (\Delta N^0 - \Delta N_T)\frac{h\nu_L V}{\tau} \tag{5-4}$$

where

h = Planck's constant

ν_L = laser frequency

V = volume of the active medium

P_c = power emitted in to the cavity

To render this equation more useful, ΔN^0 has to be related to the pumping conditions and ΔN_T to the cavity and medium properties. The quantity ΔN^0 is given in terms of R_2, the rate of pumping. If P is the electrical power into the flash lamps, then:

$$R_2 = \frac{P\eta_1 \eta_c' \eta_q}{h\nu_p V} \tag{5-5}$$

where

η_1 = the efficiency of the conversion of electrical power to light power in the pump bands

η_c' = the efficiency with which the light power is coupled into the cavity

η_q = the quantum efficiency

ν_p = the "average" pump photon frequency

Putting this into Eq. (5-2c) and then using the ΔN obtained in Eq. (5-4), we find:

$$P_c = (P - P_T)\,\eta_1\,\eta_c'\,\eta_q\,\frac{\nu_L}{\nu_p} \tag{5-6}$$

The power coupled out of the cavity, P_{out}, is given by:

$$P_{out} = P_c\,\frac{T}{T+A} \tag{5-7}$$

where T is the output mirror transmission and A is the distributed loss per pass or $1-e^{-\alpha L}$ (where α is the loss per centimeter and L the path length in the active medium).

Finally, the sheath effect must be taken into account. This is an effect that arises whenever an active medium is clad in another material, as it always must be in a liquid laser. A problem related to this has been discussed by Devlin,[101] McKenna[102] and Sooy,[103] and we restrict ourselves to the approximate treatment of Devlin. In a cell configuration, the wall functions as a lens focusing the isotropic radiation of the close coupled enclosure. Light incident on the outer cell wall is refracted so that an active medium of radius $\rho_M = \frac{R}{n}$ (where R is the outer radius of the cell and n is the refractive index of the cell material) would intercept all the refracted rays. An active medium of radius ρ smaller than ρ_M would intercept only ρ/ρ_M of these rays. This is an explicit factor in the η_c', and taking it out, we can write the power output equation as:

$$P_{out} = (P - P_T)\,\eta_1\,\eta_c\,\eta_q\,\frac{\nu_L}{\nu_p}\,\frac{\rho}{\rho_M}\,\frac{T}{T+A} \tag{5-8}$$

Eq. (5-8) is strictly applicable to an infinitely long pulse or cw operation. To apply it to pulsed operation, we assume that the pulse is long enough so that the steady state approximation is valid, and we further assume a square pulse. With these assumptions, the power quantities become energies and Eq. (5-8) is applicable in the pulsed domain.

If the experimental data are organized according to Eq. (5-8), the threshold energy and slope efficiency can be readily determined. The threshold energy for a given sample and enclosure is dependent on the output mirror transmission and the distributed material losses. The latter are constant and can be evaluated by varying the former in a known way. To see how this comes about, we note that the condition for oscillation is:

$$R_1\,R_2\exp(\sigma\Delta N_T - \alpha)\,L = 1 \tag{5-9}$$

where R_1 and R_2 are the reflectivities of the cavity mirrors, σ the absorption cross-section, and the other quantities have been previously defined. Expressing ΔN_T in terms of energy and a proportionality constant β (assuming the steady state approximation) Eq. (5-9) can be recast to read:

$$E_T = \frac{\alpha}{\beta\sigma} - \frac{\ell n\,R_1\,R_2}{\beta\sigma L} \tag{5-10}$$

The loss obtained from Eq. (5-10) is the dynamic loss, that is, under pumping conditions. It will, therefore, be larger than the passive losses discussed in Section 2.

We will make extensive use of Eqs. (5-8) and (5-10) for analyzing the energy output data of the various lasers. Eq. (5-10), of course, provides the information on loss. Eq. (5-8) can also be used for this by plotting $\frac{1}{\eta_s}$ against $\frac{1}{T}$ and, from the equation of the resulting straight line, the quantity A can be obtained. In general, this is less reliable than the use of Eq. (5-10) for this purpose. The principal use of Eq. (5-8) is to provide information on the product of the efficiencies, $\eta_1 \eta_c \eta_q$. These relate to the flash lamps, the enclosure and the laser material; if any two are kept constant, information on the third can be extracted provided the dynamic loss is known.

5.2 ENERGY OUTPUT OF STATIC LIQUID LASERS

The experimental work on the subject of energy output is concerned with a comparison of three liquid laser materials ($SeOCl_2$:$SnCl_4$, $POCl_3$:$SnCl_4$ and $POCl_3$:$ZrCl_4$) with each other and with a glass (LG 55, Schott). In addition, the effect of Nd^{+3} concentration and the effect of variable cell bore diameter (with a fixed cell outer diameter) were studied. The cells used in this work were described in Section 3, and the resonator was of the plane parallel type. In these experiments similar flash lamps, in a close wrapped configuration, were used. The output was detected by a TRG 105B thermopile, with care taken to ensure that all the output radiation entered the detector. Experimentally, the laser output was determined for a set of different electrical input energies to the capacitor bank. Two measurements were made for each input energy and sufficient time allowed between shots so that there was no residual thermal history. The time required for this was determined in a separate set of experiments.

A peculiarity observed with the laser liquids used is the requirement of a "break-in." For a given electrical input energy, the laser output increases, at first, with the number of shots. After a large number of shots, the output stabilizes at a value between 50 and 100% larger than the first one. All the solutions used were fired until this steady value was reached.

Typical experimental data are illustrated in Figure 5-2 and 5-3. From these it is seen that there is always an initial linear region with an increasing slope efficiency as T increases (R decreases) in conformity with Eq. (5-8). At higher values of input energy, there is a break in the curve and a change to a lower slope efficiency; this will be discussed later. For the present, we will concentrate on the initial linear range (lower input energies) and the extrapolated threshold energies.

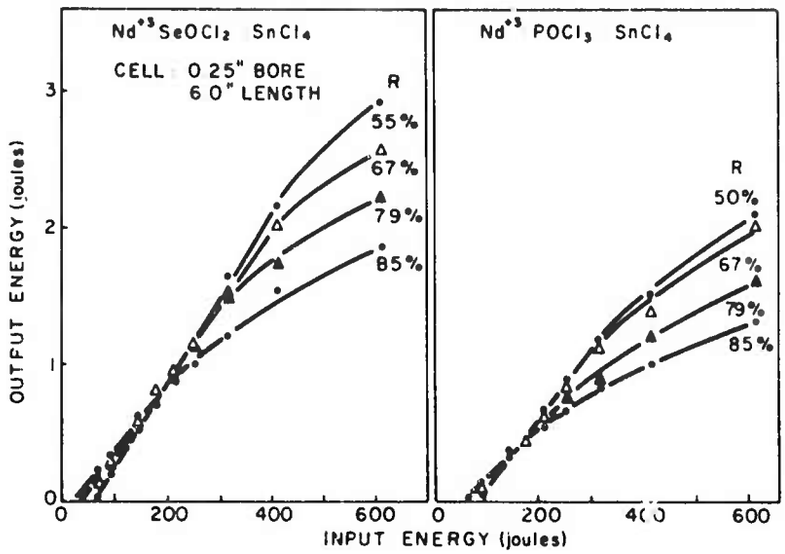

Figure 5-2. Energy Output as a Function of Energy Input

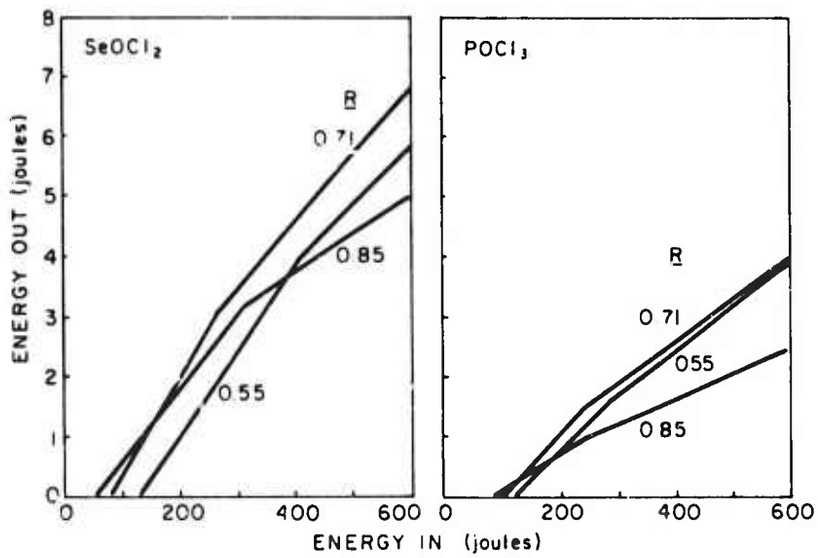

Figure 5-3. Energy Output as a Function of Energy Input

The extrapolated threshold energies are plotted as a function of $-\ell nR$ (corrected for the reflectivity of the second side of the flat mirror) in Figures 5-4 and 5-5, where we use only the corrected output mirror reflectivity, since the second mirror was totally reflecting. The points are fitted by a straight line consistent with Eq. (5-10). In addition to the experiments with the liquid laser solutions, a similar set was carried out with an 0.25 inch diameter LG 55 glass rod. To make the results comparable, the glass rod was sheathed in similar manner to the liquids; the opening in the sheath was just large enough to make a close fit with the laser glass rod. The loss values obtained are summarized in Table 5-1.

TABLE 5-1

LOSS FACTORS (% cm^{-1})

Cell Diameter (inches)	$POCl_3$:$SnCl_4$	$POCl_3$:$ZrCl_4$	$SeOCl_2$	Glass
0.25	1.9	1.2	0.12	2.4
0.375	1.0	0.89	0.60	
0.500	2.10		0.83	

There are several features of this table deserving comment. The high loss values observed in the $POCl_3$:$SnCl_4$ system are related to a solubility problem associated with this system. It was found that the loss in these solutions increases with time and that when it approaches a value a few times higher than the values given in Table 5-1, a macroscopic precipitate appears. A fresh solution typically has a loss in the 0.5 to 1.0 percent cm^{-1} range. The value of 0.12 percent cm^{-1} reported for one of the $SeOCl_2$:$SnCl_4$ experimental sets is anomalously low, and in fact, is the lowest value observed for all of the solutions used. The losses are principally due to scattering and are not associated with any one of the solution components, but only when all the components are together as in a laser solution. This has been confirmed by the light scattering measurements reported in Section 2. The high value reported here for the $POCl_3$:$ZrCl_4$ solution most likely arises from the fact that these measurements were made on some of the first solutions prepared. Subsequent development improved the quality of these solutions markedly and, as will be seen later in the section on circulating

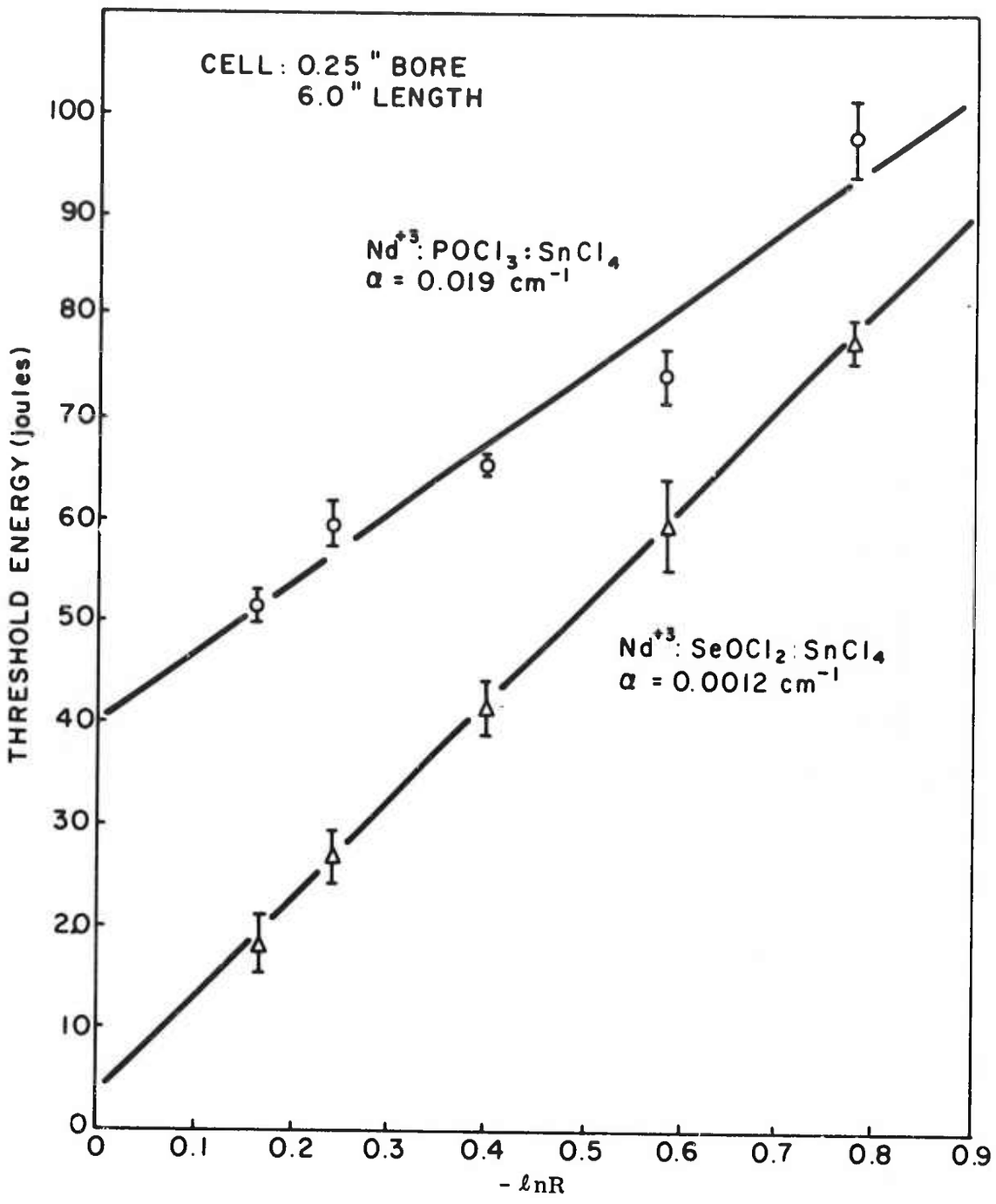

Figure 5-4. E_T vs. ℓ n R for Data Presented in Figure 5-2

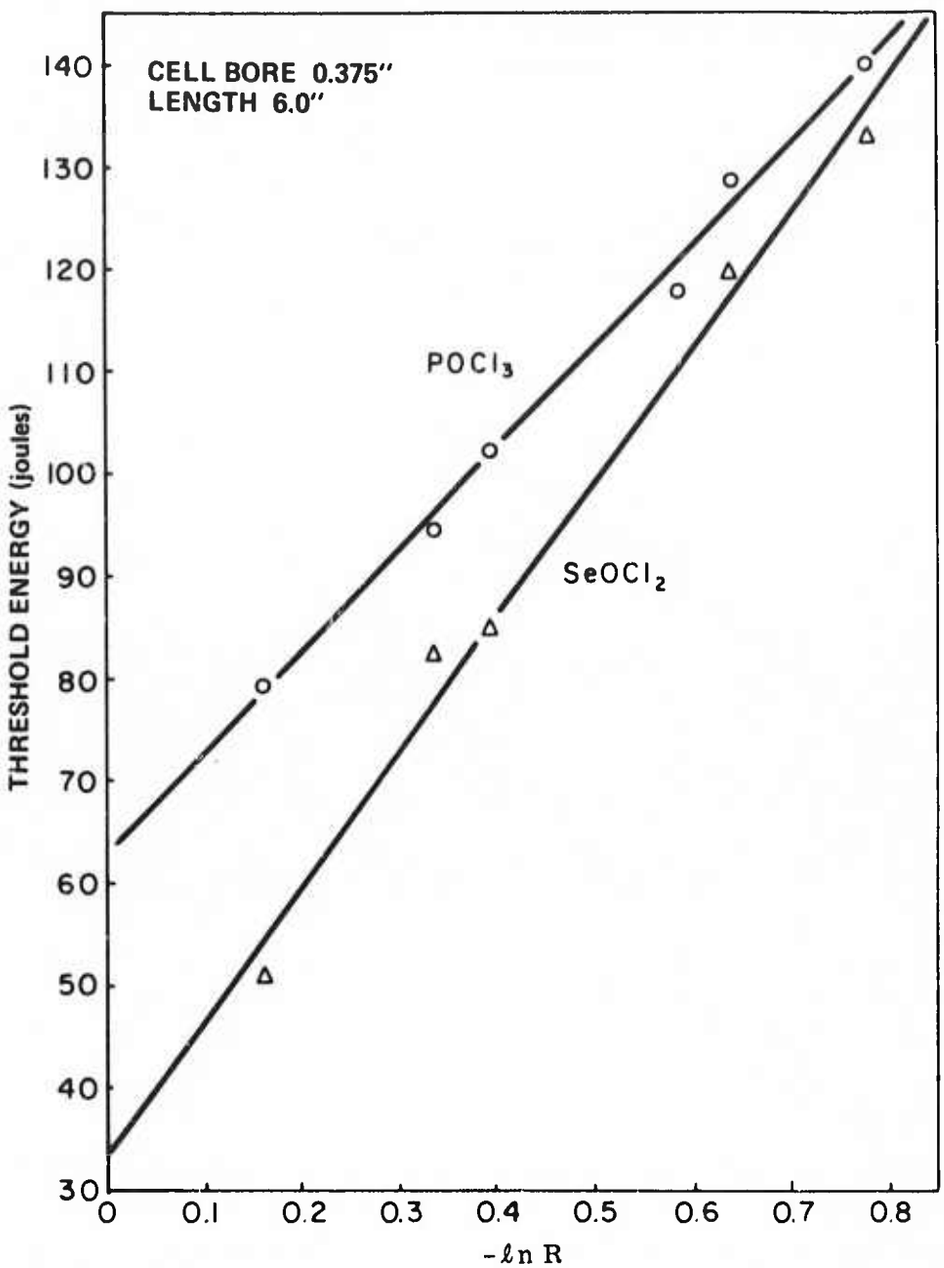

Figure 5-5. E_T vs. $\ell n\, R$ for Data Presented in Figure 5-3

liquid laser systems, dynamic losses were usually less than 0.5% cm^{-1} and frequently in the range 0.2 to 0.3% cm^{-1}. The loss value obtained for the LG 55 glass appears to be somewhat high, but not anomalously inconsistent with the results of other workers.[104] The conclusions to be drawn from this study is that the liquids have a lower dynamic loss than LG 55 glass and that their dynamic loss is, in general, probably comparable to that of glass.

The next factor to be considered is the efficiency product of $\eta_1 \eta_c \eta_q$. This is obtained from the experimental slope efficiency (efficiency above threshold) and Eq. (5-8) using the known transmission and loss factors and the ratio ρ/ρ_M. The factor ν_L/ν_p need not be taken out, since this is approximately the same for all the Nd^{+3} based systems. A comparison of results of data reduced in this way for $SeOCl_2$:$SnCl_4$ and $POCl_3$:$SnCl_4$ solutions of concentration $1.8 \times 10^{20}/cm^3$ (0.3M) and different cell diameters is listed in Table 5-2.

Averaging these results over the different output mirror reflectivities and the results of similar experiments in the $POCl_2$:$ZrCl_4$ solvent, the results in Table 5-3 are obtained. These results were obtained for a concentration of $1.8 \times 10^{20}/cm^3$. Since the same lamps and flash enclosures were used in all the experiments, these results reflect the material efficiency factors involved in η_q. The conclusion here is that the laser liquids are at least comparable to, if not better than, LG 55 glass. We also note a tendency for the efficiency factors to increase with the bore diameter. Since the differences in coupling arising from changes in bore diameter (ρ/ρ_M) have been taken into account, the differences must reside in an improved utilization of the pump radiation because of the longer path length in the active medium.

The next material parameter studied was the concentration of Nd^{+3}. Threshold values do not vary significantly over the range of concentration studied (0.6, 1.8 and $3.0 \times 10^{20}/cm^3$), but there is more information in the efficiency factors. The results obtained from experiments with an 0.50 inch bore diameter cell are listed in Table 5-4. Here we observe a tendency for the efficiency to increase with increasing concentration. This is due to an increasing coupling efficiency due to the increasing optical density of the solution. Qualitatively, these results are similar, and are based on the same optical effect as those on increasing the bore diameter. Comparable concentration studies were not carried out with the $POCl_3$:$ZrCl_4$ solvent, but based on the general similarity in the behavior of this with the other liquid system in other studies, similar results would undoubtedly be obtained.

TABLE 5-2

EFFICIENCIES $\eta_1 \eta_c \eta_q$

Cell Diameter (inches)	$POCl_3$	$SeOCl_2$	Glass
	R = 85%		
0.25	0.0635	0.0288	0.0324
0.375	0.0483	0.0590	
0.500	0.0595	0.0705	
	R = 75%		
0.25	0.0522	0.0277	0.0283
0.375	0.0523	0.0522	
0.500	0.0652	0.0762	
	R = 67%		
0.25	0.0497	0.0288	0.0262
0.375	0.0516	0.0540	
0.500	0.0586	0.0591	
	R = 53%		
0.25	0.0449	0.0317	
0.375	0.0442	0.0448	
0.500	0.0510	0.0549	
	R = 45%		
0.25	0.0472	0.0269	0.0235
0.375	0.0324	0.0437	
0.500	0.0525	0.0507	

TABLE 5-3

AVERAGE EFFICIENCIES $\eta_l \eta_c \eta_q$

Cell Diameter (inches)	$POCl_3$:$SnCl_4$	$POCl_3$:$ZrCl_4$	$SeOCl_2$:$SnCl_4$	Glass
0.25	0.0515	0.0345	0.0287	0.0276
0.375	0.0468	0.055	0.0507	
0.500	0.574		0.0623	

The input-output curves in Figures 5-4 and 5-5 all show a break toward lower slope efficiency as the input energy is increased. Related effects have been observed by other workers. R. Lang[105] for example, observes an extreme case of this and noted that using a K_2CrO_4 solution as a cell coolant rather than water alone corrected the situation markedly. These deviations from linearity in the experiments were observed at input energies in excess of one kilojoule. Yamaguchi et al.[106] report a similar effect setting in at pump energies of about 500 J. Hongyo et al.,[107] however, indicate a linear relationship up to input energies of 1.5 KJ with a water coolant. Above this value, there is a relatively small departure from linearity which is corrected by the use of a $NaNO_2$ solution as a coolant. In general, such effects have been attributed to optical distortion arising from the pump flash and is supported by some work, such as that of Nanjo,[108] on the optical quality of pumped liquid laser solutions.

A closer look at the results shown in Figures 5-4 and 5-5 indicates a more complex phenomenon. The break in the curve, for each cell diameter and output mirror reflectivity, occurs at different values of the input energy. Were this purely a thermal-optical effect, such a result would not be expected. It looks more like an effect depending on the cavity power density. The average power density in the active medium can be calculated from the expression:

$$P = \frac{E_{out}}{ATt} \qquad (5\text{-}11)$$

TABLE 5-4

COMPARISON OF $\eta_1 \eta_c \eta_q$ VALUES AS A FUNCTION OF Nd^{+3} CONCENTRATION

R(%)	$SeOCl_2$:$SnCl_4$ Conc $\times 10^{-20}/cm^3$			$POCl_3$:$SnCl_4$ Conc $\times 10^{-20}/cm^3$		
	0.6	1.8	3.0	0.6	1.8	3.0
85	0.115	0.071	0.92			
75	0.071	0.076	0.079	0.033	0.065	0.064
65	0.055	0.059	0.068	0.029	0.059	0.081
55		0.055	0.058	0.024	0.051	
45	0.046	0.051	0.047	0.025	0.053	0.057
Loss Factor a	0.0134	0.021	0.022	0.0168	0.0083	0.017
Average	0.057 ± 0.006	0.062 ± 0.004	0.069 ± 0.007	0.028 ± 0.002	0.057 ± 0.002	0.067 ± 0.009

where

E_{out} = the output energy

A = the cross section area of the active liquid

T = the output mirror transmission

t = the time duration of the laser pulse

Putting in the energy at which the break is observed and using 100 μs as the laser pulse length (an average of the times observed in the experiments), Table 5-5 can be constructed.

TABLE 5-5

POWER DENSITIES AT ENERGY BREAK (kW/cm^2)

Output Mirror Transmission %	Cell Diameter (inches)					
	0.25		0.375		0.500	
	$SeOCl_2$	$POCl_3$	$SeOCl_2$	$POCl_3$	$SeOCl_2$	$POCl_3$
0.15	159	106	177	66	170	54
0.21	227 167	113 83				
0.29			128	88	88	61
0.33	193	108	91	31	120	62
0.45	162	83	94	47	90	62
0.48			93	45	91	41
Average	182	99	117	49	112	56

The scatter in these results is rather large, and this can be attributed to uncertainties in accurately locating the energy at which the break occurs and mostly to the use of a single value for t. Clearly, however, there is an effect which depends on the power density of the laser flux in the cavity, and it is different for $POCl_3$ and $SeOCl_2$ based solutions. It is tempting to attribute this to a stimulated scattering process, but the

thresholds for these (Section 2.4.2) are almost an order of magnitude higher than the power densities determined. A possible explanation, but one by no means established, is that the distortion could be due to transient bubbles caused by the high power density.

This is not to propose that there are no thermal effects due to the flash lamps, and indeed, we shall later characterize these. With proper precautions, such thermal effects can be minimized. The results observed by the other workers might largely be attributed to flash lamp saturation, experimental variables or improper attention to existing non-isothermal conditions. As an example of high flash lamp input energies without such deviations from linearity, we present the results of two experiments on a cell built as a prototype for a circulating liquid laser; this is shown in Figure 5-6. The solid line represents the actual experimental data in which a marked curvature is observed. However, if the flash lamps are corrected for saturation, that is, the light output is adjusted to correspond to the electrical input energy required if the flash lamp output were linear in electrical input, the dotted curves are obtained. These are linear. It should also be noted that the dotted curves correspond to slope efficiencies in the range of 5 to 8%.

A final set of experiments relating to threshold and output efficiency were carried out to determine a cell design feature. This relates to whether the inner surface of the cell should be smooth or rough. To avoid laser modes arising from internal reflections, the inner wall of the cell is usually roughened. To see the extent of this effect, two cells of 0.50 inch diameter (one rough and one clear) were compared and the results are given in Table 5-6. A detailed comparison of threshold energies is difficult because the values scatter badly; there are, however, no major effects. The slope efficiency values, on the other hand, show a consistent behavior; they are significantly lower for the smooth cells. In fact, if the loss factors are removed from the efficiency values as in the last row of Table 5-6, it is clear that there is a reduction of efficiency in the smooth cells to almost 55% that of the rough cells. This could be explained by a decrease in coupling efficiency, but such an explanation is inconsistent with the absence of a corresponding effect in the values for threshold energy. It is more probable that the smooth cells support a significant number of off-axis laser modes, and that a considerable amount of laser radiation is coupled out through the sides of the cell. This would lead to a significant reduction in efficiency with little change in threshold values. The roughening of the cell inner wall is, then, a significant feature in cell construction. A factor which has not been studied is the roughening of the exterior wall of the cell.

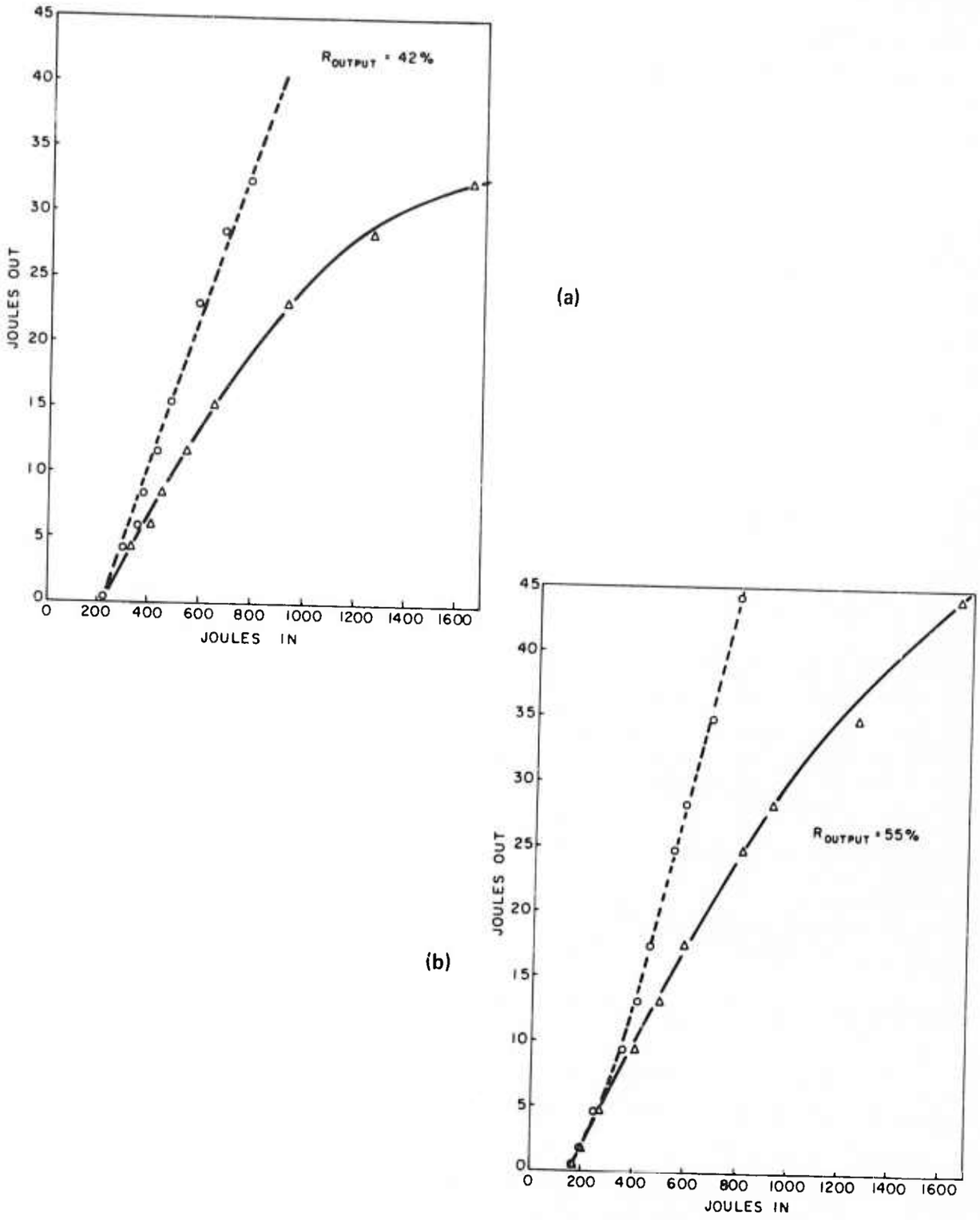

Figure 5-6. Energy Output as a Function of Energy Input for a 25-cm Long, 19.5-mm-Diameter Cell in a Double Elliptical Flash Housing: (a) R Output = ±2%; (b) R Output = 55%

This is frequently done with solid state rods to frustrate internal reflection. However, it also tends to make the pumping radiation more isotropic, and this would be useful.

TABLE 5-6

COMPARISON OF ROUGH AND SMOOTH CELLS

	$SeOCl_2$				$POCl_3$			
	Rough		Smooth		Rough		Smooth	
R(%)	E_T	η_S	E_T	η_S	E_T	η_S	E_T	η_S
85					79.4	0.0061	71.9	0.0046
75	82.4	0.017	77.2	0.0082	94.7	0.0094	86.7	0.0060
67	84.8	0.015	137.3	0.0093	102.0	0.0102	110.5	0.0083
55	119.9	0.016	127.3	0.0093	125.0	0.0107	128.8	0.0084
45	132.6	0.015	172.5	0.0082	139.0	0.012	170.2	0.011
Loss Parameter a		0.0083		0.0098		0.021		0.0094
Average: $\eta_S \frac{T+A}{T}$		0.026		0.015		0.025		0.013

In summary, the laser liquid, if properly prepared and handled, does show a low dynamic loss as anticipated from the passive loss measurements described earlier (Section 2). As expected from the spectroscopic properties, thresholds are generally lower than those found in glass laser materials. Output efficiency is strongly dependent on the cavity configuration and can be as high as 4% (using existing flashlamps) in a good cavity. The material efficiency, as far as could be determined, is better than that of LG 55 glass.

5.3 Q-SWITCHING, SELF Q-SWITCHING AND MODE LOCKING

The three parts of this section are to some extent interrelated but are, for the most part, independent areas of investigation. Most of the work on Q-switching was oriented to the task of making a master oscillator for an amplifier system. Thus, it was designed as a circulatory system in order to have a reasonable repetition rate. It was, however, not used for this purpose and since the circulatory aspect played a somewhat secondary role, this work will be discussed in this section. Self Q-switching is an interesting phenomenon and was, perhaps, first observed in liquid lasers. Mode locking, with liquid systems, has a slightly different character than in glass laser systems and deserves mention. We shall consider these independently.

5.3.1 Q-Switching

The main objective of the Q-switched oscillator work was to develop a master oscillator to use in a high brightness oscillator-amplifier system. As a consequence, great attention had to be paid to the mode structure and the beam quality of the pulse. For this purpose, the nature of the resonator was as important as the medium.

The laser itself employed a circulating liquid. The circulatory system consisted of the pump, heat exchanger and the cell. For our purposes here, we shall focus only on the cell and flash head and accept as a given fact that the other components functioned to provide an acceptable optical medium and not discuss them. The cell and flash head used for this laser are illustrated in Figure 5-7.

A series of experiments was performed to characterize the laser system from the standpoint of optical losses in the laser liquid, and laser output energy. Since the presence of small particles or other optical scatter inside the laser resonator leads to serious degradation in the laser output properties, this factor must be controlled very carefully if optimum results are to be expected. These experiments were simply to operate the laser in the long-pulse mode and measure the laser output while changing the flashlamp input and output mirror reflectivities. From the extrapolated laser thresholds and slope efficiencies for a series of different output couplings, a direct measure of dynamic laser resonator losses can be made. Figure 5-8 shows schematically the resonator structure used in these experiments. The 8 mm aperture was placed inside the laser cavity and near the end of the laser cell, to cut off any lensing effects due to temperature inhomogeneities in the laser liquid near the liquid-cell wall boundaries.

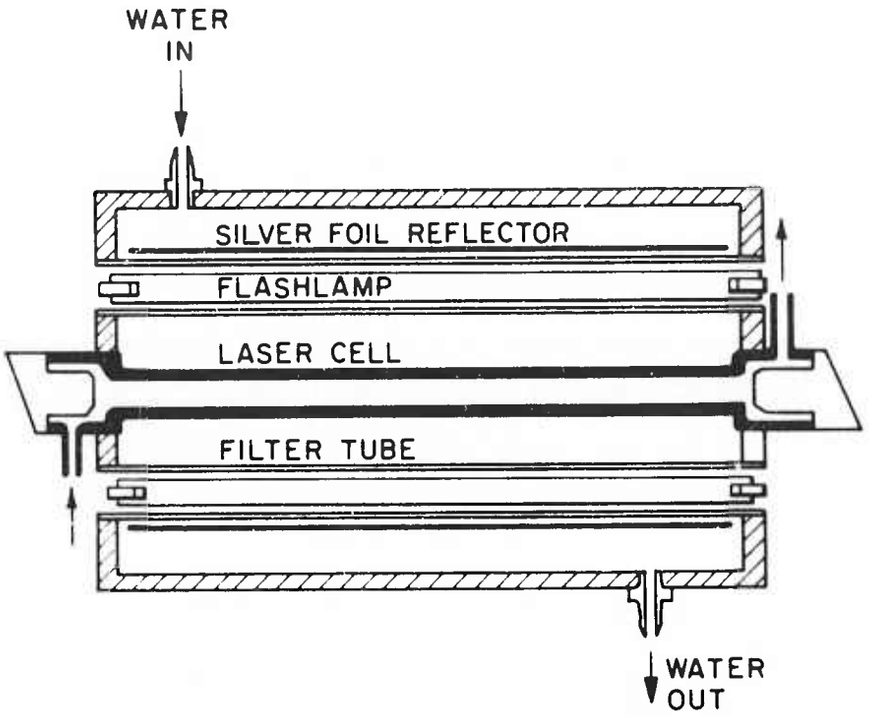

Figure 5-7. Cross-Section of the Flash Enclosure and Cell Used in the Q-Switching Laser Experiments

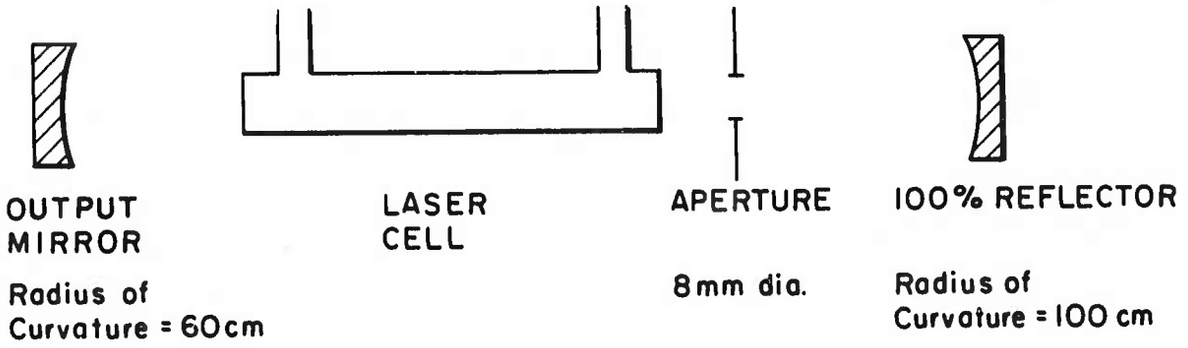

Figure 5-8. Laser Resonator for Long Pulse Experiments

Since the laser cell had a bore diameter of 16 mm, this aperture limited the output energy. Threshold, however, was only slightly affected while the beam divergence was reduced and the beam uniformity improved.

The data obtained are presented in Table 5-7 and Figure 5-9. In these experiments the laser was pulsed at the rate of 0.5 pps and output was measured for ten or more pulses. At this pulse rate, no significant decrease in output was seen from the first pulse to the last indicating that, at this 400 watt average input power level, temperature stability of the laser liquid in the optical path is good. Also, as may be seen from Figure 5-9, the change in laser threshold energies with liquid volume flow rate are small, and both data sets indicate a scattering loss of about 0.46% cm^{-1}.

TABLE 5-7

RESULTS OF LONG-PULSE OSCILLATOR DATA*

		0.96 GPM**		2.26 GPM**	
R_{out}	$-\ell n\ R_{out}$	η_s (%)	E_T (J)	η_s (%)	E_T (J)
90.5%	0.0998	0.368	99.8	0.374	92.3
82.0%	0.198	0.541	159.5	0.555	161.1
75.0%	0.287	0.662	182.7	0.672	184.7
71.0%	0.342	0.765	215.5	0.800	219.9
71.0% (Rerun)	0.342	0.589	217.4	---	---
60.0%	0.510	0.709	278.5	0.675	284.1
57.0%	0.562	0.667	279.7	0.675	284.0

*Slope efficiency and threshold calculated using all data points (1st pulse + 3rd pulse + 10th pulse).

All η_s and E_T's are results from computer least-squares fit.

** Volume flow rates through laser cell in gal·min^{-1}.

To make optimum use of the high peak powers generated by pulsed condensed-phase lasers, it is necessary to control the angular divergence of the laser beam. For some high brightness applications, such as ranging, the beam spread must be reduced to the smallest possible value. The Nd^{+3} liquid laser is similar to the other condensed

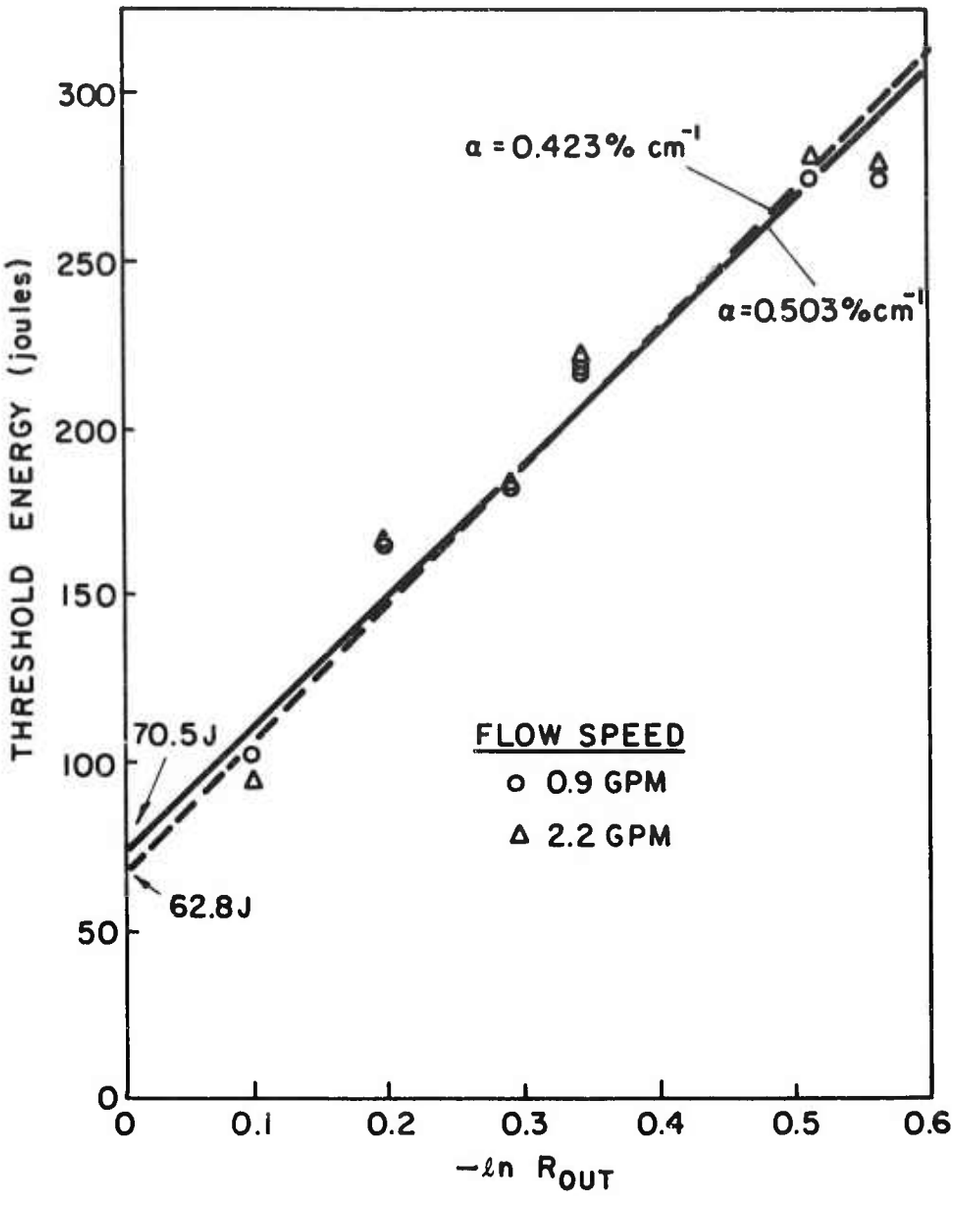

Figure 5-9. Threshold Energy vs. $\ell n\ R_{output}$ for Long Pulse Experiments at Two Different Pump Speeds

phase pulsed lasers in that the active medium aperture-to-length ratio is about an order of magnitude greater than that in most gas lasers. For gas lasers with reasonably-sized laser resonators (up to one meter length), the tube bore diameter restricts the number of available transverse laser resonator modes possible. However, in the case of Nd^{+3} liquid or glass lasers this restriction does not usually apply. For this reason, a liquid or glass laser of 1/2 inch diameter by 6 inch length produces a multimode output with a beam divergence angle on the order of 10 milliradians or more. If such a beam were to be focused to a spot with a lens of focal length f, the resultant spot diameter would be no smaller than

$$d = f\theta_d \tag{5-12}$$

where θ_d = far-field full beam divergence angle.

For this reason, a considerable effort has been directed towards designing a laser resonator for the liquid laser that limits the laser beam divergence angle (BDA), but at the same time, maintains adequate pulse output in the Q-switched mode of operation. Therefore, an investigation into the use of intra-cavity apertures, to limit the number of transverse laser modes possible in the resonator, was undertaken. Figure 5-10 shows the schematic laser cavity of the Q-switched oscillator. The output mirror and totally reflecting mirror, with respective radii of curvature R_1 and R_2, are separated by the effective optical distances d_1 and d_2 from the plane of the minimum TEM_{00} mode radius w_0. The effective optical distances, d_1 and d_2, must take into account the effects of index of refraction of the laser liquid and cell windows, the KD*P Pockels cell Q-switch, and the Glan-Laser prism polarizers. Aperture stops of various diameters are placed at the beam minimum to limit the number of modes the cavity could sustain.

Following Kogelnik [109] the beam radii and effective optical distances can be calculated from:

$$w_1^4 = (\lambda R_1/\pi)^2 \left(\frac{R_2-\ell}{R_1-\ell}\right)\left(\frac{\ell}{R_1+R_2-\ell}\right) \tag{5-13}$$

$$w_2^4 = (\lambda R_2/\pi)^2 \left(\frac{R_1-\ell}{R_2-\ell}\right)\left(\frac{\ell}{R_1+R_2-\ell}\right) \tag{5-14}$$

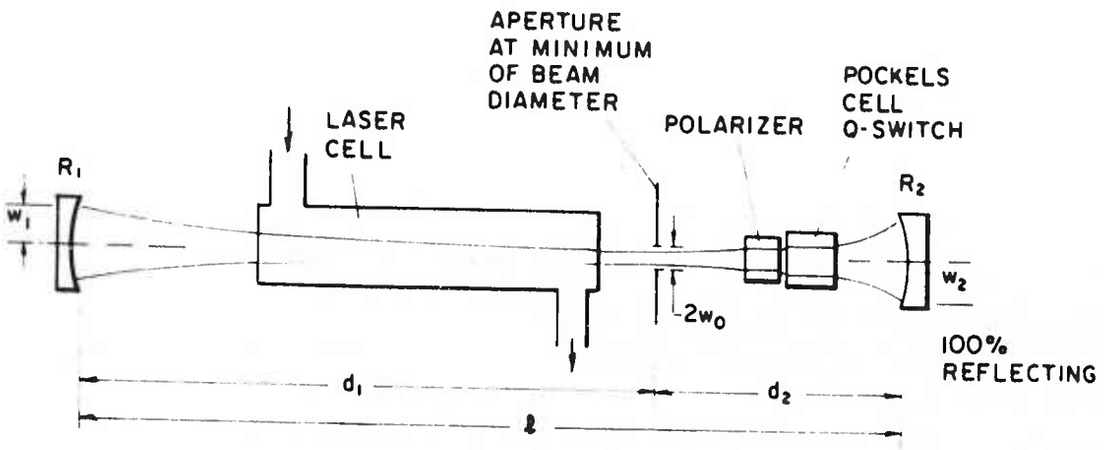

Figure 5-10. Laser Resonator for Pockels Cell Q-Switched Operation

$$w_0^4 = (\lambda/\pi)^2 \left[\frac{\ell\,(R_p - \ell)\,(R_2 - \ell)\,(R_1 + R_2 - \ell)}{(R_1 + R_2 - 2\ell)^2} \right] \tag{5-15}$$

$$d_1 = \frac{\ell\,(R_2 - \ell)}{R_1 + R_2 - 2\ell} \tag{5-16}$$

$$d_2 = \ell - d_1 = \frac{\ell\,(R_1 - \ell)}{R_1 + R_2 - 2\ell} \tag{5-17}$$

where all variables are defined by Figure 5-10. The stability condition for the resonator is given by:

$$0 < \left(1 - \frac{\ell}{R_1}\right)\left(1 - \frac{\ell}{R_2}\right) < 1 \tag{5-18}$$

If the plane of the minimum spot size is taken as $z = 0$, the beam radius at the $1/e^2$ intensity point of the TEM_{00} beam is described by the equation:

$$w(z) = w_0 \left[1 + \left(\lambda z/\pi\, w_0^2\right)^2\right]^{1/2} \tag{5-19}$$

The hyperbola described by Eq. (5-19) has, in the far field, asymptotes separated by the angle θ_{00} given by:

$$\theta_{00} = \lim_{z \to \infty} \left[2w(z)/z\right] = 2\lambda/\pi\, w_0 \tag{5-20}$$

and far-field zone of the laser is defined by the relation:

$$z > \pi\, w_0^2/\lambda \tag{5-21}$$

For a given pair of mirrors R_1, R_2, and effective cavity length ℓ, Eqs. (5-15) and (5-20) allow us to predict the smallest BDA the resonator structure will support. Then the measured BDA of the oscillator with various aperture stops can be compared to see how close to diffraction-limited operation (TEM_{00} mode) the laser will work.

Two types of Q-switching were tried on the liquid laser, a Pockels cell with prism polarizer and a rotating roof prism. Both methods produced Q-switched pulses but the Pockels cell was by far the best method in terms of laser output reproducibility and beam quality.

Figure 5-10 shows the location of the Pockels cell Q-switch inside the laser resonator. The Pockels cell was a commercial KD*P unit, AR coated on both exit and entrance faces, with a quarter wave voltage of 3.7 kV. The polarizer element was an air-spaced Glan-Thompson prism, also AR coated on both faces. A commercial, high-voltage pulse unit switched the quarter-wave voltage to the Pockels cell with a rise time of less than 10 nanoseconds. Cavity apertures used were stainless steel electron-gun apertures and ranged in diameter from 7.9 mm to 4.9 mm. The resonator mirror radii were varied in these experiments.

The experiments were run with a constant, laser-power input of 760 joules/pulse at a repetition rate of 0.5 pps. Laser output, especially when the smaller pinholes were used as aperture stops, was reproducible on both shot-to-shot and long term bases, but not enough data were collected to make a detailed statistical analysis. Experiments were prematurely terminated because of laser damage to the polarizing prism from the high peak-power densities generated in the resonator. As the manufacturer's specification for damage threshold in the calcite polarizer was 150 megawatts/cm^2, rather large power densities were obviously being generated in these experiments.

Representative data from this series of experiments is presented in Table 5-8 and a typical oscilloscope trace of a single pulse of full-width-at-half-maximum of about 25 ns is shown on Figure 5-11. No double-pulsing is observed with this energy input to the laser and the trace shows no modulation. Laser output beam patterns are rather uniform, although obviously, from the data of Table 5-8, the beam consists of several transverse laser modes oscillating simultaneously. The best output beam quality was obtained with the 5 meter radius of curvature cavity mirrors. In this case, the minimum spot diameter $2w_0$ was about a factor of 5 smaller than the aperture diameter, while the measured beam divergence angle was only a factor of 3 larger than the theoretical TEM_{00} divergence angle.

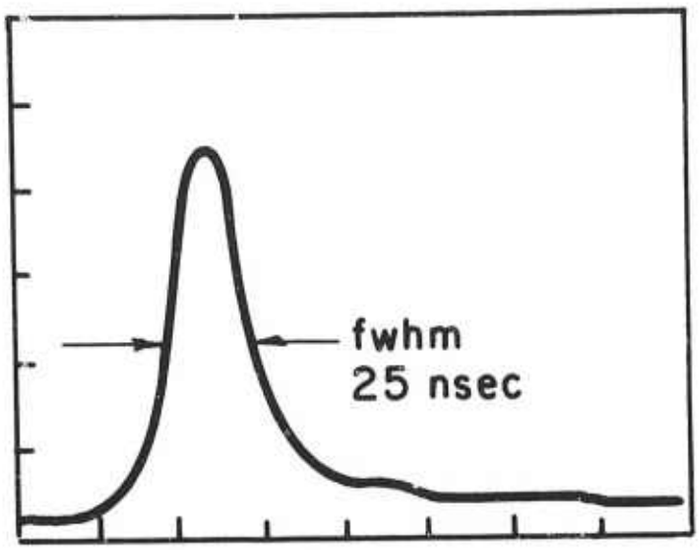

Figure 5-11. Q-Switched Output Pulse. Time Scale is 10 ns per Division

TABLE 5-8

Q-SWITCHED OSCILLATOR PERFORMANCE

Mirror Combination	Aperture Diameter (mm)	Energy Output (Joules)	Measured BDA (mrad)	w_0* (mm)	TEM_{00}** BDA (mrad)
75% Refl., 60 cm R_c, 100% Refl., 100 cm R_c	7.9	0.86	12.4	0.367	2.2
75% Refl., 60 cm R_c, 100% Refl., 100 cm R_c	4.9	0.15	9.1	0.367	2.2
65% Refl., 5M R_c, 100% Refl., 5M R_c	4.9	0.10	4.4	0.528	1.3

*w_0 is TEM_{00} minimum spot radius calculated from Eq. (5-4).

**θ_{00} calculated from w_0 and Eq. (5-9).

A rotating prism Q-switch was also tried as the totally reflecting cavity mirror. A 40 cm focal-length lens was placed between the rotating prism and the laser cell to produce a rotating mirror of 80 cm radius of curvature. The prism was driven at a speed of 30,000 RPM (500 RPS). Figures 5-12a and 5-12b show typical results obtained in this manner. Because the laser output was so erratic from shot-to-shot, the figure shows only representative sketches of the results. Typical laser output consisted of a pulse train about 4 μs in duration composed of from 3 to 9 giant laser pulses, randomly distributed, with individual pulse durations on the order of 200 ns. The laser output beam was smeared in the direction of rotation of the spinning prism and had very poor uniformity. The laser beam divergence for this mode of operation was not measured.

From the above work it is concluded that Q-switching with good beam quality and output reproducibility is best accomplished with a Pockels cell. Apparently, not enough mechanical stability is easily obtained with a spinning prism to assure reproducibility of output. Also, ordinary prism Q-switches are plagued by multiple-pulsing due to their lower switching speed. The KD*P Q-switch with intra-cavity aperture mode control resulted in reproducible, single giant pulses with relatively uniform beam patterns; however the high intra-cavity laser power densities generated resulted in damage to optical components.

5.3.2 Self Q-Switching

Self-Q-switching is the production of giant pulse laser spikes without the intervention of an active or passive Q-spoiler external to the laser material. Because of the high gain of the liquid laser material, it can be operated conveniently at low output mirror reflectivities with moderate thresholds. As the output mirror reflectivity is decreased to below 50%, giant spikes become interspersed with the more normal, lower power, microsecond-long spikes characteristic of the free running output. At yet lower output mirror reflectivities the giant spikes begin to dominate the output. With only the cell output window for feedback, the output consists exclusively of the giant spikes, usually only a few of them. The power in these spikes has been determined to be as high as 500 MW. Most of the work to be described was done with the $SeOCl_2$ solvent system, but it has also been observed in the $POCl_3$ solvent.

If the resonator consists of a 100% reflecting mirror and the cell output window only, the output spectrum extends over a range of 5 to 10 Å and consists of a series of sharp lines with a spacing characteristic of the interferences arising from a plane-parallel element having the thickness of the output window. If the cell forms its own

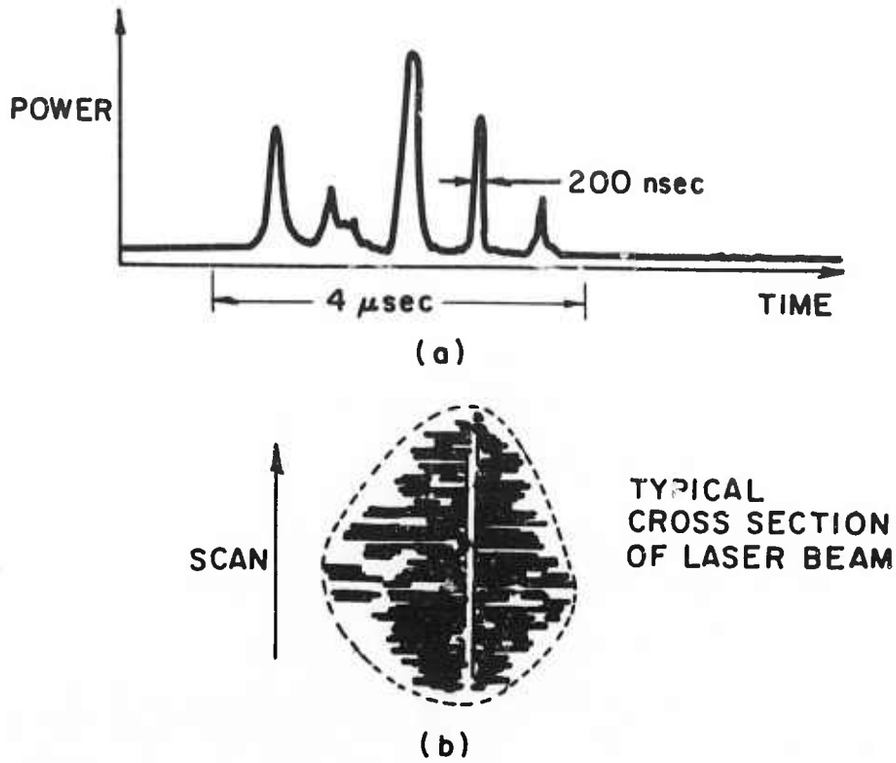

Figure 5-12. Typical Rotating Prism Q-Switched Results

cavity, the feedback consists only of the Fresnel reflection from each end-window, and the output consists only of a few giant pulses as high as 500 MW. The output spectral distribution shows fewer lines (never more than the number of spikes) spanning a width of less than 5 Å. In the case of multiple lines, their frequency separation usually does not correspond to any known interference element in the cavity.

In those cases where there is a totally reflecting mirror, the beam diverges and transverse mode patterns (of high order) are usually detectable. With no external mirrors, the output beam is quite divergent and the mode patterns more clearly discerned.

In the absence of feedback from the cell window, it was not possible to generate the giant spikes, at least within the available range of input energies. This does not prove that yet higher energies would not produce the effect, but does indicate that a small amount of feedback is very helpful. A tentative explanation, put forward for the effect, was that some small amount of feedback, possibly arising from stimulated Brillouin or Rayleigh scattering due to the high flux in the active medium, acts like a mirror that is suddenly turned on. Thus, it behaves as if there were an internal Q-switch.

At about the same time that the work reported here was done, Freund[110] and Collins, Braun and Dean[111] reported a similar effect in ruby. In these experiments, the transition to giant spiking was observed as the totally reflecting mirror was gradually misaligned to a very small extent. Freund tried, but could not produce the same effect in Nd^{+3}:glass. Birnbaum and Finchner[112] were able to achieve self Q-switching in Nd^{+3}:YAG and ruby using a pulsed argon laser for excitation. Here, also, a principal factor was an element of misalignment, either the resonator or the pumping beam with respect to the resonator.

While the effects observed in the solid and liquid media are similar, the main factors appear to be different. In the liquid, it was always the cavity reflectivity that was dominant and this was irrespective of the liquid employed (the effect is also observed in $POCl_3$ solutions). It is, of course, difficult to estimate misalignment in the liquid systems. It was always clear that the cavity was aligned; however there could be a slight misalignment in the cell end windows that would be difficult to detect .

The basic explanation for the effect was hard to find. While, in theory, the proposed stimulated Brillouin scattering was a possible mechanism, the experimental evidence for it was lacking. The spectrum of these giant spikes always shows one line per spike and no second one separated by the frequency shift associated with Brillouin scattering. Selden[32] was able to make a more plausible case for stimulated Rayleigh back scattering as the mechanism for the enhancement of the cavity Q. In effect, he puts forward the idea that a normal pulse and the associated electromagnetic wave produce a grating by thermal refractive index modulation; this leads to the required back scattering. Where there is a high field, the stimulated emission rate is high and more transitions occur at that point. The heat associated with the relaxation from the terminal laser level to the ground state is greatest there, and a corresponding decrease in the refractive index occurs. This mechanism appears to be most consistent with the observations and has the lowest threshold for all the stimulated scattering processes.

5.3.3 Mode Locking

Mode locking is related to Q-switching, in that it is observed in almost all kinds of Q-switched pulses and is generated when a passive Q-switch (a saturable absorber) is employed. The particular interest in the Nd^{+3} liquid laser materials from this point of view is that there is a large bandwidth for the fluorescence (~ 180 Å) and the broadening appears to be largely homogeneous.

Experiments performed with Nd^{+3}:$SeOCl_2$ employed the apparatus shown in Figure 5-13a. The laser cell was 15 cm long and the other components are described in the figure. The Kodak 9740 Q-switch solution was used with absorption constants, α, ranging from 0.19 cm^{-1} to 1.63 cm^{-1}. In these experiments, all the mirrors were plane parallel and the return mirror for the two-photon fluorescence dye cell was separated and removed from the cell. The peak power was a maximum of 170 MW for an α of 1.25 cm^{-1} and decreased for higher and lower values of α, as shown in Table 5-9. The giant spikes observed, were invariably mode-locked and the period of 4.5 ns agreed very well with measured optical length of the cavity. The individual pulses of the mode-locked train had a width of about 2 ns in the Tektronix-519 oscilloscope trace, indicative of poor or complex mode-locking. This was confirmed by the two-photon fluorescence experiments which showed a substantial substructure to the pulses, due to the subsidiary resonances in the cavity.

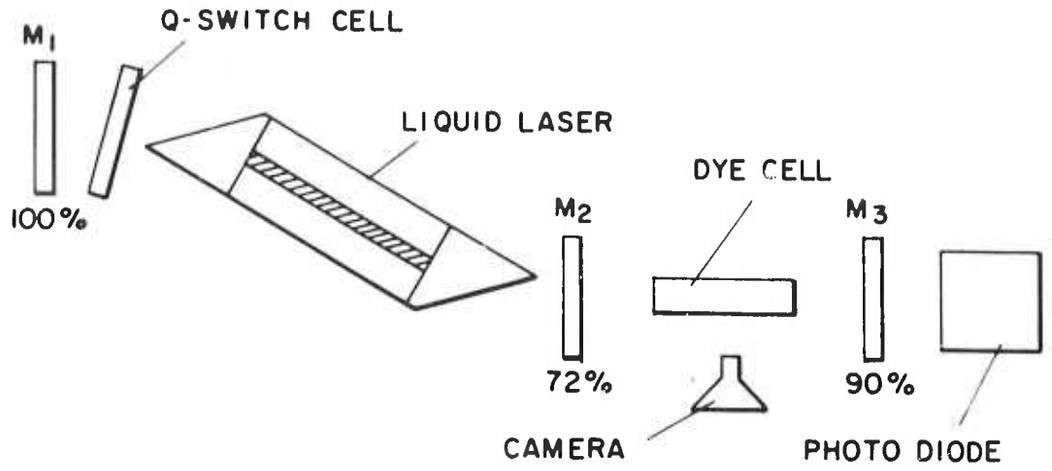

Figure 5-13a. Schematic of the Experimental Arrangement for Studying Mode-Locked Pulses

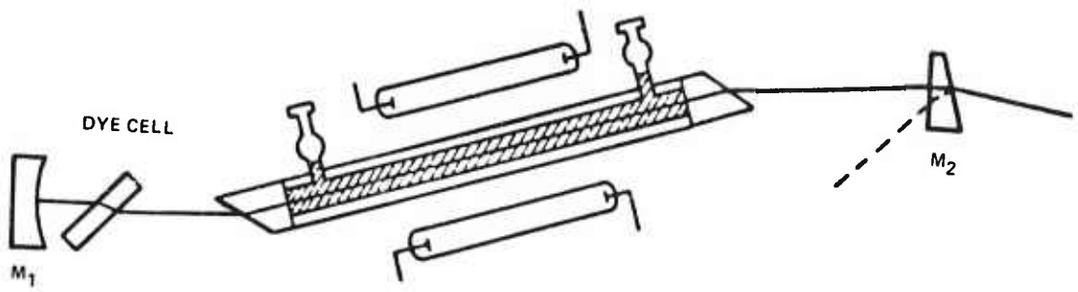

T_c = 7.5 ns

Figure 5-13b. Schematic Arrangement of Mode-Locked Liquid Laser

TABLE 5-9

PEAK POWER OUTPUT

Dye Absorption Constant α (cm^{-1})	Input (J)	Output (MW)
0.19	640	15
0.32	360	25
0.63	640	80
0.88	810	125
1.25	810	170
1.63	810	60

Further experiments were carried out with the experimental arrangement shown in Figure 5-13b using the $Nd^{+3}:POCl_3:ZrCl_4$ material. This experimental arrangement is more carefully designed than the previous one and eliminates the spurious reflections. The length of the active medium is 25 cm and the diameter is 1.0 cm. M_1 has a 10M radius of curvature and a reflectivity of 100%; while M_2 is wedged with an angle between 1 and 5°, and its reflectivity was varied from 4% to 80%. The laser was Q-switched with Kodak 9860 dye, having a transmission between 60 and 70% and the dye cell is anti-reflection coated.

The spectral output of the laser is shown in Figure 5-14. The spectrum extends over 100 cm^{-1} and shows no structure except for a sharp line near the line center of 1.052μ. There is also an emission due to stimulated Raman scattering displaced 488 cm^{-1}, which is the Raman frequency for $POCl_3$.

The pulse trains themselves, often lasting microseconds, show a "clean" mode-locking with a 7.5 ns spacing characteristic of the cavity. These are illustrated in Figure 5-15.

Stimulated Raman emission always accompanies the usual emission in the spectra of mode-locked pulses, but may or may not occur on normal Q-switching. A Brewster-Brewster Nd^{+3} $SeOCl_2$ laser of cavity length 70 cm, cross-section ~1 cm^2, and active medium length 25 cm was Q-switched with a 60% transmission Kodak 9860

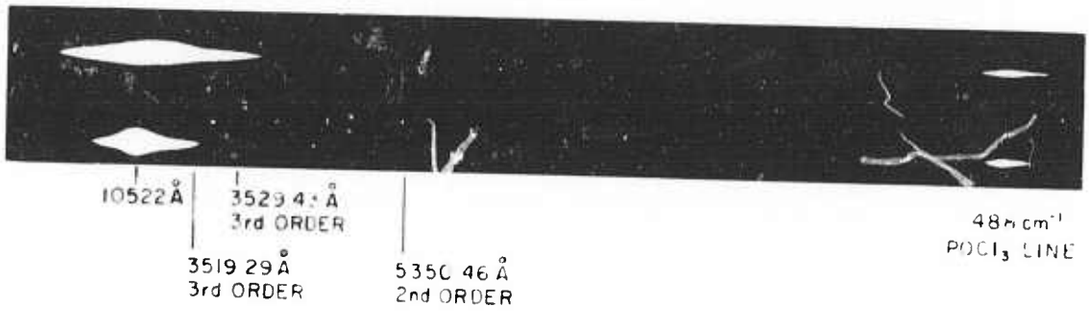

Figure 5-14. Spectra of Mode-Locked Liquid Laser. Two Shots Show $\approx 100\ cm^{-1}$ Central Band and Raman Shifted Light

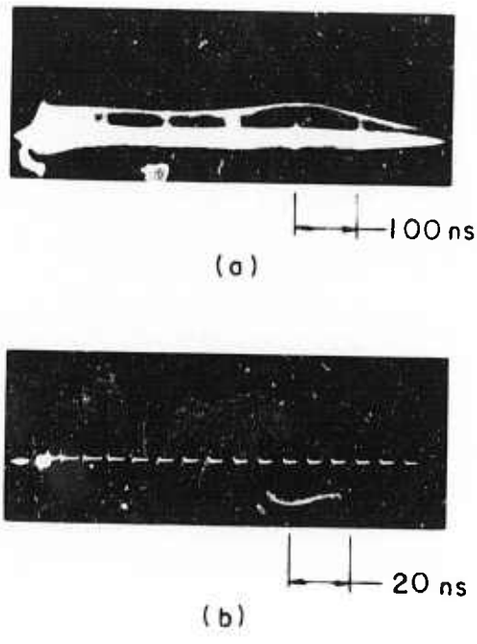

Figure 5-15. Typical Oscilloscope Traces of Laser Pulse Train. (a) 100 ns/cm; (b) ns/cm (airbrushed).

dye. When this laser was operated in a Q-switched but nonmode-locked mode, as shown on a Tektronix 519 scope, no SRS was observed in the output. When regular trains of short pulses were emitted, however, intense SRS was observed. Both first and second Stokes of the $ScOCl_2$ 386 cm^{-1} line were recorded on sensitized Kodak 1-Z plates. The Raman emission occurred in a band ~ 6 cm^{-1} wide with a laser excitation spectra bandwidth of ~ 6 cm^{-1}, also. A Bausch and Lomb two-meter spectrograph was used to detect the spectral output. The laser pulse width, as measured by two photon fluorescence, was ~ 6 ps. With an Nd^{+3} $POCl_3$ laser of similar construction as the Nd^{+3} $ScOCl_2$ laser, intense stimulated Raman scattering was observed when the laser was operated in the mode-locked mode, Q-switching with a saturable absorber, and also in the self-Q-switched mode. When the laser was Q-switched and mode-locked, first Stokes and anti-Stokes lines of $POCl_3$ (488 cm^{-1}) were recorded with a 1/2-meter Jarrell Ash spectrograph and with Polaroid infrared No. 57 film. Highest-order Stokes lines were not recorded because the film was insensitive at longer wavelengths. Raman scattering occurred on almost every shot. Raman scattering in the first Stokes and first and second anti-Stokes modes were recorded with the laser self-Q-switched. Self-Q-switching was obtained by using a quartz wedge as an output reflector and by removing the Q-switching dye cell. Figure 5-16 shows a typical self-Q-switched spectra and 519 scope trace. It should be noted that the scope trace shows some degree of self-mode-locking. Raman scattering, during self-Q-switching only, appeared on the most intense shots.

5.4 SPECTROSCOPIC PROPERTIES OF THE LASER OUTPUT

The spectroscopy of the laser output is often useful in understanding some of the properties of the material itself. While these observations may not always be conclusive, they often provide a great deal of information. Thus, in the previous section, the spectral output of the self-Q-switched laser provided the evidence to rule out one mechanism. In the present section, we shall discuss the output of the free running laser in terms of its spectroscopy.

In this work, we use a streak camera to trace the time evolution of the spectrum of the spikes in a laser pulse. This camera is put in place of the plate-holder at the exit of the spectrograph. The spectrograph output strikes the surface of a highly-polished, rapidly-rotating stainless steel parallelopiped and focuses on the film pack of a Polaroid camera back. The phase of the rotating steel parallelopiped and the trigger pulse are adjusted so that at least 150 μs of the laser pulse is photographed.

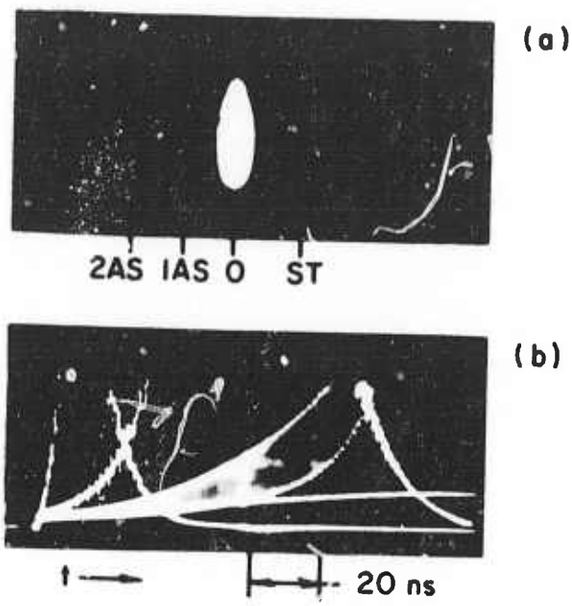

Figure 5-16. (a) Self-Q-Switched Spectrum Showing Stokes and Anti-Stokes Raman Scattering;
(b) Time Output on Tektronic 519 Oscilloscope.

5.4.1 Free Running Laser

The output of the free running laser depends on the nature of the feedback. One of the first experiments done was to compare output spectra from mode-supporting and nonmode-supporting cavities; the results for the $SeOCl_2$ solvent are illustrated in Figure 5-17. It is seen that in the high reflecting cavity, the laser action is confined to a range of about 15 to 20 Å. The spacing between the lines is determined by the multiple beam interference spectrum of the front window and the partially transmissive output mirror. With a nonmode-supporting cavity, the output spectrum narrows to 3.9 cm^{-1}. This sort of behavior is quite different from that of glass, and suggests that the 180 Å spontaneous line width is principally homogeneously broadened, and that the inhomogeneous width is of the order of 3 Å.

To explore the nature of the line broadening in more detail, the streak camera was used to display the laser emission spectrum. The experimental arrangement consisted of a static cell, 6 inches long and 0.25 inch in diameter placed in a close-wrapped configuration between two FX 45 linear flash tubes, with the cavity mirrors mounted external to the laser sample. The output was focused on a pinhole which replaced the

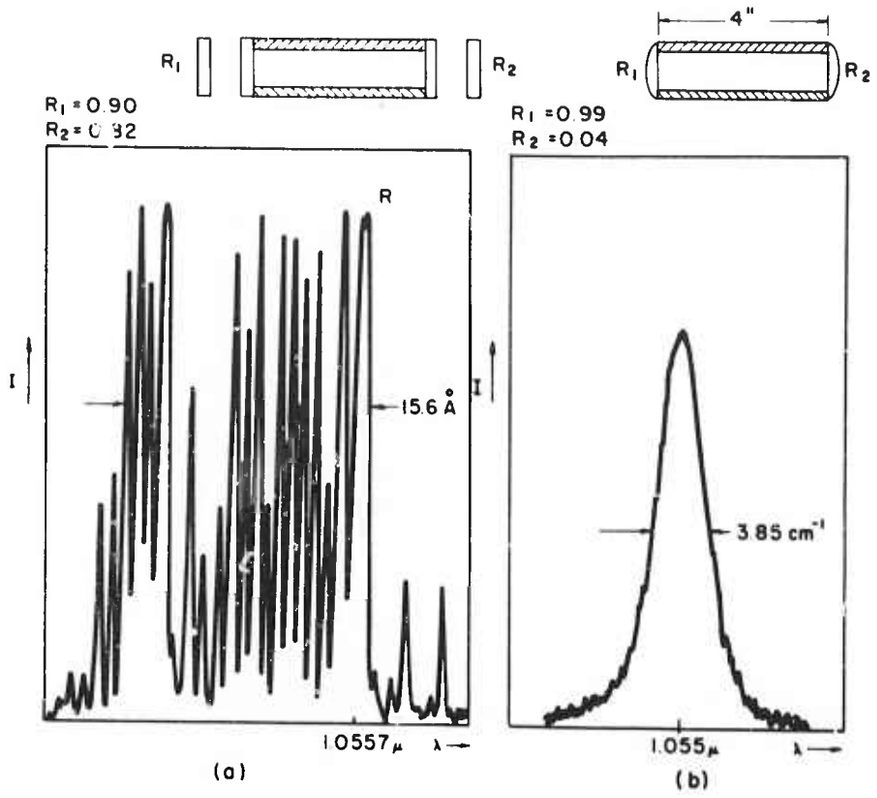

Figure 5-17. Spectra of Laser Emission. (a) High-Reflectivity Mode-Supporting Cavity (b) Nonmode-Supporting Cavity.

slit of a Bausch and Lomb dual-grating spectrograph, and the plate camera of the spectrograph was replaced by a rotating mirror streak-camera with a linear sweep speed of about 20 μs/cm at the film and a linear dispersion of 1.7 cm^{-1} per millimeter. The replacement of the slit by the pinhole greatly improved the time resolution of the streak. Nd^{+3}:$SeOCl_2$:$SnCl_4$ was the liquid system used.

A typical spectrum obtained when plane parallel mirrors are used on the laser is shown in Figure 5-18. The laser emission occurs at several wavelengths with a spread of 10-20 cm^{-1}. At higher input energies, the density of spikes (and dots on the streak) increases without significant broadening of the lasing spectral range. This result indicates a basic difference in the behavior of liquid from that of glass lasers whose spectral width tends to broaden with input power.[113] A more pronounced difference is observed when a confocal, rather than a plane-parallel, cavity is used. The

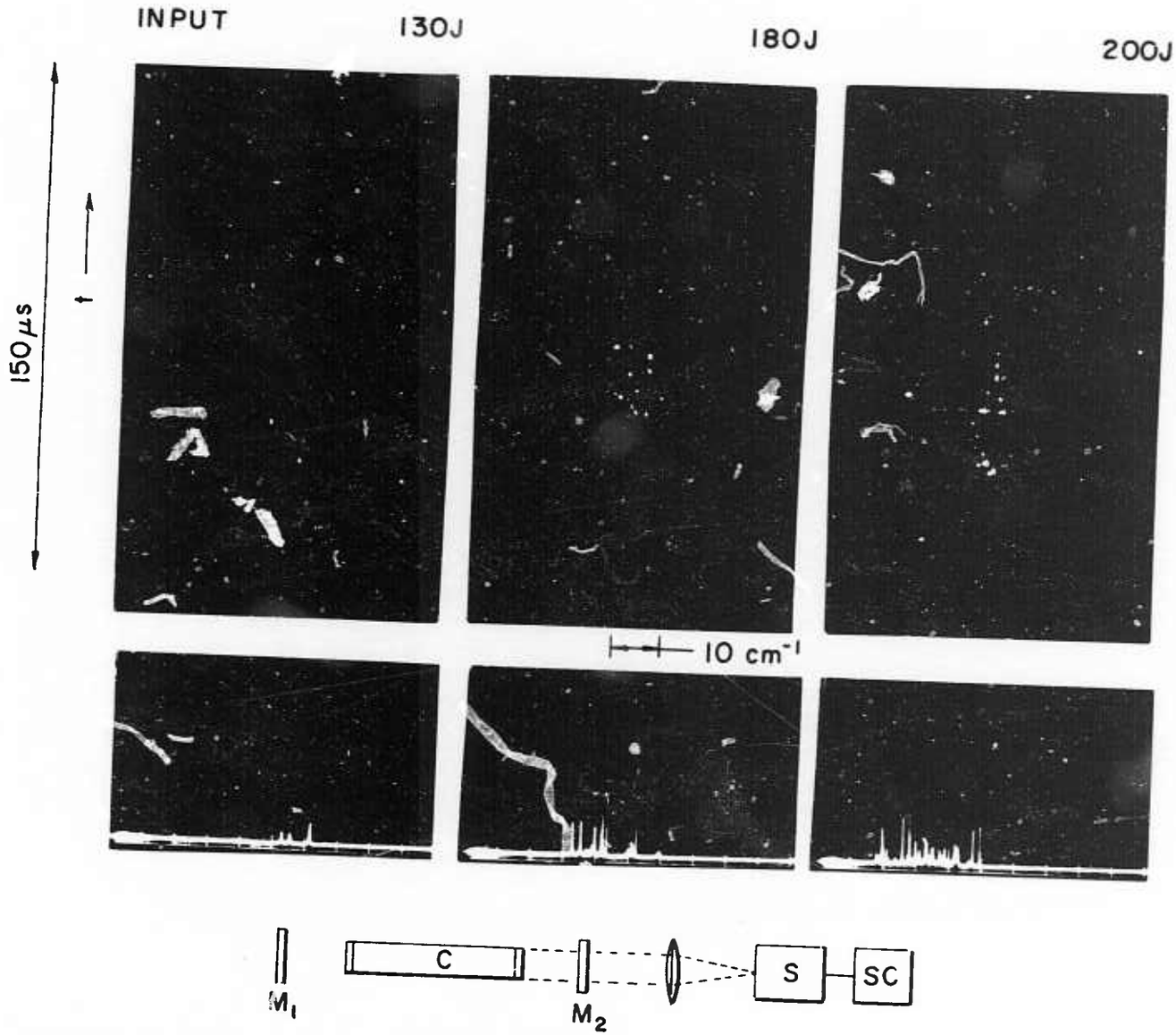

Figure 5-18. Time-Resolved Spectra of a Plane-Parallel Laser at Three Levels of Input Energy and Corresponding Spike Traces. Experimental Arrangements Consisted of a Cell C, Mirrors M_1 and M_2, Spectrograph S and Streak Camera S-C.

results for the liquid, shown in Figure 5-19, indicate that the spectral range is quite narrow, 2 to 4 cm^{-1}, and remains narrow at higher input powers. Under the same conditions, glass lasers show a pronounced broadening and eventual hole-burning effects. The implication of this result is that the predominant line-broadening mechanism in liquids is homogeneous and, thus, quite different from that encountered in glass. The homogeneous nature of fluorescent line also makes it possible to obtain a narrow emission from a plane-parallel laser cavity. This is advantageous, since the plane-parallel geometry can utilize the full volume of the material without a great increase in beam divergence. To explore the spectroscopy more fully, an output mirror consisting of a variable spacing Fabry-Perot interferometer was used, as illustrated in Figure 5-20. The windows of the cell and the outer surfaces of the interferometer were antireflection coated, and the interior faces of the interferometer were coated with dielectric films having a reflectivity of 54%, giving it a finesse (F) of 5 and a maximum resonant reflectivity of 92%.

The condition of oscillation of a laser can be expressed as:

$$R(\nu)\, e^{[\sigma(\nu)\,\Delta N - \alpha]L} = 1 \tag{5-22}$$

which takes the dispersive nature of R into account. The other symbols have the same meaning as before. Eq. (5-22) can be rewritten as:

$$\sigma(\nu)\,\Delta NL - \alpha L = \ln R(\nu) \tag{5-23}$$

The first term on the left-hand side is proportional to the gain of the laser. The second term can be assumed nondispersive and therefore a constant. The whole left-hand side can, thus, be considered as a generalized "gain curve," having the same shape as the fluorescence line and translatable along the ordinate axis. The function $R(\nu)$, for the case of an output mirror consisting of a Fabry Perot interferometer, is given by:

$$R(\nu) = \frac{4F^2 \sin^2 (2\pi\nu d)}{\pi^2 + 4F^2 \sin^2 2\pi\nu d} \tag{5-24}$$

where F is the finesse and d the interferometer spacing. The negative logarithm of this function has a periodic series of positive infinities and minima spaced at one half the inter-order spacing $\Delta\nu = 1/2d$.

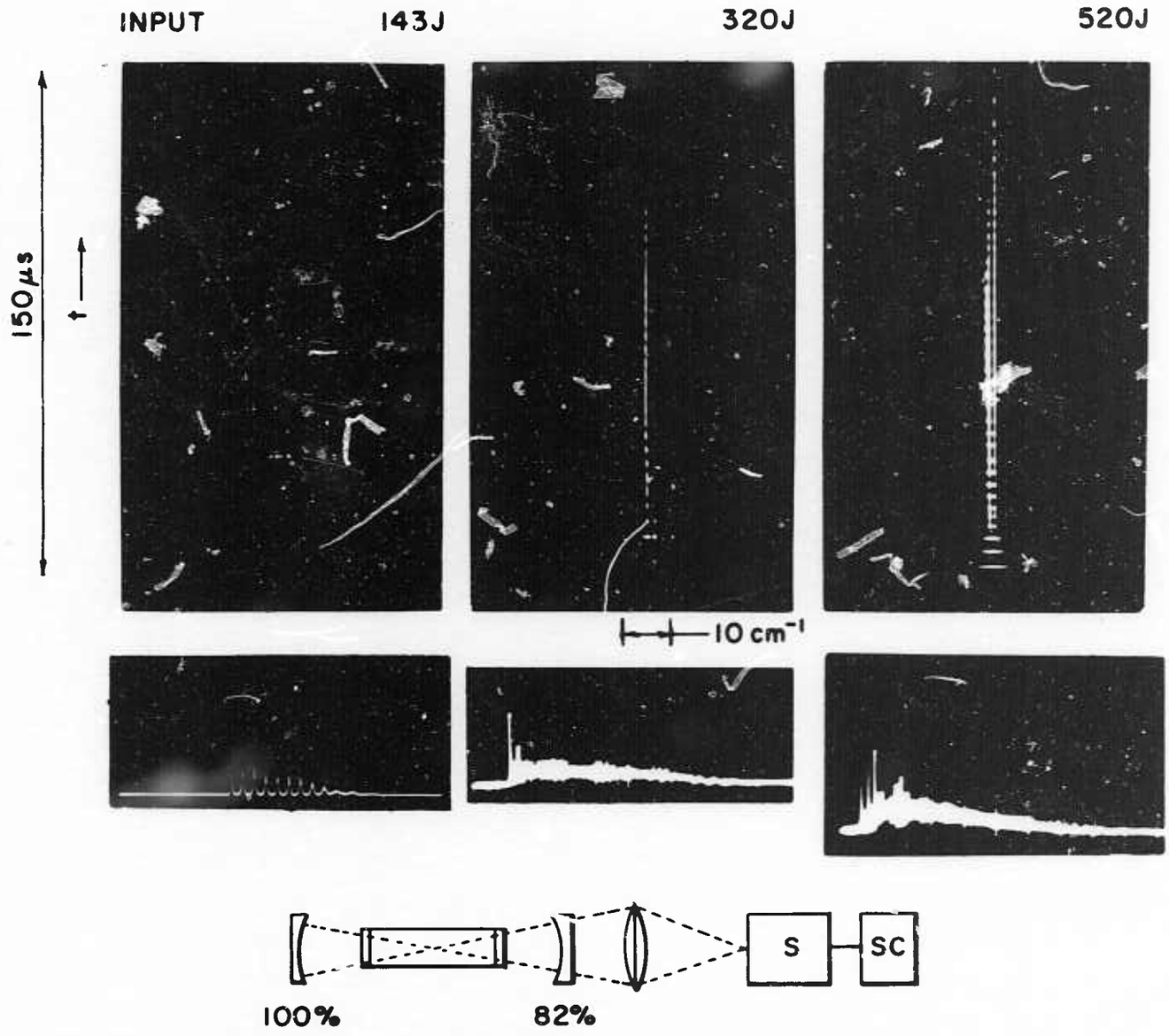

Figure 5-19. Time-Resolved Spectra of a Confocal Laser at Three Levels of Input Energy and Corresponding Spike Traces.

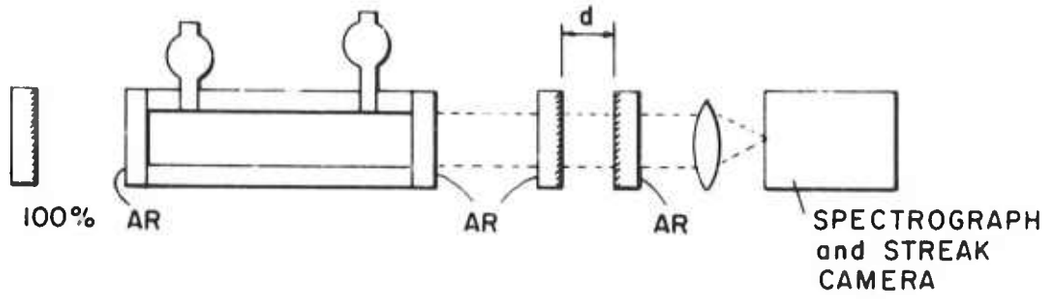

Figure 5-20. Experimental Arrangement for the Study of Streak Spectra Using Variable Spacing (d) Fabry Perot Interferometer as the Output Reflector. AR-Antireflection Coated Surface.

Consider a plot of the function $-\ell nR(\upsilon)$ versus ν, which represents the frequency-dependent part of the loss and which will be called the "loss curve." The oscillation condition, Eq. (5-23), requires that the loss curve make at least one point of contact with the gain curve. This is illustrated in Figure 5-21 for an interferometer spacing of 0.02 cm. Since nothing is known about the absolute phase of the reflection, both curves can be translated horizontally with respect to each other. The gain curve may also translate vertically until it re-establishes a point of contact with the loss curve. In general, at most two such points of contact are possible, if the maximum of the gain curve falls between the minima of the loss curve. The same is true of the case illustrated in Figure 5-22, which shows a loss curve corresponding to a larger spacing of the interferometer (d = 0.1 cm). In this idealized case both interferometer spacings should permit oscillation at one or two frequencies.

The oscillation condition, Eq. (5-23) is, of course, only valid in the steady state. In a pulsed laser, the dynamics of the situation permits the crossing of the loss curve by the gain curve beyond the point of contact. It is, however, obvious that this is far more likely to occur for the large interferometer spacing (Figure 5-22), in which the minima occur close together in frequency and a number of them lie close to the gain curve. The output spectra of the laser, with the two different interferometer spacings, are shown in Figure 5-23 and confirm the qualitative predictions. When the inter-order spacing of the interferometer exceeds 20 to 25 cm^{-1}, the liquid laser oscillates in a narrow line without any tendency to spread.

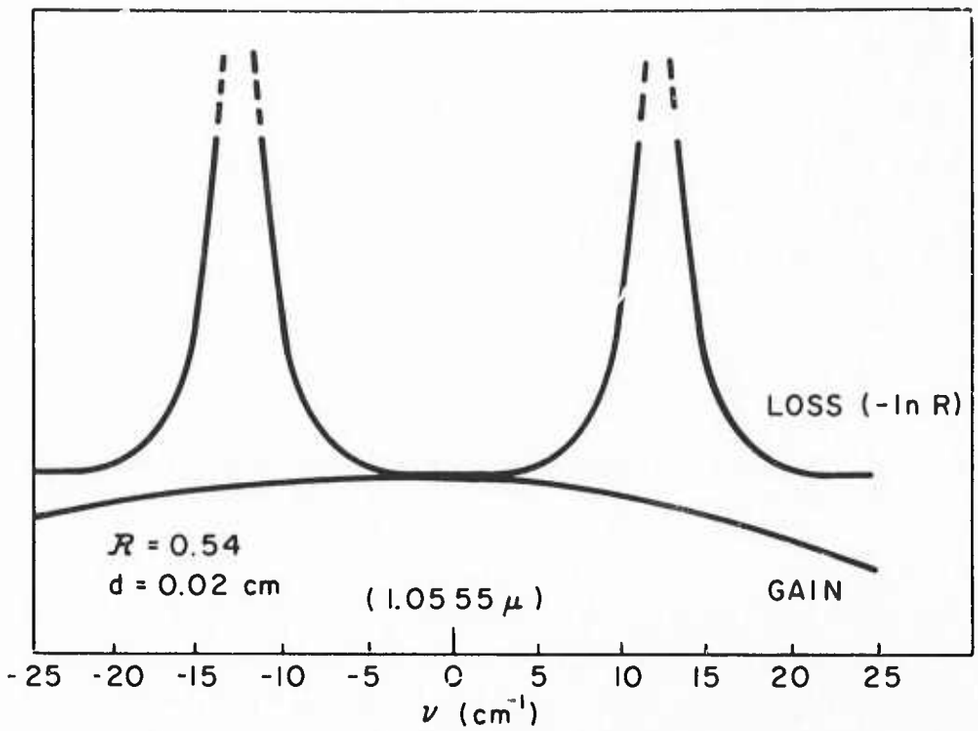

Figure 5-21. Gain and Loss Curves for an Interferometer Spacing of 0.02 cm.

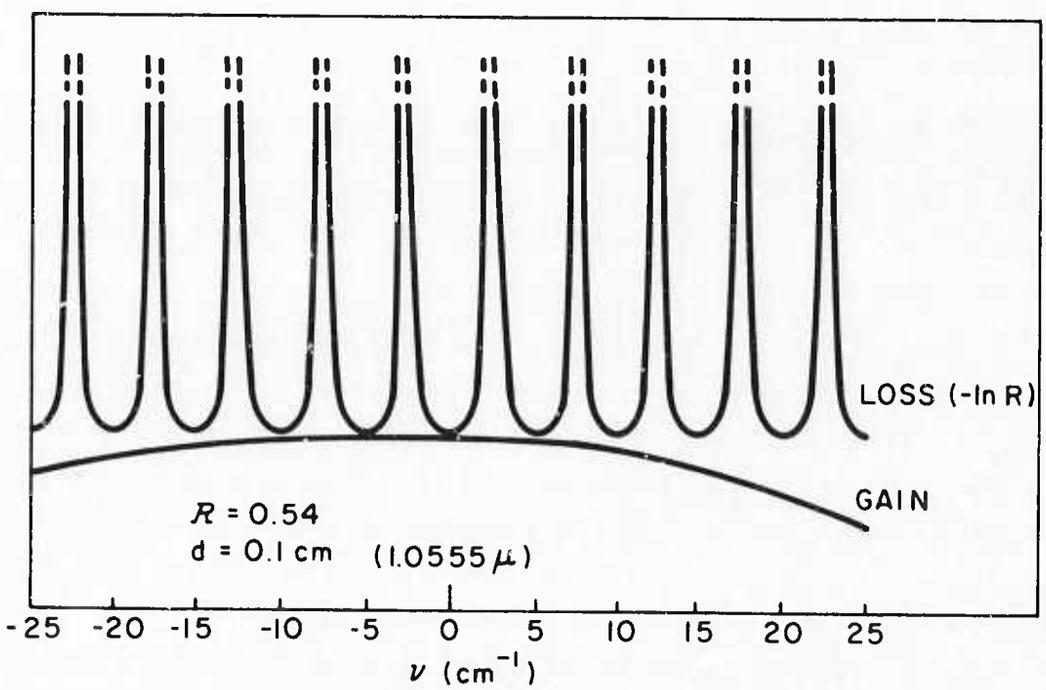

Figure 5-22. Gain and Loss Curves for an Interferometer Spacing of 0.1 cm.

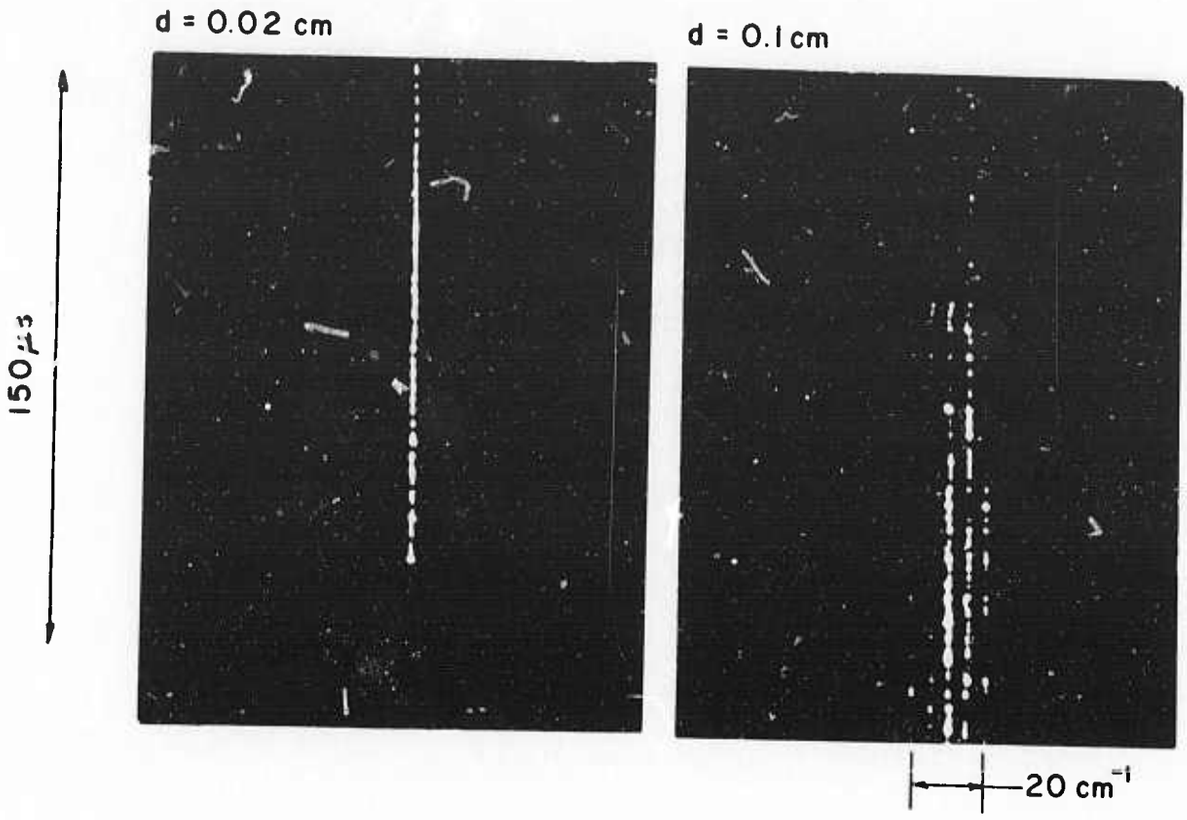

Figure 5-23. Streak Spectra Obtained with Interferometer Spacing of 0.02 and 0.1 cm.

5.4.2 Spectral Broadening

The final phenomenon to be discussed in this section is spectral broadening. This can be observed in simple, plane-parallel resonators at intermediate input powers and when self-Q-switching does not occur. The work to be reported was done with the $SeOCl_2$ solvent. The experimental arrangement shown in Figure 5-24 consisted of a 15-cm laser cell placed between mirrors of reflectivities R_1 = 95% and R_2 = 80 or 20%. The output beam (passing through R_2) is directed into a Bausch and Lomb 1.8-m spectrograph, whose plate holder has been replaced by a rotating mirror streak camera with a sweep of 18.7 μs/cm. To obtain improved time resolution, the vertical entrance slit was replaced by a 0.4-mm pinhole placed at the focal point of a f = 20 cm lens. With this arrangement, only light diverging less than 2 mrad can enter the spectrograph. The spectrograph and streak camera combined produce a 1.7X magnification of the

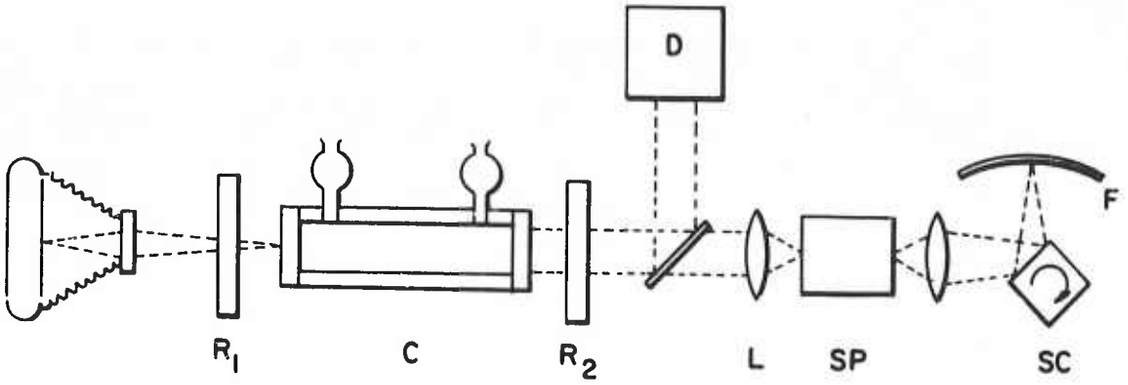

Figure 5-24. Experimental Setup: C - Laser Cell; $R_1 R_2$ - Mirror; D - Detector; L - Lens; Sp - Spectrograph; Sc - Streak Camera; F - Film.

entrance pinhole. A camera placed behind the R_1 mirror was focused on the plane of the cell window giving a 3X magnification. Since the laser emits in the region of 1.06μ, an infrared-sensitive film (Polarid type 413) was used in both cameras. Each experiment consisted of recording the time-resolved spectrum, the near-field pattern (from the back) and the laser intensity.

Figure 5-25a shows the results obtained at low input energy. The streak spectrum is seen to be composed of large dots (images of the entrance pinhole). Multiple wavelengths arise from the mode-selecting properties of the laser cell, windows and mirror R_2. The near-field pattern shows evidence of high-order modes indicating that under these conditions the laser behaves very much like any solid-state laser. At slightly higher input energies (Figure 5-25b), the character of the streak patterns change abruptly with the occurrence of spectral broadening; this is evidenced by the formation of "strings of beads" extending a few tens of cm^{-1} with a slight asymmetry towards the Stokes side. When the rear mirror reflectivity is increased from 95 to 99.9%, the broadening and beading becomes more pronounced. A streak spectrum taken under these conditions is shown in Figure 5-26. Note that diameter of the "beads," being smaller than that of the large dots, is not determined by the size of the entrance pinhole. It represents therefore a high degree of collimation of the light. The streak camera does not have sufficient sweep-speed and resolution to measure the true time duration of the laser spikes. All we can say is that the spikes responsible for the "beads" are of

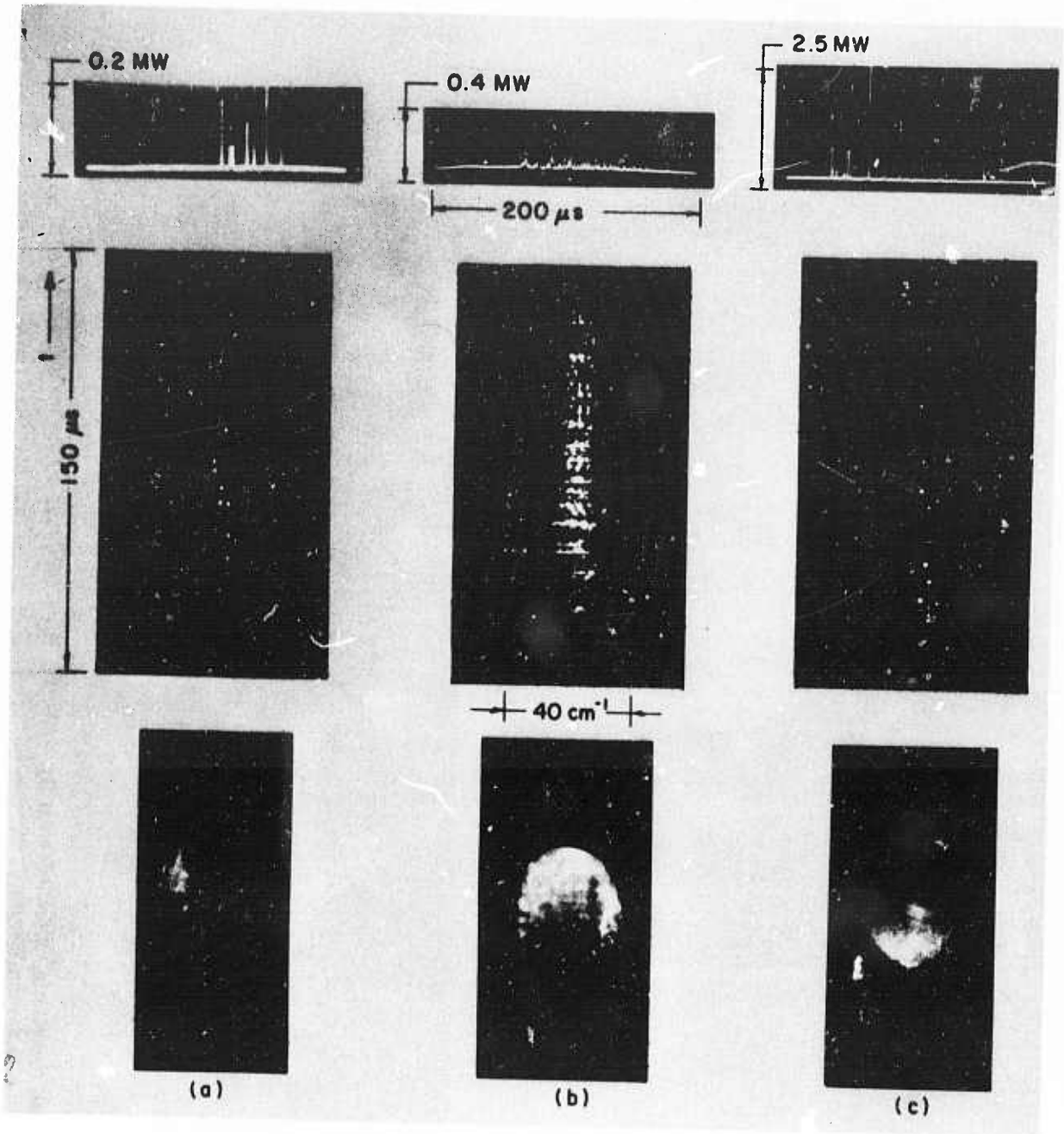

Figure 5-25. Laser Output Under Different Conditions. Top row: laser spikes; middle row: time resolved spectra. Center of streak corresponds approximately to 1.06μ. Bottom row: near field pattern at 3X magnification. (a) R_1 = 95% R_2 = 80% input energy 80 joules (just above threshold). (b) R_1 = 95% R_2 = 80% input energy 120 joules. (c) R_1 = 95% R_2 = 20% input energy 800 joules.

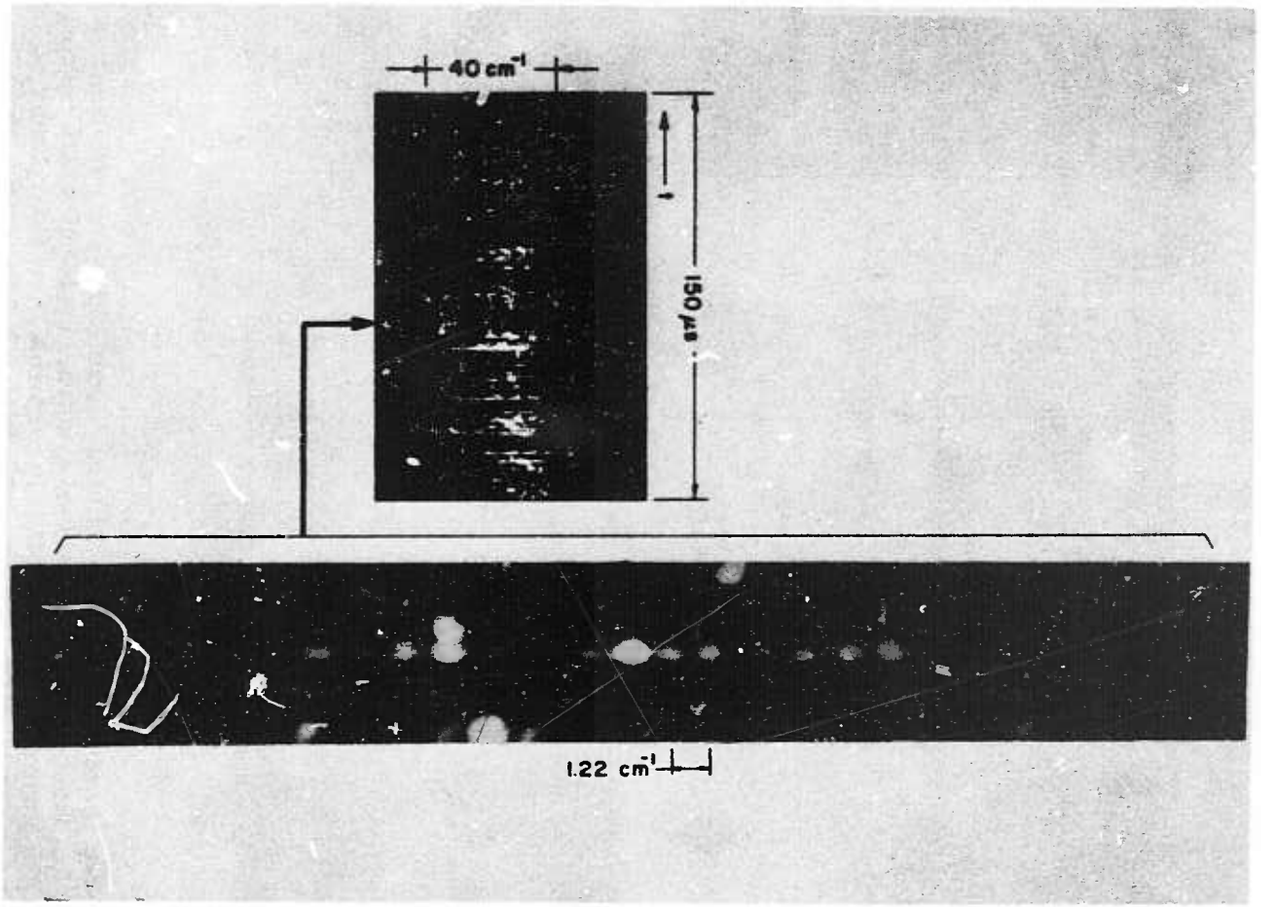

Figure 5-26. Streak Spectrum Obtained with R_1 = 99.9% R_2 = 80% and a Single Magnified Row of "Beads." Spacing Between Beads 1.22 cm^{-1}.

shorter duration ($< 0.63\ \mu s$) than those giving rise to the large dots. The spectral broadening is accompanied by the disappearance of mode patterns. The near field shows, instead, the occurrence of bright filaments. In some cases when the spike density is low, it is possible to correlate particular spikes with particular "strings," although not with filaments whose picture is time integrated. Examination of a large number of photographs shows that the occurrence of filaments is invariably accompanied by the broadening or "beading" of the streak spectrum and vice versa. Neither of these phenomena could, however, be correlated with the spike heights. This is understandable, since filament formation is likely to depend more critically on field configuration rather than intensity.

The diameter of the filaments was estimated in two different ways. If we assume that the diameter d of a "bead" can be identified with the Airy disc of a diffracting filament, then the diameter D of the filament is given by $D = 1.22\ f\lambda/d$ where m is the magnification of the optical system. Typical values of D are of the order of 1 mm. The second estimate can be obtained from direct photographs and yields values between 0.5 and 0.8 mm. Neither of these can be taken as too accurate because of the obvious difficulty in focusing at 1.06μ.

In another experiment (see Figure 5-24), the lens L was placed so that its focal point was 20 cm in front of the spectrograph pinhole. With wire stops placed at this focus, no light from the laser could be detected entering the spectrograph independent of the position of another lens placed between the stop and the pinhole. This demonstrates that light emerging from the laser, including filament light, is very nearly parallel. This parallelism, together with the estimated diameters of the filaments, indicates that the observed phenomena are due primarily to large scale trapping.[114]

It has been shown earlier that at very low reflectivities ($\leq 1\%$) of the output mirror, the peak power of the laser spikes can be increased to multimegawatt levels and their duration reduced to 20-40 ns. Under these conditions the giant spikes give rise to simple mode patterns. Figure 5-25c shows the results obtained with $R_2 = 20\%$ which represent an intermediate case. Both the spectral broadening and the filaments have disappeared and some mode patterns are again discernible. Hence, in this regime, like in the case (Figure 5-25a) of high reflectivity and low pump energy, the laser again does not appear to be dominated by effects leading to filament formation.

The enlarged "string of beads" shown in Figure 5-26 shows some intensity modulation along its length. This is often, but by no means always, observed. Many strings show a monotonic intensity decrease towards the Stokes and anti-Stokes sides. Other features which distinguish this broadening from that observed in CS_2[114] are the lack of elongation of the beads, and the constancy of their spacing. This spacing, which is equal to 1.2 cm^{-1}, is constant within one string, from one "string" to another and from one experiment to the next. It is also independent of the mirror spacing. We conclude, therefore, that the theory of the broadening proposed by Shimizu[115] and Cheung et al.,[116] based on the modulation of the refractive index, is not appropriate for the present case. Rather, an iterative effect similar to the optical mixing observed by Wiggins et al.[117] would appear to be more likely. It is difficult, however, to account for the rather large spacing of 1.2 cm^{-1} in terms of either Brillouin or Rayleigh scattering. Backward Brillouin scattering (at 6940Å) gives a shift of 0.2 cm^{-1} and stimulated Rayleigh shift is expected to be even smaller on account of the high viscosity of the laser solutions (~10 centipoise).

The disappearance of the broadening and the filaments under conditions of high laser peak power is not understood, but may be related to the duration of the laser pulses. If the molecular reorientational time τ is involved in the mechanism of the phenomena described here, we may expect their time constant to be large. Since the laser solutions are viscous and presumably contain large solvated entities, the relaxation times could well be in the 10^{-8} - 10^{-7} s range. This would make them comparable to the duration of the spikes.

6. LONG-PULSE, HIGH AVERAGE POWER OSCILLATOR

On the basis of the spectroscopic data and a comparison with both the YAG and glass materials doped with Nd^{+3}, we were able to project that high output pulse energies were to be expected from the liquid laser systems. This was, indeed, shown in the experimental work on static, liquid-laser systems and the achievement of high average powers depends on attaining a reasonable repetition rate. In the work to be described, repetition rates used ranged up to 10 pps, depending on the input pulse energy.

In repetitively-pulsed operation, serious thermal and thermo-optical problems arise as the average power input increases. All laser systems involve a significant dissipation of pump power as heat, and in four-level laser systems, such as Nd^{+3}, there is an additional energy arising from the relaxation between the terminal laser level and the ground state that is also dissipated as heat. For Nd^{+3} laser systems, the total dissipation can amount to as much as 50% of the absorbed power. The deposition of this heat is radially asymmetric for cylindrical laser geometrics, and leads to severe thermo-optical distortions resulting in substantial loss in output and deterioration of beam quality.

Various approaches have been used in coping with the thermal problems of repetitively pulsed lasers. In one of the more common approaches the active material is segmented and the coolant circulated between the segments as well as around the outside of the active material. This has met with some success but has difficulties associated with it. The alternative of the liquid medium has obvious advantages. The medium is circulated and the heat deposited in it is removed convectively by the gross movement of the liquid through an external heat exchanger. If the active volume in the cell can be exchanged for each excitation pulse, a fresh isothermal laser medium is always available. A second problem is, however, created by the use of liquid media and that is the cell. This, too, absorbs pump power and its temperature rises. The thermal problem here is somewhat easier to deal with, since it is a thin cylindrical shell and can be cooled inside by the laser liquid and outside by a circulating coolant.

In this section we describe the results on three different experimental arrangements. In the first, the cell has no external coolant and in the others, there is external cell cooling but the design is different. We also set up a model for reducing the experimental data, discuss the dynamic losses of the laser system,

and present the experimental behavior of the repetitively pulsed laser. We then discuss the results in terms of the hydrodynamic-thermal model developed in Section 4.

6.1 BRIEF DESCRIPTION OF THE LASER SYSTEMS STUDIED

The principles involved in the construction of the circulatory liquid laser system and in the design of the components have been given in Section 3. In Section 3 the principles were applied, in detail, for the final system constructed, but the development of various components was traced through from beginning to end. In the course of this development, three different long-pulse oscillator systems were constructed and tested; the results of these experiments will be presented in this section. First, however, we will briefly describe the laser systems so that the experimental results can be related to the system structure and understood in these terms.

6.1.1 Laser System No. 1

The first, repetitively-pulsed, liquid laser system was of a very simple construction. The circulatory system was a shaft-seal pump described in Section 3.2.3.5 in series with a nose-piece type of cell, 10 inches long and 0.5 inches in diameter. The cell had no external water jacket and was enclosed in a dual elliptical flash head. A shell and tube type heat exchanger completed the circuit. The power supply used was the one manufactured by Hadron, Inc. and series injection triggering was used to fire the flash lamps. Four different fills of laser liquid were used and before each fill, various modifications were made to the circulatory system, principally in the shaft-seal arrangement on the circulatory pump.

6.1.2 Laser System No. 2

To increase the high-average, power performance with an improvement in beam quality, a number of modifications were made to the design of the exploratory Laser System No. 1. In this laser, there were two four-lamp flash heads, one close-coupled and the other a quadruple ellipse. In the close-coupled head external cell, cooling was provided by flooding the volume of the head between the cell and the reflector. While in the quadruple ellipse, the cell itself was equipped with an external water jacket. The other modifications to the circulatory system were the installation of a 2μ porosity-fritted, quartz-liquid filter in a bypass arrangement, an improved heat exchanger, and the use of the Liquidyne pump. The filter path was so arranged

that about 10% of the laser liquid passed through the filter on each circuit. The Liquidyne pump, described fully in Section 3, proved to be an ideal solution to the pump problem since it eliminated the shaft seal problem completely.

The Systomation, Inc. power supply replaced the Hadron unit used in Laser System No. 1 and it proved to be more reliable and reproducible.

The output detection and measuring system was also modified. The laser output was collected by a lens, and passed into a beam splitting arrangement so made that the measured output was not dependent on any possible polarization of the laser output. A part of the output was sent to an EG&G Lite-Mike, functioning in the integrating mode. The output from the photodetector was sent to a Honeywell Visicorder recorder. Another part was directed to another port that could be equipped with a second photodetector or blocked off. The bulk of the beam was transmitted directly through the beam splitter arrangement and could be used for other purposes or simply absorbed.

The thermal load of the dissipated power was divided between two cooling circuits. One included the flash lamps, flash head and cell water jacket and the other the laser liquid. The temperatures of the cooling water in the two circuits were monitored and separately controlled, so that a temperature differential between the laser liquid and the cell coolant could be established. In principle, the cooling system was satisfactory, however the temperature regulation process was too slow and the thermal inertia of the cooling system too large for any long time experiments.

6.1.3 Laser System No. 3

The new features incorporated into this laser relate to the design of the cells and to the cooling system. The water jackets in these cells were thinner and constructed in conformity with the calculations of Section 3.2.4.5. In each case, the cell jacket and cell wall thickness were designed so that the entire cell volume would be pumped when the optical focussing properties of the material, external to the cell volume, were taken into account.

The cooling system was improved by the addition of a unit designed for this application and purchased from Systomation, Inc. The basic unit provided deionized water for the flash lamp, cell water jacket and flash head cooling. This was the bulk of the thermal load. The second was used to cool the laser liquid when it passed through the heat exchanger. The temperatures were controlled by Harrell

proportional controllers and the sensors were thermistor units, one monitoring the temperature of the laser liquid after it exited from the third cell and the other monitoring the temperature of the deionized water as it entered the cell water jacket. Similarly placed iron-constantan thermocouples measured these temperatures and either the actual temperatures or their difference could be read. The difference in temperature was also recorded on one of the channels of the Honeywell Visicorder used to record the laser output. The difference temperature variation was kept to $\pm 0.1^{\circ}C$ during a run. The laser output was recorded as in the previous experimental arrangement.

This cooling arrangement proved far more satisfactory than that used in Laser System No. 2. The circulatory system contained three laser heads, one a quadruple ellipse and the other two double ellipses. The dimensions of the cell in the quadruple ellipse was 0.875 inch diameter and 10 inches in length, while those in the double ellipses were 0.625 inch diameter and 10 inches in length, and 0.5 inches diameter and 6.5 inches in length, respectively. These dimensions were selected to provide flexibility to the system. Individually, the cells could function as long-pulse oscillators in different repetition-rate and pulse-output energy regimes or, if used simultaneously as an amplifier chain or in an oscillator-amplifier mode.

6.2 EXPERIMENTAL PROCEDURE TREATMENT OF THE DATA

Before presenting the experimental results, the experimental procedure will be described and the parameters clearly delineated so that a reasonable means for reducing the mass of data can be obtained.

A run is made in the following manner. For a predetermined temperature differential between the laser liquid and the cooling water in the cell water jacket (ΔT), a series of laser pulses is run off at preset repetition rates and pulse input energies. The laser output for each pulse is detected and recorded as is the temperature differential during the run. The number of pulses in a given run is large enough so that the transient pulse output, usually encountered in the first few seconds, has died down and the pulse output energy has become sensibly constant. The number of pulses in a train for any other than a quasi single-shot experiment is never less than 15 and can be as large as 80. For a given temperature differential, the set is completed by repeating the above procedure until the desired set of repetition rates and pulse-input energies has been spanned. The pulse-output energy characteristics of a given set of conditions is taken to be the steady state value, since by this time, the thermal conditions have also become steady.

The independent variable is the average input power, the dependent variable is the average output power, and the parameter is the temperature differential set between the water coolant external to the laser cell and the laser liquid. The average power input is, of course, the pulse energy times the repetition rate. However, this is only an approximate variable. In terms of the heat deposited in the laser liquid, average power is not important as long as there is at least one exchange of the active volume per pulse. The real effect is in the cell wall itself. The heat deposited here has to be removed by convection and conduction. Let us consider the particularly simple example of a thin sheet of material in contact with an infinite reservoir maintained at a fixed temperature. Now, let the temperature of the sheet be suddenly increased. The rate of cooling will follow an exponential law

$$\Delta T = \Delta T_0 e^{-Kt} \tag{6-1}$$

where ΔT is the temperature of the sheet above the reservoir at time t, ΔT_0 is the initial rise in temperature, and K a constant governing the heat transfer between the sheet and the reservoir. For a fixed average power input, the response of the system will vary with the repetition rate, as can be readily shown. We take as the lowest repetition rate one pulse per second and assume that the energy of this pulse raises the temperature by ΔT_0. We further assume that at a higher repetition rate, α, the temperature increment is $\Delta T_0/\alpha$ per pulse. Then at the end of N pulses, just before the delivery of the (N + 1) pulse, the temperature increase of the sheet is:

$$\Delta T = \frac{\Delta T_0}{\alpha} \sum_{\beta=1}^{N} e^{-\frac{\beta K}{\alpha}} \tag{6-2}$$

The behavior of this function as a function of time (N/α) is shown in Figure 6-1. For a fixed value of K, $\Delta T/\Delta T_0$ increases faster and reaches a higher steady value for higher repetition rates. Furthermore, the steady values for $\Delta T/\Delta T_0$ decrease with increasing K, as shown in Figure 6-2. This analysis indicates that the average power input is only an approximate variable when describing the thermal behavior of the laser; it is, however, the most convenient. In using it, we expect to find that the experimental points will scatter, but that we can get a semiquantitative understanding of the processes involved.

During the course of an experiment, the cell wall temperature will rise and, if the system were initially isothermal, there will ultimately be a thermal gradient, due to the difference in temperature between the circulating laser liquid and the cell

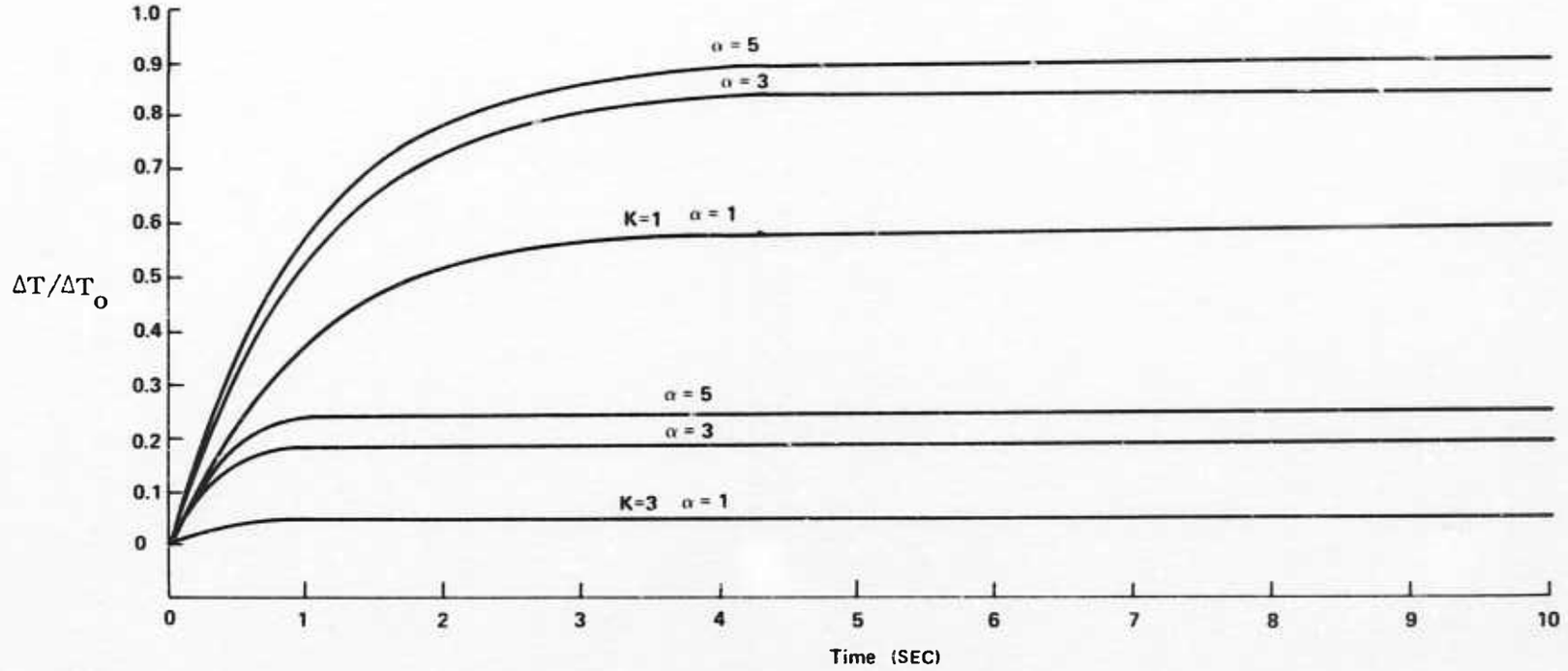

Figure 6-1. Behavior of Cell Wall Temperature for Different Heat Transfer Constants (K) and Pulse Repetition Rates (α)

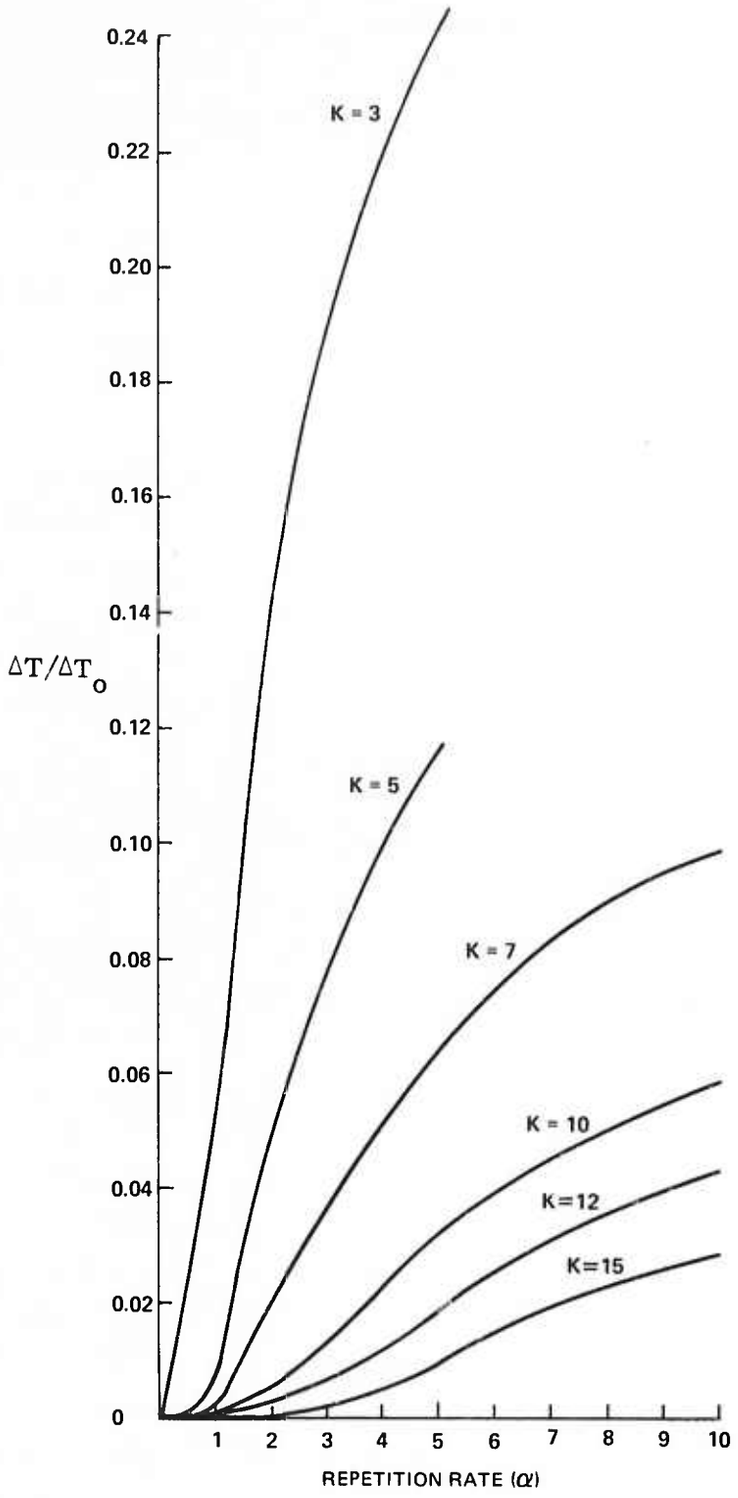

Figure 6-2. Steady Values of $\Delta T/\Delta T_o$ for Different Values of Heat Transfer Constant (K) as a Function of Pulse Repetition Rate (α)

wall, that will lead to optical distortion of the laser medium and a consequent deterioration of the output. Experimentally, as we shall see, this is readily observed as an initial decrease in laser output with each pulse until the steady state sets in. If the thermal constant, K, is large enough and the repetition rate low enough, the system will recover between pulses, (for example, a rate of one pulse per second and a value of $K \geq 7$ in Figure 6-2). The output will show no significant variation for the duration of the pulse train. This has been observed experimentally under isothermal conditions. The pulse output, in this case, is the same as observed from a properly executed single shot experiment and is affected only by the flash induced distortions. This is the maximum that can be obtained from a given system under a given set of pumping conditions and it becomes the normalization value. The steady-state, pulse-output energy under other thermal and pumping conditions normalized to the value described above is the dependent variable. A series of such curves, parametrized by the externally imposed temperature differential between the laser liquid and the external water coolant, constitute the reduced experimental data. A second parameter is the circulation rate of the laser liquid; this affects the Reynolds number and the heat transfer rate between the cell wall and the laser liquid.

6.3 SINGLE SHOT OUTPUT AND DETERMINATION OF DYNAMIC LOSS

When the repetition rate is low enough (≤ 1 pps) and the laser solution and cell are isothermal, the output from each pulse of a train is constant. In terms of output, this is equivalent to a static experiment. The circulation of the liquid has, however, resulted in a marked increase in the repetition rate. The output data for Laser System No. 1, for different output reflectivities, is shown in Figure 6-3. Output data for Laser Systems No. 2 and No. 3, under similar thermal and repetition rate conditions, are illustrated in Figure 6-4. These are for a 52% output mirror reflectivity. The improvement in performance for the quadruple elliptical head of Laser System No. 3 over that in System 2 is related to the improved coupling of the flash lamp radiation to the laser liquid. This, as is seen, resulted in nearly 100 J output pulses for a 4000 J input pulse. That these results are virtually independent of repetition rate and do constitute an isothermal reference output is shown in Figure 6-5. The data were obtained from Laser System No. 2. For one part of the experiment, the pulse repetition rate was kept constant at 0.5 pps independent of the pulse input energy. For the other part, the repetition rate was decreased as the pulse input energy increased so that the average power input remained constant at 350 watts.

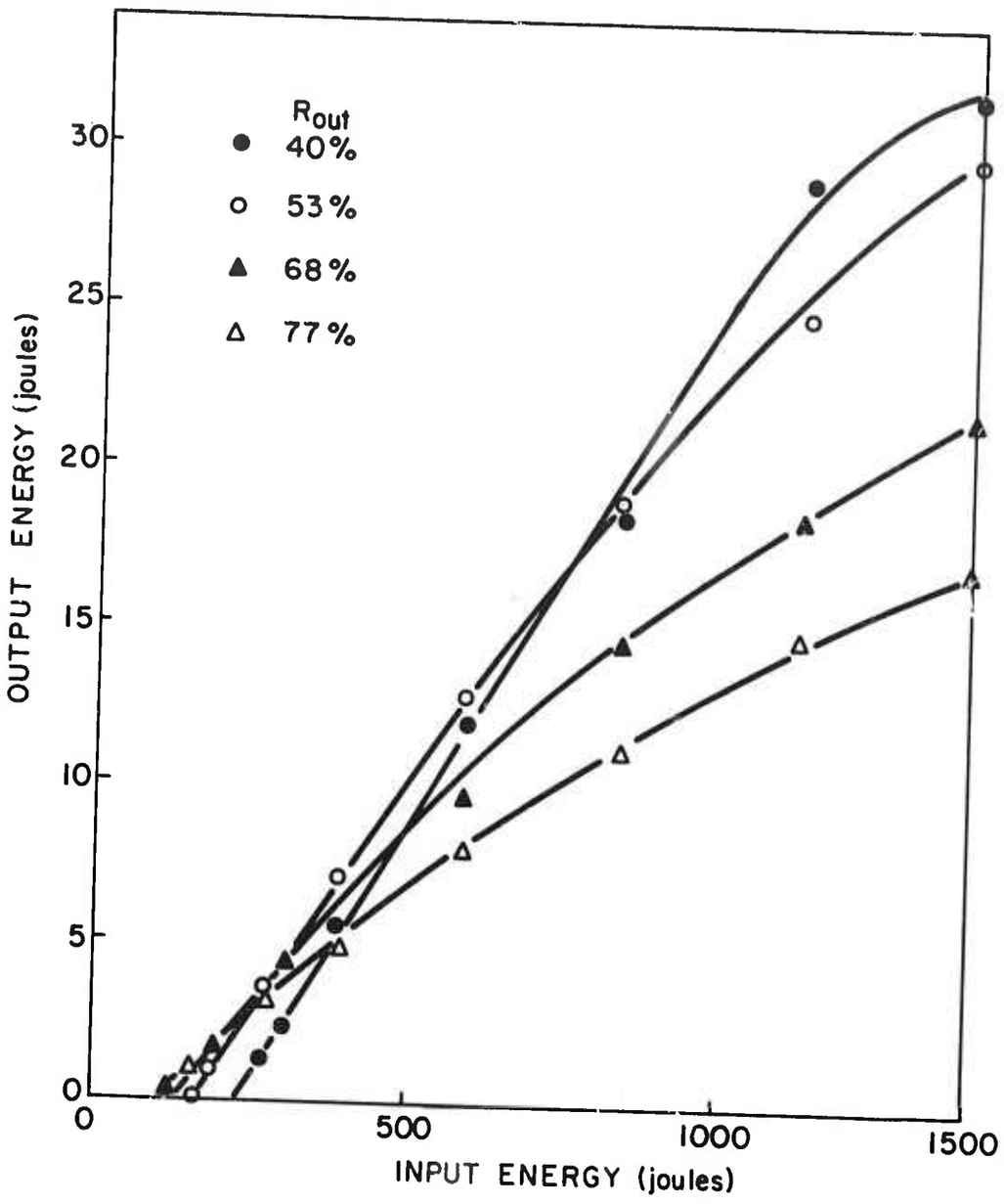

Figure 6-3. Energy Output as a Function of Energy Input of the Liquid Laser for Different Output Mirror Reflectivities

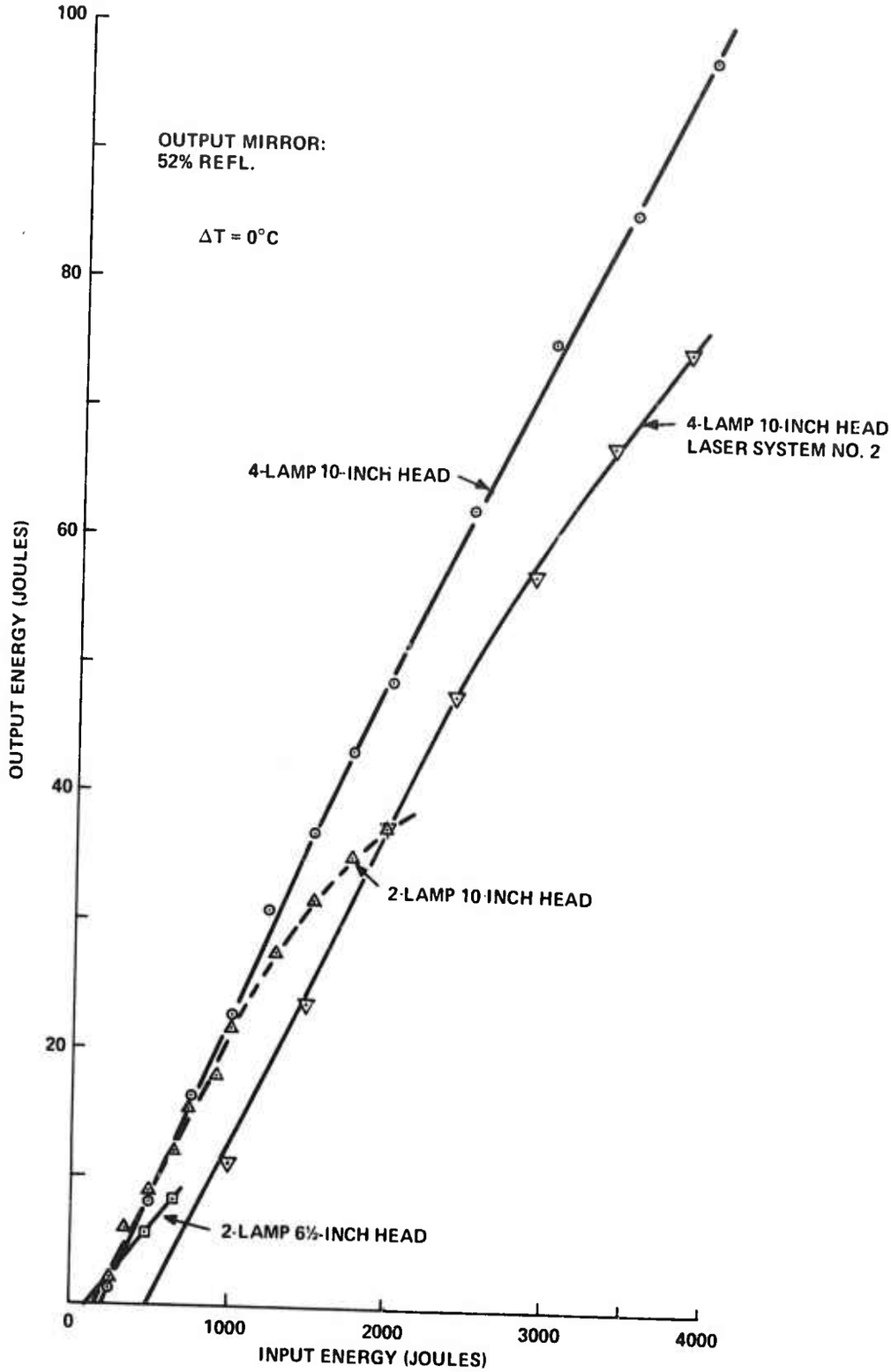

Figure 6-4. Output Energy vs. Input Energy for the Three Laser Heads With $R_{out} = 0.52$ and $\Delta T = 0$. Re for four-lamp head = 6,000. Re for two-lamp 10" head = 8,400 and Re = 10,000 for the two-lamp 6.5" head.

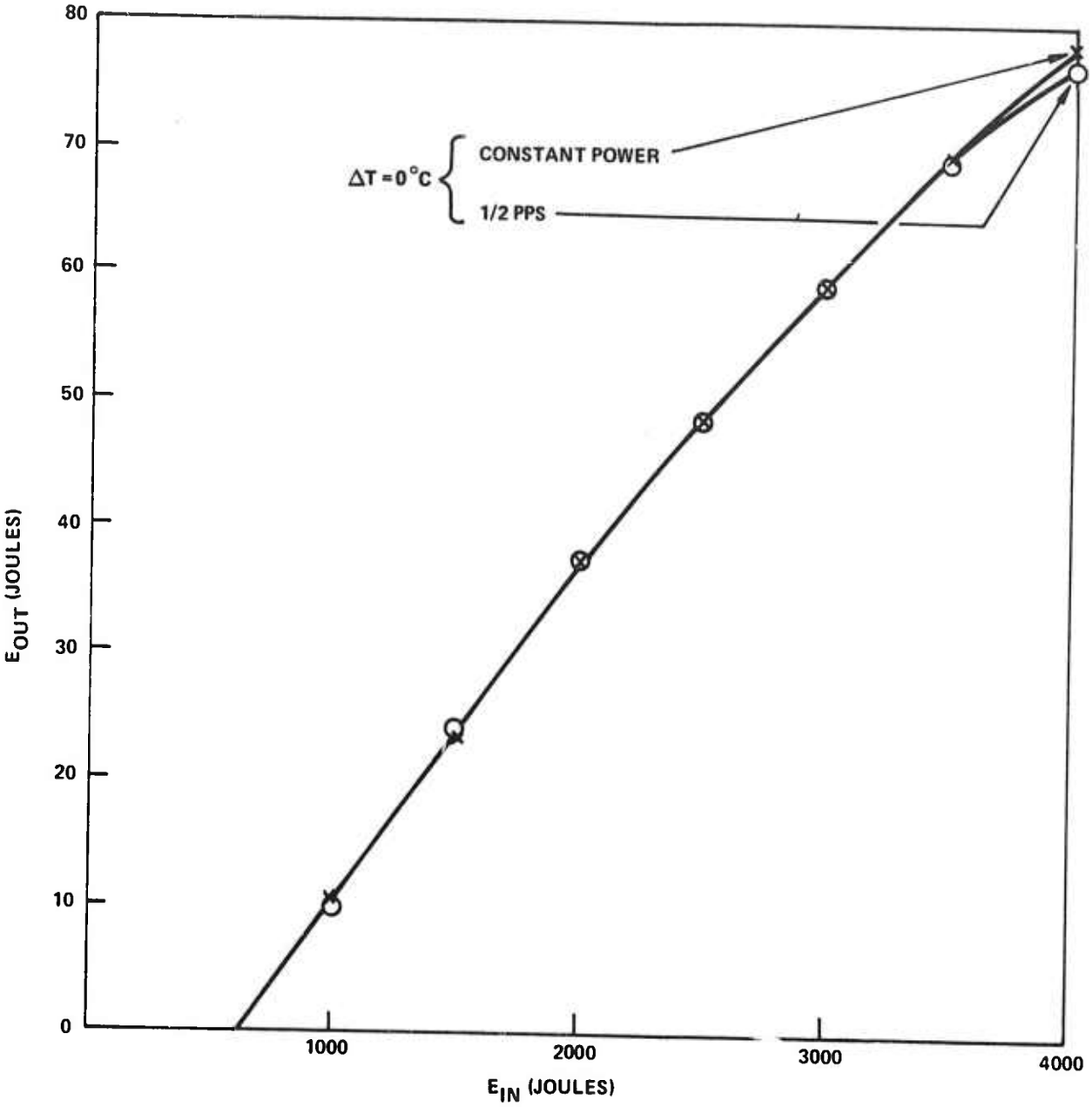

Figure 6-5. Output Energy Versus Input Energy at a Low Average Input Power

As is seen, the pulse output energies are indistinguishable except at the 4000 J input level. From this, it is concluded that up to 0.5 pps cumulative thermal effects are negligible with the laser medium circulated. These output results are used to normalize the output energies obtained under other thermal and repetition rate conditions. In general, they represent the maximum pulse output for a given pulse input.

Dynamic Loss

The single-shot experiments were also used to determine the dynamic loss. To do this, the intercept and slope information, obtained from experiments as illustrated in Figure 6-3, were treated according to Eqs. (5-8) and (5-10). For Laser Laser System No. 1 only, the threshold information was used and is plotted in Figure 6-6; the dynamic loss is 0.35% cm^{-1}. A similar plot for Laser System No. 2 is shown in Figure 6-7 and the dynamic loss here is 0.25% cm^{-1}.

For Laser System No. 3, both the threshold and slope efficiency information was used to obtain the dynamic loss. Typical threshold plots, E_T versus $-\ln R_{out}$, for the three lasers are shown in Figure 6-8. In the case of slope efficiency, η_s^{-1} is plotted against T_{out}^{-1} (T_{out} = output mirror transmission) and these are shown in Figure 6-9. The losses are presented in Table 6-1.

TABLE 6-1

LOSS IN % cm^{-1}

System	E_T vs. $-\ell nR$	η_s^{-1} vs. T_{out}^{-1}
10" Quadruple Ellipse	0.36	0.52
10" Dual Ellipse	0.38	0.89
6.5" Dual Ellipse	1.30	1.95

Based on threshold energy, the values obtained for the larger lasers are typical of what is expected from the laser material. A substantially higher value for the small laser was obtained because this system was studied when the laser liquid had already begun to deteriorate. It should be noted that the loss values obtained from the slope efficiency information are higher than those from the threshold information. This seems always to be the case, and generally, from the way the points tend to scatter in these and other experiments, the values derived from the thresholds are probably more reliable.

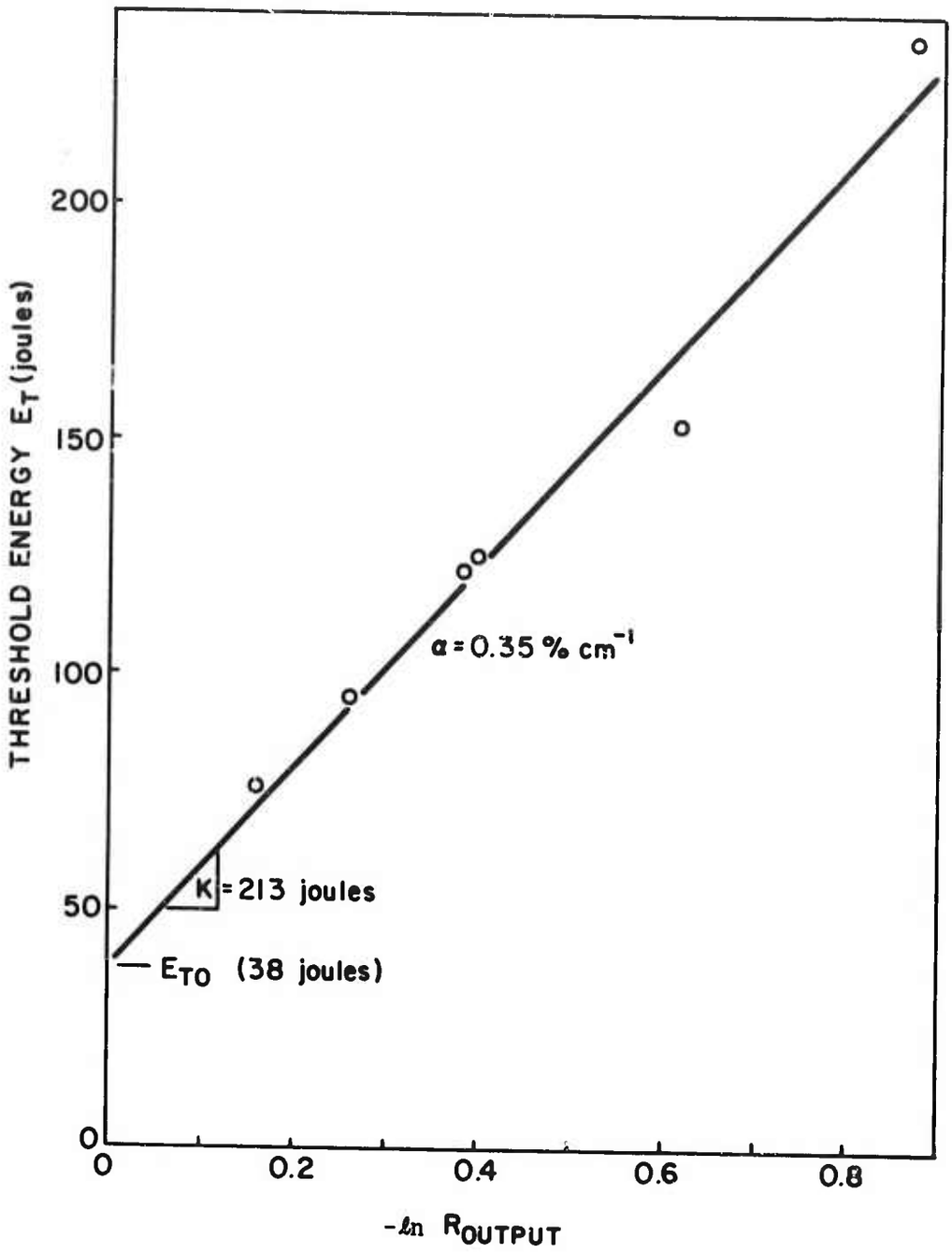

Figure 6-6. Laser Threshold as a Function of the Natural Logarithm of the Output Mirror Reflectivity

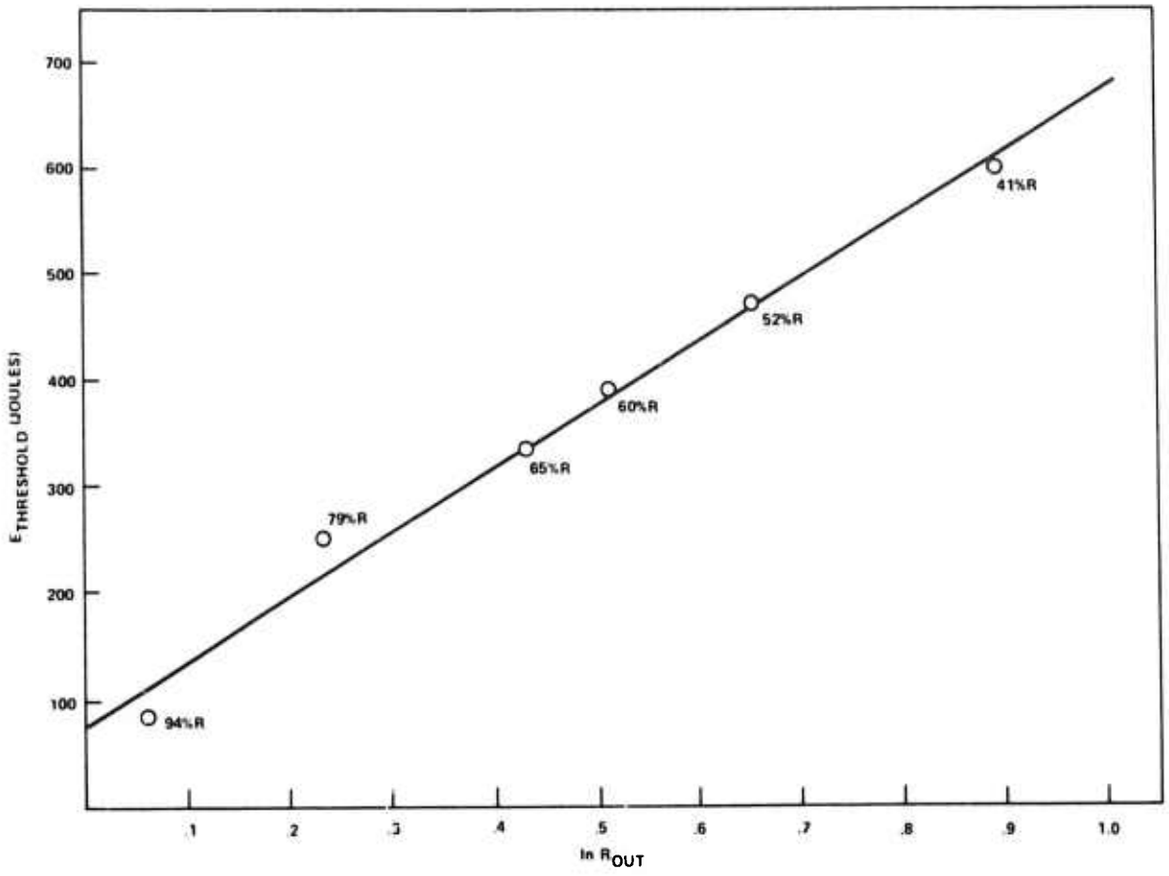

Figure 6-7. Plot of E_T Versus ln R for Focused Four-Lamp Flash Head in Laser System No. 2

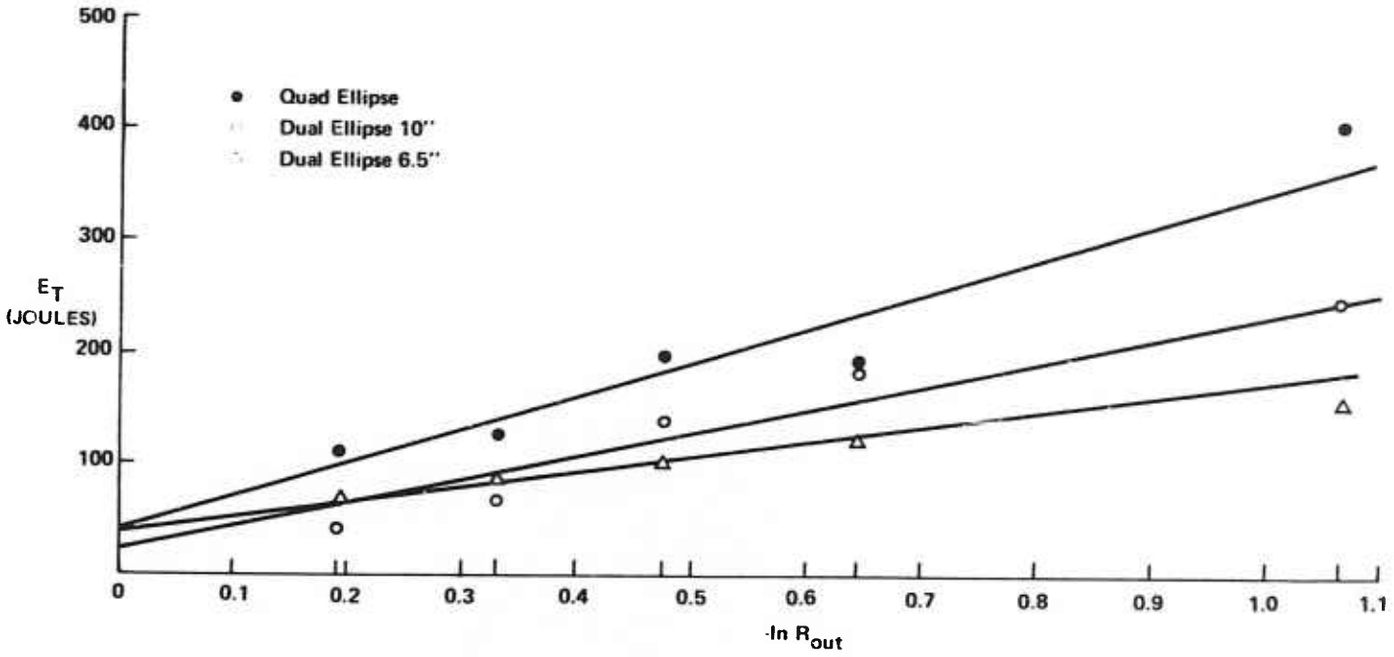

Figure 6-8. Plot of E_T Vs. $-\ln R_{out}$ for the Three Lasers in Laser System 3

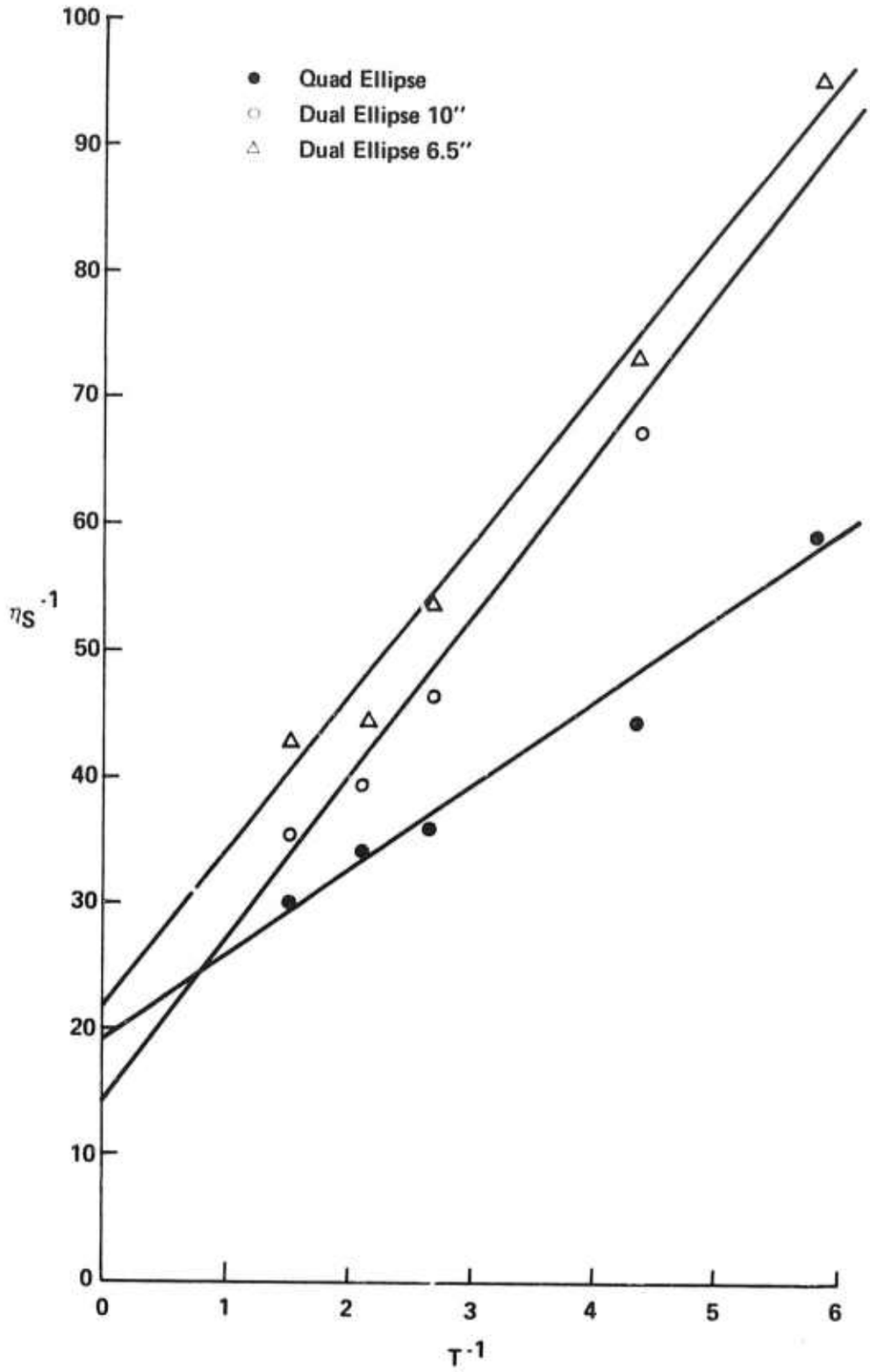

Figure 6-9. Plot of η_S^{-1} Vs. T^{-1} for the Three Lasers in Laser System 3

6.4 OUTPUT UNDER REPETITIVE PULSING

As was seen in the preceeding section (6.3), nearly 100 J output pulses are available under single-shot conditions. High average output power is most easily achieved by increasing the repetition rate, but under these conditions the cumulative thermal problem must be considered. The significance of this will become clear when the results of the three different laser systems are compared. In this section, we present the results of the repetitive pulse experiments.

6.4.1 Laser System No. 1

The purpose of this set of experiments was purely exploratory. Rather than present all the detailed results obtained, we will present only a summary of them stressing those results more pertinent to the behavior of repetitively pulsed liquid lasers. Typical output pulse trains are shown in Figure 6-10. These are obtained by deflecting a part of the output from a beam splitter into an EG&G Lite-Mike photodetector operating in the integrating mode. The output of the photodetector was put into an oscilloscope. The photodetector-oscilloscope combination was calibrated in single-shot experiments using a thermopile to measure the laser output. In each oscillogram, the upper trace is the laser output and the lower trace is the voltage to the capacitor bank. In general, the voltage variations are reflected in the laser output as a modulation of the overall decrease in output with time.

The salient characteristics of these traces are the decrease in pulse output energy with time and the time required to reach the steady state. At the 3 pps rate, the output decreases to about 60% of its initial value in a time of about five seconds. At the higher repetition rates, the steady value is usually less than 50% of the initial value, and the time required to reach it is perhaps slightly larger. The case of 4 pps at a Reynolds number (Re) 3300 is more like that of 3 pps at Re = 2200. In a qualitative way, these results bear out the temperature considerations of Eq. (6-2) for the case K = 1. That is, that there is an increase in the wall temperature resulting in a radial thermal gradient into the liquid and a consequent drop in output. This wall temperature effect is more pronounced at higher repetition rates and higher average input powers. The deleterious effect is decreased at higher flow rates, probably because of a more efficient heat transfer rate (larger value for K).

The best steady-state output power available from this system was about 75 watts, with an efficiency slightly greater than 1%. Part of this was due to the fact that the light output from the flash tubes began to saturate markedly at the higher pulse

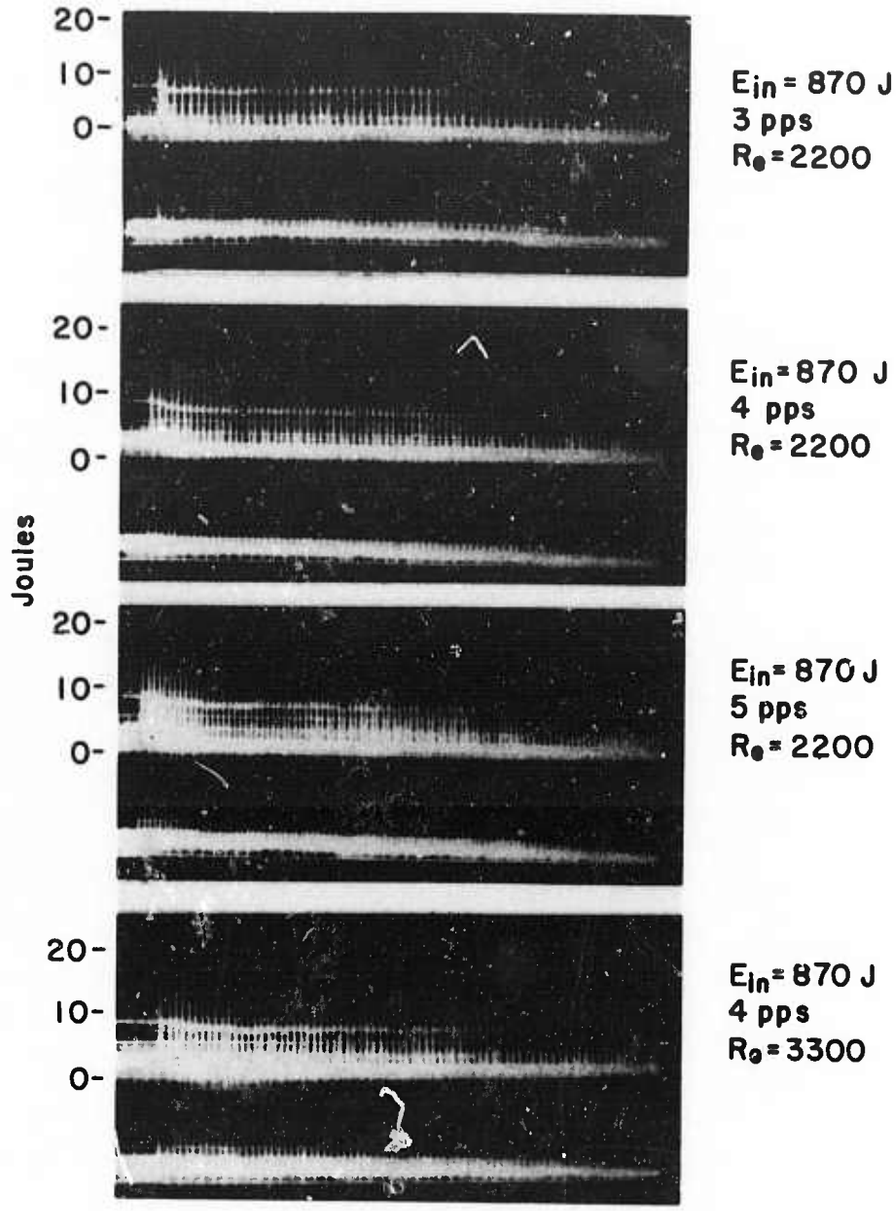

Figure 6-10. Output Pulses of Repetitively Pulsed Liquid Laser System No. 1 for Conditions Stated in Figure

input energies, but principally due to the lack of good control of the cell wall cooling and limited liquid flow speed.

6.4.2 Laser System No. 2

The basic work done with this laser was a study of the output in the repetitively pulsed mode of operation. The independent parameters were the pulse repetition rate, the pulse input energy and the temperature differential ΔT. The first two led to an average input power, while the third was an important factor in the steady state thermal condition of the laser. The dependent variable was the pulse output energy of the laser. For a given experiment, the input energy flow speed and repetition rate were selected and the laser was repetitively fired long enough to insure that a steady value of the pulse output energy was obtained. The output mirror reflectivity for these experiments was 52%, which is either at or near the optimum.

The most convenient way to represent the data is to plot the reduced pulse output as a function of average input power. The reduced pulse output is taken to be the pulse output energy under the given input power and temperature conditions, divided by the pulse output energy under isothermal conditions ($\Delta T = 0$), at a repetition rate of one pps or less at the flow speed used. The results for $\Delta T = 6.4°C$ and 8°C are illustrated in Figures 6-11 and 6-12, respectively. It should be noted that at low average power inputs, the normalized output, E/E_o, is significantly less than unity. At intermediate average input powers, E/E_o increases and then falls off again as the input is further increased. The curves for all the temperature differentials studied are illustrated in Figure 6-13.

The general characteristics of these curves clearly bear out the properties expected from a qualitative understanding of the thermo-optical behavior of a laser medium. All the curves (except for $\Delta T = 18°C$) pass through a maximum in E/E_o as a function of average input power. The maximum occurs at higher values of average input power as ΔT increases. On the low average input power side of the maximum, E/E_o fall off fairly sharply to a lower intercept at zero input power for increasing ΔT. On the high input power side, the curves tend to fall off more gradually in more or less the same way. A discussion of the experimental results will be given after those on Laser System No. 3 are presented.

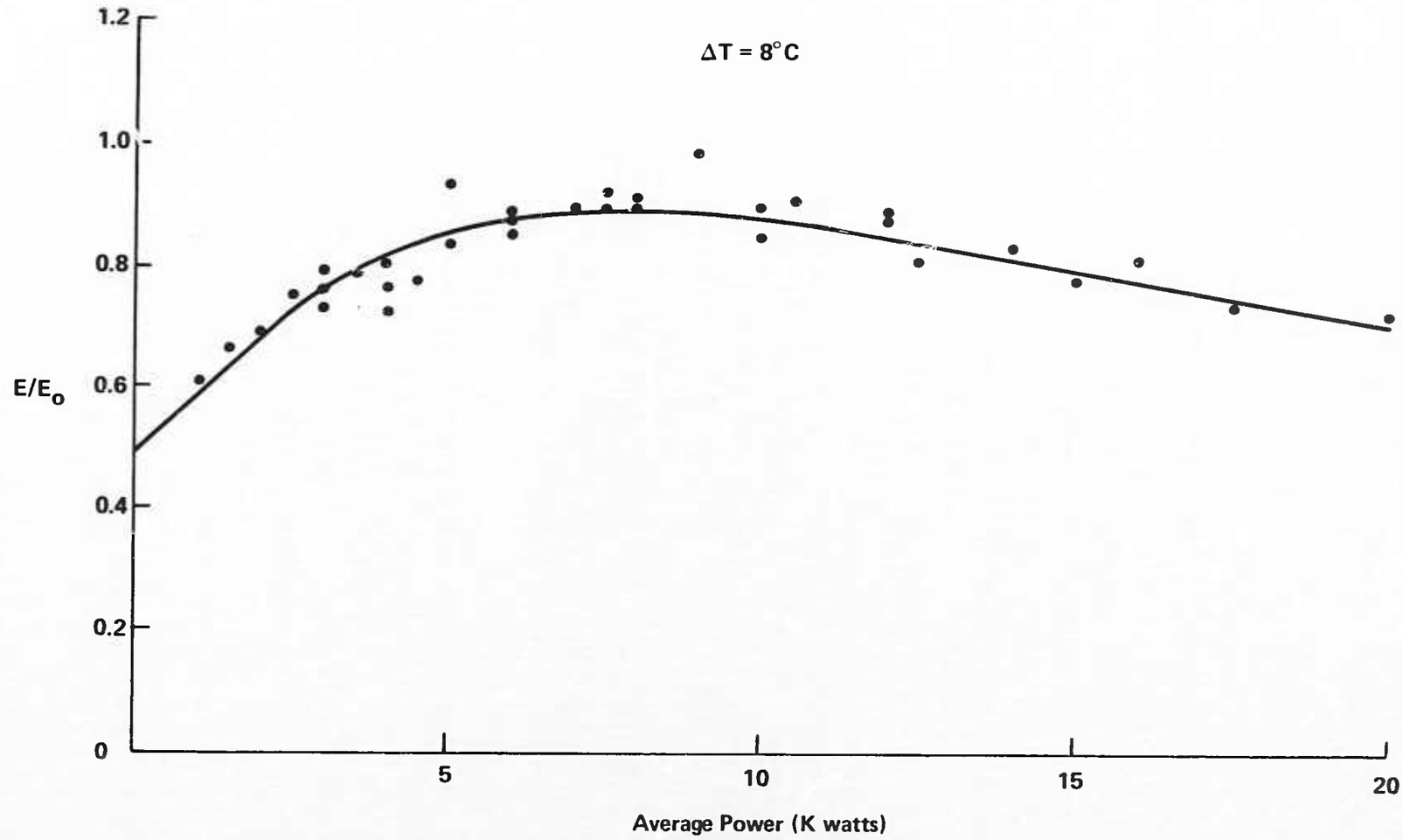

Figure 6-11. Reduced Output as a Function of Average Power Input for Laser System 2

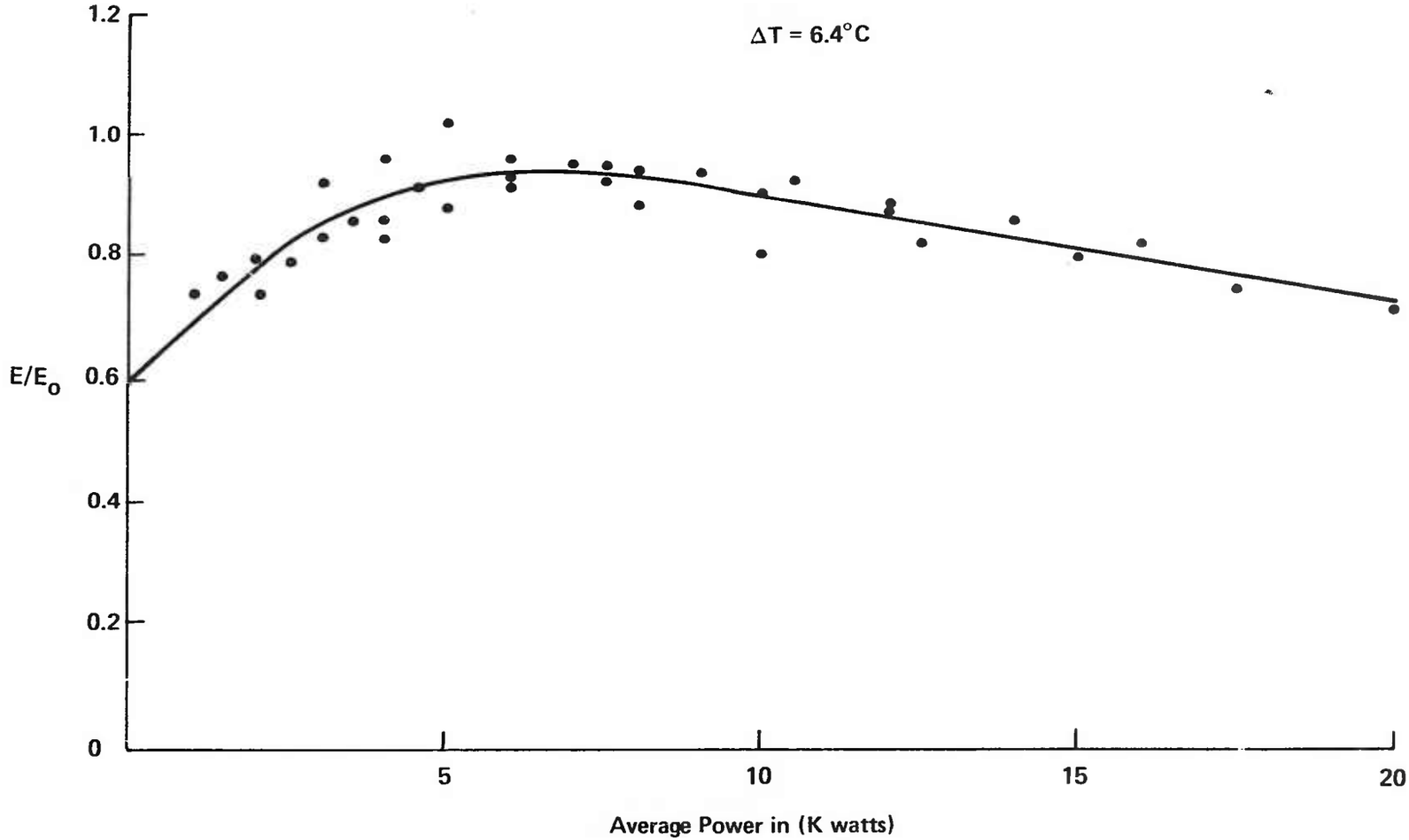

Figure 6-12. Reduced Output as a Function of Average Power Input for Laser System 2

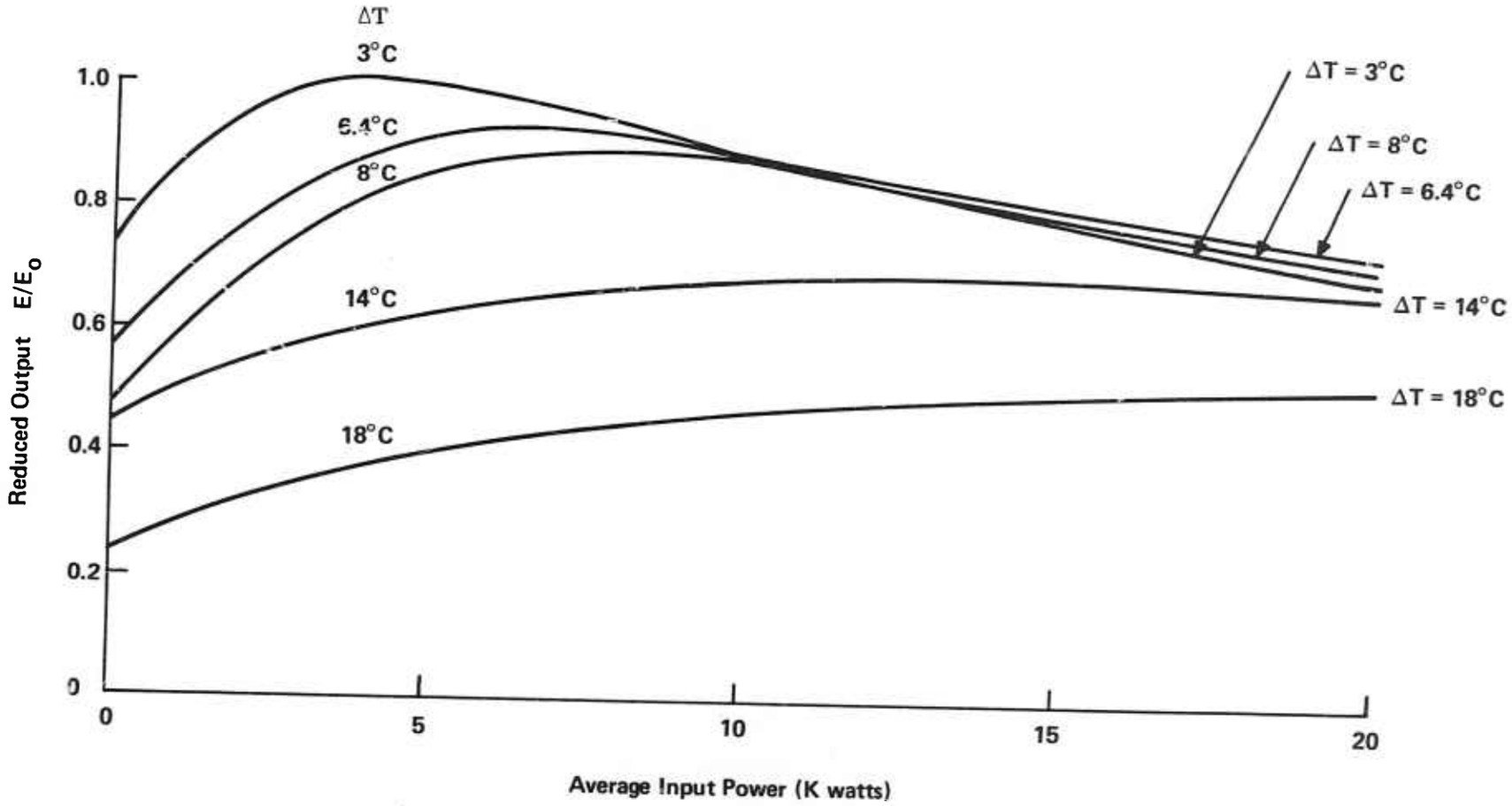

Figure 6-13. Reduced Output as a Function of Average Power Input for Laser System 2

6.4.3 Laser System No. 3

In the work on this system, considerable difficulty was experienced with the laser liquid and before proceeding to the actual experimental results, the state of the laser medium merits some discussion. The principal experience we had with the laser medium $Nd:POCl_3:ZrCl_4$ in a circulatory system was that of the experiments described in the preceding section (6.4.2). In this system, and in the Q-switched oscillator described earlier in Section 5, a single fill of the laser system was used for more than nine months. At the end of this time, the output and laser performance was indistinguishable from the results obtained after the initial break-in period was passed. This certainly is ample evidence for the long term stability of the laser liquid when it is properly prepared. In our own experience, sealed, one-liter ampoules have exhibited a shelflife in excess of three years and there is evidence of even longer shelf life (yet ongoing) from the experience of others. At the time the system we are now discussing was activated, new production runs of the laser liquid were used. In four different instances, the solution deteriorated rapidly. Twice, in fact, the degradation was detected before the ampoules were opened. The cause for this problem was ultimately traced to a relaxation in quality control steps on the part of the manufacturer. This problem caused lengthy delays in the progress of the work and made some interpretations of the data more difficult than necessary. All the results reported in this and the subsequent sections were obtained while the active liquid was still good or, in only a few instances, just as it started to deteriorate but at a state where appropriate correction could still be made.

In this section we will report the behavior of the three lasers separately. The experiments were carried out with three different fills but overlapping experiments indicate the results were comparable. Typical examples of the type of pulse trains observed are given in Figure 6-14. It is seen that the initial transient decayed reasonably rapid and that the steady state arrived in a time of two seconds or less. Similar results were observed with Laser System No. 2 and are to be contrasted with those of Laser System No. 1. In the latter systems (2 and 3), the steady state set faster and the drop off in output energy was not nearly as large.

A typical curve for $(E_{out}/E_o)_{\Delta T}$ versus average input power is illustrated in Figure 6-15 and the composite for all ΔT values at this Reynold's number flow are shown in Figure 6-16. The composite curves for Reynold's numbers of 8400 and 10,000 are shown in Figure 6-17 and 6-18, in which the individual data points have been suppressed for clarity. Figures 6-19 through 6-22 compare the data for different flow speeds at a fixed value of ΔT.

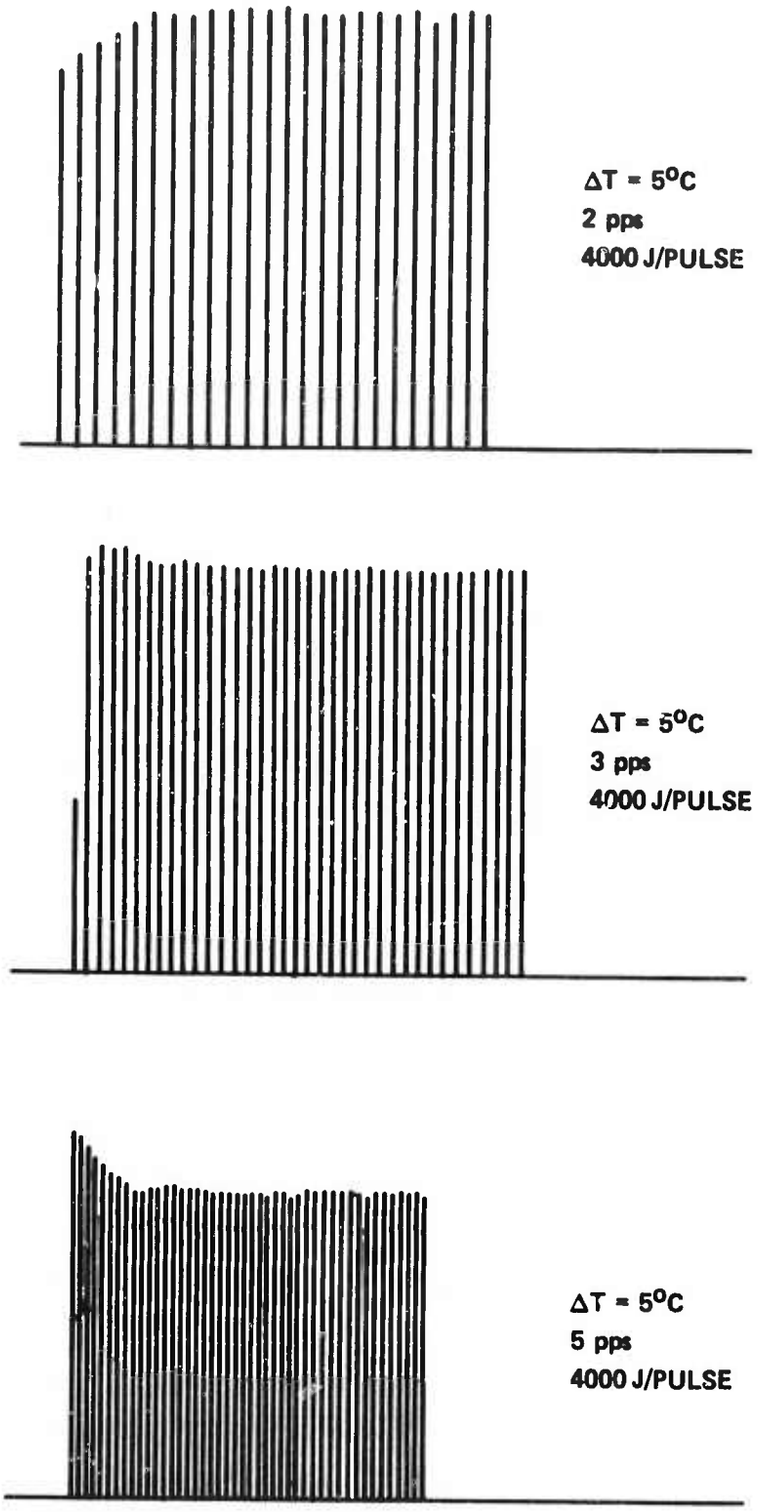

Figure 6-14. Three Typical Pulse Trains of Laser Output Energy vs. Time for the Same Initial Temperature Difference ΔT and Input Energy per Pulse. Pulse Repetition Rate Variable

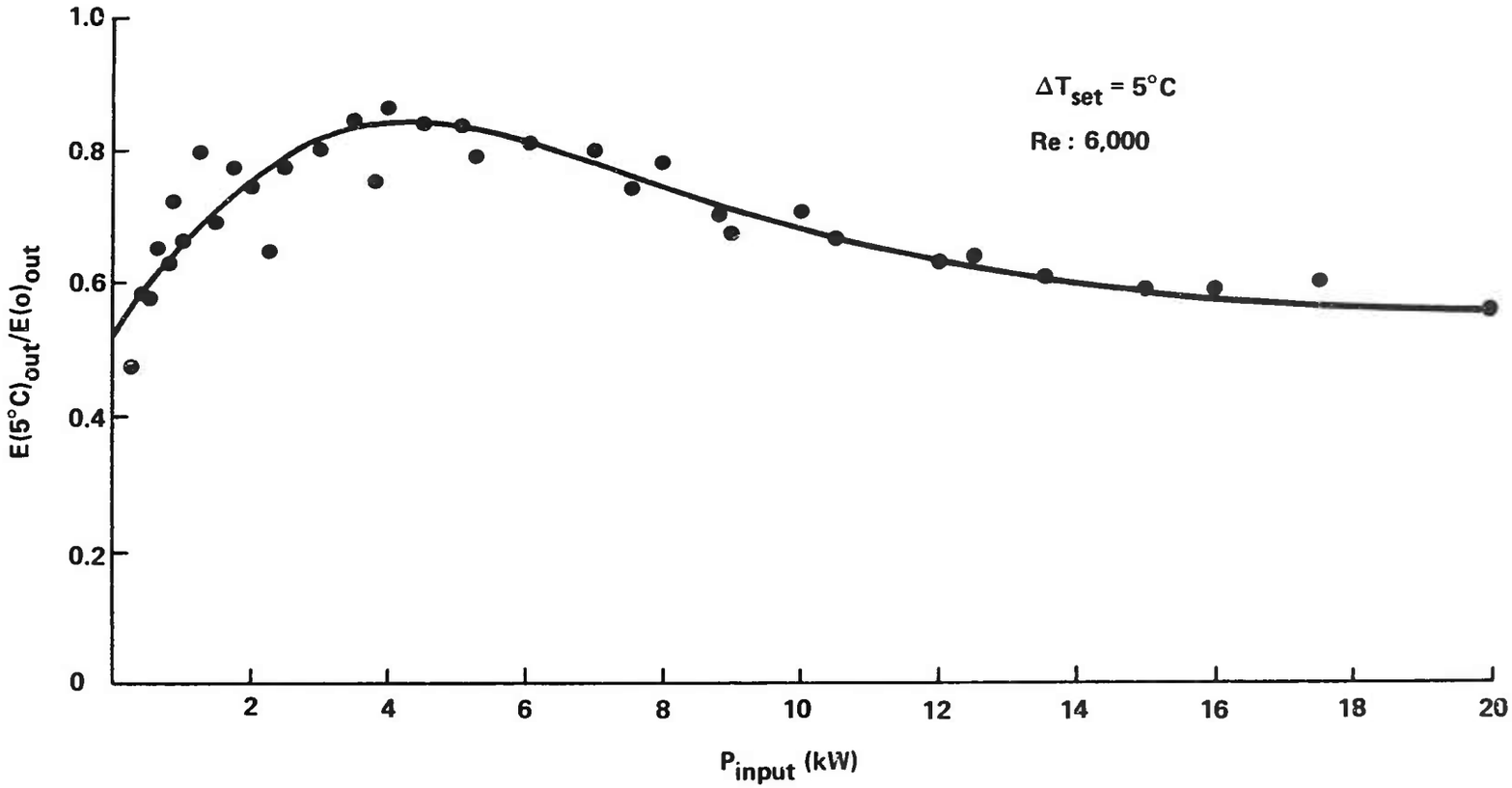

Figure 6-15. Laser Output for $\Delta T = 5\,^{\circ}C$ Normalized to Single-Shot Output for $\Delta T = 0$ vs. Average Input Power. Reynolds number: 6,000. Data points retained to show scatter.

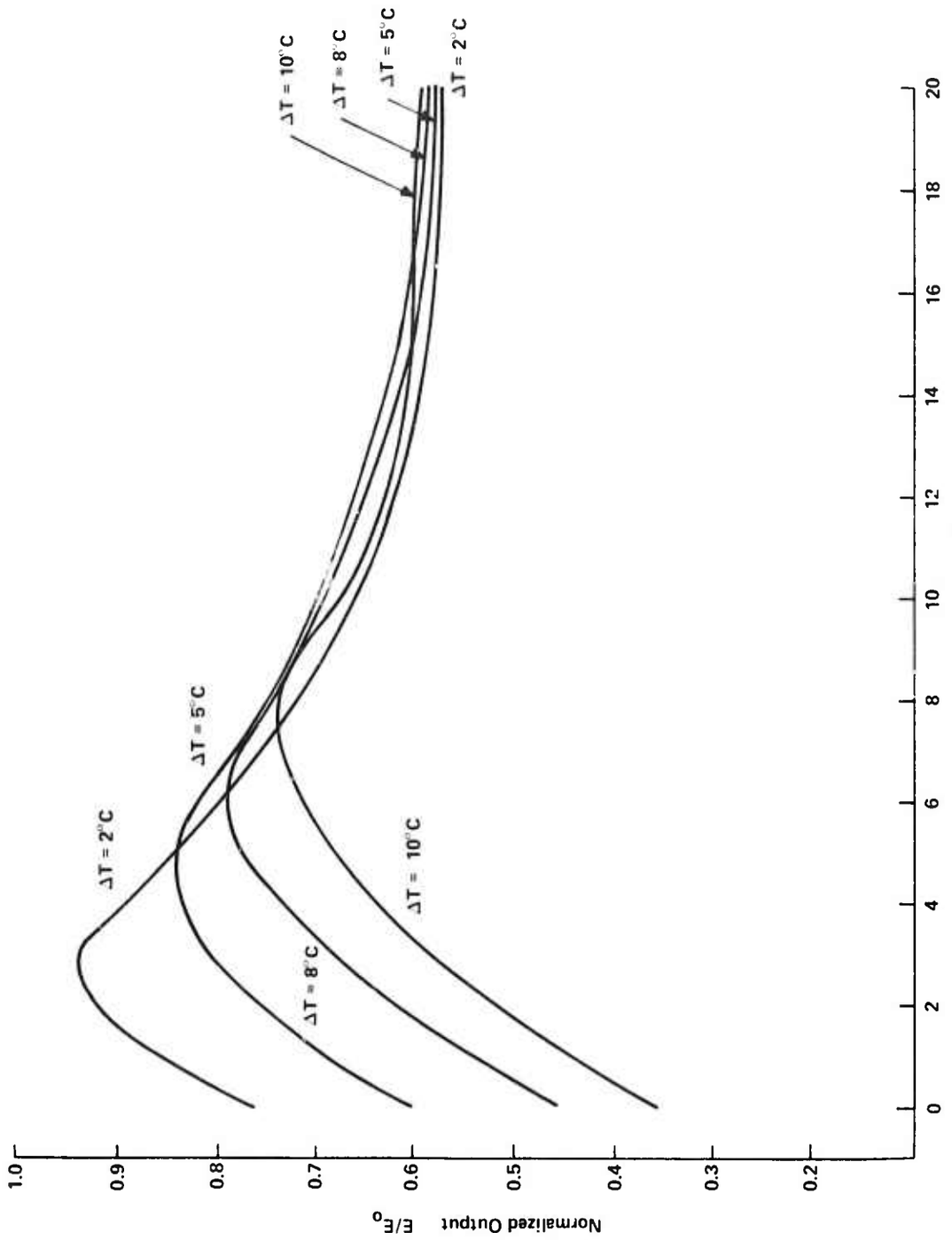

Figure 6-16. Quadruple Ellipse Reynolds Number 6000

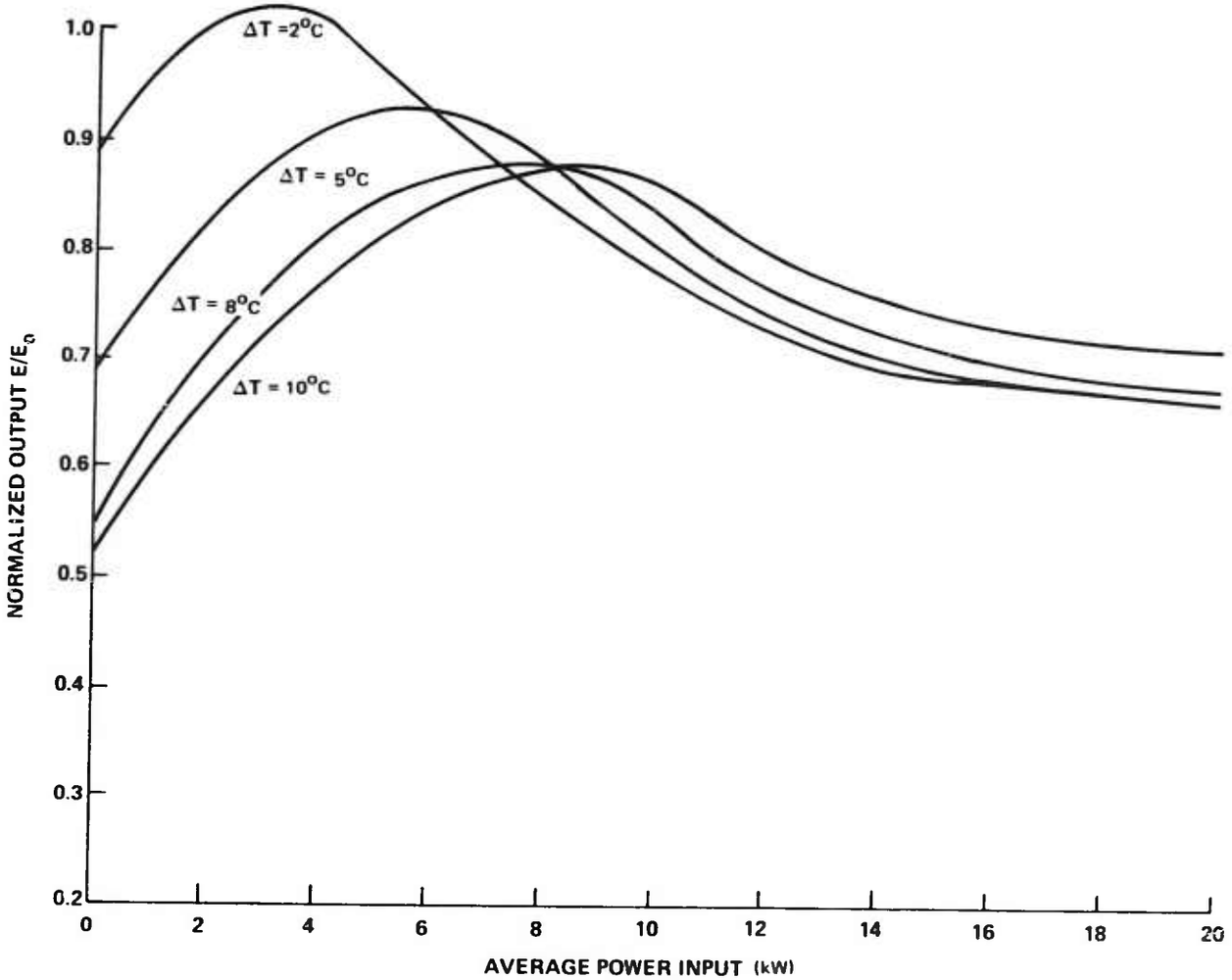

Figure 6-17. Quadruple Ellipse Reynolds Number 8000

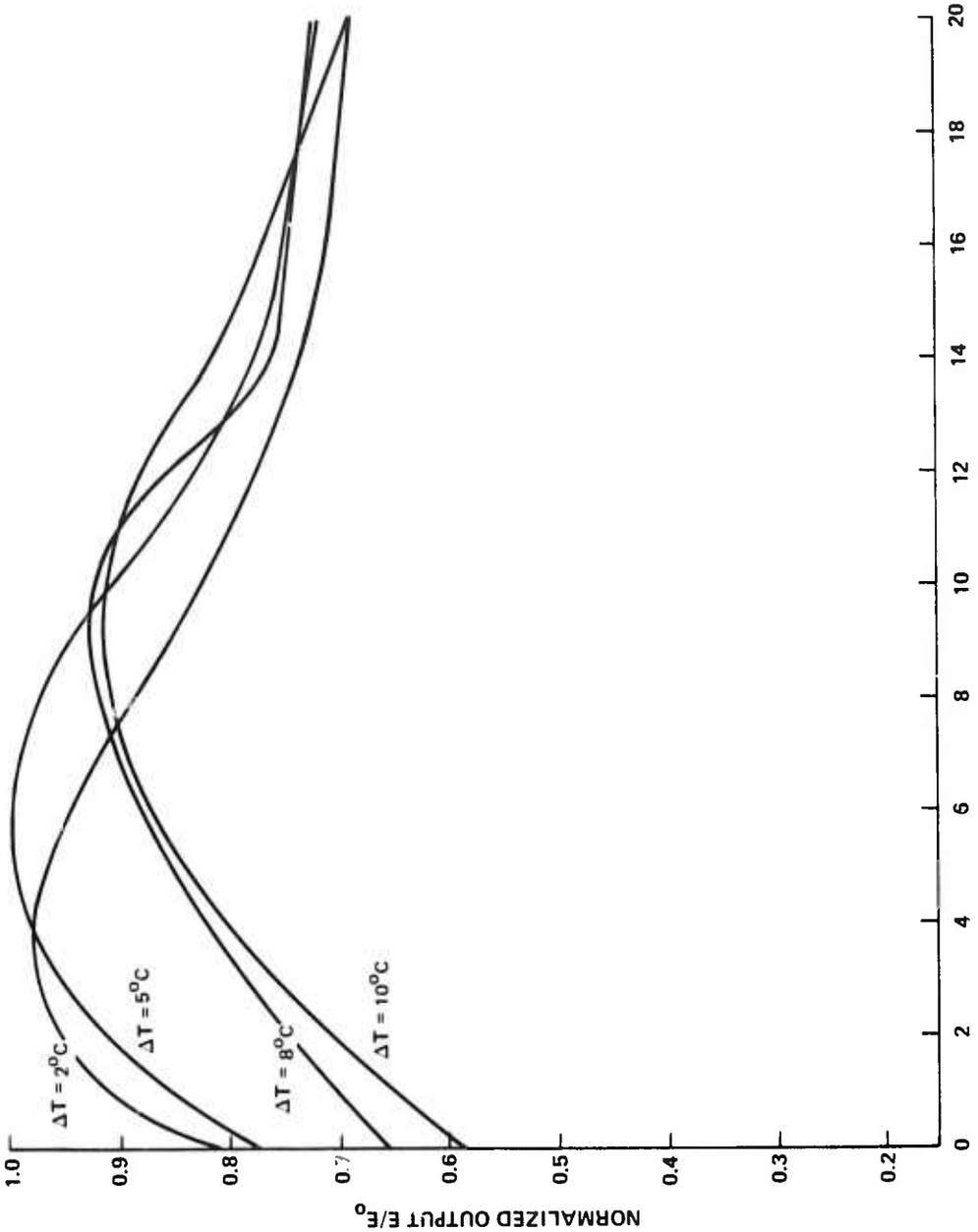

Figure 6-18. Quadruple Ellipse Reynolds Number 10,000

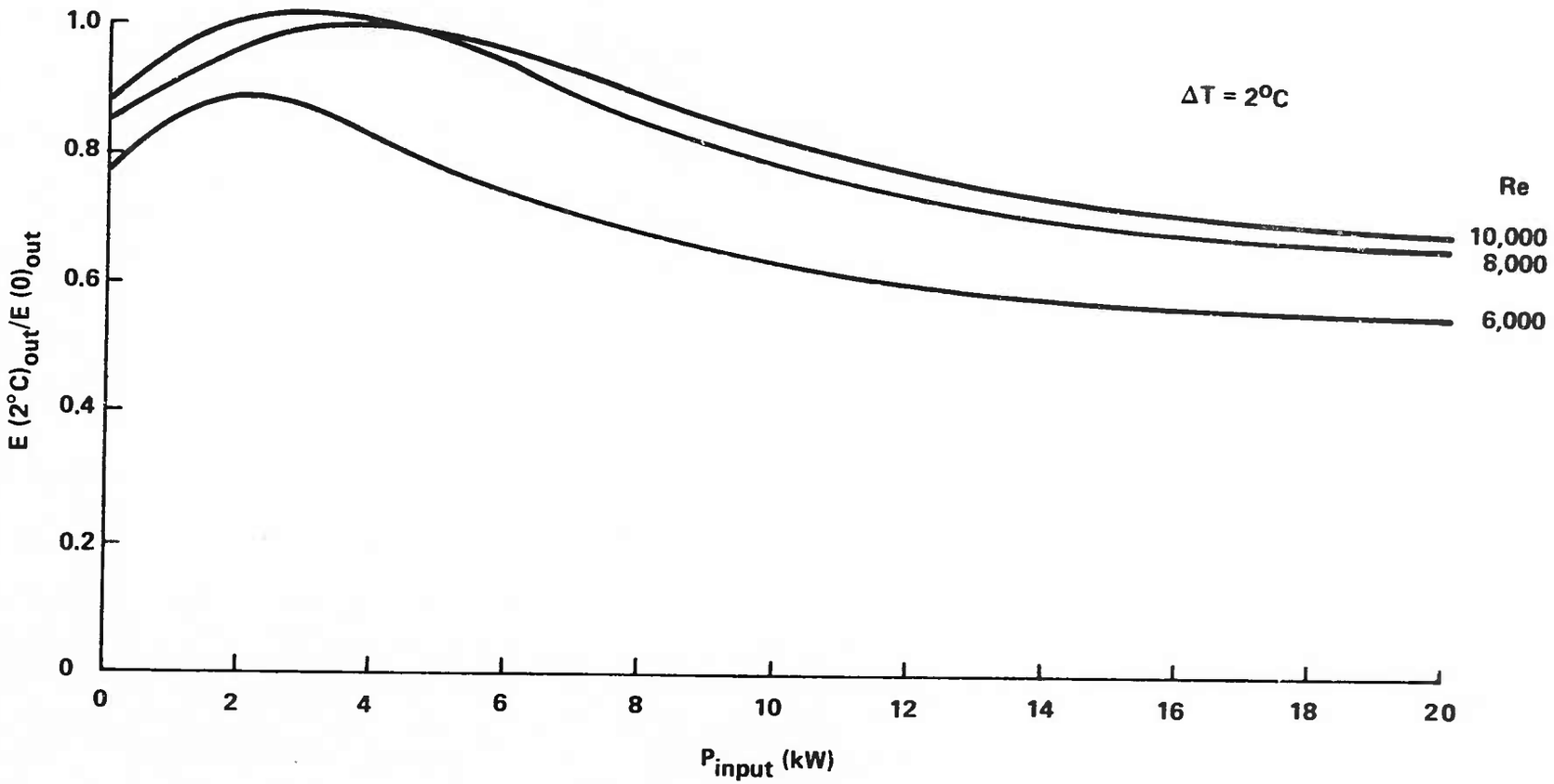

Figure 6-19. Normalized Laser Output for Four-Lamp 10-Inch Head with $\Delta T = 2°C$ and Re = 6,000, 8,000 and 10,000 vs. Average Input Power. Data points suppressed for clarity.

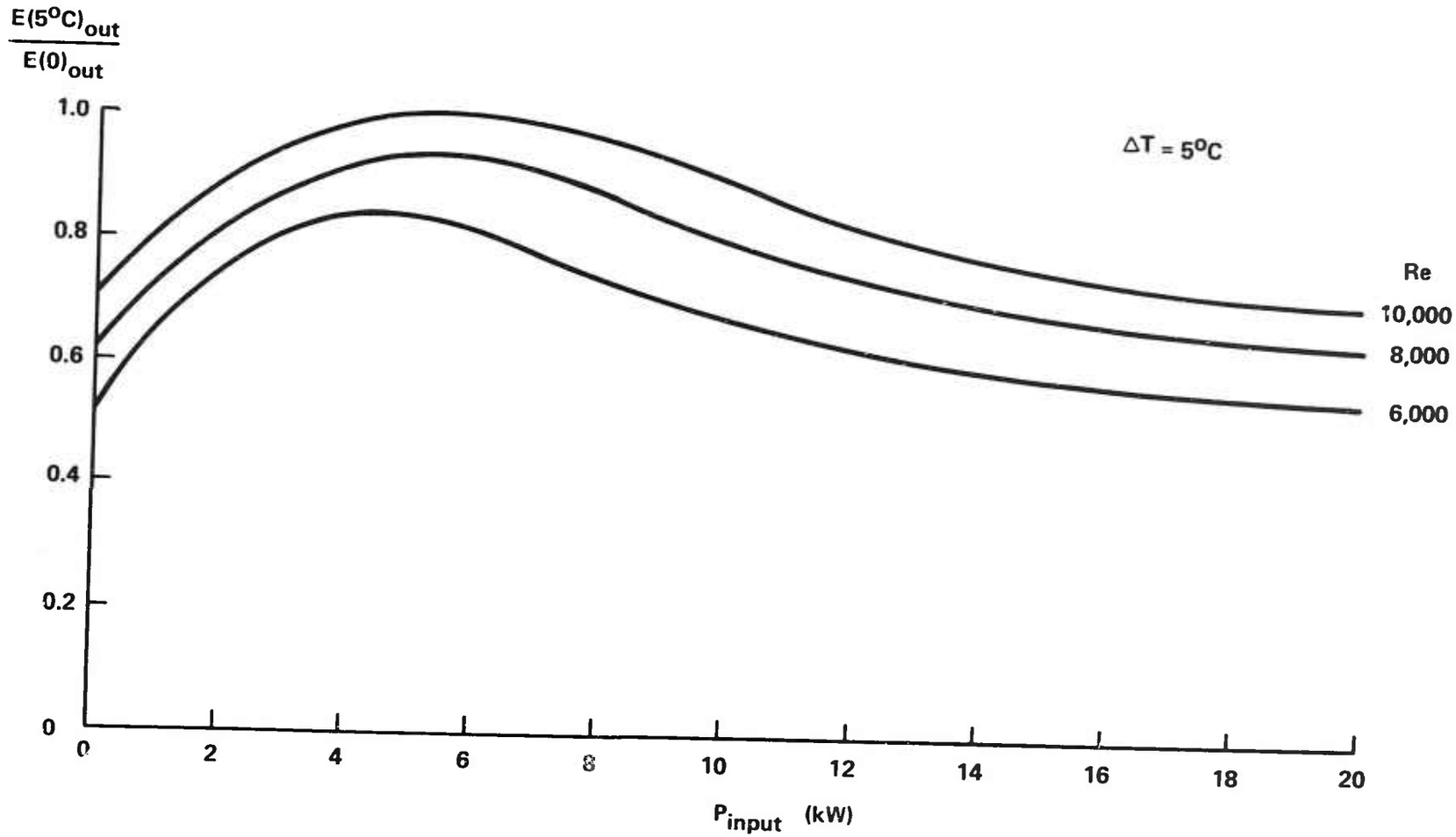

Figure 6-20. Normalized Laser Output for Four-Lamp 10-Inch Head with $\Delta T = 5\,^{\circ}C$ and Re = 6,000, 8,000 and 10,000 vs. Average Input Power. Data points suppressed for clarity.

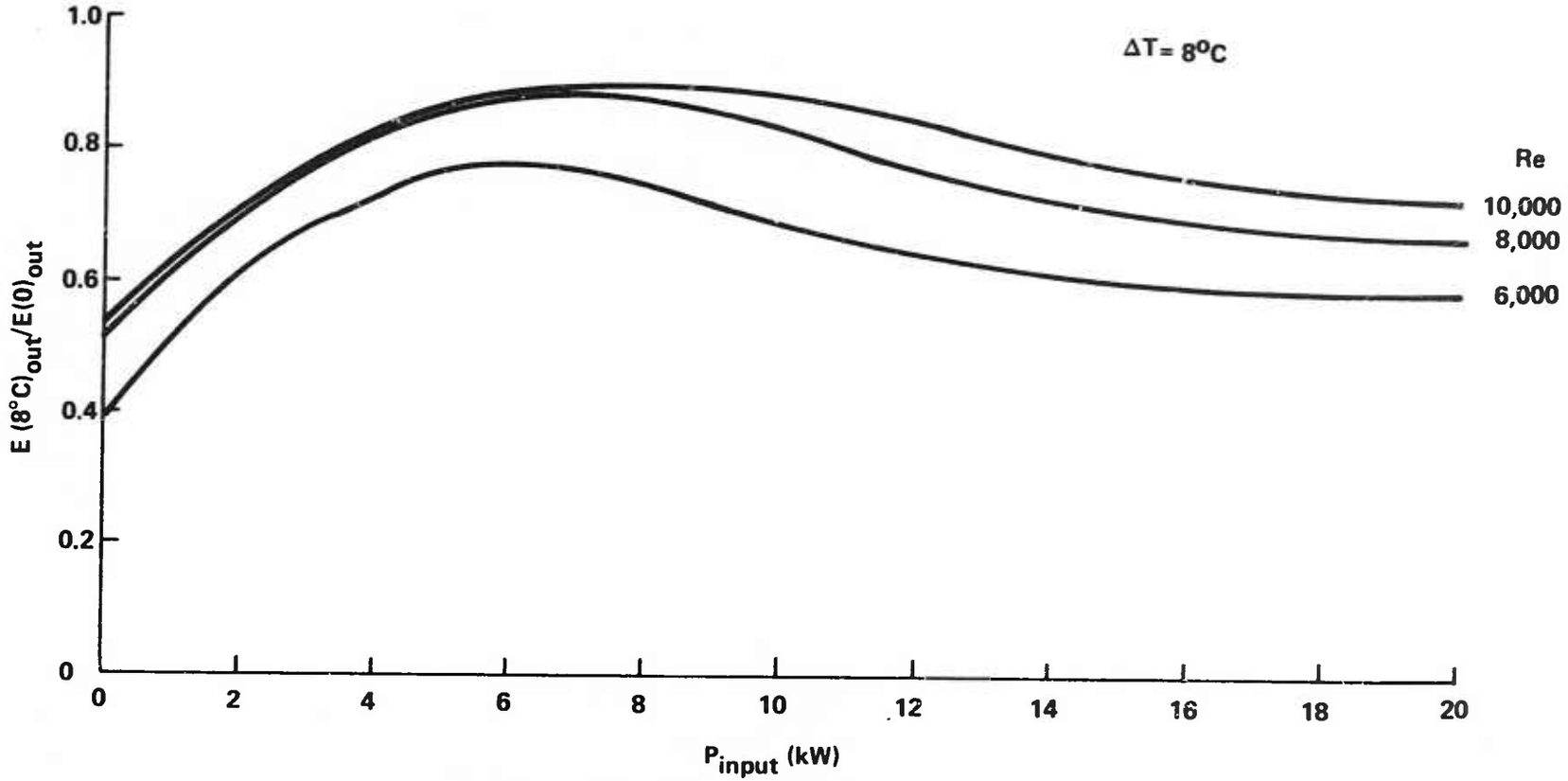

Figure 6-21. Normalized Laser Output for Four-Lamp 10-Inch Head with $\Delta T = 8\,^{\circ}C$ and Re = 6,000, 8,000 and 10,000 vs. Average Input Power. Data points suppressed for clarity.

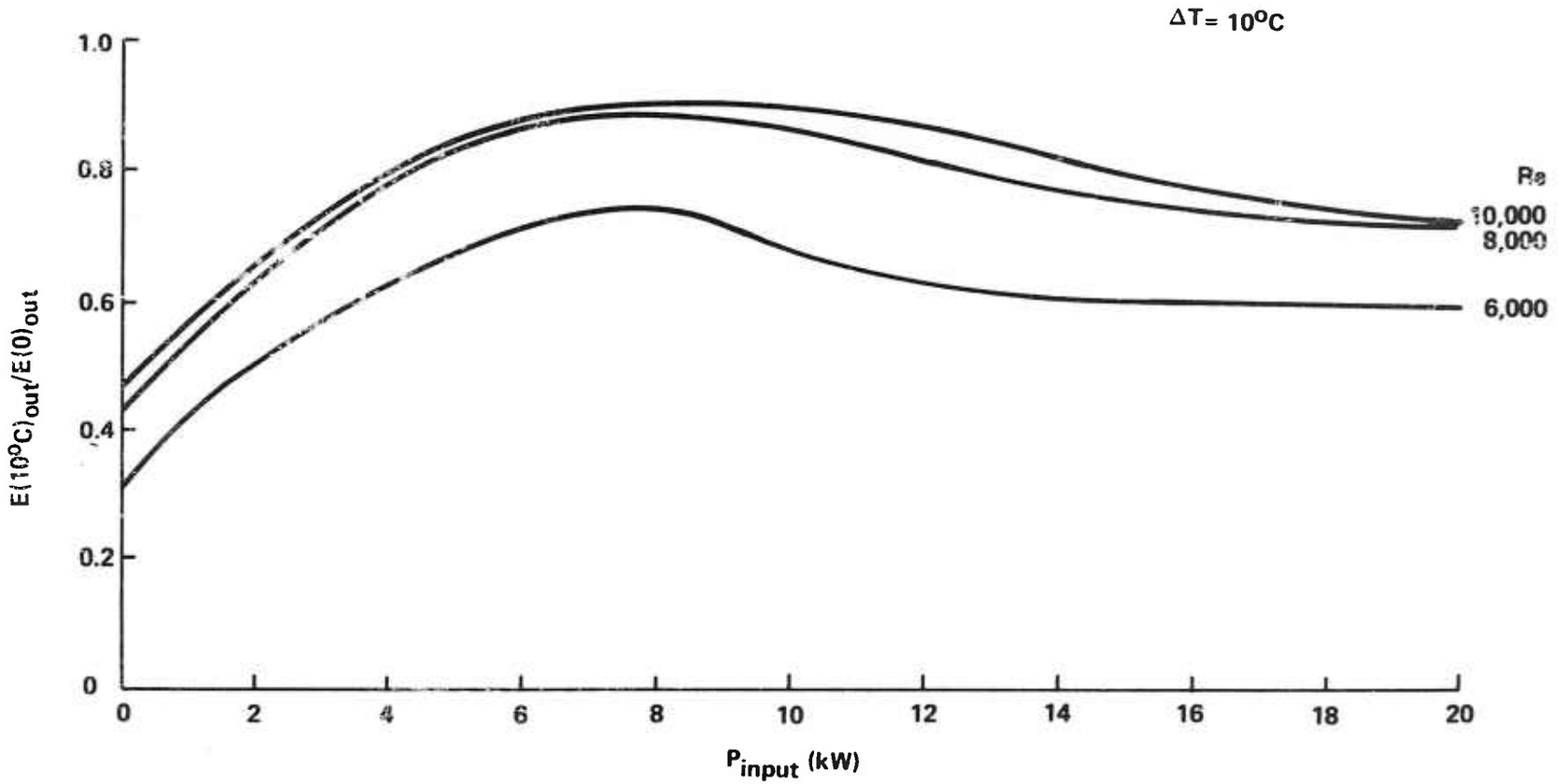

Figure 6-22. Normalized Laser Output for Four-Lamp 10-Inch Head with $\Delta T = 10^{\circ}C$ and Re = 6,000, 8,000 and 10,000 vs. Average Input Power. Data points suppressed for clarity.

For the dual elliptical flash head containing the 10-inch laser cell, the reduced output data are shown in Figure 6-23. In these experiments, the Reynold's numbers for the flow were 8400 and 11,000 and the repetition rate extended to 8 pps. The maximum average input power was limited to 10 kW, so that the maximum repetition rate was not used at pulse input energies in excess of 1250 J although pulse input energies up to 2000 J were used at lower repetition rates. The output curves are compared for the different flow speeds and ΔT values of 3°C and 5°C in Figures 6-24 and 6-25.

The temperature effect is shown in Figures 6-26 and 6-27 for the dual elliptical head containing the 6.5 inch laser cell. In these experiments, the input power was limited to 4.8 kW again with maximum pulse repetition rate of 8 per second and a maximum pulse input energy of 600 J. In this set of experiments, a curve for $\Delta T = 0$ is also included. The data are plotted in Figures 6-28 and 6-29 so that the effect of the flow Reynold's number can be readily seen.

6.5 DISCUSSION

We will restrict our consideration to systems 2 and 3, since only these systems provide the essential temperature control of the cell wall by means of the water cooling jacket. Qualitatively, the experimental results are easily understood. In the absence of any externally imposed temperature gradient ($\Delta T = 0$), the reduced pulse output decreases with increasing pumping power. This decrease is obviously due to the thermal gradient-based optical distortions arising from the power loading. To counteract this, an external thermal gradient ($\Delta T > 0$) is imposed. At low power loadings, the cell wall temperature is lower than that of the laser liquid and, because of the decrease in refractive index of the liquid with temperature, the active medium behaves as a negative lens. The resulting divergence of the cavity flux severely restricts the effective volume, resulting in a marked decrease in laser output. As the power loading is increased, the thermal gradient decreases and the strength of the lens also decreases. As a consequence, the effective laser volume increases and the output also increases. A continued increase in the power loading will ultimately lead to a change in sign of the gradient and the lens will become converging. This, too, will result in decreased output but the drop-off will not be as severe.

There are three detailed aspects of these data that merit further consideration. The first is the behavior of the ratio E/E_o at zero power input. In all cases, this is an extrapolated value and, because of the scatter of the experimental points, the

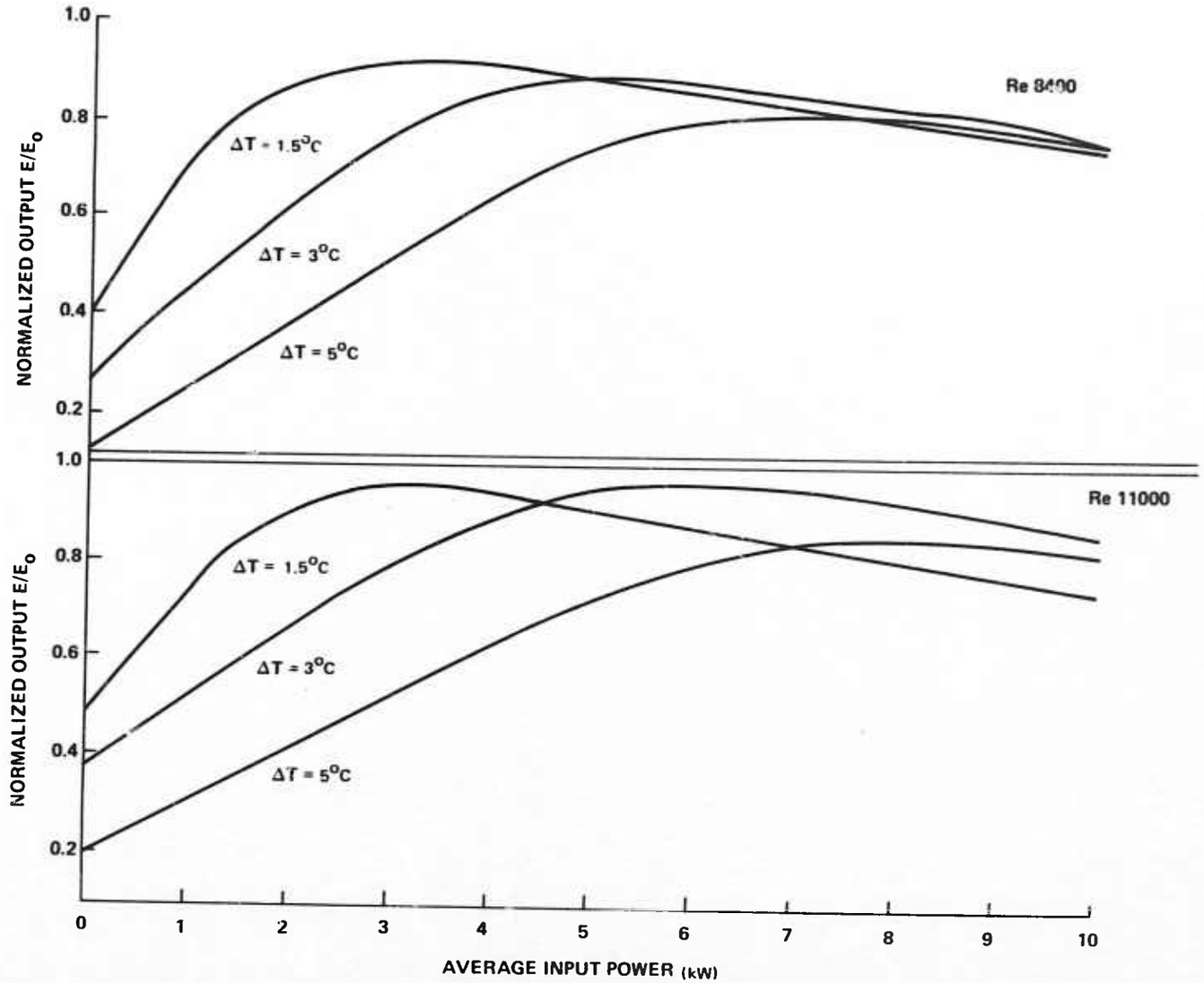

Figure 6-23. Normalized Laser Output for Two-Lamp 10-Inch Head for Re = 8400 and 11000. Data points suppressed for clarity.

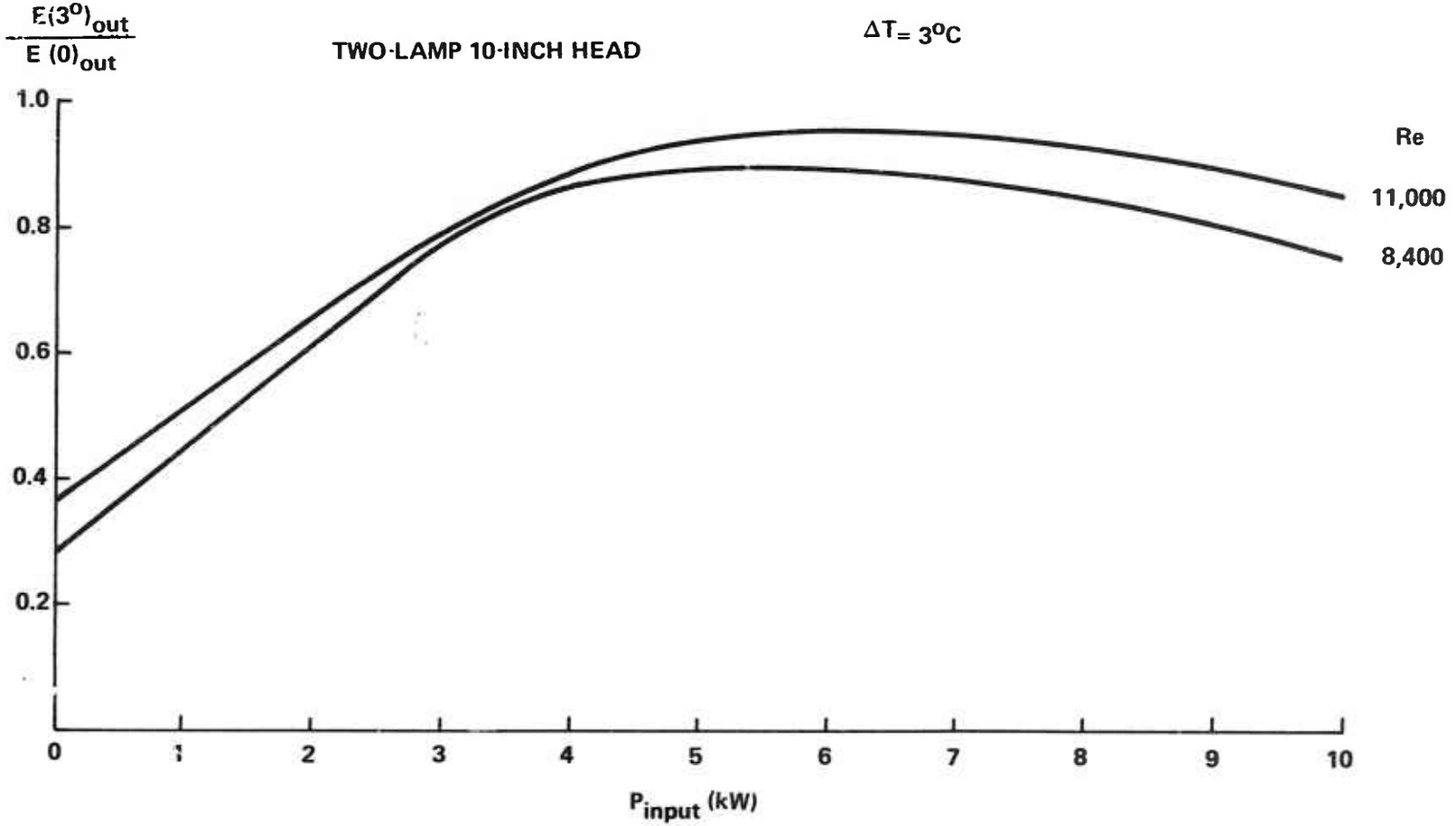

Figure 6-24. Normalized Laser Output for Two-Lamp 10-Inch Head with $\Delta T = 3^{\circ}C$ and Re = 8,400 and 11,000 vs. Average Input Power. Data points suppressed for clarity.

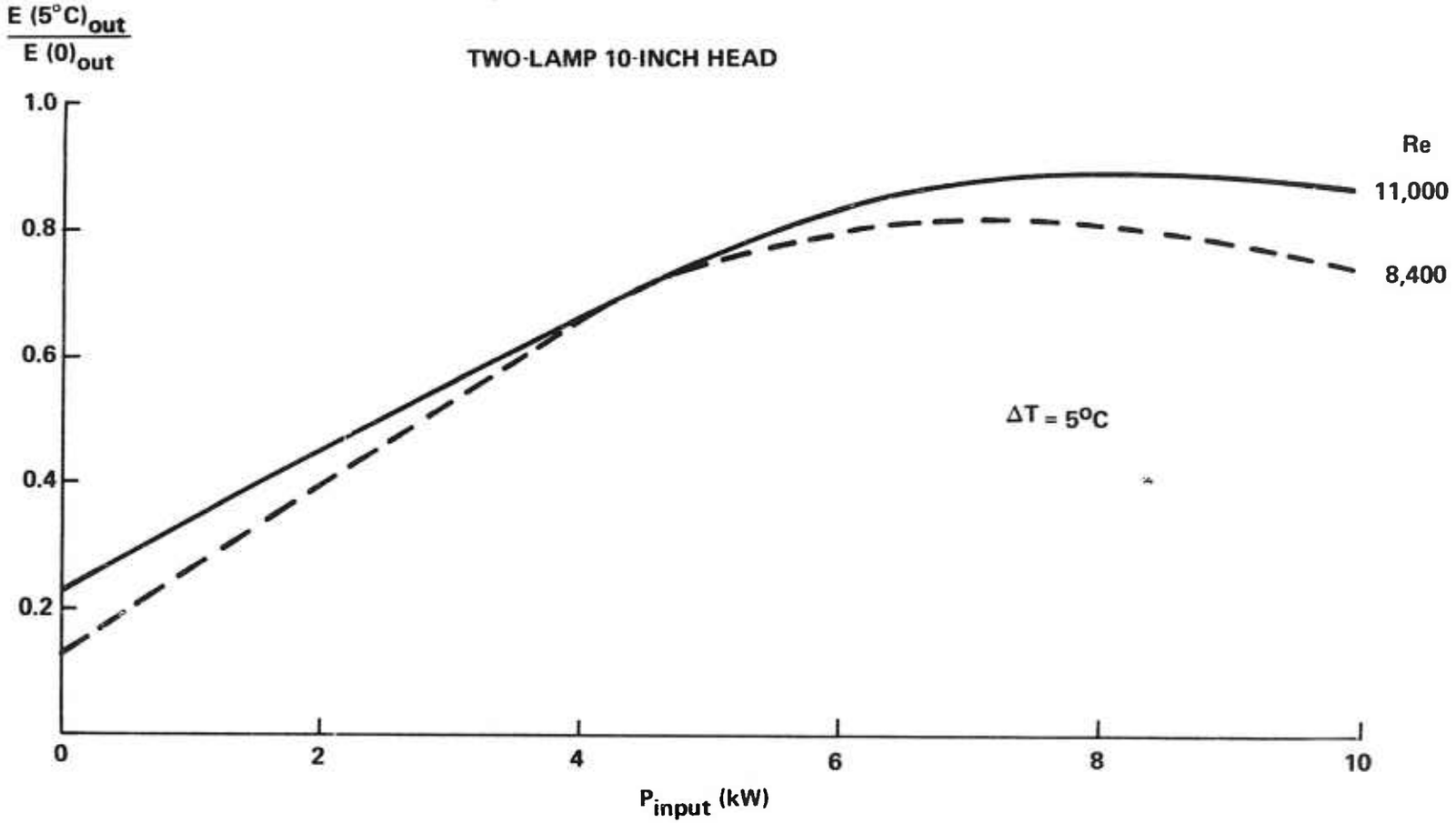

Figure 6-25. Normalized Laser Output for Two-Lamp 10-Inch Head for $\Delta T = 5°C$ and Re = 8,400 and 11,000 vs. Average Input Power. Data points suppressed for clarity.

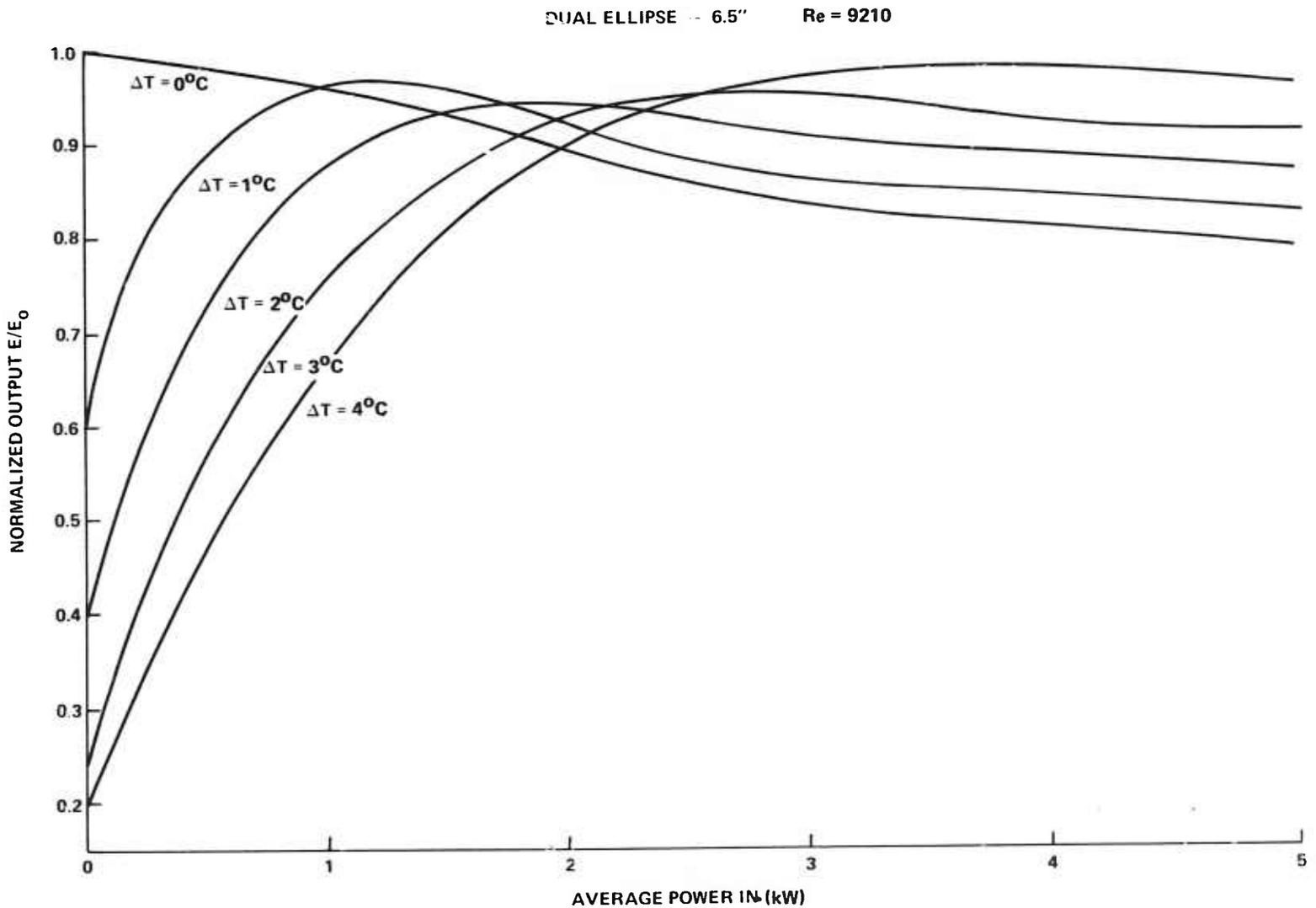

Figure 6-26. Redueed Output as a Funetion of Average Input Power at Re = 9210. Data points suppressed for clarity.

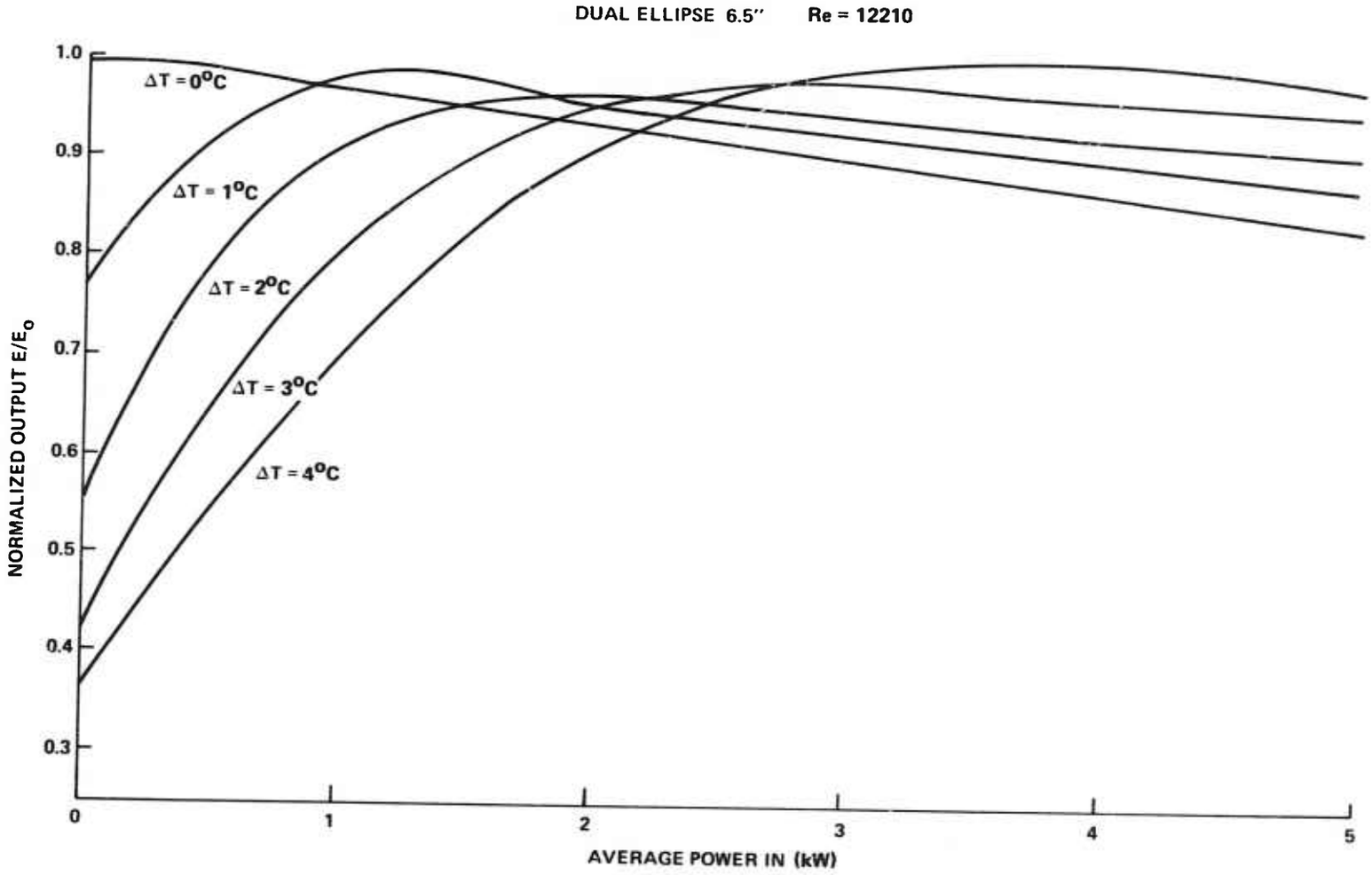

Figure 6-27. Reduced Output as a Function of Average Input Power at Re = 12210. Data points suppressed for clarity.

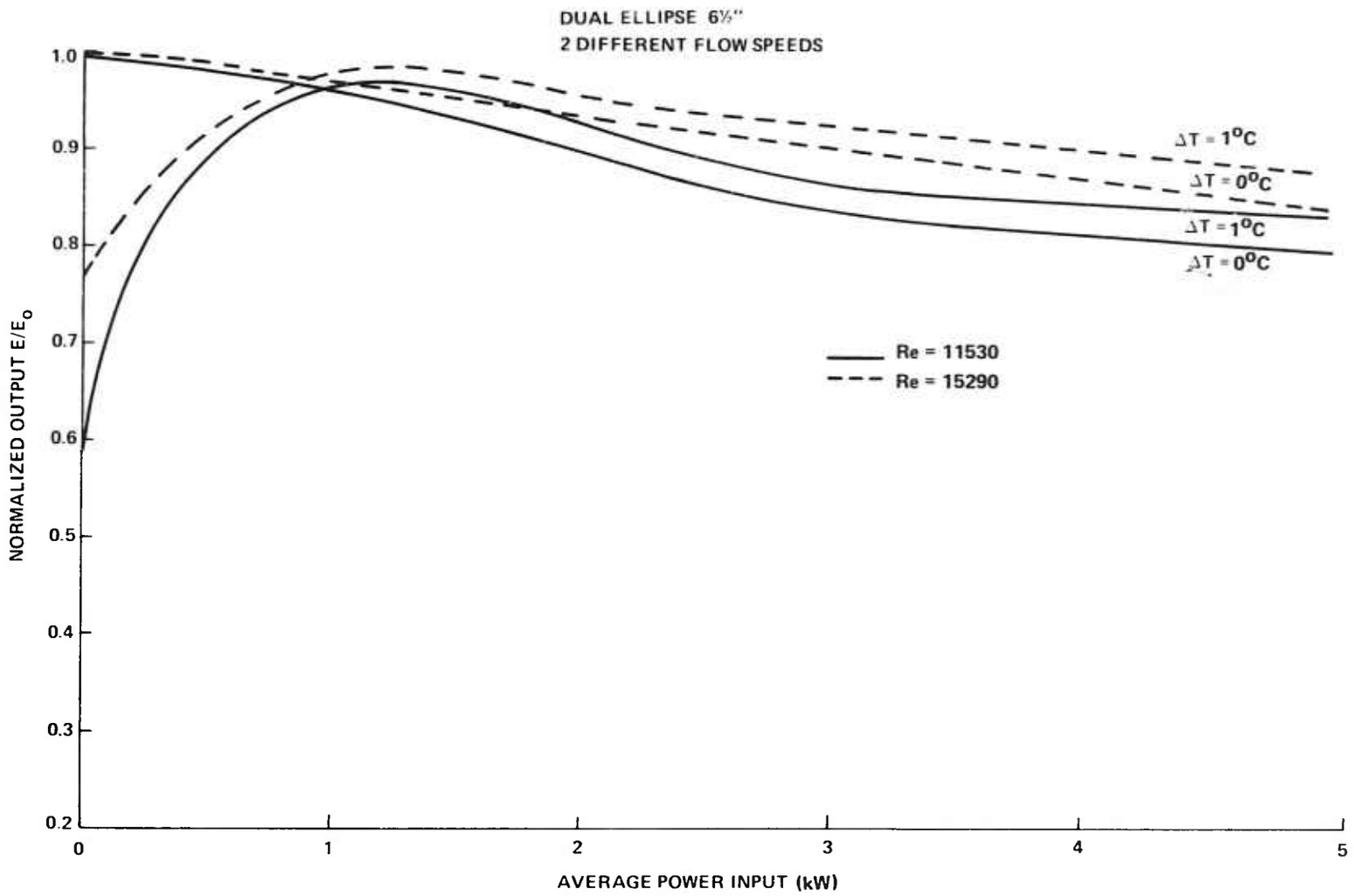

Figure 6-28. Reduced Output as a Funetion of Average Input Power Showing Effect of Flow Speed

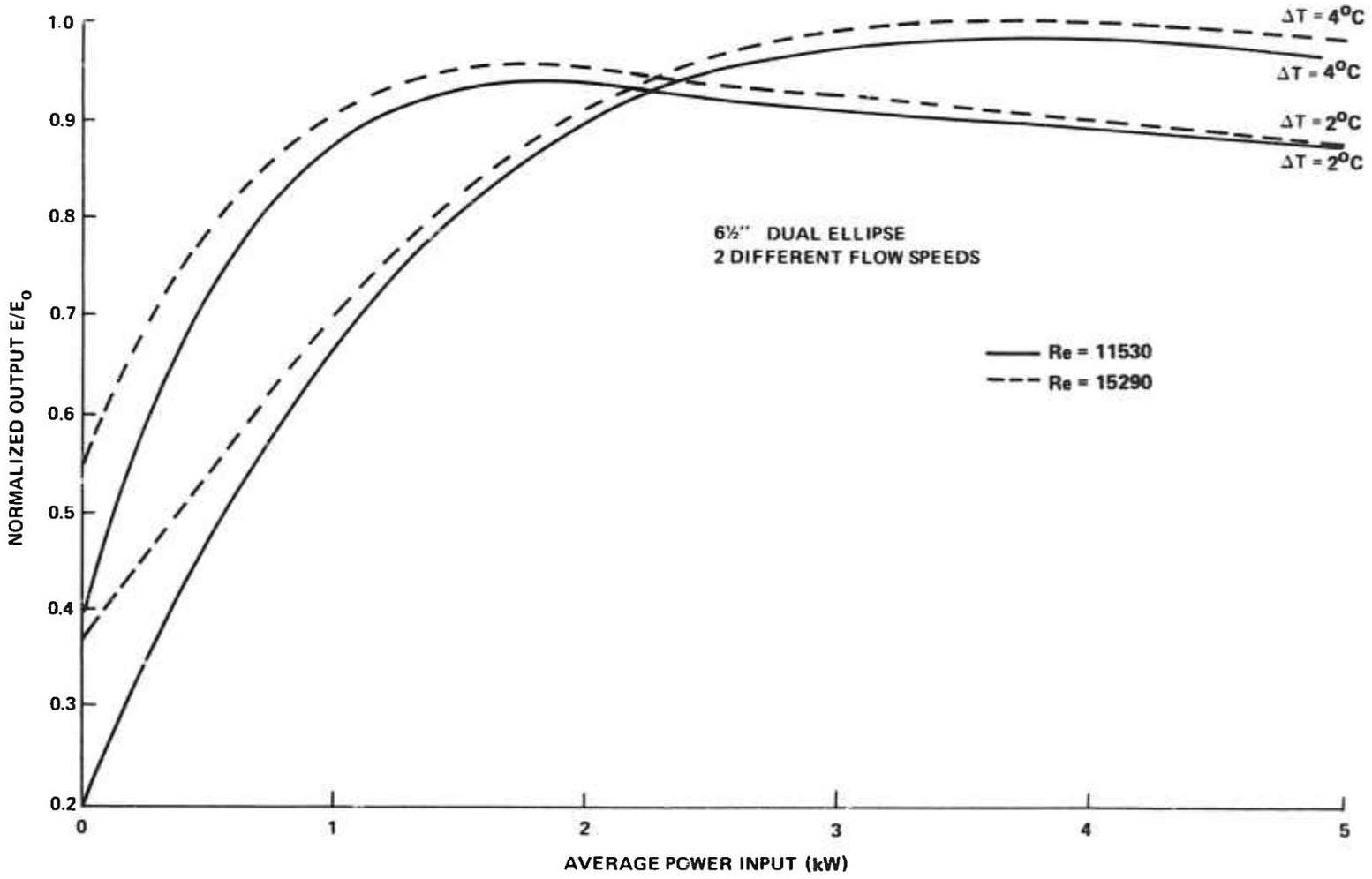

Figure 6-29. Reduced Output as a Function of Average Input Power Showing Effect of Flow Speed

extrapolation is rather difficult to make. However, since the power loading at this point is zero, it is easy to make a connection with the hydrodynamic theory described earlier. The second point of interest is the average input power at which the value of E/E_o is a maximum. This will be a function of both ΔT and the Reynold's number and usually defines the range of most efficient operation. The third point of interest is the behavior at $\Delta T = 0$. This provides some information on the effect of repetition rate at constant power input.

6.5.1 Temperature Dependence of Output at Zero Input Power

An inspection of the reduced output curves shows that for increasing temperature differentials, the values of E/E_o decrease on the low average, input-power side of the maximum. At zero input, the conditions under with the hydrodynamic model, presented in Section 4 are met. This provides an opportunity to relate the model to the experiment.

If the extrapolated values of E/E_o are plotted as a function of the imposed temperature differential as in Figure 6-30 and 6-31, it is seen that the semi-logarithmic representation provides a reasonable fit. Further, it is seen that the rate at which $(E/E_o)_{p=o}$ falls off with increasing ΔT is, in all cases, lower for the higher Reynold's numbers. Now, both ΔT and the Reynold's number determine the magnitude of the radial temperature gradient. As was shown, the radial temperature gradient will cause the light flux in the active medium to diverge, the amount of divergence increasing as the cell wall is approached. The divergence can become so large that, in effect, the effective volume of the laser is decreased and the output becomes less.

This model can be made more quantitative. Assume that $(E/E_o)_{p=o}$ is proportional to the effective laser volume or, its equivalent, the effective cross section of the laser beam in the resonator. Further assuming that the entire cross section is effective at $\Delta T = 0$, a critical or effective radius, r_c, at $\Delta T = 0$ can then be calculated from $(E/E_o)_{p=o}$ at this ΔT. Then, with this value of r_c, a value of $(dn/dr)_{r=r_c}$ can be obtained from the hydrodynamic analysis using the appropriate flow parameters. The results of such calculations are given in Table 6-2.

Over a wide variety of flow conditions and imposed gradients, the value of dn/dr at the critical radius appears to be constant for each cell, as would be expected within a given experimental arrangement. The value of the index gradient is, however, different for each laser cell and there are probably two reasons for this. The first is the aspect ratio of the cell and the resonator length. The higher the aspect ratio

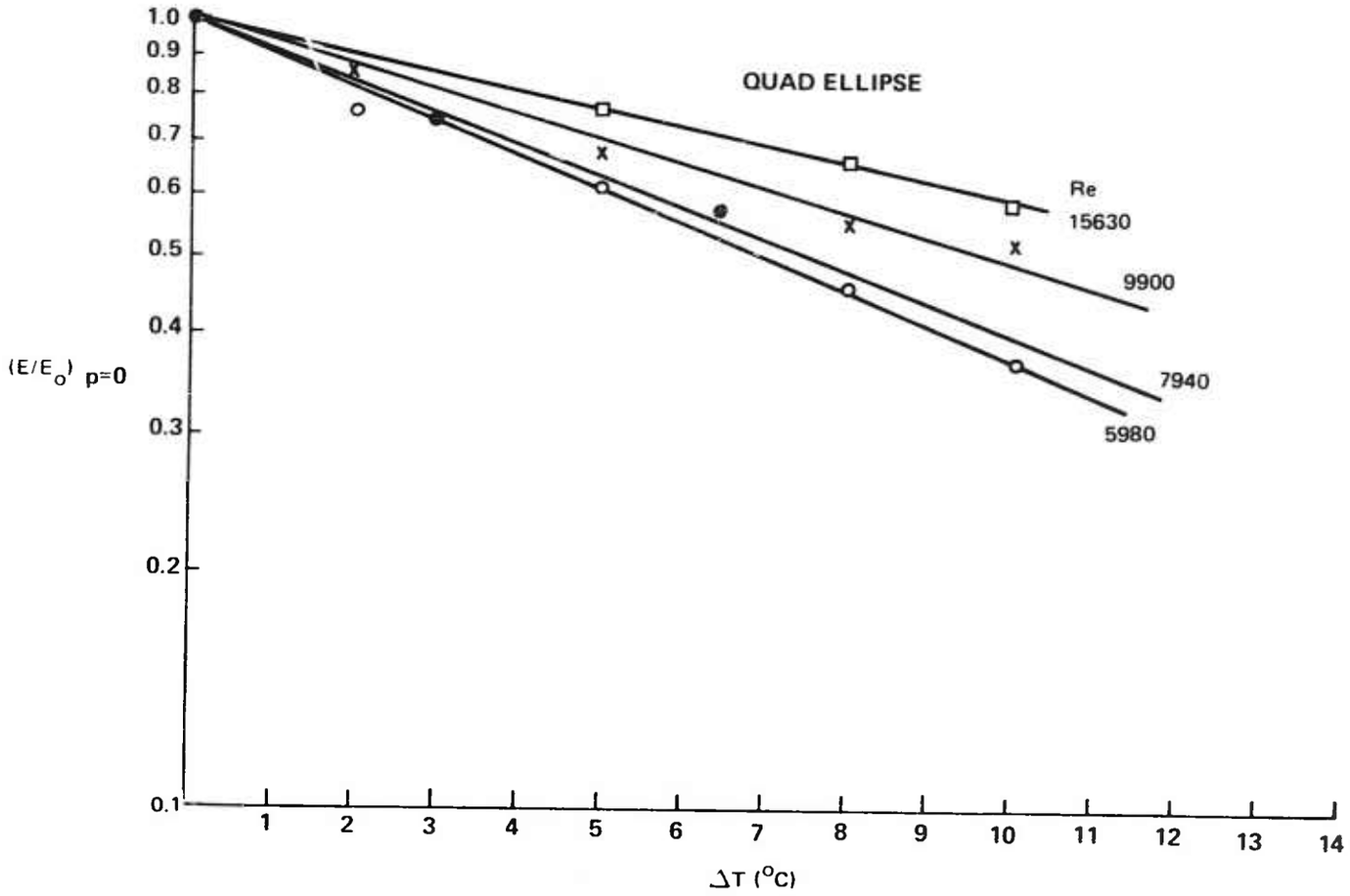

Figure 6-30. Extrapolated Value of E/E_o at Zero Input Power as a Function of the Externally Infrared Temperature Differential (ΔT)

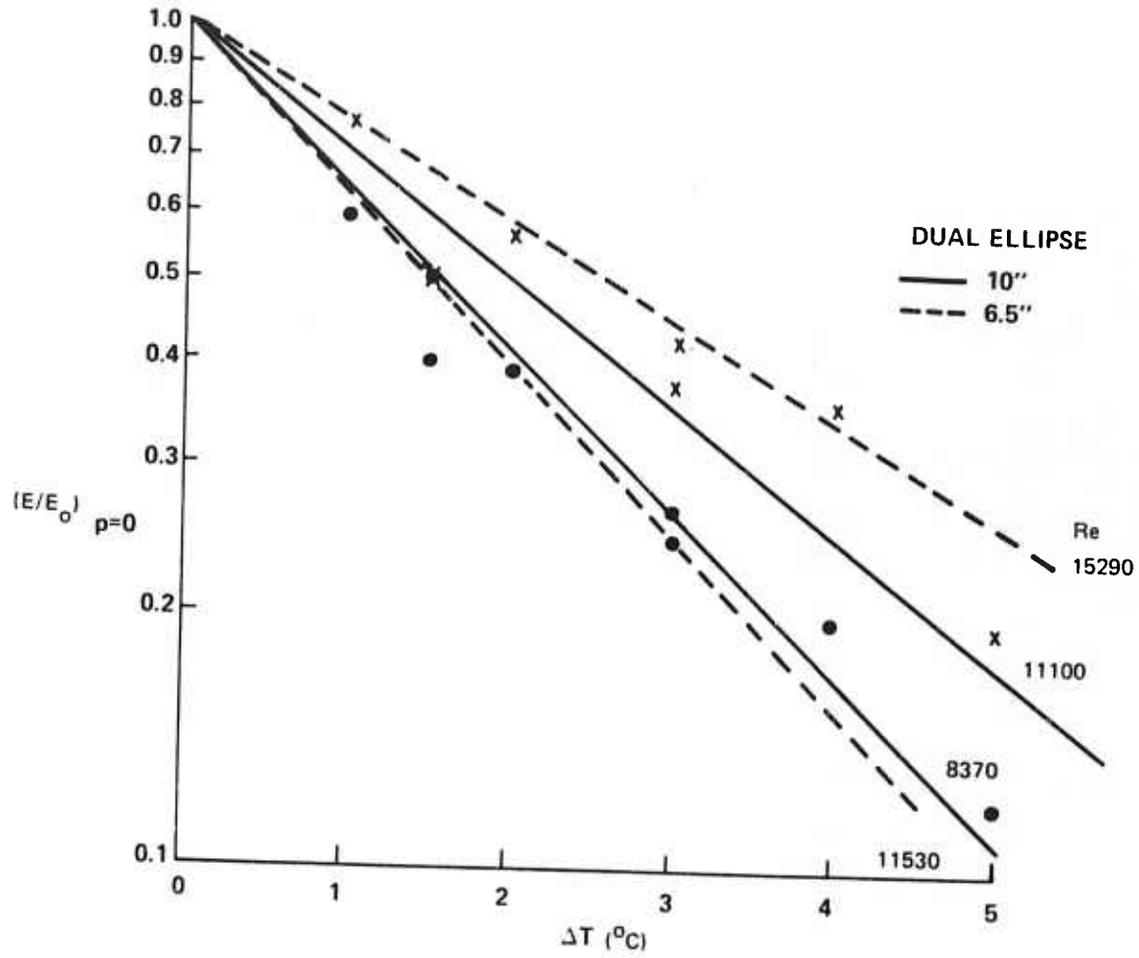

Figure 6-31. Extrapolated Value of E/E_o at Zero Input Power As a Function of the Externally Infrared Temperature Differential (ΔT)

TABLE 6-2

REFRACTIVE INDEX GRADIENT AT THE CRITICAL RADIUS

a) FOUR-LAMP LASER HEAD

$\Delta T(^\circ C)$	R_e	r_c(cm)	$\left(\frac{dn}{dr}\right)_{r=r_c} \times 10^{-5}(cm^{-1})$
3.5	5980	0.87	6.78
5	5980	0.81	7.76
6.5	5980	0.76	8.65
8	5980	0.685	8.74
10	5980	0.62	9.50
13	5980	0.545	10.72
5	7940	0.865	8.01
8	7940	0.80	13.65
10	7940	0.72	10.06
5	9900	0.94	10.06
8	9900	0.815	9.25
10	9900	0.76	9.72
6.4	15630	0.92	7.55
8	15630	0.88	7.85
14	15630	0.76	9.01
18	15630	0.665	9.11
			9.15 Av.

b) TWO-LAMP, 10-INCH, DUAL ELLIPSE

1.5	8370	0.51	1.85
3	8370	0.43	2.89
5	8370	0.30	3.35
1.5	11100	0.545	1.79
3	11100	0.485	2.84
5	11100	0.38	3.56
1	9210	0.52	1.20
2	9210	0.495	2.20
3	9210	0.42	2.64
4	9210	0.365	3.05

TABLE 6-2 (Continued)

b) (Continued)

$\Delta T(^\circ C)$	R_e	r_c(cm)	$\left(\frac{dn}{dr}\right)_{r=r_c} \times 10^{-5}$ (cm^{-1})
5	9210	0.31	3.24
1	12210	0.71	3.33
2	12210	0.66	4.08
3	12210	0.54	3.21
4	12210	0.51	3.87
5	12210	0.41	3.56
			2.91 Av.

c) TWO-LAMP, 6.5-INCH, DUAL ELLIPSE

1	11530	0.545	3.48
2	11530	0.425	2.99
3	11530	0.375	3.62
4	11530	0.275	3.42
1	15290	0.560	3.36
2	15290	0.485	3.36
3	15290	0.415	3.50
4	15290	0.365	3.78
			3.43 Av.

(length/diameter), the smaller is the value of $(dn/dr)_{r=r_c}$. A second factor of possible significance is the optical pumping arrangement. In the four-lamp head, optical pumping is more symmetric than in the two-lamp heads, and this could play a role in the substantially larger, refractive-index gradient at the critical radius.

6.5.2 Temperature Dependence of the Maximum of E/E_o

We now consider the average input power level at which the reduced or normalized pulse output energy is a maximum. In general, these maxima are broad in terms of the average input power, and tend to decrease in the peak E/E_o value as the temperature differential (ΔT) increases. The two trends that are most significant are that the maxima move to higher input powers as ΔT and the Reynold's number increase. This is displayed graphically in the log-log plot of Figure 6-32. The slopes of these lines tend to increase as the cell diameter or the cell length decreases but the overall average slope is 0.70 ± 0.02. There is a definite shift to higher average powers as a function of increasing Reynold's number for a given laser configuration, but the slope is not significantly sensitive to the Reynold's number.

It is difficult to tie the quantitative aspects of the descriptions presented in Figure 6-32 to the details of the hydrodynamic model. The trend in the values of P_{max} is easy to understand, qualitatively. At higher values of ΔT, it requires more power to bring the refractive index gradient to a minimum or zero value, hence, P_{max} increases with ΔT. For a given ΔT, increasing the Reynold's number accomplishes two things. First, it improves the heat transfer rate at the cell wall and secondly, it extends the low gradient region in the laser liquid further towards the cell wall. These factors bring about the two effects seen in Figures 6-19 through 6-22, 6-24, 6-25, 6-28 and 6-29; first, P_{max} increases and, secondly, the value of E/E_o at P_{max} increases.

The comparisons and discussions of this section are the key to the understanding of the liquid medium, when used as a high average power laser oscillator. Because of the turbulent flow, one is able to extend the range of relatively efficient operation into the region of high average input power. This has been achieved with no corrective intra-cavity optics over a wide range of operating conditions.

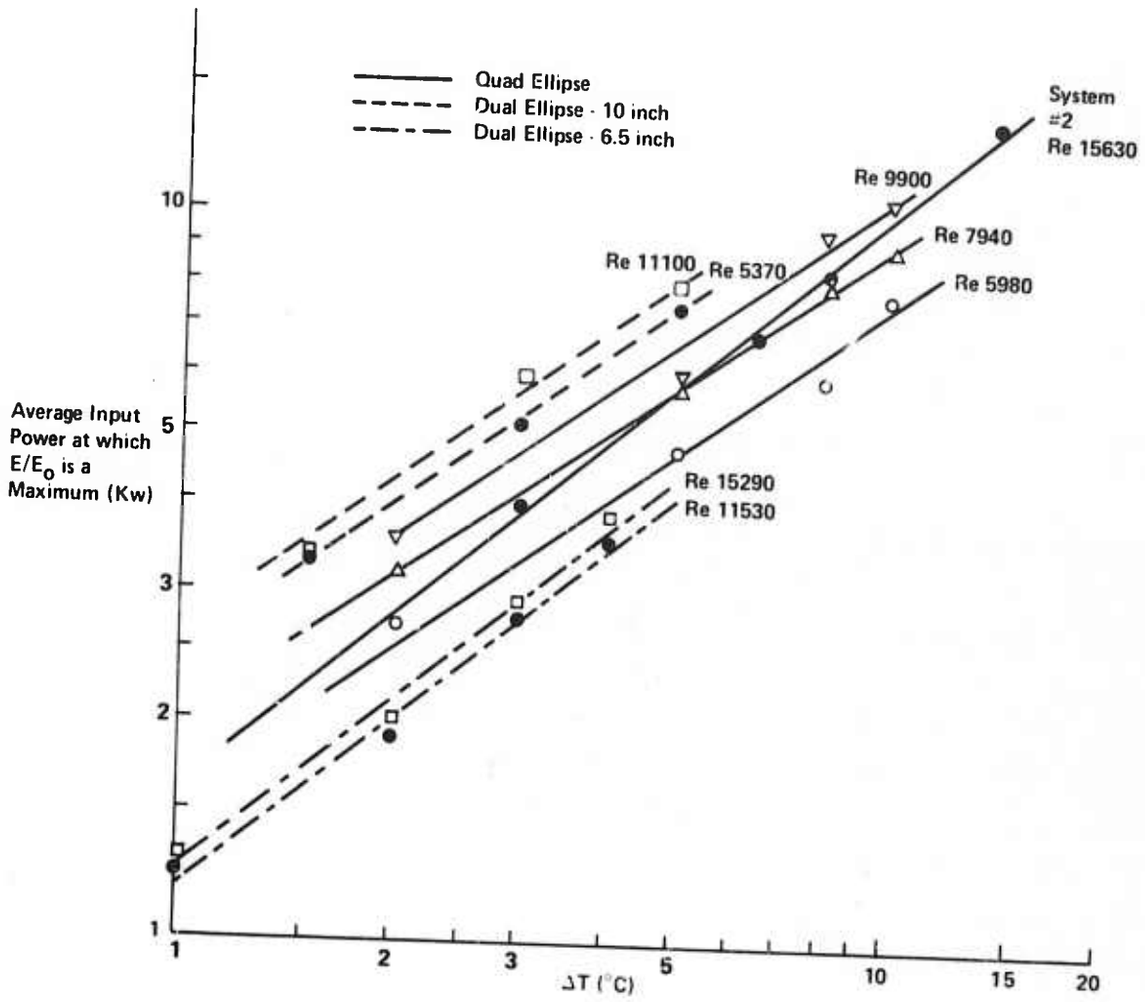

Figure 6-32. Power Input for Maximum E/E_o as a Function of ΔT

6.5.3 The Effect of the Pulse Repetition Rate

In the first part of this section, a simple analysis was presented for the cumulative thermal effect at a fixed power input in terms of the pulse repetition rate. To carry this analysis over in a simple way to the output data requires the assumption that there is no flash-induced, thermal distortion in the active medium. That is, all optical distortions arise from absorption in the cell wall and the closely associated boundary layer. As we shall see, this is not the case.

From data on the ten-inch, dual-elliptical-head laser, we construct the entries in Table 6-3. At $\Delta T = 0$, it is expected that as the repetition rate, at a constant average power input, is increased, the temperature differential should increase and E/E_o decrease. This, in fact, is the case. Furthermore, as the average input power increases, E/E_o, at a constant repetition rate, tends to decrease.

At values of $\Delta T > 0$, the picture that emerges is more confusing. First, at all input powers except 6 kW, at some value of ΔT the dependence of E/E_o on the repetition rate goes through a maximum. At the 6 kW level, there is an indication of this even at $\Delta T = 0$. Furthermore, at the 2 kW input level for $\Delta T \geq 2^\circ C$, it appears that there are two maxima. It is probable that the first maximum (at the lower repetition rate) arises from the cooperative effect of the relatively high pulse input energy and the cumulative thermal effect, while the second maximum is principally due to the cumulative thermal effect. This interaction is responsible for the scatter of the points in the E/E_o versus average power input curves, and makes the extrapolation to zero power input subject to considerable error. These effects have not been studied in any great detail.

6.6 SUMMARY

The experimental results on the long-pulse, high-average-power, liquid laser oscillator are most encouraging. What has been shown is:

1. Such high average power oscillators can be constructed quite readily with outputs in excess of 400 watts and overall efficiencies over 2%.
2. If proper precautions are taken in the manufacture and use of the laser liquid, the systems are capable of providing long service.
3. In a circulatory system, the dynamic loss of the laser medium is low.

TABLE 6-3

E/E_o FOR FIXED INPUT POWER AND TEMPERATURE DIFFERENTIAL AT DIFFERENT REPETITION RATES

ΔT°C \ Watts input	pps	1000	2000	4000	6000
0	1	1.0	1.0	0.95	0.94
	2	1.0	0.98	0.93	0.95
	4	0.85	0.95	0.83*	0.75
	6		0.93*	0.75	
	8		0.77		
1	1	0.94	0.98	0.96	0.90
	2	0.97	1.02	0.95	0.85
	4	0.77	0.96	0.84**	0.77
	6		0.83*	0.79	
	8		0.85		
2	1	0.88	0.91	0.98	0.91
	2	0.88	0.98	0.96	0.84
	4	0.77	0.96	0.86**	0.79
	6		1.02*	0.80	
	8		0.70		
3	1	0.72	0.79	0.92	0.89
	2	0.68	0.84	0.93	0.83
	4	0.46	0.77	0.83**	0.80
	6		0.86*	0.80	
	8		0.76		
4	1	0.54	0.72	0.87	0.88
	2	0.53	0.71	0.91	0.82
	4	0.30	0.65	0.84**	0.79
	6		0.74*	0.79	
	8		0.54		
5	1	0.48	0.68	0.83	0.92
	2	0.48	0.67	0.93	0.89
	4	0.30	0.55	0.84**	0.79
	6		0.71*	0.80	
	8		0.62		

*Values for 2250 W
**Values for 4500 W

The results achieved to date can be improved. A major problem affecting the laser output and beam quality is the uniformity of the pump radiation. The pump radiation in all the enclosures used was not uniform over the circumference of the laser cell. This evidence will be presented in Section 7. An improvement in pump uniformity would bring a decrease in the divergence of the oscillator beam and probably an increase in efficiency.

7. LIQUID LASER AMPLIFIERS

This section will deal with the use of the liquid solvent systems for the Nd^{+3} ion as amplification media. Experimental investigations of Nd^{+3}:$SeOCl_2$:$SnCl_4$, as a small signal amplifier under single-shot conditions, will be presented in Section 7.1. This work was performed before the advent of the more tractable Nd^{+3}:$POCl_3$:$ZrCl_4$ laser liquid with the accompanying breakthrough in the materials problem. As a result, the reported work was done using a liquid circulatory system that was only capable of a relatively slow flow rate of laser solution through the laser cell. The laser flash head used in these experiments was a water-filled type in which the laser cell was immersed. This cooling water was maintained at the same temperature as the laser liquid. As a result of this, these experiments may be viewed as being static and isothermal, with no radial temperature gradients other than those induced by the pump flash itself. These results are exclusively single-shot, as a reliable repetitively-pulsed power supply was not available at the time of these experiments.

The next section (7.2) presents the most recent results obtained using Nd^{+3}:$POCl_3$:$ZrCl_4$ laser liquid in the most recent laser system described in the last part of Section 3. The signal source for this work is a diffraction-limited, Q-switched YAG laser, the same laser as was used to investigate the thermo-optical behavior of the liquid in the laser cell as was described in Section 4. The results here are again single-shot results.

Section 7.3 is a discussion of the results obtained in Section 7.1 and 7.2, along with a discussion of optical distortion in liquid amplifiers. This will draw heavily from the results obtained in Section 4. The final section (7.4) is an application of the results of the preceeding work and Section 6, to the case of a repetitively-pulsed liquid amplifier. As such, it outlines the region of application of the Nd^{+3} liquid amplifier for the generation of high average power, high beam quality laser outputs.

7.1 SMALL SIGNAL GAIN IN Nd^{+3}:$SeOCl_2$:$SnCl_4$

This section presents the results of a study of small signal gain amplification using the laser solution Nd^{+3}:$SeOCl_2$:$SnCl_4$. The work to be described consisted of using the attenuated output from a long-pulse Nd^{+3} glass oscillator as a signal source for a liquid amplifier. The random spiking behavior of the probe oscillator allowed the

measurement of the build-up and decay of small signal gain in the amplifier. A simplified mathematical model derived from the rate equations for inversion density and amplified photon flux is derived and applied to the data. Comparison is made at the end of this section of the results of this study and those made by other investigators.

7.1.1 Mathematical Model

To describe the amplifier behavior, two equations coupled the amplified photon flux and the inversion density are required. Following Schultz-DuBois[118] and Cabezas et al.,[119] these equations can be written:

$$\frac{dN}{dt} = -\sigma N I - \frac{N}{\tau} + W(N_o - N) \tag{7-1}$$

$$\frac{dI}{dZ} = \sigma N I - \alpha I \tag{7-2}$$

where:

Z = position variable along laser axis
N = inversion density (ions/cm^3)
N_o = concentration of Nd^{+3} (ions/cm^3)
I = amplifier photon flux (photons $cm^{-2} sec^{-1}$)
σ = amplifier stimulated emission cross-section (cm^2)
$1/\tau$ = spontaneous emission rate (sec^{-1})
α = scattering loss coef. (cm^{-1})
W = pumping rate from ground to upper laser level (sec^{-1})

For small-signal amplification, the condition that the amplifier flux be small in comparison to spontaneous losses and pumping is:

$$\sigma I < \frac{1}{\tau} + W\left(1 - \frac{N_o}{N}\right). \tag{7-3}$$

Under this condition, Eq. (7-2) can be written:

$$\frac{dN}{dt} = WN_o - \left(\frac{1}{\tau} + W\right) N, \tag{7-4}$$

and the coupled equations can be separated. The solution is:

$$N = \left(\frac{N_o W}{W+\frac{1}{\tau}}\right)\left[1 - e^{-\left(W+\frac{1}{\tau}\right)t}\right] \tag{7-5}$$

Substituting Eq. (7-5) into Eq. (7-2) and integrating over the amplifier length L, we obtain:

$$\int_{I_{in}}^{I_{out}} \frac{dI}{I} = \left\{\beta\left[1 - e^{-\left(W+\frac{1}{\tau}\right)t}\right] - \alpha\right\} L = \ell n\left(\frac{I_{out}}{I_{in}}\right), \tag{7-6}$$

where $\beta = \sigma N_o W / \left(W+\frac{1}{\tau}\right)$ and L is the single pass path length. Eq. (7-6) can be written in the following form:

$$\text{dB gain (t)} = 4.343\left\{\left(\frac{\sigma N_o L W}{W+\frac{1}{\tau}}\right)\left[1 - e^{-\left(W+\frac{1}{\tau}\right)t}\right] - \alpha L\right\} \tag{7-7}$$

Eq. (7-7) is used to relate the experimental results to the system parameters.

7.1.2 Experimental Arrangement

The apparatus was assembled as illustrated in Figure 7-1. The probing oscillator was a 6-inch Nd^{+3} glass laser rod of one-half-inch diameter (Schott LG55), whose output beam was polarized for minimum insertion loss into the amplifier by placing two glass blanks set at Brewster's angle inside the laser cavity. A pinhole was used as an aperture stop for the oscillator output and a small Galilean telescope was used to expand the beam to fill the input aperture of the amplifier. This arrangement allowed the one joule output of the oscillator to be attenuated to the range 0.01 to 0.1 J total input to the amplifier with good beam characteristics. Since the flashlamp circuits of the laser heads were not identical, a dual-trigger generator with variable time delay was used to trigger the amplifier and oscillator flashlamps independently. In practice, the oscillator was triggered some 260 μs before the amplifier so that the first spike in the oscillator long-pulse output arrived close to the start of the amplifier pumping, allowing gain build-up in the amplifier to be studied. A beam splitter and photomultiplier sampled a portion of the amplifier input signal while a photodiode monitored the amplified signal. Input and output signals were displayed simultaneously on a dual-

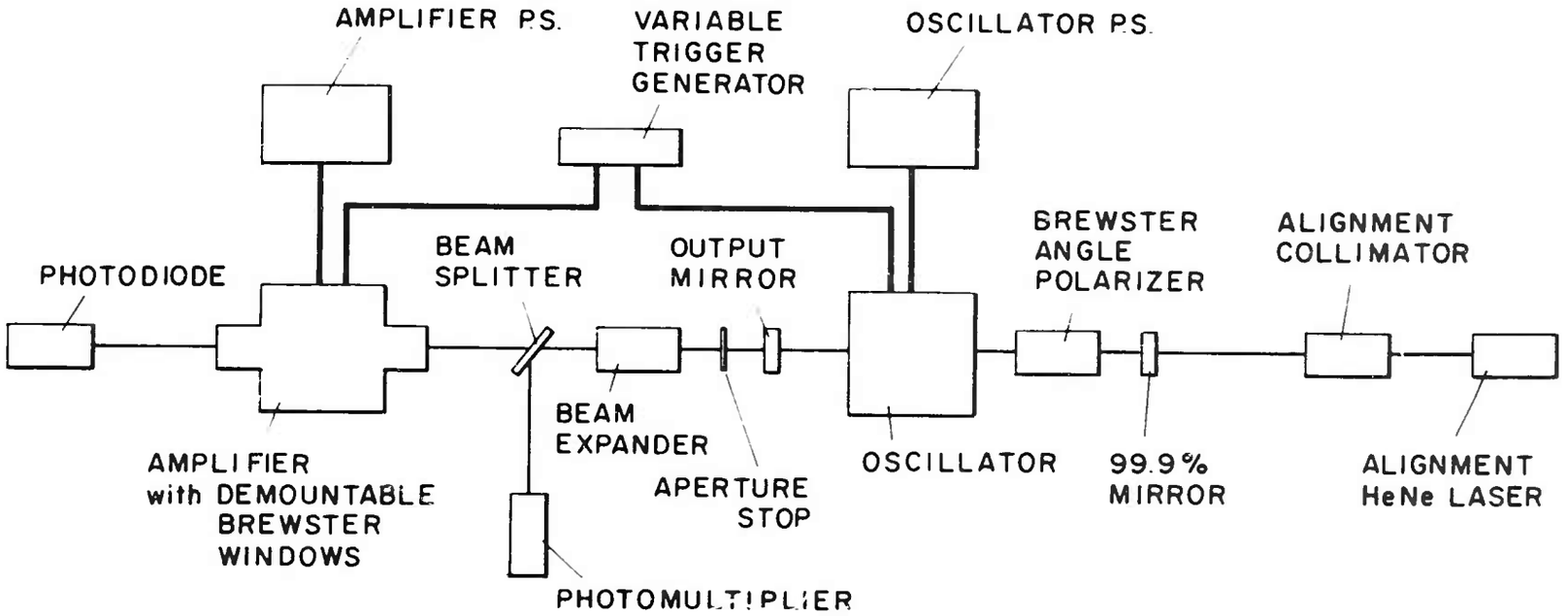

Figure 7-1. Schematic Diagram of the Sequence of Components Used in the Experimental Arrangement for Amplifier Experiments

beam oscilloscope, and amplifier gain as a function of time was measured by simply taking the ratio of corresponding peak heights. A sample of the experimental traces is shown in Figure 7-2. Figure 7-3 shows current and light output waveforms for the amplifier flashlamps which were fed by a four-section pulse-forming network. Current pulse duration is 225 μs.

A cross section of the experimental laser head is shown in Figure 7-4. The liquid laser cell was made of Pyrex and was provided with individually demountable Brewster windows as shown. The cell bore diameter was 0.55 inch and the active length 6.5 inches. Excitation of the laser was provided by two heavy-duty Xenon Corporation flashlamps (6.5-inch arc length, 12-mm bore) in series, externally-triggered from the close wrapped silver-foil reflector. The flashlamps were enclosed by special sharp-cutoff yellow filter tubing which absorbed the uv generated by the flashtube, but which transmitted radiation in the pump bands of the laser material. The entire interior of the head was filled with demineralized water to stabilize the laser cell wall temperature and provide cooling for the flashlamp filters. A small, nylon pump circulated this water through a demineralizing column and a regulated-temperature water bath. The laser liquid was $Nd^{+3}:SeOCl_2:SnCl_4$, and a separate pumping system was used for circulating the liquid laser medium. This system included a heat exchanger through which the water from the laser head passed. The whole circulating system was insulated with asbestos and cotton batting to maintain a constant temperature for both the water system and the liquid laser material. Because of the extremely corrosive nature of the laser liquid used in this system, construction materials for the circulation system were essentially limited to glass, certain types of ceramics or Teflon. The pump parts of the connecting tubing were made of Teflon. However, the liquid had an adverse long-term effect on the virgin Teflon surfaces that was manifested by a permanent staining and a decrease in resistance to abrasion. This effect showed up as small Teflon flakes suspended in the liquid after a long time. The circulation rate of the laser liquid was so slow that the liquid may safely be assumed static and isothermal.

7.1.3 Experimental Results

Data such as shown in Figure 7-2 were used to evaluate I_{out}/I_{in}. Using Eq. (7-7) with the assumption that the pump radiation of Figure 7-3 can be represented by a square pulse and with σ, τ and α known (from oscillator experiments), W can be determined. Two such fits of the measured gain to Eq. (7-7) are given in Figures 7-5 and 7-6 for input energies of 930 and 2580 J. In these calculations, the values

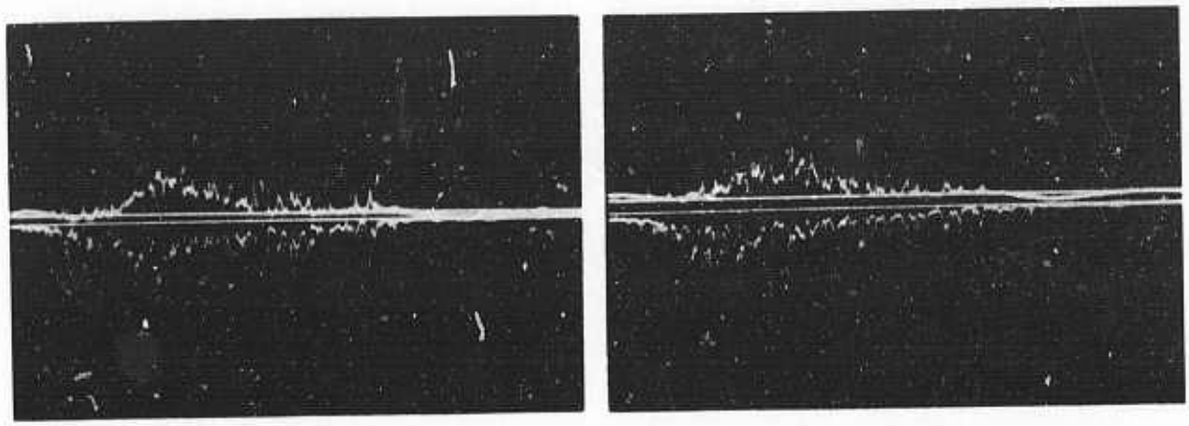

(a) E_{in} = 930 joules
(upper scale 11X lower scale)

(b) E_{in} = 2580 joules
(upper scale 45X lower scale)

Figure 7-2. Oscilloscope Traces of the Signal Input and Output Beams in the Amplifier Experiment. Upper trace: amplified signal; lower trace: input signal. Time base, 50 μs/major division.

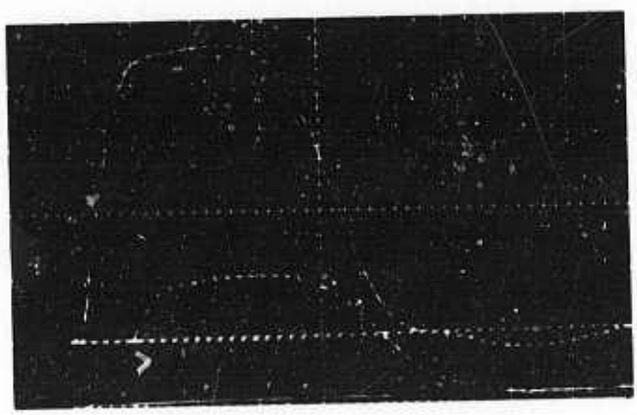

Figure 7-3. Current (Upper) and Light Output (Lower) Traces for the Flash Used to Pump the Amplifier. Input energy, 2580 joules; time base, 50 μs/major division.

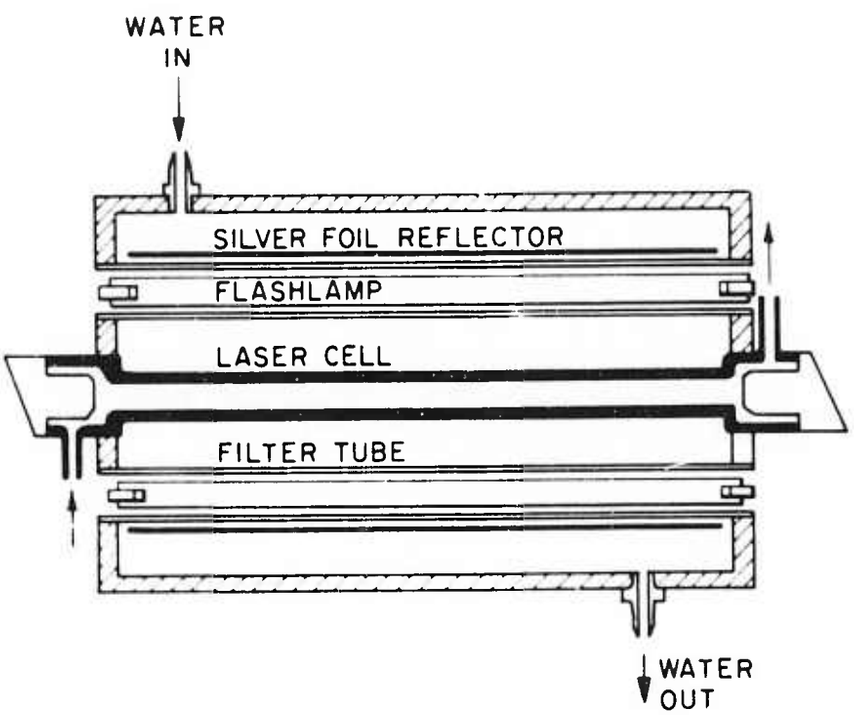

Figure 7-4. Cross Section of the Flash Enclosure and Cell Used in the Amplifier Experiments

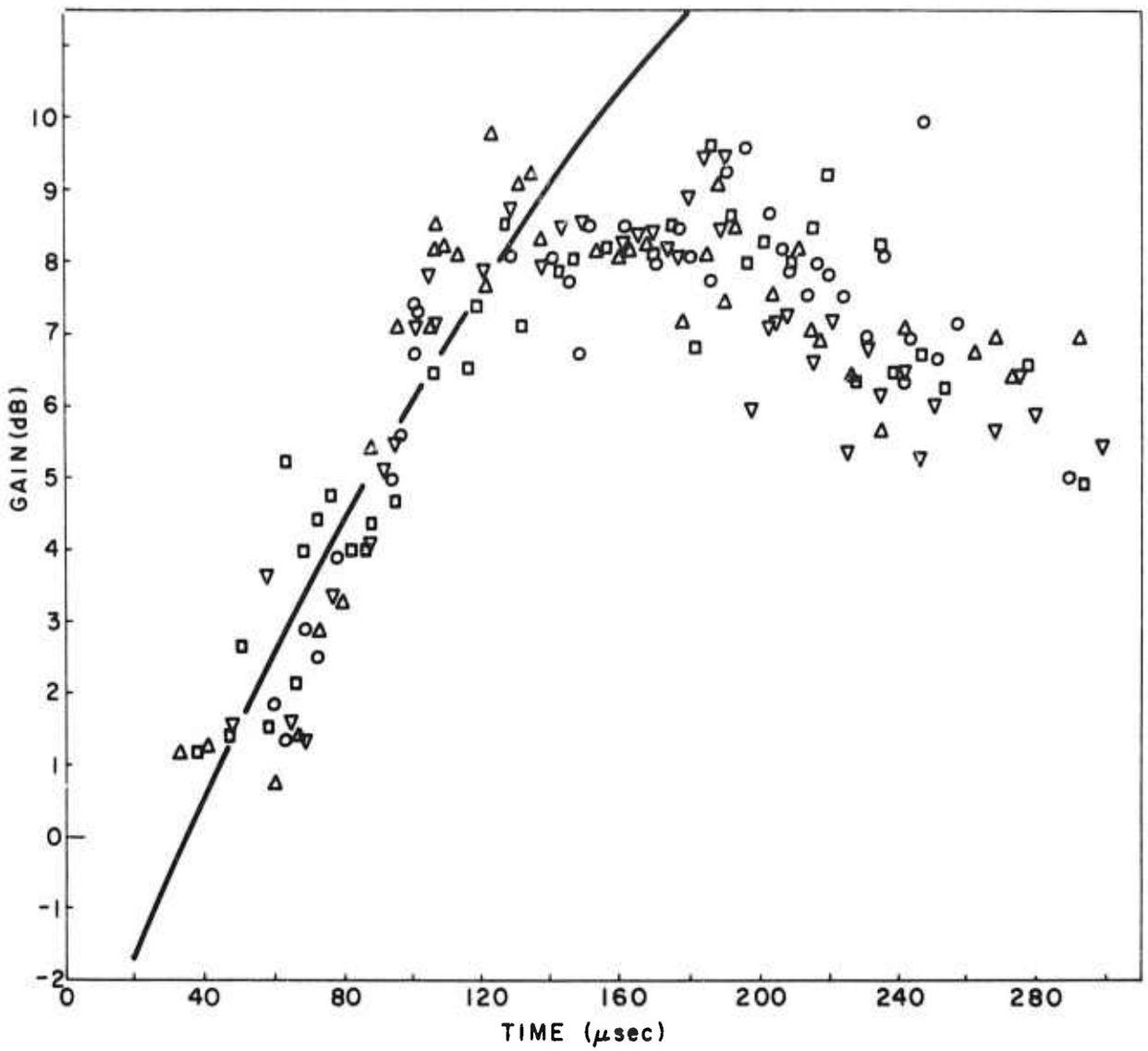

Figure 7-5. Time Development of Small Signal Gain; 930 joules Input Energy, W = 102 sec^{-1}.

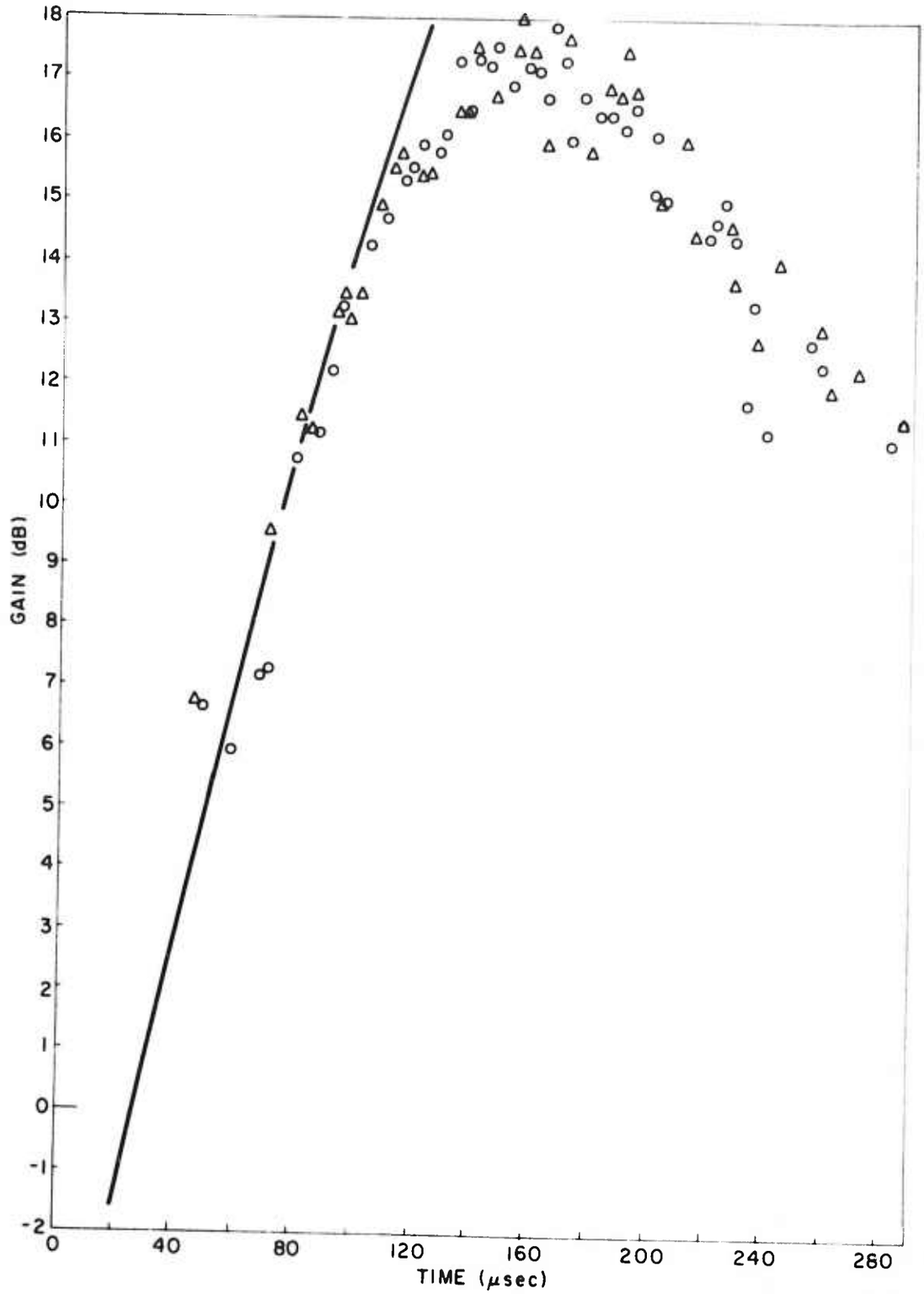

Figure 7-6. Time Development of Small Signal Gain; 2580 joules Input Energy, $W = 210\ sec^{-1}$.

$\alpha = 0.02\ \text{cm}^{-1}$, $\tau = 227\ \mu\text{s}$ and $\sigma = 8 \times 10^{-20}\ \text{cm}^2$ were used. The resulting variation of the pumping rate W with input energy is illustrated in Figure 7-7.

The variable W represents an average parameter that deseribes the interaction betweeu thc laser medium and the flux of flashlamp pumping-light inside the pumping cavity. However, it also implicitly eontains factors involving the flashlamp eonversion efficiency of eleetrical energy into light flux within the proper pumping bands, as well as the interaction between off-axis spontaneous emission and the population inversion. The first of these faetors becomes diffieult to charaeterize when fast-risetime, high current flashtube pulses (like the ones in this experiment) are used. Under these eireumstances, strong shock waves are formed inside the flashtube with shock amplitude direetly proportional to electrieal energy input,[120] and these shock waves affect flashtube conversion efficieney. As a eonsequence, there exists a maximum of flashtube eonversion efficieney with changing energy input (keeping pulse duration constant).[121, 122] Conversion effieiency is also indirectly affeeted by flashlamp "self-loading" due to the refleetive enclosure. Thus, although at first thought one would assume that flashlamp intensity and, hence, W would vary direetly with electrieal power dissipation in the lamp. Therefore, total light energy would be proportional to total electrical energy dissipated in the flash; it turns out that both flashlamp intensity and W vary directly with the current through the lamp and hence, saturate with input energy.

For amplifier gain-saturation calculations, the experimental eurve of Figure 7-7 is important. Equally important is a plot of measured-peak, small-signal gain (in decibels) against electrieal input energy (in joules) as shown in Figure 7-8. Notice that the eurve is composed of three types of data points. The points represented by circles are those derived direetly from the small amplifier experiment just described. The second set of points (denoted by the small triangles) represent threshold energies extrapolated from oscillator data as follows. In terms of small signal gain, the oscillation threshold condition may be written:

$$4.343\ (\sigma \Delta N - \alpha)L = \text{dB gain} = -5 \log_{10} \left(R_1 R_2 \right) \qquad (7\text{-}8)$$

where $R_1 R_2$ is the product of thc cavity mirror reflectivities. Here we denote dB gain to mean the measured (or effective) gain, including any distributed losses present in the oscillator excluding transmission losses at the mirrors. Thus, by extrapolating the oscillator input-output energy eurve to interseet the energy input axis, we derive a point on the small-signal gain curve for each value of $R_1 R_2$ used.

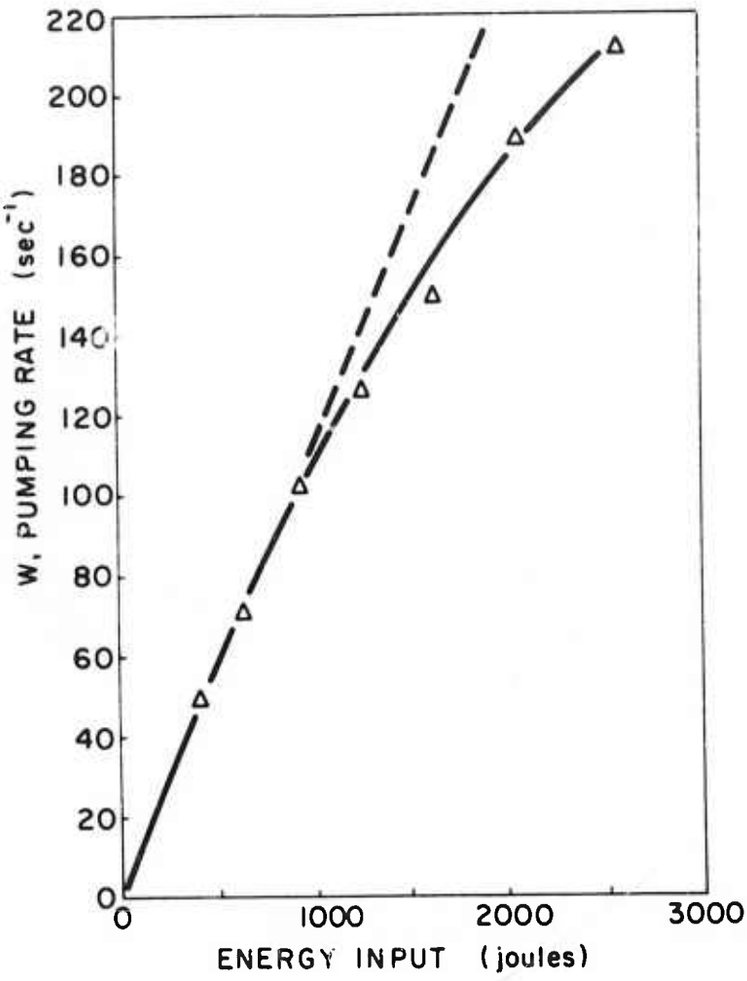

Figure 7-7. Pumping Rate W as a Function of the Input Energy to the Amplifier

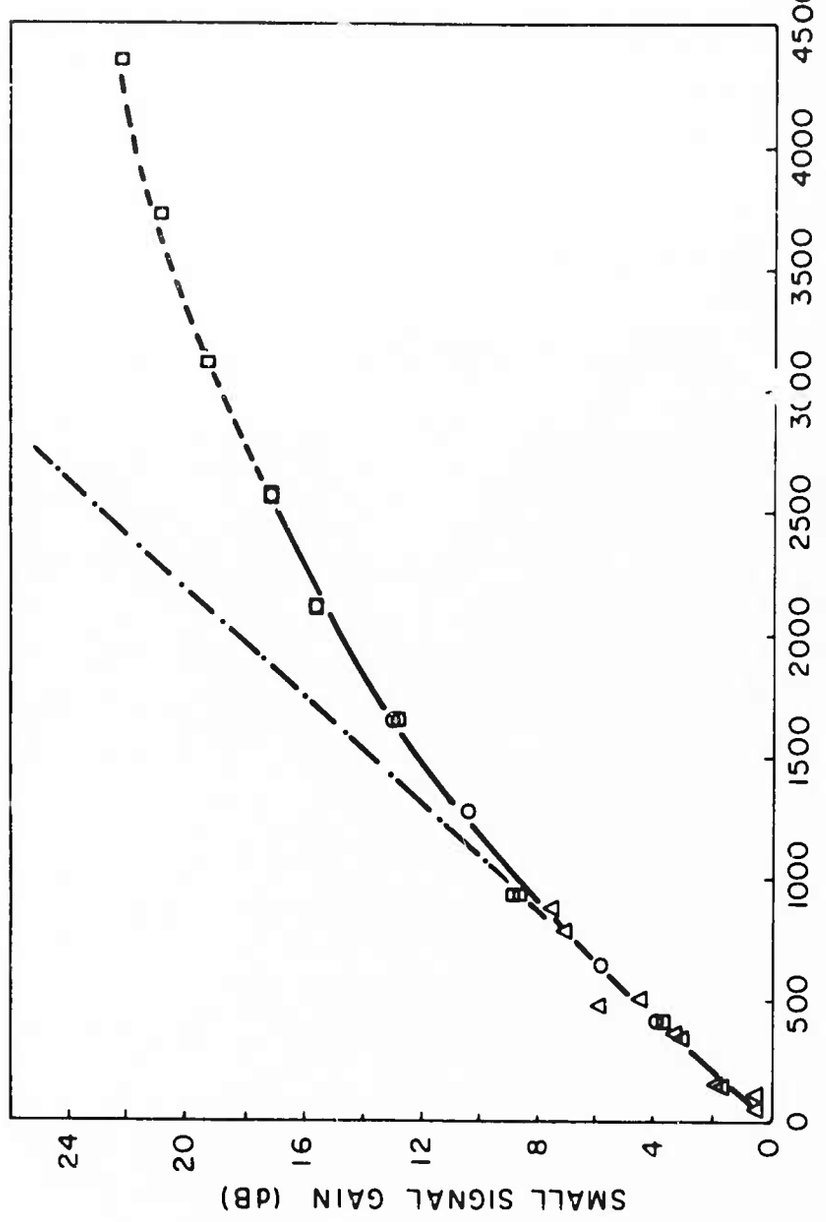

Figure 7-8. Peak Small-Signal Gain as a Function of Input Energy to the Amplifier;
O - Direct Measurements, Δ - Extrapolated Threshold Energies,
□ - from Light Output Data.

A third series of data points are plotted on Figure 7-8 by the crosses. These points represent a measurement of the broadband time-integrated light output of the flashlamps operating inside the laser enclosure. The dB gain values for the integrated pump light output are obtained by assuming this light output is proportional to the gain, and determining the proportionality constant using the 17.1 dB gain and the measured integrated light value at 2580 J input. As may be seen by this figure, the fit to the experimental small-signal gain curve is good. This fact is most significant in that these points are directly a measure of the total flashlamp radiant energy output. Likewise,

$$\text{dB gain (peak)} = 4.343 \left(\sigma \Delta N_{max} - \alpha L \right) \tag{7-9}$$

and the peak small-signal gain is directly proportional to the energy stored in the laser material in the form of the population inversion. The correspondence between the gain points and the flashlamp points in Figure 7-8 means that, for at least up to 2580 J into the laser flashlamps, amplifier performance was not being significantly degraded by premature depletion of the population inversion due to the high gain of the laser material and spontaneous emission within it (internal depumping losses). We are, therefore, left with the conclusion that the observed "saturation" of both small-signal gain and pumping rate parameter W with the lamp input energy is due to the degradation of flashlamp efficiency with increasing input energy.

The fluorescence maximum or peak gain frequency for $Nd^{+3}:SeOCl_2$ is about 50 cm^{-1} higher than for the glass oscillator. In the small signal experiments described above, no discernible difference was observed between the gain observed at the peak frequency (oscillator experiments) and the amplifier experiments (Figure 7-8). Sasaki et al.,[123] however, observe that the closer the frequency is to the peak, the higher the amplification factor. Their experiments were carried out at high probe power and saturated gains of about a factor of 3 were observed.

Fill[28] has carried out a series of amplifier measurements using $Nd^{+3}:POCl_3:ZrCl_4$. In this solvent, using a cell of diameter 9-mm and 33-cm long small-signal gains of about 28 dB have been observed for 2000 J of flashlamp input energy. The dB gain was linear up to 1500 J but deviated slightly at higher input energies. In these experiments, a Q-switched liquid or glass oscillator was used as the probe, and the ratio of the small-signal gain observed agreed within experimental error with the ratio of the fluorescence intensities (or absorption cross-sections) over the

80 Å difference in wavelength. Saturated gains of 17 dB, agreeing well with those calculated from the gain saturation parameter, were also obtained.

Andreou[124] has also carried out a series of amplifier experiments using $Nd^{+3}:POCl_3:ZrCl_4$. In this case, both the oscillator and amplifier were of the same material and the amplifier cell was 22.8 cm long, and 0.9 cm in diameter. Gains of nearly 20 dB were obtained. The amplification of an 0.5 J, 11 ns pulse to a pulse of 0.57 GW power with no distortion of pulse shape is reported. The shape of the output beam at the high input energies does show distortion. In a later work, Andreou, Selden and Little[29] describe the amplification by a liquid amplifier of mode locked pulses from a glass oscillator. Gains of 9 were observed from a 15.5 cm long amplifier at an input of 1 kJ. The beam patterns again showed significant distortion.

The thrust of this interest, as well as ours, in the high power amplifier work is the high gain and damage free operation of liquid laser amplifiers. The work described here bears out the promise; high gains have been measured experimentally and no damage has been observed. The main problem is associated with the beam distortion and we shall address ourselves to this later.

7.2 AMPLIFICATION OF A Q-SWITCHED PULSE IN $Nd^{+3}:POCl_3:ZrCl_4$

The work to be described in this section parallels that of Andreou[124] in that a Q-switch pulse is used as input to a liquid amplifier. It differs from this work in that the probe oscillator used here is a flash-pumped YAG with laser emission centered about the wavelength 1.0648 μ. This wavelength is quite removed from the peak of the fluorescence emission of the laser liquid as shown by Figure 7-9, and the relative fluorescence intensity of the laser liquid at this wavelength is only 51% of the peak value at 1.052 μ. Fill[28] has measured small-signal gains both at the peak of the fluorescence emission in this liquid and at 1.060 μ, and found that the ratio of measured small-signal dB gain agreed within experimental error with the ratio of the fluorescence intensities at the two wavelengths.

7.2.1 Experimental Setup and Equipment

A sketch of the arrangement used to study amplification in the laser liquid is shown as Figure 7-10. The pulsed YAG laser, used in these experiments, is the same device used in the Mach-Zehnder experiments described in Section 4. It is a Sylvania Model 610 laser modified for flash pumping. An intra-cavity aperture for

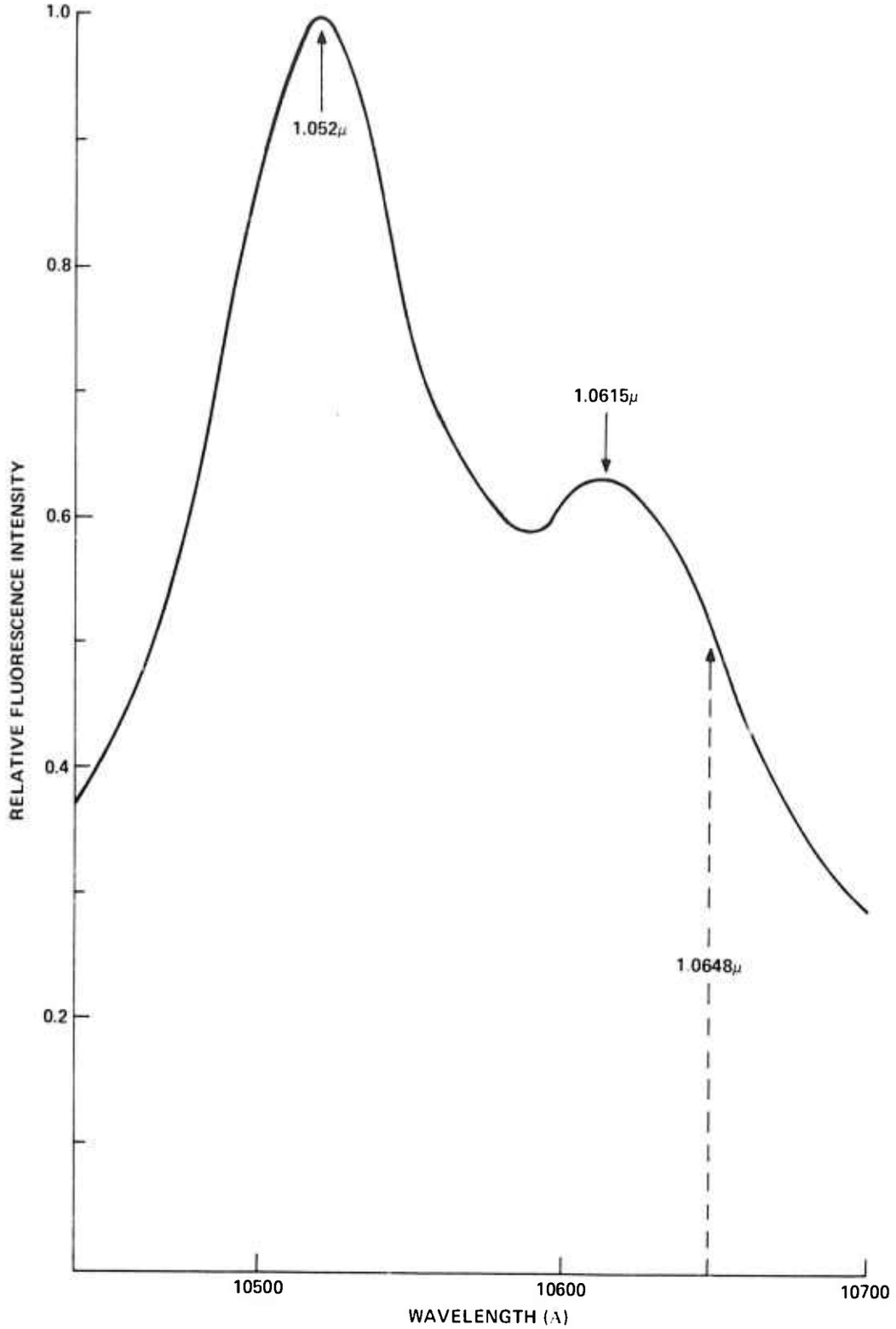

Figure 7-9. Fluorescence Spectrum of $Nd^{+3}:POCl_3:ZnCl_4$

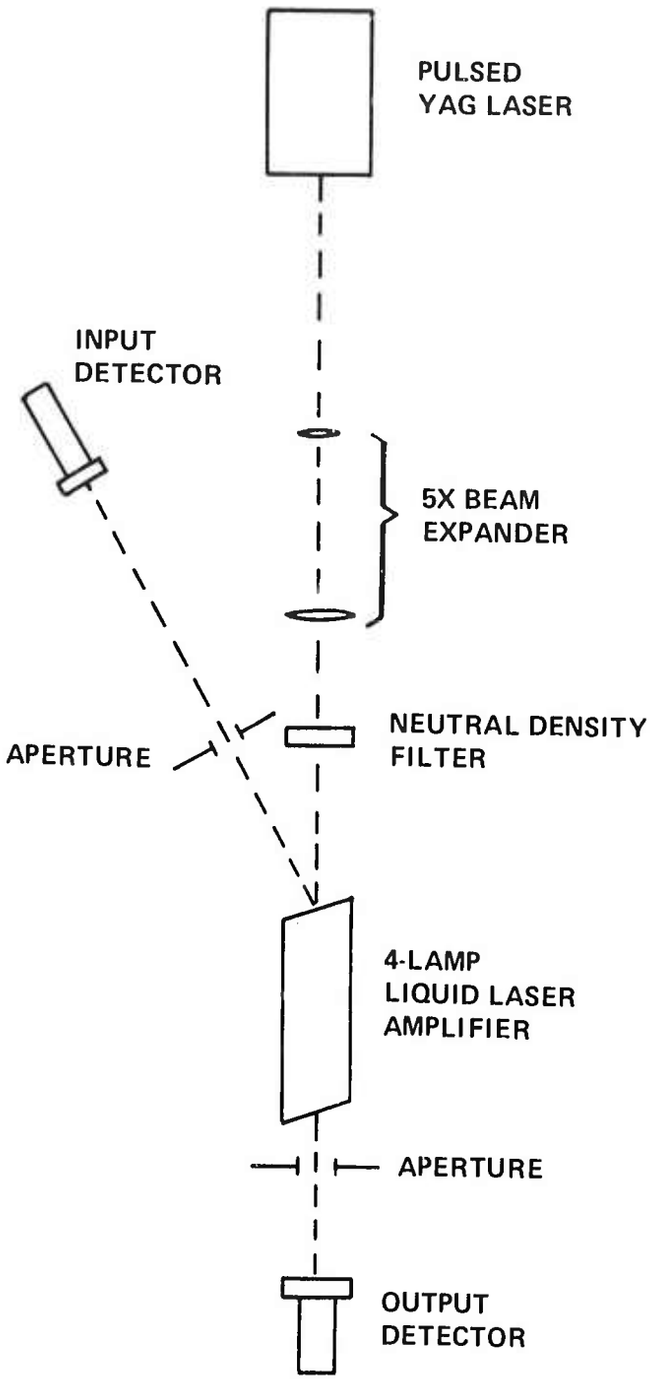

Figure 7-10. Amplifier Experimental Setup

transverse mode selection and a KD*P Pockels cell Q-switch were also added to the original laser. The total bank capacitance used with the flashlamps was 50 μF and triggering of the lamps was by series-injection. Although bank voltages in excess of 1000V were occasionally used, all the data reported here was taken with a bank voltage of 800 V ($E_{in} = 1/2\ CV^2 = 16$ J). At this input to the flashlamps, the resulting Q-switched output pulse was quite reproducible. Figure 7-11 is an oscillogram of the pulse generated under these conditions. It is apparent that the pulse is partially mode-locked, as the spikes on the pulse envelope occur at a period of about 2 ns which corresponds to the laser cavity transit time. Total pulse energy measured calorimetrically averaged about 1.3 mJ for this setup. Assuming the pulse envelope is roughly Gaussian of form:

$$I = I_o \exp\left(-\frac{t^2}{T^2}\right) \tag{7-10}$$

where T≈12 ns from Figure 7-11, the peak pulse power is approximately given by $I_o = 6 \times 10^4$ W.

The YAG laser beam intensity profile was measured using a calibrated closed-circuit TV camera and dual-time base oscilloscope in a method developed by C. Luck.[125] In this method, the CCTV camera Vidicon acted as a time-integrating detector for the Q-switched pulse in that the intensity distribution of the laser beam was "stored" as a charge pattern on the Vidicon photoconducting layer until read out by the scanning electron beam. By using a dual time base oscilloscope (Tektronix 545A), an individual TV line from the raster field could be selected, displayed on the CRT and photographed. A small TV monitor was used, with video blanking derived from the oscilloscope sweep-gate pulse, to observe the beam spot with the TV line displayed on the oscilloscope indicated as a dark line across the monitor. Because the "gamma" of the Vidicon is not unity and varies from tube to tube, the CCTV camera was calibrated in terms of video voltage vs. illumination on the Vidicon. Once this was done, the CCTV camera video output could be converted into illumination and the laser beam intensity profile measured.

Figure 7-12 shows the results obtained using this method for the raw laser beam at a distance of about four and a half meters from the laser. As may be seen from this graph, the output beam is not purely Gaussian (TEM_{00} mode), but has a bit of ripple superimposed on the Gaussian form. The slight distortion is a result of using a slightly larger-than-necessary intra-cavity aperture. As has been shown by Freiberg and Halsted[126] in their study of low order transverse modes in argon ion lasers, as the intra-cavity aperture is increased, higher order transverse modes begin to appear in the laser output beam. The next laser mode to appear after the Gaussian TEM_{00} mode will be in the donut-shaped TEM_{01}* mode. In our case, the data of Figure 7-12 indicates

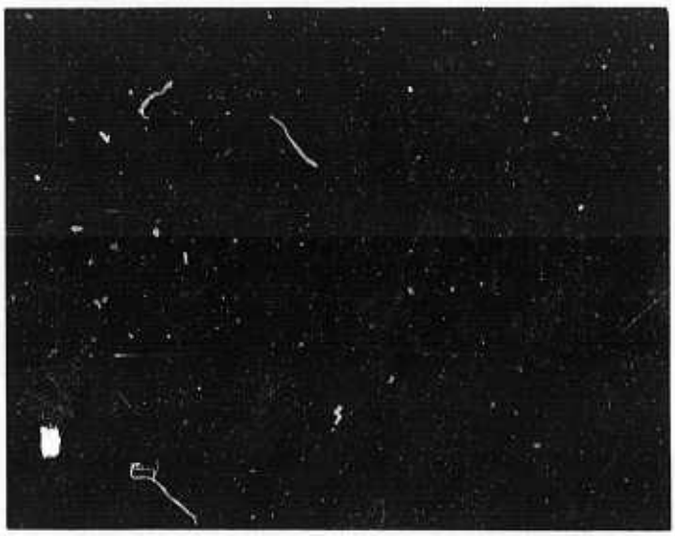

Figure 7-11. Oscillogram of YAG Laser Output Horizontal Time Scale: 20 ns/div.; pulse full-width-at-half-maximum (FWHM): 20 ns.

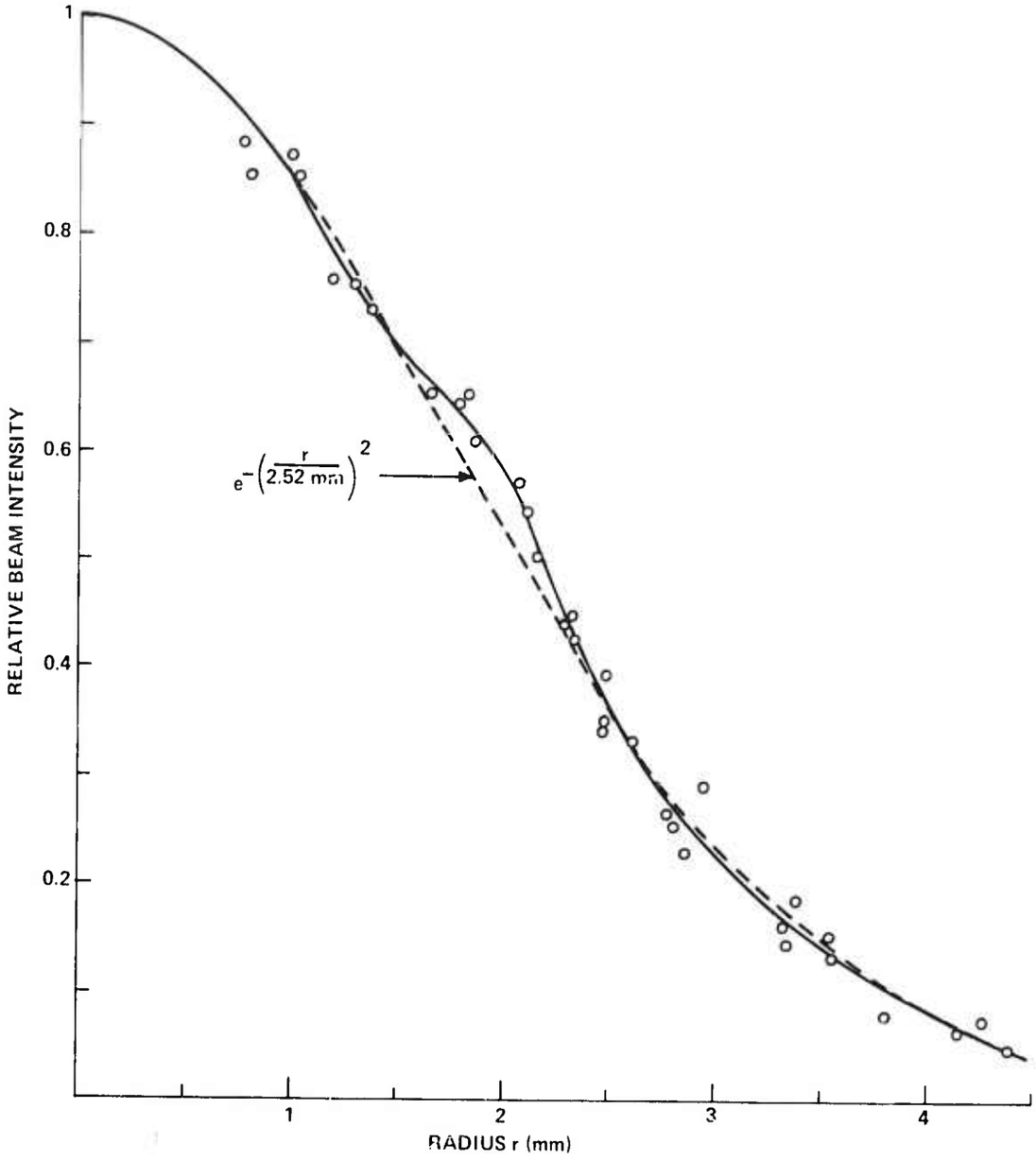

Figure 7-12. Pulsed YAG Laser Beam Profile at 450 cm From the Laser

that roughly 20% of the output energy of the beam can be ascribed to the TEM_{01}* mode, while the remainder is in the lowest-order TEM_{00} mode. A calculation of the expected spot size inside the resonator at the plane of the aperture, using the method of Kogelnik and Li[109] along with the data of Freiberg and Halsted,[126] shows remarkable agreement with the observations.

Returning to the experimental setup for measuring amplifier gain shown by Figure 7-10, the raw beam from the YAG laser was passed through a 5-times beam expander consisting of a 10 cm focal length and a 50 cm focal length converging lens combination. These lenses were manufactured by the Continental Optical Corp. to yield spherical aberrations less than or equal to the Rayleigh limit. The beam expander could be removed from the optical path to increase the input power density at the amplifier. To decrease the input pulse energy, neutral-density filters could be inserted in the beam after the beam expander. These were filters from the NG series by Schott.

Only one liquid amplifier was studied in this work. This was the large 22 mm (7/8 inch) bore diameter by 25 cm long laser cell in the 4-lamp quad-ellipse flash enclosure. This was the same laser cell used to investigate the thermo-optical distortions in the flowing liquid; the results of which were described in Section 4. The same cell was used in the long-pulse, repetitively-pulsed oscillator work presented in Section 5. The cell was equipped with end windows with a 5° wedge angle to frustrate multiple reflections inside the cell. The reflected portion of the input YAG beam, off the outer face of this window, was sent to a detector which monitored input beam energy, and an identical detector was used on the beam transmitted through the laser cell to measure output energy. These detectors were E. G. &G. "Lite-Mike" photodiode detectors, whose output current was electronically integrated to give a voltage step signal with magnitude proportional to the energy received by the photodiodes. Infrared filters and scattering plates were used in front of the photodiodes, and apertures were placed between the detectors and the laser cell to cut down the effects of stray flashlamp radiation. The detectors were calibrated in energy using a small ballistic thermopile as a secondary standard, and were cross-calibrated relative to each other through the known transmission of the laser cell at the laser wavelength from the results of the long-pulse oscillator experiments. The outputs from the two detectors were displayed on a dual-beam oscilloscope, two representative photos of which are shown as Figure 7-13. The bottom photograph shows the effect of flashlamp radiation on the detectors by the gently rising portions of the oscilloscope traces. The break in the curves occurring 400 μs after the start of the traces is the Q-switch laser pulse. As was mentioned before, the magnitude of this step is proportional to the energy in the pulse.

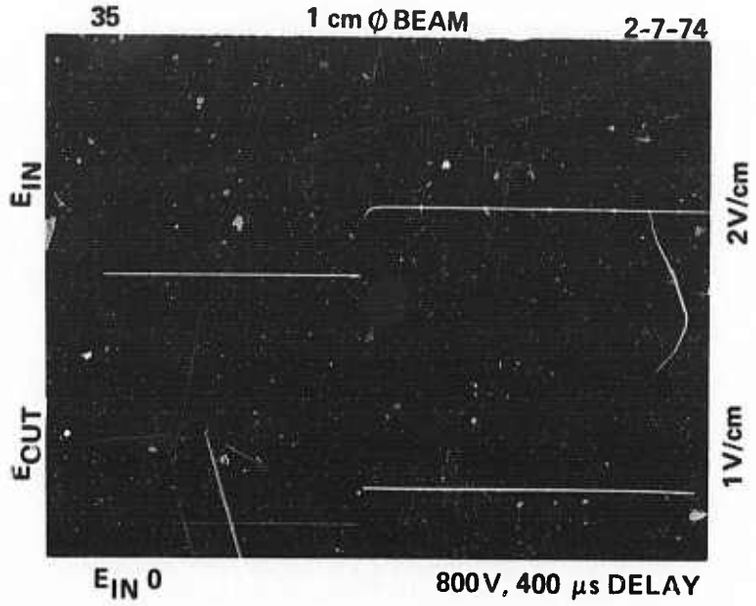

(a) Amplifer Flashlamp Input Energy Zero

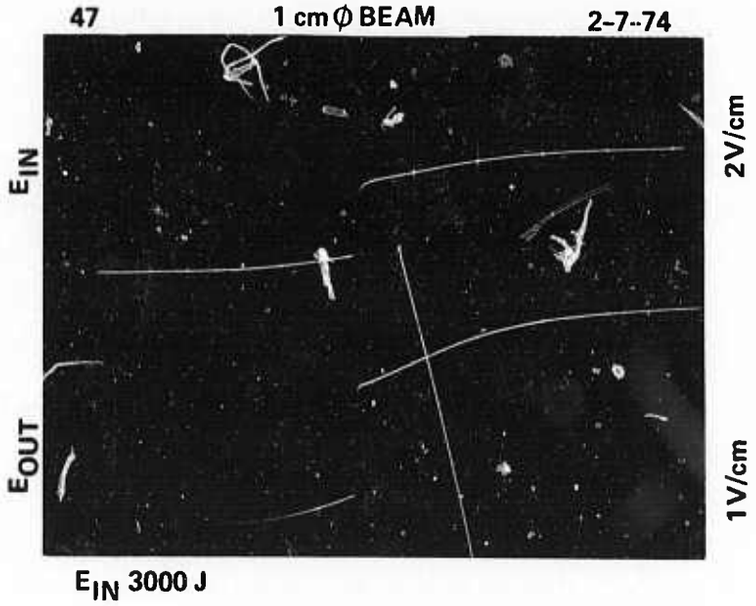

(b) Amplifier Input Energy 3000 Joules

Figure 7-13. Oscillogram Data of Amplifier Experiment. Upper trace on each photo is from input detector and lower trace is output energy.

7.2.2 Data and Calculations

All data was taken under the following circumstances:

a) Reynold's Number of liquid flow through the laser cell was held constant at 6000.

b) The laser liquid and the cell coolant temperatures were made equal ($T_{CL} - T_0 = 0$).

c) The YAG probe pulse was kept at a constant time delay from the start of the amplifier flashlamp pump pulse of 400μs.

Under these constant conditions, the amplifier input energy was varied along with the YAG pulse input power density by using filters with and without the 5x beam expander in place. The greatest attenuation of input power density was obtained by using the 5x beam expander with a neutral density filter of transmission 0.0303. The combination of these two factors is a maximum attenuation factor for the pulse input power density ($W\,cm^{-2}$) of:

$$0.0303 \times \left(\frac{1}{5}\right)^2 = 0.00121 = 1.21 \times 10^{-3}.$$

The experimentally-measured amplifier gains did not change with input power density over this entire range. This point is most significant and will be addressed a bit later.

In the same way as was done in Section 7.1.3, the long-pulse oscillator threshold-energy points for different output mirrors can be used to establish small-signal gains for the amplifier at the peak of the fluorescence emission (1.052 μ). This data can be extended to larger lamp input energies by measuring the flashlamp integrated-energy output as a function of input energy. The results of doing this, along with the averaged data from the YAG- amplifier experiment, are presented in Table 7-1.

The average of the ratios of the measured gains is 0.54, which is quite close to the ratio of the fluorescence intensity of the liquid at the two wavelengths (0.51), as shown previously by Figure 7-9. Actually, we did not take a spectra of the YAG Q-switched output. It is possible that the center of the laser emission was not quite at the 10,6480 Å assumed. In fact, if the center of the laser emission from the YAG were shifted just 40 Å toward the blue, the ratio of fluorescence intensities would be equal to 0.54. At any rate, the data from this experiment confirms the results of Fill[28] that the gain away from the line center in the laser liquid is proportional to the fluorescence intensity.

TABLE 7-1

AMPLIFIER GAINS MEASURED FOR 4-LAMP LIQUID LASER

Input Energy (J)	Oscillator Results ($\lambda = 1.052\ \mu$) Gain (dB)*	YAG Results ($\lambda = 1.064\ \mu$) Gain (dB)*	Ratio $\frac{\text{Gain @ } 1.064\ \mu}{\text{Gain @ } 1.052\ \mu}$
500	1.98	1.08	0.543
1000	3.92	2.18	0.556
1500	5.89	3.21	0.545
2000	7.60	4.06	0.534
2500	9.01	4.81	0.534
3000	10.28	5.52	0.537
3500	11.35	6.15	0.542

*neglecting scattering losses.

Let us now return to the calculation of gain in the liquid amplifier. Rigrod[127] expresses the gain relation in an amplifying medium with distributed loss α and gain $g_o = \sigma \Delta N$ as:

$$(g_o - \alpha) L = \ell n\left(\frac{E_o}{E_i}\right) - \frac{g_o}{\alpha} \ell n \left[\frac{g_o - \alpha\left(1 + \frac{E_o}{E_c}\right)}{g_o - \alpha\left(1 + \frac{E_i}{E_c}\right)}\right] \qquad (7\text{-}1)$$

where:

$g_o = \sigma \Delta N\ (cm^{-1})$

E_o, E_i = output, input energy densities $(J\,cm^{-2})$

E_c = saturation energy density $= \frac{h\upsilon}{\sigma}\ (J\,cm^{-2})$

α = distributed loss coef. (cm^{-1})

The values of the respective quantities (evaluated at the YAG laser wavelength) are:

$$\sigma = (0.51) \times (6 \times 10^{-20} cm^2) \simeq 3.1 \times 10^{-20} cm^2$$

$$E_c = \frac{h\upsilon}{\sigma} = 6.2\ J\,cm^{-2}.$$

Eq. (7-11) expresses the saturation of energy gain of the amplifier with increasing input energy density. Because the duration of the Q-switched input ($T = 12$ ns) is small, as compared to the spontaneous lifetime of the upper laser level in this material (~ 300 ns), the effect on the amplifier population inversion of spontaneous emission and pumping may be neglected.[118, 119, 128, 129, 130, 131] As a result, the purely material parameter E_c becomes a figure of merit for the amplifier medium.[132] The larger the saturation energy density of the material becomes, the more energy can be extracted from the population inversion before pulse sharpening of the amplified signal becomes a problem. This may be best seen by rewriting Eq. (7-11) in the form:

$$R \alpha L = \ell n\left(\frac{E_o}{E_i}\right) - (R+1)\ \ell n\left(\frac{RE_c - E_o}{RE_c - E_i}\right) \tag{7-12}$$

where:

$$R = \left(\frac{g_o}{\alpha} - 1\right) > 1 \text{ for any realistic amplifier.}$$

Two regimes of Eq. (7-12) are of interest. If $E_i, E_o \ll RE_c$, the amplifier is operating in the small-signal gain regime. Under this condition Eq. (7-12) becomes:

$$R \alpha L \simeq \ell n\left(\frac{E_o}{E_i}\right) - (R+1)\,\ell n\,(1) = \ell n\left(\frac{E_o}{E_i}\right)$$

and

$$E_o = E_i e^{R \alpha L} = E_i e^{(g_o - \alpha)L} \tag{7-13}$$

The output energy is, therefore, given by the difference between distributed gain and loss in the amplifier. On the other hand, when the input energy density becomes very large so that $E_i, E_o \gg RE_c$ [Eq. (7-12)] becomes reduced to:

$$R \alpha L \sim \ell n\left(\frac{E_o}{E_i}\right) - (R+1)\,\ell n\left(\frac{E_o}{E_i}\right) = R\,\ell n\left(\frac{E_o}{E_i}\right)$$

then

$$\ell n\left(\frac{E_o}{E_i}\right) = -\alpha L$$

and

$$E_o = E_i e^{-\alpha L} \tag{7-14}$$

and the amplifier acts simply as an attenuator. In the intermediate region when either E_i or E_o is comparable to RE_c, Eq. (7-12) must remain a transcendental equation that cannot be easily reduced. It should also be noticed that Eq. (7-12) has a singularity at $E_i = RE_c$ and that Eq. (7-12) becomes undefined in the region $E_i < RE_c < E_o$. The traditional region of gain-saturated amplification is, therefore, defined by the conditions $E_i \geq E_c$ while $E_o < RE_c$.

The quantities g_o and α (and therefore, R) must be measured by experiment on the particular amplifier under investigation. In the liquid amplifier under discussion, the distributed loss coefficient α was measured by using the laser as a long-pulse oscillator to be $\alpha = 7 \times 10^{-3} cm^{-1}$. The distributed gain coefficient g_o naturally depends on the energy input to the amplifier flashlamps. If we set the flashlamp input energy equal to 3000 J, we can calculate g_o from the measured data of Table 7-1 and Eq. (7-9) as:

$$4.343\, g_o L = 5.52 \text{ dB}$$

$$g_o = \frac{5.52}{4.343 \times 25.4 \text{ cm}} = 5 \times 10^{-2} cm^{-1}.$$

The quantity R is, therefore:

$$R = \frac{g_o}{\alpha} - 1 = \frac{5 \times 10^{-2}}{7 \times 10^{-3}} - 1 = 6.15$$

The region of gain saturation for the amplifier under these conditions will be defined by:

$$E_i \geq E_c = 6.2 \text{ J cm}^{-2}$$

$$E_o \geq RE_c = 38 \text{ J cm}^{-2} \qquad (7\text{-}15)$$

The maximum energy density at the input to the amplifier E_{max} will occur when the raw YAG beam is propagated without the beam expander through the liquid amplifier. If we assume that YAG beam intensity profile is Gaussian and use the results from the TV measurement on the beam intensity presented previously, we can calculate the peak on-axis energy density in the laser beam. The beam "spot size" at the input to the amplifier was measured to be w = 2.96 mm. The (normalized) energy

distribution of the input beam may be therefore written as:[126]

$$E_i(r) = \frac{2E}{\pi w^2} \exp\left(\frac{-2r^2}{w^2}\right) \tag{7-16}$$

where E = total energy in pulse = 1.3×10^{-3} J and the reader may verify for himself that:

$$\int_0^\infty 2\pi r E_i(r)\, dr = E. \tag{7-17}$$

The peak on-axis energy density of the beam is therefore:

$$E_{max} = E_i(o) = \frac{2E}{\pi w^2} = \frac{2.6 \times 10^{-3} \text{J}}{\pi (0.296 \text{ cm})^2} \simeq 1 \times 10^{-2} \text{J cm}^{-2}. \tag{7-18}$$

The energy density is at least two orders of magnitude smaller than that necessary, as given by Eq. (7-15), to reach the gain-saturated amplification regime. As the calculated E_{max} was the largest input power density used in these experiments, all values of gain measured were well in the small-signal regime.

7.3 GAIN AND OPTICAL DISTORTIONS IN LIQUID AMPLIFIERS

As was shown in the previous section, the laser stimulated emission cross-section is inversely proportional to the saturation energy density E_c, which can be used as a figure-of-merit of the amplifying medium. Table 7-2 below lists the relevant physical parameters of Nd^{+3} emission in the various host materials.

It may be seen from this table that Nd^{+3}:glass is capable of storing from about two to twenty times the energy density of Nd^{+3} in the liquid hosts at the same small-signal, single-pass gain (dB). It would appear from this conclusion that Nd^{+3}:glass is the optimum amplifier material for high-brightness laser systems. One of the serious problems encounted in the construction of high brightness systems is the target feedback problem. If the small-signal gain of the amplifier chain is made too large, back reflections of the target or optics in the amplifier chain can drive the system above threshold leading to oscillation. In may cases, this can lead to damage to the chain or optical components. What is needed for these systems is a large energy storage capacity with as low a single-pass small signal dB gain as possible. Table 7-2 shows that Nd^{+3}:glass is best suited to these requirements, while Nd^{+3}:YAG would be the worst choice of materials; the aprotic liquid solvents would fall in between these two host materials.

TABLE 7-2

PROPERTIES OF Nd^{+3}—DOPED LASER MATERIALS

	Absorption Cross-Section (cm^2)	Fluorescence Lifetime (μs)	E_c ($J\ cm^{-2}$)	Peak Emission Wavelength (μm)
$Nd^{+3}:SeOCl_2:SnCl_4$	8×10^{-20}	280	2.35	1.058
$Nd^{+3}:POCl_3:SnCl_4$	6×10^{-20}	310	3.14	1.054
$Nd^{+3}:POCl_3:ZrCl_4$	6×10^{-20}	330	3.15	1.052
Nd^{+3}:glass[19, 20, 21, 14]	$0.3 - 3 \times 10^{-20}$	100-1000	6-60	1.058 - 1.064
Nd^{+3}:YAG[19, 22, 23]	$30 - 90 \times 10^{-20}$	240	0.2 - 0.6	1.062 - 1.065

In terms of optical distortions, as was shown previously, these are of two types in the liquid laser: distortions arsing from the flash pumping and those arising from the flow of the liquid medium itself. The latter type of distortions occur on two distinct time and space scales: a macro- and steady-state scale and a micro- and millisecond scale. Both of these latter manifestations are related to the turbulent flow nature of the liquid media and arise from thermal gradients in the liquid.

In Section 4 of this report, a steady-state physical model of turbulent flow was presented and calculations based on this model were performed. These calculations were shown to be in excellent agreement with experiment. The success of the physical model in predicting the steady-state, large-scale distortions observed in the liquid laser enabled us to qualitatively explain the results of a series of repetitively-pulsed oscillator experiments with the liquid laser as due to radial thermal gradients. We have shown how these gradients can be partially compensated in the case of the long-pulse oscillator under kilowatts of average input power. In the final part of this section, we want to address ourselves to the possibility of constructing high-beam quality, high-average power liquid amplifiers.

7.4 HIGH-AVERAGE POWER LIQUID AMPLIFIERS

We have shown, both by direct experiment and by way of a physical model developed through theory and confirmed by experiments, that by proper design of a water-jacketed, axial-flow laser cell with independent temperature control of the laser

liquid and the cell coolant average power inputs of several kilowatts can be handled. Long-pulse oscillator outputs, under these circumstances, were identical to single-shot outputs, showing that large-scale thermal lensing problems can be overcome in the liquid by a combination of rapid circulation plus thermal control of the medium. These extremely positive results must now be tempered in the case of a repetitively-pulsed amplifier for Q-switched laser pulse.

As was shown in Section 4 by the Mach-Zehnder interferograms, lens-like optical distortions are generated in the liquid laser due to absorption of the pump light. When the pump radiation incident on the outside of the laser cell is not circumferentially symmetric, distortions are produced in the laser medium. In this respect, the liquid behaves no differently than any other condensed-phase, optically-pumped laser medium. By proper design of the flashlamp pumping geometry, as is necessary for any other good amplifier, this asymmetry can be eliminated. Flash pumping would then result only in a radial thermal gradient. In principle, the magnitude of this radial thermal gradient can be controlled by the concentration of the active Nd^{+3} ions in solution and the bore diameter. As has been shown in Section 4, the present laser cell behaves as a converging lens under flash pumping. Since the variation of refractive index with temperature (dn/dT) is negative for the liquid, this means that the layers of liquid near the cell wall absorb more pump radiation and, therefore, become hotter than the liquid near the cell axis. The effective focal lengths, induced in the present laser cell, were measured to be as short as one meter during the pump pulse. Although this is not as severe as had been estimated by early workers in this field,[93] the lensing is strong enough to require compensation measures. Malyshev and Salyuk[87] observed the same results as this in the liquid $Nd^{+3}:POCl_3:SnCl_4$. They pointed out that the one-meter focal length in a laser cell of the same numerical aperture, but almost twice as long as the one we used, was about the limit for compensation by a simple diverging lens because for focal lengths smaller than one meter aberrations in the effective lens caused by the flash pumping increase rapidly. These authors point out that the power of the effective lens induced in the liquid may also be decreased by increasing the bore diameter of the laser cell while keeping the product of Nd^{+3} concentration and bore diameter constant. This latter suggestion would probably be desirable in any case to decrease the inversion loss rate due to stimulated fluorescence along the cell axis. It would thus appear practical, by a proper combination of all these methods, to reduce the flash-induced distortions in the liquid amplifier at a given time during the pump pulse to those of a simple converging lens that could be compensated by diverging lenses external to the laser cell.

The next effect to be considered is the long-term cumulative heat effect of repetitive-pulsing on the amplifier optics. As has been shown in the long-pulse oscillator work, maintaining the coolant in the laser cell water jacket at a lower temperature than the bulk laser liquid temperature can restore the output of the laser to that observed under isothermal conditions. For each laser cell studied, a particular temperature differential was found to compensate for the effects of a specific average input power to the flashlamps. This relationship was found to break down when the pulse repetition period became comparable to the mean liquid transit time through the laser cell. The mechanism of this compensation was postulated to be the removal of residual heat from the liquid near the cell wall by radial forced convection to the coolant surrounding the laser cell. The efficiency of this process is dependent on Reynold's Number of the liquid flow through the cell, and the thermal conductance through the cell wall itself. Good radial heat transport can be assured by using Reynold's Numbers on the order of 10,000, as was shown by the work reported earlier. The thermal impedance of the cell wall could be decreased by using quartz rather than the Pyrex used in the cells here. These relatively simple changes would be possible even with a greatly increased cell diameter, desirable for the reasons stated previously.

The final question to be answered is what are the limiting factors in the design of the liquid amplifier? Certainly one limitation is the nonlinear optical effects in the laser liquid measured by Alfano and Shapiro.[54] Although self-focusing was not observed in the liquid, stimulated Brillouin scattering (threshold: 35 MW/cm^2) and stimulated Raman scattering (threshold: 100 MW/cm^2) were seen. In the latter case, large amounts of Raman conversion will, therefore, occur at flux densities of typically 100 MW/cm^2 and cell lengths of 50 cm. The lower SBS threshold will place an even lower limit on the gain attainable in the liquid amplifier. For example, if we say we want to limit the input power density of a 20 ns FWHM laser pulse to 30 MW/cm^2 to avoid SBS, the peak energy density at the amplifier input will be roughly:

$$E_{in\,(max)} = 3 \times 10^7 \ \frac{w}{cm^2} \times 2 \times 10^{-8} \text{ sec} = 0.6 \text{ J/cm}^2. \qquad (7\text{-}19)$$

This number is about 1/5 of the saturation energy density for the $Nd^{+3}:POCl_3:ZrCl_4$ laser liquid.

Another limitation on amplifier output brightness might be the effect of small-scale fluctuations induced in the fluid by the turbulent flow. These were seen in the interferograms of Section 4 under single-shot conditions where $T_{CL} - T_0 > 0$. It is

not clear, from the data that we have collected, if these will be present under repetitive-pulsing when the average input power balances out the temperature differential near the cell wall. The results of the long-pulse oscillator work indicates that the extent of these fluctuations should be small, but it should be pointed out that the oscillator output occurs over several hundred microseconds in this case. The long-pulse data only indicates that the optical state of the flowing liquid averaged over this period is similar to that of the isothermal case. The instantaneous state of affairs in the cell is another matter entirely. A final series of experiments was planned to investigate this point, but the laser liquid in the system precipitated before these experiments could be run.

8. EVALUATION AND RECOMMENDATION

The subject matter presented and discussed in this report concerned the field of inorganic liquid lasers in its entirety. It includes materials and systems as well as the laser and amplifier output properties. Although these divisions interact with each other, they form a convenient and useful basis for the evaluation of the results. The objectives of this research were to evaluate the potential of Nd^{+3} aprotic liquids as the active medium for use in high average power oscillators and in high brightness oscillator-amplifiers. It is the purpose of this final section to make such an evaluation in terms of the divisions stated. We will also suggest directions for further work consistent with these objectives.

8.1 MATERIALS

The molecular system, involving $ZrCl_4$ and $POCl_3$, developed in this work, is a reasonably satsifactory laser material. A severe disadvantage is its sensitivity to water in that such contamination ultimately leads to a precipitate. A definite improvement would be to find a Lewis acid that would isolate the Nd^{+3} ion, still scavenge the contaminating water but would not lead to a precipitate. One could investigate such chlorides as those of Vanadium, Hafnium or Niobium as possibilities. Apart from the work of Weichselgartner and Perchermeier[27] there has been no systematic investigation of the Lewis acids.

The spectroscopic properties of Nd^{+3} in the $POCl_3$ system are ideal for the long pulse oscillator application and satisfactory for use as a Q-switched oscillator. The laser absorption cross-section and gain are high and this leads to low threshold and high efficiency operation. In the Q-switched mode of operation, high peak powers (of the order of gigawatts) have been observed. For a power amplifier, however, the gain is too high and the energy storage is too small. To overcome this, a more extensive materials investigation has to be undertaken. Control of the chemical environment surrounding the Nd^{+3} ion should be possible and this, in turn, must affect the cross-section of the laser transition. At this point, such a suggestion is tentative, because very few sound ideas have been put forward and no such work has been reported.

8.2 THE CIRCULATORY SYSTEM

The circulatory system, in its present stage of design, is adequate for this laser system. The materials of fabrication are stable to the laser liquid and would not require any modification should a less corrosive solvent system be employed. The size of the pump and the piping are in the proper range for the repetition rates used. Should these rates be increased, the system would require higher flow speeds and pressurization would be necessary to prevent cavitation; this feature is already built in. The major improvement required is a more efficient heat exchanger for the laser liquid.

8.3 THE LASER SYSTEM

In terms of average output power, it may be possible to attain a value of 1 kW with some modification to the present system. Basically, this involves using a six- or eight-lamp flash head in a close-coupled arrangement. This would allow for an increase in average input power and, equally important, would lead to a more uniform distribution of the flashlamp radiation. The uniformity is a significant factor in coupling efficiency and in beam quality.

As far as the amplifier is concerned, our experiments have shown that the average optical quality of the liquid medium is similar to that of solid state materials. We have also shown that there are small scale fluctuations which, for a short pulse, may not be averaged out. This could be a serious limitation in the beam quality of amplified Q-switched pulses. Just how limiting this may be has not been ascertained and would require more work.

8.4 SUMMARY

Overall, we have shown that in the long-pulse oscillator mode, the liquid laser is capable of high average power outputs with good efficiency. The limitations may actually lie in the power supplies, flashlamps and the available heat exchange rates. Furthermore, the ability to control two temperatures leads to good efficiencies at high average power inputs. For amplifiers, there appear to be basic limitations; a good measure of which has yet to be made.

The laser system itself has reached a level of design and development that is adequate and reliable. Improvements in this aspect are fairly straightforward.

The laser liquid requires more study. The present material is in many respects the first acceptable one in terms of safety and system compatibility. It has a disadvantage in that it is difficult to manufacture with reproducible quality. Good quality control is essential at every step, and this is not easily achieved. It would be surprising if the present liquid were the only acceptable material, but this can be ascertained only with more research effort.

9. PUBLICATIONS AND PATENTS

9.1 PUBLICATIONS

1. A. Lempicki, C. F. Buhrer and A. Heller, "The Kerr Constant of Selenium Oxychloride," Applied Optics 6, 1141 (1967).

2. A. Lempicki and H. Samelson, "Q-Switching and Mode Locking of Nd^{+3}:$SeOCl_2$ Liquid Laser," J. Appl. Phys. 39, 6115 (1968).

3. H. Samelson, A. Lempicki and V. A. Brophy, "Output Properties of the Nd^{+3}:$SeOCl_2$ Liquid Laser," J. Quant. Electr. QE4, 849 (1968).

4. A. Lempicki and H. Samelson, "Rare Earth Liquid Lasers," Ann. N.Y. Acad. Sci. 168, 596 (1970).

5. A. Lempicki and H. Samelson, "Liquid Lasers," Naval Research Reviews 23, 10 (1970).

6. H. Samelson, C. Brecher and A. Heller, "Determination of the Absorption Cross-Section of the Laser Transition of the Nd^{+3} Ion in Nd^{+3}:$SeOCl_2$ System," J. Opt. Soc. Am. 58, 1052 (1968).

7. H. Samelson, A. Lempicki and V. A. Brophy, "Self Q-Switching of the Nd^{+3}:$SeOCl_2$ Liquid Laser," J. Appli. Phys. 39, 4029 (1968).

8. C. Brecher and K. W. French, "Comparison of Aprotic Solvents for Nd^{+3} Liquid Laser Systems," J. Phys. Chem. 73, 1785 (1969).

9. C. Brecher and K. W. French, "Spectroscopy and Chemistry of Aprotic Nd^{+3} Laser Liquids," J. Phys. Chem. 77, 1370 (1973).

10. R. Pappalardo and A. Lempicki, "Brillouin and Rayleigh Scattering in Aprotic Laser Solutions Containing Neodymium," J. Appl. Phys. 43, 1699 (1972).

11. R. R. Alfano, A. Lempicki and S. L. Shapiro, "Non-Linear Effects in Inorganic Liquid Laser," IEEE J. Quant. Electr. QE7, 416 (1971).

12. C. Brecher, K. French, W. Watson and D. Miller, "Transmission Losses in Aprotic Liquid Lasers," J. Appl. Phys. 41, 4578 (1970).

13. H. Samelson, R. Kocher, T. Waszak and S. Kellner, "Oscillator and Amplifier Characteristics of Nd^{+3}:$SeOCl_2$ Liquid Lasers," J. Appl. Phys. 41, 2459 (1970).

9.2 PATENTS

Patents acquired under this contract are:

1. Method of Preparing an Active Medium for a Liquid Laser, 3558504, C. Brecher and K.W. French.

2. Active Medium for a Liquid Laser and Method of Preparation Therof, 3623995, K.W. French.

3. Cell for Use in Circulatory Liquid Laser, 3668216, R. Kocher, F. Moore and H. Samelson.

4. Cell for Use in Circulating Liquid Laser, 3663891, R. Kocher and H. Samelson.

5. Transverse Flow Laser Cell, 3678410, R. Kocher, F. Moore, H. Samelson and W. Watson.

10. REFERENCES

1. A. Heller, J. Amer. Chem. Soc. 88, 2058 (1966).
2. G.A. Crosby and R.E. Whan, J. Mol. Spectry 8, 315 (1962).
3. H. Samelson, A. Lempicki, V.A. Brophy and C. Brecher, J. Chem Phys. 40, 2547 (1964).
4. A.N. Sevchenko and A.K. Trofimov, Zh. Eksper i Teor Fiz 21, 220 (1951).
5. H. Samelson and A. Lempicki, Phys. Lett. 4, 133 (1963).
6. E. Schimitschek, Appl. Phys. Lett. 3, 117 (1963).
7. C. Brecher, H. Samelson and A. Lempicki, J. Chem. Phys. 42, 1081 (1965).
8. A. Heller, J. Amer. Chem. Soc. 89, 167 (1967).
9. A. Heller, J. Molec. Spectroscopy 28, 101 (1968).
10. A. Heller, J. Amer. Chem. Soc. 90, 3711 (1968).
11. T.M. Shepherd, Nature 216, 1200 (1967).
12. D.J. Hunt and T.M. Shepherd, United Kingdom Atomic Energy Authority A.W.R.E. Report No. 041/70.
13. A. Heller, J. Molec. Spectroscopy 28, 208 (1968).
14. J.R. VanWazer, Phosphorous and Its Compounds, Interscience, New York, New York (1961).
15. N. Blumenthal, C.B. Ellis and D. Grafstein, J. Chem. 48, 5726 (1968).
16. F. Collier, M. Michon and Ch. LeSergent, Comptes Rendus 272, 945 (1971).
17. D. Kato and K. Shimoda, Jap. J. Appl. Phys. 9, 581 (1970).
18. D. Kato and K. Shimoda, Jap. J. Appl. Phys. 7, 548 (1968).
19. P.M. Buzhinskii, M.E. Zhabotinski, N.M. Zhavoronkov, V.G. Levedev, B.I. Malyshev, Y.V.P. Rudnetskii, V.V. Tsapkin and G.V. Ellert, Doklady Akad Nauk SSSR 185, 1306 (1969).
20. A. V. Aristov, I. M. Batyaev, E. I. Lubimov, Y. S. Maslywkov and A. S. Cherkasov, Optics and Spectroscopy 26, 365 (1969).
21. M.E. Zhabotinski, N.M. Zhavoronkov, V.G. Levedev, B.N. Malyshev, Ya. P. Rudnitskii and G.V. Ellert, Vestnik Akad Nauk SSSR 39, 52(1969).
22. Ch. LeSergent et al., Comptes Rendus 268, 1501 (1969).

23. P. Braun and P. Caro, Comptes Rendus 274, 1072 (1972).

24. E.J. Schimitschek, J. Appl Phys. 39, 6120 (1968).

25. E.J. Schimitschek and J.A. Trias, 6th International Quantum Electronics Conference, Kyoto, Japan, Sept. 7-10, 1970.

26. E.J. Schimitschek and J.A. Trias, Tenth Rare Earth Research Conference, April 30 - May 3, 1973, p. 819, Vol. 2.

27. H. Weichselgartner and J. Perchermeier, Z. Naturforsch 25a, 1244 (1970).

28. E.E. Fill, Z. Angew Phys. 32, 356 (1972).

29. D. Andreou, A.C. Selden and V.I. Little, J. Phys. D. Appl. Phys. 5, 1405, (1972).

30. D. Andreou and V.I. Little, Optics Comm. 6, 180 (1972).

31. A.C. Selden, Optics Comm., 5, 62 (1972).

32. A.C. Selden, Optics Comm. 6, 415 (1972).

33. C. Brecher and K.W. French, J. Phys. Chem. 73, 1785 (1969).

34. C. Brecher and K.W. French, J. Phys. Chem. 77, 1370 (1973).

35. E.J. Schimitschek and J.A. Trias, Inorg. Nuc. Chem. Lett. 6, 761 (1970).

36. E.J. Schimitschek, J.A. Trias and C.Y. Liang, Spectro Chemica Acta. 27A, 2141 (1971).

37. C.Y. Liang, E.J. Schimitschek and J.A. Trias, J. Inorg, Nucl. Chem. 34, 1098 (1971).

38. K. Hauptmanova, J. Pantoflicek and K. Patek, Phys. Status Solidi 9, 525 (1965).

39. C.K. Asawa and M. Robinson, Phys. Rev. 141, 257 (1966).

40. A. Einstein, Physikalische Zeitschrift 18, 121 (1917).

41. H. Samelson, A. Heller and C. Brecher, J.O.S.A. 58, 1054 (1968).

42. J.K. Neeland and V. Evtuhov, Phys. Rev. 156, 244 (1967).

43. T. Kushida, H.M. Marcos, and J.E. Geusic, Phys. Rev. 167, 289 (1968).

44. A.C.G. Mitchell and M.W. Zemansky, "Resonance Radiation and Excited Atoms," Cambridge University Press, New York (1961).

45. M.N. Tolstoi, E.L. Lyubimov and I.M. Batyaev, Opt. and Spectroscopy 28, 389 (1970).

46. M. Birnbaum and J. Gelbwachs, J. Appl. Phys. 43, 2335 (1972).

47. F. Collier, G. Girard, M. Michon and J.P. Pocholle, IEEE J. of Quantum Electr. QE7, 519 (1971).

48. N.L. Boling and G. Dubé, IEEE J. of Quant. Electr. QE8, 388 (1972).

49. V.R. Belan, V.V. Grigoryants and M.E. Zhabotinsky, Opto Electron 1, 33 (1969).

50. E. J. Schimitschek, private communication.

51. A. Einstein, Ann. Physik 33, 1275 (1910).

52. T.L. Fabelinskii, 'Molecular Scattering of Light," Plenum, New York (1968).

53. S. Bhagavantam, "Scattering of Light and the Raman Effect," Chemical Publishing Company, Inc., New York (1942).

54. R.R. Alfano, A. Lempicki and S.L. Shapiro, IEEE J. Quant. Electr. QE7, 416 (1971).

55. H.Z. Cummings and R.W. Gammon, Appl. Phys. Lett. 6, 171 (1965).

56. E. Garmire, Ph.D. Thesis, M.I.T. (1965).

57. W.R.L. Clements and B.P. Stoicheff, Appl. Phys. Lett. 12, 176 (1968).

58. R.W. Hellwarth, Phys. Rev. 130, 1850 (1963).

59. G.G. Bret and H.P. Weber, IEEE J. Quant. Electr. QE4, 807 (1968).

60. R.C. Leite, R.S. Moore, S.P.S. Porto, and J.E. Ripper, Phys. Rev. Lett. 14, 7 (1965).

61. Ohlmann, R.C. et al., Applied Optics 7, 905-13 (May 1968).

62. W. Rohsenow and H. Choi, Heat, Mass, and Momentum Transfer, p. 105, Prentice-Hall, Inc., Englewood Cliffs, N.J. (1961).

63. R. Binder, Fluid Mechanics, Third Ed., p. 123, Prentice-Hall, Inc., Englewood Cliffs, N.J. (1955).

64. Bird, Stewart and Lightfoot, Transport Phenomena, p. 183-8, Wiley and Sons, New York (1962).

65. F. Pollman, Hydraulics and Pneumatics 21, 90-5 (Feb. 1968).

66. High Energy Pulse Liquid Laser Semiannual Technical Summary Report, 28 February 1972.

67. A. Heller, Appl. Phys. Letters 9, 106 (1966); J.A.C.S. 88, 2058 (1966).

68. H. Samelson, A. Lempicki and V. Brophy, IEEE J. Quant. Elect. QE4, 849 (1968).

69. H. Samelson, R. Kocher, T. Waszak and S. Kellner, J. Appl. Phys. 41, 2459 (1970).

70. L. Daasch and D. Smith, Anal. Chem. 23, 853 (1951).

71 E. Lanning and P. Cukor, private communication.

72. "Neodymium Inorganic Aprotic Liquid Laser," Technical Report AFAL-TR-69-13 (December 1968), p. 21.

73. "High Energy Pulsed Liquid Laser," Semiannual Technical Summary Report (30 January 1969), p. 25.

74. The description of the optical procedure which follows is based on Abbe's Theory of Microscopic Vision. A useful general reference may be found in C. Meyers' book, The Diffraction of Light, X-Rays, and Material Particles, University of Chicago Press, Chicago, Ill. (1934), Chapter 7, Section 7.

75. J. Markiewicz and J. Emmett, J. Quantum Elect. QE-2, 707 (1966).

76. S. Epstein, J. Appl. Phys. 38, 2715 (1967).

77. A.E. Blume and K. F. Tittle, Appl. Optics 3, 527 (1964).

78. G. Benedetti-Michelangeli and S. Martellucci, Appl. Optics 8, 1447 (1969).

79. F.W. Quelle, Appl. Optics 5, 633 (1966).

80. D.C. Burnham, Appl. Optics 9, 1727 (1970).

81. R. Townsend, C. Stickley and A. Maio, Appl. Phys. Lett. 7, 94 (1966).

82. E.P. Riedel and G.D. Baldwin, J. Appl. Phys. 38, 2720 (1967).

83. G.D. Baldwin and E.P. Riedel, J. Appl. Phys. 38, 2726 (1967).

84. T. Houston, L. Johnson, P. Kisliuk and D. Walsh, J. Opt. Soc. Am. 53, 1286 (1963).

85. D. White and D. Gregg, Appl. Optics 4, 1034 (1965).

86. W. Koechner, J. Appl. Phys. 44, 3162 (1973).

87. B.N. Malyshev and V.A. Salyuk, Sov. Phys. Tech. Phys. 16, 1331 (1972).

88. B.N. Malyshev, et al., Sov. J. Quant. Elect. 1, 103 (1971).

89. T. Von Karman, Trans. ASME 61, 705 (1939).

90. R.C. Martinelli, Trans. ASME 69, 947 (1947).

91. M. Jakob, Heat Transfer, Vol. 1, p. 134, John Wiley & Sons, N.Y. (1949).

92. M. Jakob, Op. Cit. p. 547.

93. H. Winston and R.A. Gudmundson, Appl. Optics 3, 143 (1964).

94. H. Kogelnik, Bell Sys. Tech. J. 44, 455 (1965).

95. J. Bradford and R. Eckardt, Appl. Opt. 7, 2418 (1968).

96. A. Cabezas, L. Komai and R. Treat, Appl. Opt. 5, 647 (1966).

97. H. Welling, C. Brichart and H. Andresen, IEEE J. Quant. Elect. QE-1, 223 (1965).

98. S. Sims, A. Stein, and C. Roth, Appl. Opt. 5, 621 (1966).

99. A. Yariv, Proc. IEEE 51, 1723 (1963).

100. A. Yariv, Quantum Electronics, J. Wiley & Sons, New York, Chapters 13-16, (1967).

101. G.E. Devlin, J. McKenna, A.D. May and A.L. Schawlow, Applied Optics 1, 11 (1962).

102. J. McKenna, Applied Optics 2, 303 (1963).

103. W.R. Sooy and M.L. Stitch, J. Appl. Phys. 34, 1719 (1963).

104. C.B. Greenberg and P.W. French, J. Opt. Soc. Am. 59, 1294 (1969).

105. R. Lang, Private Communication.

106. G. Yamaguchi, F. Endo, S. Murakawa, S.O. Kamura and C. Yamanaka, Japan J. Appl. Phys. 7, 179 (1968).

107. M. Hongyo, T. Sasaki, Y. Nagao, K. Veda and C. Yamanaka, IEEE J.Quant. Elect. QE8, 192 (1972).

108. M. Nanjo, G. Yamaguchi, S.O. Kamura and C. Yamanaka, Tech. Repts. Osaka Univ. 16, 181 (1966).

109. H. Kogelnik and T. Li, Applied Optics 5, 1550 (1966).

110. I. Freund, Applied Phys. Lett. 12, 388 (1968).

111. R.J. Collins, L.O. Braun, and D.R. Dean, Applied Phys. Lett. 12, 392 (1968).

112. M. Birnbaum and C.L. Finchner, Proc. IEEE 57, 804 (1969).

113. E. Snitzer and C.G. Young, Chapter on Glass Lasers in "Lasers," Vol. II, Ed. A.K. Levine, Marcel Dekker, New York, pp. 191-256 (1968).

114. R.Y. Chiao, M.A. Johnson, S. Krinsky, H.A. Smith, C.H. Townes and E. Garmire, IEEE J. Quant. Electr. QE2, 467 (1966).

115. F. Shimizu, Phys. Rev. Lett. 19, 1097 (1967).

116. C. Cheung, D.M. Rank, R.Y. Chiao and C.H. Townes, Phys. Rev. Lett. 20, 786 (1968).

117. T.A. W ggins, R.V. Wick, N.D. Foltz, C.W. Cho and D.H. Rank, J. Opt. Soc. Am. 57, 661 (1967).

118. E. Schultz-DuBois, Bell Syst. Tech. J. 43, 625 (1964).

119. A. Cabezas. G. McAllister and W. Ng, J. Appl. Phys. 38, 3487 (1967).

120. K. Lang and F. Barnes, J. Appl. Phys. 35, 107 (1964).

121. A. Bach, R. Erickson and F. Barnes, J. Appl. Phys. 34, 2115 (1963).

122. H. Edgerton, J. Goncz and P. Jameson, "Xenon Flashlamp Limits of Operation," Technical Report, E.G.&G. Co., Inc., Boston, Mass.

123. T. Sasaki, T. Yamanaka, G. Yamaguchi and C. Yamanaka, Japan J. Appl. Phys. 8, 1037 (1969).

124. D. Andreou , Private Communication.

125. C. Luck, "Technique for Measuring Near and Far Field Intensity Distributions of a Laser Beam," Technical Report LADC-T-73-1, Raytheon Co., Waltham, Mass. (1973).

126. J. Freiberg and A. Halsted, Appl. Optics 8, 355 (1969).

127. W. Rigrod, J. Appl. Phys. 34, 2602 (1963).

128. R. Bellman, G. Birnbaum and W. Wagner, J. Appl. Phys. 34, 780 (1963).

129. L. Frantz and J. Nodvik, J. Appl. Phys. 34, 2346 (1963).

130. J. Davis and W. Sooy, Appl. Optics 3, 715 (1964).

131. P. Avizonis and R. Grotbeck, J. Appl. Phys. 37, 687 (1966).

132. C. Young, Proc. IEEE 57, 1267 (1969).

133. J. Thornton, W. Fountain, W. Flint and T. Crow, Applied Optics 8, 1088 (1969).

134. C. Young, Report on Glass Lasers, Microwave Journal, 69-78 (July 1968).

135. E. Snitzer, Applied Optics 5, 1487 (1966).

APPENDIX A

DETERMINATION OF THE ABSORPTION CROSS SECTION OF THE LASER TRANSITIONS OF THE Nd^{+3} ION IN THE $Nd^{+3}:SeOCl_2$ SYSTEM

Reprinted from JOURNAL OF THE OPTICAL SOCIETY OF AMERICA, Vol. 58, No. 8, 1054-1056, August 1968
Printed in U. S. A.

Determination of the Absorption Cross Section of the Laser Transitions of the Nd^{+3} Ion in the Nd^{+3}:$SeOCl_2$ System

H. SAMELSON, A. HELLER, AND C. BRECHER

The Bayside Laboratory, Research Center of General Telephone & Electronics Laboratories Incorporated, Bayside, New York 11360

(Received 19 February 1968)

The absorption cross section of the ${}^4F_{3/2}$–${}^4I_{11/2}$ (1.056 μ) and ${}^4F_{3/2}$–${}^4I_{13/2}$ (1.334 μ) transitions of Nd^{+3} in $SeOCl_2$, and the overall radiative lifetime of the ${}^4F_{3/2}$ state, have been calculated from spectroscopic measurements. Values of the order of 8.5×10^{-20} cm² for σ_ν of the 1.056-μ transition and 288 μsec for τ_{overall} were found, implying a quantum efficiency of the order of unity.

INDEX HEADINGS: Absorption; Lasers; Neodymium; Selenium; Spectroscopy.

THE cross section for stimulated emission is one of the important constants of laser materials. In principle, this quantity can be measured directly; in practice, however, such measurement may be quite difficult. Therefore, indirect methods are frequently used.

In the case of Nd^{+3}, where the terminal laser state is about 2000 cm^{-1} above the ground state, direct measurements require high temperature and large samples. Mauer[1] reports such a measurement for Nd^{+3} doped borate and silicate glasses, based on the measurement of the absorption constant for the laser transition and a determination of the population of the terminal level. Another method reported by Edwards[2] is based on a measurement of the change of gain coefficient with the change of energy stored; the laser material is used as an amplifier in this experiment. A purely spectroscopic method is reported by Pantoflicek[3] and is based on the relationship between the oscillator strength and the absorption cross section as given by Mitchell and Zemansky[4] or Smakula.[5] A method reported by Belan, Grigoryants, and Zhabotinski[6] directly measures the rate of stimulated emission in the laser transition. Finally, a method is reported by Neeland and Evtuhov[7] which does not depend on the determination of a quantum yield or any of the assumptions ancillary to such a determination; the method reported here is essentially the same.

METHOD FOR DETERMINING THE ABSORPTION CROSS SECTION OF THE LASER TRANSITION

The basic equations underlying the application of this method are those given by Mitchell and Zemansky[4] and Lengyel,[8]

$$\int k(\nu)d\nu=\frac{\lambda_0^2}{8\pi n^2}\frac{g_2}{g_1}\frac{N_1}{\tau_{21}}\left(1-\frac{g_1}{g_2}\frac{N_2}{N_1}\right)\approx\frac{\lambda_0^2}{8\pi n^2}\frac{g_2}{g_1}\frac{N_1}{\tau_{21}}, \quad (1)$$

$$f_{12}=\frac{mcn}{N_1\pi e^2}\int k(\nu)d\nu=37.680\frac{n}{N_1}\int k(\nu)d\nu, \quad (2)$$

and the combined equations

$$f_{12}\tau_{21}=\frac{mc}{8\pi^2e^2n}\frac{g_2}{g_1}\lambda_0^2=\frac{1.499}{n}\frac{g_2}{g_1}\lambda_0^2. \quad (3)$$

These equations are concerned with the transition between any lower state 1 and any upper state 2.

The symbols are defined as follows:

$k(\nu)$	absorption constant at ν, per centimeter
N_i	population of state i
λ_0	peak wavelength of the transition (= 8750 Å)
n	index of refraction (= 1.65)
g_i	degeneracy of state i
f_{12}	oscillator strength of the transition
m, e	electronic mass, charge
c	velocity of light
τ_{21}	radiative lifetime of the transition.

First, the oscillator strength is determined for a transition having an easily measurable absorption; in the case of Nd^{+3} this is the ${}^4I_{9/2}\rightarrow{}^4F_{3/2}$. With a value for f_{12} we can then readily determine τ_{21}. Since the laser transition and resonance transition arise from the same excited state, the ratio of the radiative lifetimes is the same as that of the fluorescence intensities. Thus τ_{laser} is determined and f_{laser} follows from Eq. (3). Finally, the absorption cross section σ_ν for the laser transition can be found,

$$\sigma_\nu=(\lambda_0^2/8\pi n^2\Delta\nu)(1/\tau_{\text{laser}}), \quad (4)$$

where $\Delta\nu$ is the half-width of the line.

[1] P. Mauer, Appl. Opt. 3, 433 (1964).
[2] J. G. Edwards, Nature 212, 752 (1966).
[3] J. Pantoflicek, Czech. J. Phys. B17, 27 (1957).
[4] A. C. G. Mitchell and M. W. Zemansky, *Resonance Radiation and Excited Atoms* (Cambridge University Press, New York, 1961).
[5] See P. Curie, *Luminescence Cristalline* (Dunod Cie., Paris, 1960), p. 78.
[6] V. P. Belan, V. V. Grigoryants, and M. E. Zhabotinski, J. Quantum Electron. QE-3, 425 (1967).
[7] J. K. Neeland and V. Evtuhov, Phys. Rev. 156, 241 (1967).
[8] B. Lengyel, *Lasers* (John Wiley & Sons, Inc., New York, (1962).

4.2

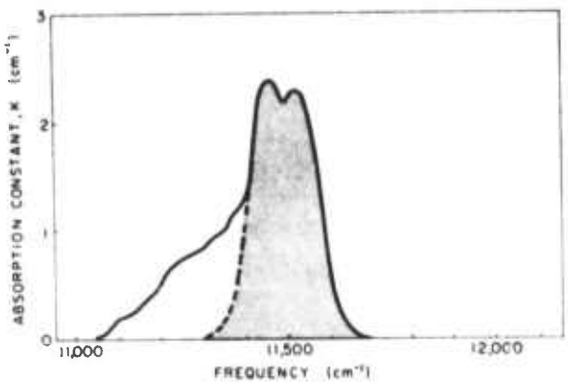

FIG. 1. Absorption spectrum of $^4I_{9/2}$–$^4F_{3/2}$ transition of Nd^{+3}. The shaded area defines the resonance region.

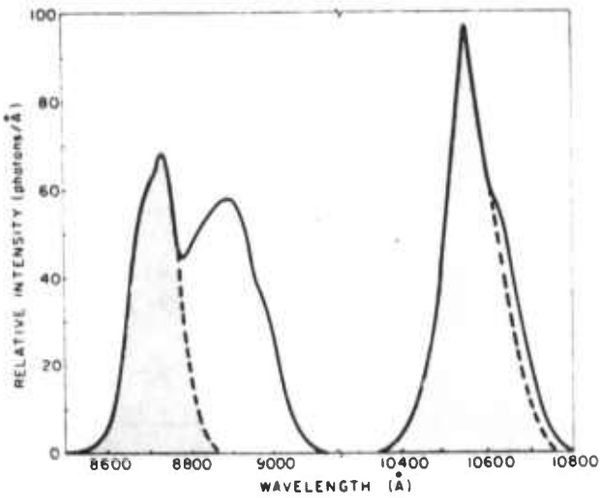

FIG. 2. Emission spectrum of $^4F_{3/2}$–$^4I_{9/2}$ and $^4F_{3/2}$–$^4I_{11/2}$ transitions of the Nd^{+3}. The shaded areas define the portions used in the cross-section determination.

DETERMINATION OF ABSORPTION CROSS SECTION FOR Nd^{+3}:$SeOCl_2$ SYSTEM

In practice, the application of the method outlined is not quite direct since complications arise from the lifting of the degeneracy of the $^4I_{9/2}$ and $^4I_{11/2}$ states of Nd^{+3} in the $SeOCl_2$–$SnCl_4$ solution. Examination of the absorption and emission spectra of these solutions yields some information about the energy-level structure of Nd^{+3} in this system. The first point is that both components of the $^4F_{3/2}$ level are seen, so that only the Kramers degeneracy remains. The Kramers degeneracy, however, applies to all the levels and can be neglected since only the ratios of degeneracies are involved in the calculations. In this sense, the components of the $^4F_{3/2}$ can be considered nondegenerate. Similarly, the $^4I_{9/2}$ state can have at most five components, of which four, located at 0, 25, 130, and 260 cm^{-1}, have been identified. For the fifth component, there is some questionable indication of a level at 350 cm^{-1} as well as the possibility that any of the four above-mentioned identified levels may be doubly degenerate. Thus some ambiguity in assigning the population remains; taking all these possibilities into account we obtain for the partition function, $Q=\sum_i g_i \exp(-E_i/kT)$, values of 3.71 or 3.60 if one of the two lowest levels is degenerate, and 3.25, 3.00, or 2.90 otherwise. With no rational basis of choice, we will use the average values, 3.65 and 3.05 respectively, in the later calculations. Finally, about all that can be said about the $^4I_{11/2}$ level, the state on which the main emission terminates, is that it can have as many as six components, although some of these may be degenerate.

The transition between each ground state ($^4I_{9/2}$) component and each upper state ($^4F_{3/2}$) component should now be considered. For the transition between the ith component of the lower state and the jth component of the upper, Eq. (1) can be rewritten

$$\int k_{ij}(\nu)d\nu=\frac{\lambda_0^2}{8\pi n^2}\frac{g_j}{g_i}\frac{N_i}{\tau_{ji}}=\frac{\lambda_0^2}{8\pi n^2}\frac{N_0\exp(-E_i/kT)}{(Q\tau_{ji})}, \quad (5)$$

since, with the upper state completely split, $g_j=1$. This expression is then summed over all of the individual transitions within the resonance band. However, since it is difficult to break the spectrum down and find each of the individual τ_{ji}'s, we must be satisfied with an overall value, which we find as follows.

The absorption spectrum in the region of the $^4I_{9/2}\rightarrow{}^4F_{3/2}$ is shown in Fig. 1. The part arising from the two upper levels of the $^4I_{9/2}$ multiplet can be readily separated from that arising from the pair of levels at 0 and 29 cm^{-1}. The separation of the latter pair is less than between the two levels of the $^4F_{3/2}$ ($\simeq 53$ cm^{-1}) and no further resolution can be made. However, since these two ground levels are so close together and since their populations differ by only about 10%, we will not attempt to distinguish between their respective contributions to the absorption. Over this region of the spectrum (see Fig. 1), the value of $\int k(\nu)d\nu$ is 1.37×10^{13} cm^{-1} sec^{-1}. The state population of the two lower states is 0.78 N_0 if one of these states is doubly degenerate (Case 1), and 0.62 N_0 otherwise (Case 2). Then, substituting these values into Eqs. (1)–(3) (with $N_0=1.8\times10^{20}$ cm^{-3}), we get

	Case 1	Case 2
$1/\tau_{12}$	6.08×10^{6}	7.59×10^{6}
τ_{21}	762 μsec	917 μsec.

Having found these values for the resonance transition, we can now calculate the corresponding values for the laser transition. For this, we use the ratio of the number of photons emitted in the transitions from the $^4F_{3/2}$ state to the two ground levels and to the $^4I_{11/2}$ state, respectively. Denoting this ratio by R, we can readily show that, neglecting dispersion,

$$R=\tau_{1\text{aser}}/\tau_{21} \quad \text{or} \quad \tau_{1\text{aser}}=R\tau_{21}.$$

We now encounter one last complication, since the emission to the $^4I_{9/2}$ state is distorted by self-absorption,

A-3

characteristic of resonance transitions. Calculation of the proper correction for self-absorption is complicated, but experimental determination is simple. All that is required is to measure the emission (Fig. 2) in solutions of lower and lower Nd^{+3} concentration until the ratio of the integrated areas of the emission spectrum ceases to change.[9] This yields a value for R of 0.662, giving values for the radiative lifetime of the laser transition of $\tau_{laser} = 503\ \mu sec$ (Case 1) or $\tau_{laser} = 606\ \mu sec$ (Case 2). Finally, to find the absorption cross section for the laser transition, we substitute these values into Eq. (4) (with $\Delta\nu = 3.5\times10^{12}\ sec^{-1}$), obtaining values of $\sigma_\nu = 9.22\times10^{-20}\ cm^2$ (Case 1) or 7.66×10^{-20} (Case 2).[10]

In the same manner, we can calculate the cross section for the ${}^4F_{3/2}$ - ${}^4I_{13/2}$ transition at 1.334 μ. Here $R = 6.47$, giving radiative lifetime of 4920 μsec (Case 1) or 5920 μsec (Case 2). With a $\Delta\nu$ of $6.6\times10^{12}\ sec^{-1}$, this yields values for the absorption cross section of $0.800\times10^{-20}\ cm^2$ (Case 1) or $0.665\times10^{-20}\ cm^2$ (Case 2).[11]

For comparison with experiment, we can also calculate the total radiative decay time for the ${}^4F_{3/2}$ state, from which all the emissions originate. Here, we divide the number of photons emitted in the transition from the ${}^4F_{3/2}$ state to the two ground levels by the total number emitted in all transitions originating from this state. This new ratio is defined as

$$R' = \frac{1}{\tau_{21}} \Big/ \sum_j \frac{1}{\tau_{2j}},$$

giving

$$\tau_{overall} = R'\tau_{21}.$$

In the same manner as for the laser transition, we find, at low Nd^{+3} concentrations, a value for R' of 0.266; this yields an overall radiative decay time for the ${}^4F_{3/2}$ state (at low Nd^{+3} concentration) of 202 μsec (Case 1) or 243 μsec (Case 2). This radiative decay time should, of course, increase with higher concentrations because of the progressively greater self-absorption of the resonance transition; from the ratio of the integrated emission intensities, we find that for a Nd^{+3} concentration of 0.3M, the lifetime should increase by about 19% over the low-concentration value, giving 239 μsec (Case 1) or 288 μsec (Case 2). The measured decay times are found to range from 220 μsec at low concentrations to 280 μsec at 0.3M. Thus, although these results have a probable error of at least 10%, it would appear that Case 2 is the case more consistent with reality. In any event, it is apparent that the quantum efficiency in the Nd^{+3}:$SeOCl_2$ liquid laser system is of the order of unity, considerably greater than the best value reported by Pantoflicek.[3]

TABLE I. Absorption cross section of 1.06-μ transition of Nd^{+3} in various hosts.

Material	$\sigma_\nu \times 10^{20}\ cm^2$	Reference
Silicate glass	1.26	1
Borate glass	0.82	1
Barium crown silicate	4.65	3
Lanthanum borate	6.62	3
Commercial Nd^{+3} laser glass (otherwise unspecified)	3.6	2
Silicate glass	2	6
Nd^{+3}:$SeOCl_2$ liquid	9.22 or 7.66	Present work

To afford a comparison with other neodymium-containing hosts, values of σ_ν for a number of different materials are listed in Table I. Our results on the Nd^{+3}:$SeOCl_2$ liquid may be in error by more than 10%, but even so the absorption cross section for this material is greater than that for most glasses.

The method presented here for measuring the absorption cross section is simple and straightforward. It depends only on absorption and emission measurements that can be made with a high degree of precision on accessible transitions, and does not require determination of quantum yield and the assumptions involved therein.

[9] It is assumed here that the environment of the emitting ion does not change significantly with the concentration of the ion. In a coordinating solvent, such as $SeOCl_2$:$SnCl_4$, where the ion is surrounded by a bulky solvation shell separating it from all other ions, this is not an unreasonable assumption.

[10] These figures assume that the terminal state of the laser transition is nondegenerate; if it is not, the figures given should be divided by the degeneracy. In these experiments, the actual degeneracy of the components of the ${}^4I_{11/2}$ state was indeterminate.

[11] The ratio of the cross section of the transitions terminating in the ${}^4I_{11/2}$ and ${}^4I_{13/2}$ states is 11.5, in good agreement with the inverse of the ratio of the threshold values obtained in laser experiments.

A-4

APPENDIX B

COMPARISON OF APROTIC SOLVENTS FOR Nd^{+3} LIQUID LASER SYSTEMS: SELENIUM OXYCHLORIDE AND PHOSPHORUS OXYCHLORIDE

[Reprinted from the Journal of Physical Chemistry, 73, 1785 (1969).]

Comparison of Aprotic Solvents for Nd^{3+} Liquid Laser Systems: Selenium Oxychloride and Phosphorus Oxychloride[1]

by C. Brecher and K. W. French

The Bayside Laboratory, Research Center of General Telephone & Electronics Laboratories Inc., Bayside, New York 11360
(Received December 9, 1968)

The properties of $SeOCl_2$ and $POCl_3$ as aprotic solvents for Nd^{3+} liquid lasers are compared. Details are given concerning preparative procedures, absorption and emission spectroscopy, energy levels and radiative lifetimes, and laser performance. The two solvents are shown to be equally suitable for use in high-energy liquid lasers.

Introduction

Aprotic solvents, because of their freedom from the high-energy vibrations which efficiently degrade energy from excited ions, have received considerable attention as host media in liquid laser applications.[2-5] The first such material in which laser action was achieved contained selenium oxychloride ($SeOCl_2$) as its major component; this liquid, with a dielectric constant of 46, is an excellent medium for the dissolution of ionic salts (such as those of Nd^{3+}), particularly when acidified by the addition of tin tetrachloride ($SnCl_4$) or other similar aprotic acids. Subsequently, another system based on phosphorus oxychloride ($POCl_3$) was developed; this solvent, with a dielectric constant of 14, is a less well-suited host for ionic salts but is more attractive for liquid laser uses because it is far less toxic and corrosive than $SeOCl_2$. This paper compares the chemical and spectroscopic properties of these two systems and relates them to the laser characteristics.

Experimental Section

The similarities and differences in the chemical properties of the two liquid laser systems were reflected in their preparative procedures. With $SeOCl_2$, the laser solution was prepared by directly dissolving neodymium oxide in anhydrous $SeOCl_2$ which had been acidified with $SnCl_4$ (in a volume ratio of approximately 5:1), a reaction which can be described by

$$Nd_2O_3 + 3SnCl_4 + 3SeOCl_2 \longrightarrow 2Nd^{3+} + 3SnCl_6^{2-} + 3SeO_2 \quad (1)$$

To remove hydrogen-containing contaminants (such as H_2O or HCl) which are the principal sources of nonradiative quenching,[6] the resulting mixture was distilled at a controlled pressure of 40 mm until a constant boiling point of about 90° (pure $SeOCl_2$) was reached and about one-third of the total solution had been removed. This procedure differs from that reported earlier[7] in that the lower temperature of distillation prevented the discoloration of the solution by Se_2Cl_2, obviating the need for bleaching. At this point, analysis of the remainder for tin showed a solution which contained only about half of the stoichiometric quality of $SnCl_4$ as defined in eq 1. The finished laser solution was then prepared by dilution with completely anhydrous $SnCl_4$ and $SeOCl_2$ to reach the desired concentration of Nd^{3+} and the desired acidity. For this investigation, a solution was prepared having an Nd^{3+} concentration of 0.3 M and an $SnCl_4$ concentration of 0.1 M in excess of stoichiometric concentration. This solution had a fluorescence decay time of 260 μsec.

With $POCl_3$, the dissolution of Nd_2O_3 can nominally be described by the same sort of equation as for $SeOCl_2$

$$Nd_2O_3 + 3SnCl_4 + 6POCl_3 \longrightarrow 2Nd^{3+} + 3SnCl_6^{2-} + 3P_2O_3Cl_4 \quad (2)$$

However, because of the much lower solubility of rare earth salts in $POCl_3$ (even when acidified with $SnCl_4$ in the same volume ratio as with $SeOCl_2$), concentrations of Nd^{3+} desired for laser solutions could not be achieved and maintained in the pure, completely anhydrous solvents. If, on the other hand, amounts of water were added to the acidified $POCl_3$ in a molar ratio of about 1:10, the solubility of the Nd^{3+} was dramatically increased, enabling concentrations greater than 2 M to be readily achieved. The reactions of water with $POCl_3$ have been found[8] to yield a large number of compounds

(1) This research was partially supported by Project Defender under the joint sponsorship of the Advanced Research Projects Agency, the Office of Naval Research, and the Department of Defense, under Contract No. N00014-68-C-0110.

(2) (a) A. Heller, *Appl. Phys. Letters*, **9**, 106 (1966); A. Lempicki and A. Heller, *ibid.*, **9**, 108 (1966); (b) T. M. Shepherd, *Nature*, **216**, 1200 (1967).

(3) D. Kato and K. Shimoda, *Japan. J. Appl. Phys.*, **7**, 548 (1968).

(4) V. P. Belan, V. V. Grigoryants, and M. E. Zhabotinski, IEEE Conference on Laser Engineering and Applications, Washington, D. C., 1967.

(5) N. Blumenthal, C. B. Ellis, and D. Grafstein, *J. Chem. Phys.*, **48**, 5726 (1968).

(6) A. Heller, *J. Am. Chem. Soc.*, **88**, 2058 (1966).

(7) A. Heller, *ibid.*, **90**, 3711 (1968).

B-2

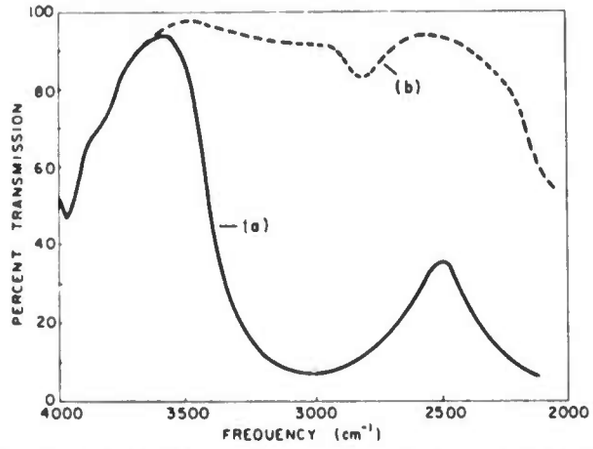

Figure 5. Infrared absorption spectrum of $SeOCl_2$ (0.3 M Nd^{3+}) laser solutions at 300°K: (a) contaminated with H_2O; (b) anhydrous.

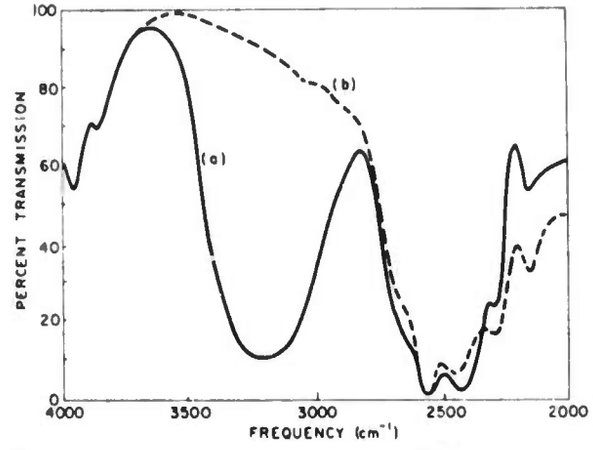

Figure 6. Infrared absorption spectrum of $POCl_3$ (0.3 M Nd^{3+}) laser solutions at 300°K: (a) contaminated with H_2O; (b) anhydrous.

$POCl_3$ system. Thus a considerably greater proportion of the total energy reaching the $^4F_{\frac{3}{2}}$ state is emitted in the desired spectral region, while the over-all transition probability from this state is decreased, making possible (in theory at least) a more efficient laser system.

On the other hand, a contradictory behavior is observed in the over-all fluorescence decay times. In $SeOCl_2$, the measured decay time is nearly identical with that calculated from spectroscopic considerations, implying an almost total absence of nonradiative losses from the emitting state and hence a quantum efficiency close to unity. In $POCl_3$, however, the measured decay time falls some 20% below the calculated value, implying the presence of some nonradiative loss. It is known that the major cause of such loss in these systems is an interaction between the ion and high-energy vibrations in the host medium, such as might be introduced by small amounts of hydrogen-containing impurities. The infrared spectra (Figures 5 and 6) show that

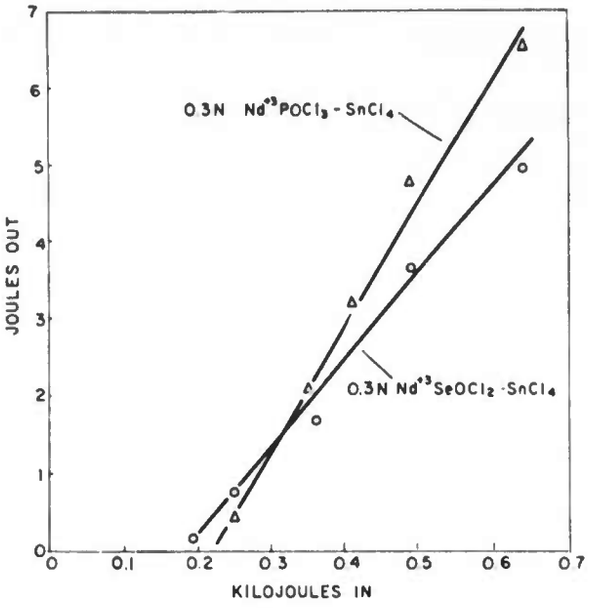

Figure 7. Energy output from 0.3 M Nd^{3+} laser solutions: ○, $SeOCl_2$; △, $POCl_3$.

neither of the solutions exhibits significant amounts of such contamination; however, the rather intense absorption in the region of the first overtone of the P–O stretching vibration (compared with the extremely weak second overtone of the Se–O vibration) suggests vibrational coupling through this transition as a possible source of nonradiative loss in the $POCl_3$ system. In any event, the points mentioned emphasize the sensitivity of the various transition probabilities of the Nd^{3+} ion to chemical interactions with the host medium.

Laser Characteristics. Laser experiments on the two liquid systems were conducted under as nearly the same conditions as possible. A Pyrex cell 6 in. long with a bore diameter of 0.65 in. was used. A cell with demountable end windows[11] was chosen because of the importance of keeping the interior faces of the cell parallel to each other in order to minimize the effect of the refractive index mismatch between the cell materials and the solutions. The laser cavity was formed by external dielectric mirrors (one with 99.9% reflectance, the other 57%) parallel to the cell window faces. The cell was filled with each of the two solutions and flashed in a close-coupled arrangement using three xenon flash lamps at input energies from zero to 640 J. Output energy measurements were made with a TRG 107 calibrated thermocouple detector and microvoltmeter. The results obtained are illustrated in Figure 7. It is seen that the slope efficiency for the $POCl_3$ system is 1.6%, almost 50% higher than for $SeOCl_2$. This is so despite the fact that the neodymium concentration and

(11) H. Samelson, A. Lempicki, and V. A. Brophy, *J. Quantum Electron.*, **4**, 849 (1968).

output reflectivities chosen were nearly optimum for energy output for the $SeOCl_2$-based system whereas it has not been established whether they are also optimum for $POCl_3$. Under these conditions thresholds occur in the region of 200 J ($SeOCl_2$ some 10% lower, $POCl_3$ 10% higher); however, with narrow-bore cells and higher reflectance output mirrors, both $SeOCl_2$- and $POCl_3$-based systems have shown thresholds as low as 10-J input.

Conclusions

On the basis of these experiments, it is clear that the differences between the two liquid laser systems are not large. The $POCl_3$ system starts with the advantages of lower corrosiveness and toxicity and under one set of experimental conditions shows a higher slope efficiency of power output. Nevertheless, its over-all decay time of fluorescence is lower (some 20% below what is calculated from spectroscopic considerations), and therefore it presumably has a lower quantum efficiency than has the $SeOCl_2$ system. On the whole, however, both systems are quite similar in their physical characteristics and the choice of one or the other would be dictated largely by experimental conditions.

B-4

APPENDIX C

SPECTROSCOPY AND CHEMISTRY OF APROTIC Nd^{+3} LASER LIQUIDS

[Reprinted from the Journal of Physical Chemistry, 77, 1370 (1973).]

Spectroscopy and Chemistry of Aprotic Nd^{3+} Laser Liquids[1]

C. Brecher* and K. W. French

Waltham Research Center, GTE Laboratories Incorporated, Waltham, Massachusetts 02154 *(Received January 2, 1973)*

Publication costs assisted by GTE Laboratories

Measurements have been made on various aspects of the spectroscopy of the $SeOCl_2$ and $POCl_3$ aprotic Nd^{3+} laser liquids, with emphasis on the latter. Unusual features in the chemical behavior are described and some apparent inconsistencies resolved. The formation of complex PO_2Cl_2-Lewis acid groups is deemed to be a major factor in the solubilizing of the Nd^{3+} ion in $POCl_3$ solution. A consistent and coherent model is proposed to explain the observations.

Introduction

One of the major advances in the liquid laser field has been the development of aprotic hosts for the Nd^{3+} ion. This ion, which is the basis for the most widely used class of crystalline and glass lasers, had never before been usable in the liquid state because of its high susceptibility to nonradiative deexcitation. The importance of high-energy vibrations in this quenching process, and the mechanism

(1) This research was partially supported by the Advanced Research Projects Agency of the Department of Defense and was monitored by the Office of Naval Research under Contract No. N00014-68-C-0110.

C-2

of the interaction, were elucidated by Heller,[2a] whose work led to the first successful utilization of an inorganic aprotic liquid, $SeOCl_2$, as a laser host medium.[2b] Subsequent work[3-6] yielded more practical systems involving the much less toxic and corrosive $POCl_3$ liquid, now the mainstay of present liquid laser research. Many individual aspects of these laser media have been studied in relation to laser applications.[7-16] There have, however, been many unanswered questions regarding the details of their chemical and spectroscopic behavior. It is the purpose of this paper to gather the pertinent observations in these areas in order to construct a coherent and consistent, if not necessarily unique, picture of the behavior of the Nd^{3+} ions in such liquid media.

Experimental Section

Chemical. Although the procedures for preparation of the solutions involved in this work have been described elsewhere,[6,8,15,16] they are sufficiently important to the subsequent discussion to be summarized here. The $SeOCl_2$-$SnCl_4$-Nd^{3+} solution is prepared by dissolving (with heating) pure anhydrous Nd_2O_3 in an anhydrous 5:1 (by volume) mixture of $SeOCl_2$ and $SnCl_4$. The mixture is then distilled under reduced pressure (40 mm) until a boiling point of about 90° (pure $SeOCl_2$) is reached and about one-third of the total solution has been removed to eliminate the last traces of protic contamination. The solution is then reconstituted to the desired Nd^{3+} concentration and acidity by addition of appropriate quantities of pure $SeOCl_2$ and $SnCl_4$. Similar procedures are followed if $NdCl_3$ rather than Nd_2O_3 is used.

The $POCl_3$-$SnCl_4$-Nd^{3+} solution was prepared in a similar manner, with the following important exception. Water, in the molar ratio of 1:10, is added to the $POCl_3$-$SnCl_4$ mixture to enable dissolution of the Nd_2O_3 or $NdCl_3$, for reasons to be discussed later. The deliberately introduced protic contamination is then removed by boiling off (at atmospheric pressure, final temperature 116°) a sufficient fraction of the total liquid volume. The solution is reconstituted to the desired concentrations by addition of the appropriate pure liquids. The $POCl_3$-$ZrCl_4$-Nd^{3+} liquid, in contrast, utilizes the pure anhydrous trifluoroacetate salt of Nd^{3+} rather than the oxide or chloride, since the presence of water causes precipitation of the zirconium. The $Nd(CF_3COO)_3$ can be prepared by crystallization from a solution of Nd_2O_3 in aqueous trifluoroacetic acid, followed by complete removal of the water by heat and vacuum. This salt dissolves directly in the $POCl_3$-$ZrCl_4$ mixture, which is then boiled to remove traces of protic contamination and reconstituted as before. Other pertinent points are mentioned in the subsequent text.

Spectroscopic. Emission measurements were made on the Nd^{3+} solutions at both liquid N_2 and room temperatures, with spot checks at various intermediate temperatures. All three liquid systems passed continuously from liquid to glassy state, with no crystallization or spectral discontinuities (except for occasional problems at low acidity). The systems are excited by a Hanovia 538C-1 xenon arc lamp through Corning 3-69 and 4-97 filters, and the emissions measured with a Jarrell-Ash 0.5-m Ebert monochromator and an ITT FW 118 photomultiplier. Some absorption measurements, particularly at low temperatures were made with the same apparatus but with a tungsten ribbon filament lamp replacing the xenon arc lamp. Room temperature absorptions were also made with a Cary-14 spectrophotometer. Decay time measurements were made with a helical xenon flashlamp surrounding the sample, with the emission detected axially. Some of the pertinent spectra are shown in Figures 1-5 and values listed in Table I; further discussion follows.

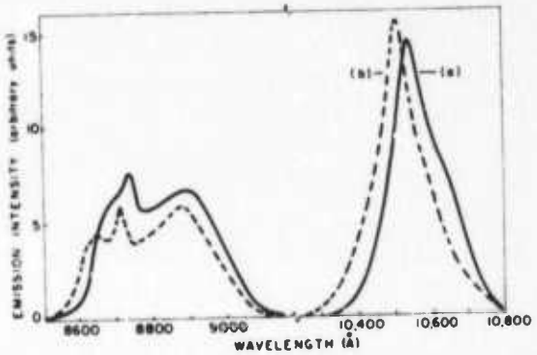

Figure 1. Emission spectrum of 0.3 *M* Nd^{3+} solutions at 300°K: (a) $SeOCl_2$, (b) $POCl_3$. Stoichiometric concentration of $SnCl_4$. Spectrum with $ZrCl_4$ not measurably different.

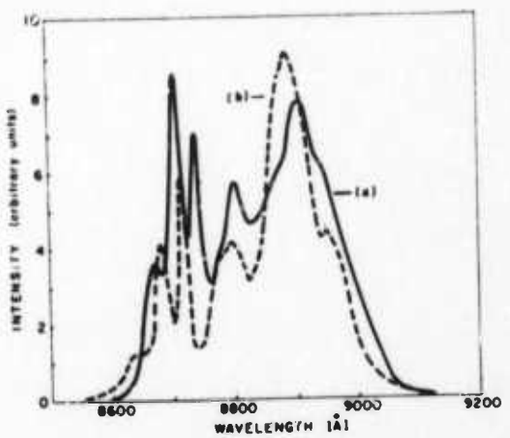

Figure 2. Emission spectrum of 0.3 *M* Nd^{3+} solutions at 100°K: (a) $SeOCl_2$; (b) $POCl_3$. Stoichiometric concentration of $SnCl_4$. Spectrum with $ZrCl_4$ differs in relative intensity of components (see Figure 4).

(2) (a) A Heller, *J. Amer. Chem. Soc.*, **88**, 2058 (1966). (b) A. Heller, *Appl. Phys. Lett.*, **9**, 106 (1966); A. Lempicki and A. Heller, *ibid.*, **9**, 198 (1966).
(3) V. P. Belan, V. V. Grigoryants, and M. E. Zhabotinski, IEEE Conference on Laser Engineering and Applications, Washington, D. C., 1967.
(4) N. Blumenthal, C. B. Ellis, and D. Grafstein, *J. Chem. Phys.*, **48**, 5726 (1968).
(5) E. J. Schmitschek, *J. Appl. Phys.*, **39**, 6120 (1968).
(6) C. Brecher and K. W. French, *J. Phys. Chem.*, **73**, 1785 (1969).
(7) D. Kato and K. Shimoda, *Jap. J. Appl. Phys.*, **7**, 548 (1968).
(8) A. Heller, *J. Amer. Chem. Soc.*, **90**, 3711 (1968); *J. Mol. Spectrosc.*, **28**, 101 (1968); *ibid.*, **28**, 208 (1968).
(9) H. Samelson, A. Heller, and C. Brecher, *J. Opt. Soc. Amer.*, **58**, 1054 (1968).
(10) H. Samelson, A. Lempicki, and V. A. Brophy, *IEEE J. Quantum Electron.*, **4**, 849 (1968); *J. Appl. Phys.*, **39**, 4029 (1968).
(11) H. Samelson and A. Lempicki, *J. Appl. Phys.*, **39**, 8115 (1968).
(12) C. LeSergent, M. Michon, S. Rousseau, F. Collier, H. Dubost, and G. Raoult, *C. R. Acad. Sci., Ser. B*, **268** 1501 (1969).
(13) H. Samelson, T. Kocher, T. Waszak, and S. Kellner, *J. Appl. Phys.*, **41**, 2459 (1970).
(14) H. Welcher, artner and J. Perchermeier, *Z. Naturforsch. A*, **25** 1244 (1970).
(15) C. Brecher, K. W. French, W. Watson, and D. Miller, *J. Appl. Phys.*, **41**, 4578 (1970).
(16) A. Heller, K. W. French, and P. O. Haugsjaa, *J. Chem. Phys.*, **56**, 2368 (1972).

C-3

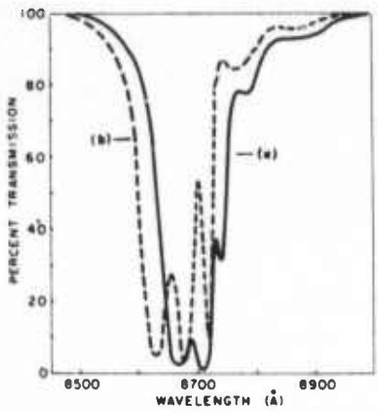

Figure 3. Absorption spectrum of 0.3 *M* Nd^{3+} solutions at 100°K: (a) $SeOCl_2$; (b) $POCl_3$. Stoichiometric concentration of $SnCl_4$.

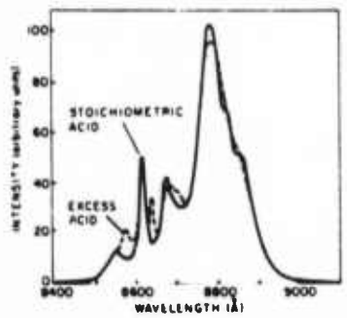

Figure 4. Emission spectrum of 0.3 *M* Nd^{3+} solutions in $POCl_3$–$ZrCl_4$ solutions at different Lewis acid concentration (at 100°K).

TABLE I: Components of the $^4F_{3/2}$–$^4I_{9/2}$ Transition of Nd^{3+} (0.3 *M*) in $SeOCl_2$ and $POCl_3$

$SeOCl_2$			$POCl_3$	
Wavelength, Å	Energy, cm^{-1}	Assignment[a]	Wavelength, Å	Energy, cm^{-1}
8668	11,537	b-1	8628	11,590
8705	11,488	a-1	8679	11,522
8738	11,444	b-2	8718	11,471
8778	11,393	a-2	8788	11,405
		b-3		
8801	11,362	a-3	8805	11,357
8865	11,280	b-4		
8905	11,230	a-4	8889	11,250
8950	11,173	b-5	8960	11,162
~8990	11,123	a-5		

[a] Components of the $^4I_{9/2}$ level are numbered consecutively from the ground state (1); for the $^4F_{3/2}$ level, a denotes the lower component and b the highe. These assignments yield the following values (cm^{-1}) for the energies of levels 1, 2, 3, 4, 5, a and b, respectively; in $SeOCl_2$: 0, 94, 125, 245, 352, 11,487, 11,537; in $POCl_3$: 0, 118, 165, 272, 428, 11,522, 11,589. See ref 6.

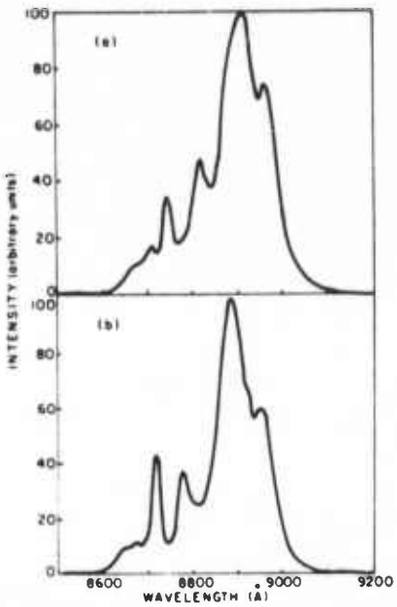

Figure 5. Emission spectrum of Nd^{3+} in two aprotic hosts (at 100°K): (a) in crystalline $Nd_2(ZrCl_6)_3 \cdot 12POCl_3$; (b) in $POCl_3$ solution at stoichiometric $ZrCl_4$ concentration.

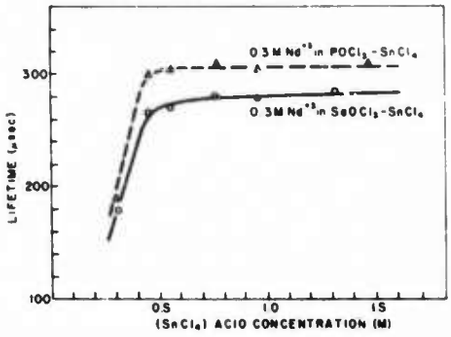

Figure 6. Fluorescence decay time of 0.3 *M* Nd^{3+} in $SeOCl_2$–$SnCl_4$ and $POCl_3$–$SnCl_4$ as function of Lewis acid concentration (at 300°K).

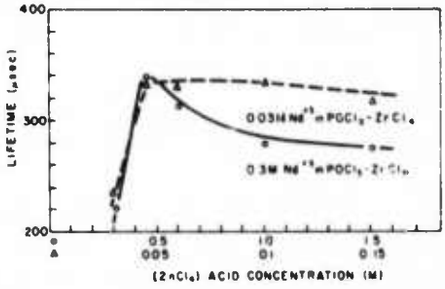

Figure 7. Fluorescence decay time of Nd^{3+} in $POCl_3$–$ZrCl_4$ as function of Lewis acid concentration (at 300°K).

Discussion

Spectroscopy. One of the sensitive optical probes is the behavior of the fluorescence decay time. The influence of the acidity is shown in Figures 6 and 7, which reveal two distinct effects. When the concentration of Lewis acid is below stoichiometric with respect to the Nd^{3+}, the fluorescence decay time and emission intensity are strong functions of acid concentration, dropping sharply as the acidity is reduced. This is true both at room temperature and at liquid N_2 temperature, in all systems studied, and in the total absence of measurable protic contamination. This behavior is accompanied by marked decrease in the chemical stability of the solutions, with precipitation occurring more and more readily. Only in the $SeOCl_2$ sys-

tems could solutions be prepared at zero acid concentration, and even they eventually precipitated out. This would indicate that the coordination sphere which solubilizes and protects the Nd^{3+} ion is becoming less and less effective, allowing external influences (Nd-Nd or Nd-solvent interactions) first to quench the fluorescence, and finally to cause the Nd to precipitate out of solution. This point will be considered later.

On the other side of stoichiometry, however, the systems behave quite differently. With $SnCl_4$ as the acid in both $POCl_3$ and $SeOCl_2$, the decay time remains essentially constant as the acidity increases to even three or four times stoichiometric. With $ZrCl_4$ in $POCl_3$ (it is insoluble in $SeOCl_2$), however, the decay time has a rather well-defined maximum, dropping significantly as the acid concentration is increased. Furthermore, as the acid concentration is increased new emission peaks appear in the fluorescence spectrum (particularly at liquid N_2 temperatures (Figure 4j), becoming continuously more intense up to the solubility limit of $ZrCl_4$. It is apparent that the $ZrCl_4$ is altering the coordination structure surrounding the Nd^{3+} ion; indeed it is likely that a Zr-containing anion is entering into the coordination structure, since the mere increase in acidity should have produced the same effect with $SnCl_4$ (which has the same shape and size). A supporting, if circumstantial, point is the remarkable structural similarity (Figure 5) in the spectra of Nd^{3+} in stoichiometric $POCl_3$-$ZrCl_4$ solutions and in the $Nd_2(ZrCl_6)_3 \cdot 12POCl_3$ salt (see Chemistry discussion). It should also be noted, as shown in Figure 7, that at a 1:10 dilution with pure $POCl_3$, the decay time drop-off for the same stoichiometry ratios is considerably slower; indeed, the effect seems to be proportional to the actual excess over stoichiometry, rather than the ratio, as would be expected for a new species in equilibrium with the old one.[17]

The decay time is also affected by the concentration of the Nd^{3+} ion itself. This arises from two characteristics of the energy level structure. First, most of the emission from the $^4F_{3/2}$ metastable state arises from transitions to either the $^4I_{9/2}$ or the $^4I_{11/2}$ lower states. The latter transition is the laser transition; the former, on the other hand, is the resonance transition to the ground state, and with increasing concentration considerable self-absorption will occur. Such self-absorption has the result of decreasing the apparent radiative probability for emission through the $^4F_{3/2}$-$^4I_{9/2}$ transition, thus effectively increasing the lifetime of the $^4F_{3/2}$ state in optically thick samples. Such behavior is observed in the $SeOCl_2$-$SnCl_4$ and $POCl_3$-$SnCl_4$ systems;[10] indeed, as seen in Figure 8, the lifetime increases by as much as 30% from its low-concentration value.

There is, however, also a second effect which arises from the fact that the energy gap between the $^4F_{3/2}$ emitting state and the $^4I_{15/2}$ state, the highest of the ^4I "ground" multiplet, is essentially the same as the energy of the $^4I_{15/2}$ state above ground. Thus when an unexcited Nd^{3+} ion is in close proximity to one excited to the $^4F_{3/2}$ state, transfer of energy between them can take place, leaving both in the $^4I_{15/2}$ state, from which they rapidly decay nonradiatively to ground. This sort of mechanism can provide a sufficiently competitive path for deexcitation to markedly reduce the lifetime of the $^4F_{3/2}$ state, and give rise to the concentration quenching observed with Nd^{3+} in many crystalline and glassy hosts.[18] Such behavior is also observed in the $POCl_3$-$ZrCl_4$ medium.

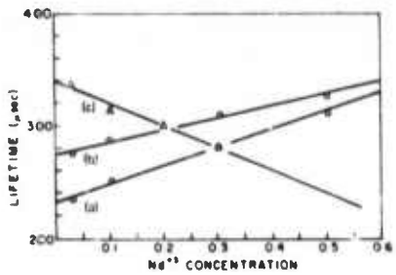

Figure 8. Fluorescence decay time of Nd^{3+} aprotic solutions at stoichiometric acidity as function of Nd^{3+} concentration (at 300°K): (a) $SeOCl_2$-$SnCl_4$; (b) $POCl_3$-$SnCl_4$; (c) $POCl_3$-$ZrCl_4$.

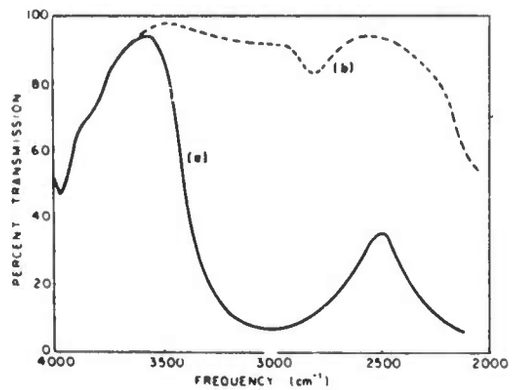

Figure 9. Infrared absorption spectrum of 0.3 *M* Nd^{3+} in $SeOCl_2$: (a) contaminated with H_2O (about 10^{-5} *M*); (b) anhydrous.

where the decay time decreased with increasing Nd^{3+} concentration even in the face of the lifetime lengthening effect of the self-absorption, which is still taking place. Since, as we have seen, the coordination in the $POCl_3$-$ZrCl_4$ liquid is such as to allow excess $ZrCl_4$ to alter it, it is not surprising that excess Nd^{3+} should do the same. This will be discussed subsequently.

The remaining important influence on the lifetime to be discussed here is that of protic contamination. It is now well established that the effectiveness of O-H and other hydrogen-containing groups in deexciting Nd^{3+}, or other ions, arises from the relatively high energy of vibrations involving the proton; so that with Nd^{3+}, only two O-H vibrational quanta are needed to bridge the gap between the $^4F_{3/2}$ and $^4I_{15/2}$ states. It is as a consequence of this mechanism that the aprotic liquid media were developed for Nd^{3+} liquid lasers. Generally, great care must be taken in the preparation of such solutions to avoid even small amounts of protic contamination, which, even at the level of 10^{-4}-10^{-5} *M*, can be readily detected both by infrared (Figures 9 and 10) and by the sharp decrease in lifetime (as much as 30-50%). Indeed, exposure of the

(17) (Nd^{3+}, solvated (I)) + $ZrCl_4$ ⇌ (Nd^{3+}-$ZrCl_4$, solvated complex (II))

$$K_{eq} \equiv [\text{species II}]/[\text{species I}][ZrCl_4]$$

or, if

$$\rho \equiv [\text{species II}]/[\text{species I}]$$

then

$$\rho = K_{eq}[ZrCl_4]$$

(18) See, for example, G. E. Peterson and P. M. Bridenbaugh, *J. Opt. Soc. Amer.*, **54**, 644 (1964); K. Hauplmanova, J. Pantollicek, and K. Palek, *Phys. Status Solidi*, **9**, 525 (1965); C. K. Asawa and M. Robinson, *Phys. Rev.*, **141**, 257 (1966); other references cited.

C-5

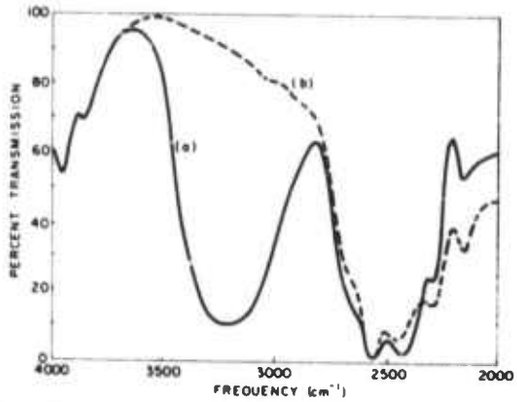

Figure 10. Infrared absorption spectrum of 0.3 *M* Nd^{3+} in $POCl_3$: (a) contaminated with H_2O (about 10^{-5} *M*); (b) anhydrous.

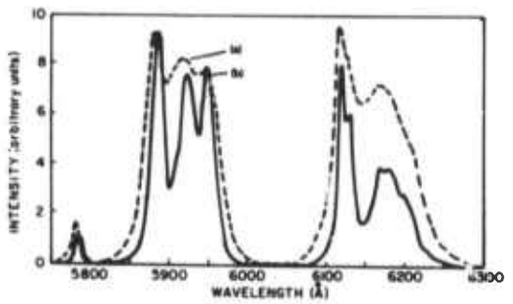

Figure 11. Emission spectrum of 0.3 *M* Eu^{3+} in $POCl_3$–$ZrCl_4$ solutions: (a) at 300°K; (b) at 100°K.

TABLE II: Emissions from Eu^{3+} (0.3 *M*) in $POCl_3$–$ZrCl_4$ Solution at 100°K

Wavelength, Å	Assignment	Energy of underlined state, cm^{-1}
5788	$^5D_0$–$^7F_0$	17,277
5884		282
5920	$^5D_0$–$^7F_1$	385
5945		456
6116		926
6127		956
6166	$^5D_0$–$^7F_2$	1,059
6182		1,101
6201		1,151

$SeOCl_2$–$SnCl_4$ and $POCl_3$–$SnCl_4$ to the open air for even a short time enables sufficient water to be absorbed to have a markedly deleterious effect on the lifetime. In contrast to this, however, the $POCl_3$–$ZrCl_4$ medium is remarkably insensitive to protic contamination. Short exposures to atmospheric moisture seem to have almost no measurable effect on the lifetime. Dropwise addition of water does have the expected effect, drastically decreasing the lifetime and the emission intensity; however (unlike the other two media), over a period of hours the solution restores itself with the lifetime and intensity regaining their original levels. This is accompanied by the slow precipitation from the solution of the white powder of $ZrOCl_2$ (or its hydrate), and the virtual disappearance of the previously intense O–H infrared absorption. The contaminated solution, if carefully filtered, becomes as good a laser solution as before.

As an explanation for the unusual behavior of the $POCl_3$–$ZrCl_4$ solutions, we observe that Zr has a much greater affinity for oxygen than has Sn.[19] For example, if water is added to pure $SnCl_4$ liquid, the crystalline $SnCl_4 \cdot nH_2O$ hydrate forms; if the same is done to $ZrCl_4$, a strong reaction takes place, with the liberation of HCl gas and formation of $ZrOCl_2$, which dissolves in water. The ability of other oxygen-containing acids, such as acetic, to displace chlorine from $ZrCl_4$, forming $ZrCl_2(OR)_2$, has been well established.[19] Thus, the following model is proposed for the behavior of aqueous contamination. The addition of water to the solution forms the protic acid

$$H_2O + SeOCl_2 \rightarrow H_2SeO_2Cl_2 \quad (1a)$$

$$H_2O + POCl_3 \rightarrow HPO_2Cl_2 + HCl \quad (1b)$$

Unless removed by boiling (with evolution of HCl), the protic acid remains in solution as a contaminant, and $SnCl_4$ has no measurable effect on its presence. With $ZrCl_4$, however, we can get further reaction

$$ZrCl_4 + HPO_2Cl_2 \rightarrow ZrCl_3(PO_2Cl_2) + HCl \quad (2a)$$

$$ZrCl_4 + 2HPO_2Cl_2 \rightarrow Zr(OH)_2Cl_2 + POCl_3 \quad (2b)$$

effectively removing the protic contamination. In eq 2a, the $ZrCl_3(PO_2Cl_2)$ in solution may then slowly rearrange to regenerate one molecule of $POCl_3$ and one of $ZrOCl_2$, which is insoluble in $POCl_3$ and precipitates out.

At this point, nothing has been said of the symmetry and structure of the coordination sphere surrounding the Nd^{3+} ion. In earlier work on Eu^{3+} liquid laser solutions,[20] it was shown that eightfold coordination around the central metal ion is almost universal in strongly bonded rare-earth compounds like chelates, with the few exceptions leading toward higher (nine- or tenfold) rather than lower coordination. It would seem quite unlikely that Nd^{3+}, with the same chemical bonding behavior and even a slightly larger ionic radius, would be satisfied with lower coordination.

Detailed information on the symmetry and stability of the various coordination structures could be unequivocally obtained because of certain unique spectroscopic properties of the Eu^{3+} ion, and it was hoped to glean similar information about the aprotic Nd^{3+} laser solutions by studying equivalent solutions made with Eu^{3+}. This hope was dashed by the highly structured spectra of the resulting solutions (Figure 11; see also ref 8c). In many cases, particularly under strongly acid conditions, more than one $^5D_0$–$^7F_0$ transition was observed, a unique positive indication of more than one coordination species. Whenever a clearly defined single $^5D_0$–$^7F_0$ transition was found (generally at stoichiometric acidity), the $^5D_0$–$^7F_1$ and $^5D_0$–$^7F_2$ transition regions showed three and five components, respectively, the maximum possible splitting.[21] This was true at both room temperature and liquid nitrogen temperatures, although of course the components were much better resolved in the latter case (Table II). Indeed, the

(19) P. Pascal, "Nouveau Traite de Chimie Mineral," Masson et Cie, Paris, 1963.

(20) H. Samelson, C. Brecher, and A. Lempicki, *J. Mol. Spectrosc.*, **19**, 349 (1966); other references cited therein.

(21) Emissions from the $^5D_1$ state to the $^7F_5$ and $^7F_6$ states, respectively, can also fall in these regions. Such emissions are generally much less intense (the observed emissions from the $^5D_1$ state to the $^7F_0$, $^7F_1$, and $^7F_2$ states are two orders of magnitude weaker) and are neglected here.

TABLE III: Analytical Results on Various Nd^{3+} Precipitates from $POCl_3$ Solutions

Material	% composition					
	Nd	Cl	O	P	Zr	
Precipitate 3 (measured)	7.9	63.0	4.6	14.9	9.6	(by difference)
$Nd_2(ZrCl_6)_3 \cdot 12POCl_3$ or $Nd_2(ZrCl_4(PO_2Cl_2)_2)_3 \cdot 6PCl_5$ (theory)	9.5	63.0	6.3	12.2	9.0	
Precipitate 2 (measured)	15.1	59.4	7.8	19.5		
$NdCl_3 \cdot 5POCl_3$ (theory)	14.2	62.7	7.9	15.2		
$NdCl_2(PO_2Cl_2) \cdot 4POCl_3$ (theory)	15.0	58.9	10.0	16.1		
Schimitschek precipitate[a] (measured)	24.2	43.8	15.0	17.0		
$Nd(PO_2Cl_2)_3$ (theory)	26.4	39.0	17.6	17.0		

[a] Reference 28

spectrum is reminiscent of those obtained from tris bidentate chelates of europium in polar solvents.[22] While an analogy between two such different systems is tenuous at best (see Appendix), this would imply that the coordination needs of rare earths in $POCl_3$ are satisfied in a similar manner, that is, with six equivalent oxygens (three bidentate groups) and two or three other (solvent) molecules. In any event, no single coordination species having a symmetry higher than C_2 is compatible with the spectrum and, while it is not unlikely that there are actually more than one symmetry species in solution, the single $^5D_0$-$^7F_0$ transition would indicate that, in the primary coordination sphere, the differences are largely matters of geometric arrangement.

Similar evidence of low symmetry and/or possible multiple species is obtained from the Nd^{3+} spectra (Figures 2 and 3). Here at least eight clearly defined components can be found in the $^4F_{3/2}$-$^4I_{9/2}$ (resonance) transition region in all three types of solution, indicating a complete splitting of both upper and lower states (ten possible energies). While this does not agree with a nearly octahedral symmetry inferred by Kato from the laser behavior[23] and Tb^{3+} spectra,[24] it is completely consistent with various studies in the Soviet Union,[25] and appears unequivocal.

The effect of acidity on the Nd^{3+} spectrum is shown in Figure 4. In all three cases, when the Lewis acid concentration is below stoichiometric there is no measurable distortion of the spectrum from the normal (stoichiometric) situation shown in Figures 1-4, indicating no significant emission from more than one species. The intensity of the emission, however, does decrease sharply, in line with the decrease in measured decay time. The $SeOCl_2$-$SnCl_4$ and $POCl_3$-$SnCl_4$ media also show no significant spectroscopic effect above stoichiometric acidity; in $POCl_3$-$ZrCl_4$, however, at least four new components do appear, exceeding the maximum of ten allowed for a single species. This supports the multiple species hypothesis inferred from the lifetime measurements, but gives no information about its nature. For further insight, we must consider other aspects of the chemistry of these solutions.

Chemistry. Although all three types of aprotic solutions were prepared with similar starting materials (a Nd^{3+} salt, a strong Lewis acid, and the aprotic solvent), there are considerable differences in the product solutions. The chemistry of the $SeOCl_2$ system has been discussed elsewhere,[8] and appears straightforward. This solvent is highly polar (dielectric constant ~46), and can thus readily dissolve ionic salts. The Nd^{3+} goes into solution, solvated by a shell of $SeOCl_2$ molecules (akin to hydration in aqueous solutions), to which it is bonded through the oxygen,[26] and which interchange readily with other solvent molecules. The Nd^{3+} chloride can even dissolve in hot $SeOCl_2$ without any Lewis acid, producing a clear solution but with considerably reduced fluorescence intensity and short (≈ 100 μsec) decay time. The cooled solution is not stable, and precipitates out in a matter of days, somewhat akin to the slow precipitation of $FeCl_{3-x}(OH)_x$ from an aqueous unbuffered solution of ferric chloride. With Lewis acid ($SnCl_4$) at stoichiometric or higher concentrations, the solution is completely stable and suitable for laser use.

Phosphorus oxychloride behaves rather differently. Its dielectric constant is only 14, and hence it will not readily dissolve most ionic salts. Thus, Nd_2O_3 will not dissolve under completely anhydrous conditions, and the addition of water is needed for the reaction to proceed. When this reaction is performed slowly, at moderate Nd^{3+} concentrations (say 0.01 *M*), with reactants cooled in an ice bath, the intermediate product (a granular light blue precipitate, denoted ppt 1) can be held for some time. If the temperature of the solution is allowed to rise, the precipitate dissolves forming a clear solution, followed by a new precipitate (ppt 2) some seconds later. The new precipitate does not dissolve, except upon addition of sufficient Lewis acid.

Similar observations are made in the third case. Here, at moderate Nd^{3+} concentrations, the $Nd(CF_3COO)_3$ can be observed to dissolve completely to form a clear blue solution, only to be followed a few seconds later by formation of a precipitate (ppt 2), which itself is soluble only on addition of Lewis acid ($ZrCl_4$). Addition of PCl_5 to the resulting stable solution causes yet another precipitate (ppt 3) to form. Analyses of these precipitates (except ppt 1, which was not stable), thoroughly dried by flowing nitrogen gas at room temperature, but not heated or pumped to drive off bound solvent of crystallization, is given in Table III.

The following mechanism is proposed to explain the dissolution of Nd^{3+} salts in $POCl_3$. First, the addition of water (or the use of the trifluoroacetate salt) forms the dichlorophosphate

$$3H_2O + 6POCl_3 + Nd_2O_3 \rightarrow 2Nd(PO_2Cl_2)_3 + 6HCl\uparrow \quad (3a)$$

(22) C. Brecher, H. Samelson, and A. Lempicki, *J. Chem. Phys.* **42**, 1081 (1968).
(23) D. Kato, *J. Phys. Soc. Jap.*, to be submitted for publication.
(24) D. Kato and K. Shimoda, *Jap. J. Appl. Phys.* **9**, 581 (1970).
(25) M. N. Tolstoi, E. L. Lyubimov, and I. M. Batyaev, *Opt. Spectrosc.* **28**, 389 (722) (1970), other references cited therein.
(26) I. Lindqvist, "Inorganic Adduct Molecules of Oxo-Compounds," Springer-Verlag, Berlin, 1963.

C-7

$$3H_2O + 3POCl_3 + NdCl_3 \rightarrow Nd(PO_2Cl_2)_3 + 6HCl\uparrow \quad (3b)$$

$$Nd(CF_3COO)_3 + 3POCl_3 \rightarrow Nd(PO_2Cl_2)_3 + 3CF_3COCl\uparrow \quad (3c)$$

The by-products go off as gases, leaving the dichlorophosphate in solution. This material, crystallized by cooling, is identified as ppt 1. However, in solution this compound is unstable in the presence of $POCl_3$,[27] reacting further and being converted to the pyrophosphoryl chloride

$$Nd(PO_2Cl_2)_3 + 3POCl_3 \rightarrow NdCl_3 + 3P_2O_3Cl_4 \quad (4)$$

The $NdCl_3$ precipitates out of solution, carrying with it approximately five molecules of $POCl_3$ as solvent of crystallization, as confirmed in Table III (ppt 2). This material differs from that obtained by Schimitschek and Trias,[28] who identified a similar precipitate as the dichlorophosphate $Nd(PO_2Cl_2)_3$. However, they isolated and dried the precipitate differently, as will be seen.

Since addition of Lewis acid causes the precipitate to dissolve, the final step (as in $SeOCl_2$) might be written as

$$2NdCl_3 + 3SnCl_4 \rightarrow Nd_2(SnCl_6)_3 \quad (5a)$$

$$2NdCl_3 + 3ZrCl_4 \rightarrow Nd_2(ZrCl_6)_3 \quad (5b)$$

in which the Lewis acid simply lowers the Cl^- concentration in the solution sufficiently to shift the equilibrium from the precipitated chloride to the solubilized $Nd^{3+}\cdot nPOCl_3$ ion. This, however, does not answer a number of specific observations on the chemical behavior:

(1) Neither this precipitate ($NdCl_3\cdot 5POCl_3$), nor pure $NdCl_3$, will dissolve in pure $POCl_3$ to which adequate Lewis acid ($ZrCl_4$ or $SnCl_4$) has been added but do dissolve if water is also added. (Except that too much water will cause $ZrOCl_2$ to precipitate.)

(2) They also dissolve when Lewis acid is added to the clear liquid from which the material originally precipitated, or to the clear liquid prepared by reaction of $POCl_3$ with the requisite amounts of water or sodium trifluoroacetate.

(3) The addition of sufficient water will cause the precipitate (or the pure chloride) to dissolve even without and Lewis acid.

(4) A precipitate prepared in the same manner, but baked out under vacuum to remove *all* solvent of crystallization (Schimitschek), does dissolve in pure $POCl_3$–$ZrCl_4$.

(5) Completely stable solutions prepared in the standard manner are caused to precipitate by addition of PCl_5 (forming ppt 3).

The behavior of Lewis acids in $POCl_3$ is complicated. The low dielectric constant is much less favorable for the formation of $POCl_2^+$ and Cl^- species than for the corresponding ions ($SeOCl^+$ and Cl^-) in $SeOCl_2$ and is even less favorable for the doubly negative $SnCl_6^{2-}$ and $ZrCl_6^{2-}$ ion. This is borne out by the low conductivity ($\sim 10^{-5}$ ohm/cm) of $POCl_3$–$ZrCl_4$ solutions. Indeed research on $POCl_3$-containing systems by many investigators[29] indicates that the validity of extending to it the ionic model appropriate to $SeOCl_2$ is extremely questionable. On the other hand, it is known that both Sn and Zr chlorides readily satisfy their coordination needs in $POCl_3$ by direct addition of two solvent molecules, forming $MCl_4\cdot 2POCl_3$, and compounds of this form have been isolated. Furthermore, as stated earlier, suitable oxygen donors (water, acetic acid, etc.) will readily displace chlorine from Zr (but not from Sn), forming stable compounds of the form $ZnCl_2(OR)_2$ (or $ZrOCl_2$ with water). We therefore propose that the important factor in the dissolution of Nd^{3+} in $POCl_3$ is the stabilization of the $PO_2Cl_2^-$ ionic species, and hence the reversal of eq 4. The Lewis acid would accomplish this, not by forming $ZrCl_6^{2-}$ or $SnCl_6^{2-}$ ions, but by direct bonding with the $PO_2Cl_2^-$ ion itself. Thus in item 1, the precipitate or the $NdCl_3$ will not dissolve in pure $POCl_3$ even with sufficient Lewis acid, because not enough $P_2O_3Cl_4$ is present to be converted back into $PO_2Cl_2^-$ (reverse of eq 4). If, however, enough is generated even by other means (item 2) dissolution will occur. Item 3 is merely item 2 carried to extreme, in which enough $P_2O_3Cl_4$ is formed to push the equilibrium in eq 4 sufficiently to the left. Item 4 is merely the result of the same leftward push of eq 4, this time by the complete removal of $POCl_3$ by heat and vacuum, followed by dissolution in pure $POCl_3$–$ZrCl_4$. And finally, item 5 is a result of the destruction of the soluhilizing species by PCl_5

$$P_2O_3Cl_4 + PCl_5 \rightarrow 3POCl_3 \quad (6a)$$

$$PO_2Cl_2^- + PCl_5 \rightarrow 2POCl_3 + Cl^- \quad (6b)$$

This leads to the following picture of the Nd^{3+} ion in $POCl_3$. With $SnCl_4$ as the Lewis acid, species of the type $SnCl_4\cdot 2POCl_3$ are present with the two oxygens donating electrons into vacant 5d orbitals of the tin and completing its octahedral coordination. The $PO_2Cl_2^-$ ion, being a stronger electron donor, displaces the $POCl_3$, forming species like $SnCl_4(PO_2Cl_2)^-$. Exchange of the $PO_2Cl_2^-$ ions would readily take place among the $SnCl_4$ molecules and between them and the Nd^{3+} ion. The primary coordination sphere of the Nd^{3+} would be occupied by these $POCl_3$ and $PO_2Cl_2^-$ groups and the $SnCl_4$ molecules associated with them, producing a number of possible coordination species. The most probable ones, because of the low dielectric constant, would bear no net charge, and would have the general composition

$$Nd(PO_2Cl_2\cdot SnCl_4)_{3-n}(SnCl_5\cdot POCl_3)_n \quad (n = 0, 1, 2)$$

where the relative proportions would be determined by the concentration of Lewis acid and by the equilibrium constants between the respective species. The remaining coordination needs for both Nd and Sn would be filled by $POCl_3$ groups, leaving only oxygen in the primary coordination sphere of the neodymium ion. The overall size of the coordination entity would necessarily be considerably larger than in $SeOCl_2$; this is supported by the rather large Rayleigh wing scattering observed in such solutions.[30] A small but nonnegligible concentration of charged species, of the same general structure but with a neutral $POCl_3$ group replacing one or more of the chlorines or the larger negatively charged groups, must also be present, as indicated by the electrical conductivity; indeed studies of the electroluminescence in similar solutions[16] lead to essentially the same chemical model.

With $ZrCl_4$ as the Lewis acid, the picture is different only in the strength of the metal-oxygen association; here the stronger Zr-O bond (involving the 4d orbitals rather

(27) J. R. Van Wazer, "Phosphorus and Its Compounds," Interscience, New York, N. Y., 1961.
(28) E. J. Schimitschek and J. A. Trias, *Inorg. Nucl. Chem. Lett.*, **6**, 761 (1970); see also E. J. Schimitschek, J. A. Trias, and C. Y. Liang, *Spectrochim. Acta, Part A*, **27**, 2141 (1971).
(29) V. Gutmann, "The Chemistry of Non-Aqueous Solvents," J. J. Lagowski, Ed., Academic Press, New York, N. Y., 1966.
(30) R. Pappalardo and A. Lempicki, *J. Appl. Phys.*, **43**, 1699 (1972).

than the much higher energy 5d's as in Sn), and the ability to form neutral $ZrCl_2(PO_2Cl_2)_2$ species, would lead to more stable Nd^{3+} coordination structures and probably ring formation of the type

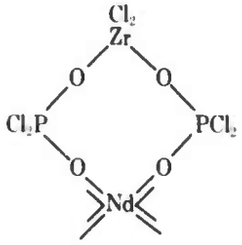

which is known to take place in other systems.[31]

This picture of the solvation of Nd^{3+} in $POCl_3$, while speculative and far from proven, has the virtue of explaining all our various experimental observations as well as those of others. It also provides a rationale for the differences in the behavior of Nd^{3+} in $POCl_3$ with the two Lewis acids. The more stable ring formations in the $POCl_3$-$ZrCl_4$ solution would be more effective in shielding in the Nd^{3+} ion from interaction with contaminants. The sharp increase in viscosity when both Nd^{3+} and Lewis acid are present in the solution, as against either one separately, is explained by the relatively large size of the agglomerations. The fact that excess $ZrCl_4$ alters the lifetime and spectrum of Nd^{3+} (see Figures 4 and 8) while $SnCl_4$ does not, arises from the ability of the $ZrCl_4$ to become directly bonded into the Nd^{3+} complex species. And finally, since at higher Nd^{3+} concentrations the -OPO-Zr-OPO groups should form bridges between different Nd^{3+} ions as readily as they form rings with only one Nd^{3+} ion, the observed concentration quenching is a straightforward result of the model. In conclusion, therefore, the foregoing picture reveals both the fundamental similarities and the disparities in detail characteristic of the most widely used Nd^{3+} aprotic liquid laser solutions, and we feel that we have derived a consistent and coherent model for their chemical and spectroscopic behavior.

Acknowledgments. The authors are indebted to H. Samelson and A. Heller for many helpful discussions on various aspects of this work.

Appendix

Spectroscopic Characteristics of Eu^{3+} Tris Chelates in Polar Solvents. The emission spectra of europium chelates were subject to intense study a number of years ago.[20] Considerable information was generated because of two particularly useful spectroscopic characteristics. First, the $^5D_0$-$^7F_0$ transition cannot be split by the coordination field, so that the observation of more than one component is a positive indication of more than one coordination structure. Secondly, the small number of components possible in the $^5D_0$-$^7F_1$ and $^5D_0$-$^7F_2$ transitions (three and five, respectively) and the great sensitivity of the latter to the symmetry of the coordination structure makes it possible to distinguish between structures having the same coordination number. It was further ascertained that for rare earths, a coordination number of less than eight is a rarity, and that tris and bis chelates will fill their unsatisfied coordination needs by associating with polar solvent molecules, either in solution or as molecules of solution in the solid. This tendency results in a low molecular symmetry and consequently a highly structured spectrum with full splitting of the known transitions.

Nevertheless, and despite differences in detail, the various europium tris chelates had many qualitative features in common, particularly in contrast to the tetrakis chelates. The $^5D_0$-$^7F_0$ transition falls between 5796 and 5800 Å, as against over 5800 Å for the tetrakis and below 5796 Å for others. The intensity of this transition is within an order of magnitude of the $^5D_0$-$^7F_2$, and some 1.5 orders of magnitude stronger than for the tetrakis. The intensity of the $^5D_0$-$^7F_1$ transition is nearly the same as that of the $^5D_0$-$^7F_2$, instead of almost 1 order of magnitude weaker. The existence of a $^5D_0$-$^7F_1$ component in the 5870-5900-Å region is characteristic of these chelates, since those for tetrakis chelates are higher. And finally, the existence of strong $^5D_0$-$^7F_2$ components in the 6160-6220 Å region is similarly characteristic of the tris species.

The large number of components makes determination of the actual symmetry difficult. The fact that there are two chemically distinct types of oxygen coordinated to the europium, to be distributed among eight (or nine) positions results in not only a low symmetry, but also the possibility of many geometric arrangements, each with its own selection rules and its own contribution to the spectrum. Since these species are virtually indistinguishable chemically, the $^5D_0$-$^7F_0$ transition will be essentially unaffected.

(31) See, for example, J. Danielsen and S. E. Rasmussen, *Acta Chem Scand.*, **17**, 1971 (1963); H. Grunze, K. H. Jost, and G. U. Wolf, *Z Anorg Allg Chem.*, **365**, 294 (1969).

C-9

APPENDIX D

BRILLOUIN AND RAYLEIGH SCATTERING IN APROTIC LASER SOLUTIONS CONTAINING NEODYMIUM

Brillouin and Rayleigh Scattering in Aprotic Laser Solutions Containing Neodymium

R. Pappalardo and A. Lempicki
Bayside Research Center, GTE Laboratories Incorporated, Bayside, New York 11360
(Received 11 August 1971)

Rayleigh and Brillouin scattering spectra have been measured at 6328 Å in aprotic laser solutions of neodymium containing $SeOCl_2$ and $POCl_3$. The intensity of the scattered radiation was mainly concentrated in the Rayleigh component of the scattering spectrum. The Rayleigh line was quite intense, while the intensity of the Brillouin line was comparable to that of benzene and other common liquids. The $POCl_3$ laser solutions were generally stronger scatterers than the $SeOCl_2$ solutions. Values of the scattering coefficients in the laser solutions have been obtained by comparison with the scattering spectra of benzene. This made it possible to derive values of the scattering losses at 1.06 μm. The values obtained are of ≃ 0.027/cm. $SeOCl_2$-based laser solutions exhibit Rayleigh-wing scattering. The width of the line indicates molecular reorientation times of the order of 50–100 psec. In $POCl_3$-based solutions such processes appear to be much slower.

I. INTRODUCTION

The characteristics of condensed-phase substances used for the generation of laser radiation can be divided into two categories: The first category deals with properties essentially determined by the active ion and its immediate surroundings, namely, quantum efficiency, radiative lifetime, linewidth, etc. The second category describes the medium and its effects on the propagation of electromagnetic radiation.

In gas lasers this latter category can often be totally neglected, since a gaseous medium, especially at low pressures, has a weak effect on the propagation of radiation. In condensed-phase lasers the properties of the medium are of great importance because they largely determine the losses through various forms of scattering, refraction, absorption, and, in the case of solids, damage. In the case of liquids all of these effects, with the possible exception of damage, also play an important role. In addition, nonlinear effects associated with the rotational motion of molecules may strongly affect the propagation of radiation through self-focusing.[1]

In an attempt to fully characterize the physical properties of aprotic laser solutions, this paper deals with spontaneous Brillouin and Rayleigh scattering of the medium. Raman scattering contributes negligibly to the loss (typically one part in a million) and has been dealt with in Ref. 1. In contrast with Raman scattering, both Brillouin and Rayleigh scattering are quasielastic and lead to the creation of frequencies which are well within the 100-cm^{-1} width of the fluorescence line of the Nd^{3+} ion. They do not, therefore, lead in a straightforward way to the creation of new frequencies in the output of the laser, as is the case with the Raman scattering, which involves shifts of hundreds of wave numbers.

Apart from contributing to the irreducible loss of a solution, however, it is felt that the Brillouin and Rayleigh scattering may play a role in some of the still unexplained phenomena in liquid lasers. It has been suggested, for instance, that self-Q-switching often observed in Nd liquid lasers is connected with Brillouin scattering.[2] The spectral broadening of the laser output[3] can perhaps be partially attributed to stimulated Rayleigh-wing scattering in much the same manner as it contributes to the broadening of a monochromatic pulse of radiation passing through CS_2.[4,5]

II. THEORY

The light-scattering effects in a homogeneous, isotropic, condensed medium, such as an aprotic laser solution, arise basically from fluctuations of the dielectric constant ϵ of the medium. In order to evaluate these fluctuations, the physical system is described by appropriate models, with an increasing degree of complexity, starting from a simple structureless continuum, suitable for a thermodynamic description, and working up gradually to a molecular model of the system. Once a given physical model is chosen, the scattering system can either be described at thermodynamic equilibrium, or its dynamic behavior in nonequilibrium conditions can be followed in detail. The theory of light scattering correspondingly increases in complexity and involves more and more physical parameters.

D-2

Thermodynamic Theory

The simplest theoretical treatment is based on the thermodynamic consideration of a structureless continuum. This is in essence the original approach used by Einstein.[6] The dependence of the variation of dielectric constant $\Delta\epsilon$ on temperature fluctuations is neglected in comparison with its dependence on the density fluctuations. Assuming a single-phase system, the following expression is derived for the intensity of the scattered light[7,8]:

$$I = I_0 \frac{\pi^2 V}{2\lambda^4 L^2}\left(\rho\frac{\partial\epsilon}{\partial\rho}\right)^2_T \beta_T kT(1+\cos^2\theta) \quad , \tag{1}$$

where I_0 is the intensity of the incident unpolarized light, V is the scattering volume, λ is the wavelength of the incident light, L is the distance from the scattering volume to the point where I is measured, ρ is the density, β_T is the isothermal compressibility, and θ is the angle between the k vectors of the incident and scattered light. Most of the quantities in (1) are external parameters, since they depend on the experimental geometry and the excitation conditions. The only internal parameters characterizing the scatterer are ρ, $(\partial\epsilon/\partial\rho)_T$, and β_T. The experimental data on scattering intensity and the theory are conveniently connected via the scattering coefficient R_θ:

$$R_\theta = \frac{I}{I_0}\frac{L^2}{V}\ (\mathrm{cm}^{-1}). \tag{2}$$

By comparison with Eq. (1) it is easy to express the theoretical value of R_θ as a function of the excitation wavelength, the scattering angle, and the physical properties of the scatterer as follows:

$$R_\theta = \frac{\pi^2}{2\lambda^4}\left(\rho\frac{\partial\epsilon}{\partial\rho}\right)^2 \beta_T kT(1+\cos^2\theta) \quad . \tag{2'}$$

The following simple relation connects the scattering coefficient for $\theta = 90°$ with the corresponding extinction coefficient h of a nonabsorbing medium[7]:

$$h = \tfrac{16}{3}\pi R_{90} \quad . \tag{3}$$

The extinction coefficient is defined from the expression connecting the initial and final intensities of a light beam after it has traversed a homogeneous medium x cm long:

$$I = I_0 e^{-hx} \quad . \tag{4}$$

The measured scattering coefficient for a laser solution can then be converted into an extinction coefficient and, as such, inserted into the expression for the gain characteristic of a laser medium, nonabsorbing at the frequency under consideration. A slight modification of (3) leads to a connection between the scattering coefficient per unit volume R'_{90} and the cross section for scattering:

$$h' = \tfrac{16}{3}\pi R'_{90} \tag{3'}$$

and

$$h' = N\sigma_{sc} \quad , \tag{3''}$$

N being the number density of scattering centers and σ_{sc} the scattering cross section per particle.

So far, no spectral distribution of the scattered light was considered. A preliminary discussion of the spectral characteristics of the scattered light *can* be derived from the following considerations: In (1) the fluctuations of the density $\overline{\Delta\rho^2}$ have been expressed as a function of the coefficient of isothermal compressibility β_T. Alternatively $\overline{\Delta\rho^2}$ can be expressed in terms of pressure and entropy fluctuations, $\overline{\Delta p^2}$ and $\overline{\Delta S^2}$:

$$I = I_{\mathrm{adiab}} + I_{\mathrm{isob}} = VG\left[\left(\frac{\partial\epsilon}{\partial\rho}\right)^2_T\left(\frac{\partial\rho}{\partial p}\right)^2_S \overline{\Delta p^2} + \left(\frac{\partial\epsilon}{\partial\rho}\right)^2_T\left(\frac{\partial\rho}{\partial S}\right)^2_p \overline{\Delta S^2}\right] \quad , \tag{5}$$

with G an "external" parameter, not containing quantities characterizing the scatterer. The pressure fluctuations obey a wave equation and will propagate, while the entropy fluctuations obey a flow equation and will not propagate. Pressure fluctuations cause Doppler-type scattering with change in frequency, while entropy fluctuations will cause no change in frequency. The first term in (5) gives rise to Brillouin scattering, the other to Rayleigh scattering. Brillouin scattering in a given direction will be maximized when Bragg's relation is satisfied and

$$2n\Lambda\sin\tfrac{1}{2}\theta = \lambda \quad , \tag{6}$$

where n is the index of refraction of the medium for the wavelength λ of the incident light and Λ is the wavelength of density waves involved in the scattering event. From (5) the following relation (Landau-Placzek formula) is obtained for the ratio of the intensity of the Rayleigh and Brillouin components of the scattered light:

$$I_{\mathrm{isob}}/I_{\mathrm{adiab}} = (\beta_T - \beta_S)/\beta_S = \gamma - 1 \quad . \tag{7}$$

γ is also the ratio of the specific heats c_p/c_v. The relative frequency shift in the scattered radiation due to pressure fluctuations can be derived from (6):

$$\Delta\omega/\omega_0 = 2n(v/c)\sin\tfrac{1}{2}\theta \quad . \tag{8}$$

From the measurement of $\Delta\omega$, ω_0, θ, and n, the value of the hypersound velocity v can be deduced.

Depolarization Effects

Both the Rayleigh and the Brillouin scattering are completely polarized because only isotropic fluctuations of the refractive index have been considered so far. Depolarization effects on the expression of the scattered intensity can be formally introduced by the use of the empirical parameter Δ_u as follows[7,8]:

$$\mathcal{I} = I\left(1 + \frac{\Delta_u(1+\rho_u)}{\rho_u - \Delta_u}\right) \quad , \tag{9}$$

$$\rho_u = i_x/i_z \quad , \tag{10}$$

$$\Delta_u = i_x/(i_z + i_z) \quad , \tag{11}$$

where $\mathcal{I}$ is the scattered intensity inclusive of scattering due to orientation fluctuations; i_x and i_z are the intensity components of the depolarized scattered light in the scattering plane and normal to it, respectively. The subscript u stands for unpolarized incident light. The expression for the scattering coefficient then becomes

$$R_{90} = \frac{\pi^2}{2\lambda^4}\left(\rho\frac{\partial\epsilon}{\partial\rho}\right)^2_T \beta_T kT\,\frac{6+6\Delta_u}{6-7\Delta_u} \quad . \tag{12}$$

The term $(6+6\Delta_u)/(6-7\Delta_u)$ is known as the Cabannes correction factor.

D-3

Relaxation Theory

The model considered so far does not take into account the existence of a band of scattered radiation found experimentally for some liquids, with a spectral distribution reaching in some cases up to 100–150 cm^{-1} away from the frequency of the incident radiation. This is the so-called Rayleigh-wing scattering, which shows pronounced depolarization. While the depolarization could be accounted for by the optical anisotropy of the scattering centers, the frequency shift would still be unexplained, and hence must be due to molecular reorientation processes in the scattering medium.

A theory has been developed by Leontovich[9] to describe by the same formalism both polarized scattering (Brillouin and Rayleigh) and depolarized scattering (Rayleigh and Rayleigh-wing scattering). This is the so-called relaxation theory, somewhat akin to the Debye theory for the electric susceptibility of polar molecules in liquids. In this approach the state of the liquid is characterized by the deformation tensor $\bar{e}_{ik}$, the anisotropy tensor $\bar{\xi}_{ik}$, and the stress tensor $\bar{S}_{ik}$. Small departures from equilibrium conditions are considered, and the return to equilibrium is characterized by a relaxation time τ that is common to $\bar{\xi}_{ik}$ and $\bar{S}_{ik}$. A specific molecular model can be introduced to connect some of the relevant parameters with molecular quantities, such as the molecular radius for spherical molecules. The fluctuations are expressed in the form of spatial sinusoidal waves. From the temporal dependence of the latter, the spectral composition of the scattered intensity is obtained by means of a Fourier transform.

Connection between Scattering Measurements and Theory

As mentioned at the beginning of Sec. II, the more refined the theory of molecular scattering, the greater the number of physical parameters required to characterize the scattering system. In the relaxation theory the scattering data must be supplemented by the elasticity and deformation constants of the fluid, measured not only under steady-state conditions, but also at high frequencies.

Since no data on the solutions studied are presently available, except for the scattering measurements and the index of refraction, the potentialities of the existing theories cannot be fully exploited. The measured data could only be related to the thermodynamic theory and to some simple aspects of the relaxation theory.

III. EXPERIMENTAL

Apparatus

A schematic representation of the experimental arrangement is given in Fig. 1. The radiation scattered by the liquid samples was provided by a He-Ne laser. The laser cavity between mirrors M_1 and M_2 was 230 cm long. Either a 2-m He-Ne laser or two 1-m tubes were placed in the cavity. The laser output polarized in a vertical direction was focused at the center of the sample cell (SC) by means of lens L_1. An interference filter for 6328 Å removed unwanted spectral components in the laser output.

The scattering volume in the sample was defined by an aperture in the light shield (LS). An additional light shield surrounded the sample cell, allowing the primary beam in and out of the sample, but removing stray light within the sample compartment. The sample compartment itself was painted black and was light-tight. All the optical components of the system were connected by sections of photographic bellows, and all metal surfaces were painted black.

The beam scattered at 90°, went through a spiked interference filter for 6328 Å with a half-passband of 6 Å, followed by a Glan-Thompson prism (to select the polarized and unpolarized components) and a collimating lens (L_2). The parallel beam emerging from L_2 was reduced in diameter by a $\frac{1}{4}$-in.-diam aperture, prior to entering the pressure-scanned Fabry-Perot interferometer. Lens L_3 (an achromat of 335-mm focal length) focused the resulting interference patterns on a pinhole situated in front of the cathode area of a cooled ITT FW 130 photomultiplier. The dc current was detected with a Keithley picoammeter. The resulting signal was sent to the y channel of an x-y recorder. A pressure transducer monitored the nitrogen pressure in the brass casing containing the Fabry-Perot interferometer, and its signal activated the x channel of the recorder. The pres-

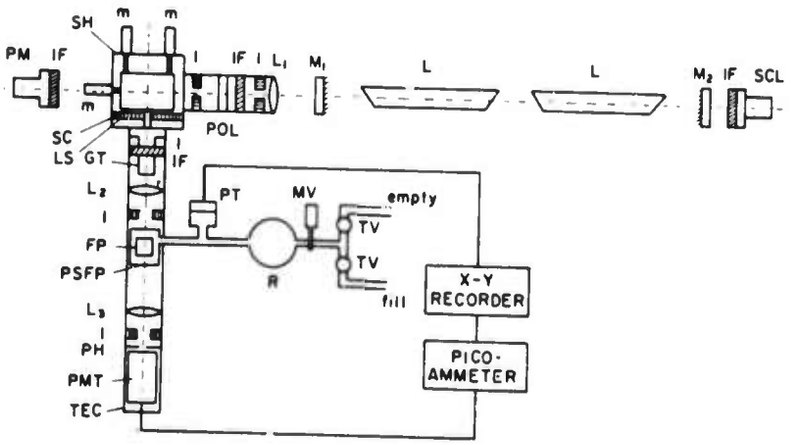

FIG. 1. Block diagram of experimental arrangement. FP—Fabry-Perot interferometer; GT—Glan-Thompson prism; I—iris-shutter combination; IF—interference filter for 6328 Å; L—He-Ne laser; L_1, L_2, L_3—lenses; LM—JEA light meter; LS—light shield; m—micrometers for positioning sample cell; M_1, M_2—dielectric mirrors; MV—metering valve; PH—pinhole; POL—polarizer; PMT—ITT FW 130 photomultiplier; PSFP—pressure-scanned Fabry-Perot interferometer; PT—pressure transducer; SC—sample cell; SCL—solar cell, laser output monitor; SH—sample holder; TEC—thermoelectric cooler; TV—toggle valve.

D-4

sure in the closed system containing the Fabry-Perot interferometer was varied from atmospheric pressure to 8 psi over atmospheric pressure. The large gas reservoir (R) acted as a ballast to smooth out pressure variations. The pressure scan rate was dictated by the requirement of matching the time constant of the PMT detection system, which varied from 1 to 100 sec.

The Fabry-Perot etalon plates were coated for 95% reflectivity at 6328 Å, the nonreflective surfaces were antireflection coated. The etalon spacing was kept constant at 10.13 mm throughout all the measurements, except for a few runs with a spacing of 3.17 mm. The time required to scan a free spectral range was typically 20 min.

The calculated finesse of our system was in excess of the finesse achieved in the measurement of the Brillouin and Rayleigh scattering, where it was limited by the intrinsic half-width of the laser line, typically 2.7×10^{-2} cm^{-1} (~800 MHz). Narrowing of the laser line was observed on introducing a 2-in. fused-quartz rod in the cavity[10] [minimum observed linewidth 300 MHz full width at half-maximum (FWHM)]. The resulting power output was, however, not constant in time, and given our rate of scan, no reliable measurements could be taken under these conditions. It has been reported in the literature[11,12] that single-mode operation in "long" He-Ne lasers can be achieved, with only a 10% loss in output power, in a cavity containing a nonlinear loss element such as Ne gas. Attempts to reproduce these results, using a 1-m intracavity loss tube of Ne gas at a fixed pressure (3 Torr) were unsuccessful. Line narrowing was observed, but power loss reduced the signal to unacceptable levels.

The free spectral range of the Fabry-Perot interferometer and the pressure excursions feasible with the pressure transducer limited the investigation of the scattering to a region ~0.25 cm^{-1} on each side of the exciting 6328 Å line. The observation of Rayleigh-wing scattering in systems based on $SeOCl_2$ raised the question of extending the observation beyond these limits, in order to confirm whether the Rayleigh-wing scattering actually covered only the region indicated by the scattering measurements with the Fabry-Perot interferometer. For this purpose some samples were studied by means of a Jarrell-Ash 1-m spectrometer provided with a high-resolution Harrison grating. The maximum resolution that could be achieved with the spectrometer was ~10^{-2} cm^{-1}, by working in the 13th or 14th diffraction order. The exciting source in these scattering measurements was the 4880-Å line from an argon-ion laser, at power levels of the order of 100 mW. The samples were contained in a cylindrical cell, positioned with its axis in a vertical direction (Fig. 2). The incident light was polarized in a horizontal direction, parallel to the plane of the spectrometer slits. The scattered light was focused on the spectrometer entrance slit; a Glan-Thompson prism in front of the entrance slit determined the polarization of the scattered radiation. The spectrally dispersed light was detected with an RCA 7265 photomultiplier and a Keithley picoammeter.

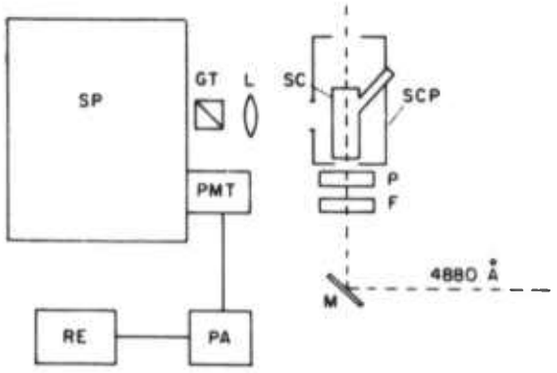

FIG. 2. Schematic diagram (side view) for scattering measurements in liquids using an argon-ion laser and a grating spectrometer. M—mirror; F—interference filter for 4880 Å; P—polarizer; SC—sample cell; SCP—sample compartment; L—lens; GT—Glan-Thompson prism; SP—spectrograph; PMT—low-noise photomultiplier; PA—picoammeter; RE—recorder.

Materials

Samples of the aprotic solvents for laser solutions and of the laser solutions themselves, which are both air-sensitive and corrosive, were contained in quartz or Pyrex cells with parallel faces. The cells were filled with the liquids under an inert atmosphere. Air or grease contamination was avoided by sealing the cells with Teflon screw caps and Teflon-coated O-rings. The cell windows were optically contacted to the cell body and then vacuum diffused to ensure parallelism to a few seconds of arc.

The composition and preparation[13,14] of the liquid samples studied are summarized in Table I. All of the $POCl_3$-based solutions had the same Nd (III) content, namely, 0.3 mole/liter. Various filtering procedures, carried out on the reactive, corrosive, and air-sensitive laser solutions, are also indicated. Only the solutions based on $POCl_3$ were filtered. No satisfactory filtering procedure has been developed yet for the solutions containing $SeOCl_2$. One of the $POCl_3$-based solutions studied was prepared by dissolving in $POCl_3$-$SnCl_4$ the trifluoracetate Nd $(CF_3COO)_3$ [or, in short, Nd $(TFA)_3$] instead of the usual Nd_2O_3. The solution F was a commercially available laser solution (available from Sylvania Precision Materials, Towanda, Pa.). One of the solutions (G) contained $ZrCl_4$ as Lewis acid instead of $SnCl_4$.

IV. RESULTS

The results of the spontaneous scattering measurements are summarized in Tables II–V and indicated in Figs. 3–7.

Brillouin-Triplet Spacing

Measured values of the Brillouin triplet spacings and values of the hypersound velocities derived from the latter using Eq. (8) are listed in Table II, columns 2

TABLE I. Composition and preparation of laser solution samples.

Sample	Components (25 : 1)	Nd content (mole/liter)	Filtered	Filter porosity
A	$POCl_3 : SnCl_4$	0.3	yes	fine
B	$POCl_3 : SnCl_4$	0.3	yes	fine
C	$POCl_3 : SnCl_4$	0.3	yes	medium
D	$POCl_3 : SnCl_4$	0.3 [$Nd(TFA)_3$]	yes	ultrafine
E	$POCl_3 : SnCl_4$	0.3		
F	$POCl_3 : SnCl_4$	0.3	yes	ultrafine
G	$POCl_3 : ZrCl_4$	0.3 [$Nd(TFA)_3$]	yes	fine
H	$SeOCl_2 : SnCl_4$	0.3	no	
I	$SeOCl_2 : SnCl_4$	0.5	no	
J	$SeOCl_2 : SnCl_4$	0.3	no	
K	$SeOCl_2 : SnCl_4$	0.1	no	

and 7, respectively. The values in column 2 of Table II pertain to the Brillouin-triplet spacings observed for 90° scattering under 6328-Å excitation. The data listed refer to various liquid constituents of the laser solutions and to the actual laser solutions. Values pertaining to other common liquids measured under the same experimental conditions are also tabulated for comparison purposes.

Intensity of Scattered Light

The data listed in Table III summarize the properties of the laser solutions with respect to the scattering intensity. The table lists: (a) the relative peak intensity of Rayleigh (central) and Brillouin components P_c/P_{MB}; (b) the over-all ratio of isobaric to adiabatic scattering I_c/I_{MB}; (c) the relative peak height of the Rayleigh line normalized to that of benzene, used as a standard and run under the same conditions; (d) the intensity of an individual Brillouin line, relative to that for benzene, that is, $P_{MB}/P_{MB}^{benzene}$. The depolarization factors of polarized incident light have been calculated under two different conditions: $\rho_v = I_{ex}/I_{ez}$ is the depolarization factor exclusive of the intensity contribution due to the frequency continuum in the free spectral range; the primed quantity ρ_v' includes the continuum contribution both in the polarized and in the depolarized scattering. The final two columns of Table III list the relative scattering intensity of the solutions studied, normalized to the intensity scattering from benzene. Again, unprimed intensity values neglect contributions to the intensity due to the frequency continuum within a free spectral range of the Fabry-Perot interferometer, while the primed quantities include these contributions.

Rayleigh-Wing Scattering

The FWHM for the depolarized Rayleigh-wing scattering in some of the systems investigated are listed in Table IV. Only solutions based on $SeOCl_2$ gave any appreciable Rayleigh-wing scattering. The FWHM was largest for $SeOCl_2$ (i.e., 0.204 cm^{-1}), and tended to decrease with increasing Nd concentration. Other liquids were studied for the purpose of comparison. Carbon disulphide gave a very wide Rayleigh-wing band with a FWHM of 6.0 cm^{-1}, while nitrobenzene exhibited a Rayleigh-wing scattering similar to that of $SeOCl_2$.

V. DISCUSSION

Brillouin-Triplet Spacing

The over-all range of the observed Brillouin-triplet spacings was bracketed between the values of 0.180 cm^{-1} (for $SnCl_4$) and 0.40 cm^{-1} (for quinoline). The largest splittings were exhibited by the aromatic liquids, such as benzene, nitrobenzene, and quinoline, run as comparison systems. $SnCl_4$ exhibited one of the smallest spacings reported so far for liquids, even smaller than that of diethyl ether. The values for the laser solutions were well within the range defined by the values for $SnCl_4$ and quinoline. The $POCl_3$-based laser solutions showed a splitting that was at most 10% wider than that of pure $POCl_3$. Since $SnCl_4$ was only a minor component in these solutions (less than 4%), the predominant $POCl_3$ component is expected to determine the Brillouin-triplet spacing. Similarly, the laser solutions based on $SeOCl_2$ exhibited a spectrum analogous to that of $SeOCl_2$. The spacing was found to increase monotonically with the Nd content of the laser solution. The 0.5-*M* solution in Nd had a triplet spacing wider by approximately 20% than that shown by $SeOCl_2$ alone.

Some of the parameter values for laser solutions listed in Table II are contrasted with values obtained from stimulated Brillouin scattering (SBS) experiments, using the 6943-Å radiation from a ruby laser. The predicted values of both the triplet spacing and the hypersound velocity at 6943 Å are contrasted for consistency with values derived from the actual observation of backward SBS (Table II, columns 5 and 8). Excellent agreement is found for $SnCl_4$ and $SeOCl_2$. A less precise agreement is found for solution I and $POCl_3 : SnCl_4$, while a definite discrepancy exists for $POCl_3$ and solution B. The values of Table II, column 4 have been derived from formula (8) on the assumption that the product $n\nu$ of the index of refraction and the hypersound velocity remained unchanged. Typical variations of the refractive index of the liquids under consideration are of the order of 0.6% in going from 6328 to 10 600 A. A much smaller variation should then occur from 6328 to 6943 A. The hypersound frequencies responsible for 90° scattering at 6328 A and for backward scattering at 6943 A from $POCl_3$ range from 3 to 4 GHz. A comparison of the values of Table II for $POCl_3$ (columns 7 and 8) would imply a dispersion of 15% in the value of the hypersound velocity in going from $\simeq 3$ to $\simeq 4$ GHz. Such a value for the dispersion is definitely too high and appears very unlikely, in view of the lack of such a dispersion for the case of $SnCl_4$ and $SeOCl_2$.

Again a comparison of the value of the Brillouin-triplet spacing for the spontaneous scattering case and the case of SBS suggests that the divergence in column 5 between the triplet spacings of $POCl_3$ and $POCl_3 : SnCl_4$ is far too large and in contrast to the corresponding lack of variation from $SeOCl_2$ to $SeOCl_2 : SnCl_4$. The increase in triplet spacing (column 5) from $SeOCl_2$ to solution K is

D-6

TABLE II. Brillouin-triplet spacings; refractive index of solutions and derived values of hypersound velocity.

Solution	Brillouin-triplet spacing[a] (cm^{-1})	Other measurements (cm^{-1})	Spacing in SBS (cm^{-1})[b] predicted[c]	Spacing in SBS (cm^{-1})[b] observed[d]	Refractive index	Hypersound velocity (m/sec) this work[e]	Hypersound velocity (m/sec) other measurements
$SnCl_4$	0.180		0.232	0.232	1.508[f]	800	803[d,e]
$POCl_3$	0.215 ± 0.005		0.277	0.234	1.457[f]	990	837[d,e]
$POCl_3$: $SnCl_4$ (25 : 1)	0.215 ± 0.005		0.277	0.294			
A	no splitting observed[h]						
B	0.235 ± 0.010		0.302	0.36	1.4879[i]	1060	1266[d,e]
C	0.220 ± 0.010		0.283		1.4873		
C	no splitting observed[h]						
F	0.225 ± 0.005		0.290				
D	0.225 ± 0.005		0.302				
F	0.230 ± 0.005						
$SeOCl_2$	0.275 ± 0.005		0.354	0.356[d]	1.648[f]	1120	1130
$SeOCl_2$: $SnCl_4$ (25 : 1)				0.356[d]			1129
H	0.290 ± 0.005		0.373	[j]			
I	0.315 ± 0.010		0.405				
J	0.295 ± 0.005		0.380		1.671[f]	1180	
K	0.285 ± 0.005		0.367	0.380[d]		1188	
benzene	0.325 ± 0.005	0.330[k]			1.5011[l]	1450	1500[m]
acetone	0.238	0.234			1.3588[l]	1175	1136[n]
diethylether	0.191	0.192[o]			1.3497[l]	950	958.5[o,p]
ethanol	~0.260[q]	0.230[n]			1.3624[l]		1112.3[n]
carbon disulphide	0.298	0.299[n]			1.6295[l]	1238	1253[o]
nitrobenzene	0.345				1.5529[l]	1490	1535[r]
quinoline	0.40				1.6245[l]	1650	1572[s]

[a] Under 6328-Å excitation; 90° scattering.
[b] Under 6943-Å excitation; backward scattering.
[c] Assuming no variation in the product nr from 6328 to 6943 Å (see discussion).
[d] Reference 1.
[e] Values derived using formula (8) and observed Brillouin-triplet spacing at 6328 Å.
[f] Interpolated value at 6328 Å.
[g] Same as footnote (e), for backward scattering at 6943 Å.
[h] Because of intense Rayleigh scattering.
[i] R. Kocher (private communication).
[j] No Brillouin components observed in stimulated backward scattering measurements.
[k] Reference 17.
[l] Index of refraction at 5893 Å (sodium lines).
[m] Reference 18.
[n] Reference 16.
[o] Reference 15.
[p] 32.5 °C.
[q] Spectrographic determination under 4880-Å excitation.
[r] Reference 19.
[s] Reference 20.

compatible with the behavior observed in spontaneous scattering both with the $POCl_3$-based and with the $SeOCl_3$-based and with the $SeOCl_2$-based laser solutions.

As already mentioned, the addition of 0.3 mole liter Nd to $POCl_3$: $SnCl_4$ and $SeOCl_2$: $SnCl_4$ produced an increase of 10% in the Brillouin-triplet spacing. At fixed geometry of observation and with the same exciting source, the increase must be due to an increase in the value of the product nr. The increment in the value of n on complex formation is 1.4% (see Table II). So the bulk of the variation must arise from a change in the hypersound velocity. The following relation connects the hypersound velocity with the density and the coefficient of adiabatic compressibility[7]:

$$r^2 = 1/\rho\beta_S \quad . \tag{13}$$

Since the density of laser solutions containing neodymium increases with respect to that of the $POCl_3$: $SnCl_4$ and $SeOCl_2$: $SnCl_4$ solutions, the coefficient of adiabatic compressibility

$$\beta_S = -\left(\frac{1}{V}\frac{\partial V}{\partial p}\right)_S$$

must be decreasing with the increase in the Nd solvation.

The results on the remaining liquids were mainly used as a check on the performance of the Fabry-Perot spectrometer. The agreement with the values reported

TABLE III. Scattering intensities and depolarization factors. (See text for symbols.)

Solution	P_c/P_{MB}	I_c/I_{MB}	P_c/P_c^{benz}	P_{MB}/P_{MB}^{benz}	P_{zx}/P_{zz} ($\times 10^2$)	$\rho_v = I_{zx}/I_{zz}$ ($\times 10^2$)	$\rho_v' = I_{xx}'/I_{zz}'$ ($\times 10^2$)	I_{zz}/I_{zz}^{benz}	$I_{zz}'/I_{zz}'^{benz}$
$SeOCl_2$	6.3	3.2	2.5	~1	5	5.7	19	2.2	2.0
H	23.5	14	5.3	0.68	4.2	4.8	18	7.0	4.5
I	45	11.2	5.3	0.7	5.4	12.2	not avail.	4.4	3.6
J	40	16	8	0.75	3.0	3.0	13	8.4	4.7
K	16	8.7	3.3	0.56	2.5	3.8	9	3.3	2.3
$POCl_3$	1.35	0.76	0.73	0.73	~0	~0	11	0.78	0.66
A[a]	not avail.	not avail.	not avail.	not avail.	5.5	not avail.	not avail.	not avail.	not avail.
B	86	not avail.	35	0.85	2.0	0.62	9	14.5	7.15
	not avail.	not avail.	234	not avail.	2.8	2.8	3	123	56
D	35	24	11	0.6	4	3.1	20	8.5	5.6
E	25	10	16	1.75	~0	~0	14	13	8.7
F	42	28	10.6	0.75	4.7	1.68	2	12.5	7
G	200	not avail.	33	~1.0	2.8	3.4	8	17	10
$SnCl_4$	~1	0.5			0				
$POCl_3$: $SnCl_4$ (25 : 1)	~4								

[a]Observed minimum FWHM of Rayleigh line was 300 MHz (0.01 cm^{-1}).

in the literature is quite satisfactory (see Table II). In the case of quinoline, a strong Rayleigh wing is present even in the polarized scattering. Since the Brillouin peaks are superimposed onto the Rayleigh wing, the accuracy in determining the Brillouin-triplet spacing is accordingly reduced in quinoline.

On the whole the Brillouin scattering from the laser solutions does not show unusual features, either with respect to the intensity of the two Brillouin components or with respect to the over-all triplet spacing. The derived values of the hypersound velocity are within the range of the values obtained for simple liquids.

Intensity of Scattered Light

The data listed in Table III are related to the intensity of the scattered light, both with regard to the spectrally integrated intensity and to the relative intensity of the scattered light in the Brillouin and Rayleigh components. The results on $SeOCl_2$ and related solutions will be considered first. The data of Table III, column 1 indicate that the relative peak height of the Rayleigh line to that of one of the Brillouin components, that is, the ratio $P_c/P_{MB} = 6.3$ is quite large for $SeOCl_2$. This is to be compared with lower values of this ratio in common liquids [Fig. 4(d), Table III]. The ratio is further increased in laser solutions.

Here again an effect related to the Nd concentration reappears, in the sense that the progressive decrease in Nd content from solution I to solution K is reflected in a monotonic decrease of the ratio P_c/P_{MB}. Similarly the intensity ratio of the Rayleigh peaks for the systems studied (relative to the benzene Rayleigh-peak), which has a value of 2.5 for $SeOCl_2$ alone, is only 3.3 for solution K, which is low in Nd content. The relative peak height of the Brillouin lines of the solutions investigated, normalized to the corresponding peak height for benzene, decreased from unity for $SeOCl_2$ to a minimum of 0.56 in solution K.

Column 8 lists the depolarization factor ρ_v'. This factor for $SeOCl_2$ was approximately 20% and was not much different in the laser solutions, except for solution K, where the depolarization appeared reduced by half. In the latter solution (low Nd content) the intensity of the polarized scattering, normalized to the corresponding depolarized scattering in benzene, was also appreciably reduced, to a value quite close to that for $SeOCl_2$ [I_{xx}'/I_{zz}'(benzene) = 2.3 and 2.0, respectively].

All of the $POCl_3$-based laser solutions had the same Nd content. The only variable parameters were the filtering procedure and the presence of $Nd(TFA)_3$. The

TABLE IV. Observed Rayleigh-wing scattering.

Solution	Observed FWHM (cm^{-1})	Other meas.	Relaxation time (10^{-11} sec)	Other meas.
$SeOCl_2$	0.204		5.2	
H	0.128		8.3	
J	0.112		9.5	
K	0.180		5.9	
CS_2	6.0	6.0[a]	0.18	
$C_6H_5NO_2$	0.225		4.7	
quinoline	0.33		3.2	4.0[b]

[a]Reference 20. [b]Reference 21.

D-8

TABLE V. Derived values of scattering coefficients $R_{90}(cm^{-1})$ and extinction coefficient h (from $I=I_0e^{-hx}$) for laser solutions. The value of $R_{90}=15\times10^{-6}$ cm^{-1} for benzene at 5461 Å was used in conjunction with formula (3).

Solution	R_{90}(6328 Å) ($\times10^{6}$ cm^{-1})	R_{90}(1.06 μ) ($\times10^{6}$ cm^{-1})	h (at 6328 Å) ($\times10^{4}$ cm^{-1})	h (at 1.06 μ) ($\times10^{4}$ cm^{-1})
$SeOCl_2$	16.8	2.13	2.82	0.356
H	37.8	4.8	6.32	0.805
I	30.2	3.84	5.02	0.645
J	39.5	5.0	6.6	0.838
K	19.3	2.45	3.26	0.41
$POCl_3$	5.55	0.70	0.93	0.117
B	60	7.6	10	1.27
C	470	59.5	79	9.95
D	47	5.95	7.9	0.99
F	73	9.25	12.2	1.55
F	59	7.5	9.9	1.25
G	84	10.65	14.1	1.785
benzene	8.4	1.07	1.41	0.18

relative intensities of the Rayleigh and Brillouin lines will be considered first. For solution A and C the Rayleigh line was so intense that the Brillouin peaks could not even be detected. Filtration of the $POCl_3$ laser solutions with the medium-porosity filter (solution C) was inadequate, as shown by the very high values of $I_{zz}/I^{benzene}$ in Table III. A marked improvement followed upon filtration on a fine frit, but no further gain in this respect derived from the use of ultrafine filters (~1 μm porosity) (Tables I and III).

In general, the central Rayleigh component in $POCl_3$-based laser solution was at least one order of magnitude

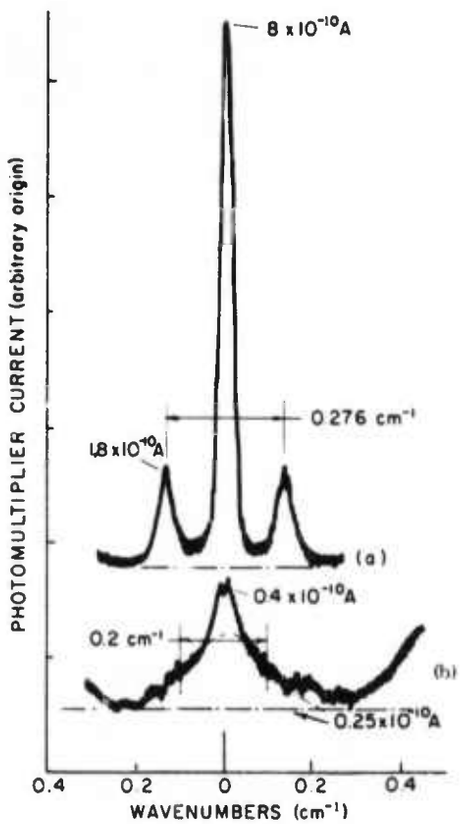

FIG. 3. Detail of the spectral distribution of scattered light at 90° from $SeOCl_2$: (a) polarized scattering (I_{zz}); (b) depolarized scattering.

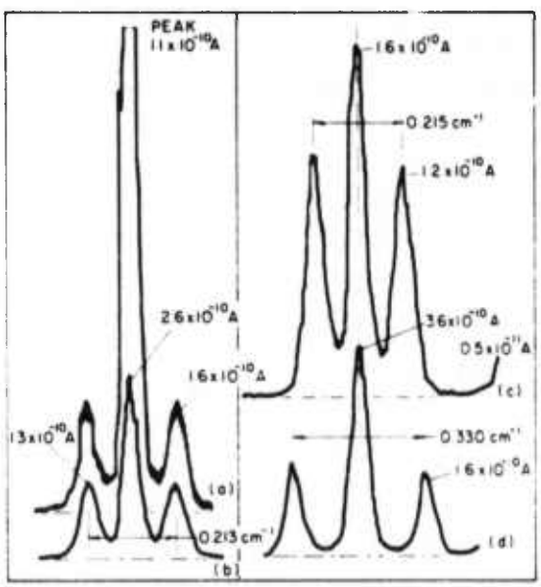

FIG. 4. "Aging" of $POCl_3$ solutions: (a) $POCl_3$ filtered liquid from distilled material; polarized scattering. Note the very strong central component. (b) Same: geometry unaltered, but next day. Both the Brillouin and Rayleigh lines, but especially the Rayleigh line, are decreased in intensity. (c) Same, but after the cell was removed from the system and later returned to it; the Rayleigh components still decreased. (d) By comparison, Brillouin triplet from benzene, run under the same conditions (I_{zz}).

D-9

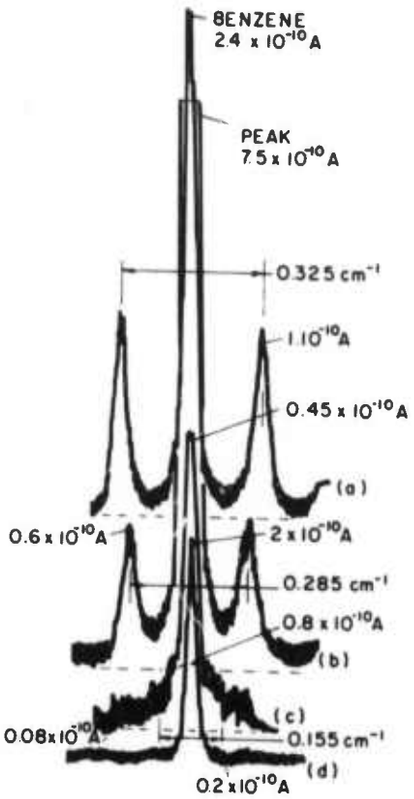

FIG. 5. Comparison of scattering spectra of $SeOCl_2$ and $POCl_3$ laser solutions: (a) Polarized scattering (I_{zz}) from benzene; the Rayleigh peak is relatively stronger than usual. (b) Polarized scattering (I_{zz}) from a selenium laser solution (K), under the same conditions as (a). (c) Same as (b), but depolarized scattering (I_{zx}). (d) By comparison, the depolarized scattering from a $POCl_3$-based laser solution ($POCl_3$-$ZrCl_4$; G). In the latter case there is no indication of Rayleigh-wing scattering.

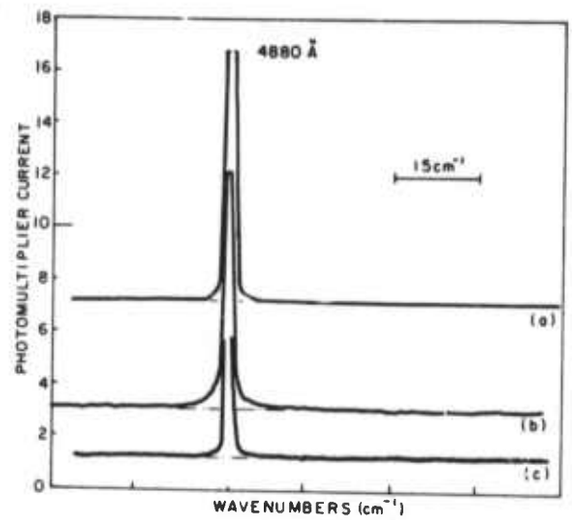

FIG. 6. (a) Polarized scattering (I_{zz}) from $SeOCl_2$ laser solution H; slits 100 μm; scale $0-1\times10^{-8}$ A. (b) Same as (a) but depolarized scattering (I_{zy}); current scale $0-1.0\times10^{-8}$ A. (c) For comparison, scattering from a diffuser (I_z); slits 100 μm. Scale $0-3.0\times10^{-9}$ A. The wing of the scattering lines from the laser solutions appears somewhat broader than the wings of the scattering line from the diffuser. The effect, though, is not very conspicuous.

more intense than in $SeOCl_2$, even in the ultrafine-filtered solutions. This was true in spite of the fact that the $SeOCl_2$ solutions were unfiltered. It would then appear that besides the solvated Nd complex, larger aggregates are formed in $POCl_3$ solutions. This hypothesis seems confirmed by the following observations on $POCl_3$: The scattering of $POCl_3$ appeared very sensitive to the preparative history of the samples investigated. Some of the samples of distilled and filtered material showed a very intense central component in the scattering spectrum, while in the best sample the ratio P_c/P_{MB} was less than 2. The scattering of the sample of Fig. 4 decreased with time. The decrease in the intensity of the Rayleigh component was not due to a trivial mechanical settling of the solution, since the sample was removed from the system, handled, and returned to the system, still maintaining its reduced scattering properties.

As evidence of a similar effect, the $POCl_3$-$ZrCl_4$ laser solution G, although fine filtered, exhibited a tremendous Rayleigh component, with a P_c/P_{MB} ratio of 200. In summary, the $POCl_3$ solutions had a considerably stronger scattering than the corresponding systems based on $SeOCl_2$. The depolarization factor was in the same range as that of the $SeOCl_2$-based solutions. As for the relative intensity of the polarized scattering with respect to benzene, the best $POCl_3$ laser solution was about 6 times more scattering than benzene.

Derivation of the Scattering Coefficient

Table V lists the value of the scattering coefficients of the solutions investigated. These values were arrived

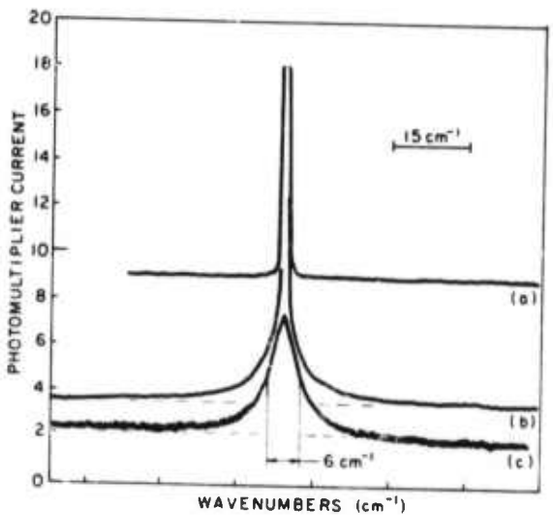

FIG. 7. Rayleigh-wing scattering in CS_2. (a) Reference scattering from a diffusing screen; polarized scattering I_{zz}; slit 100 μm; current scale $0-3.0\times10^{-8}$ A. (b) Polarized scattering from CS_2; current scale $0-3.0\times10^{-9}$ A. (c) Same as (b) but depolarized scattering; scale $0-1.0\times10^{-8}$ A. Slits 100 μm.

D.10

at by using values reported in the literature for the scattering coefficient of benzene. We assumed the value of 15×10^{-6} cm^{-1} for R_{90} from benzene under 5461-A excitation.[7] The corresponding scattering coefficients at 6328 and 10 600 Å were derived from the inverse fourth-power relation (1) involving λ. The values thus obtained are listed in Table V, columns 3 and 4. Finally the scattering coefficients were changed into the corresponding extinction coefficients. The resulting values are listed in the last two columns of Table V.

It would appear that at 1.06 μ the scattering losses even for the solutions based on $POCl_3$ would be of the order of 0.02% cm^{-1}. Somewhat higher values of the scattering losses at 1.06 μ for aprotic laser solutions containing Nd have been reported by Brecher and coworkers.[22]

Rayleigh-Wing Scattering

The scattering spectra of the $POCl_3$- based laser solutions showed no evidence of Rayleigh-wing scattering [Fig. 5(d)]. The $SeOCl_2$ laser solutions on the contrary exhibited a wing extending $\cong 0.25$ cm^{-1} on each side of the exciting line. The measurements on the grating spectrometer confirmed that the Rayleigh wing does not have an over-all spread appreciably wider than 0.5 cm^{-1} in the $SeOCl_2$ laser solutions (Fig. 6). This situation is contrasted in Fig. 7 with the pronounced Rayleigh-wing scattering in CS_2.

From the observed FWHM of the Rayleigh wing the value of the relaxation time for the anisotropy or, what is equivalent, the orientation relaxation time of the molecules in the liquid can be determined. The values thus derived are indicated in Table IV. Both for $SeOCl_2$-based solutions and nitrobenzene the relaxation time is of the order of ~ 50 psec, more than an order of magnitude longer than the very fast molecular relaxation time for CS_2.

VI. CONCLUSIONS

(i) The Brillouin-triplet spacing of the laser solutions increased monotonically with the Nd concentration, in the concentration range investigated.

(ii) The Brillouin spectra of the laser solutions and their liquid components did not exhibit unusual properties, either with respect to the spacing of the triplet or to the intensity of the Brillouin components.

(iii) It would appear that the coefficient of adiabatic compressibility decreases on complex formation in the laser solutions.

(iv) $SeOCl_2$-based laser solutions exhibit polarized scattering intensity 2.5–4.7 times stronger than the corresponding scattering from benzene. On the other hand, $POCl_3$-based laser solutions are stronger scatterers by a factor of 2 or 3 than the corresponding systems based on $SeOCl_2$. The dominant contribution to the scattered intensity in both systems arises from Rayleigh scattering. The intensity of the Brillouin scattering is only a minor component of the over-all scattered intensity.

(v) The losses due to molecular scattering in the $POCl_3$ laser solutions investigated are calculated to be of the order of 0.02% cm^{-1} at 1.06 μ. This compares with dynamic loss measurements of 0.3–0.4% cm^{-1} obtained from laser experiments performed on a flowing system.[23] This indicates that molecular scattering contributes only a small fraction of the loss encountered in lasers based on these solutions.

ACKNOWLEDGMENTS

The authors wish to thank Dr. C. Brecher and Dr. H. Samelson for many interesting discussions, K. French for making available the laser solutions, and T. Illing for technical assistance.

[1] R. R. Alfano, A. Lempicki, and S. Shapiro, IEEE J. Quantum Electron. QE-7, 416 (1971).
[2] H. Samelson, A. Lempicki, and V. A. Brophy, J. Appl. Phys. 39, 4029 (1968).
[3] H. Samelson, A. Lempicki, and V. A. Brophy (private communication).
[4] N. Bloembergen and P. Lallemand, Phys. Rev. Letters 16, 81 (1966).
[5] F. Shimizu, Phys. Rev. Letters 19, 1097 (1967).
[6] A. Einstein, Ann. Physik 33, 1275 (1910).
[7] I. L. Fabelinskii, *Molecular Scattering of Light* (Plenum, New York, 1968).
[8] S. Bhagavantam, *Scattering of Light and the Raman Effect* (Chemical Publishing Co. Inc., New York, 1942).
[9] M. Leontovich, J. Phys. USSR 4, 499 (1941).
[10] G. D. Currie, Appl. Opt. 8, 1068 (1969).
[11] V. P. Chehotayev, I. M. Beterov, and V. N. Lisitsyn, IEEE J. Quantum Electron. QE-4, 788 (1968).
[12] P. H. Lee, I. B. Schoefer, and W. B. Barker, Appl. Phys. Letters 13, 373 (1968).
[13] A. Heller, J. Mol. Spectry. 28, 101 (1968).
[14] C. Brecher and K. W. French, J. Phys. Chem. 73, 1785 (1969).
[15] R. Y. Chiao and B. P. Stoicheff, J. Opt. Soc. Am. 54, 1286 (1964).
[16] D. M. Rank, E. M. Kiess, Uwe Fink, and T. A. Wiggings, J. Opt. Soc. Am. 55, 926 (1965).
[17] H. Z. Cummings and R. W. Gammon, Appl. Phys. Letters 6, 171 (1965).
[18] Quoted by I. L. Fabelinskii (Ref. 7), as derived from Cummings and Gammon's data.
[19] V. S. Starunov, E. V. Tiganov, and I. L. Fabelinskii, Zh. Eksperim. i Teor. Fiz. Pis'ma v Redaktsiyu 4, 262 (1966); M. S. Tunin, dissertation (Moscow MOPI, 1961) (unpublished).
[20] S. L. Shapiro and H. P. Broida, Phys. Rev. 154, 129 (1967).
[21] G. I. A. Stegemann and B. P. Stoicheff, Phys. Rev. Letters 21, 202 (1968).
[22] C. Brecher, K. French, W. Watson, and D. Miller, J. Appl. Phys. 41, 4578 (1970).
[23] H. Samelson and R. Kocher (private communication).

D-11

APPENDIX E

NON-LINEAR EFFECTS IN INORGANIC LIQUID LASERS

Reprinted by permission from
IEEE JOURNAL OF QUANTUM ELECTRONICS
Vol. QE-7, No. 8, August 1971

Nonlinear Effects in Inorganic Liquid Lasers

P. R. ALFANO, ALEXANDER LEMPICKI, AND STANLEY L. SHAPIRO

***Abstract*—Inorganic liquids, phosphorous, and selenium oxychlorides, used as solvents for Nd, exhibit a number of nonlinear properties, which may reflect in the performance of liquid lasers. Spontaneous and stimulated Raman scattering have been studied. Measured cross sections and gains indicate that up to power levels of a few hundred megawatts per square centimeter the effect on laser and amplifier properties are negligible. No self-focusing has been observed. Under mode-locked conditions substantial conversion to Raman frequencies have been obtained. No connection has been found between stimulated Brillouin scattering and the phenomenon of self-*Q*-switching.**

I. Introduction

RECENTLY inorganic liquid lasers operating at high output energies and powers have been constructed [1]. Solutions of Nd in selenium oxychloride ($SeOCl_2$) or phosphorous oxychloride ($POCl_3$) have been operated in *Q*-switched, self-*Q*-switched, and mode-locked regimes [2]–[7]. Under these conditions the power available inside a liquid laser cavity can be as high as in conventional glass or ruby lasers. Since the active medium is a liquid, however, many of the nonlinear effects associated with the third-order susceptibility can be expected to occur and to affect the laser output.

The nonlinear effects associated with liquids are usually investigated by using high peak power solid-state lasers. Thus the first observation of stimulated Raman scattering was made by placing the nitrobenzene Kerr cell inside the laser cavity to *Q* switch the ruby [8]. Also, saturable absorber liquids are used in *Q*-switched and modelocked lasers [9], and anisotropic molecular liquids can be used to couple modes of solid-state lasers through the optical Kerr effect [10], [11]. Our case differs in that the entire active medium is a liquid and the effects may become "self-generated."

The specific problems that are of interest concern limitations imposed by nonlinearities on the output of liquid lasers. Thus, for instance, generation of stimulated Raman or Brillouin scattering can lead to a power limitation while self-focusing may cause the deterioration of the beam quality and thus limit the usefulness of the liquid laser. Another effect which is particularly easy to observe in liquid lasers is that of self-*Q*-switching. So far no adequate explanation of its mechanism has been given, but the suggestion [4] that it may be due to stimulated Brillouin scattering is not borne out by the present investigation.

In general, the type of effects described here have obvious pertinence to all liquid laser media, including dyes. This paper, however, is limited to the investigation of Raman scattering, Brillouin scattering, and self-focusing in inorganic liquid lasers only.

II. Materials

Inorganic laser solutions are multicomponent systems. They consist of a salt of Nd (chloride or fluoroacetate) dissolved in either selenium oxychloride ($SeOCl_2$) or phosphorous oxychloride ($POCl_3$) acidified with a Lewis acid such as tin tetrachloride ($SnCl_4$) or zirconium oxychloride ($ZrCl_4$) [3]. In addition, depending upon the Nd salt and solvent used, some reaction products can be present in solution. In the most commonly used solution, Nd^{+3}:$POCl_3$:$ZrCl_4$, Nd is introduced as a fluoroacetate ($Nd(CF_3COO)_3$). The composition of the solution is (in moles per liter): Nd–0.3; $ZrCl_4$–0.45; $POCl_3$–9; reaction product (dimer) $P_2O_3Cl_4$–0.3. The most abundant component is the oxychloride solvent, and one would expect that the main contribution to nonlinear effects should therefore be determined from the properties of $SeOCl_2$ or $POCl_3$. It should be noted that both of these molecules are highly anisotropic having symmetries of C_s and C_{3v}, respectively, and highly polarizable [12]. One can expect therefore that nonlinearities associated with molecular orientation in strong optical fields may play a role.

III. Spontaneous Raman Scattering

The study of spontaneous Raman scattering has obvious pertinence to our problem since a measurement of

Manuscript received February 25, 1971.
The authors are with the Bayside Research Center, GTE Laboratories, Bayside, N. Y.

E-2

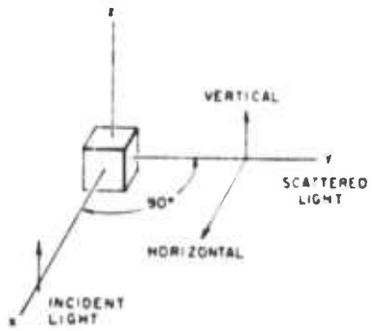

Fig. 1. Geometry of the spontaneous Raman scattering experiment.

the scattering cross section can lead to a theoretical estimate of the stimulated gain. A comparison of calculated and measured gain can in turn shed light on the occurrence of self-focusing. Since data on oxychlorides in the literature [13], [14] are rather qualitative, a quantitative experiment had to be performed.

Spontaneous scattering spectra were obtained by using the geometry shown in Fig. 1. Excitation was provided by the 4880-Å line of argon-ion laser with 50 mW power output and a vertically polarized beam. Radiation scattered at 90° was focused into the slit of a ½-m Jarrell-Ash spectrometer, and detected by an RCA 1P21 photomultiplier, Keithley ammeter, and strip chart recorder. Vertically or horizontally polarized components of the scattered light could be selected by an analyzer. The spectrometer resolution was 0.5 Å or 1.5 cm^{-1}, sufficient to measure the much broader Raman lines of $POCl_3$ and $SeOCl_2$. To provide comparison between the scattering of different liquids, solutions could be placed in identical cells.

Spontaneous Raman spectra of pure $POCl_3$ and pure $SeOCl_2$ are shown in Fig. 2. The most intense lines are the metal–halogen vibrations at 488 cm^{-1} ($POCl_3$) and 386 cm^{-1} ($SeOCl_2$). The 488 cm^{-1} $POCl_3$ line is shown under high resolution in Fig. 3(a). The FWHM was measured to be 5.2 ± 0.8 cm^{-1}. A large fraction of this width is presumably due to the presence of different chlorine isotopes. The line is almost completely polarized vertically with an extinction ratio >30.

Upon addition of the Nd ion and Lewis acid, several changes occur in the spectra of the pure solvents. The 488 cm^{-1} line of $POCl_3$ is reduced in intensity by about 10 percent and a new line appears some 5 cm^{-1} to the red of the 488 cm^{-1} line. This new line, shown in Fig. 3(b), appears to be caused by the addition of the Lewis acid since it is also present in solutions containing no Nd ion. The intensity of the 1297 cm^{-1} line is substantially reduced upon the addition of Nd presumably because it coincides with an absorption due to the ion when the exciting wavelength is 4880 Å.

The most intense feature of the $SeOCl_2$ Raman spectra is the 386 cm^{-1} Se-Cl vibration. Its lineshape in the pure solution and in laser solutions with different Nd^{+3} con-

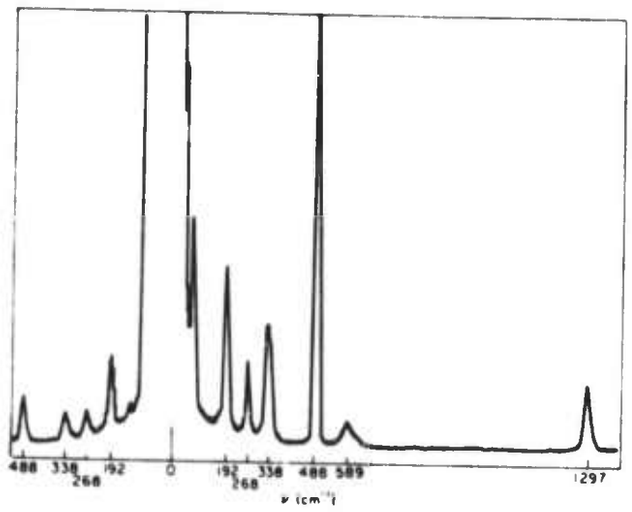

(a)

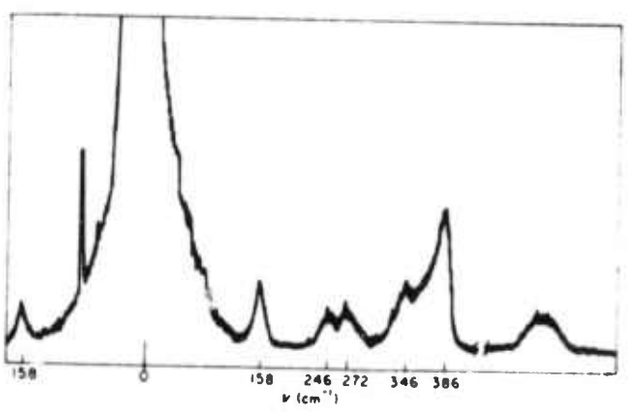

(b)

Fig. 2. (a) Raman spectrum of pure $POCl_3$. (b) Raman spectrum of pure $SeOCl_2$.

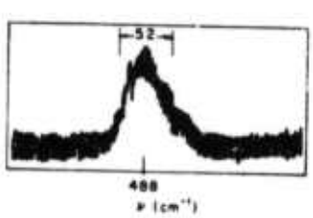

(a)

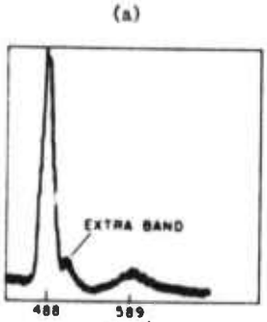

(b)

Fig. 3. (a) 488 cm^{-1} vibrational line of $POCl_3$ under high resolution. (b) 488 cm^{-1} line at a faster scan speed showing extra band in laser solution.

centrations is shown under high resolution in Fig. 4. In a pure $SeOCl_2$ solution the 386 cm^{-1} line has a complex structure $\cong 18$ cm^{-1} wide and is polarized vertically. In the laser solution of Nd^{3+} $SeOCl_2$, as in $POCl_3$, a new line appears shifted to the red of the 386 cm^{-1} line by $\cong 5$ cm^{-1}. When Nd^{3+} is removed from the laser solution, the extra line is still present indicating that the ionic complex is not responsible for this new line. At the highest molar concentrations studied (10^{-2} molar), the red shifted line is nearly as intense as the main Raman line.

For the calculation of gain in stimulated Raman scattering, it is necessary to know the magnitude of the *forward* spontaneous scattering cross section per molecule, per unit solid angle $(d\sigma/d\Omega)_{N,\theta=180°}$. This quantity is rather difficult to measure absolutely but in some special cases can be deduced from comparative measurements performed at 90°. Such a special case arises if we compare the 488 cm^{-1} and 386 cm^{-1} lines of $POCl_3$ and $SeOCl_2$ with the 656 cm^{-1} Raman line of CS_2. All of these lines are completely polarized and therefore correspond to totally symmetric vibrations [15]. The scattering cross section for vertical polarization is therefore independent of the angle θ [16], [17]. For this special case one can therefore obtain values of the forward scattering cross sections of the oxychlorides, relative to that of CS_2, by using only 90° measurements.

To obtain the cross-section ratios, spectra of the 656 cm^{-1} line of CS_2 were taken in the same apparatus. The measurable quantities such as frequencies, linewidths, and relative peak intensities are then related to the cross section in the following manner. We define [18] a *differential* cross section per unit wavelength interval, per unit solid angle and volume $d^3\sigma(\lambda)/d\lambda\, d\Omega dV$. If we assume that the dependence of the cross section is Lorentzian in wave-number space ($\nu = 1/\lambda$) we have:

$$\frac{d\sigma(\nu)}{d\nu} = \left[\frac{d\sigma}{d\nu}\right]_{\nu=\nu_0} \frac{\pi\Delta\nu}{2}\frac{\Delta\nu}{2\pi}\frac{1}{(\nu-\nu_0)^2+\left(\frac{\Delta\nu}{2}\right)^2}. \quad (1)$$

We can integrate the differential cross section over the linewidth $\Delta\nu$ and volume and obtain

$$\frac{d\sigma}{d\Omega} = \iint \frac{d^3\sigma(\lambda)\, d\lambda\, dV}{d\lambda\, d\Omega\, dV} = \iint \frac{d^3\sigma(\nu)}{d\nu\, d\Omega\, dV} d\nu\, dV$$

$$= \left[\frac{d\nu(\nu)}{d\nu}\right]_{\nu=\nu_0} \frac{\pi\Delta\nu}{2} V. \quad (2)$$

Using the parameter K_{max} defined by McClung and Weiner [18], we obtain

$$K_{max} = \left[\frac{d\sigma(\lambda)}{d\lambda}\right]_{\lambda=\lambda_0} = \nu_0^2\left[\frac{d\sigma(\nu)}{d\nu}\right]_{\nu=\nu_0}. \quad (3)$$

The cross section per molecule is obtained from (2) and (3)

$$\left(\frac{d\sigma}{d\Omega}\right)_\nu = K_{max}\frac{\pi}{2}\frac{\Delta\nu}{\nu_0^2}\frac{1}{N}\ (cm^2/sr) \quad (4)$$

where N is the number density of the substance.

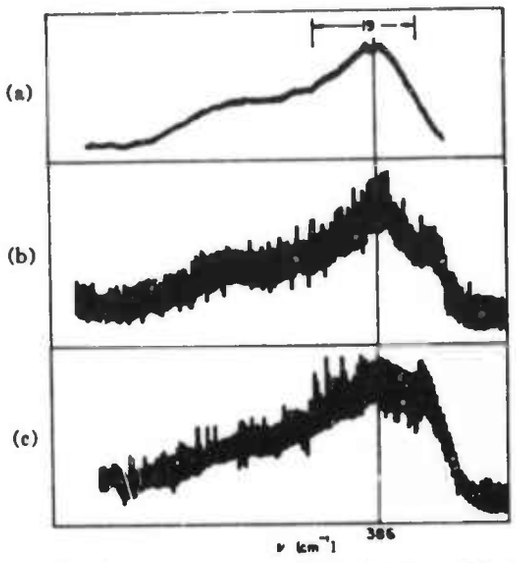

Fig. 4. (a) Raman spectrum of $SeOCl_2$ line at 386 cm^{-1}. (b) 386 cm^{-1} line in 0.3 molar Nd^{+3} laser solution showing side band. (c) 386 cm^{-1} line in 0.6 molar Nd^{+3} laser solution.

Since the quantity K_{max} is proportional to the peak intensity of the Raman line I_{peak}, we can obtain the ratio of the cross sections of two liquids (*1* and *2*) from a measurement of their peak intensities and linewidth:

$$\frac{\left(\frac{d\sigma}{d\Omega}\right)_{N,1}}{\left(\frac{d\sigma}{d\Omega}\right)_{N,2}} = \frac{I_{peak,1}}{I_{peak,2}}\frac{\left(\frac{\Delta\nu}{\nu_0^2}\frac{1}{N}\right)_1}{\left(\frac{\Delta\nu}{\nu_0^2}\frac{1}{N}\right)_2}. \quad (5)$$

The following results were obtained for the relative intensities:

$$\frac{I_{peak}(POCl_3)}{I_{peak}(CS_2)} = 0.05 \pm 0.01$$

$$\frac{I_{peak}(SeOCl_2)}{I_{peak}(CS_2)} = 0.06. \quad (6)$$

From the linewidth of CS_2 measured by Clements and Stoicheff [19], its cross section taken as 3.8×10^{-29} cm^2 [20], and our measurements of intensity ratios (6) and linewidth, we can obtain the cross sections for the oxychlorides at 4880 Å. These, together with other pertinent data, are given in Table I. To obtain cross sections for other exciting wavelengths, we can use the relationship [21]

$$\left(\frac{d\sigma}{d\Omega}\right)_{\nu_1} = \frac{\nu_1\nu_{S1}^3}{\nu_2\nu_{S2}^3}\left(\frac{d\sigma}{d\Omega}\right)_{\nu_2} \quad (7)$$

where ν_1, ν_2 are the wave number frequencies of the exciting radiation and ν_{S1}, ν_{S2} are the corresponding frequencies of the Stokes lines.

IV. Stimulated Raman and Brillouin Scattering

Stimulated scattering in liquid laser media was obtained in two different ways. For the measurement of

E-4

TABLE I
STIMULATED RAMAN SCATTERING DATA FOR OXYCHLORIDES

	$POCl_3$	$SeOCl_2$
Raman shift ν_R	488 cm^{-1}	386 cm^{-1}
Linewidth $\Delta\nu_R$	5.2 cm^{-1}	18 cm^{-1}
Forward scattering cross section $(d\sigma/d\Omega)$:		
4880 Å	3.05×10^{-29} cm^2	9.6×10^{-29} cm^2
6940 Å[a]	0.86×10^{-29} cm^2	2.7×10^{-29} cm^2
10 600 Å	0.16×10^{-29} cm^2	0.49×10^{-29} cm^2
Gain coefficient (calculated)[b]		
6940 Å	2.11×10^{-3} cm/MW	2.61×10^{-3} cm/MW
10 600 Å	1.6×10^{-3} cm/MW	1.6×10^{-3} cm/MW
Gain coefficient (measured):		
6940 Å	2.6×10^{-3} cm/MW	–

[a] Calculated from (7).
[b] Calculated from (1) and (7).

spectral shifts and energy conversion, an external laser source (ruby or Nd glass) was used and its output passed through a cell containing the liquid (Sections *A* and *B*). In a second set of experiments the ouput of a liquid laser itself was shown to contain stimulated Raman emission internally generated (Section *C*).

A. Threshold and Energy Conversion

A single transverse and longitudinal ruby laser (Korad) was used for most measurements of energy conversion into stimulated Raman scattering (SRS) and stimulated Brillouin scattering (SBS). The experimental arrangement is shown in Fig. 5. The Korad laser consists of a sapphire etalon output reflector, a 1-mm aperture, a 4-in ruby rod, a Kodak *Q*-switch dye cell antireflection coated at the ruby wavelength, and a 100 percent reflectivity rear-output reflector.

The ruby laser output pulse duration was 15 ns as measured by a TRG detector connected to a Tektronix 519 scope (0.5-μs risetime). Independent measurements of the laser output power with an EGG radiometer and a TRG calorimeter yielded a value of 1 MW. An inverted telescope reduced the beam area size to 0.5 mm^2 across the Raman cell, which was 50 cm long. The output power entering the cell was typically 0.7 MW, thus giving a power per unit area of $\simeq$140 MW/cm^2. The Raman cell was several meters from the laser and tilted to minimize optical feedback. Glass microscope slides were placed in the laser beam to vary the power. The beam polarization was perpendicular to the table. The laser output power was monitored before and after the Raman cell as was the forward and backward SRS and SBS. Glass wedges with surfaces parallel to the laser polarization reflected the light upon MgO reflectors. The diffused scattered light from the MgO plates then fell upon RCA 922 phototubes (S1 response) whose outputs were displayed on a 555 Tektronix oscilloscope. Attenuators were placed in front of the tubes so that they operated in a linear response region. The phototube responses were calibrated by conventional techniques. Conversion efficiencies were

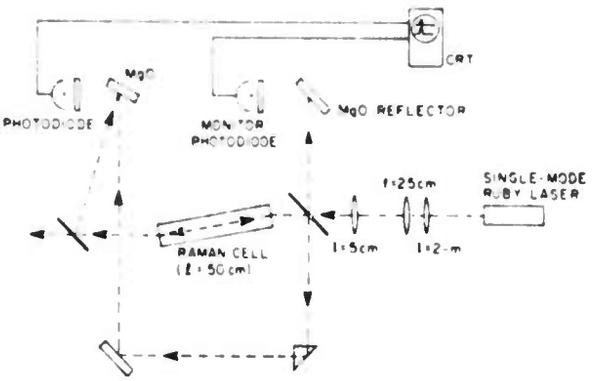

Fig. 5. Experimental arrangement for investigating stimulated Raman and Brillouin scattering.

measured by comparing the pulse heights on the scope. The forward Raman beam was observed by placing Corning 7-69 filters in front of tube 1, and the back Brillouin beam was observed by placing a narrow-band filter in front of tube 2.

Most of the stimulated Raman scattering experiments were carried out with $POCl_3$-based laser solutions. In order to separate the nonlinear effects of the main component ($POCl_3$) from possible contributions of Nd^{+3}, Lewis acid and reaction products, experiments were carried out on pure $POCl_3$, a mixture of $POCl_3$ and $P_2O_3Cl_4$,[1] and in standard laser solution with the Nd^{+3} ion replaced by Eu^{+3}. This replacement was necessary because Nd^{+3} has a strong absorption band at the ruby frequency. The use of a different rare-earth ion was not believed to change any of the relevant properties of the material.

The curve of SRS versus the ruby laser intensity for pure $POCl_3$ is plotted in Fig. 6. Only forward Raman scattering was observed from $POCl_3$. Backward SRS from $POCl_3$ was measured to be ≤ 0.01 of the forward

[1] This mixture was prepared by dissolving $Nd(CF_3COO)_3$ in pure $POCl_3$ and filtering out the Nd containing precipitates. The remainder is believed to contain a mixture of $POCl_3$ and $P_2O_3Cl_4$ in proportion occurring in standard laser solution [22].

E-5

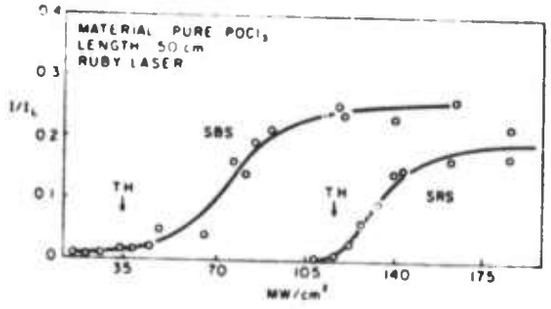

Fig. 6. Stimulated Raman and Brillouin scattering in $POCl_3$ versus ruby laser intensity.

scattering at the power levels of the experiment. Theoretically [23], the forward-to-backward ratio is one, under steady-state conditions, but this value is computed in the absence of backward SBS, which, if present, can compete against the back SRS light.

As seen from Fig. 6, substantial Raman conversion occurs over a length of 50 cm at powers of $\simeq$100 MW/cm^2. From the initial rising portion of the SRS curve, we can calculate the gain of the stimulated process by using the expression

$$I_R \propto I_L \exp(gI_L l) \tag{8}$$

where I_R is the Raman intensity as it leaves the cell and I_L is the intensity of the laser. We obtain $g(POCl_3) = 2.6 \times 10^{-3}$ (cm/MW).

The Brillouin-scattering curve shows that a large amount of laser conversion to SBS takes place at $\simeq$20 MW/cm^2. At powers where substantial Raman conversion begins, approximately 20 percent of the laser has been depleted into backward Brillouin scattering. At the highest laser powers in this experiment, as much as 40 percent of the laser beam is converted to SBS and 30 percent to SRS light.

The curves of the Raman and Brillouin intensities versus laser power reach saturation regions at high powers because of laser depletion into SRS and SBS. The laser depletion was further verified by observing that the laser beam intensity transmitted through the cell decreased as the SBS and SRS built up.

For solutions containing a mixture of $POCl_3$ and $P_2O_3Cl_4$ the only difference in Raman scattering was an increase of threshold by approximately 20 percent. This corresponds roughly to the volume decrease of pure $POCl_3$ caused by the presence of the dimer. When pure $POCl_3$ was doped with its dimer plus europium, the threshold for Raman scattering increased still further. These results show that at laser powers used in these experiments, pure $POCl_3$ is primarily responsible for SRS, and that rare-earth ions and additional liquid components act like inactive participants.

To ascertain if SRS is associated with self-focusing, photographs of SRS light were taken at the end of the cell. No filaments could be detected at the power levels used.

In another series of experiments picosecond pulse excitation was used to produce stimulated scattering. Under these conditions Brillouin scattering usually does not occur and one can expect more efficient conversion into Raman scattering [24]. The experimental set up was similar to that used for observations of self-phase modulation in liquids and solids [25]. It consisted of a mode-locked Nd:glass laser whose output was converted to the second harmonic and the beam collimated to a diameter of 1.2 mm. The energy per pulse was $\sim$5 mJ, pulse duration $\sim$4 ps, and peak power $\simeq$1 GW/cm^2. The output from the cell was passed through a 10-cm focal length lens placed at the focal distance from a 2-cm-high slit of a ¾-m Jarrell-Ash spectrograph, and recorded photographically on Polaroid 3000 speed film. Corning filters 5–60 and 5–61 were used to attenuate the fundamental frequency and pass the anti-Stokes shifted light. For observation of Stokes shifted light a 3–67 Corning filter was used. The exposed film containing both spectral and angular [24], [25] information is shown in Fig. 7. As much as eight anti-Stokes and five Stokes stimulated lines could be detected. In all probability the decreasing sensitivity of the Polaroid film limits the number of observable Stokes lines. In addition to the Raman lines a substantial amount of self-phase-modulated emission is seen to form a spectrally continuous and spatially diverging background.

No attempts were made to estimate the energy conversion into Raman and self-phase-modulated radiation under this type of excitation. The results indicate, however, that the use of liquid lasers for amplification of very-high-intensity picosecond pulses may lead to a very complex output.

B. Frequency Shifts Due to SBS

The frequency shift due to SBS was measured in order to elucidate the possible connection of this phenomenon with the self-Q-switching properties of the aprotic laser [4]. The experimental arrangement used for these measurements was similar to that described by Brewer and Shapero [26] and is shown in Fig. 8. A TRG 104 ruby laser Q switched by a rotating prism and cryptocyanine dye was used as a source. A resonant reflector consisting of two sapphire plates produced a single longitudinal-mode output.

The peak power of the pulse was measured by an ITT planar photodiode T_1. Part of the signal reflected from beam splitter B_2 was passed twice through a quarter-wave plate, rotating its polarization by 90°, and was then directed to the Fabry–Perot interferometer. The major part of the signal was focused by a 100-mm focal-length lens L into a 150-mm cell containing the liquid under study.

This lens was used to increase the power density of the ruby radiation, which otherwise was insufficient to produce SBS in Nd-containing solution. As previously noted, an absorption at the ruby frequency made this necessary. The back-scattered radiation from the cell

E-6

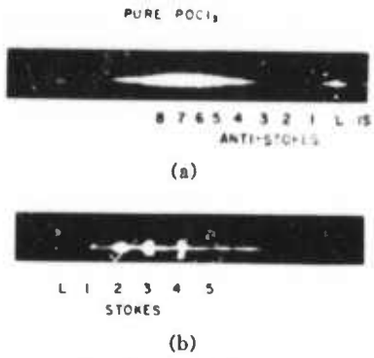

Fig. 7. Angular emission from pure $POCl_3$ under picosecond laser excitation. (a) Anti-Stokes emission. (b) Stokes emission.

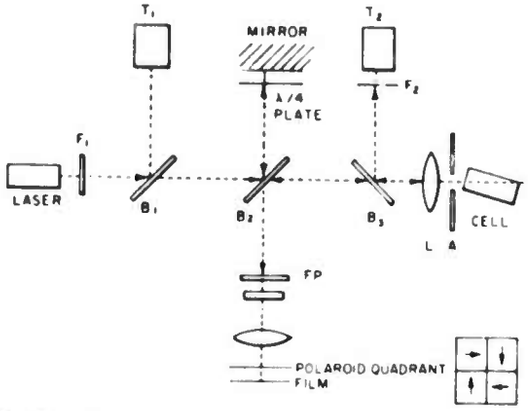

Fig. 8. Experimental arrangement for the measurement of stimulated Brillouin shifts. L—ruby laser; T_1, T_2—planar photodiodes; B_1, B_2, B_3—beam splitters; F_1, F_2—filters; L—lens.

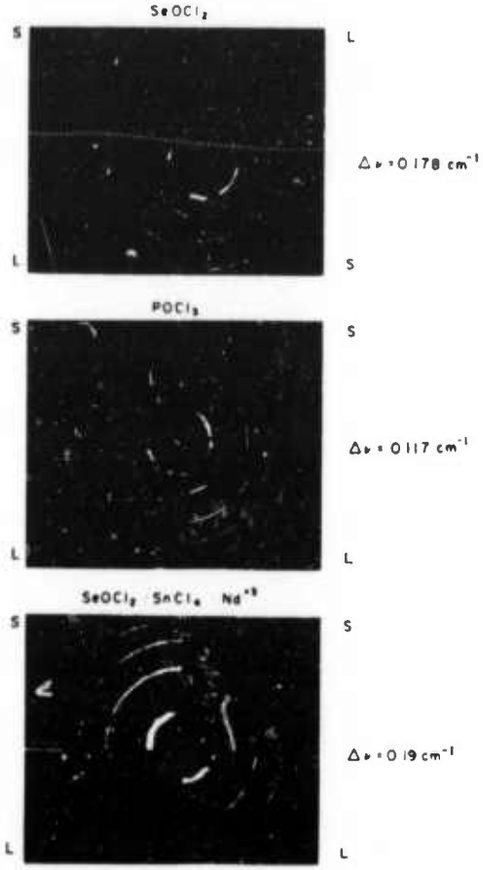

Fig. 9. Interferograms of the incident (L) and scattered (S) radiation. Inter-order spacing for $SeOCl_2$—0.494 cm^{-1}; $POCl_3$—0.27 cm^{-1}; Nd^{+3}:$SeOCl_2$:$SnCl_4$—0.494 cm^{-1}.

was detected by the photodiode T_2, and part of it was allowed to enter the Fabry–Perot interferometer. To distinguish between the incident and scattered radiation, which, upon arrival at the interferometer, are polarized at right angles, a quadrant of sheet polarizers was placed in front of the film.

Typical interferograms of the incident and back-scattered radiation are shown in Fig. 9. Table II gives the measured shifts $\Delta\nu$ for a number of solutions. From $\Delta\nu$ and the refractive index (n) at the ruby frequency ν, the velocity of sound v_s can be calculated by using the expression

$$\Delta\nu = 2\nu v_s n/c \cdot \sin\theta/2 \qquad (9)$$

where $\theta = 180°$. This is also tabulated in Table II. Assuming no dispersion in the velocity of sound, one can also calculate the Brillouin shift at the Nd-laser wavelength of 1.06 μ by using the appropriate refractive index in (9). These values are given in the last column of Table II.

No correlation was found between these shifts and the spacing of lines occurring in the spectra of self-Q-switched outputs. On this basis one can therefore rule out stimulated Brillouin scattering as the mechanism responsible for self-Q-switching. A more likely explanation of the phenomenon resides in the formation of refractive index gratings recently discussed by Key *et al.* [27].

C. Stimulated Raman Scattering: Self-Generated

The internal generation of Raman scattering in a liquid laser has been briefly reported by Alfano and Shapiro [7] and by Yand *et al.* [28].

The experimental set up in the present work is shown on Fig. 10. It consisted of a 25-cm cell of 1 cm^2 cross section placed in a dual elliptical cavity. Up to 2500 J could be discharged through two flashlamps. The cavity was formed by a 10-m radius, fully reflecting mirror, and a 50 percent reflecting flat mirror separated by 70 cm. The external surfaces of cell windows were cut at the Brewster angle, and the output mirror was wedged to reduce subsidiary resonances in the cavity. Since the refractive indices of quartz (1.45) and Nd^{3+}:$POCl_3$ (1.452) match quite well, no reflection is obtained from the quartz-solution interfaces; as a consequence, the inner surfaces of the windows can be parallel to each other, greatly simplifying the cell construction.

The laser could be operated in three different regimes: Q switched by a saturable absorber (Kodak 9860 dye); mode locked by suitably adjusting the concentration of the same dye; and self-Q-switched by removing the dye

E-7

TABLE II
BRILLOUIN SHIFTS, REFRACTIVE INDICES, AND VELOCITY OF SOUND IN LASER SOLUTIONS

Material	$\Delta\nu$(6942) (cm^{-1})	n 6942 Å	n 10660 Å	V_s (cm/s)	$\Delta\nu$(10600) (cm^{-1})
$SeOCl_2$	0.178	1.6396	1.6249	1130	0.115
$POCl_3$	0.117	1.4559	1.4501	837	0.076
$SnCl_4$	0.116	1.5042	1.4952	803	0.075
$SeOCl_2$:$SnCl_4$	0.178	1.6416	1.6268	1129	0.114
$POCl_3$:$SnCl_4$	0.147	1.457[a]	1.452[a]	1050	0.096
$SeOCl_2$:$SnCl_4$:Nd^{+3}[b]	0.19	1.6650	1.6499	1188	0.123
$POCl_3$:$SnCl_4$:Nd^{+3}	0.18	1.480[a]	1.475[a]	1266	0.117

[a] Estimated values based on increase of refractive index of $SeOCl_2$ upon addition of $SnCl_4$ and Nd.
[b] 0.3 molar concentration of neodymium.

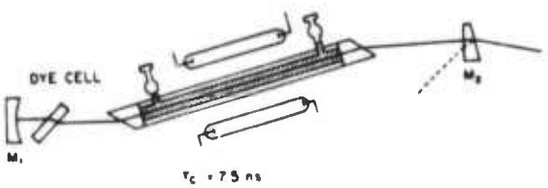

Fig. 10. Schematic arrangement of a mode-locked liquid laser.

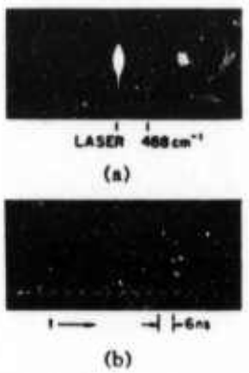

Fig. 11. (a) Mode-locked Nd:$POCl_3$ laser output showing stimulated Raman line. (b) Time output on a Tektronix 519 oscilloscope.

cell and replacing the ouput reflector by an uncoated quartz wedge. The output of the laser was directed into either a 2-m Bausch and Lomb or a ¾-m Jarrell-Ash spectrograph and recorded on sensitized Kodak 12 plates or Polaroid 57 film. A planar photodiode and Tektronix 519 oscilloscope was used to monitor the time dependence of the output.

The Nd^{3+}:$POCl_3$ laser showed stimulated Raman scattering in all three modes of operation. Figs. 11 and 12 show a spectrum and an oscilloscope trace obtained with a mode-locked laser that had a pulse duration of 3 ps and produced Raman scattering with every shot. The stimulated first Stokes line at 488 cm^{-1} is clearly visible. In other spectrograms the second Stokes line was also sometimes detected. The lasting band of about 100 cm^{-1} width is devoid of any structure except for a sharp line of about 2 cm^{-1} width, positioned to the left of the center of the band. The SRS lines were also structureless and of about the same 100 cm^{-1} width. The position of the center of the Raman emission shifts within 10 cm^{-1} from shot to shot with respect to the center of the lasing band. Since not all the pulses in the mode-locked train produce Raman scattering there should not necessarily be exact agreement between the laser bandwidth, which contains the spectrum of all the pulses, and the SRS bandwidth, which contains the spectrum of only some of them. The Raman conversion to first Stokes was measured by placing neutral density filters over the film at the location of the laser line and attenuating it until it reached the same intensity as the Raman line. By calibrating the film spectral response with a tungsten lamp at conversion of approximately 12 percent (into the first Stokes) was obtained. Spectra and oscilloscope traces obtained in the self-Q-switched mode of operation are shown in Fig. 13. In this case SRS appeared only on the most intense shots but contrary to the mode-locked case contained anti-Stokes lines as well.

With $Nd^{+3}SeOCl_2$ solutions we were able to obtain Raman generation only in the mode-locked regime. An example is given in Fig. 14. When regular trains of pulses were emitted (a rather exceptional case with $SeOCl_2$) the first and sometimes the second Stokes lines (386 cm^{-1}) were detected. The laser and Raman emission both occurred over a narrow band of approximately 6 cm^{-1}. The pulse duration measured by two-photon fluorescence was 6 ps. The narrower bandwidth and longer pulse duration can be attributed to the presence of reflections at the parallel liquid-window interfaces, which is larger than for $POCl_3$ because of poorer refractive index matching ($SeOCl_2$–1.67; quartz–1.45). The presence of parallel reflecting surfaces in the cavity is known to cause bandwidth narrowing and pulse lengthening [7].

V. DISCUSSION

The measurements of spontaneous Raman cross sections reported in Section III can be used to calculate the gain of the stimulated process that in turn can be com-

E-8

Fig. 12. Spectra of mode-locked Nd:$POCl_3$ liquid laser. Two shots show $\simeq$100 cm^{-1} central band and Raman shifted light.

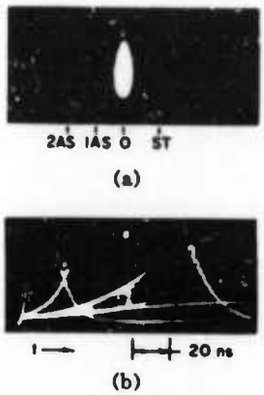

Fig. 13. (a) Self-Q-switched spectrum showing Stokes and anti-Stokes Raman scattering. (b) Time output on a Tektronix 519 oscilloscope.

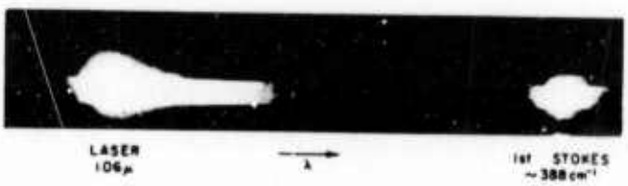

Fig. 14. Stimulated Raman scattering from Nd^{+3}:$SeOCl_2$:$SnCl_4$ laser Q switched with a dye.

pared with the directly measured values of the gain. The gain coefficient g defined by (8) is given by [29]

$$g = \frac{8\pi cN}{\hbar\omega_s^3 n\,\Delta\nu}\left(\frac{d\sigma}{d\Omega}\right)_N \tag{10}$$

where ω_s is the angular frequency of the first Stokes line and the other symbols have their usual meanings.

Using (10) we can calculate the gain coefficient g for $POCl_3$. The measured and calculated values are tabulated in Table I. We see that they agree within ten percent. This close agreement constitutes a strong proof that at the power levels used in SRS (150 MW/cm^2) there is no evidence for self-focusing. This confirms the earlier result (Section III), which showed absence of filaments on photographs, and indicates that the beam quality of liquid lasers is not likely to deteriorate from self-focusing—at least up to these power levels.

A knowledge of the gain for SRS permits us to make an estimate of the limitation imposed by scattering on the performance of liquid amplifiers. The question that we would like to answer is how much of the signal that is fed into an amplifier is likely to be converted into Raman scattering at the output of the device. Since we assume that the stimulated scattering will be generated from noise in the amplifier medium (the input does not contain any Stokes radiation), an accurate calculation is far from trivial and in fact cannot be obtained without approximations in an analytic form. To obtain an estimate, let us refer to Fig. 15, which shows a cell of length l and cross-sectional area A, filled with the liquid laser medium and traversed by a beam from another laser. The amount of Raman flux produced in the element dx and directed so that it will pass through the right window of the cell can be written as

$$dI_R = N\left(\frac{d\sigma}{d\Omega}\right)_N I_L \frac{A}{x^2} e^{gI_L x}\,dx. \tag{11}$$

Since Raman flux generated near the entrance window (left) will experience the greatest gain, we can replace x by l in the solid angle (A/x^2). Upon integration we obtain

$$I_R \approx N\left(\frac{d\sigma}{d\Omega}\right)_N \frac{A}{l^2}\frac{1}{g} e^{gI_L l}. \tag{12}$$

Using quantities characteristic of the experiment that lead to Fig. 6 (l = 50 cm, A = 1 cm^2, λ = 6940 Å) and an input I_L = 100 MW/cm^2, we obtain $I_R \approx 2 \times 10^{-3}$ MW/cm^2, which is about three orders of magnitude less than what is observed. This result leads us to believe that the relatively high SRS output shown in Fig. 6 is the result of residual feedback that changes the cell from a Raman noise amplifier to a multiple-pass oscillator.[2] This possibility makes it very important to eliminate optical feedback whenever a liquid is used as an amplifier. This is, of course, standard practice even if no SRS is generated. With good design, SRS from liquid amplifiers should not impose any limitations at power inputs in the 100–200 MW/cm^2 range.

Self-generation of SRS in liquid laser oscillators will be governed by similar consideration. Here the problem is somewhat more critical since it imposes a condition

[2] An alternative explanation would be that self-focusing does occur in the cell. This, however, would contradict the remarkable agreement between calculated and measured gains cited above.

Fig. 15. Geometry leading to (11) Laser beam of intensity I_L traverses a cell of length l and cross sectional area A, and produces a single-pass Raman output I_R.

on the resonator mirrors to have optimum reflectivity for the fundamental and essentially zero reflectivity for the Raman frequencies. The difficulty in observing Raman emission under Q-switched conditions indicates, however, that no serious loss due to SRS does occur at power levels of 100 MW/cm^2.

A somewhat different picture is presented in the case of very high-peak-power picosecond pulses where SRS emission accompanies every shot and conversion efficiencies to SRS of 12 percent have been measured. Quantitative estimates of the conversion would require the use of transient gain equations [30] and a knowledge of dispersion effects. Additional data on thresholds and gains would be needed to warrant such treatment.

In conclusion, we would like to emphasize that results presented in this paper were obtained using stationary (not flowing) liquid laser media. The natural regime of operation of these devices is in the flowing mode, which greatly improves the reproducibility of results. The technology of flowing Nd liquid lasers only recently has been developed, and as their levels of performance climbs to higher values, the effects of nonlinear properties of the medium will become more clearly defined.

Acknowledgment

The authors wish to express their thanks to K. French for providing liquid laser solutions and information on their chemistry, to C. Fallier who took most data on Brillouin scattering, and to T. Illing and S. Hussain who assisted in all phases of the experimental work.

References

[1] A. Lempicki and H. Samelson, "Rare-earth liquid lasers," *Ann. N. Y. Acad. Sci.*, vol. 168, 1970, pp. 596–609.
[2] H. Samelson, R. Kocher, T. Waszak, and S. Kellner, "Oscillator and amplifier characteristics of lasers based on Nd^{+3} dissolved in aprotic solvents," *J. Appl. Phys.*, vol. 41, 1970, pp. 2459–2469.
[3] C. Brecher and K. French, "Comparison of aprotic solvents for Nd^{3+} liquid laser systems: selenium oxychloride and phosphorous oxychloride," *J. Phys. Chem.*, vol. 73, 1969, pp. 1785–1789.
[4] H. Samelson, A. Lempicki, and V. Brophy, "Self-Q-switching of the Nd^{3+} $SeOCl_2$ liquid laser," *J. Appl. Phys.*, vol. 39, 1968, pp. 4029–4030.
[5] G. Yamaguchi, F. Endo, S. Murakawa, S. Okamura, and C. Yamanaka, *Japan. J. Appl. Phys.*, vol. 7, 1968, pp. 179–180.
[6] H. Samelson and A. Lempicki, "Q-switching and mode-locking of Nd^{3+}:$SeOCl_2$ liquid laser," *J. Appl. Phys.*, vol. 38, 1968, pp. 6115–6116.
[7] R. R. Alfano and S. L. Shapiro, "Picosecond pulse emission from a mode-locked Nd^{3+} $POCl_3$ liquid laser," *Opt. Commun.*, vol. 2, 1970, pp. 90–92.
[8] G. Eckhardt, R. Hellwarth, F. J. McClung, S. E. Schwarz, D. Weiner, and E. J. Woodbury, "Stimulated Raman scattering from organic liquids," *Phys. Rev. Lett.*, vol. 9, 1962, pp. 455–457.
[9] A. J. DeMaria, D. A. Stetser, and H. Heynau, "Self-mode-locking of laser with saturable absorbers," *Appl. Phys. Lett.*, vol. 8, 1966, pp. 174–176.
[10] J. P. Laussade and A. Yariv, "Mode-locking and ultra-short laser pulses by anisotropic molecular liquids," *Appl. Phys. Lett.*, vol. 13, 1968, pp. 65–66.
[11] J. Comly, E. Garmire, J. P. Laussade, and A. Yariv, "Observation of mode-locking and ultrashort optical pulses induced by anisotropic molecular liquids," *Appl. Phys. Lett.*, vol. 13, 1968, pp. 176–178.
[12] G. Nagarajan and A. Muller, "Thermodynamische funktionen and molekulare polarisierbarkeiten von thionyl und seleninylhalogeniden," *Z. Naturforsch., A*, vol. 216, 1966, pp. 612–617.
[13] H. Gerding, E. Smit, and R. Westrik, "Die ramanspektren und die molekulstrukturen des selenoxychlorids und des thionylchlorids," *Rec. Trav. Chim.*, vol. 60, 1941, pp. 514–522.
[14] D. Kato, "Raman spectroscopy in the $SeOCl_2$–$SnCl_4$ liquid," *J. Phys. Soc. Jap.*, vol. 29, 1970, p. 1103.
[15] G. Herzberg, *Molecular Spectra and Molecular Structure II Infrared and Raman Spectra of Polyatomic Molecules*. Princeton, N. J.: Van Nostrand, 1968, p. 277.
[16] T. C. Damen, R. C. C. Leite, and S. P. S. Porto, "Angular dependence of the Raman scattering from benzene excited by the He-Ne cw laser," *Phys. Rev. Lett.*, vol. 14, 1965, pp. 9–11.
[17] L. Nafie, P. Stern, B. Fanconi, and W. L. Peticolas, "Angular dependence of Raman scattering intensity," *J. Chem. Phys.*, vol. 52, 1970, pp. 1584–1588.
[18] F. J. McClung and D. Weiner, "Measurement of Raman scattering cross-section for use in calculating stimulated Raman scattering effects," *J. Opt. Soc. Amer.*, vol. 54, 1964, pp. 641–644.
[19] W. R. L. Clements and B. P. Stoicheff, "Raman linewidth for stimulated threshold and gain calculations," *Appl. Phys. Lett.*, vol. 12, 1968, pp. 246–248.
[20] E. M. Garmire, "An investigation of stimulated Raman emission," Ph.D. dissertation, Mass. Inst. Technol., Cambridge, Mass., 1965.
[21] R. H. Pantell and H. E. Puthoff, *Fundamentals of Quantum Electronics*. New York: Wiley, 1969, p. 240.
[22] K. French, private communication.
[23] N. Bloembergen, "The stimulated Raman effect," *Amer. J. Phys.*, vol. 35, 1967, pp. 989–1023.
[24] S. L. Shapiro, J. A. Giordmaine, and K. W. Wecht, "Stimulated Raman and Brillouin scattering with picosecond light pulses," *Phys. Rev. Lett.*, vol. 19, 1967, pp. 1093–1095.
[25] R. R. Alfano and S. L. Shapiro, "Emission in the region 4000 to 7000 Å via four-photon coupling in glass," *Phys. Rev. Lett.*, vol. 24, 1970, pp. 584–585.
[26] R. G. Brewer and D. C. Shapero, "Multiple stimulated Brillouin scattering," in *1965 Proc. Phys. Quantum Electron. Conf.*, San Juan, Puerto Rico, P. L. Kelly, B. Lax, and P. E. Tannenwald, Eds. New York: McGraw-Hill, 1966, pp. 216–221.
[27] P. Y. Key, R. G. Harrison, V. I. Little, and J. Katzenstein, "Bragg reflection from a phase grating induced by nonlinear optical effects in liquids," *IEEE J. Quantum Electron.*, vol. QE-6, Oct. 1970, pp. 641–646.
[28] R. S. Lang, H. Baumbacker, and E. E. Fill, "Stimulated Raman scattering in an inorganic Nd liquid laser," *Phys. Lett.*, vol. 32A, 1970, pp. 433–434.
[29] M. Maier, W. Kaiser, and J. A. Giordmaine, "Backward stimulated Raman scattering," *Phys. Rev.*, vol. 177, 1969, pp. 580–599.
[30] R. L. Carman, M. E. Mack, F. Shimizu, and N. Bloembergen, "Forward picosecond Stokes-pulse generation in transient stimulated Raman scattering," *Phys. Rev., Lett.*, vol. 23, 1969, pp. 1327–1329.

E-10

APPENDIX F

THE KERR CONSTANT OF $SeOCl_2$

Reprinted from **APPLIED OPTICS**, Vol. 6, page 1141, June 1967

The Kerr Constant of Selenium Oxychloride

C. F. Buhrer, A. Heller, and A. Lempicki

General Telephone & Electronics Laboratories Inc., Bayside, New York 11360.
Received 15 February 1967.

Selenium oxychloride, an inorganic solvent recently employed in liquid lasers[1], has a high dielectric constant[2], a high density[3], a high index of refraction[4], and may have a high polarization anisotropy.[5] All of these properties suggest that this liquid should exhibit a large electrooptic birefringence or Kerr effect. (The experimental Kerr constant B is given by $B = n_{\parallel} - n_{\perp}/(\lambda E^2)$, where $n_{\parallel}$ and $n_{\perp}$ are the refractive indices for light polarized parallel and perpendicular to the applied electric field E and λ the wavelength of the light *in vacuo*.) Furthermore, because of the low vibrational energies of the molecule[6], it is transparent throughout the near ir as well as most of the visible spectrum. If so, it may be useful for fast Kerr shutters in the ir where other Kerr liquids such as nitrobenzene are absorbing.

For the measurement of the birefringence we used a cell with 1 cm × 10 cm tantalum electrodes spaced 0.50 cm apart. When the cell was filled with purified $SeOCl_2$, its resistance was approximately 1000 Ω. A pulsed voltage technique was therefore used to attain a high field with low average power dissipation. Microsecond-long pulses between 10 kV and 25 kV were applied to the cell between crossed polarizers such that the electric field was at a 45° angle to the light polarization. Pulse heights were adjusted to the values at which the birefringence was an integral multiple of a wavelength, as indicated by extinction during the pulse as well as when the field was off. These voltages therefore correspond to values of electric field strength E satisfying the relation $\Delta = n\lambda = BlE^2\lambda$, where Δ is the optical path difference, n is an integer, λ is the wavelength, B is the Kerr constant, and l is the optical path length within the field region. Using this technique for nitrobenzene, we obtained a Kerr constant of 345 × 10^{-7} cm statvolt^{-2} at the sodium D line. This is somewhat greater than the published value of 326 × 10^{-7} cm statvolt^{-2} [Ref. (7)].

Table I. Kerr Constants of Selenium Oxychloride

λ (Å)	Lamp	Filter	$B \times 10^7$ esu[a]
5,461	Hg	Interference	203 ± 5
5,893	Na	Corning 3-66	192 ± 4
7,800	Rb	Corning 7-69	133 ± 8
10,600	Incandescent	Interference	100 ± 2

[a] cm × statvolt^{-2}; 1 statvolt = 300 V.

The measured values for selenium oxychloride are summarized in Table I. A plot of B vs $1/\lambda$, shown in Fig. 1, gives the expected linear relation.

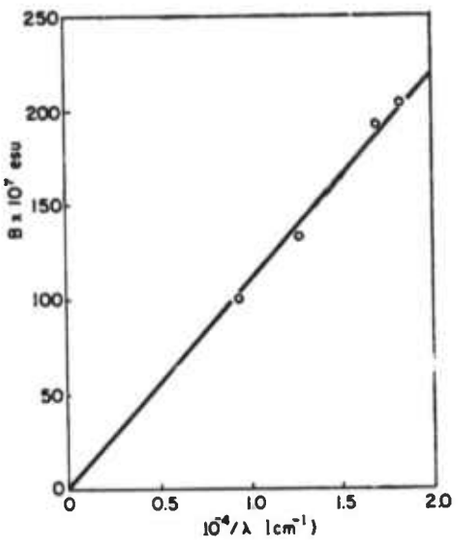

Fig. 1. Variation of the Kerr constant of $SeOCl_2$ with reciprocal wavelength.

We see that, as predicted, the Kerr constant of selenium oxychloride is among the highest known. In spite of the relatively low resistivity of this material, the high Kerr constant and its transparency in the ir should make this liquid useful for fast electrooptical shutters in this region as well as for other ir applications where a high electrooptical birefringence is desired.

References

1. A. Heller, Appl. Phys. Letters **9**, 106 (1966).
2. J. E. Wildish, J. Am. Chem. Soc. **42**, 2607 (1920).
3. T. W. Parker and P. L. Robinson, J. Chem. Soc. **1931**, 1316 (1931).
4. C. P. Smyth, G. L. Lewis, A. J. Grossman, and F. B Jennings, J. Am. Chem. Soc. **62**, 1220 (1940).
5. G. Nagarajan and A. Muller, Z. Naturforsch. **21B** 612 (1966).
6. H. Gerding, E. Smit, and R. Westrik, Rec. Trav. Chim. **60**, 515 (1941).
7. C. B. West and R. O'B. Carpenter, in *American Institute of Physics Handbook*, D. E. Gray, Ed. (McGraw-Hill Book Co. Inc., New York, 1963), 2nd ed., pp. 6–187.

F-2

APPENDIX G

TRANSMISSION LOSSES IN APROTIC LIQUID LASERS

Reprinted from JOURNAL OF APPLIED PHYSICS, Vol. 41, No. 11, 4578–4581, October 1970

Transmission Losses in Aprotic Liquid Lasers

C. BRECHER, K. FRENCH, W. WATSON, AND D. MILLER
Bayside Research Center of General Telephone and Electronics Laboratories, Incorporated, Bayside, New York 11360
(Received 27 May 1970)

Transmission losses in phosphorus oxychloride- and selenium oxychloride-based laser solutions have been measured by four different methods. These solutions have intrinsic scattering losses in the range of 0.1%–0.3% per cm. A possible explanation of this scattering loss is presented.

I. INTRODUCTION

Since their inception, Nd^{+3} aprotic liquid laser materials have been subjects of great interest.[1–6] Some of the chemical properties have been ascertained[6–10] and many of the output characteristics have been defined and described.[11–15] However, one of the most critical problems that has been limiting the application of these lasers as useful devices, particularly for cw operation, has been the optical transmission loss in the medium. It is, consequently, of considerable importance to ascertain the cause of this loss, to measure it, and to determine the lower limit below which such loss is intrinsic to the nature of the medium; this is the problem to which this paper is addressed.

II. CHEMICAL BACKGROUND

Of the many different variations of aprotic liquid media investigated in these laboratories, only three have been used to any great extent for laser systems applications. The first utilized $SeOCl_2$ acidified with $SnCl_4$ as a solvent, in which Nd_2O_3 was dissolved[1]; the second was similar, but with $POCl_3$ instead of $SeOCl_2$[4]; while the third, which also used $POCl_3$ as solvent, utilized $ZrCl_4$ instead of $SnCl_4$ as the acidifying agent and $Nd(CF_3COO)_3$ instead of the oxide as the solute.[16] Formally, the chemical equations for formation of the respective laser media are quite similar:

$$Nd_2O_3+3SnCl_4+3SeOCl_2\rightarrow Nd_2(SnCl_6)_3+3SeO_2 \quad (1)$$

$$Nd_2O_3+3SnCl_4+6POCl_3\rightarrow Nd_2(SnCl_6)_3+3P_2O_3Cl_4 \quad (2)$$

$$2Nd(CF_3COO)_3+3ZrCl_4+12POCl_3\rightarrow Nd_2(ZrCl_6)_3 + 6P_2O_3Cl_4+6CF_3COCl. \quad (3)$$

The differences on the right side of the equations arise from the different stabilities of the products. SeO_2 is a known stable compound, but PO_2Cl, its phosphorus counterpart, is not and reacts further with additional $POCl_3$ to form $P_2O_3Cl_4$ and higher polymers of the polyphosphoryl chloride type.[17] Similarly, the reaction of the CF_3COO^- group forms yet more of these polymers, while itself escaping as the gaseous acyl chloride. In all cases, the Nd^{+3} ion remains in solution solvated with an undetermined number of molecules of the reaction products and the $POCl_3$ solvent.

Historically, the stability of Nd^{+3} solutions in $POCl_3$ has always been a difficult problem. This arises from the fact that $POCl_3$ has a low dielectric constant, less than 14 as against 46 for $SeOCl_2$ and 80 for H_2O, so that the solubility of ionic salts must be inherently much lower. Indeed, it has not been possible to dissolve pure anhydrous Nd^{+3} ionic salts in *pure* $POCl_3$ with any Lewis acid tried ($SnCl_4$, $ZrCl_4$, $SbCl_5$, $TiCl_4$, among others). On the other hand, if sufficient quantities of polyphosphoryl chloride polymers are added to the solvent during the preparation of the solution, either by direct addition of the material or by reaction of $POCl_3$ with H_2O or the CF_3COO^- or other suitable anions, the solubility of the Nd^{+3} ion is greatly increased, and a stable solution is produced. Degradation of the polymer, readily accomplished by addition of PCl_5 to the liquid, invariably leads to precipitation of the Nd^{+3} out of solution.

III. OPTICAL LOSS MEASUREMENTS

In a high-gain liquid-laser material such as we are dealing with here, the most critical parameter governing its utility in a practical system is the optical transmission loss. With Nd^{+3} there is a residual transmission loss (below which we cannot go), which is determined by the absorption of the ion at the laser wavelength due to the steady-state population of the terminal state ($^4I_{11/2}$) of the transition involved. From the measured absorption cross section of the laser transition[9] and the thermal population of the state (some 2000 cm^{-1} above ground), the residual absorption at the laser wavelength is approximately 0.15% per cm. This absorption will be an effective loss only insofar as the light which is reabsorbed at this wavelength is re-emitted in the other fluorescent transitions from the $^4F_{3/2}$ state. Under lasing conditions, however, this absorption should not present an effective loss, since the light flux is then so high as to stimulate re-emission of the energy at the same wavelength (and direction) before any significant redistribution of fluorescence can occur.

Four different methods have been used for obtaining a measure of the optical loss in laser solutions. These are direct transmission, laser static loss, laser dynamic loss, and right-angle scattering. Because of their various levels of difficulty, not all these methods were used on all solutions, but enough measurements were made to enable correlation between them.

G-2

The first method, direct measurement of the transmission, is the simplest in principle, but because of the relatively low level of the losses, the least precise. This method involves the use of matched 10-cm cells with windows antireflection coated at 1.06 μ; the reference cell is filled with distilled $POCl_3$, the sample cell with laser solution. Measurements here range downward from 0.5% per cm $\pm$0.1%.

The second method, more precise but more difficult, involves the use of Nd^{+3} YAG laser in cw operation (see Fig. 1). The cell (10-cm long, antireflection coated) containing the liquid is placed within the laser cavity, and the threshold for lasing is ascertained. The cell is then removed from the cavity and replaced by a quartz plate which introduces a known reflective loss as a function of the angle the plate makes with the beam; this angle is then varied until the same threshold for laser action is obtained as before, whereupon the loss can be calculated. This method is limited to solutions with losses less than about 0.5% per cm, and thus is usable in the low-loss range where direct transmission measurement is least precise. Measurements in the two regions are quite consistent with each other.

The dynamic loss method consists of direct measurement on the solution during its actual use as a liquid laser. This is a rather involved and tedious process, requiring measurement of the energy output from the laser as a fraction of energy input, with mirror reflectivities varied over a wide range as a parameter. It can be shown[15] that the dependence of the threshold energy for laser action obeys the equation

$$E = (\alpha/c) - (1/cl)\ \ln R_1 R_2, \qquad (4)$$

where E is the threshold energy (joules); α is the dynamic loss coefficient (cm^{-1}); c is the gain per joule per cm which equals $\alpha \cdot \beta$ (where α is the absorption coefficient of laser transition and β is the total conversion efficiency of electrical energy into inversion); l is the length of the cell, and R_1, R_2 are the mirror reflectivities. Thus by plotting the threshold energy against the logarithm of the mirror reflectivities, one can get a direct measure of the effective loss per centimeter in an actual operating laser. This was done for a number of different solutions, as shown in Table I, producing loss values only slightly higher than those from other methods. This method is the only one which measured the loss of the medium itself during the lasing process; however, the length of time required for measurement precluded its extensive use.

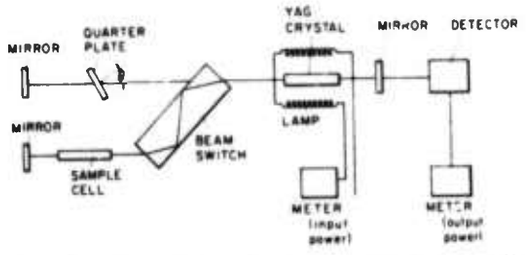

FIG. 1. Simplified schematic of transmission loss measurement. The beam switch directs light through either of the two legs (adjusted for optical equivalence). The threshold is determined (plot of output power vs input power) alternately in the two legs, and the quartz plate (which introduces known reflective loss as fraction of angle) is rotated to obtain same threshold. Measurement is repeated with cell in, and loss introduced by cell can be calculated.

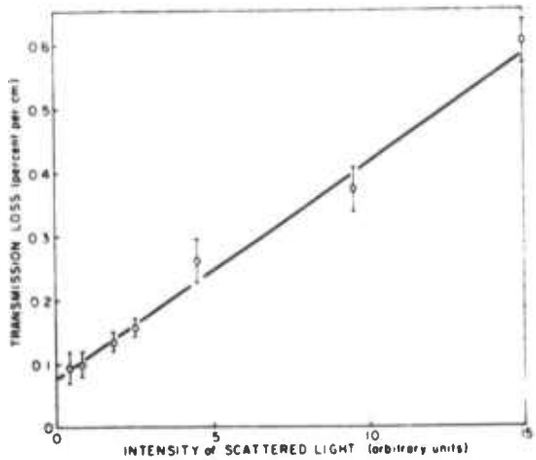

FIG. 2. Correlation between transmission loss (at 1.06 μ) and intensity of scattered light (at 6328 Å). Scattered light was measured perpendicular to the beam, transmission loss was measured as in Fig. 1.

The right-angle scattering method is the simplest and most widely used, but the most indirect. This involves simply the placing of a cell containing the liquid into the beam from a He–Ne laser (such that the beam passes through the center of the cell) and detecting with a photomultiplier the light scattered at right angles to the beam. This provides a measure of the concentration of scattering centers within the solution, which must be minimized. It does not, of course, measure any losses due to absorption. However, as shown by Table I and Fig. 2, there was a reasonably good linear correlation between the transmission and static loss values on one hand, and the scattering on the other, so that the latter method could be used to give a measure of the former.

IV. RESULTS

A number of significant points were revealed by the measurements. The laser solutions must be filtered to prevent a high scattering loss. Hence, all solutions studied in detail were filtered through an ultrafine sintered glass frit having a nominal pore size of 1 μ. Measurements were made on many different solutions, although not all methods were used on all samples. The solutions studied include

pure liquids: water, alcohol, benzene, CCl_4, $SeOCl_2$, $POCl_3$;

mixtures of various components: $SeOCl_2+SnCl_4$, $POCl_3+SnCl_4$, $POCl_3+ZrCl_4$, $Nd(CH_3COO)_3+H_2O$;

TABLE I. Light scattering and transmission loss in various liquids.

Material	Light scatter (Arbitrary units)	Transmission loss at 1.06 μ (% per cm)	Method
Water	0.15	>1	Transmission[b]
Ethanol	0.25	>1	Transmission[b]
Benzene	1.0	>1	Transmission[b]
CCl_4	0.4	0.10	Static loss
$POCl_3$	0.4	0.10	Static loss
$POCl_3+ZrCl_4$	0.6		
$H_2O+ZrCl_4$	0.5	>1	Transmission[b]
$H_2O+Nd(TFA)_3$	0.4	>1	Transmission[b]
0.3-*M* Nd^{+3} in $SeOCl_2$–$SnCl_4$	2.2		
(Contaminated with H_2O)		0.6	Dynamic loss[a]
0.3-*M* Nd^{+3} in $POCl_3$–$SnCl_4$			
(Contaminated with H_2O)		2.0	Dynamic loss[a]
0.3-*M* Nd^{+3} in $POCl_3$–$ZrCl_4$	2.5	0.16	Static loss
		0.2–0.3	Transmission
(Contaminated with H_2O)	4.5	0.26	Static loss
(Contaminated with H_2O)	15.0	0.60	Static loss
(Contaminated with H_2O)		1.0	Dynamic loss[a]
0.9-*M* $P_2O_3Cl_4$ in $POCl_3$	0.8		Static loss

[a] Dynamic loss values from Ref. 15.
[b] Loss values greater than 1% per cm by direct transmission measurement indicate that absorption band in the medium, rather than scattering, is a major loss.

various standard laser solutions: 0.3-*M* Nd^{+3} in $SeOCl_2+SnCl_4$, in $POCl_3+SnCl_4$, in $POCl_3+ZrCl_4$, with and without H_2O contamination;

dilutions of standard laser solutions with pure solvent: 0.1-*M* and 0.03-*M* Nd^{+3};

solutions prepared by reaction of sodium trifluoroacetate with $POCl_3$ to produce various concentrations of $P_2O_3Cl_4$.

The results of the measurements are listed in Table I. To summarize the more important points: All the pure components of the laser solutions ($POCl_3$, $POCl_3+ZrCl_4$, $SeOCl_2$, Nd^{+3} in H_2O) as well as some other pure liquids (alcohol, water) give scattering measures of 0.2–0.5; however, when Nd^{+3} is present in the $POCl_3$ or $SeOCl_2$ mixture, the scattering measure is 2.5–3.0, a factor of 6–8 higher. It is also noteworthy that the ratio of the scattering values for the two pure solvents CCl_4 and benzene (0.4) is in good agreement with that found by others (0.37).[18]

A linear correlation was found between the scattering values and the transmission losses. These losses range between 0.1% and 0.3% per cm, sufficiently below the effective 0.5% upper bound[19] for the attainment of cw lasing action. The scattering loss for the pure $POCl_3$ liquid comes out as about 0.015% per cm at 1.06 μ, and the absorption loss as about 0.06% per cm. The latter value is higher than expected, probably due to trace amounts of contamination by H_2O which has a significantly intense absorption of 1.06 μ. The scattering loss for the complex itself is 0.1% per cm at 0.3-*M* concentration.

$POCl_3$ solutions that have been contaminated with H_2O (even if subsequently dehydrated by distillation) invariably have high scattering (of the order of 10 or higher) and high loss (greater than 0.5% per cm) and are also quite viscous. This is attributed to an excessively high concentration of polyphosphoryl chloride polymer. Reduction of the viscosity can be accomplished by addition of PCl_5 (which selectively degrades this polymer), but the scattering does not go below the "base level" of 2.5, and further addition of PCl_5 causes the Nd^{+3} to precipitate. Since solutions containing only the polyphosphoryl chloride polymer gave scattering values considerably less than laser solutions of equal polymer concentration, it would appear that the scattering entity is a complex containing both Nd^{+3} and the polymer.

V. CONCLUSION

The results of this investigation have led to the following conclusions:

(1) A distinct scattering loss is characteristic of those aprotic liquid laser solutions, even after all particulate matter is removed.

(2) This scattering loss can be reduced to a minimum value intrinsic to the medium, below which we cannot go without deleterious chemical effect. This value is, however, less than originally thought and below the approximately 0.5% per cm effective upper bound for the attainment of cw operation.

(3) The scattering appears to be caused by a highly

G-4

polarizable complex of Nd^{+3} and $P_2O_3Cl_4$ (and also longer polymeric phosphoryl chlorides). The latter compounds are components of the $POCl_3$-based laser solution and are essential to the solubility of the active ion.

ACKNOWLEDGMENTS

The authors are grateful to H. Samelson for helpful discussions and to J. Lech and G. Alexander for their technical assistance.

[1] A. Heller, Appl. Phys. Lett. **9**, 106 (1966); A. Lempicki and A. Heller, *ibid*. **9**, 108 (1966).
[2] T. M. Shepherd, Nature **216**, 1200 (1967).
[3] D. Kato and K. Shimoda, Jap. J. Appl. Phys. **7**, 548 (1968).
[4] N. Blumenthal, C. B. Ellis, and D. Grafstein, J. Chem. Phys. **48**, 5726 (1968).
[5] E. J. Schimitschek, J. Appl. Phys. **39**, 6120 (1968).
[6] P. M. Buzhinski, M. E. Zhabotinski, N. M. Zhevoronkov, V. G. Lebedev, B. I. Malyshev, Yu. P. Rudnitski, V. V. Tsopkin, and G. V. Ellert, Dnkl. Akad. Nauk SSSR **185**, 1306 (1969).
[7] A. Heller, J. Amer. Chem. Soc. **50**, 3711 (1968).
[8] A. Heller, J. Mol. Spectry. **28**, 101 (1968); A. Heller, *ibid*. **28**, 208 (1968).
[9] H. Samelsnn, A. Heller, and C. Brecher, J. Opt. Soc. Amer. **58**, 1054 (1968).
[10] C. Brecher and K. W. French, J. Phys. Chem. **73**, 1785 (1969).
[11] H. Samelson, A. Lempicki, and V. A. Brophy, IEEE J. Quantum Electron. **4**, 849 (1968).
[12] H. Samelson, A. Lempicki, and V. A. Brophy, J. Appl. Phys. **39**, 4029 (1968).
[13] H. Samelson and A. Lempicki, J. Appl. Phys. **39**, 6115 (1968).
[14] C. LeSergent, M. Michon, S. Rousseau, F. Collier, H. Dubost, and G. Ranult, Compt. Rend. **B268**, 1501 (1969).
[15] H. Samelson, R. Kocher, T. Waszak, and S. Kellner, J. Appl. Phys. **41**, 2459 (1970).
[16] E. J. Schimitschek (private communication).
[17] J. R. VanWazer, *Phosphorus and its Compounds* (Interscience, New York, 1961).
[18] R. C. C. Leite, R. S. Moore, S. P. S. Porto, and J. E. Ripper, Phys. Rev. Lett. **14**, 7 (1965).
[19] J. Foster (private communication).

G-5